A geochemical study of the Middle Group chromitites, Helena mine, Bushveld complex, South Africa

by

Janine Kottke-Levin

Submitted in accordance with the requirements for the degree of

Doctor of Philosophy

Faculty of Natural and Agricultural Sciences,
Department of Geology
University of the Free State, Bloemfontein
Republic of South Africa

November 2011

Promoter:
Prof. Dr. Marian Tredoux
Co-Promoter:
Prof. Dr. Christoph Gauert

Statutory declaration

I hereby confirm, that the Ph.D. thesis in hand with the title “A geochemical study of the Middle Group chromitites, farm Helena, eastern Bushveld complex, South Africa” has been written by myself and only the reported assistive equipment was used.
Citations or similar, which derive word for word or analogously from other sources are declared. To date, the thesis hasn’t been submitted to another university, whether in the same nor in a similar form. It also hasn’t been published elsewhere.

I am aware of legal consequences in case of false witness.

Place, date Signature

Acknowledgement

I would like to thank the Department of Geology of the University of the Free State (UFS) in Bloemfontein, South Africa, and the Martin-Luther University Halle-Wittenberg (MLU), Germany, for providing the resources for research throughout this Ph.D. project.

The author is grateful to the UFS as well as the Hans-und Eugenia-Jütting Foundation in Stendal, Germany, for providing financial support by scholarships. Furthermore, I want to thank the Society of Economic Geologists for a student research grant to accomplish the investigations with the MLA after my return to Germany.

The first person I would like to thank is my supervisor Prof. Dr. Marian Tredoux. Her long-termed interest in the platinum-group elements let me feel to be in good hands all the time throughout the Ph.D. project. Her many good advice and fair comments have always been a valuable help in finishing this project. The typical South African hospitality she overwhelmed me with made it easier for me to stand the time without my husband in Bloemfontein. Lots of thanks!

Xstrata Alloys, in particular Pieter-Jan Gräbe, I thank for uncomplicated provision of sample material as well as for financial aid for analytical investigations.

Scientific discussion with Prof. Dr. Christoph Gauert (University of the Free State, South Africa) and Dr. Iain McDonald (University of Cardiff) has widened my understanding for liquid-magmatic processes and the behaviour of the PGE. In addition I would like to thank Dr. McDonald for instructing and supervising me during realization of the NiS fire assay and the ICP-MS as well as LA-ICP-MS analyses I worked on during my stay in Cardiff. It was an excellently organized week I learned much about analytical procedures.

Prof. Dr. Gregor Borg (MLU) I thank for providing support and infrastructure at the MLU.

I would like to thank Dr. Robert Schouwstra and Corne Schalkwyk, and the staff of the Anglo Research Lab in Johannesburg for the well-organized week I worked on the MLA.

The study has profited from logistical support provided by Prof. Willem van der Westhuizen, Jonas Choane, Andries Felix as well as Piet Roodt (all UFS). My special thanks go to Rina Immelman (UFS), who handled all the necessary bureaucracy with surprising facility and always put a smile onto my face.

Thanks to Dirk Sandmann from the Technical University Bergakademie Freiberg (TU Freiberg), Germany, for realizing the time-consuming analyses with the MLA on an additional sample set.

Dr. Jörg Reichert (Deutsche Rohstoff AG) and Sabine Walther (MLU) I would like to thank for proof-reading of part of the thesis and the suggestions for improvements in expression and layout.

My special thanks also go to family Gauert, who took me in with great hospitality and introduced me to the South African culture.

My deepest gratitude belongs to my husband Mario and my parents. They not only supported me financially, but also encouraged me many times during the time of the Ph.D. Their patience and love were essential for the work at this project. Thanks to God that I have people like you by my side!

Abstract

The study in hand reports on compositional variations in mineral and whole-rock geochemistry of the chromitite and silicate layers occurring in the Middle Group of the eastern Bushveld Complex. Special attention is paid to the platinum-group element (PGE) content and mineralization as well as the nature of platinum-group minerals (PGM) within the MG sequence.

A general progressive evolution of the MG chromitite layers can be deduced from chromite composition showing decreasing Mg# and enrichment of Fe and Al relative to Cr as well as from the decreasing whole-rock Mg#. At the LCZ/UCZ transition no marked change in mineral and whole-rock geochemistry can be observed, indicating that the MG sequence derives from a continuously progressive evolving melt. The presence of one parental magma for the formation of the MG is further substantiated by the chondrite-normalized PGE patterns of the MG chromitite layers, which resemble each other. They further resemble that of the UG2, which suggests that they derive from the same magma and a similar style of mineralisation applied. One marked reset to compositions even more primitive than the MG1 chromitite layer is present at the level of the MG4A chromitite layer, which is illustrated by a low $Mg\#_{chr}$, low whole-rock Mg#, low mineral and whole-rock $Cr^{3+}/(Cr^{3+}+Fe^{3+})$ ratios and increasing mineral and whole-rock $Cr^{3+}/(Cr^{3+}+Al^{3+})$ ratios and TiO_2 contents. It strongly suggests the addition of hot and primitive magma at this level of the MG stratigraphy.

Whole-rock geochemistry of the silicate layers is strongly governed by mutual influence of co-precipitating minerals competing for major elements like Mg, Fe, Al or Cr, and hence a statement to general trend with respect to evolution from bottom to top of the stratigraphic column of the MG sequence can't be made. Nevertheless, a strong decrease in whole-rock Mg# and low whole-rock Al_2O_3 concentrations at the level of the MG4A pyroxenite is illustrated, which can be ascribed to the same event of addition of primitive magma concluded for the MG4A chromitite layer.

The existence of Na-rich silicate inclusions occurring in chromite of all the MG chromitite layers most likely proves chromitite formation by mixing of primitive melt with a siliceous melt. Hence, the general process for the formation of the chromitite layers and their corresponding silicate layers in the MG seems to be mixing of a primitive (mafic-ultramafic) parental melt with siliceous roof-rock melt deriving from the granophyric Rooiberg felsites.

Although Cu deriving from the base metal sulphides (BMS) seems to migrate away from the chromitite layers, local Cu enrichment in the chromitite layers to concentrations

up to >6000 ppm can be observed. This excess Cu most likely derives from an external source e.g. country rocks, which could have ‘generated’ metal-loaded hydrothermal fluids. Excess S occurring in the silicate layers may result from limited, probably hydrothermal, dissolution of BMS from the respective chromitite layer below.

Chromitite samples have been investigated with the mineral liberation analyzer (MLA) for their PGM. The study focused on the mineral association of the PGM, i.e. whether they occur liberated, locked or attached to gangue or the BMS, since the mineral association is important to conclude on PGE mineralization and PGM formation. The majority of the PGM occurring in the chromitite layers of the MG sequence are Pt-Rh -sulfides (26.2%), followed by laurite (25%), Pt-Pd -sulfides (24.3%) and Pt -sulfides (13.8%). The remaining 10.7% comprise PGE –sulphoarsenides and PGE- arsenides, Pt - and Pd –alloys and Pt - and Pd –tellurides.

Except laurite, which is commonly locked in chromite (66%), the PGM are dominantly associated with silicate minerals, and to a lesser extend with the BMS only. According to this discrepancy in the PGM association, PGE mineralization of the MG chromitite layers most likely can’t be modelled in terms of the *R*-factor and therefore PGE concentration by the cluster model is favoured by the author.

Alteration of the primary silicate minerals in the MG chromitite layers to amphibole, chlorite, talc, mica and quartz can be observed locally. Since the primary BMS assemblage (chalcopyrite, pyrite and pentlandite) shows losses of Fe, Cu and S, and millerite, a Ni-rich sulphide of secondary origin, occurs, the influence of hydrothermal fluids on the chromitite layers was concluded. Besides affecting the BMS, the fluid most likely also redistributed the PGE occurring in solid solution in the BMS, i.e. Pt and Pd, as especially the negative slope from Pt to Pd in the chondrite normalized PGE patterns of the MG chromitite layers suggests.

Enrichment of the high-temperature PGE (HT-PGE) over the low-temperature PGE (LT-PGE) is depicted in the chondrite normalized PGE patterns of the MG chromitite and silicate layers. The fact that the HT-PGE are enriched relative to the LT-PGE in the lowermost MG chromitite layers as well as in the MG4A suggests that temperature could play a role in PGE fractionation. Temperature control on PGE fractionation has also been concluded from changing Pt/Ir ratio in dependence of the whole-rock Al_2O_3 content from bottom to top of the MG sequence, with increasing Al_2O_3 concentrations considered to point to decreasing temperature. Hence, Al-depletion, i.e. decreasing Al_2O_3 content, of chromite relative to Cr may result in enrichment of the HT-PGE relative to the LT-PGE. The LT-PGE are preferentially concentrated by increasing amounts of plagioclase within the chromitite layers.

Abbreviations

%An	anorthite content
BC	Bushveld Complex
BMS	base metals sulphide
CFB	continental flood basalt
CZ	Critical Zone
D	partition coefficient
ECD	equivalent circle diameter
EDX	energy dispersive X-rays
EMP	electron microprobe
En	enstatite content
fO_2	oxygen fugacity
HT	high-temperature
IAB	island arc basalt
ICP-MS	inductive coupled plasma mass spectrometry
ISL	immiscible sulphide liquid
Iss	intermediate solid solution
LA-ICP-MS	laser ablation inductive coupled plasma mass spectrometry
LCC	lower continental crust
LCZ	Lower Critical Zone
LG	Lower Group
LT	low-temperature
LZ	Lower Zone
MaZ	Marginal Zone
MG	Middle Group
Mg#	Magnesium number
MLA	Mineral liberation analyzer
MORB	mid-ocean ridge basalt
Mss	monosulphide solid solution
MZ	Main Zone
OIB	ocean island basalt
PGE	platinum-group elements
PGM	platinum-group minerals
Ppb	parts per billion
Ppm	parts per million
Ppt	parts per trillion
REE	rare earth elements
RLS	Rustenburg Layered Suite
R_S	Spearman rank correlation coefficient
RSD	relative standard deviation
SEM	scanning electron microscope
Sr_i	initial Sr ratio
Sss	solid solution series
TML	Thabazimbi-Murchison-Lineament
UCC	upper continental crust
UCZ	Upper Critical Zone
UG	Upper Group
UZ	Upper Zone
XRD	X-ray diffractometry
XRF	X-ray fluorescence

Table of content

List of tables

List of figures

1. Introduction

The Bushveld Complex in South Africa is the largest preserved intrusion on Earth and extends over an area of ca. 65 000 km^2: 350 km from Villa Nora in the north to Bethal in the south, and 450 km from Zeerust in the west to Burgersfort in the east (Fig. 1.1). It comprises a great variety of lithologies ranging from dunite, pyroxenite, anorthosite and oxide layers in the ultramafic to mafic suite (i.e. Rustenburg Layered Suite, RLS) to the granophyres and granites of the felsic suites (Eales and Cawthorn, 1996; Cawthorn *et al.*, 2006). Both rock series are host to a number of important ore deposits. Chromium, the platinum-group elements (PGE), vanadium, iron and titanium are mined from the RLS, whereas in the felsic rocks deposits of tin, fluorspar and andalusite can be found (Cawthorn *et al.*, 2006). The location of some platinum, chromite, vanadium, tin and flourite mining sites in the Bushveld Complex are presented in figure 1.1.

This study focuses on chromium and the PGE. For a reason not yet completely understood, PGE mineralization is linked to the occurrence of chromitite layers in stratiform deposits, e.g. the Bushveld Complex in South Africa or the Great Dyke in Zimbabwe, or to chromitites occurring in podiform deposits in several ophiolite complexes. Many researchers have been dealing with the formation of monomineralic chromitite layers coupled with elevated PGE concentrations, which led to the evolution of very different models (e.g. Irvine *et al.*, 1983; Irvine and Sharpe, 1986; Scoon and Teigler, 1994; Rice and von Gruenewaldt, 1995; Tredoux *et al.*, 1995; Kinnaird *et al.*, 2002).

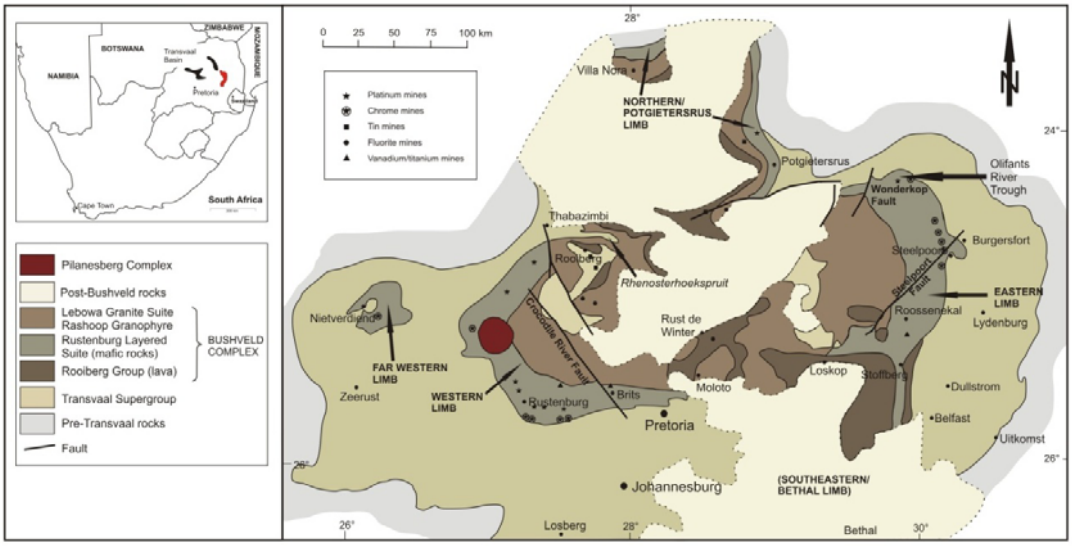

Figure 1.1 Mining sites for chrome, platinum, vanadium, tin and fluorspar in the Bushveld Complex (modified after Viljoen and Schürmann, 1998 and Cawthorn *et al.*, 2006; used with the permission of the authors).

The study in hand came into being by the wish of Xstrata Alloys to extract platinum-group minerals (PGM) as a by-product to their production of ferrochrome[1] from the Middle Group chromitite layer 1 (MG1) of the eastern Bushveld Complex. In the western Bushveld Complex, Xstrata is already mining one of the most prominent chromitite layers for its PGM: the Upper Group chromitite layer 2 (UG2). So far, the PGE contents of the MG1 and the other chromitite layers of the MG have been sub-economic. But from a strong increase in the demand for the PGE coupled with rising prices at the stock markets (Fig. 1.2), the PGE-producing industry is looking for new deposits. Exemplarily, the MG chromitite layers and its silicate interlayers have been chosen to be investigated for its PGE content and its mineability for PGM. The outcome of this study is presented in the work in hand.

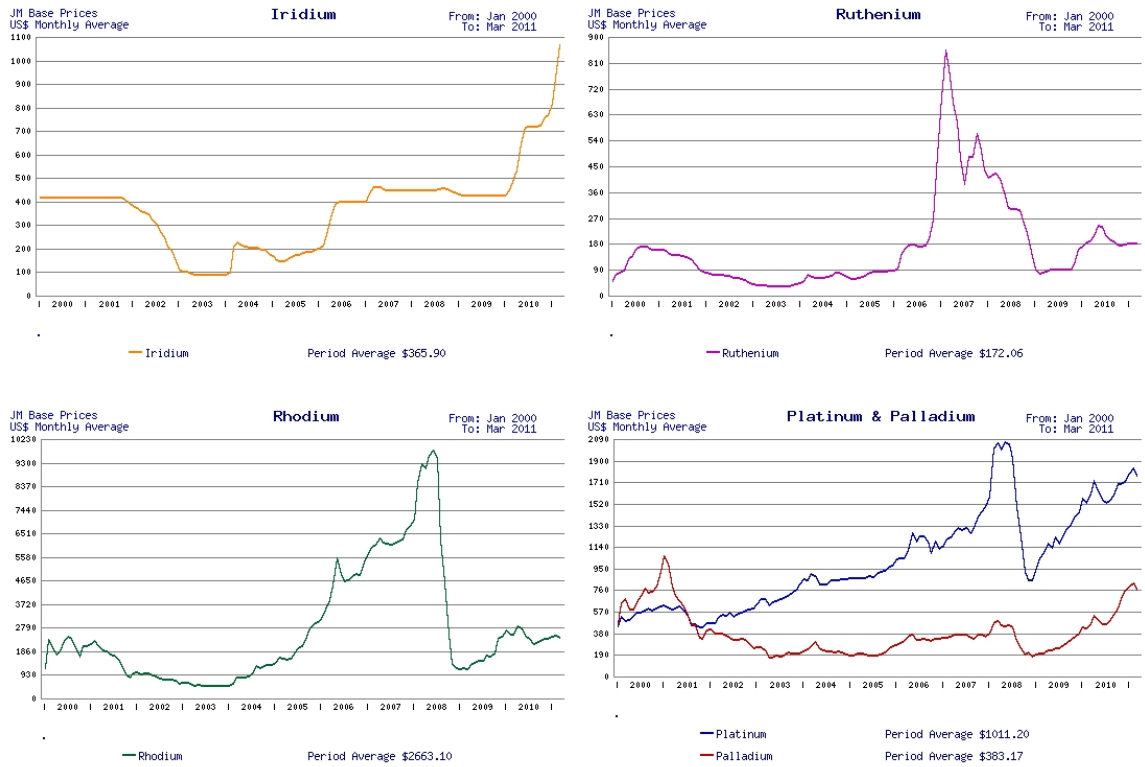

Figure 1.2 Development of PGE prices from January 2000 until March 2011 (Matthey, 2011).

[1] Ferrochrome is a silver grey alloy of mainly chromium (48-52%) and iron (35-37%), 7-8% carbon and 3-5% silicon.

1.1 Bushveld exploration history and applications of the PGE and chrome

In 1865, the German geologist Karl Mauch first discovered the presence of chromite in the Bushveld Complex, but it took nearly 100 years before South Africa became a major force in the chromium industry. Earnest chromite production already started in the eastern Bushveld Complex in 1924 near Steelpoort and Burgersfort, 16 years after detailed reports published by Hall and Humphrey (Schürmann *et al.*, 1998). Today, chrome has become a strategic mineral commodity that is mainly used by the technologically high developed industrial nations. Approximately 50% of the world's chromium (Cr) production comes from chrome mined in the Bushveld Complex (Cawthorn *et al.,* 2006).

The mineral chromite is the only ore-source of chromium. Its ideal composition is $FeO{\cdot}Cr_2O_3$, but variations in composition occur due to partial replacement of iron by magnesium and of chromium by aluminium and ferric iron (Schürmann *et al.*, 1998).

Figure 1.3 illustrates the world's largest producer of chrome in 2010 with South Africa being by far the most important one. Additionally, approximately 95% of the world's chromium resources are geographically concentrated in South Africa and Kazakhstan (Tab. 1.1).

Table 1.1 Chromium - world production and reserves in 2010. Mine production units are thousand metric tons, gross weight, of marketable chromite ore. *NA* = data not available; USGS (2011a).

Country	*Mine Production 2010*	*Reserves (shipping grade)*
India	3,800	44,000
Kazakhstan	3,400	180,000
South Africa	8,500	130,000
Other countries	6,300	NA
World total (rounded)	22,000	> 350,000

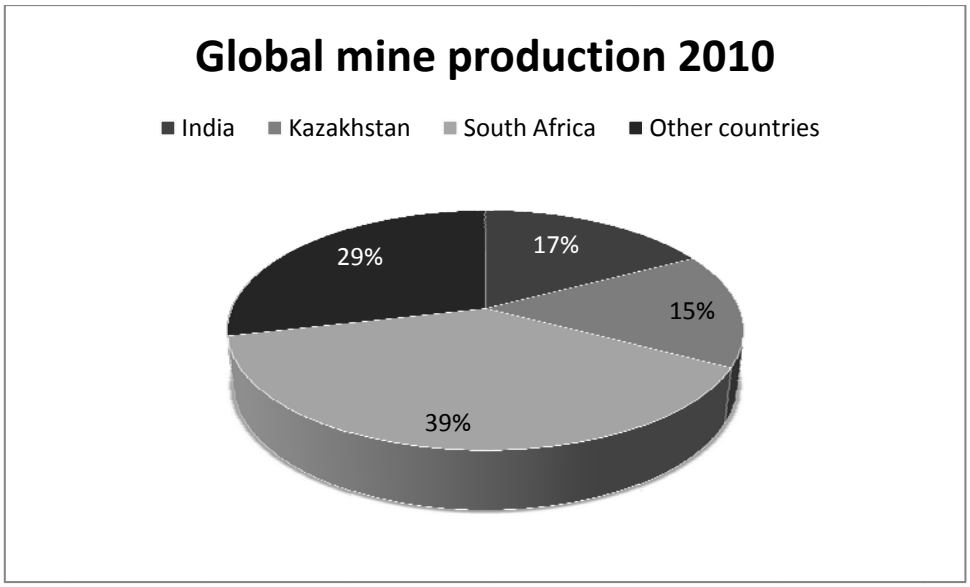

Figure 1.3 World production of chrome 2010. Data are according to the 2011 USGS Minerals Commodity Summaries/Chromium (USGS, 2011a). Data are given in table 1.1.

The chromite consumption is divided into several categories based on compositional grades (Tab. 1.2). The Bushveld chromite ores can be classified as metallurgical or ferrochrome. Due to its grade, ferrochrome can be further subdivided into six categories, which brings along different applications as well. The *stainless-steel grade* is used in cutlery, oil refining, chemical plant and building construction. The *briquetting grade* is used as feed to ferroalloy furnaces; to enhance properties like corrosion and oxidation resistance, and hardening ability of various alloys the *low-carbon ferrochromium grade* is applied. Another grade is used to produce corrosion- and abrasive-resistant equipment, heat-resistant steels for furnace components, turbine parts and nuclear reactors. In addition to it, a high-carbon grade and a ferrochromium-silicon grade exist (Schürmann *et al.*, 1998).

Table 1.2 Different chromite grades and their chemical classification (from Schürmann *et al.*, 1998). It must be noted that chrome ore from the Bushveld Complex doesn't comply with the grades presented in this table.

Grade	*Chemical classification*
Metallurgical/Ferrochrome	$Cr_2O_3 \geq 46\%$, Cr/Fe ratio > 2
Chemical	$Cr_2O_3 \geq 40 \leq 46\%$, Cr/Fe ratio 1.5 ≤2
Refractory	$Al_2O_3 + Cr_2O_3 > 60\%$, $Al_2O_3 > 20\%$

Besides being one of the world's major producers of chrome, South Africa is also the world's largest producer of PGE. The largest reserves that can be mined economically are in the Bushveld Complex, South Africa (Fig. 1.4). Since Hans Merensky in 1924 identified economic deposits of platinum in the Bushveld Complex, it has become the world's biggest resource that hosts 75 to 80% of the reserves of PGE (Jones, 1999). Dunite pipes, which discordantly cut through the layered ultramafic to mafic sequence of the Bushveld Complex, were the first to be mined for PGE from 1924 to 1930, but aren't economically significant today (Viljoen & Schürmann, 1998). Three PGE mineralized horizons within the RLS of the Bushveld Complex are currently mined for their PGE content: the Merensky Reef (which is named after its discoverer Hans Merensky), the UG2 reef and the Platreef (Merkle and McKenzie, 2002). In addition to that, all chromitite layers in the Critical Zone (CZ) of the RLS contain elevated but sub-economic concentrations of PGE (Viljoen and Schürmann, 1998).

Table 1.3 PGE - world production and reserves in 2010. Data in kg. *NA* = data not available; USGS (2011b).

Country	*Mine Production 2010*		*Reserves*
	Platinum	**Palladium**	**PGMs**
United States	3,500	11,600	900,000
Canada	5,500	9,400	310,000
Columbia	1,000	NA	NA
Russia	24,000	87,000	1,100,000
South Africa	138,000	73,000	63,000,000
Zimbabwe	8,800	6,600	NA
Other countries	2,400	9,800	800,000
World total (rounded)	183,000	197,000	66,000,000

The platinum-group elements consist of six elements: osmium (Os), iridium (Ir), ruthenium (Ru), rhodium (Rh), platinum (Pt) and palladium (Pd). They all belong to the Group VIII transition metals in the periodic system of the elements and thus having similar chemical and physical properties (Tab. 1.4). Consequently, they tend to concentrate together during geological processes.

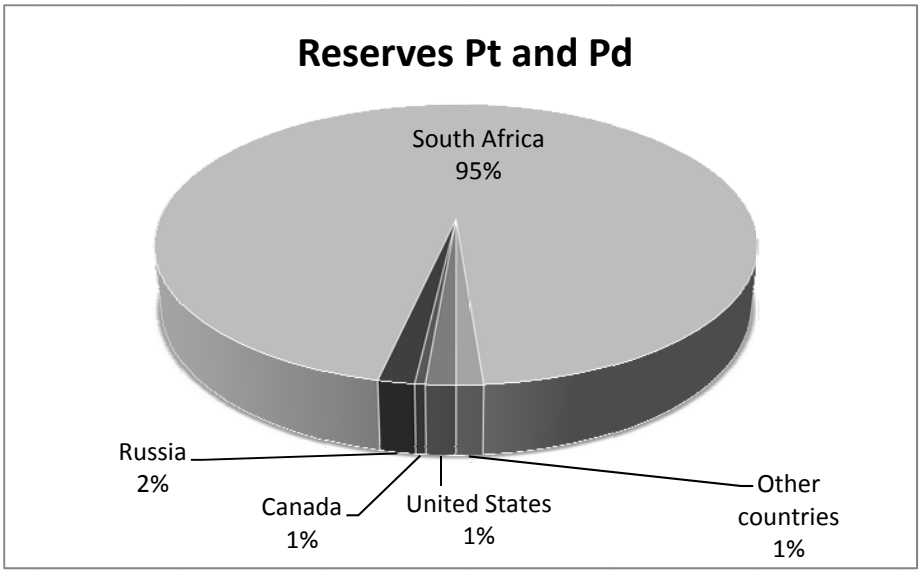

Figure 1.4 World reserves of PGM ore deposits. Data are according to the 2011 USGS Minerals Commodity Summaries/Platinum (USGS, 2011b) (cf. Table 1.3).

Table 1.4 Chemical and physical properties of the platinum-group elements (from Viljoen and Schürmann, 1998).

	Osmium	*Iridium*	*Ruthenium*	*Rhodium*	*Platinum*	*Palladium*
Atomic weight (g)	190.2	192.22	101.07	102.9	195.09	106.14
Relative density	22.61	22.65	21.41	12.41	21.45	12.02
Melting point (˚C)	3050	2443	2310	1960	1768	1552
Boiling point (˚C)	5027	4130	3900	3727	3827	3040
Crystal system	hexagonal	isometric	hexagonal	isometric	isometric	isometric
Atomic radius	1.34	1.38	1.32	1.34	1.38	1.37
Hardness (Mohs scale)	7	6.5	6.5	6	3.5	4.75
Colour	bluish	white-grey	grey-white	blue-white	grey-white	silver

The PGE have a wide range of applications. Until the early 1900s, ***platinum*** was used only for laboratory ware, as catalysts in the manufacturing process of sulphuric and nitric acids and in jewelry (Cole and Ferron, 2002). Today it is very important in the chemical, electrical and electronic industries, in the manufacture of glass and glass fibre and in the jewellery as well. The automobile industry uses a mixture of platinum, palladium and rhodium to build autocatalysts to decontaminate automobile exhaust.

The importance of ***palladium*** has increased, as it is lower in price than Pt and more widespread in its distribution. In jewellery, it is used as a substitution for Pt. Its most common application lies in the production of electronic components (Fig. 1.5).

For the recording of fingerprints as well as for staining and preserving fluids in microscopy, ***osmium*** finds its application (Viljoen and Schürmann, 1998). It can be find in the tips of ball point pens, in alloys and electronics.

Iridium often is a constituent of alloys to increase the hardness of metals. Thus, it is used in the mechanical and medical engineering.

Ruthenium is put to a number of uses as catalyst. As an alloy with Pt and Pd it increases the resistance to abrasion of electrical switch contacts. Ruthenium is also used in some advanced high-temperature single-crystal superalloys, with applications including the turbine blades in jet engines.

Rhodium is used for the production of catalytic converters. Due to its low electrical resistance and high corrosion resistance it is also used as an electric contact material.

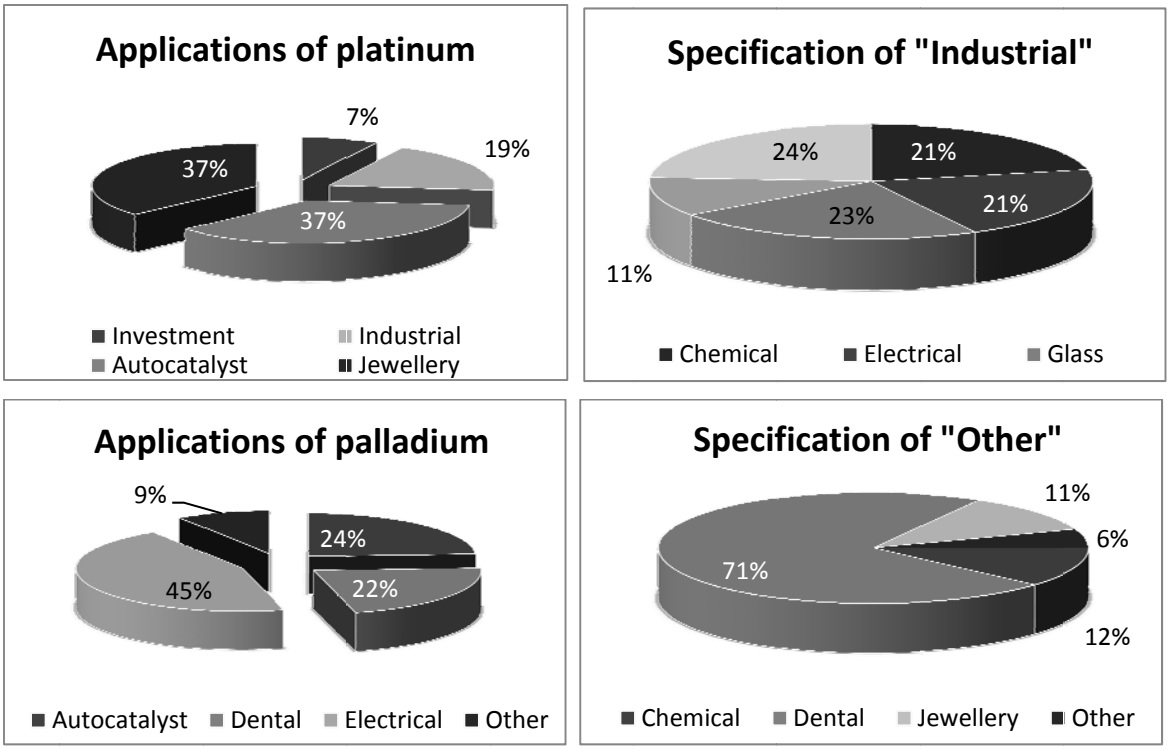

Figure 1.5 Applications of platinum and palladium (after Viljoen and Schürmann, 1998).

With a premium price of 10,100 USD/oz at the stock markets on 19th June 2008 and further continuously high prices (Matthey, 2011), Rh is even much more valuable than Pt and Pd, but unfortunately any data for presentation (as has been done for Pt and Pd) have been found.

1.2 Aims and objective of this study

The chief aim of this study is an improved understanding on the formation of the PGE mineralization in chromitite layers. The thesis focuses on the MG chromitite layers and their silicate host rocks from drill core extracted in the eastern Bushveld south of the Steelpoort fault, some 40 km northwest of Lydenburg, Mpumalanga Province. The MG has been chosen since it hosts the transition of the Lower Critical Zone (LCZ) to the Upper Critical Zone (UCZ) that is marked by a change in lithology from ultramafic to mafic rocks. Despite the lithological change of the host rocks of the chromitite layers no significant changes in mineral and whole-rock geochemistry (Cameron, 1977; Scoon and Teigler, 1994) or Sr-isotope data (Hamilton, 1977; Kinnaird *et al.*, 2002) in connection with this transition have been observed. In fact, the initial $^{87}Sr/^{86}Sr$ ratio (Sr_i) steadily increases from bottom to top of the CZ and the chromite content of the chromitite layers decreases, both indicating fractional crystallization resulting in progressive evolution of the melt in the Bushveld magma chamber. Hence it is surprising that the chromitite layers in the vicinity of the transition LCZ/UCZ, namely the MG2 and MG3 layers, show the highest PGE concentrations (e.g. Lee and Parry, 1988; Scoon and Teigler, 1994; Naldrett *et al.*, 2009; this study).

High PGE contents in chromitite layers have been linked to elevated amounts of sulphur and base metal sulphides (BMS) (Naldrett and von Gruenewaldt, 1989; von Gruenewaldt and Merkle, 1995), but low S contents of the chromitite layers of the MG cast doubt on that (e.g. von Gruenewaldt *et al.*, 1986; Scoon and Teigler, 1994; Kinnaird *et al.*, 2002). This study will investigate in detail the chromite as well as chromitite geochemistry to specify possible reasons for a chromite-linked PGE mineralization.

Furthermore, the presence of platinum-group minerals within the chromitite layers of the MG is investigated. Since the occurrence of different PGM species influences the PGE patterns of the chromitite layers, their formation (primary igneous or secondary by hydrothermal fluid) is important for PGE fractionation. In connection with information about minerals associated with the PGM an estimation about the recovery of PGE from the chromitite layers of the MG is proposed.

The application of different models for PGE mineralization and fractionation is discussed and the data are compared to data from the same stratigraphic unit deriving from different localities in the Bushveld Complex.

1.3 Outline of this document

The thesis has been subdivided into six chapters. The first two chapters deal with general information about the Bushveld Complex, i.e. the general stratigraphy as well as PGE and chromite mineralization models. The relationship between chromite and the PGE that have been observed in mafic intrusions and ophiolites worldwide is described.

The techniques used to analyze the sample material are given in chapter three. In chapter four the results of mineral, whole-rock and PGE data deriving from the analyses are presented. In addition to that, the data produced during this study are compared to literature data from the MG layers of other areas of the Bushveld Complex.

The interpretation of the results in connection with chromite and PGE mineralization models is given in chapter five. The final chapter six summarizes the outcome of this study.

In the appendix data tables summarizing analytical data can be found.

2. Geological setting and mineralization models

2.1 The association of chromite and the PGE – a world-wide phenomenon

Besides being produced from placer deposits or Cu-Ni-sulphide ores, the PGE today often are extracted as a by-product during chromium production from chromite ore. There are three types of chromite deposits known for their high PGE concentrations: (1) the stratiform; (2) the podiform (or Alpine-type); and (3) the laterite deposits. They are associated with ultramafic or anorthositic rocks and types (1) and (2) yield about half of the world's chromite production (Evans, 1997; Schürmann *et al.*, 1998).

The ***stratiform deposits*** host over 90% of the world's chromite resources (Schürmann *et al.*, 1998). Typically, they are made up of layers that have formed in the lower parts of stratified igneous complexes, e.g. the *Bushveld Complex* and the *Great Dyke*, or in sill-like intrusions, e.g. the *Stillwater complex*. Significant features are their intrusion into stable cratons and their Precambrian age (Naldrett, 1981; Evans, 1997).

The shape as well as the mass of a ***podiform deposit*** is highly variable. However, the most common morphology is sheet-like to pod-like with masses ranging between a few kilograms to several million tonnes. This type of chromite deposit is located in major tectonic belts; often as ophiolites or parts of dismembered ophiolites. The chromite is hosted by irregular peridotite masses or peridotite-gabbro complexes, and typically occurs near the contacts of peridotite and gabbro (Evans, 1997; Schürmann *et al.*, 1998). They can have different ages; most of them are Palaeozoic, but some of them are Mesozoic or even Tertiary. All major podiform deposits can be found in ophiolites formed in marginal basins (Pearce *et al.*, 1984). Due to their chemical composition two ore types can be distinguished: high-chromium chromite (46-55% Cr_2O_3) and high-aluminum chromite (22-34% Al_2O_3, 33-38% Cr_2O_3) (Schürmann *et al.*, 1998).

The largest known deposits are located in the Ural Mountains, and the Tethyan Mountains in Albania, Greece and Turkey (Schürmann *et al.*, 1998); smaller ones can be found in Canada, Newfoundland, Cuba and Greece (Evans, 1997).

Iron- and nickel-rich ***laterites***, which are formed by weathering of peridotites, can also host considerable amounts of chromite. An example is the Rama-River Ni-chromite laterite deposit lately discovered in Papua New Guinea (Schürmann *et al.*, 1998).

2.1.1 PGE distribution in chromite deposits and ultramafic and mafic rocks

The PGE mineralization within the different rock types is unique for each of them, which is probably due to the different geological settings they occur in. Figures 2.1 to 2.5 should illustrate this relationship by presenting PGE concentrations normalized to C1 chondrite. Corresponding data are summarized in table 2.1. Because the samples of this study originate from ultramafic and mafic rocks as well as chromitite, the PGE patterns presented below are restricted to those rock types only, all of them deriving from partial melt of mantle material. The PGE are plotted in order of decreasing melt temperatures.

The PGE distribution patterns of ***mantle rocks*** are shown in figure 2.1. They include abyssal peridotites of oceanic origin (P-1) that refer to ultramafic rocks recovered in drilling from mid-ocean ridges. Furthermore, the PGE patterns of mantle nodules are presented with dunitic (N-1), harzburgitic (N-2) and lherzolitic compositions (N3-N4). According to their host rock, they derive from oceanic (i.e. oceanic island basalt (OIB); N-3) or continental environments (kimberlites; N-1, N-2 and N-4).

Generally, the slopes of all the patterns are very flat indicating a very small degree of fractionation only, with Pt/Ir ratios ranging between 0.7 and 1.7. Although lower in PGE concentration, the dunitic nodule (N-1) deriving from Oahu in Hawaii shows a weak negative slope suggesting an enrichment of the high-temperature PGE (HT-PGE) relative to the low temperature PGE (LT-PGE)[2] (Pt/Ir = 0.54). All profiles show distinct negative Pt anomalies as well as low Pd concentrations.

Komatiites are ultramafic rocks with >18% MgO, which is due to the high degree of partial melting (30-50%) of mantle peridotites at temperatures of 1700°C or higher (Arndt and Nesbitt, 1982) – parameters that promote PGE fertility of this rock type. Similar to the mantle nodules, komatiitic melts also show relatively flat profiles but with a clear positive trend from Os to Pd (Pt/Ir = 6.1 or 9.1 for lower and upper field boundaries, respectively) (Fig. 2.2). High-MgO basalts, rocks that are associated with komatiites, show a similar PGE pattern but with a higher degree of fractionation between the HT-PGE and the LT-PGE (Pt/Ir = 24.1). This fractionation trend is only slightly indicated in the komatiite patterns, but is probably caused by cooling and crystallization within the lava flows, removing HT-PGE and –silicates (i.e. forsterite) from the melt.

[2] According to Tredoux *et al.* (1995) the high-temperature PGE comprise Os, Ir and Ru; the low-temperature PGE are made up of Rh, Pt and Pd. These two groups coincide with the two PGE groups defined by Barnes *et al.* (1985), namely IPGE and PPGE, respectively.

Table 2.1 Whole-rock PGE analyses for different rock types. * For the UG2 the average consists of data from the western, eastern and northern limbs; for the Merensky Reef whole-rock averages from the Impala lower and Impala upper chromitite layers have been taken. MORB data are global averages. Data for OIB are averages comprising data from the Hawaiian Islands and from islands in the Indian Ocean, the South Pacific and the North and South Atlantic Oceans. CFB data are averages from Deccan, Parana, Karoo and Columbia River Provinces.

	Remarks		**Os**	**Ir**	**Ru**	**Rh**	**Pt**	**Pd**	**n**	**References**
			ppb	ppb	ppb	ppb	ppb	ppb		
Mantle rocks										A (7,58,60)
Abyssal peridotite	oceanic peridotite	P-1	2.2	3.5	6.2	0	7.6	6.1	2	A (56)
Nodule	continental dunite	N-1	0	0.7	1.4	0	0.4	0.4	1	A (28,56)
Nodule	continental harzburgite	N-2	2.2	3	5.3	1.4	5.6	2	1	A (12,48)
Nodule	oceanic lherzolite	N-3	1.4	4.4	0	0	0	7.1	1	A (28,32,47,48)
Nodule	continental lherzolite	N-4	2.2	3	5.3	1.3	4.4	2.8	1	
Melts of deep mantle origin										A (2,9,11,18,51,54,57,67)
Komatiite	upper field boundary		2.5	2.5	5.3	1.7	15	15	4	A (2,4,9,18,51,54,65,68,73)
Komatiite	lower field boundary		0.5	0.8	3.8	1	7	5.1	5	A (3,9,11,68)
High-MgO basalts	assoc. with komatiites		0.3	0.5	0.8	0.9	11.8	15.8	3	A (45)
Kimberlite 1 from southern Africa	on craton		1.6	1.3	2.8	0.8	4.4	3.2	1	A (45)
Kimberlite 2 from southern Africa	off craton		1.2	1.3	2.7	1	13.5	8.3	2	
Rocks generated in:										A (27,46,51,55)
subduction environments	island arc basalts	IAB	0.5	0.7	0.1	0	3.5	10.3	global av	A (5,13,22,30,33,37,42,50,55,
diverging plate settings	mid-ocean ridge basalts	MORB	0	0	0.1	0	0.4	0.5	global av	57,60,62)
intraplate settings 1	ocean island basalt	OIB	0.3	0.3	0.4	0.2	4.3	4.6	global av	A (7,12,14-16,21-3,29,35,36,41-43,50,53,55,57,59,60,69,70,71)
intraplate settings 2	continental flood basalt	CFB	0.6	0.1	0.3	0.3	6.2	8.8	global av	A (1,8,10,17,19,20,24-26,30, 34 39,40,44,49,52,61,63,64,66,72,74,75)

Ophiolitic complexes										
White Hills Peridotite, Newfoundland	chromitite lens	OC-1	277.5	314.5	507	91	209.5	21.5	2	B
Lewis Hills, Bay of Islands, Newfoundland	chromite-rich dunite	OC-2	7	9.5	30	3	5	5	1	B
Thetford complex, Quebec	chromitite	OC-3	31	32	30	5	10	15	1	B
British Columbia Ultramafics	chromite-rich dunite, chromitite	OC-4	79.5	87.4	149.4	16,.1	39.4	39.4	8	B
Vourinos Complex, Greece	chromite-rich dunite, chromitite	OC-5	14	20.5	40	7	20	27.5	2	B
Stratiform complexes										
Bird River Sill, Manitoba	chromite-rich dunite, diss. chromite	BRS	23.4	15.5	120	14.6	21	10	5	B
UG2 reef, Bushveld Complex	chromitite layer	UG2	93	159.7	792	462.7	2763	1850.3	3	C
Merensky Reef, Bushveld Complex	chromitite layer	MR_chr	564	908	4424	1903	30073.5	3114.5	2	C
Great Dyke, Zimbabwe	Main Sulfide Zone pyroxenites	GD	13.9	43.9	91	104.7	1165.6	1004.4	25	D
Stillwater complex, Montana, USA	Chromite Seam A	Still	---	178	372	384	1288	2176	6	E

References: A – Crocket, 2002; **B** – Talkington and Watkinson, 1986; **C** – Barnes and Maier, 2002; **D** - Oberthür *et al.*, 2003; **E** – Talkington and Lipin, 1986. *References in brackets (1-75) represent references used by Crocket, 2002: 1. Barnes and Francis, 1995; 2. Barnes and Giovenazza, 1990; 3. Barnes and Picard, 1993; 4. Bickle et al., 1993; 5. Blusztajn et al., 2000; 6. Brandon et al., 1999; 7. Brandon et al., 2000; 8. Brooks et al., 1999; 9. Brügmann et al., 1987; 10. Brügmann et al., 1993; 11. Crocket and MacRae, 1986; 12. Crocket and Skippen, 1966; 13. Crocket and Teruta., 1977; 14. Crocket et al., 1973; 15. Crocket, 2000; 16. Crocket, 2002; 17. Crocket, unpubl.; 18. Dowling and Hill., 1992; 19. Ellam and Cox, 1989; 20. Ellam et al., 1992; 21. Fryer and Greenough, 1992; 22. Gottfried and Greenland, 1972; 23. Gottfried et al., 1972; 24. Gottfried et al., 1990; 25. Greenland, 1971; 26. Greenough and Fryer, 1995; 27. Hamlyn et al., 1985; 28. Handler and Bennet, 1999; 29. Hauri and Hart, 1993; 30. Hertogen et al., 1980; 31. Hertogen et al., 1995; 32. Jagouts et al., 1979; 33. Keays and Scott, 1976; 34. Keays, 1984; 35. Lassiter and Hauri, 1998; 36. Lassiter et al., 2000; 37. Laul et al.. 1972; 38. Lightfoot et al., 1997; 39. Maier et al., 2001; 40. Mangan et al., 1993; 41. Marcantonio et al., 1995; 42. Martin, 1991; 43. Martin et al., 1994; 44. Massey et al., 1983; 45. McDonald et al., 1995; 46. McInnes et al., 1999; 47. Mitchell and Keays, 1981; 48. Morgan et al., 1981; 49. Nielsen and Brooks, 1995; 50. Oguri et al., 1999; 51. Pearson and Woodland, 2000; 52. Peate, 1969; 53. Pegram and Allégre, 1992; 54. Puchtel and Humayan, 2000; 55. Ravizza and Pyle, 1997; 56. Rehkämper et al., 1997; 57. Rehkämper et al., 1999a; 58. Rehkämper et al., 1999b; 59. Reisberg et al., 1993; 60. Roy-Barman and Allégre, 1994; 61. Schaefer et al., 2000; 62. Schiano et al., 1997; 63. Shirey, 1997; 64. Thériault et al., 1997; 65. Tredoux and McDonald, 1996; 66. Vogel and Keays, 1997; 67. Walker et al., 1988; 68. Walker et al., 1999; 69. Wasson and Baedecker, 1970; 70. Widom and Shirey, 1996; 71. Widom et al., 1999; 72. Wooden et al.,1993; 73. Zhou, 1994; 74. Horan et al., 1995; 75. Rowe, 1969.*

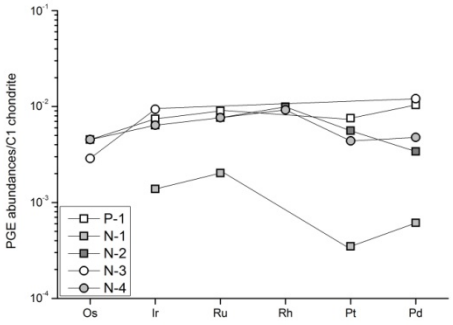

Figure 2.1 C1 normalized PGE patterns for mantle nodules (*N*) and abyssal peridotites *(P*). Data from Crocket (2002) and references therein.

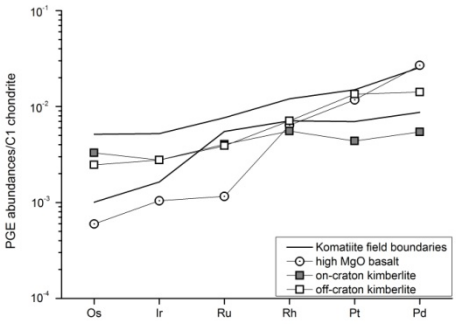

Figure 2.2 C1 normalized PGE patterns for a range of komatiites and rocks associated with them (high-MgO basalt). Furthermore, PGE profiles for kimberlites occurring on or off the Kaapvaal craton are presented. Data from Crocket (2002) and references therein.

Another example for melts of deep mantle origin is ***kimberlite***. Exemplarily, mean concentrations for kimberlites occurring on or off the Transvaal craton, Southern Africa, are plotted (Fig. 2.2). On-craton kimberlites show flat profiles with a Pt anomaly similar to those presented for mantle nodules. A fractionation between HT-PGE and LT-PGE is most obvious in the pattern of the off-craton kimberlites, since the slope abruptly increases from Ru to Pd. The Pt/Ir ratio for the latter suite is 10.4, whereas for the on-craton suite it is 4.4 only.

Figure 2.3 presents the PGE patterns for basalts generated in different geological settings. The pattern for ***island arc basalt*** (IAB) deriving from a subduction environment comprises averaged values including picrites, andesites and boninites from various localities (see table 2.1). Compared to the other patterns in figure 2.3, the IAB has the highest HT-PGE concentrations. Furthermore, the IAB shows strong negative anomalies for Ru and Rh and a positive slope from Ru to Pd. Thus it seems that the PGE fractionated within three distinct groups, which are Os-Ir, Ru-Rh and Pt-Pd.

Basalts generated at diverging plate margins (***mid-ocean ridge basalts*** – MORB) have very low PGE concentrations depicted in their pattern. They generally show a positive slope (Pt/Ir = 13.67) and a negative Rh anomaly. Several authors showed (e.g. Czamanske and Moore, 1977; Hamlyn *et al.*, 1985; Keays, 1995) that the PGE in MORB are concentrated by immiscible sulphide liquid generated contemporaneous to magma generation. Since the sulphide melt is separated from the silicate melt during cooling, the MORB are depleted in the PGE.

PGE concentrations of the two types of intra-plate volcanism resemble each other except for Os and Ir (Fig. 2.3), but both with positive slopes. For the ***ocean island basalts*** (OIB) as well as the ***continental flood basalts*** (CFB) a deep mantle origin of the melt is considered that is produced and transported by a convective mantle plume. The PGE in the CFB are stronger fractionated than in the OIB, as can be obtained by their Pt/Ir ratios (77.5 or 15.36, respectively). The high Os content in the CFB profile cannot be confirmed to be a general feature of flood basalts, since Os data are available for Karoo and Noril'sk only (Crocket, 2002). However, the CFB show lower concentrations of the HT-PGE when compared to OIB, which is due to assimilation of crustal material.

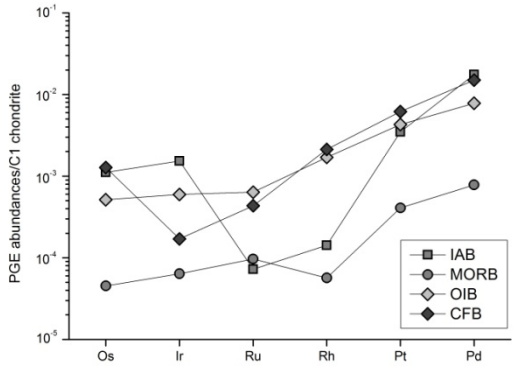

Figure 2.3 PGE patterns for melts generated in subduction environments (IAB), at diverging plate margins (MORB) and in intracontinental settings (OIB, CFB). Data from Crocket (2002) and references therein.

Compared to the various silicate rocks above, the chromitites in ophiolitic complexes and major PGE-bearing horizons in stratiform intrusions are enriched in the PGE, which is very well illustrated in their PGE patterns (Fig. 2.4 and 2.5). Since both types are or have been mined for PGE, their PGE mineralogy is described additionally.

All the profiles from ***ophiolitic complexes*** (Fig. 2.4) show negative slopes with only minor differences. Except for the chromitite lens from the White Hills peridotites, Newfoundland (OC-1), the patterns have distinct negative Pt anomalies and generally higher amounts of HT-PGE relative to the LT-PGE. This circumstance is also deflected in the Pt/Ir ratios all being <1. Additionally, in the profiles of OC-2, OC-4 and OC-5 slight positive Ru anomalies can be observed.

Except for the Bird River sill, Manitoba, all the PGE patterns of the ***stratiform complexes*** show positive slopes with high degrees of fractionation between the HT-PGE and the LT-PGE (Fig. 2.5): the Pt/Ir ratio ranges between 7.2 for the Stillwater complex and 33.1 for the Merensky Reef chromitites (MR_chr). Additionally figure 2.5 shows that the MR_chr is the most enriched layer when compared to the other patterns.

When compared to C1 chondrite, it is also the only one that shows higher PGE concentrations for each single PGE. Except the Bird River sill, this is generally only true for the LT-PGE within the other stratiform complexes.

The concentrations of the HT-PGE in ophiolitic complexes and most of the stratiform complexes except the Merensky Reef chromitites are quite similar (approximately 0.2 times C1 chondrite), whereas the LT-PGE show another chemical trend in each case: the LT-PGE concentrations in the ophiolitic complexes are around 0.2 times the C1 chondrite concentrations. In the stratiform complexes except for the MR chromitite the LT-PGE concentrations vary strongly and range between 1.8 to 7.3 times the concentration of C1 chondrite. This results in PGE patterns with generally negative slopes for the ophiolitic complexes. Higher abundances of the LT-PGE are depicted by positive slopes for the major PGE-bearing horizons of the stratiform complexes.

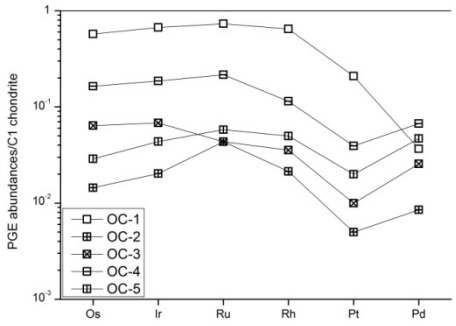

Figure 2.4 Averaged PGE patterns of chromite-bearing ultramafic rocks and chromitites from various ophiolitic complexes. Data from Talkington and Watkinson (1986). *OC-1:* White Hills Peridotite, Newfoundland; *OC-2:* Lewis Hills, bay of Islands, Newfoundland; *OC-3:* Thetford complex, Quebec, Canada; *OC-4:* British Columbia Ultramafics; *OC-5:* Vourinos complex, Greece.

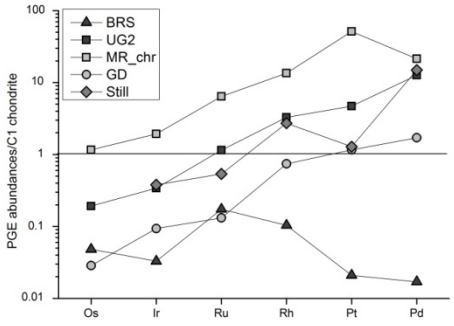

Figure 2.5 PGE profiles of major PGE-bearing horizons from different stratiform complexes. Data compiled from Talkington and Lipin (1986), Talkington and Watkinson (1986), Barnes and Maier (2002) and Oberthür *et al.* (2003). *BRS:* Bird River Sill, Manitoba, Canada; *UG2:* Upper Group chromitite layer 2, BC, South Africa; *MR:* Merensky Reef chromitite, BC, South Africa; *GD:* Great Dyke, Zimbabwe; *Still:* Stillwater complex, Montana, USA.

According to Page and Talkington (1984) and Talkington *et al.* (1984) high absolute abundances of Os, Ir, and Ru can be correlated to the presence of laurite [$(Ru,Os,Ir)S_2$] and (Ru,Os,Ir)-bearing alloys. They occur as discrete inclusions within chromite grains

of chromitites in ophiolite complexes. Data on grain sizes differ highly: <10 µm (Legendre and Augé, 1986), <15 µm (Talkington and Watkinson, 1986) or <40 µm, as described by Talkington *et al.* (1984). However, it is agreed upon the habit, being euhedral to subhedral with square, rectangular, triangle or hexagonal crystal forms.

Laurite inclusions have also been observed by Talkington and Lipin (1986) and McLaren and de Villiers (1982) within chromitite layers of the Stillwater complex or the UG2 layer of the Bushveld Complex, respectively. Its grain size is <20 µm; the euhedral habit showing the same forms described for the ophiolite complexes. In the UG2 chromitite layer, laurite also occur along grain boundaries or associated with the BMS (McLaren and de Villiers, 1982). Thus, laurite seems to be the most common PGM associated with chromitites in stratiform (Page, 1971; Page and Jackson, 1967; Page *et al.*, 1976; McLaren and de Villiers, 1982) as well as in ophiolite complexes (Legendre and Augé, 1986). As the stratiform complexes show even higher concentrations of Ru (see Fig. 2.5) it can be assumed that 'pure' laurite (RuS_2) is more abundant here.

The scarcity of Pt-, Pd- and Rh-bearing PGM within ophiolites is generally ascribed to their compatible behaviour relative to the silicate melt if sulphide saturation is not attained (Talkington and Watkinson, 1986). This aspect also has been observed by Talkington and Page (1984) and Talkington *et al.* (1984) and seems to be a characteristic feature of ophiolite complexes. If present, the Pt-, Pd- and Rh-bearing phases occur as intercumulus phases associated with the base-metal sulphides, i.e. pyrrhotite, pentlandite and chalcopyrite. Contradictory to that are the findings of Legendre and Augé (1986) who investigated chromitites from different ophiolite complexes, too. According to them, all PGM found were inclusions within chromite crystals and can be assigned to one of four groups: (1) PGE-alloys; (2) PGE-sulphides; (3) PGE-sulpharsenide; and (4) PGE-alloys with other transition metals. The authors didn't observe any PGM being interstitial or trapped within interstitial silicates. However, they also mentioned laurite to be the most frequent PGM in ophiolitic chromitite.

Besides laurite as the dominant PGM species, abundant Pt-, Pd- and Rh-bearing PGM can be found within stratiform complexes. They comprise sulphides like cooperite (PtS), braggite [(Pt,Pd,Ni)S] and vysotskite (PdS) in the UG2 of the Bushveld Complex (McLaren and de Villiers, 1982) and the Main Sulphide Zone (MSZ) of the Great Dyke, Zimbabwe (Oberthür *et al.*, 2003). The latter furthermore contains (Pt,Pd)-bismuthotellurides and (Ir,Rh,Pt)-sulphoarsenides, which together make up 74% of all the PGM species (Oberthür *et al.*, 2003). It must be noted that in the Great Dyke laurite is very rare due to the scarcity of chromite. All the PGM in the two stratiform complexes mentioned above form discrete grains that are predominately associated with the BMS,

i.e. pentlandite, chalcopyrite and pyrrhotite, or they occur along grain boundaries or locked in silicates. For the UG2 they can furthermore be locked within chromite.

The presence of PGM containing abundant Pt, Pd and Rh additionally to abundant laurite is considered to cause the positive slopes of the PGE patterns of stratiform complexes, as have been shown in figure 2.5.

All rock types presented above are thought to derive from partial melts of the mantle. If one compares the PGE patterns (Fig. 2.6) it can be seen that the mantle rocks, represented by a harzburgitic (N-2) and a lherzolitic mantle nodule (N-3), are very similar. The latter can be interpreted to be the source material for mantle melts; the harzburgite as the refractory residue. This is especially nice depicted in their Pt and Pd contents. The source material is still enriched in these two PGE; with a partial melt event fractionating Pt and Pd into the melt leaving a depleted restite (i.e. harzburgite).

Komatiitic melts comprise as much PGE as mantle rocks, which is caused by a very high degree of partial melting (30-50%) (Lorand *et al.*, 2008). They are only slightly enriched in Pt and Pd and depleted in Rh and Ir when compared to their source rocks. This kind of melt generation is extinct and restricted to the Archean. In contrast, the PGE pattern for the MORB is extremely low and those for the chromitites (OC-1 and UG2) enriched in all the PGE relative to mantle rocks, which indicates a process that enriches the PGE during fractionated crystallization of the parental melt.

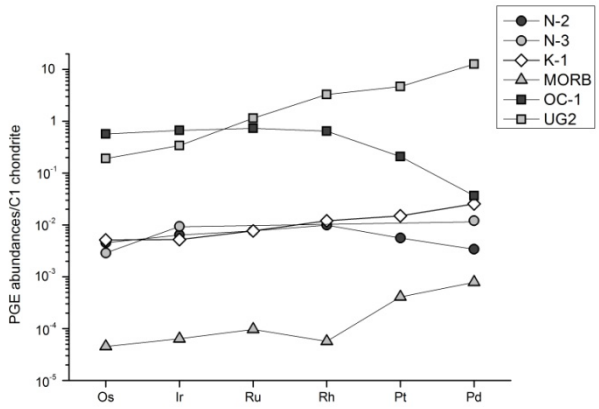

Figure 2.6 Chondrite-normalized PGE abundances in (residual) mantle rocks and mantle derived magmas.
N-2: harzburgitic mantle nodule; *N-3*: lherzolitic mantle nodule; *K-1*: komatiite, upper field boundary from Fig. 2.2; *MORB*: mid-ocean ridge basalt; *OC-1*: chromite lens from White Hill Peridotite. Newfoundland; *UG2*: UG2 chromitite layer, Bushveld Complex. Data are the same as for figures 2.1 - 2.5. See also table 2.1.

According to Morgan (1986), Pattou *et al.* (1996) and Burton *et al.* (2002) the upper mantle contains about 0.1% of Fe-Ni-Cu sulphides with PGE concentrations at the parts per million (ppm) level. This is three orders of magnitude higher than the concentration

determined for mantle-derived rocks. Since all the PGE have the same affinities for sulphide melts (sulphide melt-silicate melt partition coefficient of 10^3-10^6; Ballhaus *et al.*, 2006) the PGE patterns presented cannot completely be explained by different degrees of partial melting only.

From the data given above it seems that the occurrence of Rh- Pt- and Pd-bearing PGM is linked to high abundances of BMS. In fact, Alard *et al.* (2000) and Lorand and Alard (2001) discovered that more than 90% of the PGE in mantle lherzolites resides in two sulphide populations, both occupying different sites of crystallization and with different mineralogical and geochemical compositions. The first population comprises Os-Ir-Ru- and Rh-rich sulphides occurring as rounded Fe-Ni monosulfide solid solution (mss) inclusion in olivine. Analyses with laser ablation inductively-coupled-plasma mass-spectrometry (LA-ICP-MS) yielded a similar chondrite-normalized PGE pattern as residual (depleted) mantle peridotites with a negative slope. The second population consists of Ni sulphide and Cu sulphide (pentlandite and chalcopyrite-isocubanite) that occurs intergranular and is enriched in Pd. They produce positively sloped chondrite-normalized PGE pattern.

Due to these findings it can be concluded that during partial melting of the mantle, the intergranular Ni-Cu-sulphides are consumed first, entraining Pd and Pt into the melt. This results in the typically negative sloped PGE pattern for mantle restites, since Os, Ir, Ru and Rh remain in there. If the degree of partial melting is high enough (≥ 20 ± 5%) all the mss is expected to be consumed by the magma. This causes the liberation of micrometer-scale Ru-Os-Ir sulphides and Os-Ir-Ru-bearing alloys, which retain the HT-PGE inside the residual mantle rocks (Luguet *et al.*, 2007).

Surely, these considerations are very well applicable to PGE deposits with elevated amounts of sulphides, e.g. Ni-Cu-PGE sulphide deposits, but rather difficult explain high concentrations of PGE within sulphide-poor chromitite layers as the Middle Group of the eastern Bushveld Complex. The reason for preferentially PGE enrichment in chromitite is still not known exactly and is continued to be debated. To give an overview, the following chapter presents mineralization models for the formation of chromitite layers and the associated PGE mineralization.

2.2 Models for chromitite formation and PGE mineralization

2.2.1 The formation of chromitite layers

As mentioned in the chapter before, modal layering is very common within the RLS. Especially in the CZ, the appearance of several chromitite-harzburgite-pyroxenite-norite-anorthosite sequences gives rise to cyclic units, which are defined as a group of rock units that occur in a certain, commonly repetitive order (Bates and Jackson, 1995). Individual layers within these cyclic units can be followed over distances of several 100 km.

There are many hypotheses for the formation of especially the chromitite layers, including increases in oxygen fugacity (fO_2), pressure changes and gravitational sorting. Chromitite layer formation by crystal settling or gravitational sorting is one of the oldest ideas and deals with crystals that (depending on their size and density) settle through the liquid to the bottom of the magma chamber (Wager *et al.*, 1960; Jackson, 1967). Large and heavy crystals (e.g. chromite grains) thus would sink to form a dense layer and small and light crystals would remain in suspension. A major problem for this model is the assumed convection of the magma due to temperature and compositional gradients (Eales, 2001). If the convection velocity exceeds the settling velocity due to field strength of the magma, settling of chromite grains would be prevented (Campbell, 1978).

After Lipin (1993), who worked on the Stillwater complex, a periodic increase in the pressure would instantaneously change the crystallizing mineral assemblage, driving the magma into the chromite field of the ternary diagram olivine-chromite-quartz and resulting in chromite precipitation. The increase in total pressure is caused by the formation of CO_2 bubbles rising to the top of the magma chamber. During this process they enlarge their volume by four to six times. Lipin (1993) suggested that this process works for the entire complex, thus explaining the great lateral persistence of individual chromitite layers. However, Eales and Cawthorn (1996) noted that a pressure increase would also increase the stability of pyroxene relative to plagioclase indicating that plagioclase precipitation is suppressed. They also questioned sufficient roof stability for a magma chamber as large as the Bushveld Complex to develop a pressure increase at the bottom of the chamber. Due to Cameron (1977, 1980) such a change in pressure can also be achieved by tectonism affecting the magma chamber during crystallization for which he found evidence around the Schwerin fold in the eastern Bushveld. The stresses produced directly impinged on the walls of the chamber, which temporarily caused increase of pressure on the liquid. Concurrently, further magma addition enlarged the height of the magma column and thus supports pressure increase, which shifted the crystallization path into the chromite field.

Although it seems unlikely that the oxidation of magma will be easily achieved, Ulmer (1969) suggested that an increase in the fO_2 will support the stability of chromite and thus will allow the mineral to be the only one to crystallize for a short period of time. According to Ulmer (1969) the high fO_2 is accompanied by a magnesium enrichment of spinels and co-precipitating silicates. The crystallization of chromite again changes the composition and the fO_2 of the melt resulting in further crystallization of silicate minerals. Experimental analyses done by Hill and Roeder (1974) have shown that at high fO_2 a large amount of chromite with a Cr_2O_3 content of about 45% crystallizes over a small temperature interval (1230°C-1196°C). With decreasing temperature the amount of chromite even increases, but the composition changed to slight enrichment in Fe and Ti with contemporary decreasing Cr, Al and Mg concentrations. In contradiction to that, Irvine *et al.* (1983) stated the fO_2 to be a function of the parent liquid compositions and thus their influence is internal to the system as part of the compositional effects of the mixing process. Thus, the compositional changes are rather the result of magma mixing than of changing fO_2. Additionally, since the fO_2 increases presumably as a result of contamination, the lateral extent of layers cannot be explained by local increase in fO_2.

Models dealing with magma mixing and double-diffusive convection have gained much more attention and will be described in more detail below.

Irvine (1975; 1977) was the first who provided a model for chromite formation based on magma mixing. He suggested two initial geologic situations: (1) an evolved primitive liquid is mixed with “new” primitive liquid or is contaminated with granitic roof rock melt; and (2) the addition of plagioclase-saturated magma to an evolved primitive melt (Irvine *et al.*, 1983). With the phase diagram olivine-chromite-silica Irvine (1975; 1977) explained the crystallisation paths occurring during the mixing events. Both are able to shift the ‘normal’ crystallization path into the stability field of chromite, thus resulting in the precipitation of chromite only (Fig. 2.7 (a) – 2.7 (d)). The mixing occurs at diffusive interfaces between liquid layers that formed because of different temperatures and densities within the magma chamber (Irvine, 1982). It is in these interfaces only, where minimal chemical diffusion but rapid heat transfer takes place, which is why this process is called double-diffusive convection (Fig. 2.8). Only here the chromite precipitation is induced.

Dick and Bullen (1984) showed that variations in the Si/Al ratio of the magma are depicted in the Cr/Al ratios of chromite, saying that mixing of primitive and plagioclase-saturated melts in different proportions would result in chrome spinels with different compositions. Chromite composition in the Bushveld Complex is quite systematic within the stratigraphic column and laterally uniform. Thus Eales and Cawthorn (1996) concluded that the second geologic situation involving the addition of plagioclase-

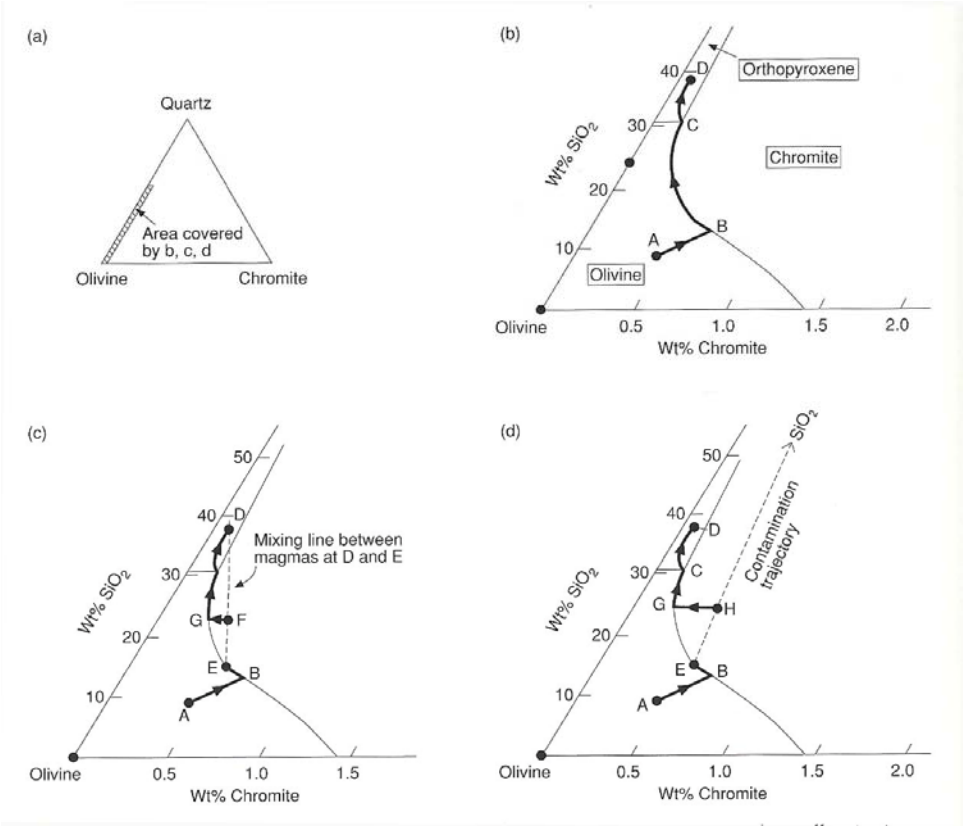

Figure 2.7 Normal crystallisation paths of a mafic magma shown in a section of the ternary system chromite-olivine-quartz (**a,b**). The normal crystallization path for a basaltic magma starts with the precipitation of olivine only until the cotectic phase boundary olivine – chromite is reached (A-B). Here a small amount of chromite (~ 1%) starts to coprecipitate with olivine, and the magma composition then would evolve along the cotectic towards C. Now the SiO_2 content of the magma has increased to a level where olivine and chromite can no longer be the stable liquidus assemblage and orthopyroxenes starts to crystallize (C-D). As fractional crystallization continues, plagioclase will eventually appear together with orthopyroxene, which is not shown in this diagram.
To form monomineralic chromitite layers as can be found in the Bushveld Complex, the crystallization path needs to be shifted into the stability field of chromite. This is either achieved by magma mixing (**c**) or magma contamination (**d**). The first one deals with the injection of a new and more evolved magma into the magma chamber at point E. Mingling of the two magmas would result in a mixture whose composition would lie somewhere along the mixing line DE, but in most cases in the stability field of chromite (F). For a short period chromite would thus be the only mineral that crystallizes, leading to the formation of a monomineralic layer. Contamination of the magma with siliceous material could force the magma composition into the chromite field (**d**). The composition of the contaminated magma would lie somewhere on the mixing line H-SiO_2, leading to the crystallization of chromite only (from Robb, 2005; after Irvine, 1977; used with the permission of the author).

saturated melt is not applicable to the Bushveld Complex. Another problem with this model is the huge volume of magma needed to deposit a chromitite layer. Mixing in such

a scale also seems to be implausible, especially if the magma is added as a dense, basal flow (Eales and Cawthorn, 1996). The absence of cryptic variations in orthopyroxenes below and above chromitite layers also questions the accuracy of this model (Cameron, 1980; Hulbert and von Gruenewaldt, 1985; Eales *et al.*, 1988; Cawthorn and Barry, 1992; Eales *et al.*, 1993).

The theory of layering formation has also been used by Rice and von Gruenewaldt (1991; 1995) to model the formation of chromitite layers in the Bushveld Complex. They coupled their theory with observations from industrial engineers, who experimentally proved the development of layering. They also observed the formation of thin boundary layers between two liquids of different composition and density, in which early precipitated crystals settled. The crystallization process is ascribed to particle aggregation caused by shear conditions in fluids that result from the collision of particle matter. The scavenging takes place, where the shear is greatest: in the convecting boundary layers. As described by Irvine *et al.* (1983), the formation of the layering in the magma chamber is caused by a temperature gradient decreasing from bottom to top. Due to convection, every layer is well mixed and thus of uniform temperature and composition. It is only at the thin boundary layers between the liquid layers where temperature and composition change (Fig. 2.9 and 2.10). Since the uppermost layer tends to be the coolest, chromite precipitation starts here. The crystals are hold in suspension by convection until they are too heavy and sink. Carried as a slurry, they become concentrated in the boundary layer of the convective cells and eventually form a chromitite layer. Excessive crystallization in the boundary layer of an upper convecting layer will begin to drive crystals into the liquid layer below. As this is hotter, partial or total resorption of the entering chromite crystals takes place. The added material is then mixed with the liquid of the lower layer. That way, Rice and von Gruenewaldt (1991; 1995) give another possibility for chromite formation apart from repetitive magma injections but on the basis of convection and mixing. The process is repeated from top to bottom of the magma chamber during cooling and produces chromitite layers with increasing concentrations of Cr downwards.

Kinnaird *et al.* (2002) picked up the idea of contamination proposed by Irvine (1975) leading to the formation of monomineralic chromitite. They corroborated the contamination path with detailed Sr_i data gathered from interstitial plagioclase from chromitites of the entire CZ and different silicate host rocks. According to them, the influx of new magma into the magma chamber (Sr_i = 0.705–0.706) interacts with the overlying granophyric roof rocks (Sr_i > 0.72). The siliceous melt is incorporated into the new primitive liquid, which immediately induce chromite saturation. The contamination with the highly siliceous melt yielded short events of chromite precipitation, which settled to the floor of the magma chamber (Fig. 2.11). Therewith Kinnaird *et al.* (2002) confirm the statement of Eales and

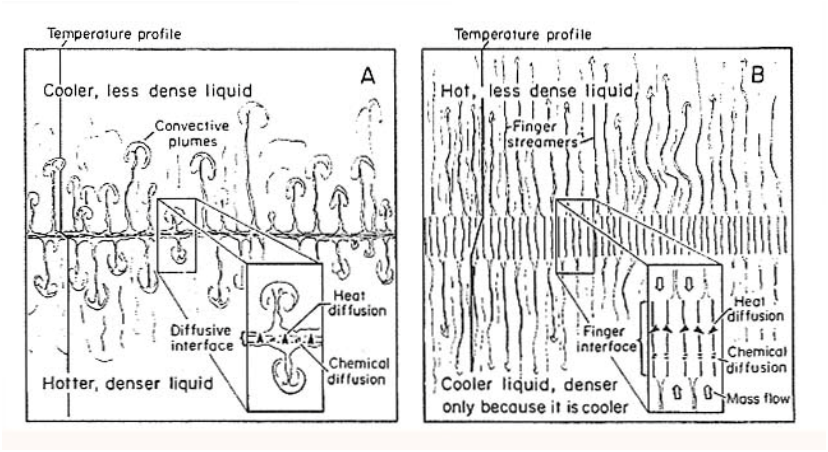

Figure 2.8 Mixing interfaces between liquid layers in double-diffusive convection systems; (**A**) diffusive interface, (**B**) finger interface. (**A)** Chemical transfer of components is in either or both directions depending on the composition of the liquids. The heat transfer is from the hotter (i.e. lower) to the cooler liquid only and is much faster. This results in unstable areas in the vicinity of the interface leading to the formation of convective plumes. Hence, with decreasing diffusion the liquid mixing becomes increasingly mechanically. (**B)** If new liquid is added in a jet or fountain like way, a hot, less dense liquid overlies a cooler liquid layer, which is denser only because it is cooler. When the hotter liquid cools its density increases and mixing with the underlying layer occurs by "finger mixing". The downward thermal diffusion causes the density relationships gradually to reverse, which is achieved by mass flow. The exchange occurs by way of vertical tubular structures ('finger streamers') in both directions. Hence, the liquids become combined mechanically. At the same time, diffusive chemical exchange takes place (from Irvine *et al.*, 1983; used with the permission of the author).

Cawthorn (1996) mentioned above that there is no need for the addition of huge volumes of plagioclase-saturated melt to form a chromitite layer. After Kinnaird *et al.* (2002), small fragments of magma are thought to be dragged by the chromite mass producing interstitial silicates with enriched isotopic ratios. At the same time, the newly introduced melt interacts with the resident liquid in the magma chamber by entrainment. The long-term process within the magma chamber of the Bushveld is thus magma-mixing resulting in the formation of the very different silicate cumulate rocks observed in the RLS with the chromitites being produced by short mixing events only.

A study on silicate melt inclusions in chromite grains from the Stillwater Complex led Spandler *et al.* (2005) to a similar conclusion for chromite formation that has been suggested by Kinnaird *et al.* (2002): a new magma influx interacting with the roof of the Stillwater magma chamber that leads to partial melting of the roof rock and mixing with the residual melt in the magma chamber. Spandler *et al.* (2005) interpret the inclusions to be trapped melt that has been locked into chromite during chromite growth and hence

provide information on chromite formation. Their chemical composition show variable degrees of mixing between parental magma, i.e. high-Mg basalt, and a Na-rich trondhjemitic melt, the latter probably deriving from partial melting of country rocks. As described for the Bushveld Complex by Kinnaird *et al.* (2002), magma mixing within the magma chamber of the Stillwater Complex led to extensive chromite formation. More recent research by Spandler *et al.* (2007) has shown mobility of rare earths elements (REE) through olivine and chromite by lattice diffusion that led to complete re-equilibration of the REE pattern of trapped melt inclusions at magmatic temperatures. This has cast doubt on whether these silicate inclusions record pristine melt compositions, but the unusually Na-rich character of the Stillwater inclusions and the highly radiogenic Sr isotope signatures found in plagioclase associated with chromite still support the idea that chromite crystallisation took place in the presence of unusually siliceous melt.

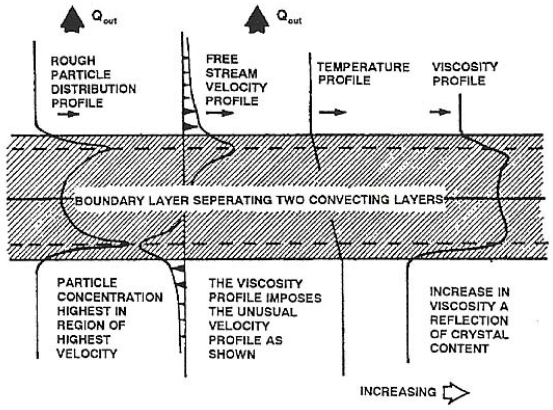

Figure 2.9 Detail of a boundary layer. Big arrows depict the upward transport of heat. Crystals migrated into the boundary layer because of dispersive pressure (shear-grading) form two maxima in crystal content at the top and the bottom of the boundary layer. The maxima coincide with those for the velocity profiles. With increasing crystal content, the velocity profile is further skewed, which also affects the viscosity. All parameters have increasing values to the right (Rice and von Gruenewaldt, 1991; 1995; used with the permission of the author).

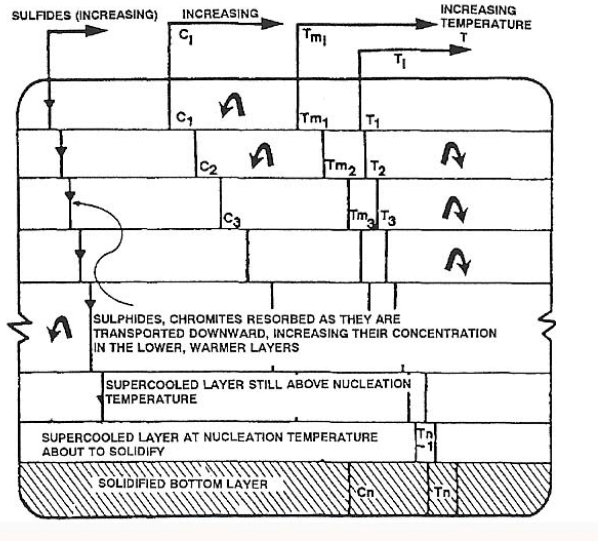

Figure 2.10 Magma chamber split into several layers due to different temperatures and densities. Thin boundary layers (horizontal solid lines) separate the convecting layers; it is only in them where compositional and temperature changes occur. After crystallisation of refractories in the uppermost (i.e. coolest) layer, they are transported downward into the next (warmer) layer. Here the crystals equilibrate or are resorbed, which enriches this layer in chromite, sulphide, PGE etc. (Rice and von Gruenewaldt, 1991; 1995; used with the permission of the author).

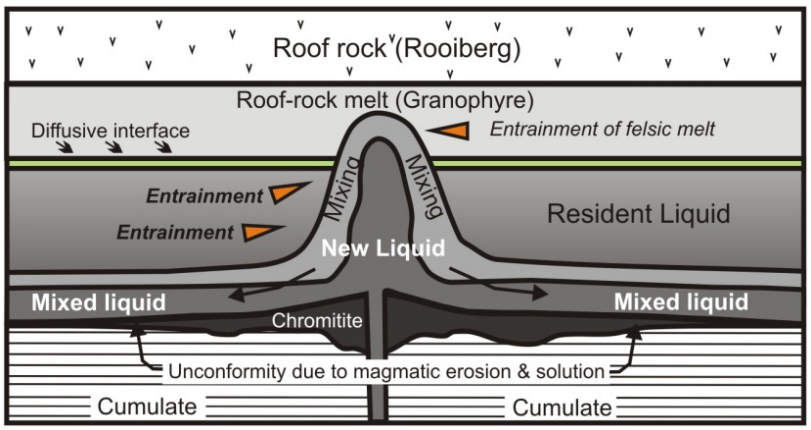

Figure 2.11 Schematic diagram of chromite formation by magma intrusion and mixing of resident and new liquid. Introduction of a new primitive magma (Sr_i = 0.705 - 0.706) as an active fountain resulted in the entrainment of resident mafic liquid. If the upward momentum was sufficient, contamination with a silica-rich component (i.e. granophyric roof-rock melt) took place, forcing the crystallization of chromite (from Kinnaird *et al.*, 2002; used with the permission of the author).

Although the discussion about the formation of the chromitite layers is manifold, there still is the problem how such high chromite concentrations as in the chromitite layers of the Bushveld Complex can be achieved. One possibility to obtain a chromitite layer with a chromium content in excess of 30 wt% from a basaltic magma with a concentration of Cr of about 1000 ppm only is convective scavenging, as suggested by Rice and von Gruenewaldt (1991; 1995). The authors stated that without the scavenging process an enrichment of 300 times would be necessary to yield chromitite formation. However, most of the researchers working on large layered intrusions as the Bushveld Complex doubt their emplacement in a single magma injection, and rather prefer the emplacement from multiple magma addition (e.g. Sharpe, 1980, 1981; Irvine *et al.*, 1983; Cawthorn and Walraven, 1998; Kruger, 2005;). To achieve a chromitite layer of approximately 1 m thickness and a Cr_2O_3 content of 45%, a magma pile of approximately 3000 m thickness is required (Murck and Campbell, 1986; Cawthorn and Walraven, 1998). This seems very unlikely, as adequate volumes of Cr-depleted residua are missing (Eales, 2000).

As stated by Eales (2000), there is more Cr present in the Bushveld Complex than can be accounted for by its solubility in the mafic parental magmas, assuming that the present stratigraphic column represents the entire magma mass.[3] He suggests the presence of <3% microphenocryts of chromite in the intruding melt for the formation of the CZ in addition to the Cr being dissolved in the magma. Mondal and Mathez (2007)

[3] Laboratory experiment on basaltic melts by Hill and Roeder (1974) showed that at a log fO_2 of -8 at 1200°C the maximum solubility of Cr in basaltic melts is between 200 to 300 ppm only. This is due to the relative insolubility of Cr^{3+} in silicate melts.

adopted the model proposed by Eales (2000) to explain the formation of the thick UG2 chromitite and its pyroxenitic host rock without the necessity of a huge magma pile.

The ultramafic sills of the eastern Bushveld Complex described by Sharpe and Hulbert (1985) are interpreted to represent crystal mushes that have been formed in a crustal chamber prior to their intrusion into the Bushveld floor rocks. This crystal laden injection of magma thus should give evidence for the model proposed by Eales (2000).

Unfortunately, every single model has its limitations concerning the application on such a huge magma chamber as the Bushveld Complex. Furthermore, no genetic model completely meets all geochemical and mineralogical characteristics and field observations of the cyclic units. Thus, probably a mixture of multiple injections, fractionation and mixing with previously fractionated magma combined with convective scavenging and changes in pressure and $fO2$ lead to the formation of chromitite layers in the RLS.

2.2.2 PGE mineralization models associated with massive chromitite

As already mentioned in the introduction, the PGE with other elements, e.g. Fe, Co and Ni, belong to the Group VIII transition metals, which chemical similarities give a reason for their tendency to be concentrated together during geological processes. To give a general introduction into PGE concentrating processes, table 2.2 presents the concentrations of Fe, Co, Ni and the PGE in carbonaceous chondrite (i.e. C1 chondrite), the Earth's crust and mantle. The transition metals are quite rare in the crust with concentrations of 1/100 to 1/1000 of the bulk earth (Naldrett, 1981). This is a result of the siderophile character of these elements that dissolved in molten iron in the early history of the earth and sank to the Earth's interior due to gravitational settling forming the core. Compared to the crust, the Earth's mantle is two to 86 times enriched in the transition metals, but still no economic concentrations are achieved.

Table 2.2 Abundances of some Group VIII transition metals. Fe, Co and Ni in ppm; PGE in ppb.

	Fe	Co	Ni	Ru	Rh	Pd	Os	Ir	Pt
Carbonaceous chondrite[1]	182,800	502	10,640	692	141	588	486	470	1,004
Earth's crust[2]	521,568	26.6	59	0.57	n.a.	1.5	0.041	0.037	0.5
Earth's mantle[3]	630,000	102	1,860	4.55	0.93	3.27	3.4	3.2	6.6

[1] Lodders (2003); [2] Rudnick and Gao (2003); [3] Palme and O'Neill (2003); *n.a.:* data not available.

The transfer of the transition metals from the mantle to the crust is possible in two ways:

- Along subduction zones or major lateral faults, large slabs of mantle may be thrust into the crust. After the mantle rocks have been exposed to weathering, Ni-laterites and PGE placer deposits can form.
- Partial melting of mantle peridotites results in the formation of ultramafic or basaltic magma that intrudes into the crust or extrudes as lava, i.e. at mid-ocean ridges (MORs) (Naldrett, 1981).

The latter is thought to have caused the emplacement of the Bushveld Complex, and in the following several PGE mineralization models are presented that may have been responsible for the economic PGE concentrations that can be found in the chromitite layers of the CZ of the complex. Since the PGE mineralisation is linked to the precipitation of chromite in some way, most of the models described above for the genesis of chromitite layers can also be taken to explain the PGE mineralization of them (e.g. Irvine *et al.*, 1983; Rice and von Gruenewaldt, 1991, 1995; Kinnaird *et al.*, 2002).

From the considerations presented above it can be seen that generally the different processes of PGE mineralization can't be separated. It has been done here to show the reader which major process the authors focus on.

2.2.2.1 Sulphide association

Petrogenetic models for PGE mineralization are typically based on the separation of an immiscible sulphide liquid (ISL) from a silicate magma after it reaches sulphur saturation scavenging base and precious metals due to their high silicate/sulphide partition coefficients (D) and the so-called *R*- factor (Naldrett, 1989; Naldrett and von Gruenewaldt, 1989, Li *et al.*, 2001).[4] This model is based on the proposed chalcophile character of the PGE. It is assumed that the sulphide liquid separates as small droplets sinking through the liquid column and scavenging chalcophile elements like the base metals and the PGE. Experimental studies showed that the first phase to crystallize from the cooling sulphide liquid is a monosulphide solid solution (mss) at ca. 1000°C (Naldrett, 1989; Ballhaus *et al.*, 2001; Mungall *et al.*, 2005). Os, Ir, Ru, Rh and Ni are highly compatible in the mss, whereas Cu, Pt, Pd and Au concentrate in the residual sulphide liquid. With further cooling, at approximately 900°C, a Cu-rich solid (intermediate solid solution; iss)

[4] The R-factor is a mass ratio that results from the available amount of silicate melt relative to sulphide liquid.

separates from the liquid, forming magmatic chalcopyrite. The mss decomposes into a Ni-rich part crystallizing pentlandite, and a Fe-rich proportion crystallizing magmatic pyrrhotite. Both are thought to contain Os, Ir, Ru and Rh in solid solution. However, Pt, Pd and Au are incompatible relative to the iss and tend to concentrate with other trace elements, e.g. As, Bi, Te. At temperatures <650°C they start to form discrete PGM.

According to Campbell *et al.* (1983) high *R*-factors can be achieved by turbulences in the magma that occur, when newly introduced magma is added as jets or plumes into the magma chamber. Applied to the PGE several problems arise: (1) silicate magma has very low abundances of PGE only (in the order of parts per billion (ppb)); (2) the PGE need to be heterogeneously distributed to optimize the ore formation by scavenging; (3) experimentally determined D values for the PGE vary extremely. Bezmen *et al.* (1994) determined D values as high as 10^6, whereas Barnes and Maier (1999) give values of about 10,000 only. Campbell *et al.* (1983) even calculated a D value of 5×10^5 to obtain the grades of mineralization in the UG2. A concentration of 10 to 15 ppb of Pt and Pd each is estimated for the Bushveld parental magma (Maier, 2005). Hence, it requires an immense concentration to reach PGE concentrations of 5000 to 6000 ppm, as for example in the Merensky Reef (Barnes and Maier, 2002). The source of the PGE can be found in the mantle, where the PGE are mainly hosted by sulphides (Lorand *et al.*, 2008). Due to the highly chalcophile character of the PGE, they would probably remain in the mantle during partial melting, as a basaltic magma can only dissolve a maximum of 1000 ppm PGE at upper mantle pressure (Maier, 2005). To prevent the PGE from remaining in the mantle, a high degree of partial melting is required (approximately 25%) (Barnes *et al.*, 1985). Furthermore, the mantle-derived ultramafic or mafic melt should be initially sulphide undersaturated to prevent PGE loss on its way up.

After the emplacement of the melt into the lower crust, a trigger for the separation of a PGE-enriched ISL is needed. Several possibilities can be found in the literature. The simplest way to obtain sulphide saturation is the increase of the S content during magma differentiation, since sulphur isn't incorporated into crystallizing oxides and silicates (Maier, 2005). Haughton *et al.* (1974) experimentally tested the influence of several factors on the sulphur solubility of a basaltic magma, i.e. fO_2, bulk composition and temperature, and found that the principal control is the ferrous iron content: an increase in FeO content resulted in contemporary increasing sulphur solubility. Thus, the fractionation of Fe-rich minerals like olivine, orthopyroxene and chromite may cause decreasing sulphur solubility and hence sulphide saturation. Li and Ripley (2005) suggest the mixing of two sulphide undersaturated magmas with very different compositions to obtain sulphide saturation. In contradiction to that, Irvine *et al.* (1983) suggest the mixing of an ultramafic (U_1) with an anorthositic (A_0) magma to trigger precipitation of ISL, but if the

silicate liquids are not initially saturated with sulphide, the authors doubt the immediate precipitation of ISL.

Another possibility to achieve sulphur saturation is contamination of the magma. This can be realized by assimilation of external sulphur, i.e. from country rocks as suggested by Lesher and Campbell (1993); or by assimilation of siliceous partial melt of the country rocks (Irvine, 1975). According to Haughton *et al.* (1974) contamination of the magma could cause an increase in the fO_2, which in turn results in the crystallization of chromite and hence decreasing FeO concentration of the magma. Since S is bonded to Fe^{2+}, decreasing FeO contents lower the capacity of the magma to carry sulphur, which again leads to sulphide saturation.

Finally, the droplets if the ISL sink to the base of the magma chamber, meanwhile the PGE partition into the sulphide droplets due to their chalcophile character. In large intrusions as the Bushveld Complex, the immiscible sulphide melt moves through a large volume of magma, thus scavenging more PGE and hence giving a high *R*-factor. Additionally, convection due to turbulences would also increase the *R*-factor.

However, the coexistence of two PGE-bearing sulphide species in chromitite layers below the UG2 led von Gruenewaldt *et al.* (1986) to the conclusion, that pure PGE concentration by high *R*-factor is an oversimplification, since the individual PGE show different behaviour in terms of being concentrated in various PGM species. Additionally, they observed very low S contents of these chromitite layers and the virtual absence of pyrrhotite. They suggest that postcumulus desulfurization and redistribution of the PGE modified the originally present PGE mineralization within the chromitite layers below the UG2.

On the basis of the work from Gain (1985) and von Gruenewaldt *et al.* (1986), Naldrett and Lehmann (1988) present a model dealing with Fe and S loss of sulphides during cooling, which should explain the poorness of S of chromitite layers in the Bushveld Complex. By interaction with chromite, Fe from the sulphides fills vacancies that exist in high-temperature chromite grains. Due to the equation

$$4/3\ Fe_2O_{3\ spinel} + 1/3\ FeS \Leftrightarrow Fe_3O_{4\ spinel} + 1/6\ S_2 \uparrow,$$

a part of the S is lost to the surroundings. That way, the primary magmatic sulphides contain much more metal (base metals and PGE) relative to S than can be expected by mass ratio. Naldrett *et al.* (2009) extended this model by postulating a multi-stage magma chamber, in which the FeS component of earlier sulphides is gradually dissolved by sulphide-undersaturated magma passing through the staging chamber. The remaining sulphide will thus become enriched in Ni, Cu and especially the PGE. Cawthorn (1999) in

turn suggested that oxidation processes are responsible for the loss of Fe and S from the chromitites, and rejected a desulphidation process. He considered that, because of low BMS abundances in the chromitite layers, the sulphides have never been there.

Experiments on partial desulfurization of Fe-Ni-Cu sulphides done by Peregoedova *et al.* (2004) confirms the considerations of Naldrett and Lehmann (1988) in so far that partial loss of S may redistribute the original sulphide and PGM assemblage within a PGE ore. By reaction with surrounding chromite grains the sulphides trapped between them lose Fe to the chromite and S to the surrounding, thus realizing conditions of low sulphur fugacity (fS_2). It is in this milieu, where Pt and Ir can exsolute from the BMS to form PGE alloys. The loss of S is accompanied by decreasing Cu, Ni and Pd contents in the primary BMS. S and the metals are transported in the form of a vapour phase and crystallize elsewhere as Pd-bearing Cu-Ni sulphide. Thus, the authors present a possible explanation for the observed separation of the PGE resulting in changing Pt/Ir or Pd/Ir ratios, respectively.

According to direct field evidence as well as experimental data some authors propose that especially Os, Ir and Ru can directly precipitate as phenocryst phases from a silicate magma in the form of laurite or Ru-Ir-Os alloys (Brenan and Andrews, 2001; Bockrath *et al.*, 2004). For this process the magma should not be saturated in S, since then these PGE would partition into the mss as described above.

Peach and Mathez (1996) studied partition coefficients of the PGE in order to explain their fractionation from each other. They found stratigraphic variations in chalcophile element concentrations in the UG2 and concluded that the metals must have been redistributed after their deposition as sulphides, which is either caused by different mobilities of the chalcophile elements relative to each other or by concentration by another mechanism than with sulfides. The latter the authors see confirmed by the very similar $D^{\text{sulfide melt/silicate melt}}$ of Ir and Pd and their observed fractionation within natural systems.

2.2.2.2 PGE mineralization associated with chromite precipitation

Similar to the formation of an ISL, the PGE mineralization associated with chromite precipitation is thought to be caused by magma mixing. Here, the PGE mineralization is a by-product of the chromite formation and is initiated simply by changes in physics and chemistry which the magma underwent during contamination and mixing (Kinnaird *et al.*, 2002). The same applies for the scavenging model provided by Rice and von Gruenewaldt (1995), which is equally applicable for PGE mineralization. Teigler (1990)

ascribed the increasing content of the LT-PGE relative to HT-PGE with height in the stratigraphic column of the RLS to the same process.

Another model have been proposed by Hiemstra (1985) and Scoon and Teigler (1994) suggesting that discrete high-temperature PGM (i.e. Os, Ir, Ru) were enclosed by crystallizing chromite grains, which they proposed on basis of petrographic studies. Although the PGM are mainly sulphides and a few alloys, the question to what extend S acted as a PGE collector arises, since the early formed PGM must have been shielded from equilibration with later impoverished liquids. After Scoon and Teigler (1994) this kind of 'chromite control' on PGE precipitation is restricted to sulphide-poor chromitite layers, i.e. those below the UG2. Magma mixing resulting in chromite precipitation is thought to trigger local sulphide saturation and direct nucleation of PGM.

PGM occurring within chromite grains have been considered to result from exsolution during cooling by several authors (Gjibels *et al.*, 1974; Capobianco *et al.*, 1994). Capobianco *et al.* (1994) for example experimentally determined partition coefficients of the PGE between Fe-oxides (magnetite and hematite solid solutions) and silicate melt. They found that Ru and Rh are strongly compatible while Pd is slightly incompatible into the Fe-spinels and thus give a possible fractionation trend of the PGE.

Due to their high $D^{\text{sulfide melt/silicate melt}}$ the PGE Ir, Ru, Rh are highly compatible into chromite spinels, whereas Pd and Au are found to be incompatible (Righter *et al.*, 2004) and thus confirm the findings of Capobianco *et al.* (1994). The authors observed that with decreasing fO_2 the Ru content of the spinels increases, which is explained by changing valences of Ru from 4+ to 3+. Ru^{3+} would thus be able to replace Cr^{3+} in the spinel lattice. Apart from that, Pt has been found to be mildly compatible into clinopyroxene.

According to Merkle (1992), who investigated PGM in chromitite layers of the Middle Group from the western Bushveld Complex, the PGE values reported from authors above (e.g. Gijbels *et al.*, 1974) aren't due to substitution into the crystal lattice of chromite. Evidence comes from the presence of discrete PGM inclusions in chromite, mainly laurite, which is interpreted to be a high-temperature mineral enclosed as chromite crystallizes. Although Merkle (1992) generally coincides with the model of sulphide extraction and postmagmatic modification of the BMS mentioned above, he states that there is a severe problem in modeling PGE concentrations in terms of *R*-factors (Naldrett, 1989; Naldrett and von Gruenewaldt, 1989).

Substantial experimental evidence for the co-precipitation of laurite with chromite recently was given by Bockrath *et al.* (2004) and Ballhaus *et al.* (2006), who found that especially Ru preferentially nucleated onto the chromite surface. Due to the further growth of chromite, the Ru-bearing alloy of the experiment was enclosed.

2.2.2.3 PGE enrichment by metasomatic processes

In recent years several studies have generated the idea of PGE mineralization and/or redistribution of the PGE by aqueous fluids (e.g. Molnar *et al.*, 1997, 1999, 2001; Wood, 2002; Li *et al.*, 2004; Hanley *et al.*, 2005; Mathez and Webster; 2005). One has to distinguish between low temperature (LT) hydrothermal fluids (<500°C) and high temperature (HT) magmatic volatiles and post-cumulus magmatic fluids (>500°C). The LT fluids are inevitably linked to postmagmatic hydrothermal alteration (Farrow and Watkinson, 1992; Li and Naldrett, 1993; McCormick and McDonald, 1999; Molnar *et al.*, 2001). The occurrence of high salinity fluid inclusion containing Cl^- as the principal anion as well as the presence of Cl-rich hydroxysilicate minerals has led several authors to suggest that PGE transport and redistribution took place by chloride complexation. However, experimental studies showed that complexation of Pt and Pd with Cl^- below 500°C only occur under highly oxidizing or highly acidic (pH ~2) conditions (Gammons and Bloom, 1993; Wood, 2002), which makes it almost impossible to create PGE-bearing chloride complexes in magmatic Ni-Cu-PGE deposits. Thus, complexation with bisulphide (HS^-) seems to be more successful. However, Cl-rich fluids selectively remove BMS, as have been reported by Li *et al.* (2004) from the Merensky Reef. Here, local replacement of PGM-hosting BMS by amphiboles, epidote and calcite can be observed. According to this, the textural association of PGM with secondary minerals may be an artifact of PGM-hosting primary magmatic BMS that have been removed by Cl-rich fluids and don't necessarily indicate a hydrothermal origin of PGM.

A different picture can be drawn for the HT fluids. Evidence exists that the HT deuteric fluids interacted with the PGE-bearing sulphide liquid, the silicate melt as well as the solidifying cumulate pile resulting in the complexation of the PGE with Cl-rich volatile phases (e.g. Ballhaus and Stumpfl, 1986; Boudreau *et al.*, 1986; Willmore *et al.*, 2000; Mathez and Webster, 2005). Fleet and Wu (1993) gave experimental evidence for PGE solubility at high temperatures (800-900°C) saying that Cl^- acts as the major ligand. According to Boudreau and Meurer (1999) a Cl-rich volatile phase exsolves from the interstitial liquid due to water saturation and compaction. It dissolves PGE, S and base metals from pre-existing sulphides in the cumulus pile and migrates upward until it reaches a silicate liquid that is not yet fluid saturated. This way, the metal, S and water content is added to the undersaturated fluid. This process is repeated, until saturation is reached and BMS and PGM can precipitate out of the fluid. Evidence for the existence of Cl-rich volatile phases are given by the presence of halogen-bearing minerals like apatite and mica, the occurrence of pothole structures, which are interpreted to represent

"fumarolic" structures (Reid *et al.*, 1993), as well as discordant ultramafic pipes and breccias (Schiffries, 1982).

There are several studies deriving from the Sudbury complex as well as the UG2 and Merensky Reef of the Bushveld Complex (BC) involving PGE mineralization by aqueous fluids (e.g. Molnar *et al.*, 1997, 1999, 2001; Wood, 2002; Li *et al.*, 2004; Hanley *et al.*, 2005; Mathez and Webster; 2005). Evidence for this process was found to be given by the association of a secondary silicate mineral assemblage being closely associated with the PGM. The fluids are supposed to be deuteric in origin (Boudreau and Meurer, 1999; Voordouw *et al.*, 2009) or derive from country rocks the BC intruded into (Schiffries and Rye, 1990). In contradiction to the Sudbury Igneous complex, an extensive PGE mineralization by aqueous fluids in the BC has not been substantiated so far. It rather occurs redistribution of the primary PGM assemblage associated with BMS, the latter which are (partly) dissolved by the corrosive Cl-rich fluids and most likely transporting also some PGE (Li *et al.*, 2004). On the other hand, a secondary PGM assemblage has been observed in the UG2 chromitite by Voordouw *et al.* (2009) dominantly consisting of PGE-sulphoarsenides.

2.2.2.4 The cluster model

All the models presented above have robust difficulties to explain PGE enrichment solely by chemical or physical changes. Based on experimental evidence, Tredoux *et al.* (1995) suggest a PGE mineralization model apart from chemical and physical aspects, i.e. magma mixing, changes in fO_2 and pressure, and sulphide saturation. According to PGE data from different mafic and ultramafic rocks of the Kaapvaal craton it seems that with increasing melt temperature the PGE content increases, too. Hence the authors concluded that the behaviour of the PGE is correlated to the melt temperature and subdivided the PGE into two groups: the high-temperature PGE (HT-PGE) comprising Os, Ir and Ru, and the low-temperature PGE (LT-PGE: Rh, Pt, Pd). These groups are equivalent to the IPGE and PPGE of Barnes *et al.* (1985). Since the melt temperature of the individual PGE are extremely high (cf. Tab. 1.4 in section 1.1), Tredoux *et al.* (1995) further suggest that the most refractory PGE occur in the melt as inter-PGE alloys in the form of micro-xenocrysts. Build on that and the heterogeneous distribution of the PGE within rocks the idea of PGE mineralization by clusters is born, which is explained in more detail below.

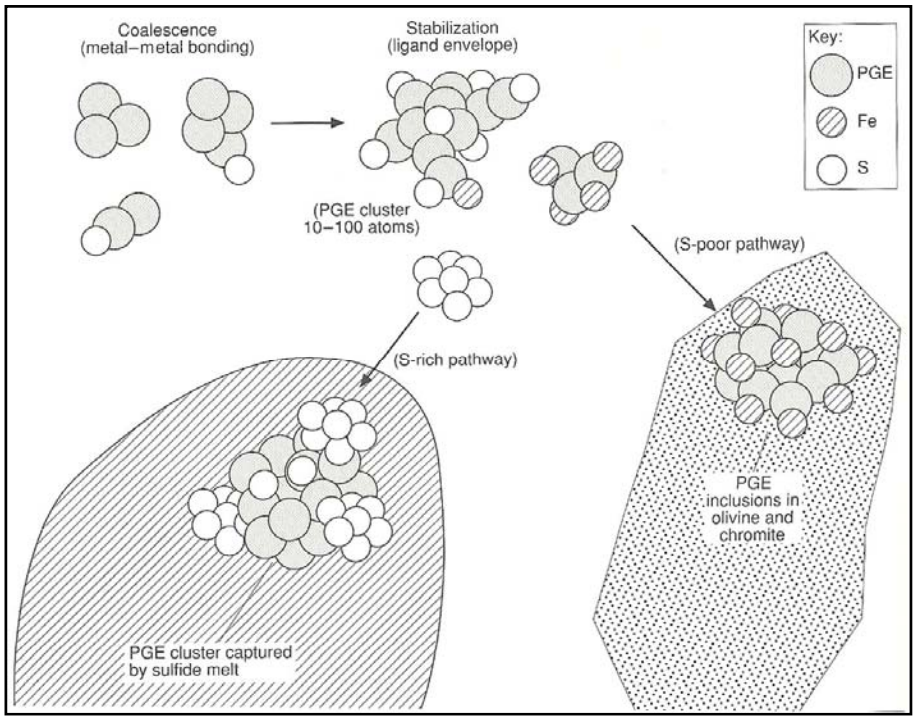

Figure 2.12 Formation of PGE clusters in a magmatic system. Both, the S-rich path and the S-poor path are presented, probably resulting in the inclusion of PGE clusters in either an immiscible sulphide fraction or in a oxide or silicate cumulus phase (from Robb, 2005; after Tredoux *et al.*, 1995, used with the permission of the author).

The PGE are present as metallic clusters (~ 50-100 atoms per cluster) in the melt, which are stabilized by surface adsorption of chalcogenides, like S, As, Sb and Te. In a S-rich environment, the clusters will associate with the sulphide melt and will precipitate to form PGE- arsenides, -antimonides, -tellurides, -alloys and complex sulphides (Fig. 2.12). Remaining clusters will precipitate with the BMS and form sub-microscopic inclusions within them. On the other hand, in a S-poor environment the clusters will remain in the silicate melt. Eventually, they will coalesce to form PGE alloys and thus probably can act as nucleation centres for early-forming oxide and silicate minerals (Fig. 2.12). The high melting points of Os and Ir, as well as their tendency to form the most stable clusters, coincide with the appearance of these two elements with early cumulates, i.e. chromite. Submicroscopic inclusions of PGM within the BMS and the fractionation of the HT-PGE relative to the LT-PGE may be indications for the existence of PGE clusters.

LA-ICP-MS analyses done by Sylvester (2001) on synthetic chromite crystals showed several peaks or spikes of Pt that have been interpreted to represent such clusters included in chromite grains. This has casted doubt on the accuracy of PGE partition coefficients measurements (Ertel *et al.*, 1999). It especially affects the partition coefficients determined by Righter *et al.* (2004) for the PGE between spinel and silicate liquid, from

which the authors deduced the incorporation of PGE into the chromite lattice. However, due to the dearth of LA-ICP-MS analyses on natural chromite this conclusion is lacking substantial evidence.

2.3 Geological setting and stratigraphy of the Bushveld Complex

According to the South African Commission for Stratigraphy, the term Bushveld Complex describes three lithological units that make up the entire complex: (1) the ultramafic to mafic sills underlying the (2) Rustenburg Layered Suite consisting of ultramafic to mafic layered rocks; and (3) the granophyres and granites overlying the RLS (SACS, 1980). After recent age determinations, Cawthorn *et al.* (2002) summarized the stratigraphic relationships within the Bushveld Complex as follows: (1) mafic sill emplacement into the Transvaal Supergroup representing an early phase of Bushveld magmatism; (2) the felsic and minor mafic volcanics of the Rooiberg Group dated at 2.06 Ga by Eriksson *et al.* (1995) underlying the (3) RLS comprising mafic to ultramafic rocks; and (4) the Rashoop Granophyre Suite and the Lebowa Granite Suite both overlying the RLS. The author of this work will apply this new definition to the work in hand.

Several rocks of the RLS have been dated by Walraven *et al.* (1990) close to 2.06 Ga. Considering the age of the Rooiberg Group, which has also been dated at 2.06 Ga (Eriksson *et al.*, 1995), it is most likely that the Rooiberg Group is an initial phase of Bushveld magmatism. Further support for this is given by field data obtained from Harmer and Sharpe (1985). A special feature of the stratigraphic relations between the RLS and the Rooiberg Group is that the latter is partly underlying and partly overlying the RLS (Fig. 2.13). Covering approximately 65000 km^2 and with a thickness of 7-9 km, the RLS of the Bushveld Complex is the largest layered intrusion on earth.

Figure 2.13 furthermore illustrates the relationship between the various lithological units of the Bushveld Complex and the Pretoria Group, into which the entire complex intruded. The Pretoria Group, which is part of the Transvaal Supergroup consists of a succession of sediments of 6-7 km thickness. It is predominantly made up of mudrocks alternating with quartzitic sandstones and subordinate conglomerates, diamictites and carbonate rocks. Minor basaltic to andesitic lavas are significantly interbedded with the sediments, which have undergone low-grade metamorphism (Eriksson *et al.*, 2006). The only radiometric age available for the Pretoria Group is for its lavas having been dated at 2.224 ± 0.021 Ga (Rb-Sr whole rock, Burger and Coertze, 1973-74). In most areas, the stratiform sediment packages of the Transvaal Supergroup slightly dip towards the centrally located Bushveld lithologies (Eriksson *et al.*, 2006).

2.3.1 The Rustenburg Layered Suite

Owing to outcropping at the surface or geophysics and borehole material, the Rustenburg Layered Suite can be subdivided into five compartments: (1) the Western limb; (2) the Eastern limb; (3) the Northern limb; (4) the Far Western limb and (5) the Bethal limb (cf. Fig. 1.1 in chapter 1). Except the latter, all limbs appear on the Earth's surface, with the Far Western limb being an eroded remnant extending to the Botswana border that crops out at Zeerust. The Bethal limb has been identified by a gravitational high and its lithology is only known from borehole information (Cawthorn *et al.*, 2006). Several satellite intrusions are thought to be coeval with the RLS, e.g. the Molopo Farms complex in Botswana and the Uitkomst, Losberg, Moloto and Rhenosterhoekspruit Intrusions (Cawthorn *et al.*, 2006) (Fig. 2.14).

By far the best known limbs are the western and the eastern ones. Due to structural features occurring within them they can be further subdivided into smaller sectors. The emplacement of the Pilanesberg complex separates the western part of the RLS into a northern and a southern sector. The eastern limb is divided into a central and a southern sector by the prominent Steelpoort fault. The Wonderkop fault again separates a northwestern sector from the central part (Cawthorn *et al.*, 2006).

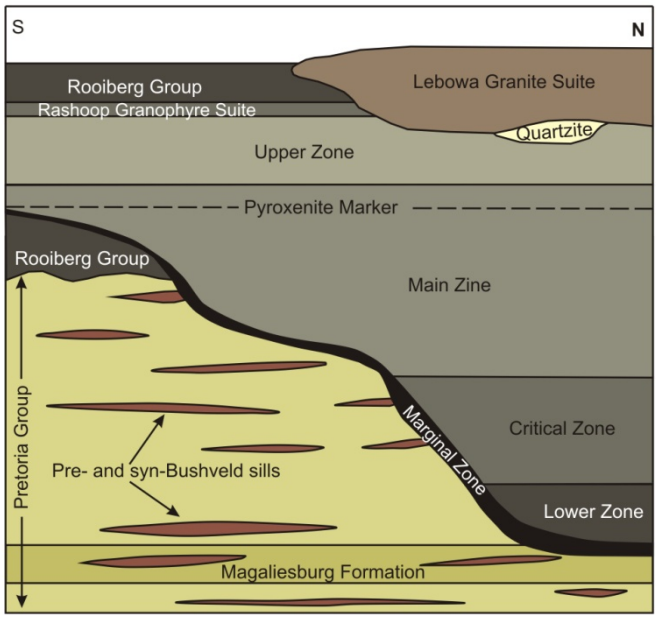

Figure 2.13 Schematic north-south section from Dullstroom to Steelpoort in the eastern limb showing the relationship between the Bushveld Complex and the Pretoria Group and the expansion of the RLS in the magma chamber (after Harmer and Sharpe, 1985).

The term 'layered suite' is attributed to rock types of varying mineralogical composition forming layers, ranging from dunite, pyroxenite and chromitite through norite, gabbro and anorthosite to magnetite and apatite-rich diorite and thus demonstrating a

complete differentiation sequence for a mafic magma (Cawthorn *et al.*, 2006). Layering is present at various scales from millimetres to hundreds of metres. Most of the layers in the eastern and western limbs now dip at shallow angles to the centre of the complex having developed after cooling (Hattingh, 1991).

Due to the different rock types, the RLS is vertically divided into five zones: (1) a noritic Marginal Zone at the base (MaZ); (2) an ultramafic Lower Zone (LZ); (3) an ultramafic to mafic Critical Zone; (4) a gabbronoritic Main Zone (MZ) and (5) a ferrogabbroic Upper Zone (UZ) (Cawthorn *et al.*, 2006). Simplified stratigraphic columns of the western, eastern and northern limbs are presented in figure 2.15.

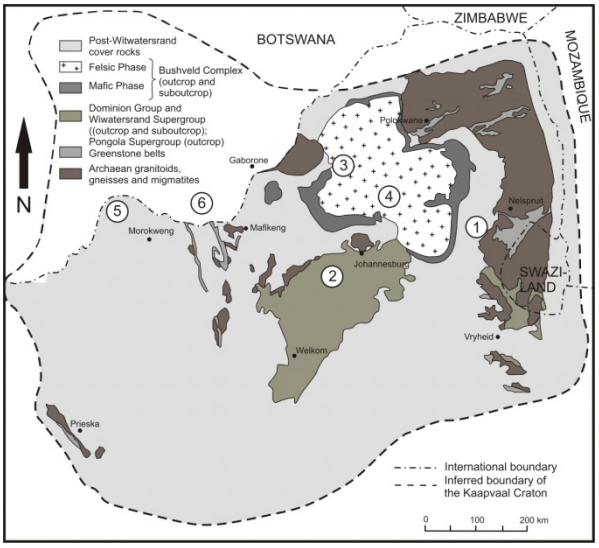

Figure 2.14 Simplified geological map of the Kaapvaal Craton and immediate surroundings showing the localities of the ultramafic-mafic igneous intrusions, which are thought to be coeval with the RLS. Numbers represent (1) Uitkomst complex; (2) Losberg complex; (3) Rhenosterhoekspruit Intrusion; (4) Moloto Intrusion; (5) Molopo Farms complex; and (6) Moshaneng complex (from Anhaeusser, 2006; used with the permission of the author).

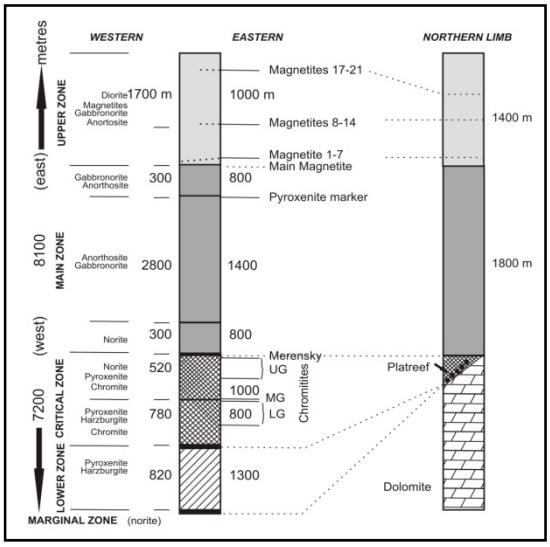

Figure 2.15 Simplified stratigraphic sections for the three main limbs of the RLS of the Bushveld Complex (western, eastern, northern) showing the rock assemblages in the various zones and their approximate thicknesses (modified after White, 1994).

The CZ holds a vast number of (monomineralic) chromitite layers forming huge deposits of chromite. Its base has been defined by Teigler *et al.* (1992) at the level where the appearance of significant olivine in the cumulate rocks is terminated. Owing to their host rock the chromitite layers are assigned to several groups: (1) the Lower Group (LG)

with ultramafic cumulate rocks; (2) the Upper Group containing mafic culumates; and (3) the Middle Group that is made up of ultramafic and mafic cumulate rocks and lies between the LG and the UG. Within the MG the first appearance of cumulus plagioclase marks a major lithological change from an ultramafic to a mafic host rock assemblage. On that basis, the CZ is further subdivided into a Lower and an Upper Critical Zone (Cawthorn *et al.*, 2006).

In general, the LCZ contains nine cyclic units of chromitite, harzburgite and pyroxenite. The chromitite layers are referred to as LG1-7 and MG1-2 (Scoon and Teigler, 1994; Barnes and Maier, 2002). The Middle Group generally contains four chromitite layers (MG1-4). As the first occurrence of plagioclase is between MG2 and MG3, in both the western and eastern limbs (Cawthorn *et al.*, 2006) the layers MG3 and MG4 already belong to the UCZ. In the UCZ eight cyclic units can be found. They differ from the LCZ by the host rock types: instead of harzburgite and pyroxenite, norite and anorthosite are present (Cawthorn *et al.*, 2006). Above the MG chromitite layers three more can be found in the UCZ: the UG1-3. The top of the UCZ is made up of two cyclic units: the Merensky and Bastard cyclic units, which are transitional to the Main Zone.

Besides huge chromite deposits the UCZ hosts two of the world's largest platinum-bearing ore bodies: the UG2 chromitite and the Merensky Reef. The latter is an exception, for it is no chromitite layer but consists of pegmatoidal pyroxenite bound by and hosting chromitite stringers (Hatton and von Gruenewaldt, 1985; Schürmann *et al.*, 1998).

A detailed compilation about the stratigraphy of the RLS from various locations of the western and eastern limbs is given by Hatton and von Gruenewaldt (1985). On the basis of local differences within the stratigraphic column they observed the existence of distinctly different northern and southern facies of the LZ and LCZ. These differences Hatton and von Gruenewaldt (1985) interpreted to be caused by differences in parental magma composition.

2.3.1.1 Connectivity of the limbs

If the limbs of the Bushveld Complex are connected is still strongly debated. Its sill-like character and lithostratigraphic correlation of cores from different localities of both the western and the eastern parts, makes it most likely that a connection exists (Eales *et al.*, 1988; Scoon and Teigler, 1994; Scoon and Teigler, 1995), although variations in thicknesses of the various stratigraphic units and ore grades are present. It also happens that one unit of the 'normal sequence' (see figure 2.15) is missing at another location, as

could be shown for parts of the MZ and the base of the UZ by Wilson (1994) for the Northern Gap in the western limb.

On basis of missing positive gravity anomaly present in the central area of the Bushveld Complex, Cousins (1959) concluded that the two major limbs (i.e. eastern and western) are not connected at depth. However, due to significant petrological similarities, e.g. the occurrence of the transition from LCZ to UCZ, similar PGE grades for the UG2 and the same initial $^{87}Sr/^{86}Sr$ ratios at the base of the Merensky Reef and at the level of the Pyroxenite marker, Cawthorn and Webb (2001) argued that a connection must exist rather than to suggest that the responsible processes could occur at identical horizons in totally separate bodies. To substantiate their theory they reinterpreted gravitational data from Meyer and de Beer (1987) and concluded that an intrusion with the size of the Bushveld Complex caused an isostatic response in the entire crust with a significant subsidence of 6 km into the upper mantle. The intrusion of thick Bushveld granite further increased the subsidence. The positive anomaly normally induced by the mafic rocks is thus balanced by the negative effect of the thickened continental crust, giving a zero anomaly. According to this interpretation it is indeed very likely that the eastern and western limbs are connected at depth.

2.4 Previous work on the cumulate rocks of the Middle Group and their PGE content

In general, published data on the PGE distribution in the silicate rocks and chromitite layers besides the Merensky Reef and the UG2 are rare but increasing research interest in the last ten years has enhanced the totals of published articles. In the following, the most important papers with regard to the Middle Group are summarized. Furthermore, a few articles about the PGE contents of the marginal rocks of the Bushveld Complex have been added, since they are thought to represent the parental magma composition for the RLS (e.g. Davies and Tredoux, 1985).

2.4.1 The chromitite layers

An early paper from Cameron (1969) deals with the texture that can be observed within the cumulate rocks of the Bushveld Complex. For the chromitite layers, he observed two ‘types’ of chromite grains. The most common one occur as a loose-packed arrangement

(“chain texture”) with relatively big grain sizes (0.4 mm), which Cameron (1969) ascribes to postcumulus growth of the grains by diffusion. Chromite grains that are ‘trapped’ in the interstitial phases of a chromitite layer, i.e. pyroxene and plagioclase, appear to have smaller grain sizes (0.1 mm). The author explains that feature with in situ nucleation of the silicate minerals trapping single chromite grains and thus shielding them from further overgrowth. The grain size enlargement is in excess of other grains and therefore Cameron (1969) concluded that >50% of the total volume of the present material must derive from the postcumulus stage. During this process, equilibration between the chromite grains and its surrounding phase, i.e. liquid or silicate crystals, takes place, yielding chromite grains without zonation.

Chromite composition changes from bottom to top of the CZ in the eastern Bushveld (Cameron, 1977). His study included data from chromite deriving from massive chromitite layers as well as from chromite grains occurring disseminated in silicate rocks. In the LCZ, the chromite in chromitite layers show increasing Cr/Fe ratios and Mg# from bottom to top, whereas in the UCZ no systematic change is present. Chromite grains in silicate rocks generally show higher concentrations of Ti and V and lower Mg# and Cr/Fe ratios when compared to those in massive chromitites. Since chromite from massive chromitite being enclosed in bronzite has the same Mg/Fe ratio as chromite in plagioclase, as could not be expected from subsolidus equilibration, the variation in composition of chromite the chromitite layers reflects the fractionation of the magma.

Lots of work on the chromitite layers of CZ of the Western Limb was done by Teigler (1990), Teigler and Eales (1993) and Scoon and Teigler (1994). Their findings are presented below.

Teigler (1990) subdivided the chromitite layers of the Lower and Middle Groups from the western Bushveld Complex geochemically into three groups according to their Cr/Fe ratios, Ti values and PGE content: 1) LG1 - LG4; 2) LG5 - LG7 and 3) MG1 - Merensky Reef chromitite. Group 1 is dominated by high HT-PGE values and especially Ru due to the occurrence of abundant laurite. The PGE content of group 3 is characterized by the dominance of LT-PGE over HT-PGE. Group 2 shows PGE characteristics that are intermittent between groups 1 and 3. With progressive evolution of the melt, the PGE seem to fractionate in the order Os < Ir < Ru < Rh < Pt < Pd. According to this, the uppermost chromitite layers, namely the UG2 and Merensky Reef show the highest Pt and Pd contents. Furthermore, the lack of decreasing HT-PGE content despite increasing LT-PGE content is explained by repeated magma replenishment into the magma chamber.

Teigler and Eales (1993) divided the chromitite layers of the Critical Zone of the northwestern sector of the RLS in the western limb into two types according to their host

rock. Chromitite layers of Type 1 are associated with ultramafic cumulates, whereas Type 2 chromitite layers occur in host rocks with abundant plagioclase cumulates It has to be noticed that this way of classification of the chromitite layers does not correspond with the conventional stratigraphic subdivision for the chromitites into Lower, Middle and Upper Groups. Within the stratigraphic column of the CZ, there is an irregular increase of the total PGE content with height, thus Type 2 chromitite layers display higher PGE contents than the Type 1 chromitite layers. The authors provide a model for the PGE mineralization associated with sulphide-poor chromitites involving mixing of sulphide undersaturated magma with supernatant liquid, which resulted in chromite formation. The nucleation of chromite changed the solubility of sulphur in the hybrid silicate liquid causing the formation of high-temperature PGM, as laurite and Os,Ir,Ru-bearing alloys. Furthermore, Teigler and Eales (1993) do not exclude the possibility of a late-stage postcumulus overprint and redistribution of the original PGE mineralization.

The division of chromitite layers mentioned above is also applied by Scoon and Teigler (1994) for their samples from Union and Brits. They interpret the regular variations of the Cr/Fe and the (Pt+Rh+Pd)/(Ru+Ir+Os) ratios with increasing height as a differentiation trend. According to the authors, the PGE mineralization in sulphide-poor chromitites is a result of chromite control, which is not yet fully understood. The formation of the chromitite layers itself is explained by repeated replenishment of the magma chamber with pristine sulphide-poor magma that mixes with resident liquid that became more and more differentiated with height. As the chromitite layers below the UG2 do not show major isotopic variations, the authors concluded that the magma must have derived from a single magma batch.

The PGE geochemistry of the Lower and Middle Group chromitites of the eastern Bushveld have been studied by Lee and Parry (1988). As the authors before, they noticed an enrichment in the PGE and Au in the chromitite layers over silicate-rich host rocks and an increasing PGE content with height. Although (Pt+Pd+Rh) appears in a greater abundance in the MG chromitites, chromitites with more than 80 vol% chromite are depleted in these elements. Due to the different concentrations of Os, Ir and Ru in the chromitite layers, the authors noticed a possible cryptic variation in laurite, the most common platinum-group mineral and host for these elements.

One of the first studies including sample material from the CZ of the western and the eastern RLS has been done by von Gruenewaldt *et al.* (1986). By analyzing the PGE and chromium content of the individual layers they found out that all the chromitite layers are enriched in PGE when compared to the surrounding silicates. Averaged proportions of the total PGE content for the individual chromitite layers are very similar in the eastern and the western complex. Hence the authors concluded that the conditions of the formation of

the chromitite layers and the PGE content associated with them must have been very uniform. This suggests that both limbs are connected and are the product of one magma chamber. Furthermore, the authors doubt the petrogenetic models for PGE mineralization in chromitite layers based on partition coefficients and the *R*-factor (cf. subsection 2.2.2.1), for these are related to high contents of S, and the chromitite layers of the CZ below the UG2 show extremely low S contents.

2.4.1.1 Platinum-group minerals in chromitite layers

Although publications on the PGE content of the chromitite layers of the Bushveld Complex are manifold, articles on the mineralogy of PGM are rather rare. Studies dealing with this topic mainly focus on the UG2 (McLaren and de Villiers, 1982; Penberthy and Merkle, 1999; Penberthy *et al.*, 2000; Voordouw *et al.*, 2009) or the Merensky Reef (Verryn and Merkle, 1994; Merkle and Verryn, 2003). Reasons for that is probably their importance as major PGE ores and the attempt to increase the recovery of PGE by understanding platinum-group mineralization. However, a detailed description of the PGM of the Middle Group has been done by Merkle (1992) for chromitite samples at Marikana, western Bushveld Complex. He observed laurite to be the dominant PGM that commonly is enclosed by chromite. Cooperite, braggite, Pt-Rh-sulphides and some arsenides also occur. The average grain size of the PGM ranges between 3-5 µm. According to Merkle (1992), the BMS assemblage within the chromitite layers, i.e. chalcopyrite, pentlandite, minor pyrite and pyrrhotite, doesn't reflect a primary magmatic assemblage and thus must have been modified. Hence he concluded, that the PGM occurring as inclusions in chromite, i.e. laurite and Pt-Fe alloys, are of primary origin only, whereas the other probably have undergone redistribution. The latter is confirmed by common indications for hydrothermal activity and thus verifies the possible redistribution of the primary PGE mineralization stated by Teigler and Eales (1993).

Another study from Schoenberg *et al.* (1999) deals with initial $^{187}Os/^{188}Os$ ratios of chromite separates and interstitial phases from chromitite layers of the CZ. Schoenberg *et al.* (1999) found that the Os concentrations of the interstitial phases are by 30 times much higher than those found for the chromite grains, which the authors interpreted to illustrate the presence of highly PGE-enriched interstitial suphides. Since initial $^{187}Os/^{188}Os$ signatures of the cumulus chromite and its interstitial minerals tend to be very similar and the development of their trends is coupled, the source for Os seems to be the same. Hence, Schoenberg *et al.* (1999) suggested that the enrichment of sulphides with PGE is due to a primary magmatic process, rather than being concentrated by fluids.

2.4.2 Silicate rocks

A textural study of anorthosites of the CZ of the eastern Bushveld has been done by Cameron (1969) as part of the study mentioned above. Adcumulus growth is also suggested for plagioclase. The appearance of plagioclase xenocrysts enclosed in bronzite is explained by early postcumulus growth of bronzite trapping settled grains of plagioclase. The same grain size relations that have been observed for the chromite grains apply: 0.12 mm for enclosed plagioclases and 0.35 mm for cumulus plagioclase. Eales *et al.* (1991) observed plagioclase inclusions in orthopyroxene and olivine of the LCZ, western Bushveld. They occur exclusively in parts where the addition of primitive liquid to the crystallizing column can be assumed by means of chemical evidence. According to Eales *et al.* (1991), these inclusions represent feldspar crystals that settled from higher liquid layers in a stratified liquid column, although the compositional range of An (An_{60}-An_{75}) is similar for cumulus and intercumulus plagioclase in the host rocks. However, there seems to be a correlation between the occurrence of these inclusions and chemical reversals in fractionation trends, i.e. increasing whole-rock Mg# from 0.77 to 0.85, similar to findings from Cameron (1980; 1982).

Cameron (1980; 1982) not only studied the chromitites but also the silicate rocks of the entire CZ of the eastern Bushveld by means of modal and electron microprobe analyses. The results indicate that the CZ developed by fractional crystallization, but changes in the enstatite portion of bronzite indicates reversal fractionation in parts of the stratigraphic column. Cameron (1980; 1982) suggests repeated impulses into the chamber to explain chemical variations as well as slow decrease of total pressure to account for the reversals in fractionation. The stratification of the complex is possibly caused by double diffusive convection.

Another study on orthopyroxenes from the LZ and the CZ of the western Bushveld Complex comes from Eales *et al.* (1993). They monitored the minor elements Al, Cr, Ti and Mn within orthopyroxene by electron microprobe analyses. For the LZ and LCZ an increase of the Al content with a contemporaneous decreasing Mg# could be demonstrated, whereas in the UCZ the Al contents decrease with further decreasing Mg#. The amounts of Ti and Mn increase throughout the entire stratigraphic column under investigation; the Cr content decreases. According to the authors the cryptic variations of Al, Cr, Ti and Mn within orthopyroxenes of the CZ are caused by the entry of plagioclase into the paragenesis, which is especially well depicted in the changing trend of Al concentration at the LCZ/UCZ transition.

Comparable studies on the PGE content of the silicate succession within the CZ are rather rare. Lee and Tredoux (1986) worked on PGE abundances in silicate cumulates of

the LZ and the LCZ of the eastern Bushveld Complex. The PGE contents range from 0.1 to 15 ppb (except Pt; 10-130 ppb). Pd was always detected in samples with higher Au contents suggesting a similar chemical behaviour of Au and Pd decoupled from the other PGE. Pt also seems to show trends of different activity as it is the only PGE that does not parallel the $C1_N$ trend of the Merensky Reef. In addition to that, the authors observed that ratios of Pt and Pd are constant throughout the development of the complex up to the Merensky Reef despite the absence of abundant Pt-Pd-sulphides enriching the chromitite layers in Pt and Pd due to their repeatedly attributed chalcophile character.

Maier and Barnes (1999) investigated the silicate rocks of the LZ, CZ and MZ at Union, western Bushveld, in association with the chromitite layers. According to the authors, the sulphur content of the silicate rocks is relatively constant (50-150 ppm), but higher than in the corresponding chromitite layers. PGE concentrations are low. Rh, Pt and Pd increase from the LZ silicates up to the UG2, whereas the contents of Os, Ir and Ru tend to be constant. The study yielded a model for PGE fractionation. The crystallization of monosulphide solid solution incorporates Os, Ir, Ru and Rh, whereas the remaining PGE (Pt and Pd) will concentrate in the residual fractionated sulphide melt. Subsequent physical separation of mss sulphide ore, i.e. precipitation into chromitite layers, from the fractionated sulphide melt probably forming the Pt- and Pd-enriched Merensky Reef may result in a zoned ore body as can be observed in the Bushveld Complex. Alternatively, the authors mention fractional crystallization of PGM from sulphur undersaturated sulphide melt as a process to produce PGE patterns observed in the silicate rocks of the LZ, CZ and MZ.

2.4.3 Marginal rocks and their PGE content

Sharpe (1982) concentrated on the PGE content of the marginal rocks of the Bushveld Complex. He found the PGE concentration to be higher than in basalts and marginal rocks of other layered intrusion. Chondrite normalized PGE patterns show enrichment of Rh and Au relative to Pt and Pd. The author concluded that the rocks from the Bushveld Complex derived from a magma source enriched in noble metals. The sulphur content of the marginal rocks is very low (< 0.5%), similarly to findings of Teigler and Eales (1993) and Scoon and Teigler (1994) for the chromitite layers of the CZ. Sharpe (1982) also determined two major subdivisions of marginal rocks: a pyroxenitic group (B1) that occurs from the base of the Lower Zone to the top of the LCZ, and a gabbroic group from the UCZ on containing several subgroups (B2, B2N, B3 and B3N). From this he suggests that the LZ and the LCZ were derived from liquids of compositions

similar to B1. The UCZ was formed from a residuum of B1 liquid that mixed with a new influx of B2N-type gabbroic liquid.

Another investigation on the PGE and Au contents of the marginal rocks and sills of the Bushveld Complex was done by Davies and Tredoux (1985). Similar to the findings of Sharpe (1982), two magma types can be announced for the formation of the RLS: an early magnesian basaltic magma and a later tholeiitic one. Comparison of chondrite-normalized patterns of the marginal rocks with those of the Merensky Reef, the Platreef and the UG2 led the authors to the conclusion that a magnesian basaltic magma appears to be the parental magma for the Merensky Reef and the Platreef. The pattern of the UG2 reef is comparable to that found for the ultramafic sills, indicating mineralogical similarities.

2.4.4 Parental magmas to the CZ

On basis of a theory to explain chromite formation within large layered intrusions, Irvine (1977) and Irvine *et al.* (1983) suggested the influence of two magmas with very different compositions for layers associated with orthopyroxene or with orthopyroxene and plagioclase, whereas the chromitite layers associated with olivine-rich cumulates could have been formed by mixing of an evolved ultramafic liquid with a newly added primitive one. Many authors (e.g. Kruger and Marsh, 1982; Sharpe, 1985; Lee and Butcher, 1990) confirmed this theory with analyses of the $^{87}Sr/^{86}Sr$ ratio from various rock types of the RLS and determined an ultramafic ("U") MgO- and SiO_2-rich and a tholeiitic ("A") lineage. The former corresponds with the B1 liquid determined by Sharpe (1982) and is thought to be responsible for the formation of the stratigraphically older rocks (i.e. LZ and LCZ) as they comprise almost entirely orthopyroxene. This lineage resembles the high Mg basaltic magma presented by Davies and Tredoux (1985). The plagioclase-rich rock types higher up in the stratigraphy of the RLS derive from tholeiitic melt, termed B2 by Sharpe (1982) and tholeiitic basaltic magma by Davies and Tredoux (1985). Their conclusions are a bit different from the conclusions of Irvine (1977) and Irvine *et al.* (1983), but confirm the existence of two parental magmas during formation of the CZ.

According to Hatton *et al.* (1986), who investigated samples of the MG from the western sector of the eastern limb and determined whole-rock Sr-isotope ratios as well as variations in the Mg/(Mg+Fe) ratios of orthopyroxene, the mixing of the parental magmas is illustrated in the antipathetic relationship of the two ratios: An U-type magma with low Sr_i (0.703 – 0.705) and a high Mg# mixes with an A-type magma having a high Sr_i (> 0.7085) and a low Mg#, which results in the observed pattern.

Kruger (1994) divided the stratigraphic column of the Bushveld Complex into two parts according to his findings on the $^{87}Sr/^{86}Sr$ initial ratios: one part deriving from an 'Integration stage' and another formed during a 'Differentiation stage'. The former reaches from the base of the LZ to the top of the UCZ and is marked by repeated irregular de- and increases of the Sr_i ratio. Increasing $^{87}Sr/^{86}Sr$ values Kruger (1994) attributed to be caused either by contamination of the magma with granophyric roof-rock melt or the magma itself derives from a crustal source region. Decreases in the ratio are thought to be caused by addition of magma from a mantle source. Hence, only one parental magma was present during the formation of the CZ. The constant Sr_i of the MZ the author ascribes to a paucity of both magma addition and contamination unless the added material had the same Sr_i values as the magma already existing in the chamber. Thus, this 'Differentiation stage' is dominated by fractional crystallization.

Later Kruger (2005) revised his findings and suggests the presence of two different parental magmas for the formation of the CZ: a Bushveld LZ (BvLz) magma forming the LZ and the LCZ, and a Bushveld CZ magma (BvCz) responsible for the formation of the UCZ. The former is ultramafic in nature and equivalent to the B1 magma of Sharpe (1982), whereas the BvCz magma has a noritic lineage, but shows a basaltic chemistry.

Sr istotope studies from Kinnaird *et al.* (2002) are based on the determination of the initial $^{87}Sr/^{86}Sr$ ratio obtained from plagioclases being interstitial to chromite and from plagioclases from different silicate host rocks of the CZ. They yielded increasing radiogenity with height in the stratigraphy of the CZ. In contradiction to the silicate host rocks, which show an increase in the Sr_i from the pyroxenite below the LG5 through to the norite below the MG4, the plagioclases being interstitial to chromite show abrupt changes in the isotopic ratio. These remarkable findings the authors interpret to prove the influence of a component of felsic roof-rock melt during chromite precipitation. They concluded that the necessity of two compositionally different parental magmas is doubtful and suggest the influence of one parental magma only (U-type) that mixes with the siliceous roof-rock melt forming at the top of the Bushveld magma chamber (cf. subsection 2.2.1).

The existence of two parental magmas has been also doubted by Teigler and Eales (1996), who investigated the Nooitgedacht (NG) sequence from the Union section of western limb comprising the LZ, the CZ and the lower parts of the MZ of the RLS. Due to the bulk data, i.e. petrographic, mineralogical as well as geochemical data, the cumulates of the NG sequence seem to derive from U-type liquid and its derivates only, since no evidence for the involvement of an A-type parental liquid was found. Only slight changes in the Cr content of orthopyroxene and variations of the Sr isotope ratio indicate slight compositional differences of the parental liquids. Hence Teigler and Eales (1996) concluded that with Sr_i values ranging between 0.7047 to 0.7060 for the NG sequence a

clear isotopic evidence for the involvement of A-type magma in the formation of the RLS below the Merensky Reef is not well pronounced. However, the authors agree with findings of Eales *et al.* (1990) that the increasing Sr_i throughout the CZ suggests a progressive mixing of liquids with a higher Sr_i, or a change in the mantle source.

McCandless *et al.* (1999) have been the first who presented initial $^{187}Os/^{188}Os$ ratios for chromite separates from chromitite layers of the CZ gathered from Brits, western Bushveld, and from Steelpoort and the Winterveld Mine, eastern Bushveld. On the basis of their data the authors propose a crustal assimilation model whereby high Os concentrations and initial $^{187}Os/^{188}Os$ ratios were incorporated into the RLS during its formation. Since the ratio increases with stratigraphic height and shows an inflection to even higher values at the LCZ/UCZ boundary, McCandless *et al.* (1999) suggest an assimilation of about 5% mafic granulitic lower crust into tholeiitic magma to explain the observed radiogenic values. Additionally, with the help of the Pd/Ru ratio the authors give evidence for the source of the PGM in the chromitites. As the relative shift in the pattern of this ratio for the chromite and its granular fraction is very similar from one layer to the next, the source of the PGM enclosed in the chromite grains, i.e. laurite, is the same as the one precipitating PGM as intergranular phases. According to the authors this proves that the PGM within the chromitite layers are unaffected by later deuteric and/or hydrothermal fluids.

3. Sample material and analytical methods

3.1 Sample material

Sample material and access to the outcrops were kindly provided by Xstrata Alloys. It derives from the diamond drill core HEX10 that was drilled during the Helena Drilling Project of Xstrata on the farm Helena 6JT in the eastern Bushveld, some 40 km northwest of Lydenburg, Mpumalanga Province (Fig. 3.1). The drillhole was drilled on surface. The core HEX10 has been chosen because the whole Middle Group is present. Figure 3.2 shows the core log of the core HEX10 and sampling positions of the silicate rocks. For geochemical analyses of the chromitite layers, three quarters of core HEX10 has been used. For the investigation of the silicate partings occurring between the chromitite layers only half a core has been used. A detailed explanation about how the core has been used is described below. Remains of the core stayed on site.

3.1.1 Sampling and sample preparation

The core HEX10 was sampled between the drilling depths 119 and 160 m. Because the chromitites and silicates have been sampled at various times and have been prepared with different methods, the preparation of the corresponding core pieces is discussed separately below.

Chromitite samples: The chromitite samples were sampled and analysed for the by Xstrata. Therefore, only little is known about the analytical procedures used. The data and thick polished sections were made available for this study.

51 chromitite samples were taken from top to bottom of the core and numbered as follows: HEX10/01 for the uppermost sample and HEX10/51 for the lowermost one. Each sample has a thickness of 12 to 17 cm (see appendix A, table A-1). One quarter has been used to prepare thick polished sections. The 2nd quarter has been used to analyze the chromitites for their major element contents, some minor and trace elements as well as for the PGE and Au. A third quarter has been crushed and milled by the author herself for the determination of the sulphur content and XRD analyses. The same sampling positions and intervals were used, as described above (see appendix A, table A-2).

Samples of the silicate host rocks (pyroxenite, anorthosite, norite): The 42 silicate rock samples basically have been taken from the hanging and footwalls of the chromitite layers. Additionally, fine sampling of the silicate interlayers between the MG2

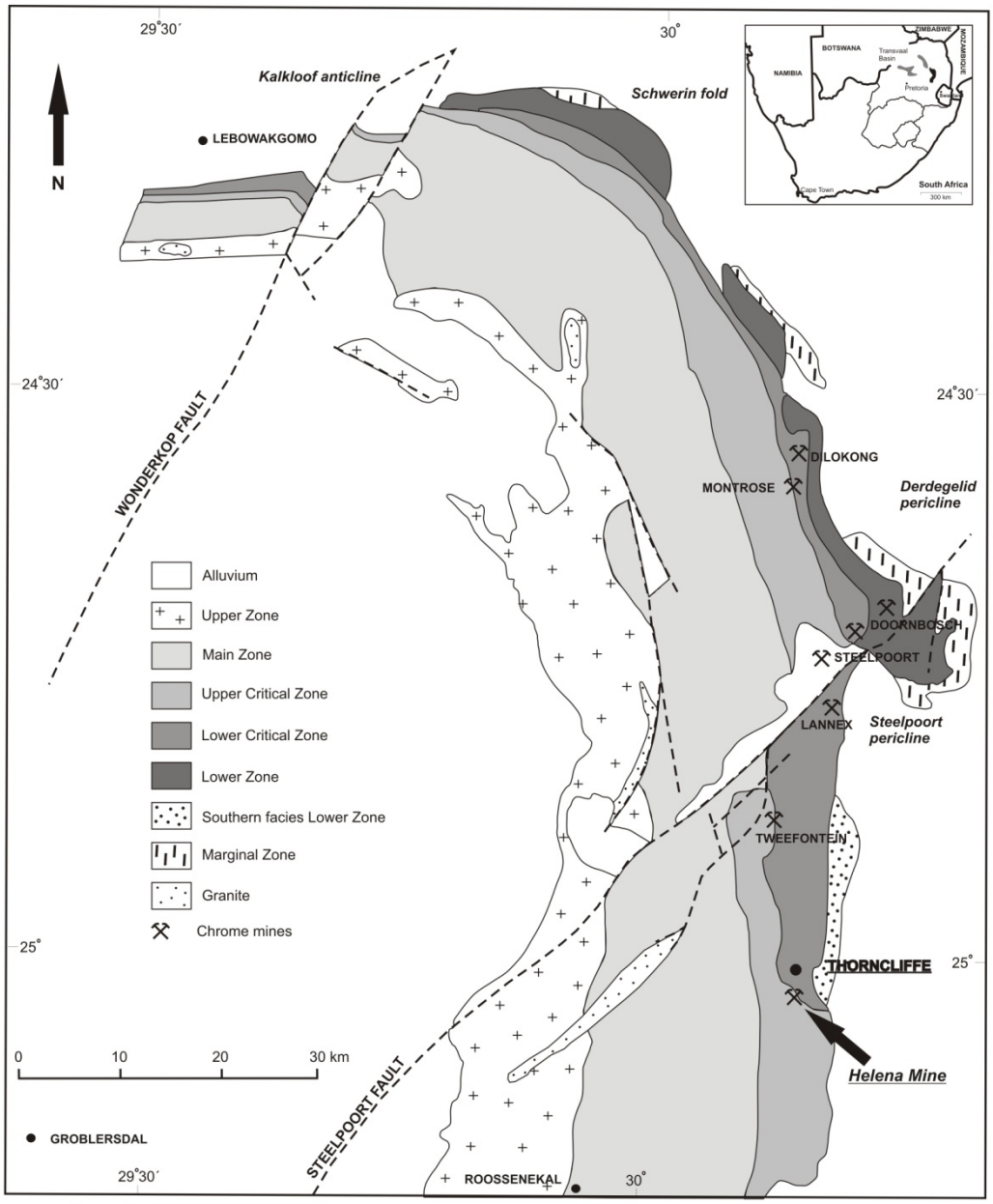

Figure 3.1 Geological map of the eastern Bushveld Complex with an arrow indicating the origin of core HEX10 (from Viljoen and Schürmann, 1998).

and MG3 (8 cm intervals) as well as between the MG4A and MG4B chromitite layers (interval of 15 cm) has been done. It was carried out by Xstrata a few months after the first sampling. The numbering of samples follows the stratigraphy from bottom to top of the core. An exception is the fine sampling of the MG4A pyroxenite, where the numbering runs from top to bottom. The sample positions are shown in figure 3.2.

After the preparation of 31 thin polished sections (appendix A, table A-3), the rest of the samples have been crushed with a hammer by hand. To avoid contamination with the

steel of the hammer plastic bags have been used, as the silicate rocks are thought to contain chromite and especially PGE in traces only. For milling, an agate pot has been used. Because of the hardness of the rocks, ethanol had been added for milling and was removed through vaporization at 80˚C.

Although the number of samples as well as the data set acquired with the individual methods described below seems to appear small, the PGE and chromitite geochemistry in the same stratigraphic sequence at other locations of the Bushveld Complex (e.g. Lee and Parry, 1985; von Gruenewaldt *et al.*, 1986; Lee and Tredoux, 1986; Eales *et al*., 1993; Scoon and Teigler, 1994) show little variation only, and thus point out that the data set acquired and presented during this study is indeed adequate for scientific discussion. Furthermore, the data set presented in the work in hand isn't based on a particular mine, but the interpretation is rather presented in the scope of a regional study.

3.2 Analytical methods

3.2.1 Optical microscope

The optical microscope was used for textural and petrographic description and modal analyses of the chromitites as well as the silicate rocks. The thick polished sections of the chromitites were investigated under reflected light and the thin sections of the silicate rocks under transmitted light. Photographs were taken by using the Microscope BX51 from Olympus coupled with the digital camera Altra 20.

The modal analyses for the chromitite samples were carried out by using the analySIS®FIVE software of Olympus. On the basis of different grey scales, the software generates a false colour image and calculates the amount of each colour in one image.

For the silicate samples the point counting method for modal analyses was applied.

3.2.2 X-ray fluorescence (XRF) analyses

To determine the whole rock major element content as well as the amount of minor and some trace elements the samples have been analyzed by XRF.

The chromitite analyses were carried out by Xstrata themselves. Hence, no information about the standards used is available.

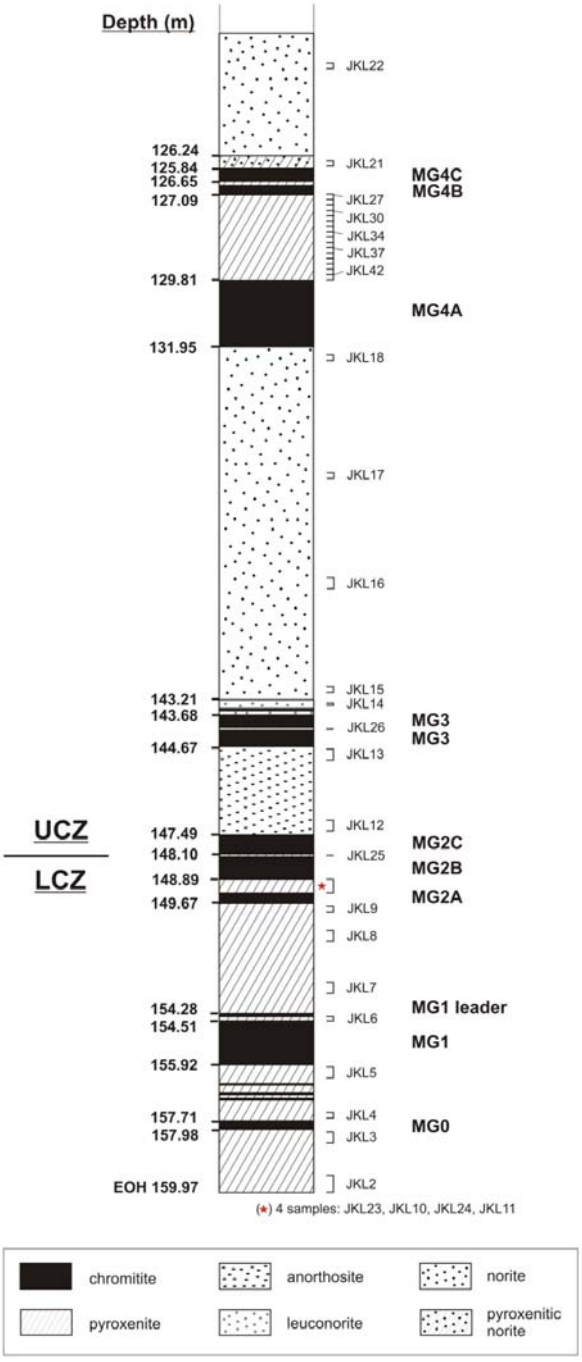

Figure 3.2 Core log of the Middle Group from core HEX10 (MG sequence). Sampling positions of the silicate layers are indicated. Depths are given in meters below surface.

The analysis of the whole rock geochemistry of the silicate rocks was done at the Department of Geology at the UFS in Bloemfontein, South Africa, using the Axios PANalytical WD X-ray spectrometer. The spectrometer works with the SuperQ Version 4 Software and an accelerator voltage of 60 kV in maximum. First, the rock powder of the silicate samples have been used to prepare fusion discs using 0.28 g of sample material

and 0.02 g Li-borate as a flux to determine the major element oxides SiO_2, Al_2O_3, Fe_2O_3, MnO, MgO, CaO, Na_2O, K_2O, TiO_2 and P_2O_5. After the determination of the loss of ignition pressed pellets have been performed by mixing 8 g of rock powder with 2 g of Hoechst Wachs C micropowder ($C_{38}H_{76}N_2O_2$) from Merck. The pellets were analysed for minor and trace elements (Sc, V, Cr, Co, Ni, Cu, Zn, Ga, As, U, Br, Rb, Sr, Y, Zr, Nb, Mo, Ba, Tl, Pb, Th) as well as for Na_2O only. The latter is necessary, since the flux used for the preparation of fusion discs contains Na, and a correction in the major element content for Na_2O has to be done. In addition to that, the content of Cr_2O_3 has been determined with an extra measuring programme on the pressed pellets, as the chromitites are too refractory for the flux used for the preparation of glass discs. The data have been calculated H_2O-free and are Na_2O and Cr_2O_3 corrected. Standards used during XRF analyses are listed in table A-4 in appendix A.

3.2.3 X-ray diffraction (XRD) analyses

XRD analyses were carried out on 13 chromitite samples (appendix A, table A-2) at the Department of Geology at the UFS, using a D 5000 BRUKER AXS diffractometer. It was done to get information about the nature of silicate minerals co-precipitated with chromite in the chromitite layers, as only thick polished sections have been available. The settings of the machine were as follows:

Accelerating voltage: 40 kV	Scanning area: 5-70˚
Step size: 0.02˚	Time: 2 s

The interpretation of the data was carried out with the software X'Pert HighScore Plus at the department of Earth Sciences at the Martin-Luther University (MLU) Halle-Wittenberg in Germany.

3.2.4 Sulphur determination

These analyses were carried out at the Council for Geoscience in Pretoria to determine the sulphur content of the chromitite layers, using an Eltra CS 800 double dual range. 19 samples with the highest PGE contents have been chosen (Tab. A-2 in appendix A), as the first analyses with the mineral liberation analyzer (MLA) showed a

dominance of PGM being sulphides and thus high PGE content could indicate high amounts of S.

In an Eltra analyses a solid sample, milled to less than 75 micron, is combusted in a stream of oxygen. Carbon and sulphur present as carbonate, graphite, organic carbon and sulphate, sulphide or elemental sulphur are converted to CO_2 or SO_2, respectively. These gasses are then detected using four infrared detectors (detection method: solid state infrared absorption). The constituents of an unknown sample can then be identified and measured by comparison with calibration standards. A sample size of 0.2 g is normally used. The analysis time is between 40 to 50 seconds. Lower detection limits for sulphur are 0.1 ppm S at 500 mg sample.

3.2.5 Inductive coupled plasma mass spectrometry (ICP-MS) analyses

The author applied the ICP-MS to 21 samples of the silicates at the School of Earth and Ocean Sciences at the University of Cardiff in Wales (see appendix A, table A-3). The ICP-MS machine used is a ThermoElemental X-series, which was chosen for its low detection limits (typically in the ppb and ppt range) and high sensitivity. The PGE and Au contents have been pre-concentrated during NiS fire assay in a furnace at 1100˚C. The resulting sulphide bead was then digested in 150 ml HCl on a hot plate. To eliminate Ni and Cu and produce a final precious metal concentrate, 1 ml of Te chloride solution as well as 3 ml of tin chloride solution was added. The developing black precipitate collected the PGE and Au that has gone into solution during the digestion. This precipitate has been separated from the solution by filtering under vacuum through a 0.45 pore size membrane filter. The membrane filter was then placed into a Teflon vial. Four millilitres of concentrated HCl and 3 ml of concentrated HNO_3 have been added to digest the filter as well as the precipitate. Once the digestion was complete, each solution was spiked with 1 ml of Tl used as an internal standard and finally analyzed by ICP-MS.

The following isotopes were analyzed: ^{193}Ir, ^{99}Ru, ^{101}Ru, ^{103}Rh, ^{195}Pt, ^{105}Pd, ^{106}Pd, ^{197}Au. The standards used are WITS-1 and WPR-1.[5]

To monitor the accuracy of the analyses, six samples have been analysed twice (JKL5, JKL10, JKL15, JKL26 and JKL39). The precision of the analyses expressed by means of the relative standard deviation (RSD) for the PGE as well as total reagent

[5] ***WITS-1*** is a standard obtained from silicified komatiite originating from the Komati River near Baberton, South Africa. It is used as a low concentration noble metal standard (Tredoux and McDonald, 1996).
WPR-1 is a reference material for an altered peridotite containing Au and the PGE. It derives from the Wellgreen Complex, Yukon Territory, Canada (Natural Resources Canada, 2011).

blanks and the reproducibility of the data are listed in table 3.1. Detection limits are summarized in table 3.2.
Further information on the described procedure can be taken from Wilson *et al.* (1989).

Table 3.1 Total PGE in blanks, the standard deviation (SD) as well as the RSD for the individual PGE isotopes analysed. Values of SD and RSD are averages from six duplicate analyses.

	^{188}Os	^{189}Os	^{193}Ir	^{99}Ru	^{101}Ru	^{103}Rh	^{195}Pt	^{105}Pd	^{106}Pd	^{197}Au
Total PGE in blanks	0.026	0.026	0.069	0.223	0.226	0.151	1.362	1.192	1.215	0.248
SD	0.066	0.065	0.090	0.272	0.270	0.123	1.062	0.488	0.539	0.041
RSD (in %)	1.552	1.183	0.865	0.714	0.659	0.598	0.753	0.560	0.570	0.781

Table 3.2 Detection limits of the ICP-MS for PGE and Au.

element	detection limit (ppb)
Os	0.005
Ir	0.008
Ru	0.010
Rh	0.006
Pt	0.010
Pd	0.010
Au	0.005

For the analysis of the content of trace elements, the PGE and Au, Xstrata did ICP-MS analyses on the chromitite layers themselves. The PGE were pre-concentrated with NiS fire assay. Standards used for PGE analyses are SARM76 (PGE-containing Merensky Reef material), SARM65 (PGE-bearing UG2 chromitite) and HGMN[6] (see also Tab. A-6 in appendix A).

3.2.6 Analyses with the scanning electron microscope (SEM)

The analyses were carried out at the Centre for Microscopy at the UFS in Bloemfontein using a Shimadzu SSX-550 scanning electric microscope and energy

[6] Reference SARM76: MINTEK (2011b), reference SARM65: MINTEK (2011a).

dispersive X-rays (EDX). Nine carbon coated thick sections of the chromitite layers have been investigated for their chromite chemistry as well as some PGM and titanium oxide inclusions (see appendix A, table A-2). In addition to that, the composition of some BMS and silicate inclusions in chromite grains has been analyzed. Analytical settings for the EDX were 15 kV beam voltage and a count time of 120 s.

The same settings have been applied for 16 thin sections of the silicate rocks (see appendix A, table A-3) determining accessory chromite chemistry. In addition to that, analyses on the composition of pyroxenes and plagioclases have been carried out.

Mineral data obtained with the SEM-EDX are generally not as correct as data from other spectroscopic methods, e.g. the electron microprobe (EMP) or the LA-ICP-MS. Table 3.3 exemplarily compares Al_2O_3 values of chromite obtained with the SEM-EDX and the LA-ICP-MS during this study as well as Al_2O_3 concentrations of plagioclase and the MgO content of orthopyroxene gained from SEM-EDX and EMP analyses. It shows that the values are quite similar and also reflect the same tenor upward the stratigraphic column of the MG sequence. Due to that, the SEM-EDX has been found to be a useful tool to analyze changes in the major element content of minerals and hence the data were used for plots and the description of trends during this study.

3.2.7 EMP analyses

Besides SEM-EDX analyses, six polished thin sections of the silicate host rocks were analyzed with the EMP (see appendix A, table A-3). The measurements took place at the Department of Mineralogy, Crystallography and Materials Science at the university of Leipzig, Germany. The microprobe works with five spectrometers using TAP, PET and LiF crystals, with which the following elements have been monitored: Na, Mg, Al, Si, K, Ca, Ti, Cr, Mn, Fe. The analytical settings were 15 kV beam voltage and 20 s measurement per element. The raster length was 10 µm. A list of standards used as well as their composition is added to appendix A, table A-5.

The analyses were mainly done to determine the exact major element contents of the pyroxenes and the plagioclases and to get information about the trace element content of the pyroxenes.

Table 3.3 Comparison of the Al_2O_3 content of chromite and plagioclase as well as the MgO content of orthopyroxene obtained with different analytical methods. *Px*: pyroxenite; *no*: norite; *an*: anorthosite. All values are given in wt%.

		chromite		**plagioclase**		**orthopyroxene**	
		SEM-EDX	LA-ICP-MS	SEM-EDX	EMP	SEM-EDX	EMP
layer	sample	Al_2O_3	Al_2O_3	Al_2O_3	Al_2O_3	MgO	MgO
MG4C	HEX10/01	13.85	13.35	-	-	-	-
MG4A_px	JKL42	-	-	33.45	30.31	30.53	30.98
MG4A_px	JKL34	-	-			32.14	31.73
MG4A	HEX10/11	18.35	18.67	-	-	-	-
MG3_no	JKL18	-	-	35.43	32.25	34.01	31.46
MG3	HEX10/23	16.03	16.23	-	-	-	-
MG2C_an	JKL13	-	-	32.87	32.27	-	-
MG2C	HEX10/28	17.21	17.37	-	-	-	-
MG2B	HEX10/37	17.20	17.35	-	-	-	-
MG2A_px	JKL10	-	-	-	-	34.04	31.45
MG2A	HEX10/38	16.15	16.10	-	-	-	-
MG1_px	JKL09	-	-	34.13	32.19	33.28	29.00
MG1	HEX10/43	16.09	16.01	-	-	-	-

3.2.8 LA-ICP-MS analyses

The LA-ICP-MS analyses were carried out using a New Wave Research UP213 UV laser system coupled to a Thermo X Series ICP-MS at the School of Earth and Ocean Sciences at the University of Cardiff, UK. The ICP-MS is coupled to a Merchanek 213 nm UV laser for laser ablation analysis of solid samples. Ablations were performed under He in the laser cell and the resulting vapour was combined with Ar before delivered into the ICP-MS. All the analyses executed used a 40 µm laser spot at a frequency of 10 Hz. Typical acquisitions lasted 60 s, with 23 s of gas blank measurement followed by 37 s ablation. A detailed description of the method is described by Dare *et al.* (2009).

The following elements were monitored: Mg, Al, S, Ti, V, Co, Ni, Cu, Zn, Ga, As, Sb, Te, Bi, the PGE and Au. Mg was used as an internal standard to calculate the contents of MgO, Al_2O_3 and TiO_2 in wt% and some trace element contents (V, Co, Ni, Zn, Ga; in ppm).

The LA-ICP-MS analyses have been done: (1) to determine possible changes in the chemical composition in single chromite grains, and (2) to look for distinctive PGE peaks, possibly representing PGE clusters.

3.2.9 Analyses with the MLA

To get a first overview of the PGM content and their sizes, nine polished section of chromitite samples (HEX10/03, -09, -17, -22, 34, -40, 41, -46, -51) were analyzed by using the MLA at MinTek, Johannesburg, South Africa.

Due to these preliminary studies two sets of six and four samples (see appendix A, table A-2) have been chosen to be analyzed in detail at the Anglo Research Lab at Crown Mines, Johannesburg, South Africa, and at the Technical University Bergakademie Freiberg, Germany, to determine the following parameters:

- Distribution of PGMs
- PGM grain size distribution
- PGM grain mode of occurrence
    - PGM association with BMS
    - PGM association with gangue (silicates and oxides)
- PGM grain liberation index

Prior to the MLA analyses, a hydro-separation has been used to concentrate the PGM using the strong differences in the densities of the individual minerals. The hydro-separator (Fig. 3.3) worked in the following way. A trapeze shaped sheet of metal is shaken in two horizontal directions by a small engine imitating movements of waves. At the narrower upper end the sample is placed under a permanent water flow, which is separating the sample material according to its densities. Thus, the silicates (densities ~3 g/cm^3) should separate from chromite (density ~ 5 g/cm^3) very easily and settle 'downstream' remaining the chromitite grains in the upper part of the metal sheet. That this kind of separation works very well is demonstrated in figure 3.4, exemplarily showing the separation result of the MG2C anorthosite (sample JKL14).

Since the PGM are thought to have extremely high densities (5.7-19.3 g/cm^3; Cabri, 2002), they should also settle within the uppermost part. With regard to these thoughts, every sample was thus separated into three aliquots: (1) a chromite-rich part; (2) a mixture of chromite and silicate minerals; and (3) a silicate-rich part (A1, A2 or A3 in Tab. 3.4, respectively).

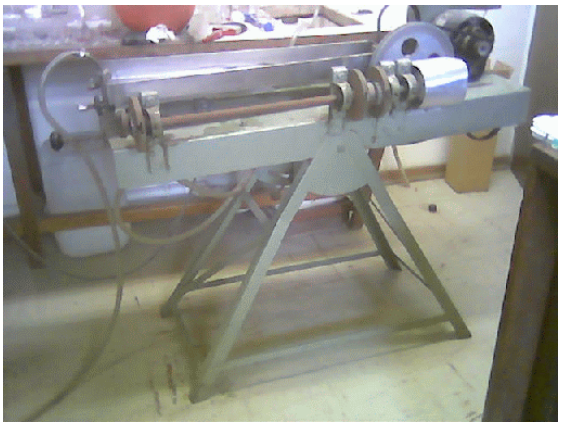

Figure 3.3 Hydro-separator.

Figure 3.4 Chromite (black) separated from plagioclase (sample JKL14).

Table 3.4 MLA samples separated by hydro-separation. *X: no data available. 'Loss'* indicates the amount of lost material during hydro-separation.

			Mass of parts (in g)				
sample	**Unit**	**Rock type**	**A1**	**A2**	**A3**	**Total (g)**	**loss (g)**
HEX10/02	MG4C	chromitite	35.8	39	33.1	107.9	18.5
HEX10/08	MG4A	chromitite	36.8	34	16.9	87.7	12.9
HEX10/15	MG4A	chromitite	13.9	36.3	34.3	84.5	12.9
HEX10/21	MG3	chromitite	46.8	29.3	10	86.1	5
HEX10/27	MG4	chromitite	44.1	44	16.3	104.4	5
HEX10/30	MG2C	chromitite	60.1	30.1	9.4	99.6	5.2
HEX10/31	MG2C	chromitite	31.4	35.7	25.5	92.6	14.1
HEX10/32	MG2B	chromitite	41.1	20.8	10.9	72.8	3.1
HEX10/38	MG2A	chromitite	39.4	72.6	38.7	150.7	16.4
HEX10/41	MG1	chromitite	41.4	49.9	30.8	122.1	15.6

Empirical values showed that the PGM tend to be associated with the silicate fraction, rather than the chromite fraction (pers. comm. Robert Schouwstra, Anglo Research Lab), which is most likely due to their small grain size. In addition to that a pre-examination of the chromite-rich parts at the MLA at the University of Johannesburg yielded in the absence of PGM in the chromite fraction. Thus, the silicate-rich part has been used for MLA analyses.

Two splits from the 'concentrated' silicate fraction of each sample have been prepared, one of them used for the preparation of ten MLA block mounts with a diameter of 30 mm each. The other split was kept in reserve in case of any mishaps.

As the PGM in the MG tend to have extremely small grain sizes (3-5 micron, cf. Merkle, 1992), the grain size fraction <75 micron of each sample was used to prepare block mounts. The mounts were analyzed until 100 PGM-bearing particles were found. If less than 100 particles per sample were found, the mounts had to be re-ground and measured again until at least 100 particles were detected and analyzed. The author decided to work on liberated samples to make an estimation about the liberation index of the PGM from their host rock, which is not possible when one uses in situ analyses.

The type of measurement used for PGM analyses was the Schwoustra analysis (SPL-DZ) (Fandrich *et al.*, 2006). It is based on the *Sparse Phase Liberation analysis* (SPL), during which BSE images are searched for particles containing phases of interest, i.e. PGM. The search is carried out by using a BSE grey scale range. For identification of PGM Cu-grey obtained from the Cu standard of the machine was used as the the lower level of brightness. When a PGM particle has been identified an X-ray analysis is performed on it. DZ stands for *double zoom* and says that the image capture is repeated at a higher resolution on particles of interest, and the SPL analyses is then repeated at the higher resolution. The measurements have been carried out at an accelerating voltage of 25 kV with a spot size of 6 µm at a 376- fold magnification. Working distance was 11 mm.

For the so-called online processing of the analyses the *MLA Process Tool 2008* was used. First, laurite is excluded from the found PGM particles, as it is commonly locked in chromite grains and therefore not recoverable (cf. Merkle, 1992). After that the correctness of identification of the remaining PGM is examined by SEM-EDX analyses.

To interpret the obtained data, the *MLA DataView 2009* software as well as the *MLA Imageview 2008* software has been applied. For detailed description of the method of PGM analyses it is referred to Gu (2003) and Fandrich *et al.* (2006).

3.2.10 Calculation of Mg-number (Mg#) and the anorthite content (%An)

The calculation of the Mg# of orthopyroxene, clinopyroxene and chromite has been carried out by calculating the proportions of cations from chemical analyses (SEM-EDX, EMP). The amounts of Fe^{2+} and Fe^{3+} have been determined by using a method described by Ulmer (2001). The Mg# of the minerals mentioned above has then been calculated as cation ratio $Mg^{2+}/(Mg^{2+}+Fe^{2+})$.

The whole-rock Mg# was calculated using the major element oxides from XRF analyses ($MgO/(MgO+FeO_{tot})$), for which the measured Fe content has been recalculated to total FeO.

The proportion of the An content in plagioclase was calculated using the norm composition of albite (11.84% Na_2O, 19.4% Al_2O_3, 68.75% SiO_2) and anorthite (20.2% CaO, 36.6% Al_2O_3, 43.2% SiO_2) involving the corresponding molecular weights of their components. For the determination of the %An content these norm compositions have then been put into relation to the results of the geochemical analyses (SEM-EDX, EMP). Thus the %An content is calculated by

$$\%An = \Delta Ab_N / (\Delta An_N + \Delta Ab_N),$$

where ΔAb_N is the difference of the SiO_2 content of norm albite and the SiO_2 content of the plagioclase analyses, and ΔAn_N the difference of the SiO_2 content of norm anorthite and the SiO_2 content of the plagioclase analyses.

3.3 Statistics

Since the data sets of mineral compositions obtained with the different analytical methods are not normally distributed and also contain numerous outliers (cf. appendix B), Spearman rank correlation matrices have been calculated to identify statistically significant correlations between pairs of element oxides.
The Spearman rank correlation coefficient r_S is calculated as follows:

$$r_S = 1 - [6*\Sigma D^2/n(n^2-1)],$$

where *D* is the difference in ranking between the x- and y-values and *n* is the number of pairs (Rollinson, 1993).

The significance of a correlation observed between x and y is described in different levels of significance, i.e. the 0.05 or the 0.01 level. If the correlation coefficient r for a single data pair falls within these levels, the probability is high that the observed relationship holds for the entire data set. For the calculation of r_S the two-sided test has been used, since the correlation coefficient of the data set $\rho \neq 0$. Statistic significance is indicated by one star for the 0.05 level (*) or two stars (**) for the 0.01 level behind the correlation coefficient (e.g. r_S= 0.876**). These levels are synonymous with 2σ and 3σ.

There are different intervals in which the strength of a correlation is divided. For this study the separation presented in table 3.5 is used (from Eckey *et al.*, 2008). The adjectives “positive” or “negative” only describe the direction of the trend the correlation shows.

Table 3.5 Strength of correlation for r_S (Eckey *et al.*, 2008).

$0 \leq r_S < 0.1$	no correlation
$0.1 \leq r_S < 0.4$	weak correlation
$0.4 \leq r_S < 0.8$	medium strength correlation
$0.8 \leq r_S < 0.9$	strong correlation
$0.9 \leq r_S < 1$	very strong correlation
$r_S = 1$	absolute correlation

4. Results

4.1 The stratigraphy of the Middle Group, eastern Bushveld Complex, yielded from core HEX10

There are four major chromitite layers in the core HEX10, namely MG1, MG2, MG3 and MG4. Due to the occurrence of thinner sub-layers, the MG2 and MG4 chromitites are further subdivided into MG2A, MG2B, MG2C or MG4A, MG4B and MG4C, respectively (Fig. 4.1). The core HEX10 extends from approximately 22.2 m above the UG1 to 2 m below the MG0 over a vertical distance of 160 m below surface. As only the MG is part of this study, the sampling was restricted to the lowermost 50 m of the core.

The MG chromitites occurring within the LCZ, namely the MG0, MG1, MG2A and MG2B chromitites, are hosted by pyroxenite only (Fig. 4.1, Fig. 4.2). The bottom of the MG2C chromitite layer represents the transition zone from the LCZ to the UCZ, and all chromitite layers above that point belong to the UCZ. The MG2C chromitite is sandwiched between a pyroxenitic footwall and an anorthositic hanging wall. The MG3 chromitite is hosted by anorthosite to its bottom and leuconorite to its top, followed by a thick pile of norite up to the footwall of the MG4A chromitite. Within the MG3 a thin (7 cm thick) pyroxenitic band occurs. The uppermost chromitite layers of the MG, i.e. the MG4B and MG4C chromitite layers, are hosted by pyroxenite. Contacts between chromitite layer and overlying silicate layer are sharp, whereas those to the silicate layer in the footwall is rather gradational. Detailed information about thicknesses, lithology and origin of samples are listed in table A-1 in appendix A.

Each chromitite layer represents the base of a cyclic unit; thus nine cyclic units are developed in the core HEX10. The ideal composition of a cyclic unit comprises a chromitite layer at its base, followed by a sequence of pyroxenite, norite and anorthosite (Jackson, 1970; 1971). As figure 4.1 shows, only the MG4C unit shows such an ideal succession. The cycles below contain two or three rock types only, but in varying compositions.

Although all the rocks of the MG are cumulate rocks (see section 4.2), they are named according to their mineral content by taking into account the IUGS classification of igneous rocks (Le Maitre, 2002) as well as the traditional Bushveld nomenclature (Wager and Brown, 1968). As a consequence, the cumulus rocks of the MG can be assigned to four major rock types: chromitite, pyroxenite, norite and anorthosite. In the following, the stratigraphy of the MG from core HEX10 is described in detail from bottom to top. With

regard to the term *cyclic units*, the description is subdivided into the sub-units MG0 to MG4C with the corresponding chromitite layer as the name giver.

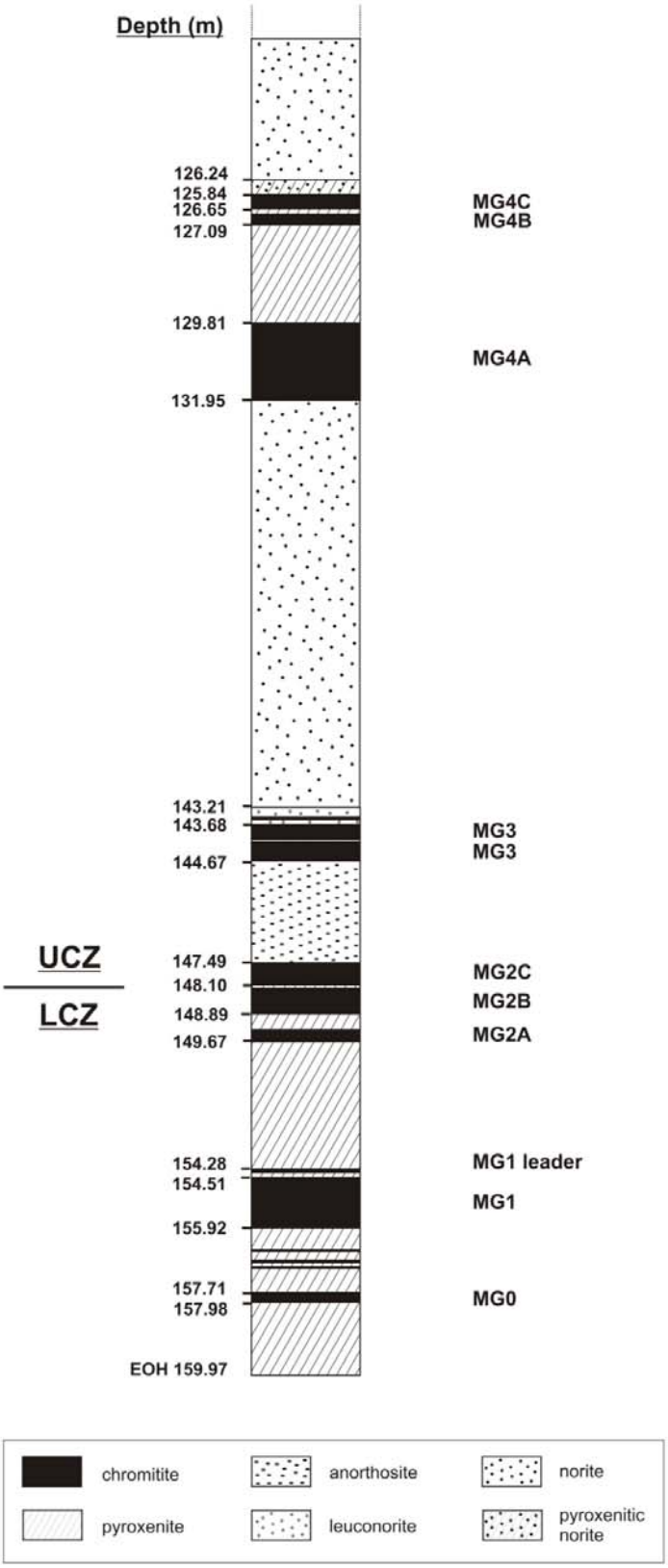

Figure 4.1 Stratigraphy of core HEX10 (MG sequence).

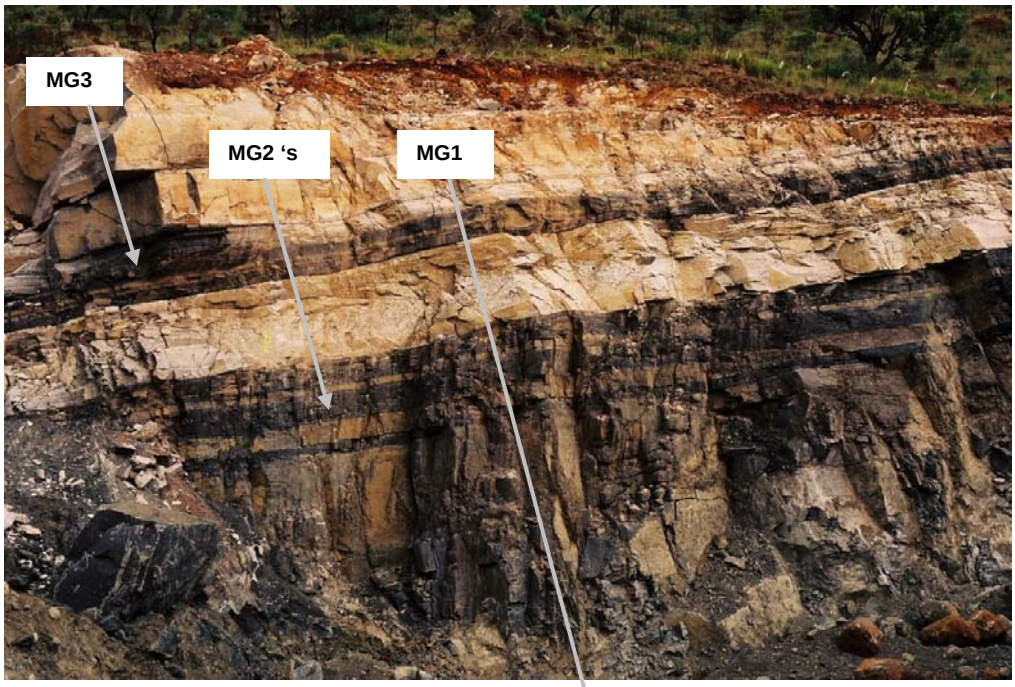

Figure 4.2 Section of the open pit of the Helena mine showing a part of the stratigraphy of the MG. MG1 is at the bottom of the pit. The transition LCZ/UCZ is markedly illustrated by change in color of the silicate rocks (arrow).

4.1.1 The Lower Critical Zone

MG0 unit: The MG0 chromitite layer is 0.27 m thick and made up of alternating bands of chromitite and pyroxenite. Its hanging wall is a pyroxenite of 1.79 m thickness that is cut by three thin chromitite stringers of varying thicknesses (0.03 – 0.11 m). The footwall of the MG0 chromitite is also a pyroxenite, which is part of the uppermost cyclic unit of the Lower Group.

MG1 unit: With a thickness of 1.41 m, the MG1 chromitite layer is the second thickest in the MG sequence after the MG4A. The pyroxenite in its hanging wall has an overall thickness of 4.67 m. It hosts the 10 cm thick MG1 leader 1, which represents the precursor of the MG1 chromitite. The MG1 leader 1 is a disseminated chromite band occurring 0.13 m above the MG1. 2.82 m further up another disseminated chromitite band, the MG1 leader 2, appears having a thickness of 7 cm. Within the thick pyroxenite succession a fracture and two quartz-filled veins have been observed. The contact to the pyroxenite in the footwall of the MG1 chromitite is sharp (Fig. 4.3).

MG2A unit: The chromitite layer at its base is 0.34 m thick and therewith the thinnest of all the chromitite layers in the MG. On its top a pyroxenite of 0.44 m thickness can be found (Fig. 4.4).

Figure 4.3 A trench in the eastern Bushveld near Lydenburg showing the sharp contact between the MG1 chromitite layer and the pyroxenite in its footwall. The short site of the scale is 6 cm.

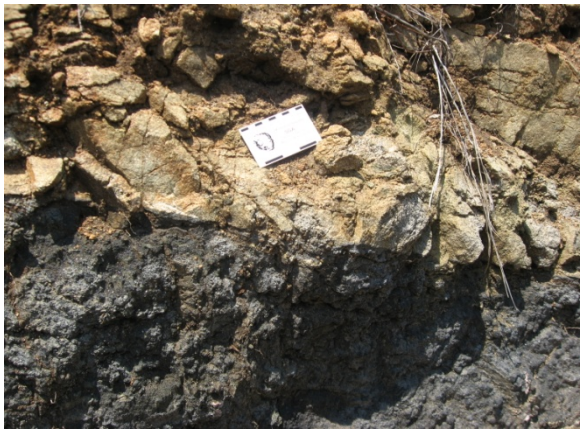

Figure 4.4 Sharp contact of the MG2A chromitite to its pyroxenitic hanging wall. The location and scale are the same as in figure 2.18.

MG2B unit: The MG2B chromitite layer has a thickness of 0.71 m. It is separated from the MG2C chromitite layer by a thin pyroxenitic band (0.07 m) that contains lots of disseminated chromite. Thus, the contacts to the chromitite layer above and below the pyroxenitic band are rather gradational than sharp.

4.1.2 The Upper Critical Zone

MG2C unit: The thickness of the MG2C layer is 0.61 m. In its hanging wall, the first cumulus plagioclase of the stratigraphic column can be observed in the mottled anorthosite (thickness 2.82 m). The anorthosite contains various amounts of disseminated chromitite. The contact to the MG2C chromitite is sharply defined (Fig. 4.5).

MG3 unit: Similar to the chromitite layers in the MG2 units, the MG3 chromitite layer is also made up of two chromitite layers that are separated by a thin pyroxenitic band (0.07 m). The lower part has a thickness of 0.70 m and the upper part is 0.28 m thick. Other than for the MG2 chromitite layers, they aren't treated separately. The hanging wall is made up of norite with a bulk thickness of 11.7 m. Due to the low amount of pyroxene its lowermost part (0.41 m) appears brighter and is therefore termed leuconorite. From figure 4.6 it can be seen that locally displacement due to post-depositional processes occurs.

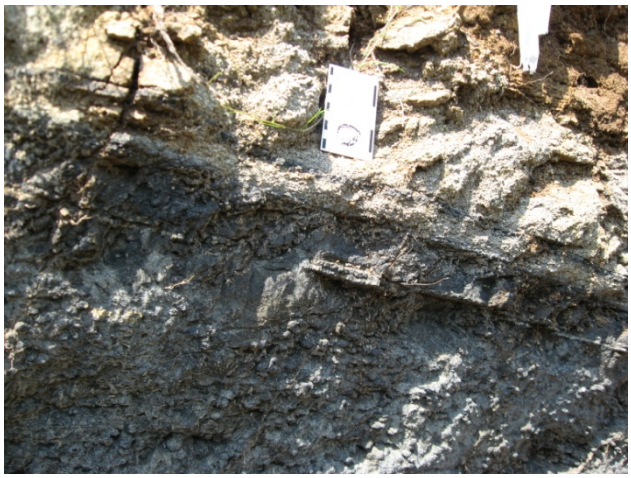

Figure 4.5 Well defined contact between the MG2C chromitite and its anorthositic hanging wall. Note the small chromitite band just below the scale, which is taken as a marker for the MG2C chromitite layer. Location and scale as in pictures before.

Figure 4.6 A dyke with a width of ca. 2 cm is displacing the MG3 unit and parts of the unit below. Location and scale as in pictures before.

MG4A unit: The MG4A chromitite layer is 2.14 m thick and overlain by a huge pile of pyroxenite of 2.72 m thickness, which comprises disseminated chromite as well as thin chromitite stringers.

MG4B unit: The MG4B chromitite layer has a thickness of 0.3 m. As with the MG2 units, the MG4B and MG4C are separated by a thin pyroxenitic band (0.14 m).

MG4C unit: The MG4C chromitite layer is with 0.41 m thicker than the MG4B. The hanging wall is made up of a thin layer of pyroxenite (0.4 m), which is overlain by a huge pile of norite (27 m) that, because of varying amounts of pyroxene and chromite, changes its appearance between melano- and leuconorite.

Later during this work data from different studies done by Cameron (1977; 1980; 1982) on samples from the northern part of the eastern Bushveld Complex are used for comparison with data from this study to demonstrate that the data of this work are regional data (cf. subsections 4.3.1 and 4.3.2). Since Cameron developed his own stratigraphic subdivision, table 4.1 presents the respective equivalent to the Bushveld nomenclature used now (Cawthorn *et al.*, 2002).

Table 4.1 Comparison of Cameron's stratigraphic intervals of the MG with the one used during this study.

Stratigraphic intervals of this study	Stratigraphic intervals by Cameron
MG4C cyclic unit	G unit
MG4B cyclic unit	
MG4A cyclic unit	
MG3 cyclic unit	F unit
MG2C cyclic unit	E unit
MG2B cyclic unit	
MG2A cyclic unit	
MG1 cyclic unit	D unit; 'Steelpoort chromite seam' is equivalent to the MG1 chromitite layer
MG0 cyclic unit	

4.2 Optical microscopy

The rocks occurring in the RLS are supposed to be cumulate rocks; i.e. rocks that consist of "crystals that precipitated from a magma without having been modified by later crystallization" (Bates and Jackson, 1995) and thus probably don't show 'normal' rock compositions. They formed during fractional crystallization by gravitational settling of crystallizing minerals. The term *cumulate* was developed by Wager *et al.* (1960) and later amplified by Wager (1963) and Wager and Brown (1968) to describe the textures of igneous rocks in slowly cooled layered intrusions. According to that, cumulus minerals are the very first precipitated crystals that accumulate on the floor of the magma chamber before any modification. The liquid coexisting in the interstitials of the cumulus crystals is called intercumulus liquid. With regard to the amount of co-existing intercumulus liquid Wager and Brown (1968) developed the following terminology. Unmodified cumulate rocks were termed *orthocumulate* (< 25% intercumulus material). *Mesocumulates* contain between 7 and 25% intercumulus material, whereas *adcumulates* comprise up to 7% intercumulus material in maximum.

As the accumulation of the cumulus crystals as well as the cooling of the crystal mush resulting from this accumulation is very slow, various modifications in the primary texture and also in the composition are most likely, which has been recognized by several authors (e.g. Hess, 1960; Cameron, 1969; Cawthorn *et al.*, 1983; Hulbert and von Gruenewaldt, 1985). Typical modifications are the enlargement of cumulus crystals accompanied with a gradually reduction of pore space, i.e. intercumulus liquid, by mechanically pushing the liquid out of the crystal mush pile. Any remaining intercumulus liquid was termed *trapped*

liquid. Hence, the subsequently crystallized pore material has the same composition as the contemporary magma (Hunter, 1996).

Because orthocumulates are rather rare and the transition to the other crystallization stages is smooth the application of the terms *orthocumulate*, *mesocumulate* and *adcumulate* is abandoned during this study. As a result, the author prefers the general terms cumulus and intercumulus mineral. However, since enlargement of grain sizes in cumulate rocks is quite common, the term 'adcumulus growth', as defined by Wager *et al.* (1960) and Jackson (1967) describing the growth of larger grains on the expense of smaller grains will be used during the work in hand.

4.2.1 Petrography of the chromitite layers

The amounts of chromite and silicate phases differ in the individual chromitite layers investigated during this study. The determination of the proportion of cumulus chromite and intercumulus silicate was carried out via phase analysis using the analySIS®FIVE software of Olympus. The results are summarized in figure 4.7. An enrichment of cumulus chromite over the silicate phases is evident from the MG1 chromitite layer up to the MG2B (60.6% to 79.5%). Coincidently with the transition from the LCZ to the UCZ, i.e. at the bottom of MG2C chromitite, the amount of cumulus chromite decreases from MG2C (79.3%) to 50.4% in the MG4B chromitite in favour of the silicate phases. A very slight increase of the cumulus chromite fraction about 0.9% can be seen in the MG4C chromitite. With more than 70% cumulus chromite, the MG2B, MG2C and the MG3 chromitite layers are the most enriched ones in chromite.

Figure 4.8 gives detailed information about grain size distribution of chromite grains in each chromitite layer. The grain size distribution is very heterogeneous, ranging between 24 µm in minimum and 584 µm in maximum dimension. Based on the measurement of 580 grains, the grain size distribution of all the chromitite layers is structured in the following way: With 34.4% the biggest part of chromite grains shows sizes between 125 and 212 µm, followed by grains with sizes between 212 and 425 µm (25.9%). Less often grains smaller than 45 µm (2.1%) occur. The MG2C chromitite layer comprises the highest amount of large grain sizes (> 212 µm), which points to the highest degree of adcumulus growth within this layer. The smallest grain sizes (< 45 µm) can be observed in the uppermost chromitite layer MG4C that can be linked to less adcumulus growth.

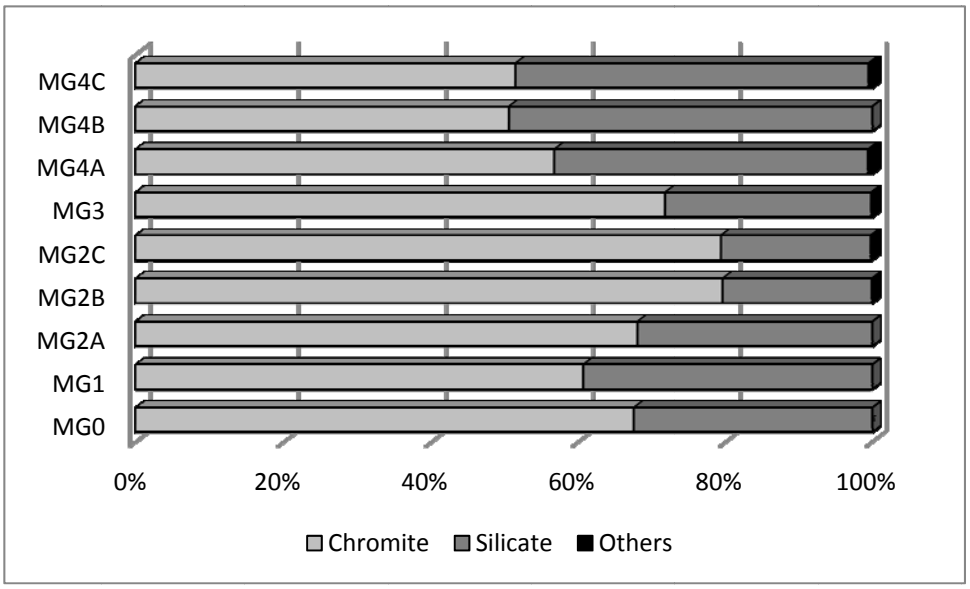

Figure 4.7 The amounts of chromite and silicate phases in the MG chromitite layers. The results are based on 88 images from thick polished sections that have been analysed with the software analySIS®FIVE. Base metal sulphides and rutile are summarized in 'others'.

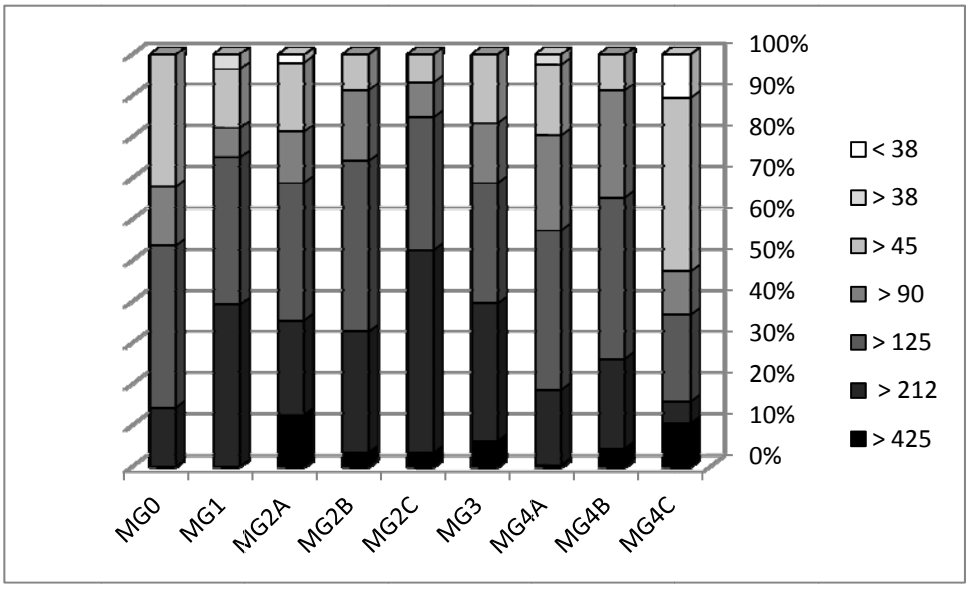

Figure 4.8 Grain size distribution of chromite in the individual MG chromitite layers. For each chromitite layer one sample has been chosen exemplarily. The size intervals have been chosen according to sieve sizes used in sedimentology.

According to different grey scales, at least two distinct silicate phases have been noticed, certainly plagioclase and orthopyroxene (Fig. 4.9A). Detailed information about the silicate phases in chromitite layers of the MG are compiled in subsection 4.4.1.1 dealing with XRD analyses.

The silicate phases occur as primary intercumulus minerals, forming a framework for the loose packed chromite grains. This arrangement is called chain texture (Cameron, 1969). Isolated chromite grains are generally rounded and partly euhedral, whereas the shape of colliding chromite grains is defined by their grain boundary geometry (Fig. 4.9D). Quite common are polygonal textures suggesting adcumulus growth of chromite grains (Fig. 4.9B and 4.9C), but this is not the only evidence that can be given. Irregular grain boundaries, which formed by some kind of welding, atoll-like structures (Fig. 4.9D) and the multiple presence of silicate inclusions (see Fig. 4.14 below) give also support for this. Due to the adcumulus growth, a general coarsening of grain sizes is achieved. According to that, the present grain size distribution presented in figure 4.8 is not the original one.

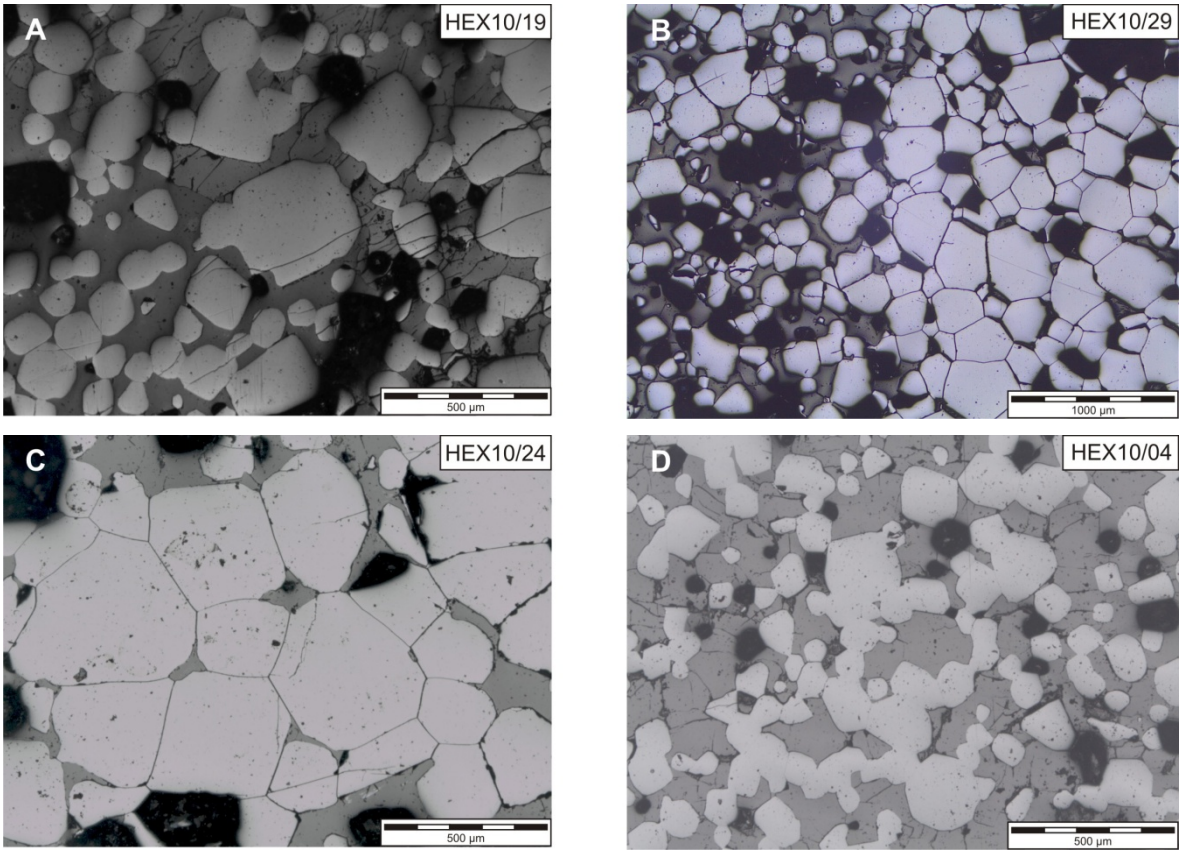

Figure 4.9 Cumulate textures in the chromitite layers of the MG sequence. (**A**) Two silicate phases as intercumulus material to chromite grains, certainly orthopyroxene (upper right) and plagioclase (lower left). (**B**) 'Transition' from massive chromitite showing polygonal texture to a lesser densified chromite ore. (**C**) Triple junction in coarse grained/massive chromitite with minor 'trapped melt' in the interstitials. (**D**) Grain shapes of solitary and welded chromite. Welding of chromite grains of different sizes leads to general coarser grain sizes. In the center of the picture an atoll-like texture is developed. Plain polarized light (PPL) images.

Poikilitically enclosed chromite grains in orthopyroxene can be especially found in the MG4A chromitite layer (Fig. 4.9A) and have also been observed by Hulbert and von Gruenewaldt (1985) in chromitite layers of the Northern limb. They are interpreted to represent original grain sizes, as their appearance as an inclusion shielded them from interaction with the intercumulus liquid and adcumulus growth. Their size ranges from 21.3 µm to 195.7 µm in maximum and thus they are smaller than cumulus chromite grains from massive parts, proving the shielding function of the enclosing mineral (Fig. 4.10).

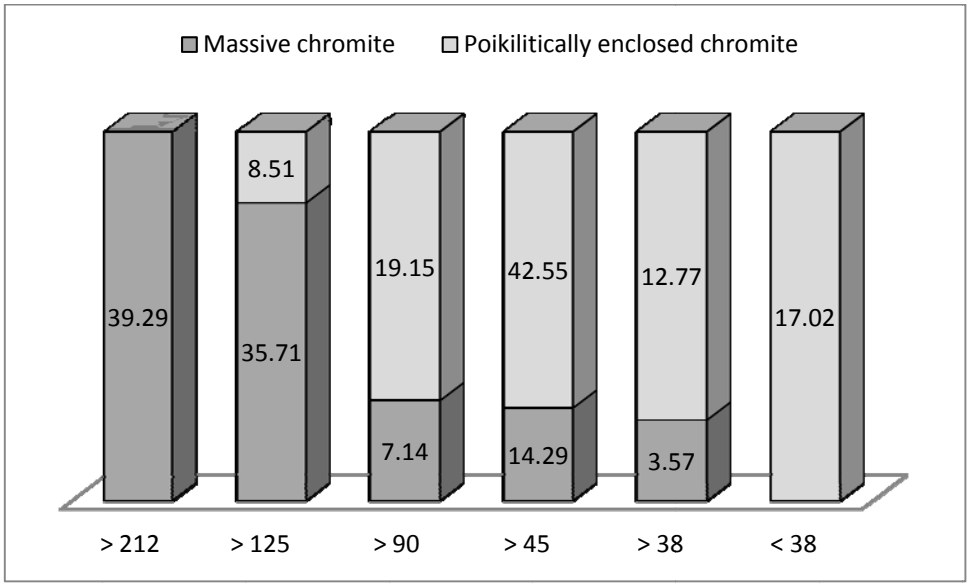

Figure 4.10 Range of grain sizes for 'massive chromite' and chromite poicilitically enclosed in intercumulus minerals exemplary for the MG1 chromitite layer. The amount of chromite grains with small grain sizes is dominantly represented by those occurring enclosed in orthoproxene. Numbers define percentages relative to 100% of the corresponding population.

The BMS are very rare (< 1 vol%). Most commonly they occur disseminated within the silicate intercumulus material, but also form small inclusions in chromite grains (Fig. 4.11A and 4.11B). Very seldom they are euhedral, but generally irregular grain boundaries dominate. Rather rare the BMS appear interstitially between chromite grains. Multi-phase sulphides, i.e. agglomerates of the various BMS in various arrangements, also occur (Fig.4.11A and 4.11B). Four different BMS species have been determined with the optical microscope: chalcopyrite and pyrite as the major BMS phases, with minor pentlandite and rarely pyrrhotite. They are interpreted to represent primary magmatic sulphide assemblage. Sometimes bornite can be seen and suggests a secondary overprint of the BMS. Cracks in pyrite, an 'alteration halo' in the silicates surrounding chalcopyrite (Fig.

4.11D) as well as their occurrence in altered silicate matrix (Fig. 4.11C) also indicate postmagmatic modifications of the BMS in the MG sequence.

The BMS assemblage seems to vary throughout the Bushveld Complex. A study on MG chromitite layers in the southwestern part of the Bushveld Complex (Marikana area) by von Gruenewaldt *et al.* (1986) yielded chalcopyrite to be the most abundant BMS, followed by minor pentlandite. They observed a relative abundance of siegenite and only very small amounts of pyrite in their samples. In the MG as yielded from core HEX10, pyrite is thus much more common, whereas pentlandite is rather rare. Von Gruenewaldt *et al.* (1986) furthermore noticed an absence of pyrrhotite, which normally is assigned to be a primary magmatic sulphide. This lack the authors explained by a possible postmagmatic modification of the primary BMS assemblage. Their observation coincides with those made for the MG in so far, as only very little pyrrhotite is present and further evidences for postmagmatic modification have been found.

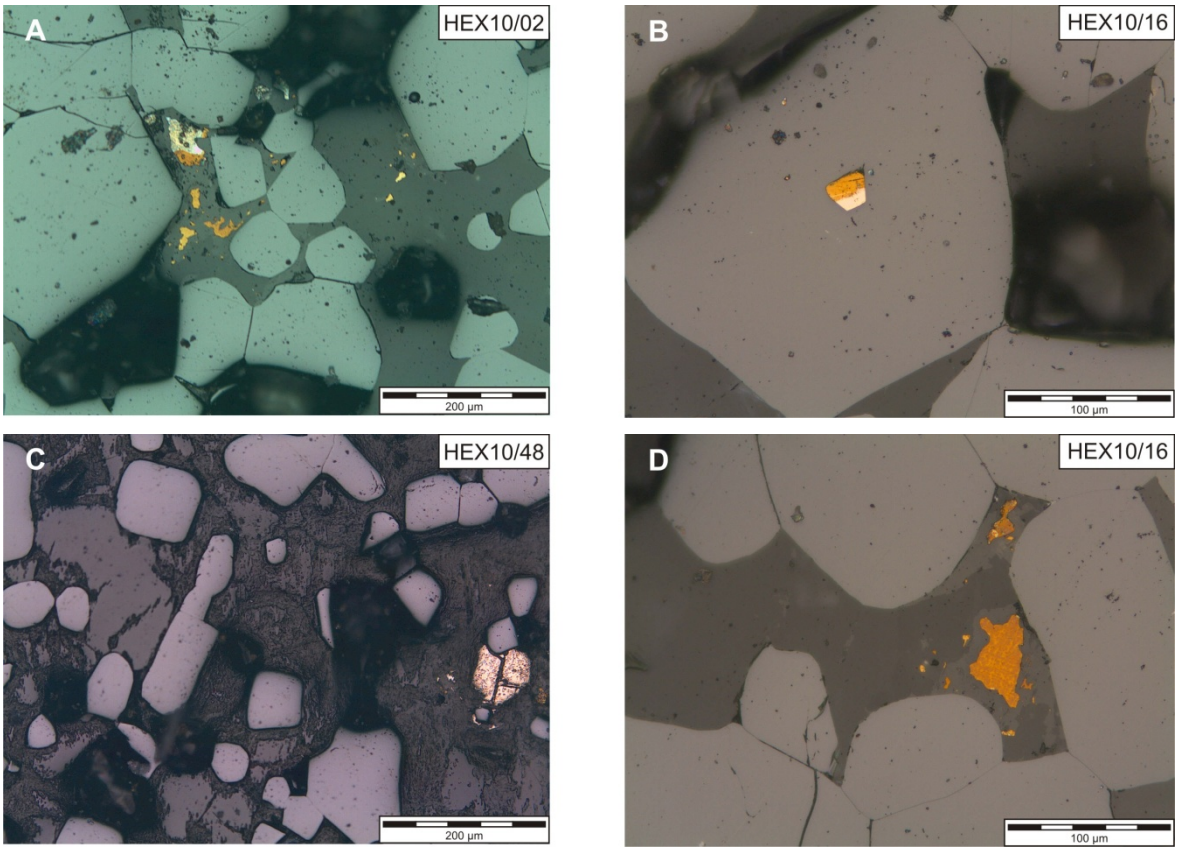

Figure 4.11 Base metal sulphides in the MG chromitite layers. (**A**) Disseminated pyrite (light yellow) and chalcopyrite (orange) in silicate intercumulus material. Note the coalescence of both BMS species. (**B**) Merged melt inclusion of pyrite and chalcopyrite in chromite. (**C**) Subhedral pyrite being cracked parallel to its cleavage surfaces. Note the strongly altered silicate matrix. (**D**) Light grey rim around chalcopyrite, probably representing an 'alteration halo' that developed in the silicates surrounding chalcopyrite due to postmagmatic modifications. PPL images.

Rutile occurs in close relation with chromite in the chromitite layers of the MG. Most common is the occurrence as tiny acicular inclusions in chromite parallel to the crystallographic directions of the chromite grain (Fig. 4.12E and 4.12F) suggesting their growth to be related to chromite structure. Bigger inclusions form single crystals with sharp grain boundaries, which can be elongated or prismatic. The latter are twinned sometimes (Fig. 4.12C and 4.12D).

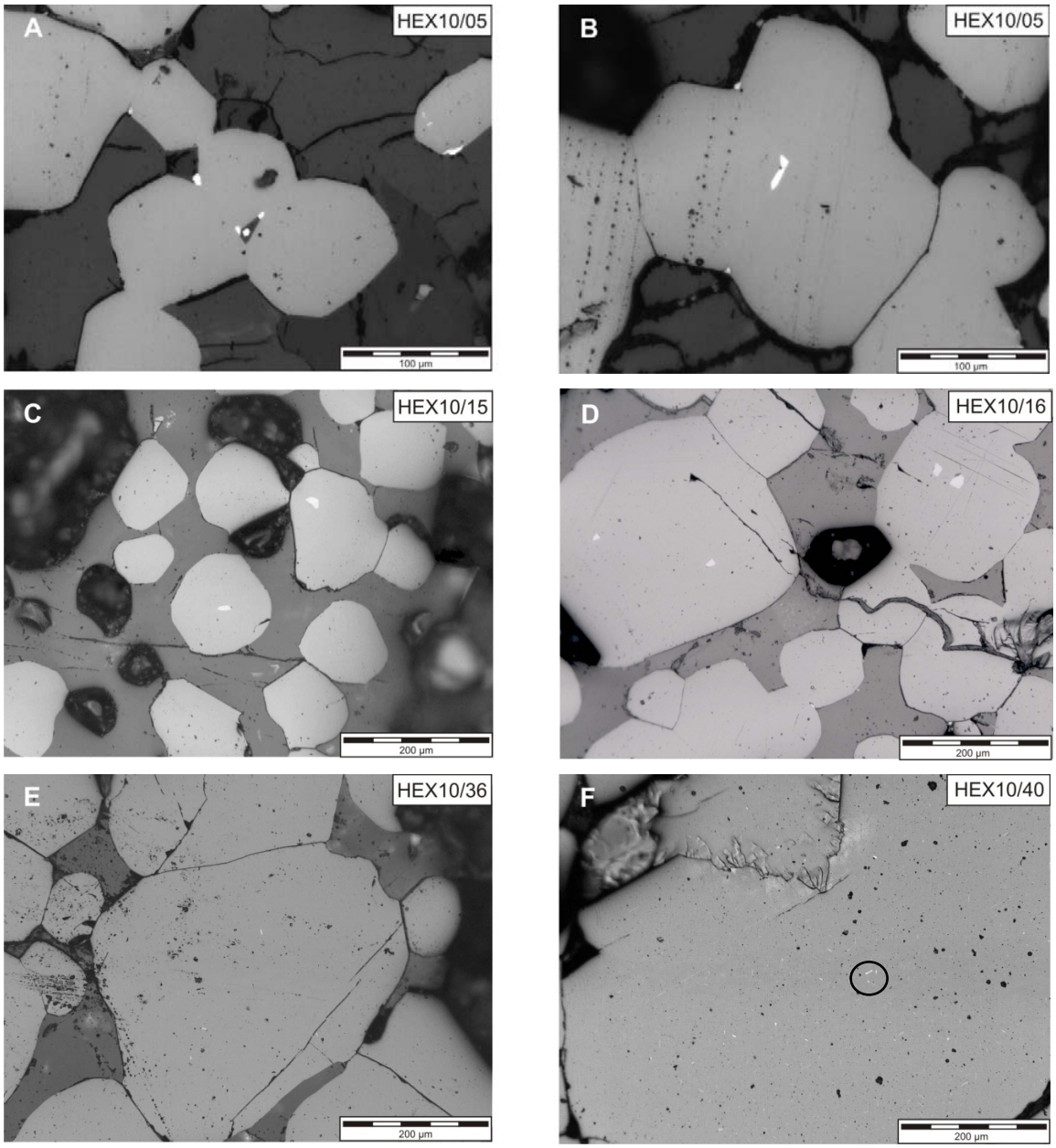

Figure 4.12 Inclusions and exsolutions of rutile in chromite grains of the MG sequence. (**A**) and (**B**) Sub- to euhedral rutile grains interstitial to chromite. Rutile occurring at margins of chromite is preferentially anhedral. (**C**) and (**D**) Typical inclusions of prismatic rutile in chromite. (**E**) and (**F**) Tiny needle-shaped inclusion orientated parallel to crystallographic directions of chromite. PPL images.

The size of the rutile inclusions varies according to their shape between 6 x 7 µm as the minimum for rounded grains and 6 x 33 µm as the maximum for elongated grains.

Anhedral rutile occurs at margins of chromite grains (Fig. 4.12A). At triple junctions or in the interstices of chromite sub- to euhedral rutile can be observed (Fig. 4.12A and 4.12B).

The occurrence of rutile is random and most of the chromite grains show any of the described features. However, its abundance increases from the MG0 to the MG4A chromitite layer.

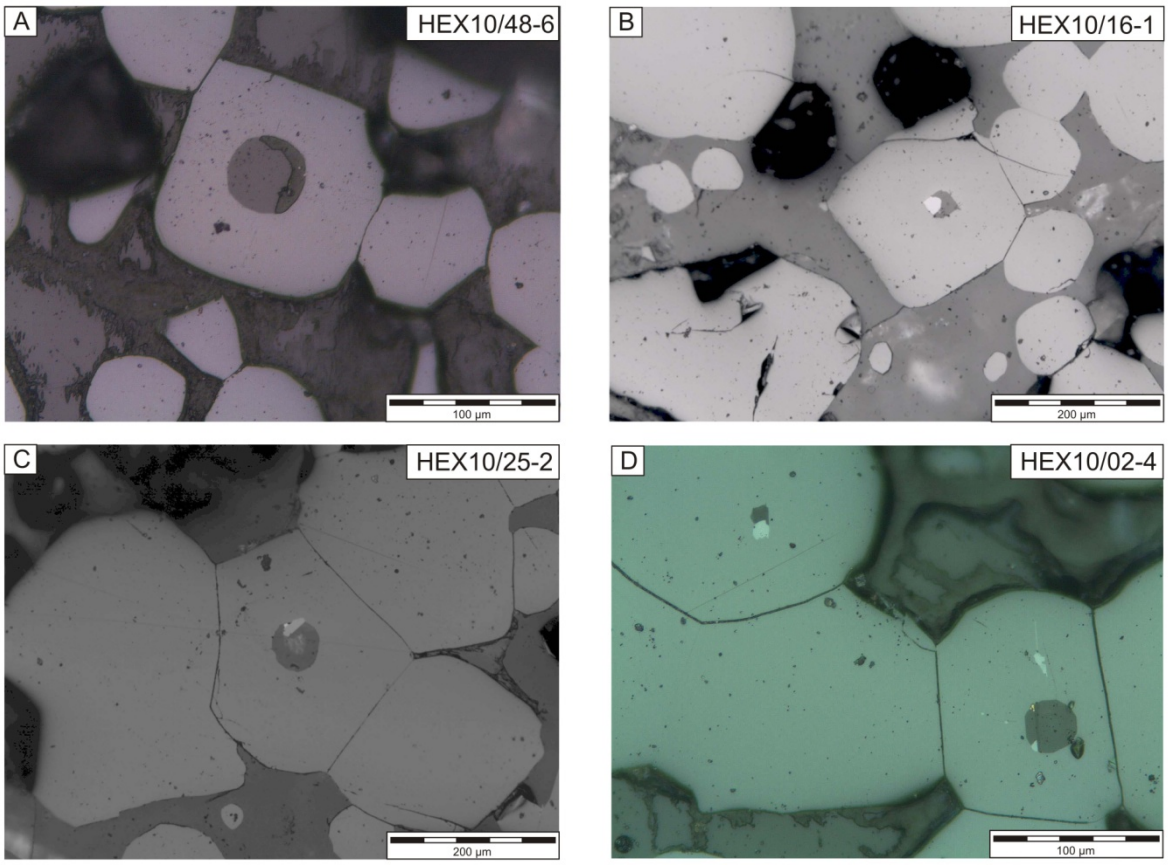

Figure 4.13 Silicate inclusions in chromite of the MG sequence. (**A**) Inclusions being composed of two silicate phases. (**B**) Inclusion made up of two silicate phases and rutile. (**C**) Inclusion of one silicate phase, rutile and pentlandite. (**D**) Big silicate inclusions with two silicate phases also containing rutile and chalcopyrite.

The tiny needle-shaped inclusions are interpreted to derive from the separation of TiO_2 from the spinel structure during cooling, since the valence of Ti doesn't fit easily into the chromite lattice at lower temperatures. Evidence for this is their orientation parallel to the crystallographic directions of chromite as shown in figure 4.12E and 4.12F. With

regard to their size and their shape the prismatic inclusions presented in figures 4.12C and 4.12D rather indicate their formation as distinct crystals before being trapped by chromite, thus pre-dating chromite crystallization. Textural relation of rutile occurring outside chromite but adjacent to it and silicate minerals point to rutile crystallisation also preceding silicate crystallisation.

In all the chromitite layers silicate inclusions within chromite grains can be found. Inclusions consisting of one silicate phase only are extremely rare. Usually, these inclusions are composite and are composed of one or two silicate phases ± rutile (Fig. 4.13A and 4.13B) or one silicate phase, rutile and a BMS (Fig. 4.13C). Quite rare are inclusions with two silicate phases and a BMS (Fig. 4.13D). Unfortunately, the nature of the silicate phases could not be determined with the optical microscope, as only thick polished sections have been available. Because of that, SEM-EDX analyses have been carried out and the results are outlined in subsection 4.3.4.3.

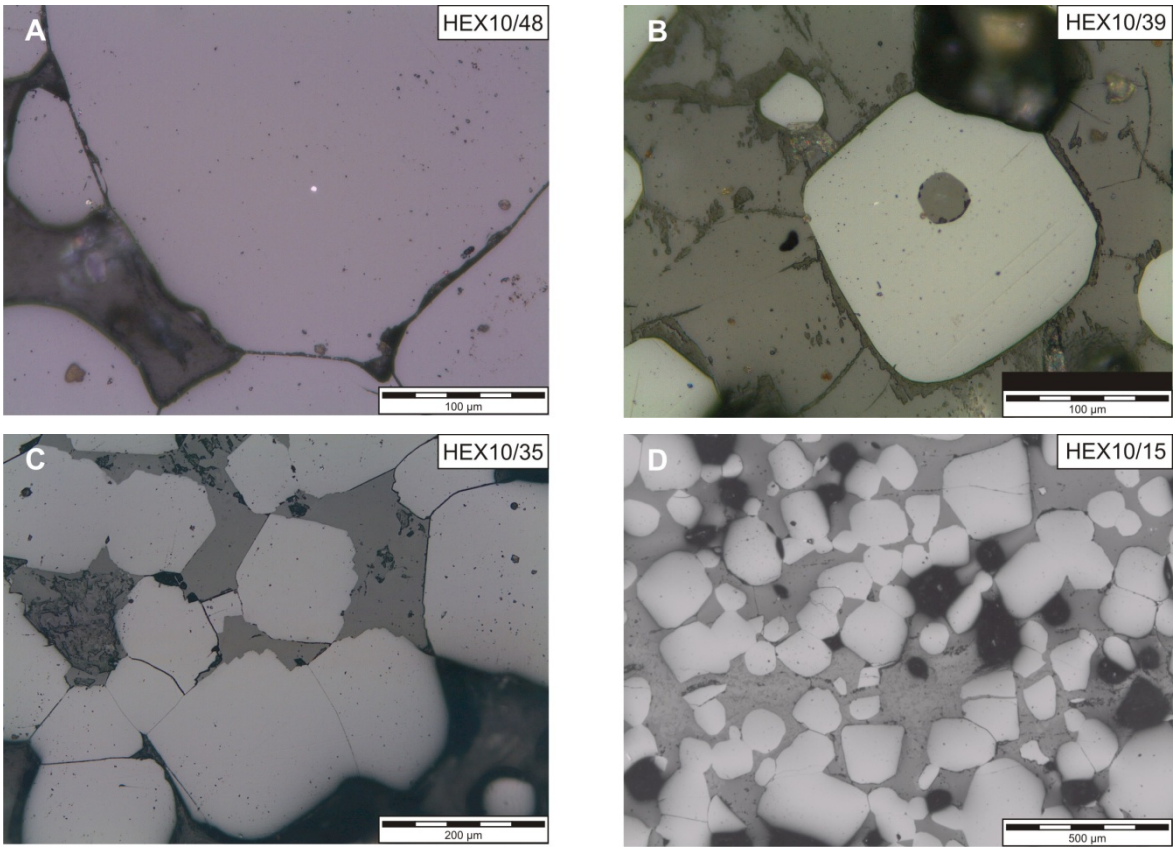

Figure 4.14 PGM and alteration in chromitite layers of the MG sequence. (**A**) Tiny PGM inclusion in chromite. Note the blurry grain boundaries caused by the high reflectance. (**B**) Alteration of silicate minerals typically beginning at their grain boundaries. Chromite grains are not affected. (**C**) Irregular grain boundary of chromite due to locally occurring disequilibrium conditions. (**D**) Vein cracking several chromite grains. PPL images.

Platinum-group minerals have only been observed by their very high reflectance (Fig. 4.14A), as they are normally too small to be seen with the optical microscope (3-5 µm on average, as pointed out by Merkle (1992)). Preliminary MLA studies resulted in the existence of nine different PGM species with a dominating amount of PGE-sulphides. Detailed results of this study are presented in subsection 4.3.8.

Signs of alteration occur within the silicate phases only, which form the intercumulus material in the chromitite layers (Fig. 4.14B and 4.14C). It is not very common and occurs mainly at grain boundaries. Irregular grain boundaries of chromite have only been observed once and have been interpreted to result from local disequilibrium conditions between cumulus phase (chromite) and intercumulus material (silicate minerals) (Fig. 4.14C). Chromitite samples of the MG4A layer are additionally characterised by cracks and small veins cutting chromite grains (Fig. 4.14D). Since polished sections were available only, the composition of the veins couldn't be determined.

4.2.2 Petrography and classification of the silicate rocks

4.2.2.1 Petrography

During the following subsection, the modal mineral content of the silicate rocks gathered via point count analyses of the MG sequence is described. Counting is carried out within predefined intervals, but since the different minerals have various grain sizes, e.g. very small for chromite and quite coarse for orthopyroxene (cf. Fig. 4.15D), the given modal percentages are only rough estimations. Additionally, the counting of huge poikilitic intercumulus minerals is very difficult.

Pyroxenitic samples

Macroscopic investigations of core pieces of the MG revealed that dark brown pyroxene is the most common mineral that appears coarse grained. Chromite as the second common mineral occurs as lenses, schlieren or disseminated within the rock, but shows much smaller grain sizes. Within one silicate layer, its content is highly variable. Generally, very few plagioclase has been observed in the pyroxenites of the LCZ, namely minor intercumulus plagioclase in samples JKL6 and JKL8. In the UCZ plagioclase occurs as a cumulus mineral in all of the samples and its content appears to increase with stratigraphy.

Microscopically, orthopyroxene is the dominant mineral within these rocks, too, ranging between 36.1 and 60.1 modal% in the LCZ, and between 30.3 and 55.5 modal%

in the UCZ. In the LCZ plagioclase occurs as often as clinopyroxene, namely 18 or 17.5 modal%, respectively. In the UCZ plagioclase is more abundant (25.6 modal%) than clinopyroxene (8.4 modal%). The chromite content is highly variable (5.2 to 49.4 modal%) and often depends on the location of the sample within the stratigraphic column. Samples deriving from hanging or foot walls of chromitite layers show higher chromite contents than those deriving from within the silicate layer. Generally occurring disseminated, the chromite in samples with high chromite content occurs as schlieren and lenses. Biotite appears randomly in LCZ and UCZ pyroxenites. Alteration minerals like serpentine and clay minerals are very common in pyroxenites of the UCZ, especially in the MG4A pyroxenite. In the LCZ they have been observed in four samples only (JKL4B, JKL5A, JKL6A, JKL7A). In the UCZ pyroxenites quartz can be found, ranging from 0.3 to 1.6 modal% (JKL20A, JKL42, JKL30, JKL21). Hematite is accessorily present in sample JKL21. A summary of the Point Count analyses is given in table B-1 in appendix B.

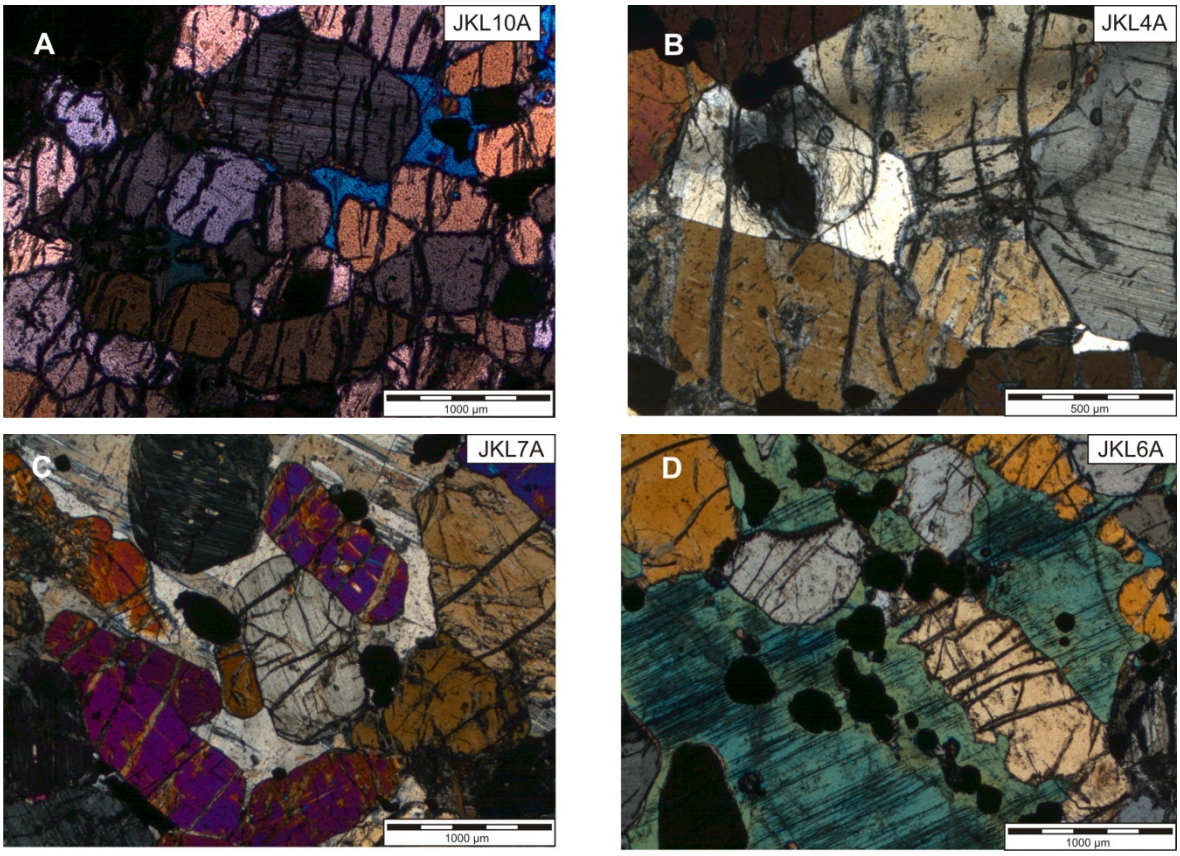

Figure 4.15 Photos from pyroxenite samples of the LCZ. (**A**) Granular texture dominantly formed by orthopyroxene. Bluish colour represents intercumulus clinopyroxene. (**B**) and (**C**) Intercumulus plagioclase in varying amounts. (**D**) Large areas of clinopyroxenitic cement enclosing cumulus minerals like orthopyroxene and chromite. Note the very different grain sizes of the two minerals and the irregular grain boundaries of the elongated orthopyroxene (beige-coloured).

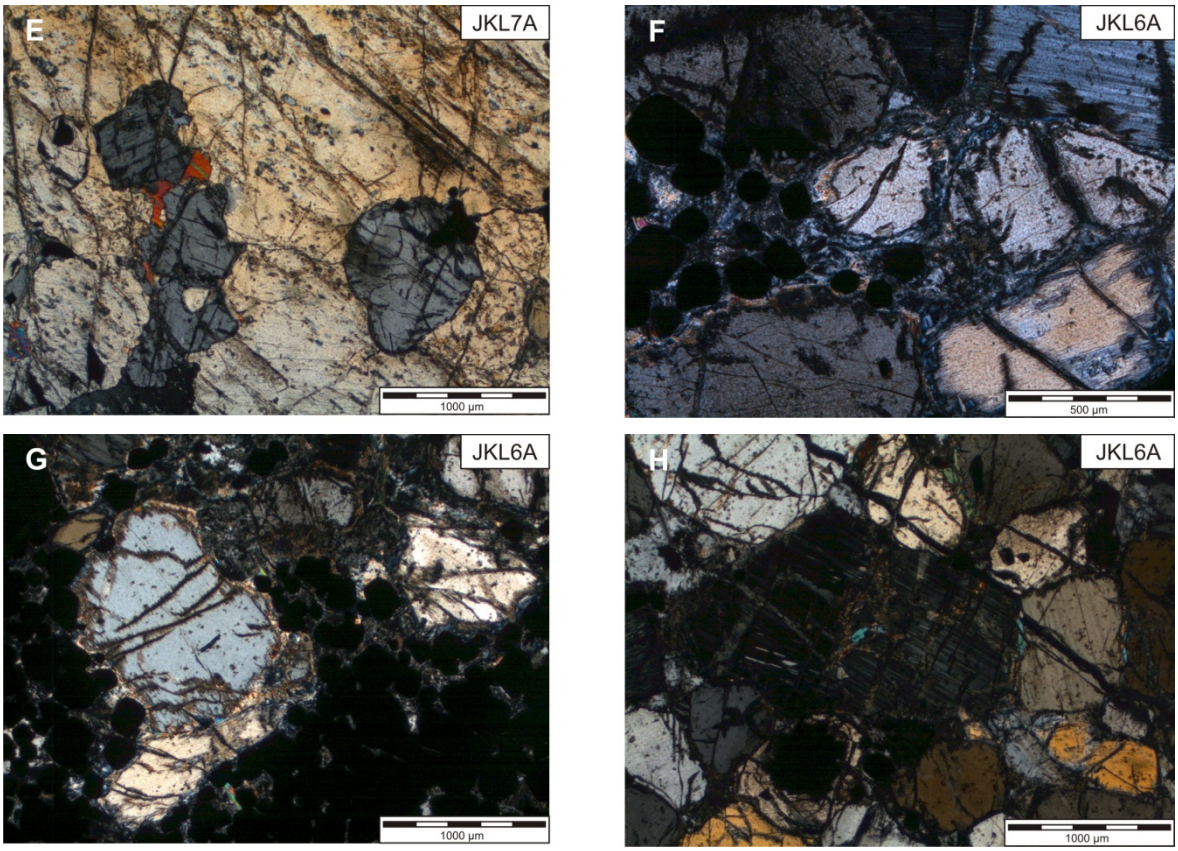

Figure 4.15 *(cont.)* (**E**) Orthopyroxene with inclusions of orthopyroxene, probably representing inherited crystals. (**F**) and (**G**) Serpentinization of orthopyroxene along grain boundaries. (**H**) Serpentinization of orthopyroxene preferably along cracks on the mineral surface. All pictures have been taken under crossed nicols.

A weak foliation of large orthopyroxene crystals can further be seen in hand specimen as well as in thin sections and is orientated parallel to the major mineralogical layering of the RLS.

Inclusions of chromite in pyroxene crystals can often be found. Rather rare is the occurrence of orthopyroxene inclusions in orthopyroxene (Fig. 4.15E). Irregular grain shapes of orthopyroxene can only be found regionally, when it is surrounded by clinopyroxene or plagioclase (Fig. 4.15D). It is probably caused by magmatic corrosion due to disequilibrium conditions (cf. Hunter, 1996; Vernon, 2004).

When occurring in the vicinity of chromite lenses or schlieren, orthopyroxene is strongly altered to serpentine minerals (Fig. 4.15F, 4.15G). This form of alteration starts at the grain boundaries of the orthopyroxene and strongly indicates solid-state diffusion during cooling. Another form of alteration is the formation of bastite as an orientated pseudomorphosis along cracks on the mineral surface (Fig. 4.15H).

The amount of intercumulus plagioclase in the UCZ is much higher than in the LCZ (Fig. 4.16A, 4.16B). Chromite occurs more massive in the pore space of the pyroxene

cumulate (Fig. 4.16C). Unlike in the LCZ, where clinopyroxenitic intercumulus material encloses cumulus crystals, in the UCZ large clinopyroxene crystals poicilitically enclose orthopyroxene, small chromite crystals and minor plagioclases (Fig. 4.16D). The inclusions show irregular boundaries and are of different size. These clinopyroxene crystals can already be seen macroscopically, forming patchy bodies of light green colour and have diameters between 0.5 to 1.5 cm.

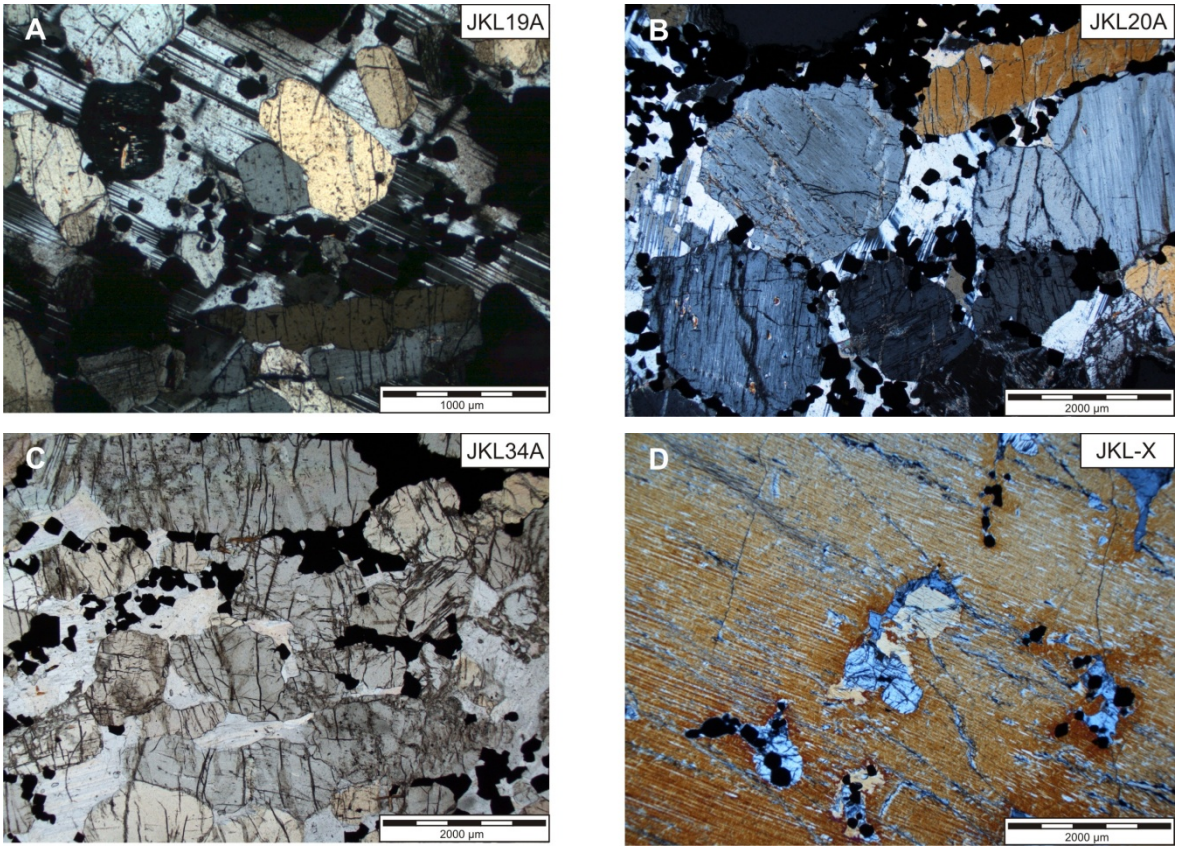

Figure 4.16 Photos of pyroxenite samples from the UCZ. (**A**) and (**B**) Increased amounts of intercumulus plagioclase relative to the LCZ pyroxenites. (**C**) Massive chromite in 'Zwickeln'. (**D**) Adcumulate of orthopyroxene and small chromite crystals poicilitically enclosed in a large clinopyroxene crystal. Except (C) pictures have been taken under crossed nicols.

Both, the pyroxenitic rocks of the LCZ but especially the ones of the UCZ comprise indications for dislocation creep, which most common feature is the bending of crystals (Hunter, 1996). In figure 4.17A and 4.17B, the bending of orthopyroxene is shown, in the latter well illustrated by the bended exsolution lamellae. Twinning lamellae in plagioclases also show bending and it doesn't seem to matter if plagioclase forms the intercumulus phase (Fig. 4.17C), or an individual crystal (Fig. 4.17D). In case of the latter, a distinct new grain has formed, caused by substantial angular rotation.

With regard to Hunter (1996), dislocation creep is caused by compaction in the sub-solidus state.

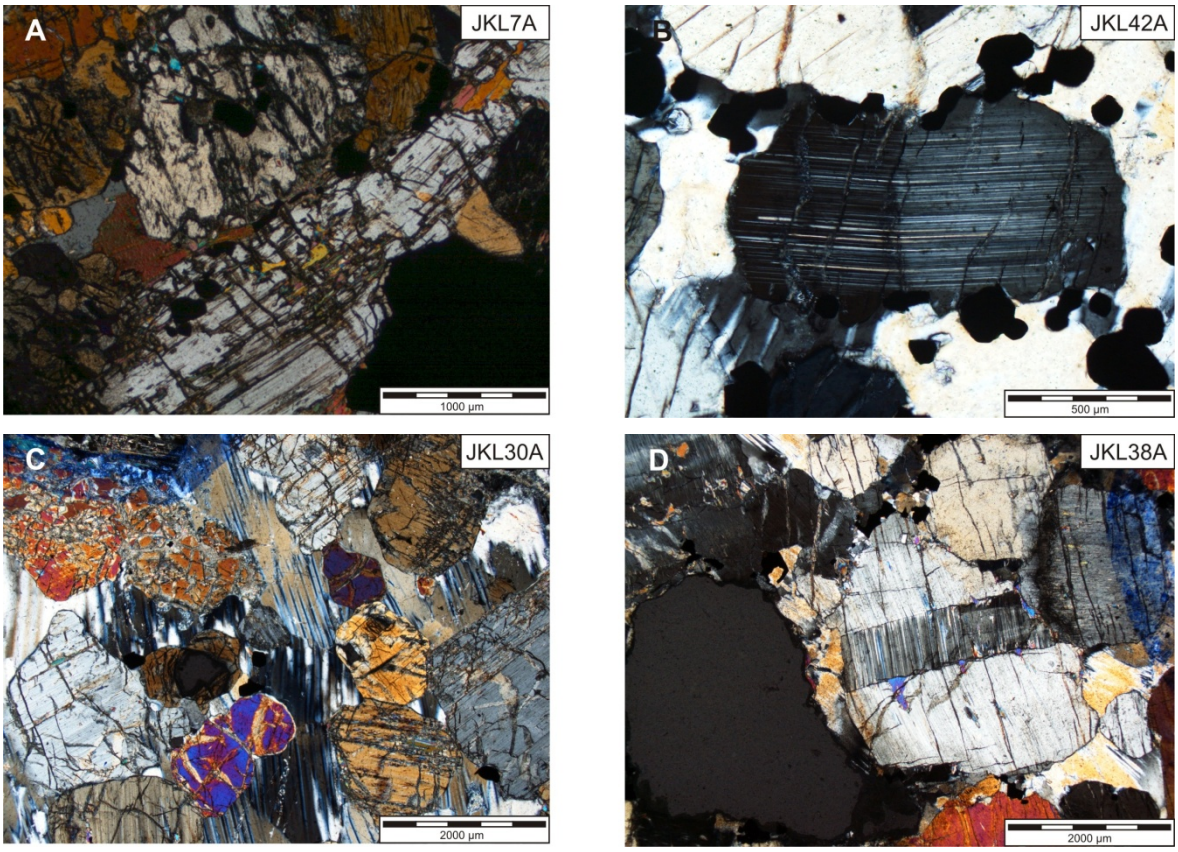

Figure 4.17 Indications for dislocation creep within pyroxenites of the MG sequence. (**A**) and (**B**) Bended exsolution lamellae in orthopyroxene of the LCZ. (**C**) Bended twinning lamellae of plagioclases of the UCZ. (**D**) Formation of a new individual plagioclase grain due to angular rotation. All pictures have been taken under crossed nicols.

Noritic samples

Macroscopically, the noritic samples of the MG consist of plagioclase as the major cumulus mineral with only minor pyroxene of dark brown colour. They are distributed in a dot pattern throughout the rock. The ratio of plagioclase to pyroxene is approximately 3:1. Chromite is an accessory phase occurring slightly disseminated.

Point count analyses revealed the modal composition of 63.7% plagioclase, 30.2% orthopyroxene and 5.1% clinopyroxene on average. The remaining 1 modal% is composed of chromite, biotite and quartz. An exception is sample JKL14 deriving from the hanging wall of the MG3 chromitite layer. It contains approximately 30% cumulus chromite.

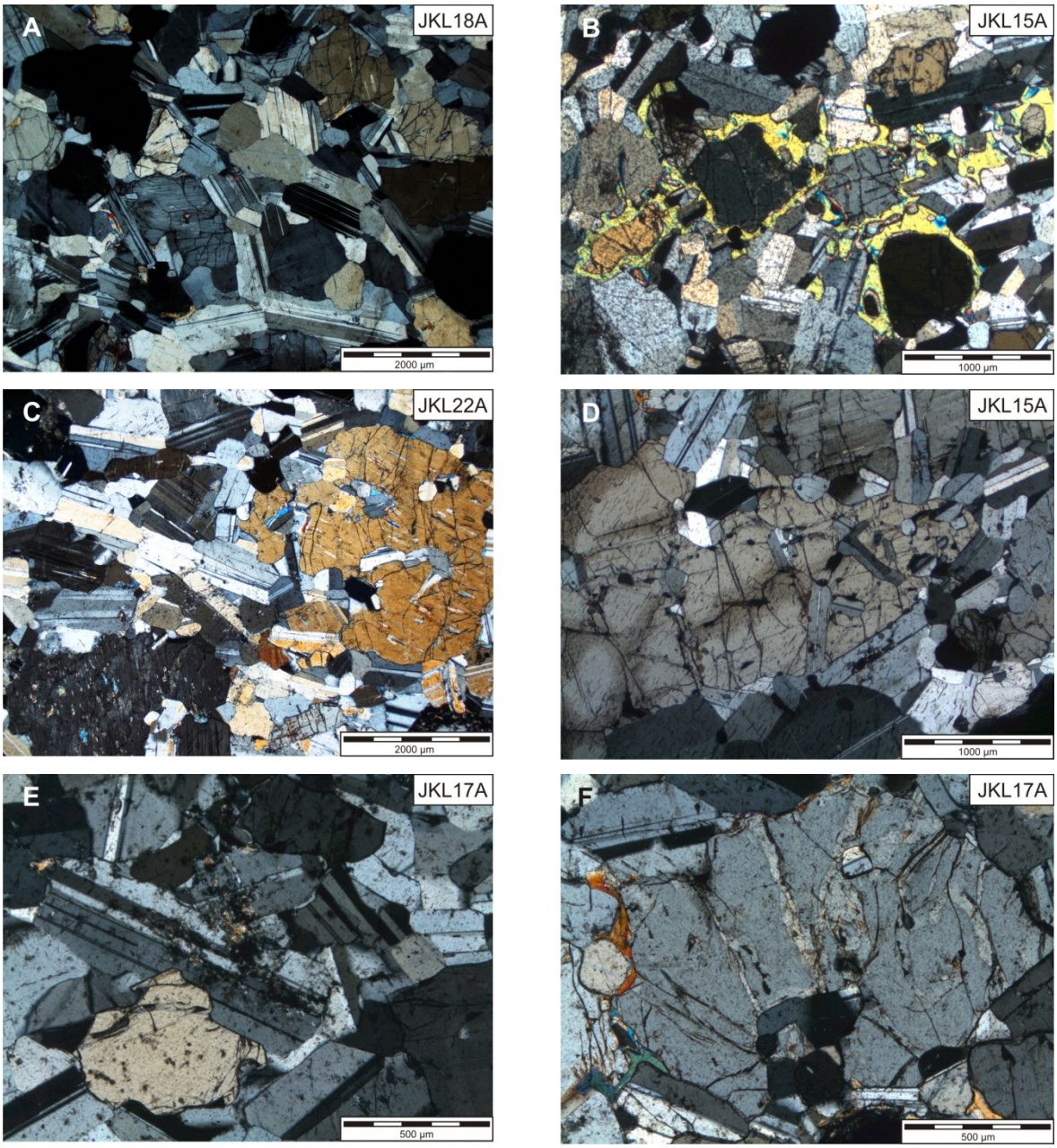

Figure 4.18 Noritic samples under the microscope. (**A**) Typical texture with elongated plagioclases and rounded orthopyroxene. (**B**) Rims of clinopyroxene around orthopyroxene. (**C**) and (**D**) Inclusions of plagioclase in orthopyroxene crystals. (**E**) Sericitization of plagioclase. (**F**) Serpentinization of orthopyroxene along cracks. All pictures have been taken under crossed nicols.

The cumulate texture in the noritic rocks is formed by elongated plagioclases showing twinning and rounded orthopyroxene (Fig. 4.18A). The latter often show embayments along its grain boundaries, which is a typical sign for magmatic corrosion (Vernon, 2004). Clinopyroxene is very rare. If present it forms rims predominantly around orthopyroxene (Fig. 4.18B), probably indicating solid-state processes between orthopyroxene and plagioclase. A common feature is the occurrence of plagioclase inclusions of various sizes

and shapes in orthopyroxene (Fig. 4.18C, 4.18D). Their spheroidal appearance is ascribed to partial resorption. Signs of alteration are seldom and are restricted to small areas (Fig. 4.18E, 4.18F). Chromite is an accessory phase only (< 1%).

Anorthositic samples

The anorthositic rocks of the MG are macroscopically composed of approximately 90% plagioclase with minor dark brown pyroxene and accessory disseminated chromite. Microscopically the plagioclase content ranges between 69.5 and 87.4 modal%, the remainder is made up of pyroxene. Dark mica and minor chromite are the only accessory minerals that have been observed. The massive texture is made up of plagioclase and minor orthopyroxene (Fig. 4.19A). The grain size of plagioclase is very heterogeneous. Intercumulus clinopyroxene forms large 'crystals' that poikilitically enclose plagioclase (Fig. 4.19B, 4.19C), but it seldom occurs.

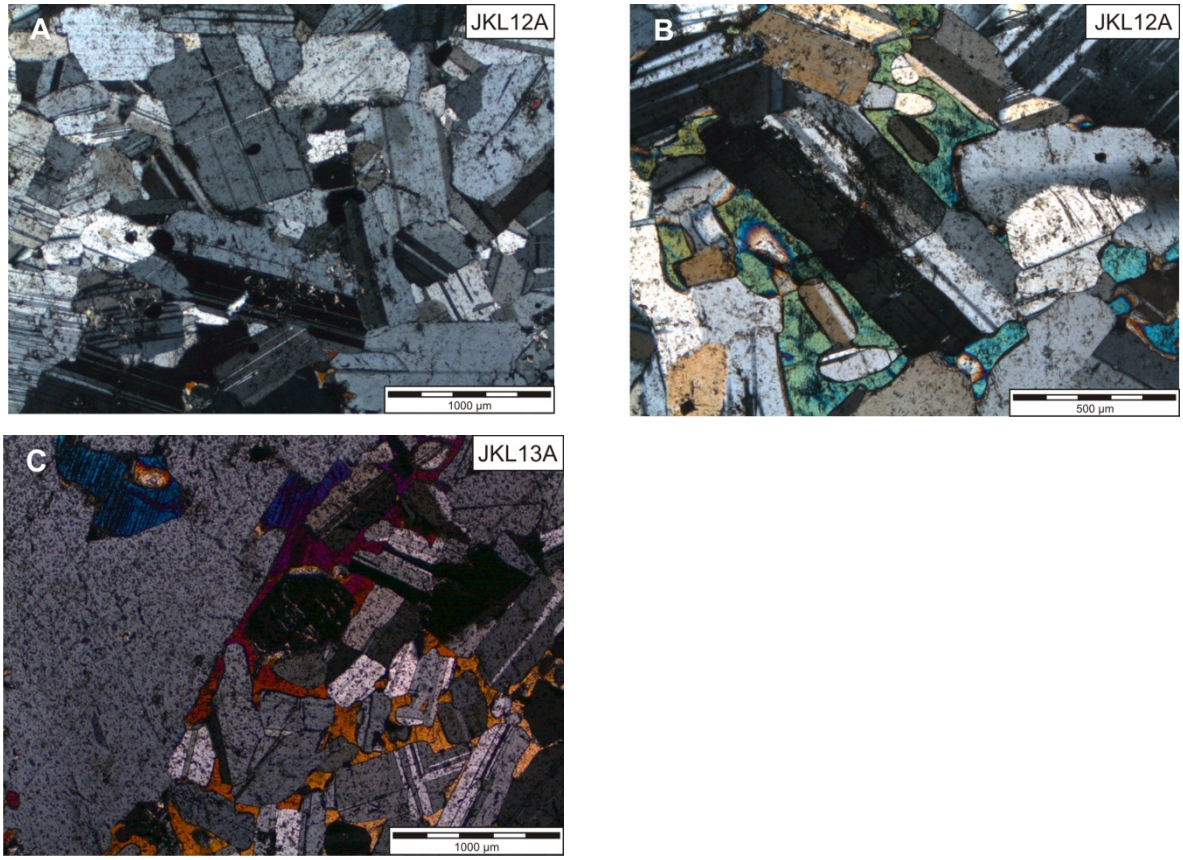

Figure 4.19 Anorthosite under the microscope. (**A**) Texture of anorthosite showing plagioclases of various sizes erratically distributed throughout the rock. (**B**) Intercumulus clinopyroxene enclosing plagioclase crystals. (**C**) Large clinopyroxene crystal poicilitically enclosing plagioclases and being enclosed from plagioclase at the same time. (B) and (C) have been taken under crossed nicols; (A) PPL image.

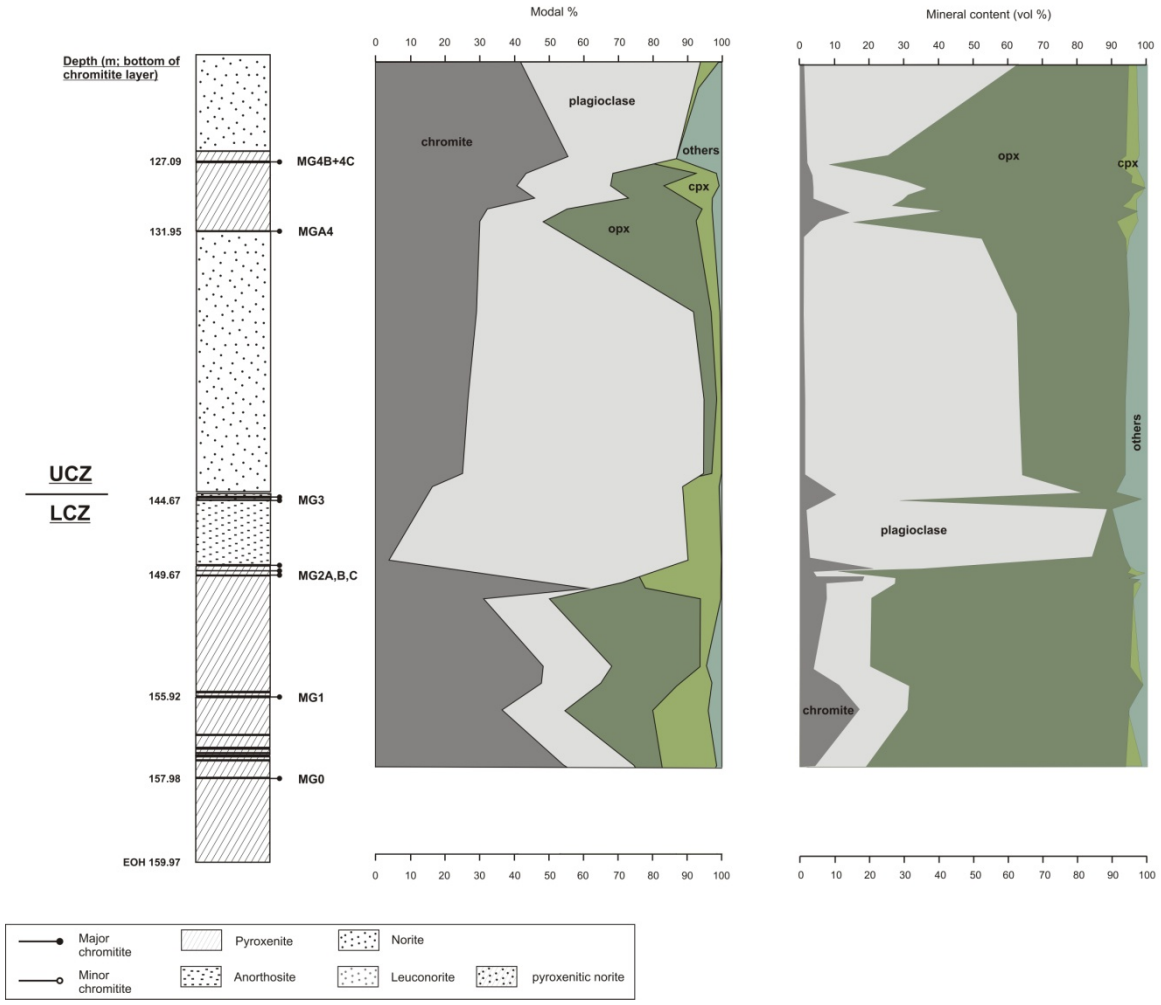

Figure 4.20 Modal proportions of chromite, plagioclase, orthopyroxene (opx), clinopyroxene (cpx) and others in the silicate samples (left) as well as CIPW norm calculations (right) from core HEX10. “Others” includes mica, alteration minerals and quartz in the modal proportions (left), and quartz, orthoclase, olivine, ilmenite, magnetite and apatite in the vol% mineral content (right). Data of Point Count analyses are given in table B-1 in appendix B, data of CIPW norm calculation in table B-2 in appendix B. Note that not every sample has been analysed by Point Count analyses (cf. Tab. A-3 in appendix A).

The results of the Point Count analyses of the individual silicate samples are summarized in Figure 4.20. Additionally, the CIPW norm calculation is shown. The strongest difference is visible in the chromite and orthopyroxene contents, which is due to the difficulties during Point Count analyses mentioned at the beginning of this chapter. The amount of plagioclase seems to be quite similar, but shows differences in its tenor upwards the stratigraphic column, i.e. increasing or decreasing amounts relative to the other minerals. Clinopyroxene is less abundant in CIPW norm calculation.

4.2.2.2 Classification

Pyroxenite, as defined by LeMaitre (2002), is a plutonic ultramafic rock essentially consisting of ortho- and/or clinopyroxene and olivine. Small amounts of garnet, spinel and sometimes biotite are common. Plagioclase occurs as an accessory only. Pyroxenites are classified according to their relative amounts of clino-, orthopyroxene and olivine in a ternary diagram olivine-orthopyroxene-clinopyroxene.

In the case of the pyroxenitic samples from the MG of the eastern BC, no olivine has been observed macroscopically, but minor amounts of plagioclase. Additionally, no olivine in any of the thin sections was detected. Thus, the ternary diagram orthopyroxene-clinopyroxene-plagioclase was used for rock classification of the pyroxenites instead of the conventional one mentioned above.

Modally, the pyroxenites of the MG sequence are gabbronorites with two samples being norites (JKL6A and JKL20A) (Fig. 4.21). It can be seen very nicely that the pyroxenites of the UCZ, i.e. from the MG4A cyclic unit, contain more plagioclase than the ones in the LCZ (MG0 and MG1 cyclic units), which already have been noticed from hand specimen. For that reason, and to avoid confusion with the traditional Bushveld classification, the pyroxenitic rocks of the UCZ are termed plagioclase-bearing pyroxenites throughout this study. For the LCZ pyroxenites the term pyroxenite is applied.
According to its mineral composition, ***'norite'*** is a special term used for gabbroic rocks consisting of plagioclase and orthopyroxene only (LeMaitre, 2002).

As can be seen in figure 4.21, most of the noritic rocks in terms of the Bushveld nomenclature plot in the norite field with two samples plotting at the boundary to the gabbronoritic rocks. Only one sample (JKL22A) plots within the gabbronorite field, which is caused by the higher amount of pyroxene (41.3 modal%). It is therefore termed pyroxenitic norite. Since its bulk content of pyroxene is modally quite low for a noritic rock (16.6 modal% relative to 31.9 modal% of the noritic rocks) sample JKL14 is rather termed leuconorite.

Anorthosite can be distinguished from an 'ordinary' gabbro by its content of mafic minerals, which should be smaller than 10% (LeMaitre, 2002). The anorthosite sample from core HEX10 (JKL12A) plots within the anorthosite field (Fig. 4.21).

From figure 4.21 it can be seen that there is a gap between the pyroxenites and the norites and anorthosites of the MG. This gap is caused by the different amounts of plagioclase within these rock groups. For the pyroxenites and plagioclase-bearing pyroxenites it ranges between 10.1 and 31.8 modal%, whereas in the noritic and anorthositic rocks the plagioclase content is between 52.4 and 87.4 modal%.

The results of the point count analyses inclusively traditional and new rock terms are summarized in table B-1 in appendix B.

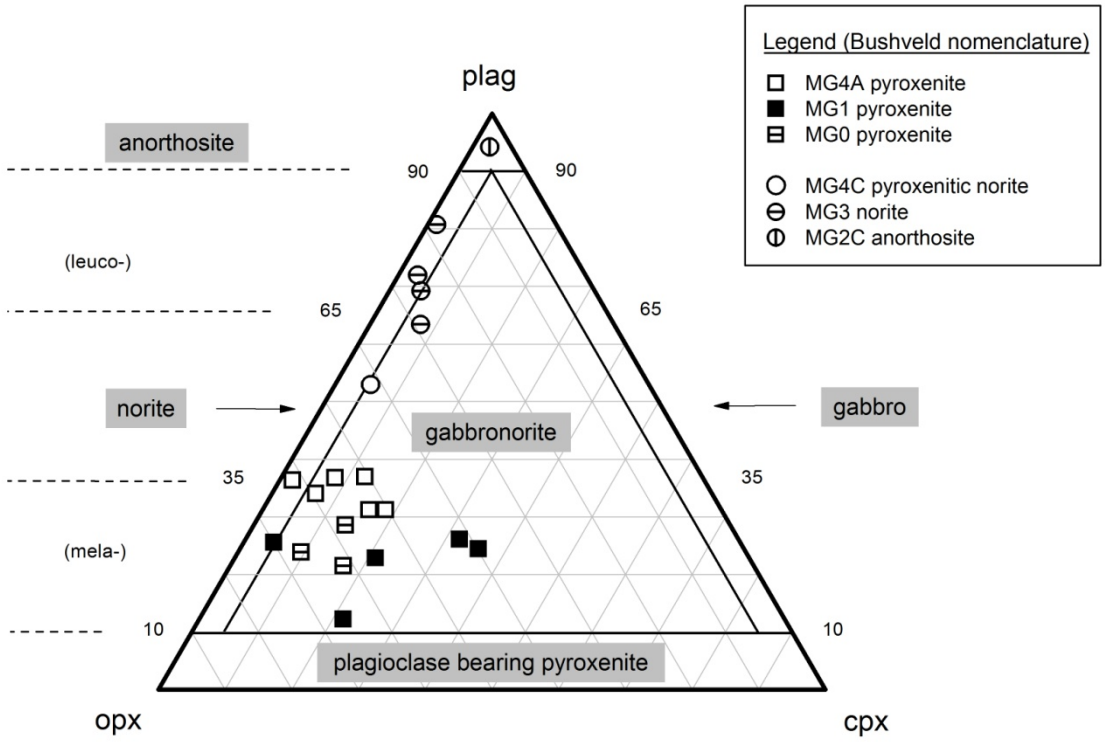

Figure 4.21 Ternary orthopyroxene-clinopyroxene-plagioclase plot based on Point Count analyses of the silicate rocks of the MG sequence (after LeMaitre, 2002).

4.3 Mineral chemistry

4.3.1 Chemistry of chromite grains from chromitite layers

Chemical data for single chromite grains were obtained by SEM-EDX for the major elements and by LA-ICP-MS for the trace elements. The results base on 55 chromite grain analyses from SEM-EDX and 208 measurements with the LA-ICP-MS. Except from MG4B and MG0 one thick polished section has been chosen from each layer to be analysed with the SEM-EDX. The SEM-EDX data have been used to estimate changes in chromite compositions within chromitite layers of the MG sequence. For LA-ICP-MS analyses three additional samples were used: one more each from the MG4B and the

MG4A chromitite and one for MG0. In total, 101 grains have been analysed by line ablation.

The ternary plot in figure 4.22 illustrates the average relative element proportions of Al^{3+}, Cr^{3+} and Fe^{3+} within the chromite grains for each layer. Cr is the major element in the chromite grains and behaves mirror inverted to Al: as the one increases the other one decreases at the same time (Tab. 4.2). It speaks for mutual substitution in the same crystal lattice position.

Table 4.2 Chromite composition gained with SEM-EDX analyses. FeO and Fe_2O_3 have been recalculated from FeO with the spreadsheet of Barnes (2005) on the assumption of stoichiometric distribution of the cations. Mg#: $Mg/(Mg+Fe^{2+})$. Major element oxides are given in wt%; n = number of grains analysed. Detailed results of individual chromite analyses are given in appendix B, Tab. B-3.

layer	**MG1**	**MG2A**	**MG2B**	**MG2C**	**MG3**	**MG4A**	**MG4C**
n	8	8	7	8	7	8	9
SiO_2	0.8	0.1	0	0.8	0.7	0.4	0.2
TiO_2	0.6	1.1	0.8	1.0	1.1	0.8	1.5
Al_2O_3	16.1	16.2	17.6	17.2	16.0	18.4	13.9
Cr_2O_3	47.5	45.4	40.6	44.6	44.9	43.6	43.7
Fe_2O_3	5.5	7.4	6.1	6.3	7.3	6.8	10.1
FeO	20.7	20.6	17.8	21.5	21.6	21.3	23.4
MgO	9.4	9.9	10.8	9.3	9.1	9.5	8.2
Na_2O	0	0.2	0.1	0.1	0	0	0.1
total	100.6	100.7	93.7	100.6	100.7	100.7	101.0
cations on the basis of 32 oxygens							
Si	0.20	0.02	0	0.19	0.18	0.09	0.06
Ti	0.12	0.21	0.17	0.19	0.21	0.15	0.29
Al	4.86	4.89	5.61	5.18	4.86	5.51	4.27
Cr	9.63	9.22	8.67	9.00	9.13	8.78	9.04
Fe^{3+}	1.05	1.42	1.23	1.20	1.41	1.30	1.99
Fe^{2+}	4.44	4.41	4.03	4.59	4.64	4.53	5.12
Mg	3.58	3.78	4.34	3.54	3.49	3.60	3.20
Na	0	0.10	0.04	0.05	0	0	0.04
Mg#	0.45	0.46	0.52	0.44	0.43	0.44	0.39
$Cr^{3+}/(Cr^{3+}+Fe^{3+})$	0.90	0.87	0.88	0.88	0.87	0.87	0.82
Fe^{3+}/Fe^{2+}	0.24	0.32	0.31	0.26	0.30	0.29	0.39
$Cr^{3+}/(Cr^{3+}+Al^{3+})$	0.66	0.65	0.61	0.63	0.65	0.61	0.68

Contradictory to the data of Teigler and Eales (1993), who described higher Al_2O_3 contents of chromite grains from chromitite layers of the UCZ relative to those from the LCZ, the chromite grains in the MG sequence don't show such striking difference. Only analyses from the MG4C chromitite layers plot in a cluster of higher Al_2O_3 contents (11-15%). The FeO contents range from 17.81 wt% to 23.37 wt% and Fe_2O_3 concentrations from 5.47 wt% to 10.10 wt%. As the Cr_2O_3 content decreases throughout the stratigraphy, the FeO_{tot} content increases, which coincides with findings from Teigler and Eales (1993). MgO content varies very little and is about 9 wt% on average. This type of Cr-spinel is termed picotite and has the chemical formula $(Fe,Mg)(Cr,Fe,Al)_2O_4$ (Rösler, 1991). However, for reasons of simplicity, the term 'chromite' is used throughout this study.

Figure 4.22 furthermore shows comparative chromite analyses done by Cameron (1977) on chromite deriving from the same stratigraphic sequence from the north of the eastern Bushveld, i.e. farms Jagdlust 418 KS and Winterveld 417 KS. There are comparatively plotted to the regional data of this study. Generally, chromite from chromitite layers in the UCZ (MG2C-MG4C) investigated by Cameron (1977) show higher amounts of Al^{3+} and Fe^{3+} and less Cr^{3+} compared to those investigated during this study. In the LCZ , i.e. from the MG1 to the MG2B chromitite layer, chromite of this study rather have higher Al^{3+} and less Fe^{3+} than those investigated by Cameron (1977), whereas the content of Cr^{3+} varies.

Figure 4.23 presents cryptic variations in chromite composition from the chromitite layers upwards the stratigraphic column of the MG sequence. For comparison, chromite data from Cameron (1977) have been added. In general, the Cr/(Cr+Al) ratio of chromite from this study increases and the $Cr/(Cr+Fe^{3+})$ ratio decreases, indicating evolution of magma composition from which the chromite grains were derived, but the values from the MG4A chromitite layer show a prominent shift to more primitive composition within this general trends. The data of Cameron basically show the same trends upwards the stratigraphic column. Exceptions are visible in the $Cr^3+/(Cr^{3+}+Al^{3+})$ ratio of chromite from the MG2C and MG3 chromitite layers, which rather show increasing amounts of Al relative to Cr then a decreasing $Cr^3+/(Cr^{3+}+Al^{3+})$ ratio as is illustrated by chromite data from this study. Depicted by the $Cr^3+/(Cr^{3+}+Al^{3+})$ ratio, Cameron's chromite analyses show higher amounts of Cr in the LCZ and more Al in the UCZ compared to chromite of this study.

In the $Cr^3+/(Cr^{3+}+Fe^{3+})$ ratio of the uppermost chromitite layers another difference in the trend can be seen, but this eventually is caused by data from different chromitite layers, i.e. MG4C (this study) and MG4B (Cameron, 1977).

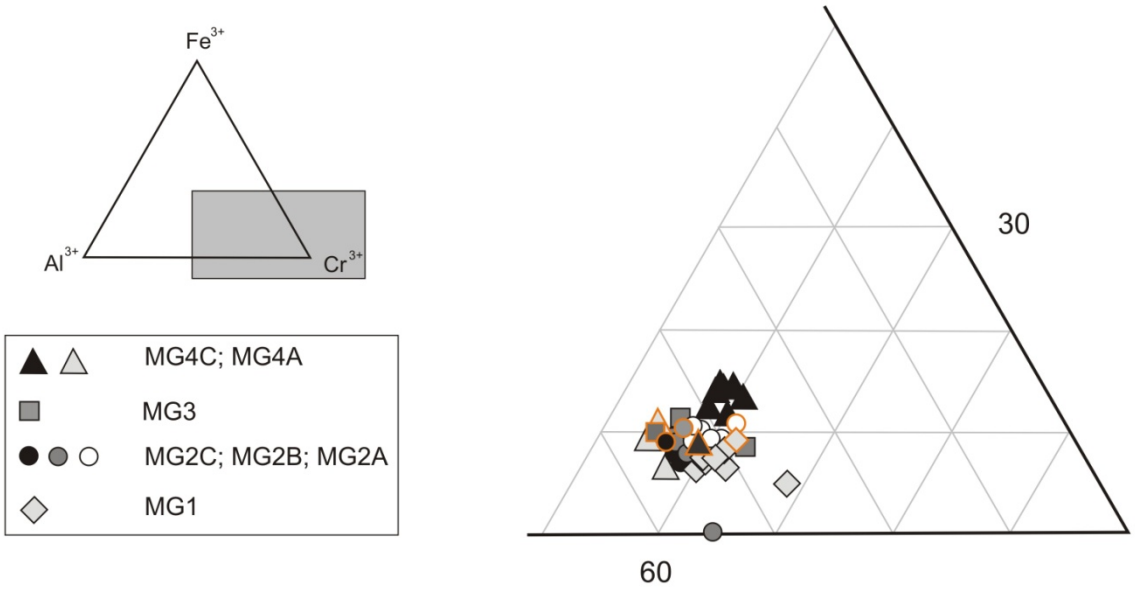

Figure 4.22 Averaged composition of chromite grains from the individual chromitite layers of the MG sequence obtained from SEM-EDX analyses. Data are given in table 4.2. Orange rimmed symbols are average data of chromite from the north of the eastern Bushveld Complex analyzed by Cameron (1977).

In the LCZ, chromite of both studies show decreasing $Cr^3+/(Cr^{3+}+Al^{3+})$ and $Cr^3+/(Cr^{3+}+Fe^{3+})$ ratios from the MG1 to the MG2B chromitite layer due to advancing Al^{3+} or Fe^{3+} concentrations, respectively. However, at the bottom of the LCZ/UCZ transition, i.e. within the MG2C chromitite layer, both ratios rise. From there on upward the stratigraphic column the ratios show a mirror inverted behaviour, which is interpreted to result from co-precipitation of cumulus plagioclase besides chromite and orthopyroxene resulting from fractional crystallization of the melt.

The tenor of the Mg# generally decreases from bottom to top of the MG sequence, which coincides with findings from Teigler and Eales (1993) for the same stratigraphic level in the western BC. Although slightly higher, the Mg# of chromite investigated by Cameron (1977) shows the same trend as those analyzed during this study.

In the UCZ of the MG sequence the tenor of the Mg# coincides with that of the $Cr^3+/(Cr^{3+}+Fe^{3+})$ ratio and it also shows the shift observed for the ratio at the MG4A chromitite layer. Decreasing Mg# in spinels is normally attributed to decreasing crystallization temperature (Harmer and Sharpe, 1985), thus an increase in Mg# could imply an increase in temperature at the level of the MG4A chromitite layer. It could illustrate the addition of primitive melt to the existing hybrid in the magma chamber at the level of the MG4A chromitite layer (cf. appendix D).

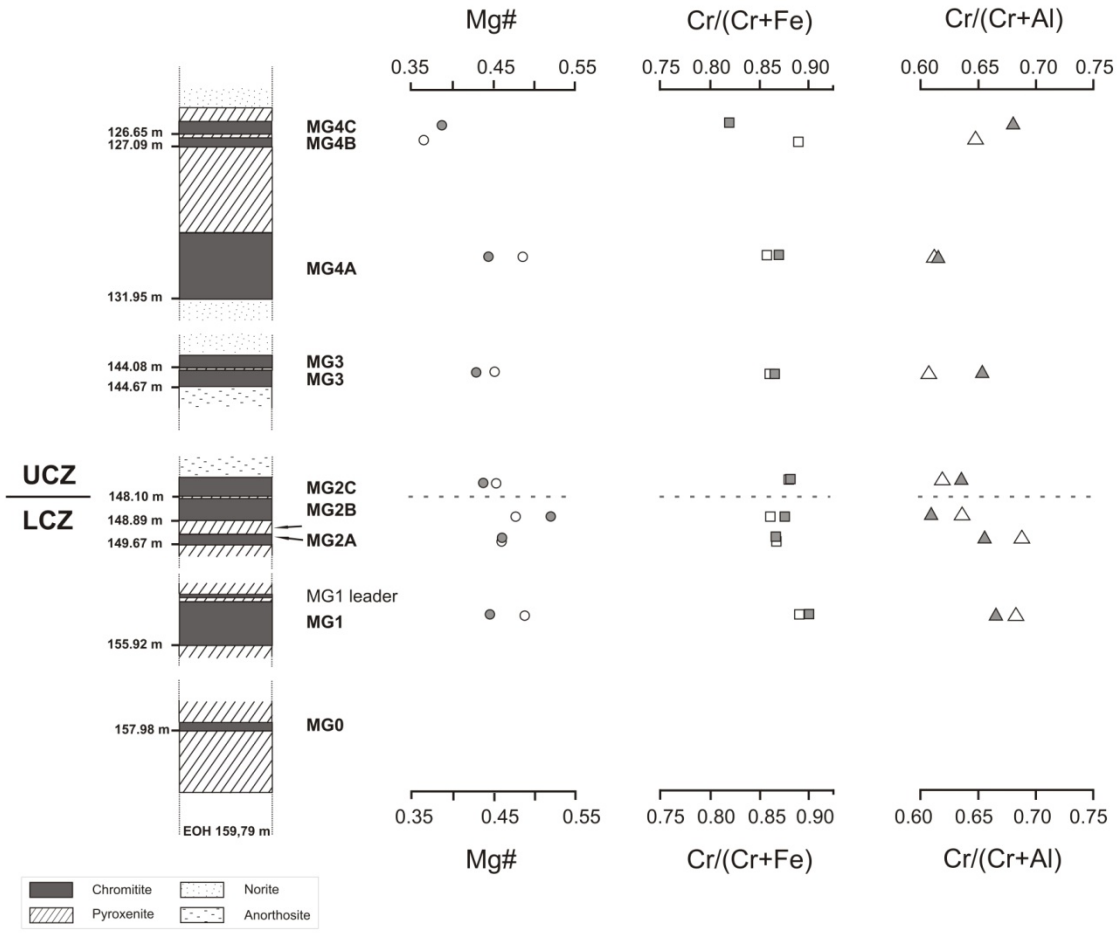

Figure 4.23 Plot of the averaged Mg# and the $Cr^3+/(Cr^{3+}+Al^{3+})$ and $Cr^3+/(Cr^{3+}+Fe^{3+})$ cation ratios of chromite grains vs. the stratigraphy of the MG sequence gathered from SEM-EDX (grey symbols). Data are given in table 4.2. For comparison, data from Cameron (1977) have been plotted, too (white symbols).

As Cameron (1977) argued, variation in chromite composition reflects fractionation of the magma, rather than subsolidus equilibration, since he couldn't find differences in the Mg/Fe ratio of chromite being surrounded by orthopyroxene or plagioclase. His observations thus confirm a general progressive melt evolution for the MG, with minor influxes of primitive melt at the level of the MG2B and MG4A chromitite layers (cf. Mg# in Fig. 4.23).

As elements relatively incompatible to chromite, the TiO_2 and V concentrations within the chromite lattice can be used as indicators for progressive melt evolution. Interestingly, such progressive melt evolution is only well depicted within the LCZ by increasing TiO_2 and V concentrations (Table 4.3, Fig. 4.24). At the level of the MG2B chromitite layer a slight decrease illustrates a period of addition of primitive melt composition.

A completely different picture can be seen in the UCZ, where the TiO_2 rather decreases and the V values stagnate if looking at averages of MG4A and MG4B+MG4C.

Within the relatively thick MG4A chromitite layer as well as in the MG4B-MG4C join progressive melt evolution is illustrated by increasing TiO_2 and V contents and thus confirm the formation of the chromitite layers in cyclic units. Low TiO_2 and V concentrations at the base of the MG4A chromitite substantiate the possibility of an influx of magma much more primitive than that forming the MG chromitite layers in the LCZ.

Righter *et al.* (2006) reported that partition coefficients for Ti and V between spinel and melt strongly depend upon temperature, fO_2 and spinel composition. Thus, decreasing melt temperature is envisaged to result in the increasing TiO_2 concentrations up to the MG3 chromitite in the MG sequence as well as increasing amounts of V. With the magma addition postulated at the bottom of the MG4A chromitite, the melt temperature raises likewise resulting in decreasing amounts of TiO_2 and stagnating V concentrations (Fig. 4.24).

Table 4.3 Trace element concentrations within chromite grains from the chromitite layers of the MG sequence. The following isotopes were analyzed with the LA-ICP-MS: Ti = 47, V = 51, Co = 59, Ni = 61, Zn = 66, Ga = 71.

layer	sample	TiO_2 %	V ppm	Co ppm	Ni ppm	Zn ppm	Ga ppm
MG4C	HEX10/1	1.6	7536.6	519.3	1530.0	1433.2	60.3
MG4B	HEX10/5	1.1	2663.7	408.8	1634.2	1025.8	59.0
MG4A_2	HEX10/6	14	6756.6	571.5	2820.9	1222.0	59.8
MG4A_1	HEX10/11	1.3	3555.0	426.9	1340.6	997.0	67.9
MG3	HEX10/23	1.8	5042.3	482.4	2744.6	1019.2	52.6
MG2C	HEX10/28	1.2	6129.3	479.4	1375.2	1183.1	60.7
MG2B	HEX10/37	0.9	3001.2	419.5	1538.2	1010.1	60.8
MG2A	HEX10/38	1.1	5066.9	418.2	1247.3	1220.3	54.8
MG1	HEX10/43	0.9	4413.6	433.0	1207.3	1037.2	50.3
MG0	HEX10/50	0.9	3021.6	394.6	1256.0	1039.5	49.1

The chromite grains show prominent amounts of Ni, Zn and Co (Tab. 4.3; average values are 1400 ppm, 1100 ppm and 400 ppm, respectively), which occur in solid solution within chromite grains. Ga contents of 58 ppm on average have also been detected. This particular set of elements have been chosen, since they substitute for the major elements in chromite (Tab. 4.4) and thus can be used as petrogenetic indicators pointing to the nature and source of the parental melt.

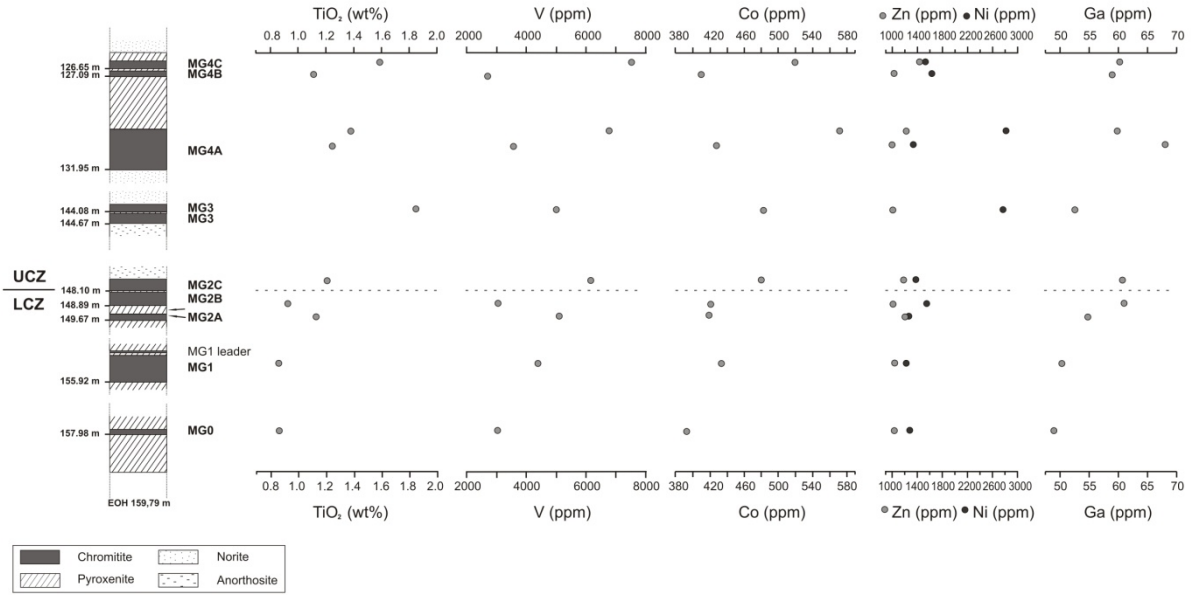

Figure 4.24 The development of the concentrations of TiO_2 and some trace elements within chromite grains upwards the stratigraphic column of the MG sequence acquired with LA-ICP-MS. Data are given in table 4.3.

Table 4.4 Position of the major and trace elements in chromite (Navrotsky and Kleppa, 1967; Nehru *et al.*, 1974; Princivalle *et al.*, 1989; O'Reilly *et al*., 1991; Canil, 2002).

Octahedral sites	Tetrahedral sites
Cr^{3+}, Al^{3+}, V^{3+}	Al^{3+}, Ga^{3+}
Mg^{2+}, Ni^{2+}	Mg^{2+}, Fe^{2+}, Zn^{2+}

Co, Ga and Zn generally show increasing trends in the LCZ (Fig. 4.24). Their tenors in the UCZ are very similar to that of V. Except for the MG2A, MG4A and MG4B chromitite layers, the tenor of the Ni concentrations is mirror inverted to those of Co, Ga and Zn. As could have been shown from the Mg# and the $Cr^3+/(Cr^{3+}+Al^{3+})$ and $Cr^3+/(Cr^{3+}+Fe^{3+})$ ratios, an increase of melt temperature at the base of the MG4A chromitite layer is most likely. This can also be observed from the data of Co, Zn and Ni, since at the same level a prominent shift in the tenors to lower concentrations appears. The Ga content is generally increasing within the LCZ as well as in the UCZ, but it often behaves different to the other trace elements. Highest Ga concentrations are present at the bottom of the MG4A chromitite layer. If primitive magma addition at this point is assumed, high amounts of Ga in Cr-spinel indicate its formation from a magma of primitive composition.

In the western Bushveld the values of **Ni** range between 393-1179 ppm for the LG, and 943-1022 ppm for the UG chromitites (Paktunc and Cabri, 1995).[7] Hence, the Ni values of the MG chromitites determined during this study (1207-2820 ppm) are considerably higher than those obtained by Paktunc and Cabri (1995) (cf. Tab. 4.3).

When compared to Ni values from other layered intrusions, as the Bird River Sill, Manitoba, and the Mechanic Intrusion, New Brunswick, the Ni values obtained for chromitites during this study range in the upper section of the cluster (Fig. 4.25). Due to the high Ni content they chemically are rather similar to ultramafic dikes.

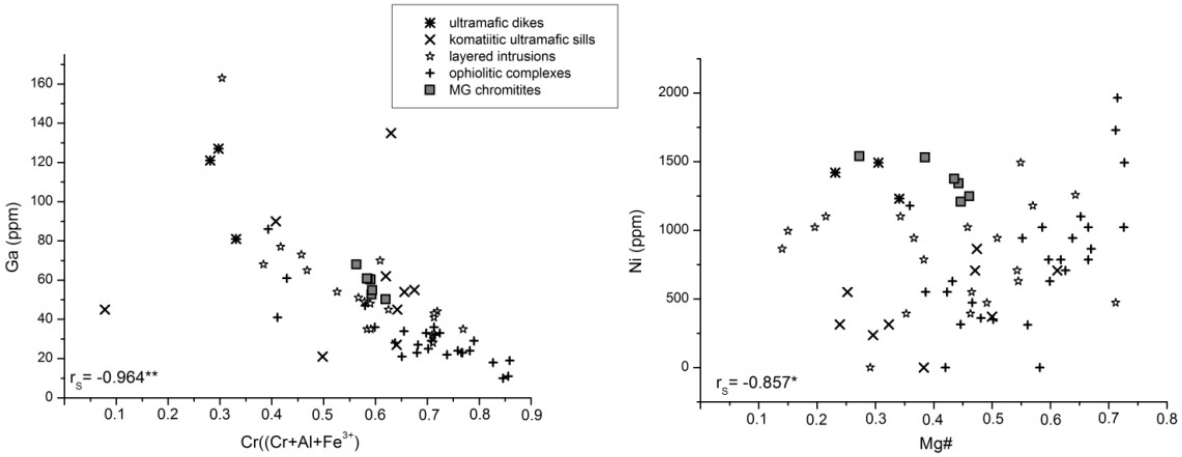

Figure 4.25 Variation of Ga with Cr/(Cr+Al+Fe^{3+}) and Ni with Mg# in chromite of the MG sequence compared to chromite from ultramafic dikes, komatiitic ultramafic sills, layered intrusions and ophiolitic complexes (data from Paktunc and Cabri, 1995). Mg# has been calculated Mg/(Mg+Fe^{2+}). r_s= Spearman rank correlation coefficient; **correlation significant at the 0.01 level; *correlation significant at the 0.05 level.

Paktunc and Cabri (1995) also determined **Zn** values from chromite grains in the LG and the UG chromitites of the western Bushveld Complex, which range between 642-5784 ppm for the LG and 884-2169 ppm for the UG chromitite layers. Zn concentration of chromite from the MG chromitite layers of this study have been determined to vary from 1000 to 1433 ppm (cf. Table 4.3). Contradictory to the Ni values, the results for Zn in chromite of the MG are rather lower than those found for the LG and UG.

Different from the data of Paktunc & Cabri (1995), there is no correlation between Zn and the Mg#, which was interpreted as a temperature control on Zn distribution in dependence of the dominant divalent cations (Mg and Fe^{2+}) (Fig. 4.26). However, a positive correlation between Zn and V exists, rather pointing to similar geochemical

[7] Pactunc and Cabri (1995) analyzed Ni and Zn in chromite with the electron microprobe and Ga with the proton microprobe.

behaviour in terms of incompatibility, and enrichment with increasing fractionation of the melt (Fig. 4.26).

Ga concentrations determined by Paktunc and Cabri (1995) range between 28-54 ppm for chromite of the LG and 70-73 ppm for chromite of the UG chromitites. Thus, the Ga concentrations of the studied MG chromitites (58 ppm on average) fall into the middle of LG and UG values. Hence an increasing trend through the stratigraphy of the CZ can be described, pointing to increasing evolution of the melt.

The inverse relationship of Ga with the $Cr/(Cr+Al+Fe^{3+})$ ratio presented in figure 4.25 can be interpreted to describe the dependence of Ga abundance on the distribution of the dominant trivalent cations Cr, Al and Fe^{3+}.

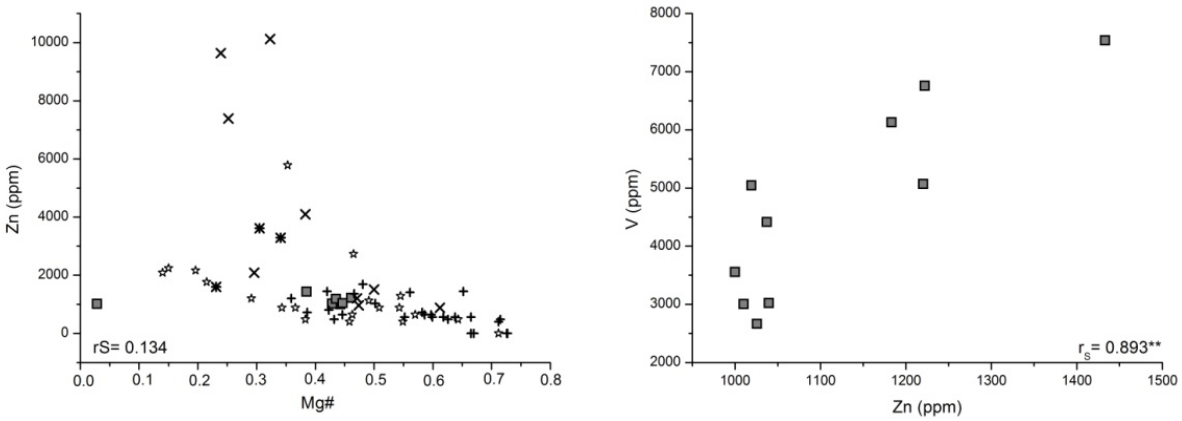

Figure 4.26 Variation of Zn with Mg# and bivariate plot of Zn versus V. Data of chromite grains from the MG chromitites are averages from chromite analyses obtained with the LA-ICP-MS. r_S: Spearman rank correlation coefficient; ** correlation significant at the 0.01 level.

Hence, only the abundances of Ga can be directly attributed to progressive melt evolution the CZ chromitites derive from. Within the stratigraphic level of the MG Ni and Zn also show increasing amounts within chromite, but relative to the LG and UG chromite grains no general enrichment from bottom to top of the CZ is present. Since the comparative data of Paktunc and Cabri (1995) derive from chromite grains of the western Bushveld, high amounts of Ni and Zn are probably a characteristic feature of the eastern Bushveld Complex.

High Ni in chromite points to a magma source being enriched in Ni, which is thought to be the peridotite from the upper mantle (Paktunc and Cabri, 1995). Zn abundances presented by Paktunc and Cabri (1995) derive from the sulphide-enriched chromitite layers of the UG and the relatively S-poor chromitite layers of the LG, thus explaining the strong variations within the values. Elevated amounts of Zn in chromite grains from the

MG sequence appear in samples at the top of the chromitite layers, especially at the top of the MG4A and MG4B-MG4C chromitite layers. It suggests some kind of enrichment process with respect to sulphides.

Since the data set of chromite composition is not normally distributed (Fig. B-1 in appendix B), correlation matrices using the Spearman rank coefficient of correlation and the two-sided test have been calculated (appendix B, Tab. B-4). Besides the melt composition, chromite composition is also influenced by subsolidus equilibration with coexisting minerals or liquid. Thus, the modal proportion of the coexisting phases has to be considered when looking at the chromite composition.

The strongest correlation exists between FeO and MgO (r_S= -0.964). It's a negative one due to progressive evolution of the melt the chromite derives from resulting in less primitive chromite compositions, as well as increasing degree of co-precipitating pyroxene (cf. Fig. 4.7 in subsection 4.2.1). This trend is also depicted in the generally decreasing Mg# of chromite with height (cf. Fig. 4.23). The same conclusions, i.e. progressive evolution of the melt, can be deduced from another strong negative correlation existing between FeO and Cr_2O_3 (r_S= -0.821). Thus, decreasing amounts of Cr_2O_3 are linked to increasing amounts of FeO within the chromite grain.

Positive correlations exist between FeO with TiO_2 and Co (r_S= 0.821 or 0.857, respectively). As has been shown before, with increasing V content the content of Zn increases simultaneously (r_S= 0.857). It means that with a general increase in the iron content the chromite grains further become enriched in the trace elements – another prove for progressive evolution of the melt, since the trace elements are rather incompatible relative to chromite.

Modified Harker diagrams have been plotted with Cr_2O_3 at the x-axis, since Cr is the dominating element in the chromite grains (Fig. 4.27). The plots have been done in relation to the stratigraphy of the MG sequence and show decreasing Cr_2O_3 contents with increasing concentrations of Al_2O_3, Fe_2O_3, FeO and MgO. It is noteworthy that the samples from the MG4C chromitite layer generally plot in a separate cluster. Chromite composition in this layer is dominated by Fe_2O_3, FeO and Cr_2O_3, which could be an indication for high amounts of co-precipitating pyroxene and plagioclase intensively consuming Mg or Al, respectively.

Cameron's (1977) data generally plot in the range of chromite data from core HEX10. Significant differences are visible in chromite chemistry from the MG3 chromitite layer from the north of the eastern Bushveld, having lower Cr_2O_3 contents. Additionally, it has lower concentrations of Al_2O_3 and FeO but higher amounts of Fe_2O_3. It thus reflects a more evolved chromite composition. Chromite from the MG2A chromitite layer also show

a quite evolved composition with lower Al_2O_3 and higher Fe_2O_3 compared to chromite chemistry of the same layer in the south.

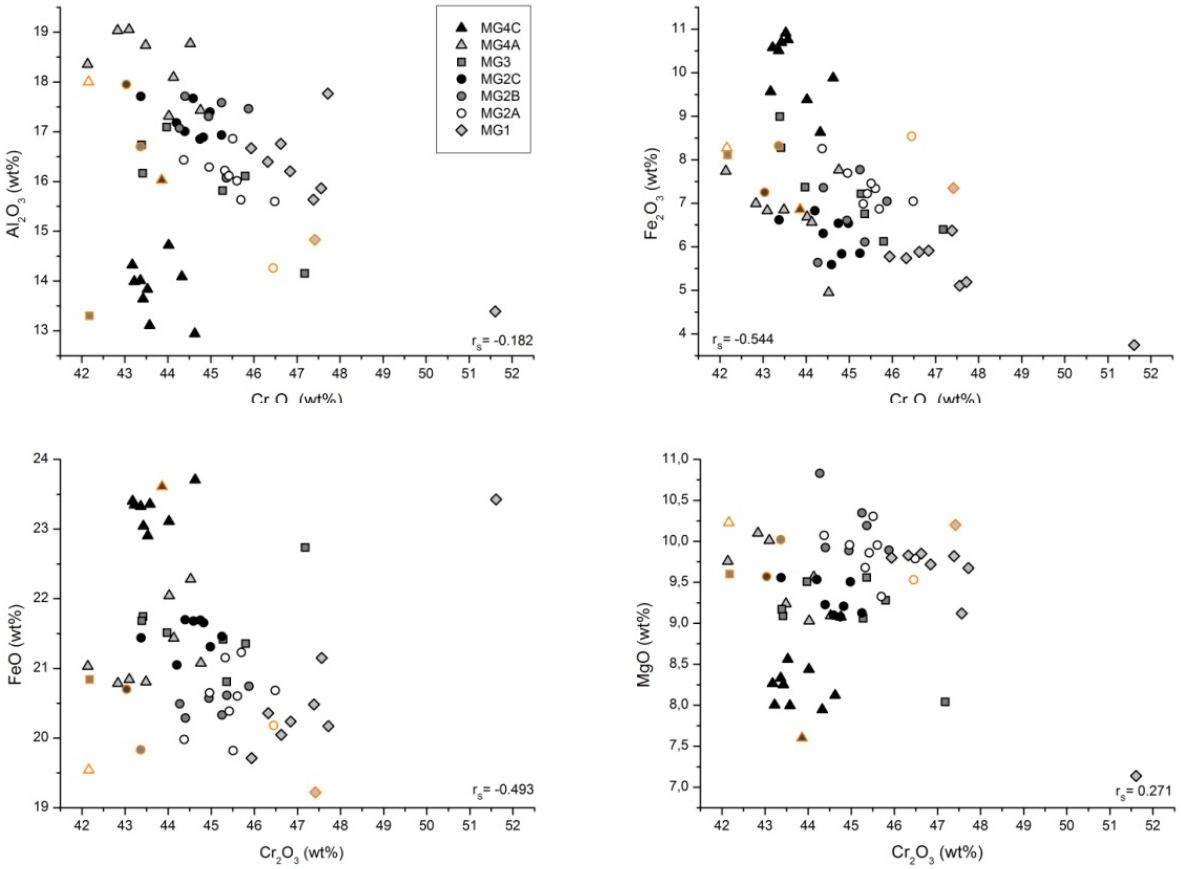

Figure 4.27 Bivariate plots showing the relationships of the major element oxides being key components in chromite. Data are given in table 4.2. r_s= Spearman rank correlation coefficient showing no significant correlation. Orange rimmed symbols are comparative data from Cameron (1977).

Table B-4 in appendix B also comprises data pairs having moderate correlation coefficients but no statistic significance. Sometimes, missing significance is due to outlier from the data set. This applies to three data pairs, which have been plotted in figure 4.28. On the one hand it shows the reverse correlation of Al_2O_3 with Fe_2O_3 or MgO, respectively, plotted with regard to the stratigraphy of core HEX10. In the LCZ Fe_2O_3 and MgO contemporaneously increase with Al_2O_3. Up to the MG3 chromitite layer the MgO contents drop, whereas Fe_2O_3 concentrations rather incline due to once more increasing amounts of co-precipitating orthopyroxene consuming Mg rather than Fe. At the level of the MG4A chromitite, Al_2O_3 and MgO concentrations are reset to most primitive compositions, which develop within a very short distance to most evolved ones up to the MG4C chromitite. The same applies for Fe_2O_3. The resetting is ascribed to the addition of

primitive magma in an amount exceeding those triggering the formation of chromitite layers below. The same result can be deduced from the correlation of FeO and TiO_2 (Fig. 4.28). Generally, progressive evolution of the melt upwards the stratigraphic column is illustrated but at the level of the MG4A chromitite layer TiO_2 as well as FeO concentrations within chromite are reset to lower values indicating the addition of more primitive magma. Even here the fast progressive evolution of chromite composition up to the MG4C chromitite is illustrated.

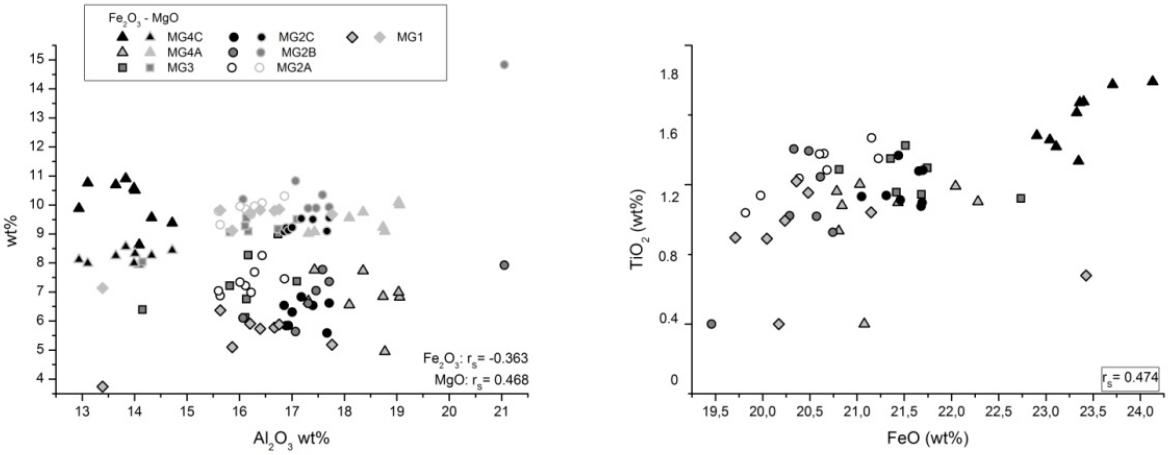

Figure 4.28 Interrelationship between selected major element oxides building up chromite. r_s= Spearman rank correlation coefficient showing no significant correlation. Data are given in table 4.2.

When the Mg# is plotted vs. the cation ratio Cr/(Cr+Al) one can distinguish four individual clusters (Fig. 4.29) according to stratigraphy. The first cluster includes chromite from chromitite layers of the LCZ, i.e. MG1, MG2A-2B. From this a reverse evolution of chromite chemistry is detectable within chromitites of the LCZ (green arrow). The increase of the Mg# indicates addition of new magma, which exceeds changes due to crystallization, i.e. chromite rather consumes Fe than Mg and the precipitation of pyroxene is not strong enough. Proceeding chromite precipitation results in the consumption of Cr from the melt with the later crystallizing chromite having lower Cr/(Cr+Al) ratios.

Progressive evolution is towards MG2C and MG3 with lower Mg#, both occurring below or above the LCZ/UCZ transition (orange arrow). Lower Mg# result from co-precipitating pyroxene consuming Mg from the melt. The slightly higher Cr//Cr+Al) ratio within chromite grains of the MG3 chromitite relative to those below is caused by the onset of cumulus plagioclase crystallization.

Up to the MG4A another negative linear trend follows, which is illustrated by the red arrow. The MG4A chromitite shows the most primitive chromite chemistry with high Mg#

and low Cr/(Cr+Al). As for the LCZ an influx of primitive magma can be assumed. Since during the formation of the norite in the footwall of the MG4A chromitite the consumption of Al was high due to plagioclase precipitation, the low Cr/(Cr+Al) ratio displays the offset of massive plagioclase crystallization leading to higher amounts of Al_2O_3 within chromite. The chromite chemistry of MG4C plots separated from the other ones and shows the most evolved compositions with regard to the low Mg#. Evolution of the melt due to crystallization of pyroxene gives chromite composition with low Mg#; the high Cr/(Cr+Al) ratio points to co-precipitation of plagioclase. Thus, the MG4C chromitite layer hosts the most ordinary chromite with high FeO and Cr_2O_3 contents.

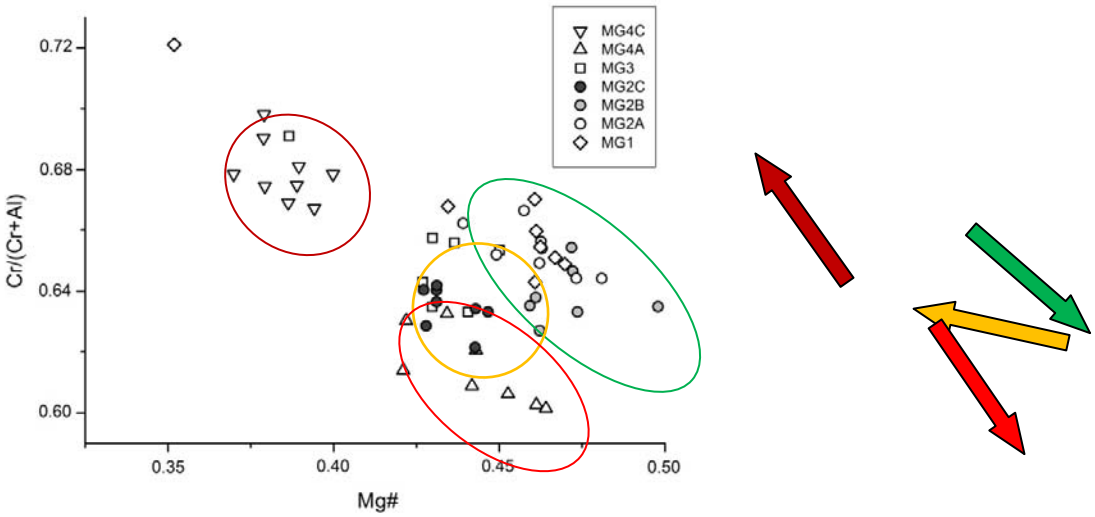

Figure 4.29 Cr/(Cr+Al) cation ratio plotted vs. Mg# ($Mg^{2+}/Mg^{2+}+Fe^{2+}$) for chromite chemistry of the individual MG chromitite layers. Green cluster: LCZ; orange and red clusters: UCZ. Arrows indicate the trends of the evolution of chromite composition upwards the stratigraphic column of the MG-sequence.

LA-ICP-MS analyses yielded in the lack of zonation of chromite grains (Fig. 4.30A and 4.30B), which can be ascribed to equilibration of chromite with interstitial liquid and/or silicates. For a few LA-ICP-MS measurements of samples from the MG4C, MG4A, MG3, MG2A and MG1 chromitite layers an evenly distribution of PGE within the chromite lattice have been detected. The most common one is Pt (detected in 6 of 97 chromite grains; Fig. 4.30D); followed by Ir (3), Rh (2) and Ru (2). Rather rare is Pd (1). Abrupt peaks of Cu, Au, Pd, Rh, Ni, Ru and rarely Os describe the existence of metal inclusions with sizes smaller than 5 µm (Fig. 4.30C). Since Fe has not been monitored, these inclusions probably represent alloys associated with Fe. Generally, these inclusions are more

common in the upper chromitite layers, i.e. MG4A and MG4C, and furthermore are dominated by the PGE and Cu.

Table 4.5 Inclusions within chromite grains.

sample	layer	type of inclusion (in order of abundance)	number
HEX10/01	MG4C	Cu; Pt, Pd; Ru, Au, PdS	11
HEX10/05	MG4B	Au	1
HEX10/06	MG4A	Rh; Pd, Ir	5
HEX10/11	MG4A	Cu; Ru	2
HEX10/23	MG3	Pd	1
HEX10/28	MG2C	Cu	2
HEX10/37	MG2B	---	---
HEX10/38	MG2A	Au	1
HEX10/43	MG1	Ni; Au	4
HEX10/50	MG0	---	---

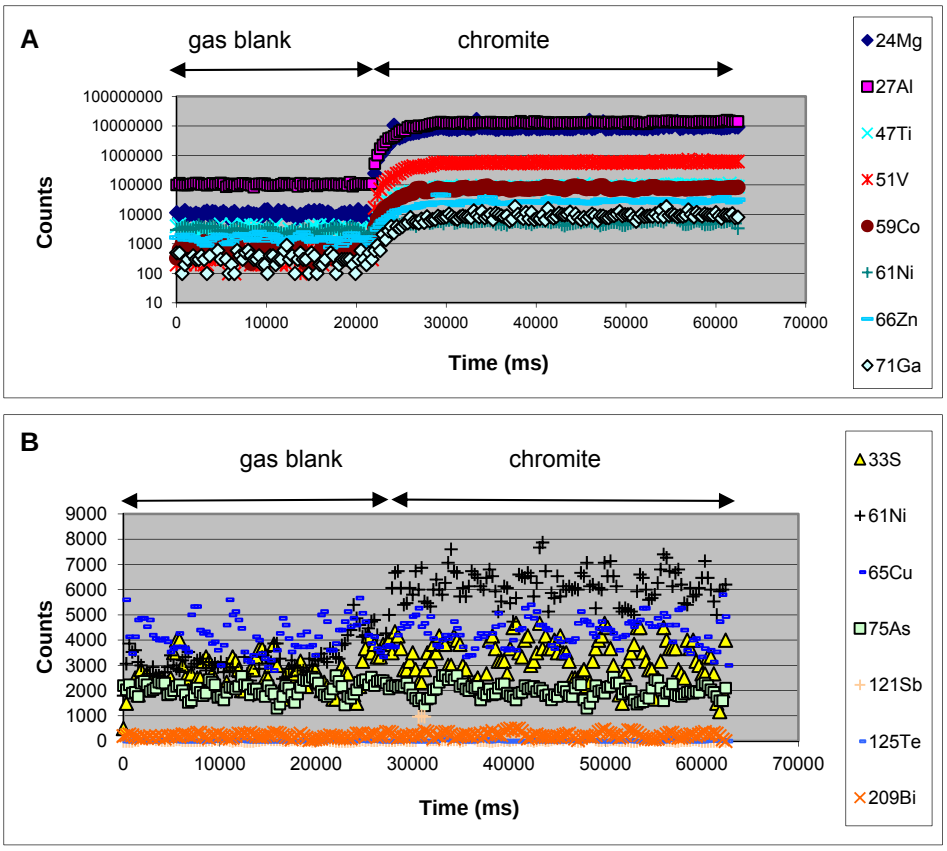

Figure 4.30 Typical spectra of chromite grains of the MG sequence. **(A)** Spectra for elements Mg, Al, Ti, V, Co, Ni, Zn and Ga. **(B)** Spectra for S, Ni, Cu, As, Sb, Te and Bi.

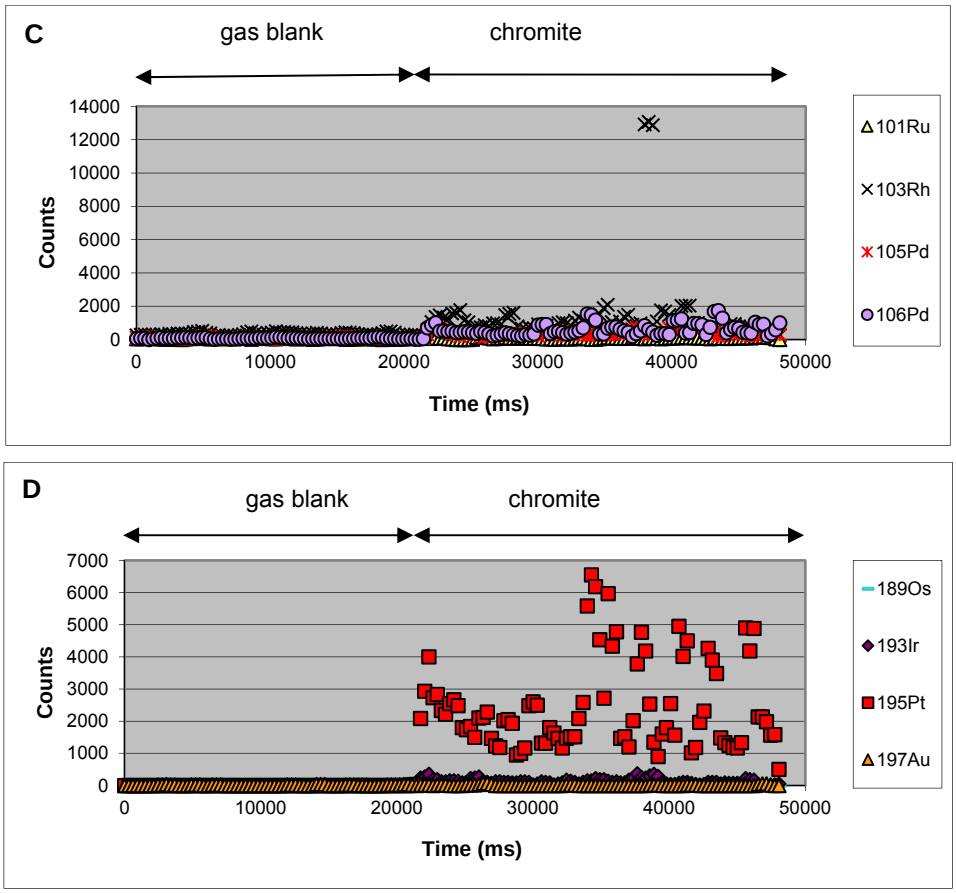

Figure 4.30 *(cont.)* Typical PGE spectra of chromite grains of the MG sequence. **(C)** Rh peak probably representing an alloy included in chromite. Rh and Pd appear to be evenly distributed within the chromite lattice. The same equally distribution is shown in **(D)** for Pt and Ir. (A) and (B) from sample HEX10/37 (MG2B); (C) and (D) from sample HEX10/01 (MG4C).

4.2.2 Chemistry of chromite grains from silicate rocks

In the following chapters, the samples are named with respect to the chromitite layer of the corresponding cyclic unit. For example, samples from the norite occurring above the MG3 chromitite layer are termed ‘MG3 norite’; pyroxenitic samples from the pyroxenite in the hanging wall of the MG2A chromitite are termed ‘MG2A pyroxenite’ and so on.

In the silicate rocks chromite occurs as cumulus chromite or as inclusion in orthopyroxene and plagioclase. Chromite composition as obtained with the SEM-EDX is presented in tables 4.6 and 4.7. Detailed results of individual analyses are given in appendix B, Tab. B-5.

The silicate layers are cumulate rocks with one or two dominating mineral phases, i.e. pyroxene and/or plagioclase. Equilibration of chromite takes place with two different kinds

of silicate minerals in maximum resulting in only slight compositional differences between cumulus chromite and chromite occurring as inclusion (cf. Tab. 4.6 and 4.7). Thus, for further interpretation the results have been summarized to create the figures of this chapter.

Table 4.6 Composition of cumulus chromite in silicate layers of the MG sequence. Fe_2O_3 and FeO have been calculated from FeO_{tot} with the spreadsheet of S. Barnes (2005). All values are given in wt%. *n*: number of grains analysed.

cyclic unit	**MG0**	**MG1**	**MG2A**	**MG2C**	**MG3**	**MG4A**
lithology	pyroxenite	pyroxenite	pyroxenite	anorthosite	norite	pyroxenite
n	2	6	2	2	4	3
SiO_2	0.3	1.2	0.7	0.5	1.0	1.3
TiO_2	0.4	0.4	0.4	1.1	0.8	1.2
Al_2O_3	16.4	18.0	21.2	10.9	17.4	13.3
Cr_2O_3	39.1	49.9	31.2	51.6	49.8	57.2
Fe_2O_3	17.9	2.9	19.4	4.9	3.6	0
FeO	22.4	21.5	18.1	28.9	22.3	22.6
MnO	0	0	0.6	0.6	0	0
MgO	5.2	5.1	6.9	2.0	4.5	3.8
CaO	0	0.1	0.3	0	0.2	0.1
Na_2O	0	1.1	1.2	0	0.8	0.4
total	102	100	100	100	100	100
cations based on 32 oxygen						
Si	0.09	0.26	0.79	0.15	0.25	0.44
Ti	0.07	0.10	0.03	0.22	0.15	0.26
Al	5.00	5.59	5.95	3.52	5.32	3.98
Cr	7.94	10.52	6.08	11.21	10.22	11.90
Fe^{3+}	3.59	0.34	3.59	1.04	0.70	0
Fe^{2+}	4.89	4.50	3.74	6.67	4.83	5.22
Mn	0	0	0.12	0.13	0	0
Mg	2.01	1.91	2.68	0.81	1.76	1.45
Ca	0	0.02	0.08	0	0.05	0.03
Na	0	0.33	0.61	0	0.41	0.18
Mg#	0.30	0.30	0.42	0.11	0.27	0.22
$Cr/(Cr+Fe^{3+})$	0.70	0.97	0.63	0.92	0.94	1.00
Cr/(Cr+Al)	0.59	0.65	0.51	0.76	0.66	0.75

Various ratios obtained from chromite chemistry have been plotted against the stratigraphic column of the MG and are shown in figure 4.31. Additionally, data from

Cameron (1977) have been plotted to illustrate differences in chemistry to chromite grains in silicate layers in the north of the eastern Bushveld.

The chromites in the silicate layers of this study generally show decreasing Mg#, as could be expected for a progressive fractional crystallisation trend. Within most of the silicate layers decreasing Mg# from bottom to top is present, resulting from progressive melt evolution due to fractional crystallization during the formation of one cyclic unit. The shifts to higher Mg# in the MG2B and the bottom of the MG4A (arrows in figure 4.31) indicate the addition of higher proportions of primitive magma as also shown by the associated chromitite layers.

Table 4.7 Composition of chromite enclosed by pyroxene in the pyroxenites and by plagioclase in norite and anorthosite. Fe_2O_3 and FeO have been calculated from FeO_{tot} with the spreadsheet of S. Barnes (2005). All values are given in wt%. n = number of grains analysed.

cyclic unit	**MG0**	**MG1**	**MG2A**	**MG2C**	**MG3**	**MG4A**
lithology	pyroxenite	pyroxenite	pyroxenite	anorthosite	norite	pyroxenite
n	1	3	1	1	7	18
SiO_2	0	6.2	12.6	0.9	0.8	0.9
TiO_2	0.9	0.3	0	1.1	2.0	1.1
Al_2O_3	13.8	18.5	26.4	11.8	15.1	20.0
Cr_2O_3	43.9	46.5	35.3	48.6	47.7	46.8
Fe_2O_3	9.4	0.5	0	2.6	6.8	3.9
FeO	28.5	19.8	10.7	31.5	22.2	21.5
MgO	4.4	6.3	13.6	1.6	6.0	5.7
CaO	0	1.6	1.3	0	0.4	0.1
Na_2O	0	0	0	1.4	0	0.4
total	100.9	99.7	100.0	99.5	100.8	100.4
cations based on 32 oxygen						
Si	0	1.30	2.79	0.24	0.10	0.18
Ti	0.74	0.21	0	0.92	4.82	0.84
Al	4.38	5.78	6.90	3.86	3.91	6.06
Cr	9.35	9.18	6.19	10.70	7.01	9.20
Fe^{3+}	1.90	0.07	0	0.55	2.97	0.90
Fe^{2+}	6.42	4.15	1.99	7.33	6.86	4.58
Mg	1.77	2.38	4.50	0.68	1.63	2.31
Ca	0	0.33	0.30	0	0.05	0.03
Na	0	0	0	0.76	0	0.17
K	0	0	0	0	0	0.02
Mg#	0.22	0.37	0.69	0.09	0.23	0.33
$Cr/(Cr+Fe^{3+})$	0.83	0.99	1.00	0.95	0.66	0.90
Cr/(Cr+Al)	0.68	0.62	0.47	0.74	0.61	0.60

Data from Cameron (1977) show lower Mg# in the pyroxenites of the LCZ without the prominent shift at the level of MG2B that have been observed from core HEX10. Chromite in the anorthosite in the hanging wall of the MG2C chromitite has a higher Mg# in the north than those in the south. Values for the MG3 norite and the plagioclase-bearing pyroxenite of the MG4A cyclic unit are within the range of chromite data from the south, i.e. this study.

The $Cr^3+/(Cr^{3+}+Fe^{3+})$ ratio increases upwards the stratigraphic column due to an enrichment of Cr, but the tenors within each cyclic unit are the same as have been observed for the Mg# illustrating fractional crystallization of chromite to more Fe rich varieties. However, with every cyclic unit a new batch of magma with new Cr is entering the system and increases the present amount of Cr. Since Cr^{3+} is relative incompatible to the crystal lattices of pyroxene and plagioclase it is incorporated into chromite only, and thus a general Cr-enrichment of chromite within the silicate layers upwards the stratigraphic column results.

An exception is the decreasing $Cr^3+/(Cr^{3+}+Fe^{3+})$ ratio of chromite from the MG4A pyroxenite. Here the chromite composition becomes enriched in Cr from bottom to top of the layer. From thin sections an enrichment of chromite approximately in the middle of the MG4A pyroxenite is recorded. Hence, this feature is reflected in geochemistry (circles around data points in Fig. 4.31) and indicates a new, but smaller influx of magma at this point. Due to that, the crystallization path seems to shift along the cotectic chromite-orthopyroxene with Fe being preferentially incorporated into pyroxene. This results in the observed Cr-enrichment of chromite within the MG4A pyroxenite.

Chromite in the MG2B pyroxenite is marked by lower $Cr^3+/(Cr^{3+}+Fe^{3+})$ ratio than chromite from the MG2A pyroxenite, which further corroborates primitive magma addition at this point (arrow in figure 4.31). For chromite at the bottom of the MG4A pyroxenite this feature is also visible, but not as clear as with the Mg#, since chromite from the top of the MG3 norite shows an even lower $Cr^3+/(Cr^{3+}+Fe^{3+})$ ratio.

Chromite date from the north of the eastern Bushveld (Cameron, 1977) show lower $Cr^3+/(Cr^{3+}+Fe^{3+})$ ratios in the LCZ, but have the same decreasing trend upwards the stratigraphic column. For the UCZ, the data for the MG3 norite are within the range of data from core HEX10, but again lower $Cr^3+/(Cr^{3+}+Fe^{3+})$ ratios can be seen in the MG2C anorthosite as well as plagioclase-bearing pyroxenite of the MG4A cyclic unit.

In the LCZ the $Cr^3+/(Cr^{3+}+Al^{3+})$ ratio behaves reverse to the development of the Mg#, indicating an enrichment of Cr in chromite relative to Al. It is interpreted to be caused by the incompatibility of Cr^{3+} into the lattices of co-precipitation silicate minerals. At the onset of the crystallisation of cumulus plagioclase in the UCZ the $Cr^3+/(Cr^{3+}+Al^{3+})$ ratio of chromite increases, since Al is intensively consumed by plagioclase. It results in Al

depletion within accessory chromite, which can especially be observed in the MG3 norite. For chromite within MG2C anorthosite as well as MG4A pyroxenite an enrichment in Cr is illustrated by the $Cr^3+/(Cr^{3+}+Al^{3+})$ ratio, as have been observed for the $Cr^3+/(Cr^{3+}+Fe^{3+})$ ratio.

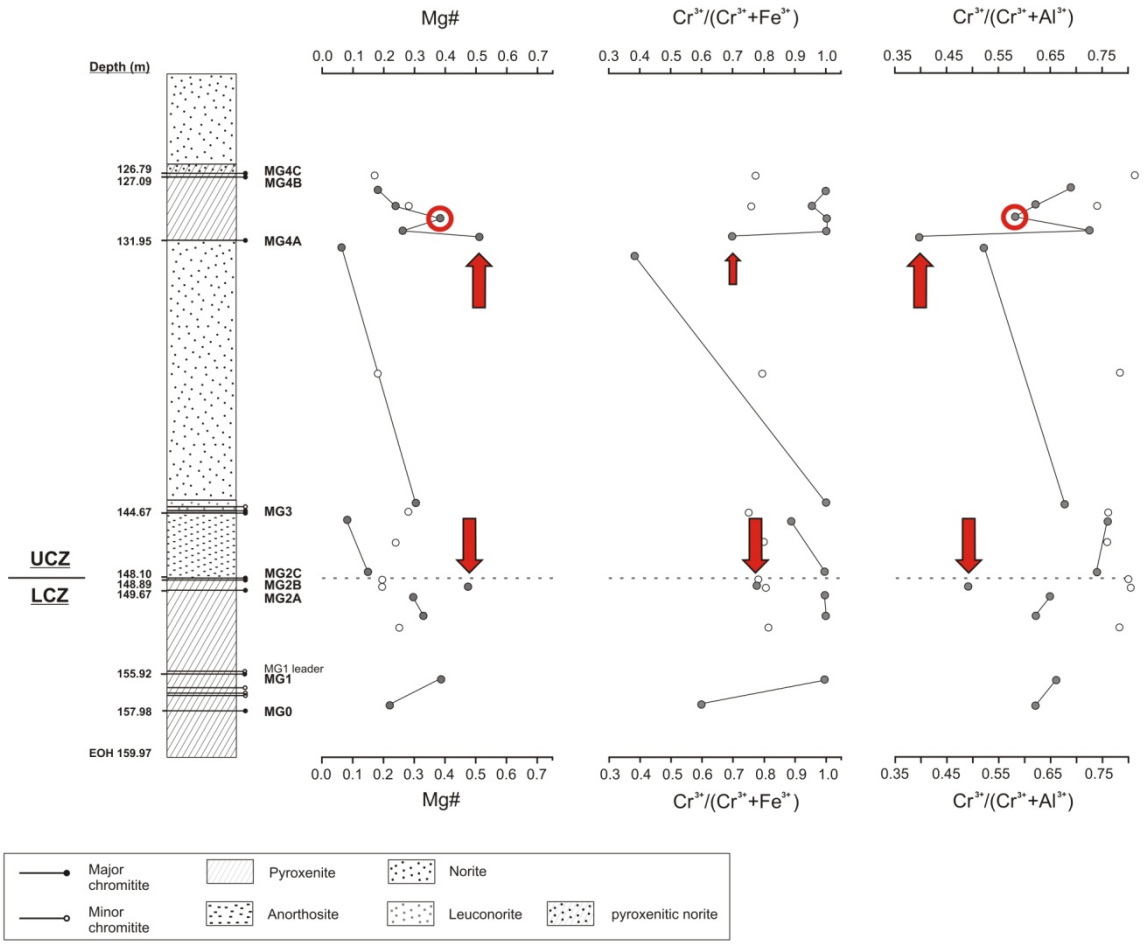

Figure 4.31 Summarized chromite composition from chromite of the MG sequence occurring as inclusion in silicate minerals and cumulus chromite in stringers or similar. Arrows indicate addition of primitive magma at points of high Mg# or low $Cr^{3+}/(Cr^{3+}+Fe^{3+})$ and $Cr^{3+}/(Cr^{3+}+Al^{3+})$ ratios, red circles indicate addition of Cr by another smaller magma influx during formation of the plagioclase-bearing MG4A pyroxenite. Data shown are averages from tables 4.6 and 4.7. White symbols represent data from Cameron (1977) and are averages from chromite analyses occurring within the silicate layers.

When compared to chromite from the other silicate layers, the ones from the MG2C anorthosite show reversed behaviour of the $Cr^3+/(Cr^{3+}+Fe^{3+})$ and $Cr^3+/(Cr^{3+}+Al^{3+})$ ratios. The chromite grains become enriched in Fe but depleted in Al, which perfectly can be attributed to the major cumulus mineral, the plagioclase. Plagioclase crystallization

intensively consumes Al, but doesn't incorporate Fe, which results in the observed composition of cumulus chromite.

Chromite from the north (Cameron, 1977) generally show higher $Cr^3+/(Cr^{3+}+Al^{3+})$ ratios with a stronger enrichment of Cr relative to Al when compared to chromite composition in core HEX10. Only the $Cr^3+/(Cr^{3+}+Al^{3+})$ ratio from chromite of the MG2C anorthosite is comparable to data from this study.

In the LCZ, the $Cr^3+/(Cr^{3+}+Al^{3+})$ ratio from chromite in the north of the eastern limb (Cameron, 1977) shows the same trend of increasing amounts of Cr relative to Al. Higher ratios in chromite from the MG3 norite and the MG4A pyroxenite in the north reflect enrichment of Cr relative to Al.

As is reflected in the Mg# and the $Cr^3+/(Cr^{3+}+Fe^{3+})$ ratio, the addition of primitive magma probably also shifted the $Cr^3+/(Cr^{3+}+Al^{3+})$ ratio of the MG2B pyroxenite and the MG4A pyroxenite to low values (arrows in figure 4.31). This seems to be a special feature of chromite from the south of the eastern limb, since the data from the north (Cameron, 1977) lack this significant shifts in the ratios.

When looking at the correlation matrix for chromite grains occurring in the silicate layers (Tab. B-6 in appendix B), the strongest correlation is present between Al_2O_3 and MgO (r_S= 0.854), which is ascribed to influxes of primitive magma and the offset of plagioclase precipitation. The latter is confirmed by coincidently increasing Mg# and $Cr^3+/(Cr^{3+}+Al^{3+})$ ratio in figure 4.31.

Progressive evolution of the melt, as illustrated by the Mg# before, can also be proved by the existence of the moderate negative correlation between Cr_2O_3 and FeO (r_S= -0.496) causing increasing Fe contents of chromite.

The moderate positive correlation of TiO_2 and Cr_2O_3 (r_S= 0.467) can be interpreted as Ti being incorporated into the lattice of chromite as the first precipitating mineral or the association of chromite with rutile, respectively.

Although moderate correlations of Na_2O and CaO with the other major element oxides exist, the concentrations of Na_2O and CaO are too low to create meaningful correlations.

4.2.3 Chromite from massive chromitite vs. chromite from silicate rocks

The ternary plot Fe^{3+}-Cr^{3+}-Al^{3+} in figure 4.32 shows the relationship of the three major cations important for composition of chromite grains occurring in the MG sequence. It can be seen that the composition of those occurring in silicate rocks scatter a lot, whereas the composition of chromite from chromitite layers are relatively the same. It gives further

support to the assumption mentioned above that the chromite composition in the silicate layers is influenced by equilibration with the co-precipitating silicate minerals.

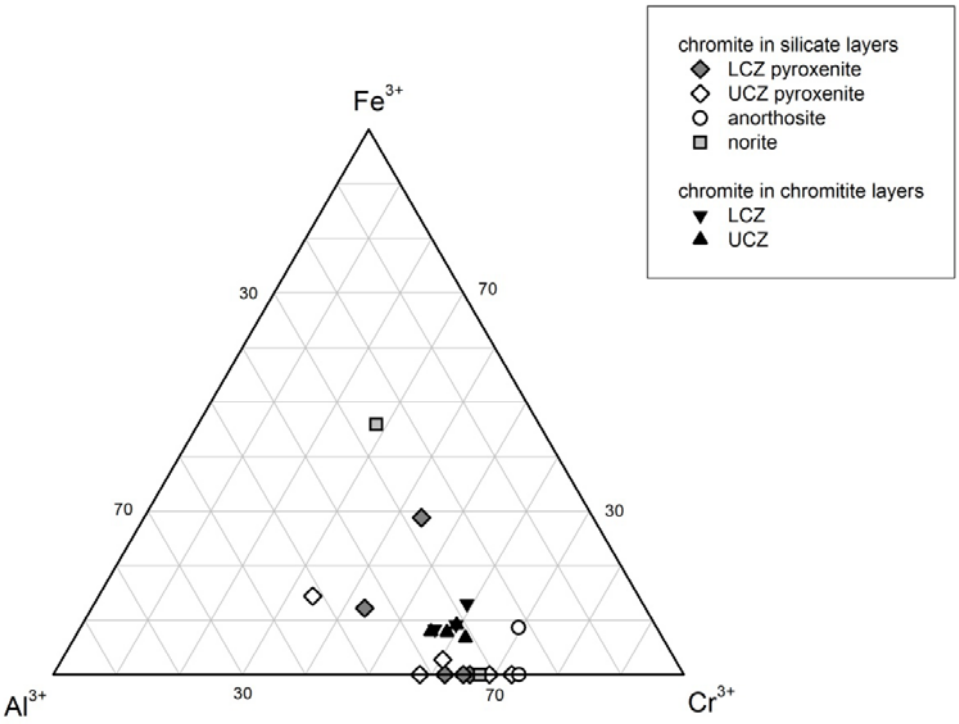

Figure 4.32 Comparative ternary plot of the composition of chromite grains occurring in the MG sequence. Data of massive chromitite layers (LCZ and UCZ) are averages for the individual layers.

In general, cumulate chromite in silicate rocks has by far the highest amounts of Cr^{3+} (> 60%), even higher than chromite grains from massive chromitite layers (< 60%). Those of the data points of chromite composition of the silicate layers showing lower Cr^{3+} concentrations occur with one exception in the hanging walls of the MG0, MG2A and MG4A chromitite layers. Cr^{3+} is here replaced by Fe^{3+} and Al^{3+}. The exception is a data point representing chromite composition in norite in the footwall of the MG4A chromitite layer, for which the highest Fe^{3+} concentrations have been acquired (46%). Teigler and Eales (1993) also found accessory chromite to be enriched in Cr_2O_3 relative to those occurring in massive chromitite layers of the UCZ. For the LCZ they noted a reversed relationship, which is not the case for the MG sequence.

The Fe^{3+} or Al^{3+} contents of chromite from massive layers differ slightly only (8-12% or 28-36%. respectively), whereas the Al^{3+} concentrations for chromite occurring in the silicate layers is highly variable (25-52%). Pyroxenitic layers generally have chromite with higher Al_2O_3 contents than noritic or anorthositic layers in the MG sequence, as in the latter Al_2O_3

is preferentially incorporated into plagioclase. In contrast and with a few exceptions, chromite from silicate layers contains almost no Fe^{3+}, which is contradictory to results from Teigler and Eales (1993) presenting chromite from massive layers being poorer in Fe^{3+} than those modally present in accessory proportions. The lack of Fe^{3+} described for accessory chromite of the MG-sequence is compensated by higher Cr^{3+} and Al^{3+} values. Plotting outside the general cluster are those four chromite data points with Fe^{3+} contents between 12-45% mentioned before.

The data presented thus in the first place illustrate the substitution of Fe^{3+} and Cr^{3+} in the chromite lattice of chromite from the silicate layers. As can be interpreted from the data points stratigraphically being situated at the hanging walls of the chromitite layers and showing low Cr^{3+}/Fe^{3+} ratios it seems that within each cyclic unit the chromite chemistry changes to more Cr enriched chromite grains, which can be ascribed to the relative incompatibility of Cr in the structures of silicate minerals, thus concentrating in chromite grains. Fe is preferentially incorporated into precipitating pyroxene into which Cr is relatively incompatible. Hence, in the silicate layers chromian spinel with the major components Cr-Al-Mg occurs, rather than picotite as observed in the chromitite layers (cf. subsection 4.3.1).

To summarize, chromite composition thus not only depends on original melt composition but strongly on the nature of its co-precipitating minerals influencing subsolidus equilibration. However, it nevertheless reflects progressive evolution of melt the MG sequence derives from and is very sensitive to changes in melt composition.

4.3.4 Chemistry of silicate minerals from the chromitite layers

4.3.4.1 Plagioclase

In the chromitite layers plagioclase occurs intercumulus to chromite and shows ambivalent composition. As can be seen from the Na_2O-CaO-K_2O ternary diagram in figure 4.33, there are two ‘clusters’ plotting in the sodium-rich and the calcium-rich corner, i.e. albite-oligoclase or bytownite, respectively. Each chromitite layer contains both, calcium- and sodium-rich intercumulus plagioclases with a general dominance of the Ca-rich variety. Only Na-rich plagioclases have been found to be part of silicate inclusions, which is discussed separately in subsection 4.3.4.3. The tenor of the %An in the LCZ increases upwards the stratigraphy (Fig. 4.34) indicating reverse fractionation. In the UCZ, i.e. from MG3 to MG4A, the %An shows a distinct evolution towards Na-rich plagioclases. Up to

the MG4C chromitite a strong increase in the %An of its plagioclases is visible as one goes from the bottom to the top of the layer**.**

Table 4.8 Averaged composition of plagioclases in the MG chromitite layers. *n*: number of single grain analyses. Total Fe as FeO. Data are given in wt%. Results of individual analyses are given in appendix B, table B-7 and B-9.

Ca-rich plagioclase						
layer	**MG1**	**MG2A**	**MG2B**	**MG3**	**MG4A**	**MG4C**
sample	HEX10/46	HEX10/40	HEX10/34	HEX10/22	HEX10/17	HEX10/03
n	7	2	6	7	1	2
SiO_2	48.91	48.52	47.49	50.57	51.72	41.80
Al_2O_3	33.05	34.46	34.94	32.09	32.11	35.25
Cr_2O_3	0	0	0.11	0	0	0
FeO	1.42	0	1.00	0	0	2.73
MgO	0.48	0.34	0.73	0.65	0.70	0.72
CaO	12.47	13.60	12.58	11.67	10.71	18.65
Na_2O	3.67	3.08	3.13	3.48	4.76	0.85
total	100	100	99.89	98.46	100	100
%An	77.7	79.3	83.3	77.3	66.7	92.1

Na-rich plagioclase					
layer	**MG1**	**MG2A**	**MG2B**	**MG3**	**MG4A**
sample	HEX10/46	HEX10/40	HEX10/34	HEX10/22	HEX10/17
n	3	2	2	1	2
SiO_2	59.39	67.78	63.93	61.38	66.37
Al_2O_3	22.74	19.56	22.14	21.56	21.53
Cr_2O_3	0	0.54	0	0	0
FeO	4.34	0	0	4.65	0
MgO	1.37	0	0.63	0	0
CaO	2.71	0	1.30	1.23	0.61
Na_2O	9.45	12.11	12.00	11.18	11.50
total	100	100	100	100	100
%An	37.6	10.2	36.2	28.8	9.3

Coincidently with data of this study, Cameron (1982) report a general decreasing amount of the %An for plagioclases upwards the stratigraphy occurring in the MG3 and MG4 chromitite layers. Cameron (1980) furthermore found the centres of plagioclase

being enriched in Ca relative to the rims, which is contradictory to findings of this study. Here zonation of plagioclases is absent in all chromitites (Fig. 4.34B).

Elevated amounts of Fe (ca. 4-6 % Fe_2O_3) have been observed in plagioclases in the direct vicinity of BMS (Fig. 4.34A), in the Ca-rich as well as in the Na-rich ones. This is rather due to a secondary event overprinting the original plagioclase composition than to the primary event of plagioclase crystallization.

Alteration of plagioclase is very common in the MG1 chromitite but less frequent in the other massive chromitite layers. The alteration product is a not specified Fe-Mg-Al-Si compound.

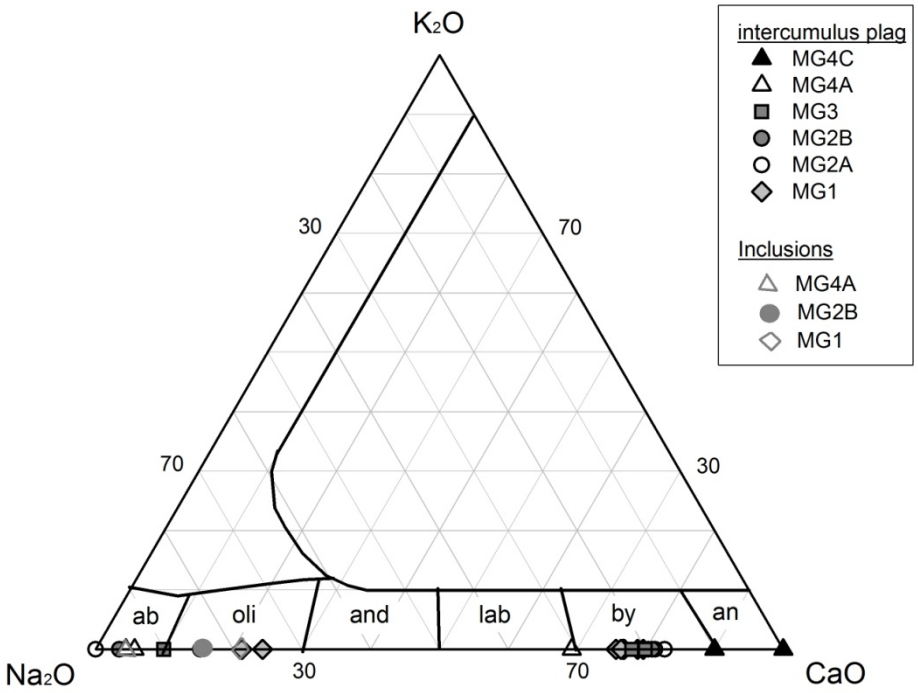

Figure 4.33 Averaged chemistry of plagioclases in chromitite layers of the MG sequence plotted in the ternary diagram Na_2O-CaO-K_2O at 900°C (modified after Deer *et al.*, 1963). *Ab*: albite; *oli*: oligoclase; *and*: andesine; *La:*= labradorite; *by*: bytownite; *an*: anorthite. Data given in table 4.8.

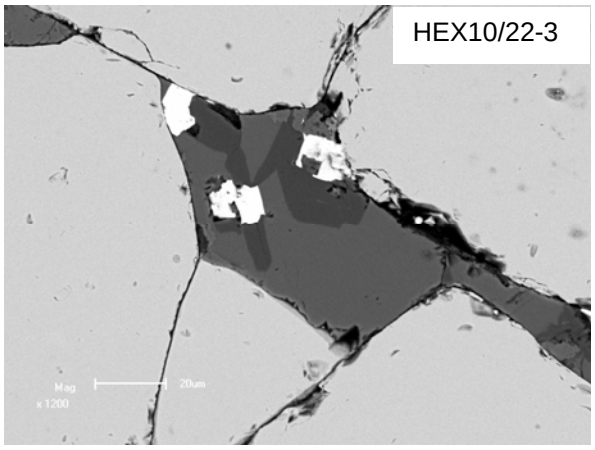

Figure 4.34A Plagioclase intercumulus to chromite (MG3). The dark grey parts surrounding the BMS (white) represent Fe-enriched albite. Bytownite in middle grey. BSE picture.

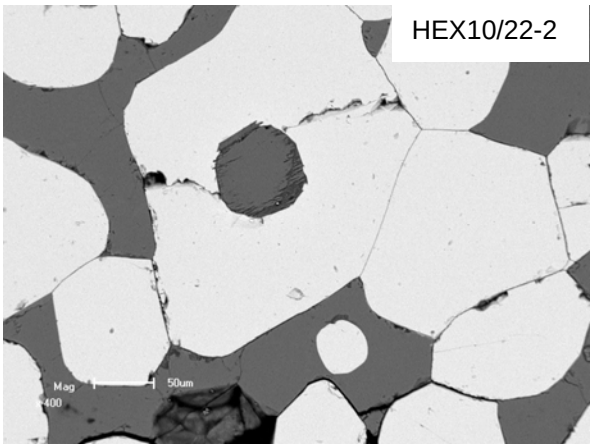

Figure 4.34B Intercumulus plagioclase (dark grey) in chromitite (MG3). Since no differences in the colour of the plagioclases are visible no zonation is present. BSE picture.

The data sets of Ca-rich and Na-rich plagioclase are not normally distributed, as can be seen in figures B-3 and B-4 in appendix B. To investigate, if there are significant correlations between the major element oxides of the Ca-rich and Na-rich plagioclases, Spearman rank correlation matrices have been calculated (appendix B: Tab. B-8 and B-10).

Normally, the negative correlation of CaO and Na_2O (r_S= -0.498) is interpreted to illustrate fractional crystallization of plagioclase and its evolution to more sodic compositions. With respect to figure 4.44, fractional crystallisation of plagioclase occurring in the chromitite layers of the MG sequence is only present in a short stratigraphic interval (MG3 to MG4A). Hence, the most significant correlations can be rather ascribed to coupled substitution typical for plagioclases: SiO_2-Na_2O; Al_2O_3-CaO; Al_2O_3-Na_2O and CaO-Na_2O (r_S= 0.695; r_S= 0.400; r_S= -0.648; r_S= -0.498, respectively). High amounts of Al_2O_3 are synonymous to more primitive composition, which is substantiated by the positive correlation of Al_2O_3 and CaO (cf. table 4.8).

4.3.4.2 Pyroxene

Generally, orthopyroxene is intercumulus to chromite, but sometimes it poicillitically encloses chromite (cf. Fig. 4.3A in subsection 4.1.1). Compositionally orthopyroxene plots in the enstatite field of figure 4.29. No clinopyroxene have been found to be analysed.

In general, the Mg# of orthopyroxene decreases upwards the stratigraphic column due to fractional crystallisation (Fig. 4.44). Although variation of the Mg# is small (cf. Tab. 4.9) two shifts to more primitive compositions, i.e. higher Mg#, are visible: one in the MG2B and another in the MG4A chromitite layer. It points to the addition of primitive liquid at these levels in the stratigraphic column, which matches the observations made from chromite chemistry (cf. subsection 4.3.1).

Alteration of orthopyroxene has also been detected with the SEM-EDX, which generally begins at the grain boundaries. It couldn't be determined, but the alteration mineral probably is vermiculite.

Table 4.9 Averaged composition of orthopyroxene in the MG chromitite layers. The data from MG2A, MG2B and MG4C chromitites are composed of analyses from intercumulus orthopyroxene as well as orthopyroxene forming inclusions in chromite grains. Data from MG1, MG3 and MG4A are made up of inclusion data only. *n*: number of single grain analyses; *px*: pyroxenite; *no*: norite. Total Fe is summarized in FeO. Mg# is $Mg^{2+}/(Mg^{+2}+Fe^{2+})$. Data are given in wt%. Individual analyses can be found in appendix B, Tab. B-11.

layer	**MG1**	**MG2A**	**MG2B**	**MG3**	**MG4A**	**MG4C**
sample	HEX10/46	HEX10/40	HEX10/34	HEX10/22	HEX10/17	HEX10/03
lithology	px	px	px	no	px	px
n	3	6	7	4	4	2
SiO_2	53.8	57.1	53.5	56	52.1	58.9
TiO_2	0.8	0	0.7	0	0	0
Al_2O_3	1.9	1.6	2.6	2	2.1	1.2
Cr_2O_3	1.1	0.2	0.5	0.4	1.6	0
FeO	3.8	3.7	4.8	4.3	5.3	4.4
MgO	34.4	34.8	34.7	35.1	36	33.6
CaO	1.7	0.3	0.9	0	0	0
Na_2O	1.4	0.8	0.4	0.5	0.6	0
total	98.4	98.4	98	98.2	97.7	98.1
Mg#	0.862	0.860	0.865	0.856	0.858	0.812

Similar to findings for plagioclases, some of the correlations calculated with the Spearman-rank correlation matrix for orthopyroxene (appendix B: Tab. B-12) are due to substitution of ions in its lattice, e.g. Al_2O_3 for SiO_2 and CaO for MgO, which are illustrated by the negative correlations SiO_2-Al_2O_3 (r_S= -0.657), SiO_2-CaO (r_S= -0.523), Al_2O_3-MgO (r_S= -0.576) and MgO-CaO (r_S= -0.556). The latter can further be interpreted as a sign for fractional crystallization, i.e. the evolution from orthopyroxene to clinopyroxene.

Progressive melt evolution can be attributed to the negative correlations of SiO_2 and Cr_2O_3 (r_S= -0.751) as well as SiO_2 and FeO_{tot} (r_S= -0.570) resulting from increasing FeO and decreasing Cr_2O_3 concentrations in the chromitite layers with stratigraphic height (cf. subsection 4.4.1). The moderate negative correlation of TiO_2 with MgO (r_S= -0.428) as well as the positive one of TiO_2 with CaO (r_S= 0.559) can also be attributed to evolution of the melt and the development of orthopyroxene to less primitive compositions upwards the stratigraphy. A significant negative correlation of MgO and FeO is missing, which coincides with the presence of more Mg-rich varieties of orthopyroxene in chromitite layers throughout the stratigraphic column of the MG sequence (cf. Fig. 4.35).

Moderate positive correlations of Al_2O_3-CaO (r_S= 0.428), Al_2O_3-Cr_2O_3 (r_S= 0.615) and Cr_2O_3-CaO (r_S= 0.488) can be interpreted to describe the purification of orthopyroxene composition due to progressive evolution of the melt: Cr is increasingly concentrated in chromite and intensified plagioclase crystallization consumes Ca and Al.

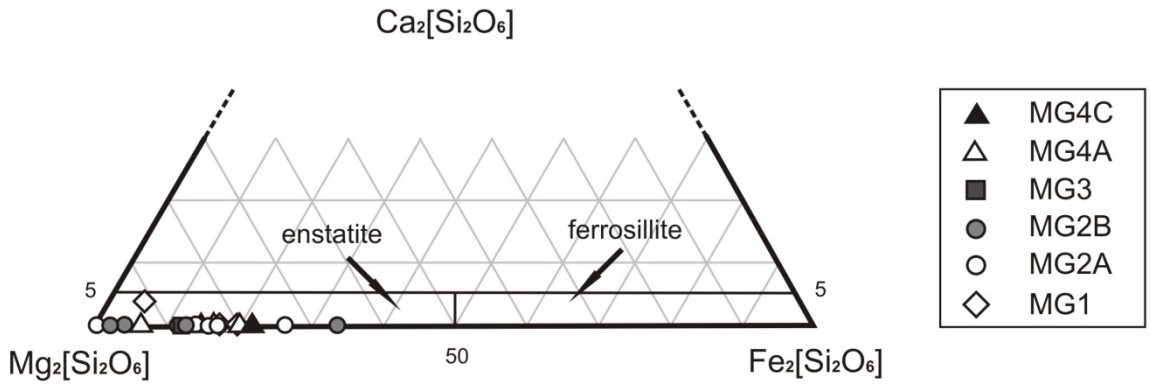

Figure 4.35 Ternary diagram $Mg_2[Si_2O_6]$-$Fe_2[Si_2O_6]$-$Ca_2[Si_2O_6]$ (after Morimoto *et al.*, 1988) showing the composition of pyroxene in MG chromitite layers.

4.3.4.3 Silicate inclusions within chromite grains

The silicate inclusions in chromite normally are rounded, indicating that they were included as melt droplets, and dominantly composed of two phases: orthopyroxene and mica (probably biotite or phlogopite). Inclusions with more than three phases are rare. Further constituents are rutile, BMS and a non-determinable component; probably vermiculite. Plagioclase and Pt-alloys also were seen, but are very rare (Fig. 4.36). The silicate inclusions in general appear more altered than the intercumulus silicate material.

Differences in the major element oxides between orthopyroxene occurring intercumulus to chromite and orthopyroxene in silicate inclusions are small (cf. table 4.9),

but there are variations in the minor elements (Fig. 4.37). Although small, the most prominent variation occurs in the Al_2O_3 content with the orthopyroxene inclusions showing less Al_2O_3. It is interpreted to be caused by equilibration with chromite during cooling, since Al^{3+} is more compatible into the chromite lattice. The same applies for the difference in the CaO content.

Orthopyroxene in silicate inclusions appears to be enriched in Na_2O and Cr_2O_3 relative to orthopyroxene occurring intercumulus to chromite. Again, equilibration is considered to have caused this feature.

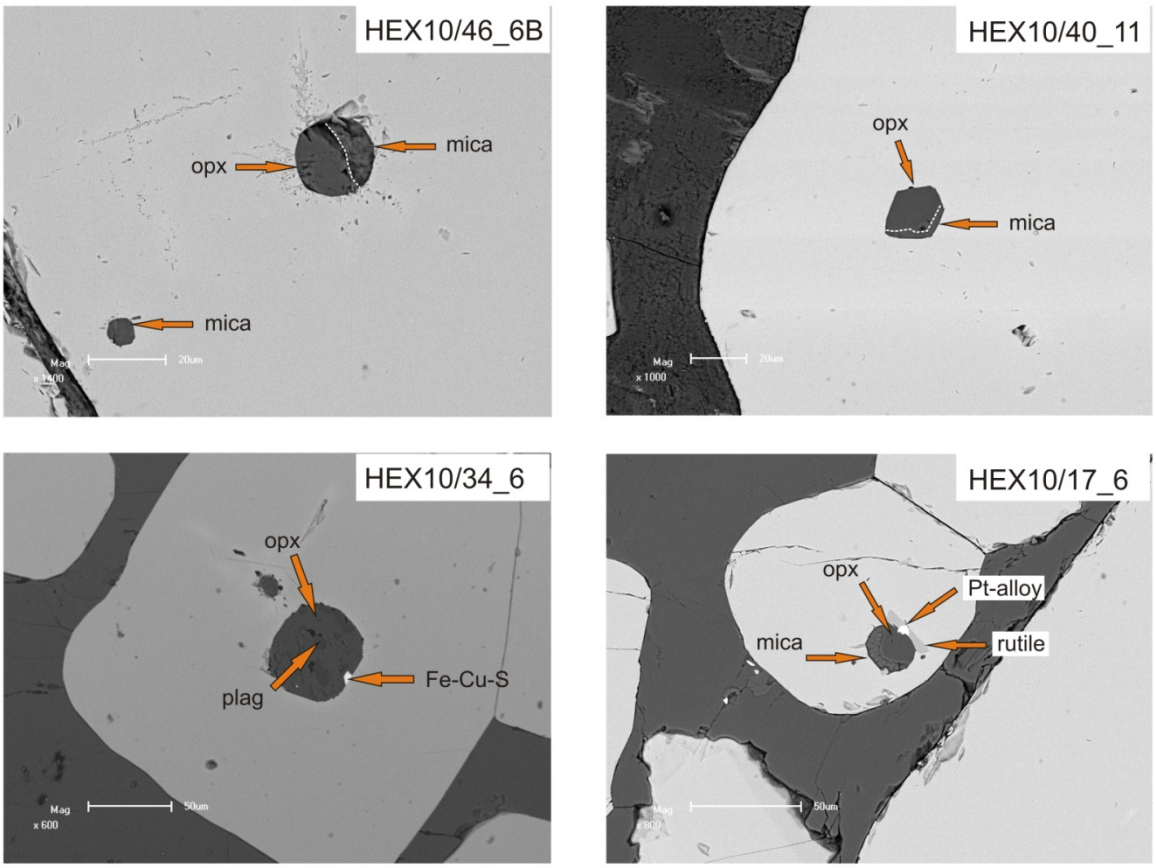

Figure 4.36 Silicate inclusions of different composition occurring in chromite. They normally have rounded shapes, but occasionally are rhomboidal. *Opx:* orthopyroxene, *plag:* plagioclase.

TiO_2 is almost absent in orthopyroxene within the inclusions. Equilibration appears to have been caused this limited only. Since chromite is the first mineral to solidify, TiO_2 is most likely incorporated into the chromite lattice due to its relative incompatibility to the silicate melt.

The plagioclase found in the inclusions are invariably Na-rich, i.e. albite and oligoclase, and do not show compositionally significant differences to Na-rich plagioclases

occurring intercumulus to chromite (Fig. 4.38). As for orthopyroxene, the variations in the major element oxides are relatively small. The most remarkable difference in the minor element oxides is present for Fe. In the areas intercumulus to chromite orthopyroxene and plagioclase equilibrate next to each other, which results in elevated amounts of Fe in the plagioclases. However, no silicate inclusion has been found containing both, orthopyroxene and plagioclase, but only one of them. Thus, Na-rich plagioclase in the melt inclusion gives its Fe to chromite, which results in lower Fe_2O_3 contents when compared to intercumulus plagioclase. To a lesser extent, the same process can most likely be applied for MgO and CaO.

As have been shown for orthopyroxene, the Na-rich plagioclases occurring in silicate melt inclusions are enriched in Cr_2O_3 relative to those in the intercumulus matrix (Fig. 4.38).

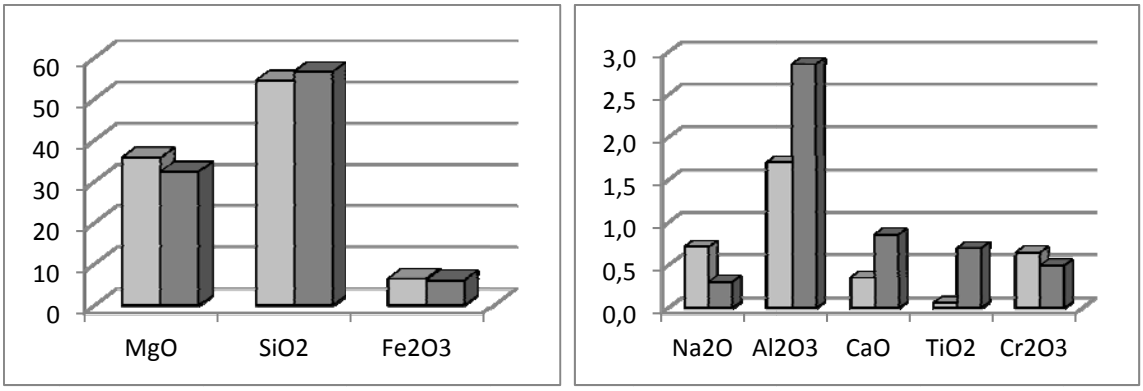

Figure 4.37 Comparison of composition of orthopyroxene occurring intercumulus to chromite (dark grey) and those being part of silicate melt inclusions in chromite (light grey). On the right hand side the major element oxides are illustrated; to the left the element oxides of minor constituents can be seen. Data are given in Tab. B-11 in appendix B.

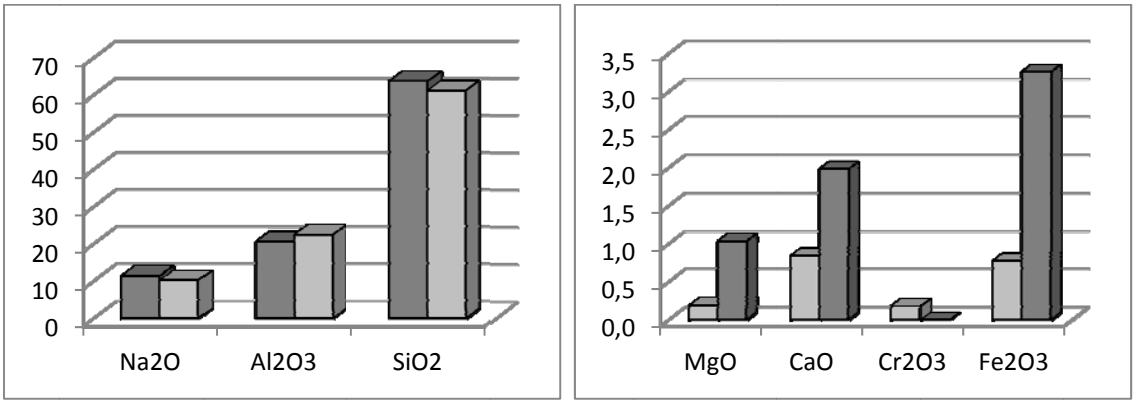

Figure 4.38 Comparison of composition of Na-rich plagioclase occurring intercumulus to chromite (dark grey) and those in silicate melt inclusions in chromite (light grey). On the right hand side the major element oxides are illustrated; to the left the element oxides of minor constituents can be seen. Data are given in Tab. B-9 in appendix B.

In the system albite-anorthite, high-temperature plagioclase with a maximum of 25% anorthite content, i.e. oligoclase, begins to crystallize at approximately 1120°C, thus being a relative late phase in fractional crystallization of plagioclase. However, experiments on parental magmas by Cawthorn *et al.* (1979) at 3 kbar yielded the existence of Ca-rich plagioclase at the temperature of 1120°C rather than Na-rich one. Additionally, a multi-component system as it happens to have been present during crystallization of the RLS certainly would lower the liquidus temperature of a Na-rich plagioclase.

Spandler *et al.* (2005) discussed Na-rich silicate inclusions occurring enclosed in chromite from the Stillwater complex and concluded that they represent partial melt of the metasedimentary country rocks mixed with small proportions of primitive parental magma. These findings raise the question, if the enclosing chromite grains in the MG also locked mixed liquid or if the Na-rich plagioclase is the result of another event.

It is suggested that during cooling the former Ca-rich plagioclase equilibrates with the enclosing chromite in that way that a substitution of Ca for Na takes place, especially since Ca^{2+} is more compatible into the chromite lattice than Na^{+}. Thus, simply equilibration can have caused the present Na-rich plagioclase in the silicate melt inclusions. Na-enrichment of orthopyroxene within silicate inclusions substantiates this conclusion. On the other hand, it is doubtful, if unequilibrated chromite hosts sufficient amounts of Na to produce albite from anorthite in the silicate inclusions. Hence, it is possible that these inclusions represent a mixture of primitive with siliceous melt, as has been suggested to trigger chromite precipitation (Kinnaird *et al.*, 2002; Spandler *et al.*, 2005). Additional analyses of chromite composition in the direct vicinity of such inclusions as well as the determination of initial Sr isotope ratio could give further information on this question.

The occurring mica and vermiculite most likely represents alteration products of orthopyroxene. Since the chromite grain should have shielded the silicate inclusion from any hydrothermal process it is the question what caused the alteration. One explanation is the existence of cracks parallel to the direction of view, which at present are either cut or hidden due to sample preparation. This would mean that, with a single exception, all inclusions analyzed are connected to the intercumulus silicate material. As this seems very unlikely, it is rather suggested that degassing during cooling resulted in the formation of a fluid phase. Due to the locking function of the chromite grain it wasn't able to escape and hence alteration of early orthopyroxene took place. This model is corroborated by small cracks leading away from the inclusion into chromite, which could have been caused by overpressure resulting from fluid formation (Fig. 4.36). Chromite is chemically relatively inert to those fluids, which would explain the lack of alteration signs of the chromite grains in the vicinity of these cracks. Hence, the ability of the silicate melt of the

MG- sequence to produce deuteric fluids during a late-stage magmatic process is indicated.

4.3.5 Chemistry of silicate minerals from silicate rocks

4.3.5.1 Plagioclase

The composition of the plagioclases in the silicate layers of the MG ranges from labradorite (An_{70-50}) to bytownite (An_{90-70}) with a few exceptions only (Fig. 4.39). This is true for plagioclase being a cumulus or an intercumulus mineral as well as for plagioclase inclusions occurring in orthopyroxene of the MG2C anorthosite and the MG3 norite (Fig. 4.40). The plagioclases occurring in the MG0 pyroxenite seem to be of a more evolved composition, since they plot in the field of andesine (An_{50-30}). Generally, the plagioclases of the MG4A pyroxenite contain more K_2O than plagioclases from the silicate layers below, which is probably due to a higher state of evolution of the liquid they derive from.
Plagioclase analyses that have been done with the EMP plot in the bytownite field only, or at the boundary to the labradorite field. It thus confirms the SEM-EDX analyses. Since fewer analyses have been done, the range in composition observed with SEM-EDX analyses probably could not be modelled.

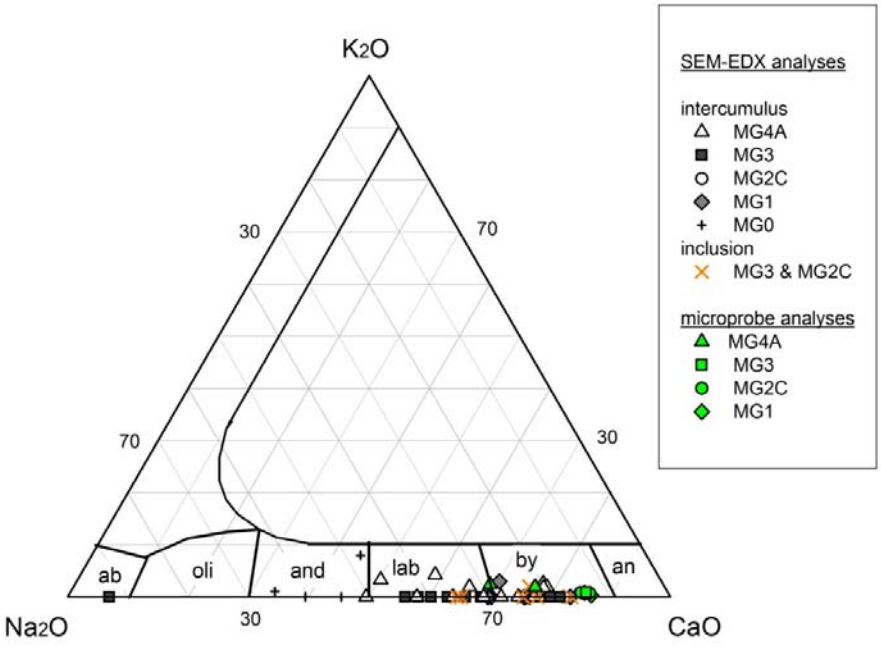

Figure 4.39 Plagioclase composition from plagioclases of the silicate layers of the MG sequence. The shorthand symbols “MG1, MG2A, etc.” represent the silicate layer above the corresponding chromitite layer the plagioclases occur in. $N_{SEM-EDX}$= 50; N_{EMP}= 10. Ternary diagram of feldspars at 900°C (modified after Deer *et al.*, 1963).

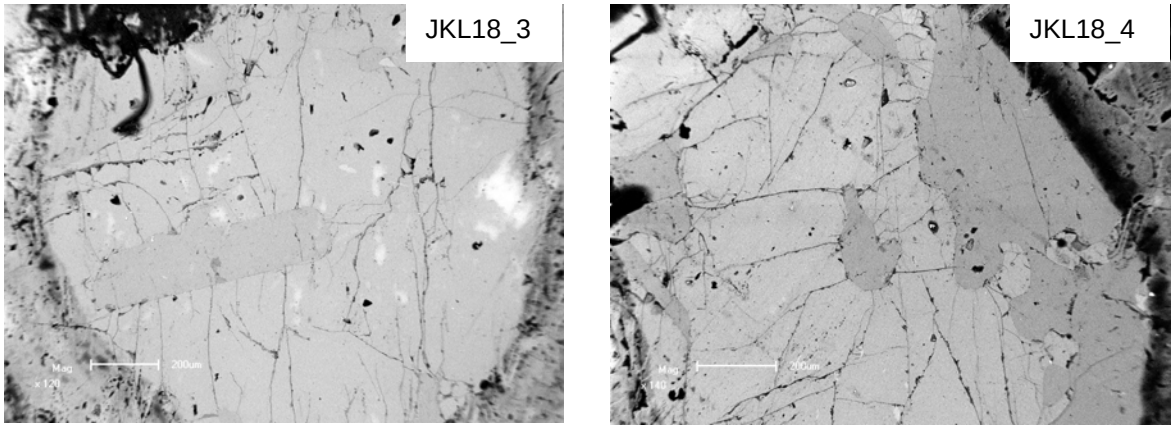

Figure 4.40 Plagioclase inclusions in orthopyroxene in norite. The shapes range from euhedral (left) to irregular (right). BSE image.

The concentrations of the major element oxide of the plagioclases as well as Cr_2O_3 from EMP analyses are shown in table 4.10. One can see that the MgO and FeO content decrease upwards the stratigraphy, indicating progressive melt evolution. The amount of CaO decreases coincidently with an increase in Na_2O and K_2O. This results in plagioclases showing a more evolved composition higher up in the stratigraphy. A general trend of decreasing anorthite content of plagioclase upwards the stratigraphic column of the MG sequence is illustrated from MG1 pyroxenite to the plagioclase-bearing pyroxenite of the MG4A cyclic unit (Fig. 4.44). This coincides with data from Cameron (1980, 1982), who investigated plagioclase from the MG deriving from the north of the eastern Bushveld Complex.

SEM-EDX analyses including cumulus and intercumulus plagioclase yielded quite evolved plagioclase compositions in the pyroxenites of the MG0 package (on average $An_{75.5}$) showing a slight increase in its anorthite content from bottom to top only. Relatively low anorthite contents of plagioclase (Mol% $An_{60\text{-}85}$) have also been recognized from Cameron (1980) from the D_2 unit, which represents the same stratigraphic unit (cf. subsection 2.3.2.2). Fractional crystallisation of plagioclase is present in the pyroxenite of the MG1 and the norite of the MG3 cyclic units from the bottom to the top of these layers (Fig. 4.42). A special feature is the low anorthite content in the leuconorite occurring directly at the top of the MG3 chromitite. Plagioclase in the anorthosite in the hanging wall of the MG2C chromitite layer shows a reverse fractionation trend, from An_{86} to An_{90}. This is in contradiction to data from Cameron (1982), who observed a general decreasing trend for the anorthite content of plagioclase within this unit.

Strong variation is visible in the plagioclase-bearing pyroxenite of the MG4A cyclic unit (Fig. 4.44). An_{90} at the bottom points to addition of primitive melt with subsequent progressive evolution to Na-rich varieties. The second shift to primitive plagioclase

composition within this layer could also derive from an influx of primitive melt. The reverse fractionation trend observed in plagioclases prior to the second magma addition could thus be caused by equilibration with the new liquid, i.e. the closer to the source of magma addition the more primitive the plagioclase composition.

Since EMP analyses are more accurate than those from SEM-EDX the results of the former have been used to calculate a Spearman rank correlation matrix (appendix B; Tab. B-14), although fewer analyses exist.

Table 4.10 Averaged major and trace element oxide contents within plagioclases of the silicate layers yielded from EMP-analyses. *N*: number of single grain analyses; *px*: pyroxenite; *no*: norite; *an*: anorthosite. Data are given in wt%. Detailed results of EMP analyses are listed in appendix B, Tab. B-13.

layer	**MG1**	**MG2C**	**MG3**	**MG4A**
sample	JKL9	JKL13	JKL18	JKL42
lithology	px	an	no	px
n	2	4	1	3
SiO_2	48.47	49.37	48.84	52.27
TiO_2	0.02	0.04	0.02	0.03
Al_2O_3	32.19	32.27	32.25	30.31
Cr_2O_3	0.01	0.01	0	0
FeO	0.30	0.29	0.19	0.20
MnO	0.01	0.01	0.03	0.00
MgO	0.13	0.02	0.02	0.03
CaO	16.29	15.32	15.95	12.75
Na_2O	2.53	2.53	2.52	4.08
K_2O	0.10	0.14	0.17	0.35
total	100.04	100.00	99.99	100.03
%An	79.5	75.9	78	64.6

As for plagioclase occurring in chromitite layers the strongest and most significant correlations indicate coupled substitution by the following relations: SiO_2-Al_2O_3 (r_S= -0.699); SiO_2-CaO (r_S= -0.988); SiO_2-Na_2O (r_S= 0.758); SiO_2-K_2O (r_S= 0.837); Al_2O_3-CaO (r_S= 0.669); Al_2O_3-Na_2O (r_S= -0.930); Al_2O_3-K_2O (r_S= -0.740); CaO-Na_2O (r_S= -0.721); CaO-K_2O (r_S= -0.762) and Na_2O-K_2O (r_S= 0.854), indications for the general evolution of plagioclase to less anorthitic composition resulting from fractional crystallisation with stratigraphy.

Positive correlation of Al_2O_3 and Cr_2O_3 (r_S= 0.737) indicates substitution of Al^{3+} by Cr^{3+} that is limited since Cr_2O_3 contents are low. The negative correlation of Cr_2O_3 and Na_2O (r_S= -0.756) suggests progressive evolution of the melt the plagioclases derive from.

4.3.5.2 Pyroxene

In the silicate layers of the MG sequence orthopyroxene and clinopyroxene are present. Both generally are cumulus minerals, but sometimes clinopyroxene also poicillitically encloses orthopyroxene or occurs as intercumulus phase. In the norite of the MG3 package it now and then forms a (reaction) rim around orthopyroxene (cf. Fig. 4.18B in subsection 4.2.2.1).

Orthopyroxene composition determined with SEM-EDX ranges between 95 and 32% $Mg_2[Si_2O_6]$ (enstatite En)(Fig. 4.41). A few grains show $Ca_2[Si_2O_6]$ contents of up to 10%. When the Mg# of orthopyroxene in the silicate layers is plotted versus the stratigraphy (Fig. 4.44) a general decrease from bottom to top of the MG sequence is visible. Several reversals with increasing Mg# can be observed: in the MG0 pyroxenite, from leuconorite to norite of the MG3 cyclic unit and in the middle of the plagioclase-bearing MG4A pyroxenite. $Mg\#_{cpx}$ deriving from EMP analyses are too few to describe distinct trends, but the values are considerably higher.

Orthopyroxene data from the MG1 pyroxenite from Cameron (1980) show slightly higher En contents (80.6 – 88.5 Mol%) when compared to data from this study (77.1 – 84.3 Mol%). At both sites the same trend of decreasing Mg# within this layer can be observed. The amount of Al_2O_3 in orthopyroxene of this study ranges between 0.89 and 1.32 wt% and thus is slightly lower than found for orthopyroxene by Cameron (1980) (1.39 - 1.84 wt%). With an average of 0.43 wt% the Cr_2O_3 content of orthopyroxene lies in the lower part of concentrations reported by Cameron (1980) (0.44 - 0.61 wt%).

For orthopyroxene in the UCZ, Cameron (1982) described the amount of En to range between 79.6 and 82 for the F unit, basically the anorthosite on top of the MG2C chromitite layer, and between 79 and 80.4 for the G unit, i.e. the MG3 norite. From this study only data from the latter are available for comparison. The En content is slightly higher than the data presented by Cameron (1982) and ranges between 81.2 and 86.4. Al_2O_3 (0.74 – 1.47 wt%) and Cr_2O_3 concentrations (0.44 – 0.54 wt%) are comparable with the data from Cameron (1982) (1.42 – 1.54 wt% Al_2O_3; 0.5 – 0.56 wt% Cr_2O_3), but the lower limits of the range are extended.

Thus, for the LCZ, i.e. the MG1 pyroxenite, one can estimate a progressive evolution of orthopyroxene composition from N to S of the eastern limb by decreasing amounts of

En as well as Al_2O_3. Although the Al_2O_3 concentrations in the MG3 norite, i.e. the UCZ, also show decreasing values, the postulated evolution cannot be verified from the En values.

Clinopyroxene shows a wide compositional spectrum; besides pigeonite and augite diopside as well as sub-calcic augite occurs (Fig. 4.41). SEM-EDX analyses of clinopyroxene forming a rim around orthopyroxene (MG3 norite) yielded less Ca than intercumulus clinopyroxene. Additionally, enrichment in Fe is present. Hence, these rims can be interpreted as reaction rims that formed during subsolidus diffusion between orthopyroxene and plagioclase. Due to low Ca content they plot in the augite field (Fig. 4.41). EMP analyses yielded in diopside composition only, but since only three minerals have been analysed no verified statement can be given (Fig. 4.341; Tab. 4.11).

Cryptic variation in the Mg# of clinopyroxene with stratigraphy (Fig. 4.44) shows the same trends that have been observed for $Mg\#_{opx}$. Here, too, EMP data show higher values.

Table 4.11 Averaged major and trace element oxide contents of orthopyroxene (left) and clinopyroxene (right) from the MG silicate layers yielded from EMP-analyses. *N*: number of single grain analyses; *px*: pyroxenite; *no*: norite. Mg# is $Mg^{2+}/(Mg^{2+}+Fe^{2+})$. Data are given in wt%. Results from individual orthopyroxene analyses are given in Tab. B-15 in appendix B.

layer	**MG1**	**MG2A**	**MG3**	**MG4A_1**	**MG4A_2**	**MG1**	**MG4A**
sample	JKL9	JKL10	JKL18	JKL34	JKL42	JKL9	JKL34
lithology	px	px	no	px	px	px	px
n	7	6	7	6	8	2	1
SiO_2	55.69	55.18	54.87	58.66	55.88	53.03	53.68
TiO_2	0.16	0.09	0.19	0.09	0.15	0.23	0.22
Al_2O_3	1.18	1.98	1.17	1.22	1.15	1.46	1.45
Cr_2O_3	0.42	0.42	0.48	0.36	0.38	0.54	0.51
FeO	11.49	9.41	10.28	7.32	9.35	4.45	3.98
MnO	0.26	0.22	0.18	0.20	0.21	0.14	0.09
MgO	29.00	31.45	31.46	30.98	31.73	15.97	17.06
CaO	1.67	1.16	1.22	1.05	1.12	23.58	22.65
Na_2O	0.10	0.07	0.10	0.11	0.03	0.52	0.31
K_2O	0.03	0.02	0.03	0.02	0.00	0.07	0.04
total	99.99	99.99	99.99	100	99.99	99.99	99.99
Mg#	0.883	0.855	0.843	0.854	0.815	0.884	0.865

A Spearman rank correlation matrix has been calculated from EMP analyses for orthopyroxene, since they are more accurate than SEM-EDX analyses (appendix B, Tab. B-16). However, for clinopyroxene the results of the SEM-EDX analyses have been used (cf. Tab. B-17, appendix B), because with the EMP only three individual grains have been analysed (appendix B, Tab. B-18).

Fractional crystallisation can be obtained from the negative correlations between FeO and MgO for orthopyroxene (r_S= -0.687), which can also be deduced from the Mg# (cf. Fig. 4.44), and the negative correlations between MgO-CaO (r_S= -0.419) and FeO-CaO for clinopyroxene resulting from Ca replacing Fe (r_S= -0.820). The latter can also be observed in orthopyroxene grains (r_S= -0.444). A moderate positive correlation of TiO_2 and FeO from orthopyroxene analyses (r_S= 0.459) gives further support for progressive evolution of the melt and crystallization of orthopyroxene of more evolved compositions. Moderate negative correlations between TiO_2 and Al_2O_3 in orthopyroxene (r_S= -0.570) and between TiO_2 and MgO in clinopyroxene (r_S= -0.460) point to fractional crystallization of pyroxene, too. Elevated amounts of Al_2O_3 and MgO limit the presence of TiO_2, the former representing elements of primitive pyroxene compositions.

In orthopyroxene, the overall increase in SiO_2 relative to decreasing Cr_2O_3, FeO and CaO is due to fractional crystallization resulting in more evolved pyroxene compositions (r_S= -0.690; r_S= -0.764 or r_S= -0.497, respectively). Furthermore, increasing quantities of co-precipitating plagioclase result in enhanced CaO consumption from the melt, leading to ‘Ca-poor’ orthopyroxenes. On the other hand, for clinopyroxene a positive correlation exists between SiO_2 and CaO (r_S= 0.745) describing the evolution to more Ca-rich varieties. Ca^{2+} in clinopyroxene is replacing Fe^{2+}, which can be deduced from the strong negative correlation FeO-CaO with r_S= -0.820. Thus, the very strong negative correlation between FeO and SiO_2 (r_S= -0.909) can be interpreted in terms of fractional crystallization of clinopyroxene illustrating decreasing FeO contents and increasing amounts of CaO. Additionally, CaO seems to be partly replaced by Na_2O (r_S= -0.643).

Positive correlation of FeO and MnO in orthopyroxene (r_S= 0.588) illustrates a limited coupled behavior of both elements. The same is true for the relation MnO-CaO (r_S= 0.497). On the other hand, a negative correlation of MnO and MgO (r_S= -0.496) represents substitution of Mg by Mn within the orthopyroxene lattice. Substitution can also be deduced from the negative correlation Cr_2O_3-MgO (r_S= -0.400).

The correlation matrices summarizing the r_S-values presented above are given in tables B-16 and B-18 in appendix B.

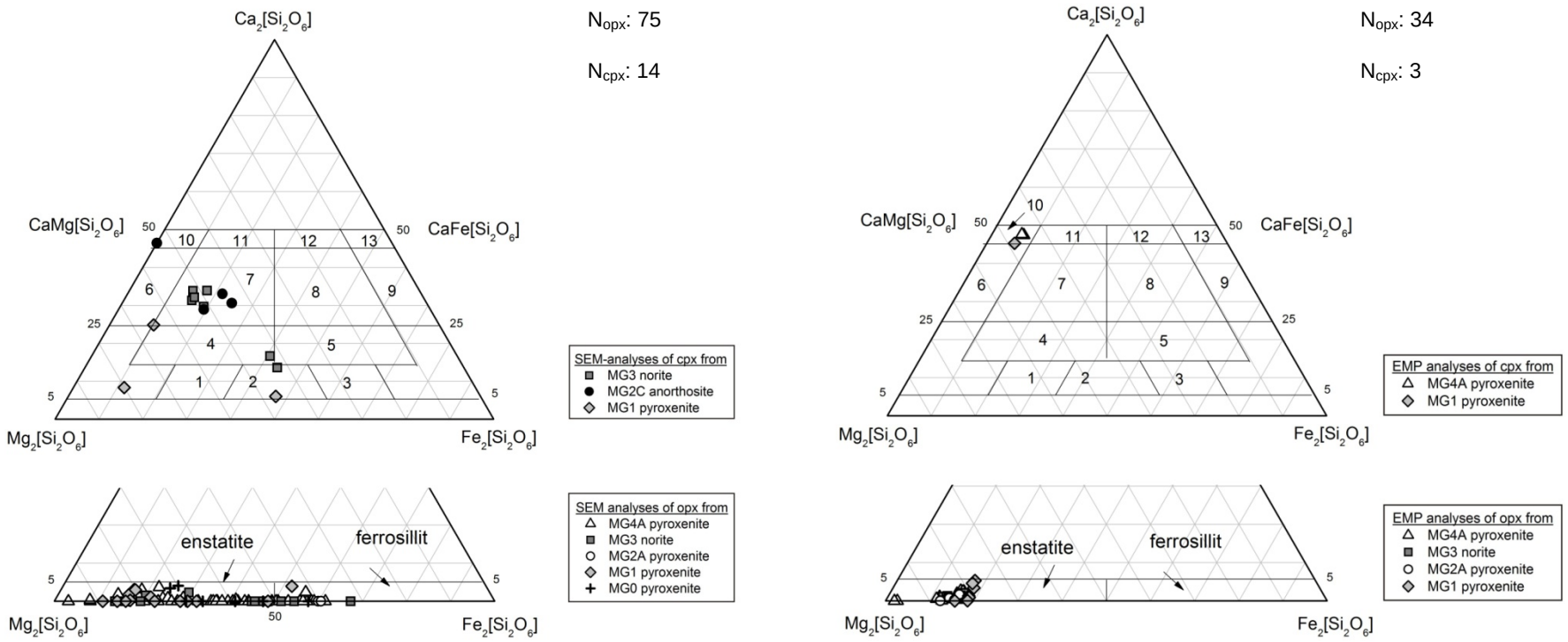

Figure 4.41 Pyroxene chemistry yielded from SEM-EDX (left) and EMP analyses (right). The lower $Mg_2[Si_2O_6]$-$Fe_2[Si_2O_6]$ pyroxene quadrilateral shows orthopyroxene composition; the ternary plot $Mg_2[Si_2O_6]$-$Fe_2[Si_2O_6]$-$Ca_2[Si_2O_6]$ above clinopyroxene composition. Numbers are: 1- magnesium pigeonite; 2- intermediate pigeonite; 3-ferriferous pigeonite; 4- subcalcic augite; 5- subcalcic ferroaugite; 6- endiopside; 7- augite; 8- ferroaugite; 9- ferrohedenbergite; 10- diopside; 11- salite; 12- ferrosalite; 13- hedenbergite. Ternary diagrams after Morimoto *et al.* (1988).

4.3.5.2.1 Minor and trace elements in orthopyroxene

The four elements Mn, Al, Cr and Ti occurring as minor or trace elements in orthopyroxene have been plotted vs. the Mg#. They have been chosen since they are sensitive to melt evolution and their amount within orthopyroxene illustrates major changes in melt composition. A special focus is directed to the LCZ/UCZ transition. For comparison, averaged data of orthopyroxene analyses from Eales *et al.* (1993) deriving from samples of the western limb have been included in each of the plots shown below.

Mg# vs. MnO. The MnO content in orthopyroxene from core HEX10 ranges from 0.24% in the LCZ to 0.20% in the UCZ on average. For the LCZ a rough trend of decreasing MnO content with contemporaneously increasing Mg# is visible, whereas for the UCZ no trend exists (Fig. 4.42). This is partly contradictory to the results of Eales *et al.* (1993), who found an inverse linear relationship proceeding from the LZ to near the roof of the UCZ.

Mg# vs. TiO_2 and Al_2O_3 vs. TiO_2. In the LCZ of core HEX10 there is a negative linear trend between Mg# and TiO_2 up to the MG3 norite, whereas in the plagioclase-bearing MG4A pyroxenite a positive linear trend impinges upon the major trend observed for the LCZ pyroxenites and the MG3 norite (Fig. 4.42). Although a few outliers exist, the relative amounts of Ti in orthopyroxene from the MG3 norite and the MG4A pyroxenite change a little only. Decreasing TiO_2 coincides with increasing Mg# within the LCZ but is unexpected, since it runs upwards the stratigraphy. Otherwise it matches the reversals in fractionation observed for the Mg# of orthopyroxene as well as the %An of plagioclase. The expected trend, i.e. decreasing Mg# and increasing TiO_2 with stratigraphy, has been described by Eales *et al.* (1993), who observed an inverse linear trend from LCZ to UCZ.

Increasing Al_2O_3 is accompanied by decreasing TiO_2 in orthopyroxene of the LCZ from core HEX10 (Fig. 4.43), consistent with the increase of the Mg# for this interval (Fig. 4.44). The data points for the UCZ scatter too much in order to form a trend, but the values are reset to concentrations similar to those of the MG1 pyroxenite. Even here the trend in the MG stratigraphy clearly differs from the positive linear trend observed by Eales *et al.* (1993).

Ti/Al ratio. The Ti/Al ratio in orthopyroxene from the MG of core HEX10 is low (0.08-0.16), but shows a sharp increase to 0.24 at the level of the MG3 norite. Low Ti/Al ratios are typical for orthopyroxene from early crystallization stages, where plagioclase is not a liquidus phase. Low Ti/Al ratios can be observed on the pyroxenitic rocks of the LCZ as well as the UCZ parts of the MG. With the onset of plagioclase crystallization, Al is consumed by plagioclase precipitation leading to increasing Ti/Al ratios. This is the case

within orthopyroxene of the MG3 norite. The incompatibility of Ti into the plagioclase lattice further impinges on the ratio.

Mg# vs. Al_2O_3. In core HEX10 an increase in Al_2O_3 from ca. 1% to ca. 1.4% is illustrated (Fig. 4.44) in the LCZ. The Mg# in the pyroxenite of the MG1 package is quite stable, but it roughly increases contemporaneously with Al_2O_3 upwards the stratigraphic column. Again, only a rude trend of the $Mg\#_{opx}$ for the LCZ is present and no trend for the MG3 norite and the MG4A pyroxenite is visible, since the data points are scattered. Eales *et al.* (1993) describe an inverse linear trend in the Al_2O_3-$Mg\#_{opx}$ relationship with an inflection at the level of the first appearance of cumulus plagioclase, i.e. at the LCZ/UCZ transition.

Cr_2O_3 vs. Al_2O_3. In the MG the LCZ pyroxenites of core HEX10 have orthopyroxene with quite consistent Al_2O_3 concentrations relative to decreasing Cr_2O_3 contents upwards the stratigraphy. Approximately the same trend can be observed in the UCZ, but the Cr_2O_3 concentration is unlike higher. Orthopyroxene in the MG3 norite shows the highest concentrations because of incompatibility of Cr in plagioclase. In core HEX10 the trend in the LCZ as well as the UCZ can be described as negative linear.

A similar, but much flatter trend is reported by Eales *et al.* (1993). Although the concentrations of Al_2O_3 and Cr_2O_3 are quite consistent, the tenor describes an inflection at the LCZ/UCZ transition.

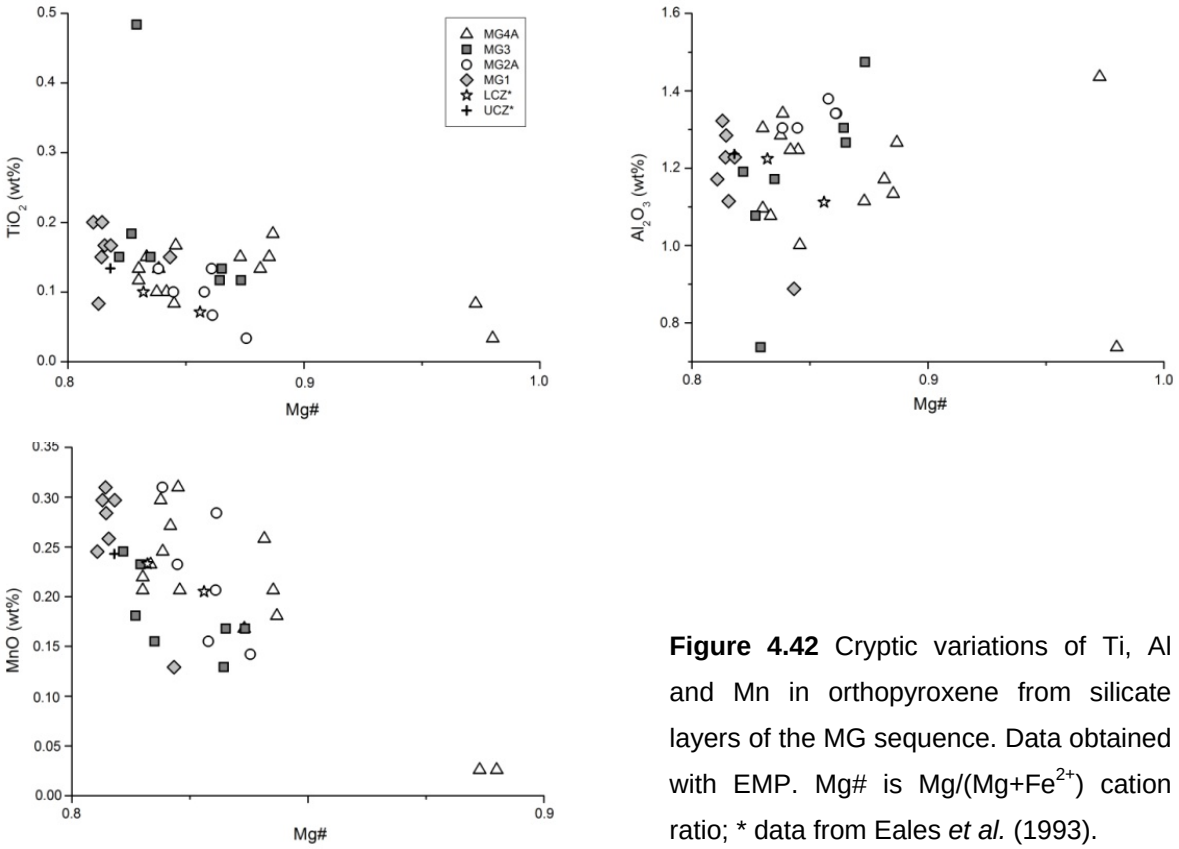

Figure 4.42 Cryptic variations of Ti, Al and Mn in orthopyroxene from silicate layers of the MG sequence. Data obtained with EMP. Mg# is $Mg/(Mg+Fe^{2+})$ cation ratio; * data from Eales *et al.* (1993).

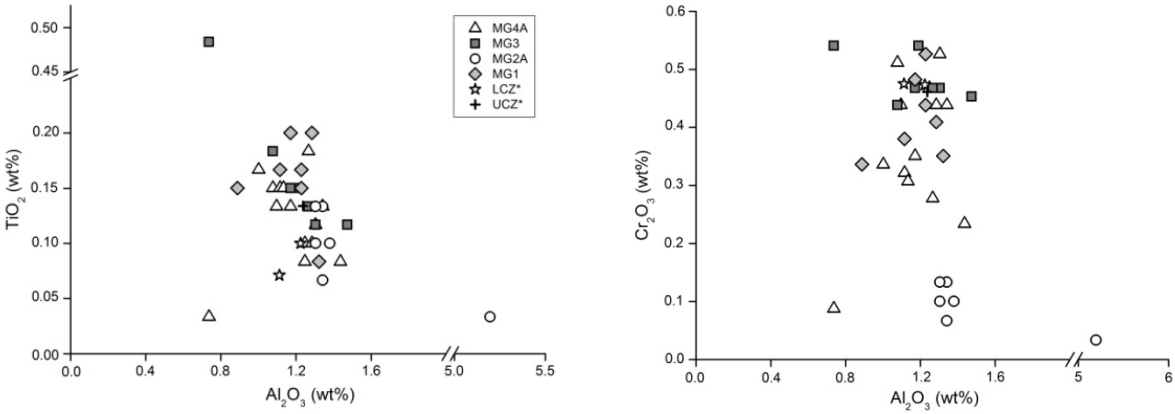

Figure 4.43 Plot of TiO_2 vs. Al_2O_3 and Cr_2O_3 vs. Al_2O_3 from orthopyroxene analyses. * Data from Eales *et al.* (1993).

However, increasing Mg# in orthopyroxene in the LCZ from core HEX10 indicates reverse crystallization. Since the specimen from the MG1 and MG2A pyroxenites have been sampled at the footwall and the hanging wall of the MG2A chromitite layer (cf. Fig. 3.2 in subsection 3.2.1), the observed trend rather reflects the end and the beginning of one cyclic unit, i.e. low Mg# in the footwall of the MG2A chromitite as 'the end' of the cyclic unit forming the MG1 package, and high Mg# in the hanging wall of the MG2A chromitite layer at the 'beginning' of a new cyclic unit. The presented results from core HEX10 are thus not directly comparable with the presented literature data from Eales *et al.* (1993). The connection of the stratigraphic position of a sample with the chemical composition is further visible in the relation Mg#-MnO, since the behaviour of Mn is linked to Fe, which shows opposite trend to Mg. The decreasing TiO_2 content relative to the increasing Mg# within orthopyroxene of the LCZ can also be ascribed to the fact of the stratigraphic position of the samples. Higher Al_2O_3 contents in orthopyroxene of the MG2A pyroxenite are due to relative fresh and not fractionated melt at the beginning of the MG2A cycle. No or very rare plagioclase precipitated and consumed Al, whereas at the top of the MG1 cyclic unit plagioclase already precipitated, which results in the lower Al_2O_3 content of orthopyroxene. The higher Cr_2O_3 concentrations in orthopyroxene from the footwall of the MG2A chromitite at constant Al_2O_3 content is probably due to the relative incompatibility of Cr^{3+} into the pyroxene lattice and thus was concentrated in the melt late orthopyroxene derived from.

Since no data from the MG2C anorthosite are available, the onset of cumulus plagioclase crystallization can nicely be read off the decreasing Al_2O_3 content within orthopyroxene of the MG3 norite, which is strongly consumed by plagioclase precipitation. The latter fades from the spotlight in the plagioclase-bearing MG4A pyroxenite, as can be seen in increasing Al_2O_3 and decreasing TiO_2 contents. As for orthopyroxene in the MG2A footwall, the Cr_2O_3 content in orthopyroxene from the footwall of the MG4A chromitite

layer is higher than those from samples of the MG4A pyroxenite. Again inducing chromite precipitation could be the reason. Further precipitation of cumulus chromite and orthopyroxene yields in slight depletion of Cr_2O_3 at constant Al_2O_3 concentrations within orthopyroxene of the MG4A pyroxenite.

The lack of trends within the UCZ in plots of the Mg# vs. TiO_2, Al_2O_3 and MnO points to disruption in normal fractional crystallization of orthopyroxene, which is probably due to changes in melt chemistry. This again is most likely caused by changing degrees of chromite precipitation (see further subsection 4.4.2) competing for these elements with orthopyroxene.

4.3.6 Comparison of silicate mineral composition from the chromitite layer with those from the silicate layers

The bivalent nature of plagioclase composition within the chromitite layers is not repeated in the silicate layers (cf. figure 4.31); here it rather spans a wider compositional range from andesine to bytownite. Pure albite is almost absent. As can be seen in figure 4.44, variations of anorthite content within intercumulus plagioclases in chromitite layers are strong in the MG stratigraphy (An_{67-92}), especially in the UCZ. Intercumulus plagioclase in the silicate layers of the LCZ also shows variations of anorthite content (An_{75-90}), but the range in the anorthite content of the cumulus phase in the UCZ even spans a wider compositional field (An_{71-95}). Intrasample variations are highest in samples with cumulus plagioclase, i.e. anorthosite, norite and pyroxenite occurring in the UCZ. Plagioclase occurring as inclusion in orthopyroxene shows the smallest range of anorthite content (An_{78-86}). Therefore, their range of the anorthite content is similar to those plagioclases occurring intercumulus in pyroxenitic layers and thus probably represent inherited specimen that crystallized during the deposition of a pyroxenitic layer. The surrounding orthopyroxene shielded them from equilibration with the other plagioclases in the plagioclase-rich cumulates, i.e. anorthosite and norite, they now occur in.

Eales *et al.* (1991), who investigated plagioclase inclusions in orthopyroxene from the LZ and CZ of the Union section in the western Bushveld Complex, found coincident anorthite contents for cumulus and intercumulus plagioclase and plagioclase inclusions (An_{60-75}) in the silicate host rocks. The plagioclases appear to be of more evolved composition at Union when compared to those investigated during this study. Since no exact data about the calculation of the anorthite content are available, the data cannot be compared with certainty.

The plagioclases investigated during this study show a trend of reverse fractionation in the LCZ and progressive fractionation in the UCZ (Fig. 4.44). As mentioned before, this trend is most likely caused by the specific position of the samples analyzed at the bottom or top of one cyclic unit, respectively. Thus, this trend doesn't represent true reversal in fractional crystallization.

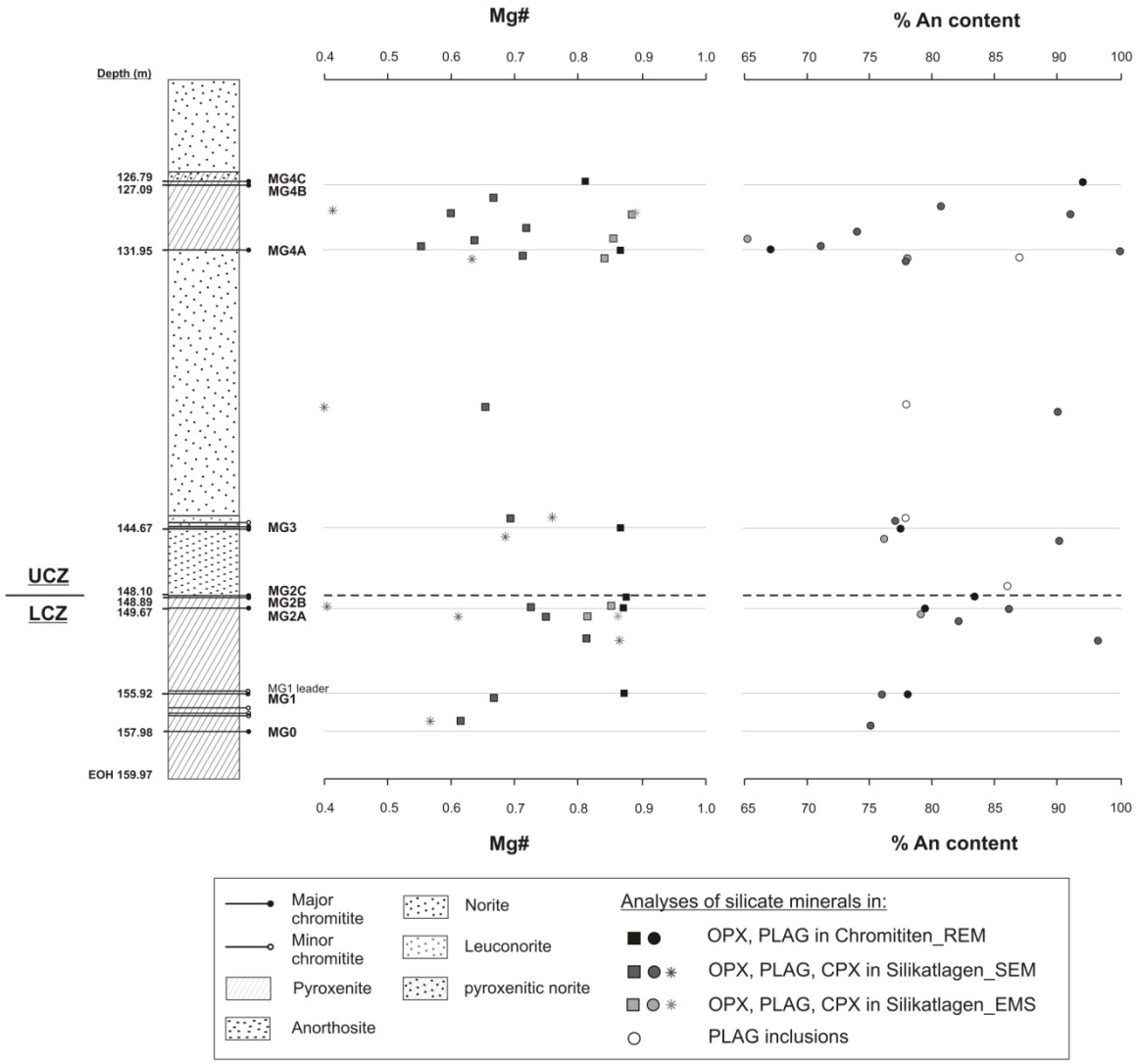

Figure 4.44 Cryptic variations of orthopyroxene (Mg#) and plagioclase (%An content) in silicate and chromitite layers through the MG sequence yielded from SEM-EDX and EMP analyses. Data are given in tables 4.8 and 4.9 for silicate minerals in chromitite layers and tables 4.10 and 4.11 for silicate minerals in silicate layers.

Figure 4.45 shows averaged pyroxene chemistry yielded from orthopyroxene in the various rock types of the MG of this study. The composition of orthopyroxene being

intercumulus in the chromitite layers is relatively constant with high MgO contents (32.3-36 wt%). By means of the Mg# (0.81-0.86; SEM-EDX data) in general progressive melt evolution with increasing amounts of co-crystallizing orthopyroxene can be deduced upwards the stratigraphic column.

Cumulus orthopyroxene in the silicate layers is richer in FeO and CaO when compared to orthopyroxene occurring intercumulus in massive chromitite. In the LCZ progressive melt evolution with stratigraphic height is detectable from the Mg# (0.62-0.82; averaged SEM-EDX data). The apparent reverse fractionation of orthopyroxene from the MG3 norite to the MG4A pyroxenite in the UCZ (0.56-0.72 respectively; averaged SEM-EDX data) derives from the addition of (multiple) primitive melt in the MG4A cyclic unit, which has been postulated before (cf. subsections 4.3.1, 4.4.1 and 4.3.2.1). Thus, the observed trend in orthopyroxene composition in the UCZ upward the stratigraphic column is not a true one.

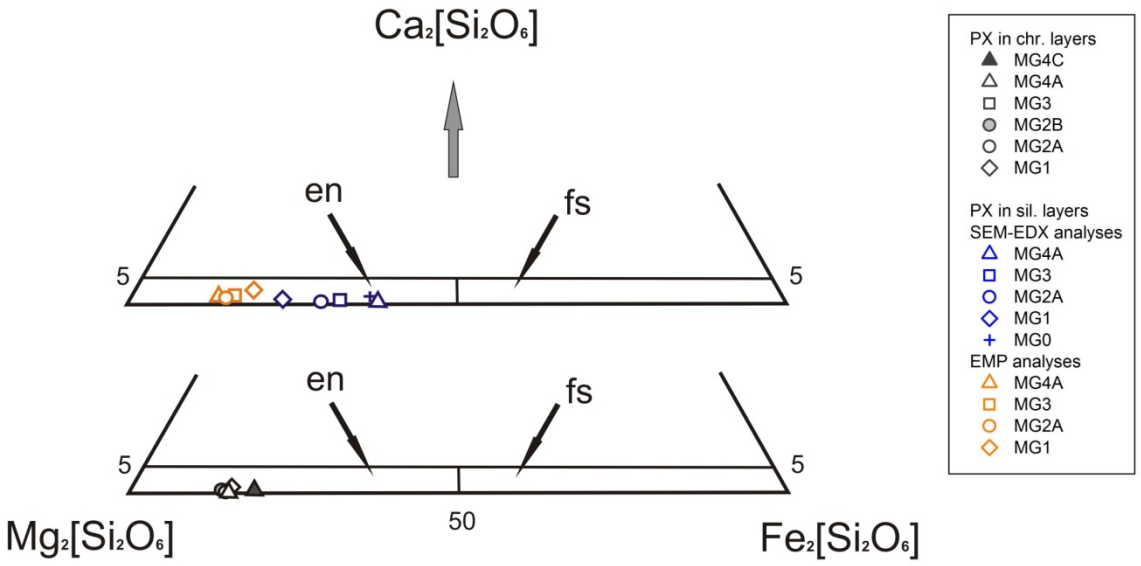

Figure 4.45 Orthopyroxene chemistry from different rock types of the MG sequence obtained during this study. *En:* enstatite; *fs:* ferrosillite. Ternary diagram after Morimoto *et al.* (1988).

4.3.7 The base metal sulphides

4.3.7.1 BMS data obtained with the SEM-EDX

As have been mentioned in subsection 4.2.1, the amount of the BMS within the chromitite layers is below 1 vol% and they mainly occur interstitial to chromite. As investigations with the MLA, the SEM-EDX analyses of the chromitite layers yielded the presence of chalcopyrite, pentlandite and millerite as well as pyrite. Their average composition is shown in table 4.12. All of them show low amounts of PGE, with the Ni-bearing sulphides preferentially containing Pt and/or Pd. Whether the PGE occur in solid solution in the BMS or represent micro-xenocrysts of PGM enclosed by the BMS cannot be specified.

Table 4.12 Average composition of the base metal sulphides analyzed with the SEM-EDX. *N:* number of analyses. Data are given in element%.

	n	Fe	Ni	Cu	Zn	Os	Ir	Ru	Pt	Pd	S	total
pentlandite	11	22.8	39.8	0	0	0	0	0	1.3	0.5	35.5	100
millerite	4	0	60.8	0	0	0	0	0	2.1	0	37.1	100
chalcopyrite	27	29.0	0	33.2		0.3	0.1	0.2	1.0	0	36.2	100
pyrite	9	42.7	0	0	0.3	0	0.2	0	0	0	55.2	100

Figures 4.46 and 4.47 illustrate compositional variations of BMS analyses from the different chromitite layers. For comparison, the norm compositions yielded from Rösler (1991) have been added to the plots.

Compared to the norm composition pentlandite hosts approximately 6% more Ni and is depleted in Fe by 10% (Fig. 4.46). Additionally, samples from the MG2B chromitite layer compositionally scatter the most. Millerite, which composition is also shown in figure 4.46, comprises less Ni (2.4 - 4.7%) but more S (0.5 – 2.7%) than norm composition indicates.

The chalcopyrite compositions determined scatter around the norm composition with generally less Fe and Cu and slight enrichment in S (Fig. 4.47). A similar situation is given for pyrite with less Fe (3 – 7%) and more S (0.4 – 4.5%) relative to the presented norm composition (Fig. 4.47).

Although some of the differences in composition can be ascribed to the relative inaccuracy with respect to microprobe analyses, a general Fe, Cu and S loss of the

primary magmatic BMS, i.e. pentlandite, chalcopyrite and pyrite, is visible. This loss is most likely to have been caused by aqueous fluids after the precipitation of the BMS, which is corroborated by manifold occurrences of secondary silicate minerals, i.e. amphibole, associated with the BMS (Fig. 4.48).

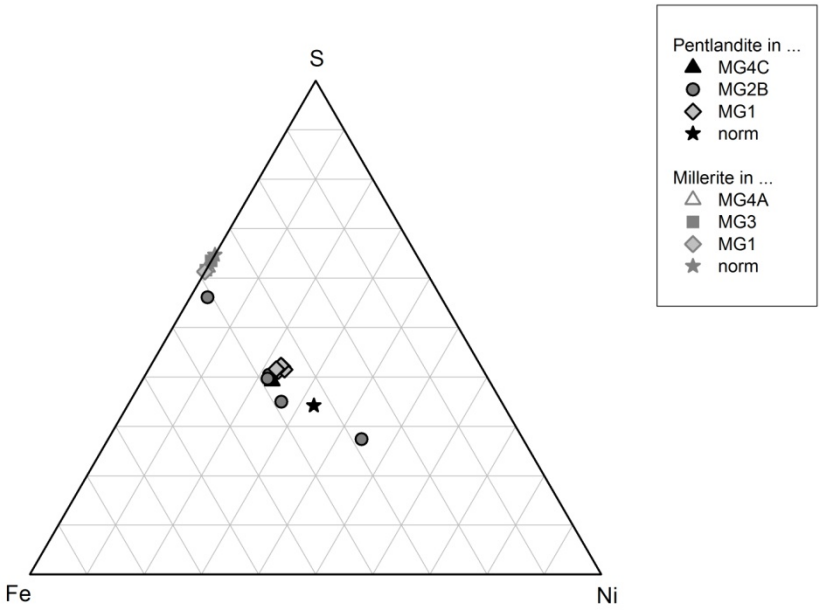

Figure 4.46 Compositional variation of pentlandite and millerite. Data are given in table B-19 in appendix B. Norm compositions are compiled in table B-20 in appendix B.

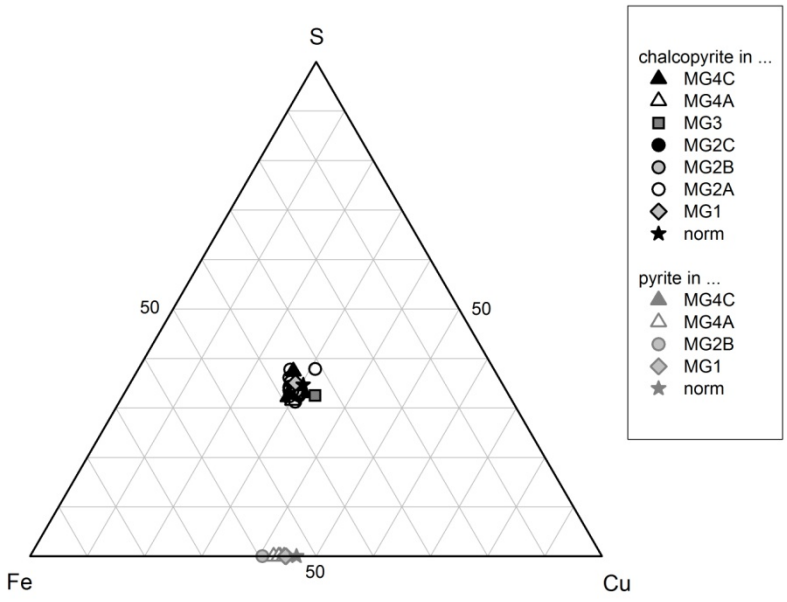

Figure 4.47 Compositional variation of chalcopyrite and pyrite. Data are given in table B-19 in appendix B. Norm compositions are compiled in table B-20 in appendix B.

During the alteration process the BMS have been cracked and dissoluted along grain boundaries (Fig. 4.49). The primary magmatic BMS show different maximum temperatures up to which they are stable, i.e. maximum thermal stability (chalcopyrite: 557°C, Barton, 1973; pentlandite: 610°C, Kullerud, 1963; pyrite: 743°C, Kullerud and Yoder, 1959). Since all of the analyzed BMS show losses in Fe, S and/or Cu the fluid must have been highly corrosive, e.g. Cl-rich, as suggested by several authors (e.g. Ballhaus and Stumpfl, 1986; Fleet and Wu, 1993; Hanley *et al.*, 2005).

Millerite is a common alteration product of pentlandite (Craig and Scott, 1974) and hence a secondary mineral. Its maximum thermal stability has been determined to be at 379°C (Kullerud and Yund, 1962). Thus, deposition of millerite occurred below this temperature, which corroborates its secondary origin.

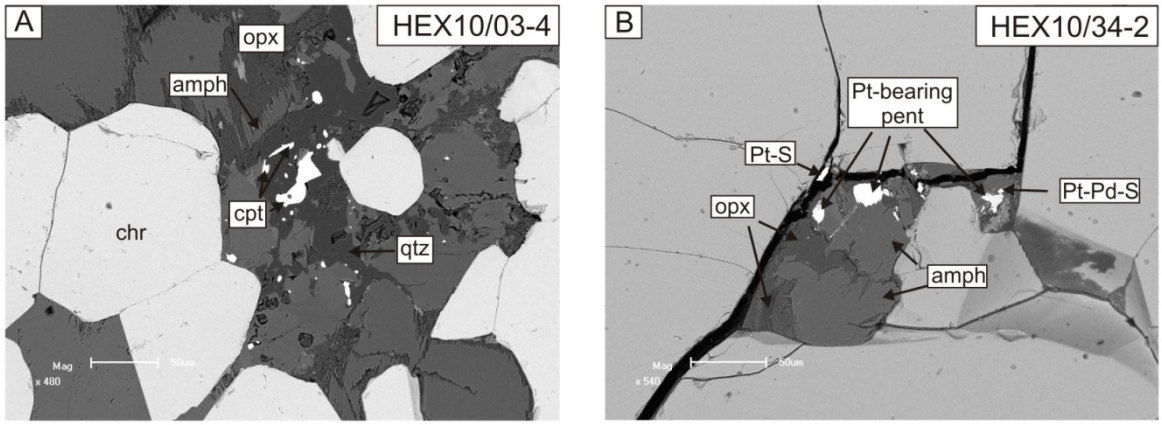

Figure 4.48 Replacement textures in the vicinity of BMS. **(A)** Chalcopyrite (cpt) with irregular grain boundaries surrounded by quartz (qtz). Orthopyroxene (opx) is replaced by amphibole (amph). **(B)** Pt-bearing pentlandite (pent) hosted by amphibole (amph) replacing formerly orthopyroxene (opx). Small grains of Pt- and PtPd-sulphides are present. BSE images.

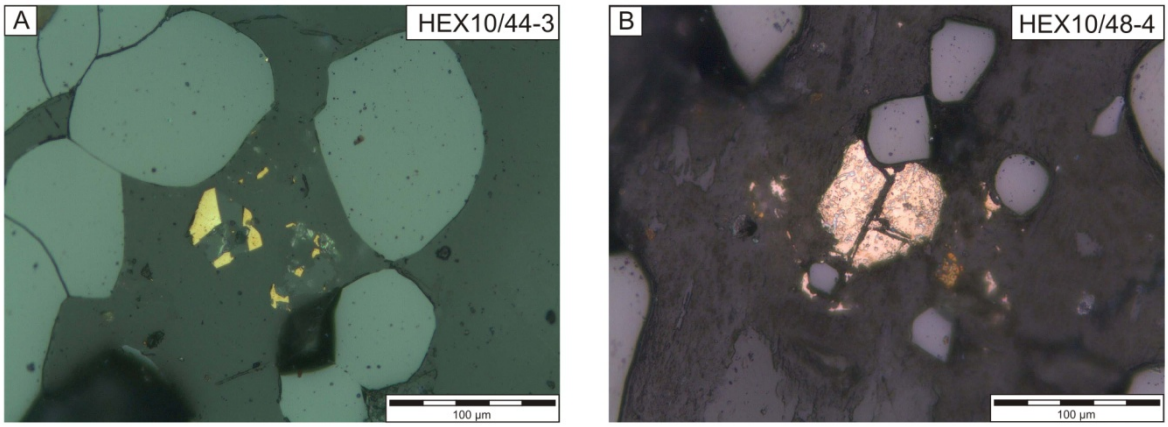

Figure 4.49 (A) Cracked chalcopyrite with alteration halo (light grey). **(B)** Cracked chalcopyrite in altered silicate matrix. PPL images.

4.3.7.2 BMS data obtained with the MLA

During investigation of MG chromitite samples with the MLA, only the BMS associated with PGM have been detected, as the PGM association was of major interest for this study (cf. subsection 4.3.8). Hence, the BMS data presented in the following do not intend to be exhaustive. However, since the BMS content of the MG chromitite layers has been found to be extremely low (cf. subsection 4.2.1), the data can be used as a rough estimation for characteristics of the BMS occurring in the MG chromitite layers.

The first observation that can be made from figure 4.50 is the lack or extreme underrepresentation of pyrrhotite, which is thought to be a primary BMS. This coincides with results from optical microscopy of the MG chromitite layers (cf. subsection 4.2.1).

In the silicate rich fraction of lowermost chromitite layers (MG1-MG2C) pentlandite is the dominating Ni-bearing BMS with the highest proportion in the MG2B chromitite, whereas in the chromitite layers above (MG3-MG4C) it is millerite. Only low amounts of pentlandite can be found here and it seems to be replaced by millerite.

From the MG1 to the MG2B chromitite the amount of chalcopyrite decreases, whereas at the same time increasing amounts of pyrite and pentlandite can be observed. In the chromitite layers of the UCZ (MG2C-MG4C) no such regular pattern is present, but the MG3 and MG4A chromitites host more pyrite relative to chalcopyrite than the MG2C and MG4C chromitite layers. Within the latter, pyrite is almost absent.

With the exception of the MG2B chromitite, chalcopyrite and pyrite make up the major portion of the BMS in the MG chromitite layers.

Table 4.13 BMS distribution within the silicate-rich fraction of the MG chromitite layers. Data for MG4A, MG3 and MG2C are averages from two samples analysed (cp. Tab. A-2 in appendix A).

mineral	MG4C	MG4A	MG3	MG2C	MG2B	MG2A	MG1
pentlandite	2.3	5.2	3.5	28.2	70.5	40.9	17.6
millerite	38.7	37.8	39.0	0.3	0	0	0
pyrrhotite	0	0	0.4	0	0	0	2.4
pyrite	2.0	49.8	49.0	35.0	9.4	19.9	21.4
chalcopyrite	57.2	6.8	8.1	36.7	20.0	40.3	60.4
total	100	100	100	100	100	101	102

After Craig and Scott (1974) millerite is a low-temperature alteration product of primary sulphides and its widespread occurrence in the UCZ paired with only minor pentlandite but lots of pyrite could be an indication for the S-loss within the UCZ chromitites as proposed by Naldrett *et al.* (1987). According to that part of the pentlandite

would recrystallize to millerite; excess Fe is used to produce secondary pyrite in the first place but can be also accounted for the Fe enrichment of chromite grains relative to Cr. S is lost to the surroundings.

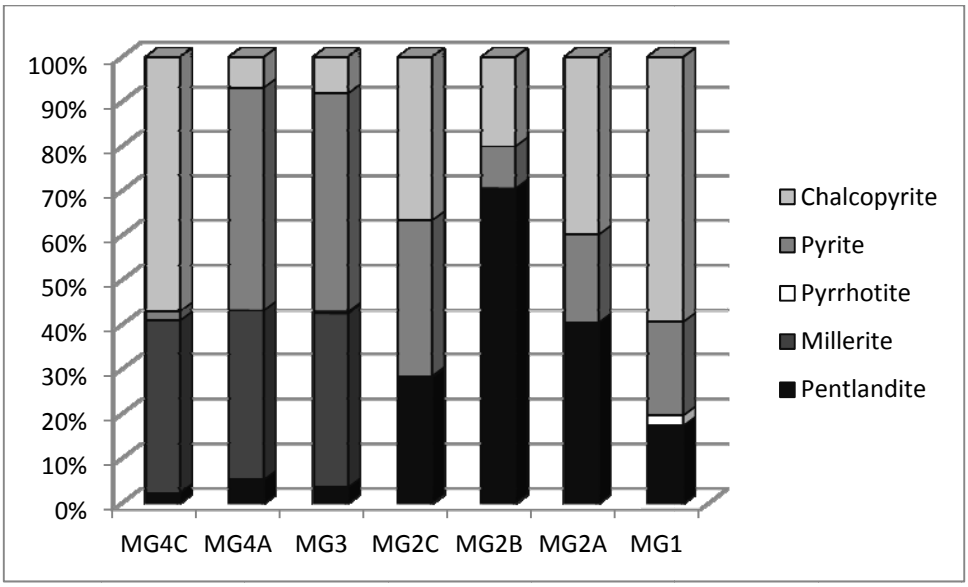

Figure 4.50 BMS distribution within the silicate rich fraction of the MG chromitite layers (area %). Data are given in table 4.13. Area % is the total area of the mineral of interest divided by the total area of the minerals of interest searched, multiplied by 100.

Grain size distribution

Grain sizes are expressed in equivalent-circle diameter (ECD), characterizing the size of a measured mineral having the same area as a circle with an equivalent diameter. It is used synonymous to µm and is calculated with the following equation:

$$ECD = 2\,x\,\sqrt{\frac{Area}{\pi}}$$

The grain size distribution of the MG chromitite layers doesn't show any regular pattern in terms of increasing or decreasing proportions in a specific size fraction (Tab. 4.14 and Fig. 4.51). In the uppermost chromitite layers (MG4C, MG4A, MG3) as well as in the MG1 chromitite the biggest proportion of the BMS has grain sizes between 20 and 45 µm. In the MG2B the grain size fractions 5-20 µm and 20-45 µm are nearly equally distributed, whereas in the MG2A chromitite almost all the BMS analysed show grain sizes between 5-20 µm. Grain sizes > 45 µm are only present in the MG2C and MG3 chromitite layers, which corresponds to highest PGE concentrations of these layers (cf. subsection 4.4.1.2).

Table 4.14 Grain size distribution of BMS grains analysed. Data for MG4A, MG3 and MG2C are averages from two samples analysed (cp. Tab. A-2 in appendix A).

Grain size	MG4C	MG4A	MG3	MG2C	MG2B	MG2A	MG1
> 45 µm	0	0	15.7	20.4	0	0	0
20-45 µm	81.9	66.9	53.2	51.8	44.8	0	77.1
5-20 µm	13.8	27.0	27.6	25.3	50.9	93.1	22.2
0-5 µm	4.3	6.2	3.5	2.6	4.3	6.9	0.7
Total	100	100	100	100	100	100	100

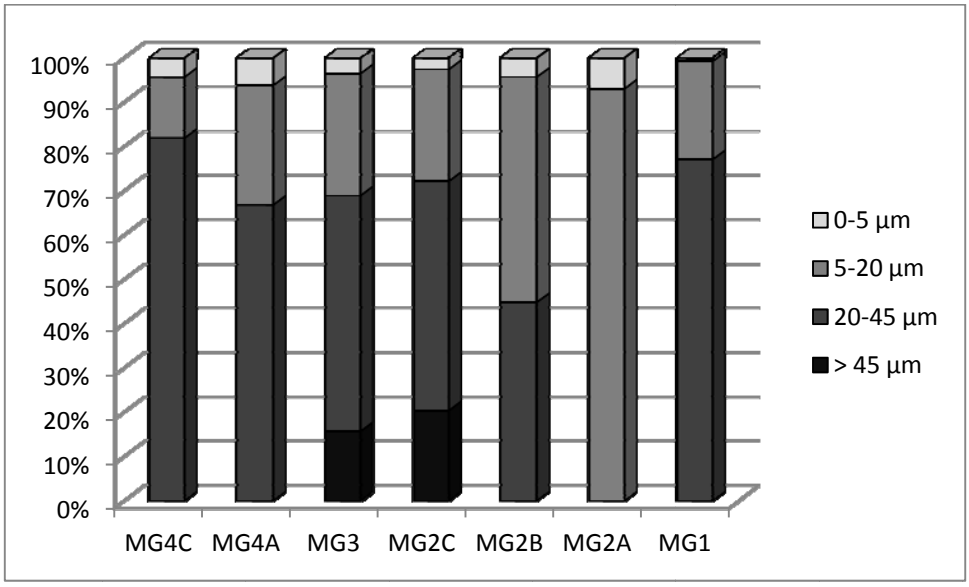

Figure 4.51 Grain size distribution of the BMS of the silicate-rich fraction of the MG chromitite layers. Data are given in table 4.14.

Mineral locking

The locking parameters generally describe the mineral association of the BMS. In this case it shows the amount of BMS being enclosed by another mineral group or the proportion of the liberated BMS, respectively, after milling of the sample material (Tab. 4.15 and Fig. 4.52). It can be used as a rough estimation of the flotation behaviour of a sample.

Locking of the BMS from the MG chromitite layers of core HEX10 doesn't show a regular pattern in terms of preference of a certain mineral group. In the MG4C and MG4A chromitites the majority of the BMS occur locked in silicate minerals. Within the MG3 and MG2B chromitite layers the highest proportion of the BMS present are enclosed by

oxides, i.e. chromite. An almost equal distribution of locking in silicate minerals or oxides can be found in the MG2C chromitite layer. A similar distribution can be observed in the MG2A chromitite, where ca. 45 wt% each of the BMS occur locked in the silicate minerals or liberated. The highest proportion of liberated BMS occurs in the MG1 chromitite layer, but it also shows a high proportion of BMS being locked by silicate minerals. Except for the lowermost chromitite layers MG1 and MG2A, the amount of liberated BMS in milled chromitite samples is generally below 30 wt% per sample.

The silicate minerals have been separated into a primary (pyroxene, feldspar) and a secondary assemblage (amphibole, mica, chlorite, talc, quartz). With the help of SEM-EDX analyses (cf. subsection 4.3.7.1) and investigations with the optical microscope (cf. subsection 4.2.1) it was suggested that part of the BMS in the MG chromitite layers have been modified by or even derive from aqueous fluids affecting the MG chromitite layers after their precipitation. Table 4.16 shows that in the MG4C, MG2B and MG1 chromitites the distribution of the BMS being locked in primary or secondary silicate minerals is nearly equal, whereas in the other chromitite layers the BMS are preferentially locked in the primary silicate minerals, especially feldspar. Hence, the MG4C, MG2B and MG1 chromitite layers were probably more affected by alteration processes than the other chromitite layers of the MG-sequence. On the other hand, BMS like millerite that are definitely of secondary origin can only be found in the chromitite layers of the UCZ, i.e the MG3-MG4C (Fig. 4.46). Thus, redistribution of the primary BMS assemblage as well as formation of secondary BMS seems to be quite limited in the MG chromitite layer relative to observations made for the UG2 and Merensky Reef (e.g. Li *et al.*, 2004; Voordouw *et al.*, 2009).

Table 4.15 Locking parameters of the BMS occurring in the silicate-rich fraction of the MG chromitite layers. Data for MG4A, MG3 and MG2C are averages from two samples analysed (cp. Tab. A-2 in appendix A).

BMS wt% locked in...	MG4C	MG4A	MG3	MG2C	MG2B	MG2A	MG1
silicate	69.9	92.8	75.9	59.6	61.8	45.6	44.0
oxides	9.4	2.6	1.5	4.7	2.7	6.5	0.6
PGM	0	1.7	7.0	0.7	3.4	0	0
other	8.2	0.5	8.2	10.8	15.7	3.4	0.2
liberated	12.5	2.3	7.4	24.2	16.3	44.5	55.1
total	100	100	100	100	100	100	100

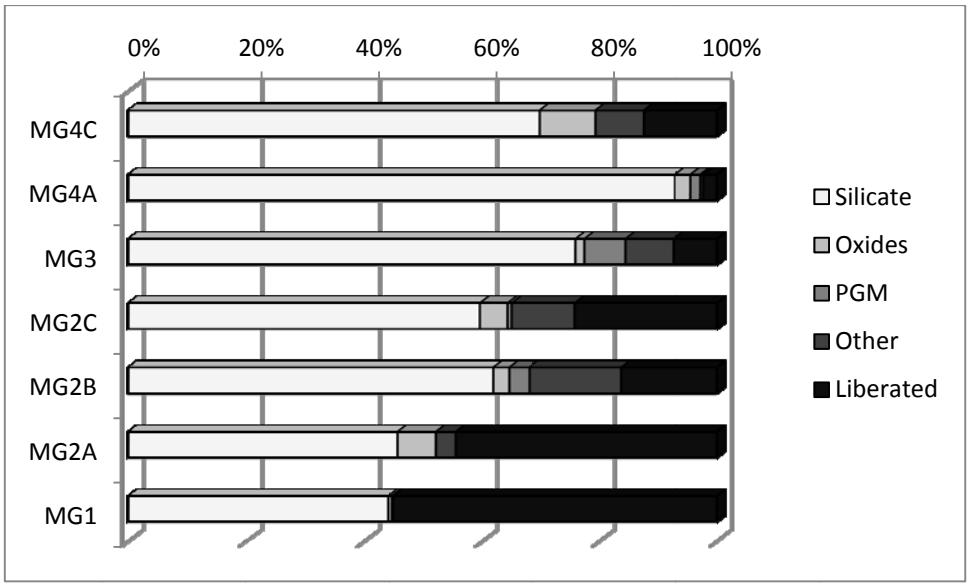

Figure 4.52 Locking of the BMS being present in the silicate-rich fraction of the MG chromitite layers. Data are given in table 4.15.

Table 4.16 Proportion of the primary and secondary silicate mineral assemblages the BMS of the silicate-rich fraction of MG chromitite layers occur locked in. Data for MG4A, MG3 and MG2C are averages from two samples analysed (cp. Tab. A-2 in appendix A). ***SIL:*** silicate minerals. 'Primary silicate minerals' comprises pyroxene and feldspar; 'secondary silicate minerals' amphibole, mica, chlorite, talc and quartz.

	MG4C	MG4A	MG3	MG2C	MG2B	MG2A	MG1
primary SIL	52.2	83.7	73.5	62.7	48.3	66.3	46.6
secondary SIL	47.8	16.3	26.5	37.3	51.7	33.7	53.4
total	100	100	100	100	100	100	100

Liberation

The **degree of liberation** (formerly referred to as "combined liberation index" (CLI)) of a mineral from a particle can be calculated by the relation of the proportion of a mineral in contact with free surface relative to that in contact with another mineral in the particle. The liberation classes are divided into intervals of 10% (i.e. 0 %, 0% < x ≤ 10%; 10% < x ≤ 20%; ...; 90% < x ≤ 100%; 100%) with x representing the mineral of interest. They are divided as follows:

- Locked: 0-30% free surface
- Middlings: 30-80% free surface
- Liberated: 80-100% free surface.

Table 4.17 BMS liberation (in %) from chromitite layers of the MG sequence.

	MG4C	MG4A	MG3	MG2C	MG2B	MG2A	MG1
liberated	12.5	2.3	37.3	38.2	34.8	44.5	55.1
middlings	44.5	40.9	38.2	49.0	48.1	0	25.5
locked	43.1	56.8	24.6	12.8	17.1	55.5	19.4
total	100	100	100	100	100	100	100

The highest degree of liberation of the BMS is present in the MG1 chromitite layer (Tab. 4.17), but more than 30% of the BMS can also be liberated from the MG2A, MG2B, MG2C and MG3 chromitites. Relatively high amounts of middlings exist for BMS in the MG2B-MG4C chromitite layers. Since 'middlings' means that 30-80% of free surface are available, finer grinding of the sample material (i.e. <75 µm) may even increase the amount of liberated BMS especially within these chromitites.
Lowest degree of liberation exists for BMS occurring in the MG4A chromitite that also shows an amount of >50% of locked BMS. The opportunity of finer grinding probably also can increase the amount of liberated BMS from the middlings.

4.3.8 The platinum-group minerals

Ten samples have been chosen to be analysed with the MLA; one for each of the chromitite layers MG1, MG2A, MG2B and MG4C and two samples of the chromitite layer most enriched in the PGE (i.e. MG2C, MG3) and also two samples from the MG4A chromitite. Their stratigraphic position can be quoted from table A-2 in appendix A. For information of the mineral association investigations with the MLA are important, since the data are acquired quickly relative to microprobe analyses and clues for PGE mineralization and conditions for PGM formation are possible.

The groupings of PGM species described in this chapter is based on the division that has been done by the Anglo Research Lab in Johannesburg for mineral liberation analyses and can be deduced from table 4.18.

Table 4.18 Division of the PGM for mineral liberation analysis (from Anglo Research Lab, Johannesburg).

mineral name	abbreviation	composition
Pt- sulphide	PtS	PtS
PtPd- sulphide	PtPdS	PtPdS
PtRh- sulphide	PtRhS	PtRhCuS
Pt- telluride	PtTe	PtBiTe
Pd- telluride	PdTe	PdTeBi
Pt- alloys	Pt-alloy	PtSbSnAs
Pd- alloys	Pd-alloy	PdSbSnAs, RuOsIr-alloys
Pt- arsenide	PtAs	PtAs
Pd- arsenide	PdAs	PdAS
PGE- sulphoarsenides	PGESAs	PtRhAsS
ferroplatinum	PtFe	PtFe
laurite	L	RuS

In the following, a brief outline of the composition of the PGM species grouped by the Anglo Research Lab is given. It should illustrate the affiliation of PGM after Cabri (2002) to the individual groups.

Pt-sulphide: Cooperite (PtS) is the only PGM that can be related to this group. Since a solid solution series (sss) with vysotskite (PdS) exists (Verryn and Merkle, 2002; Merkle and Verryn, 2003), Pt can be replaced by Pd. Verryn and Merkle (1994) reported furthermore that Pt seems also to be replaced by Ni.

PtPd-sulphide: Due to the major element contents this group is comprised of vysotskite (PdS) and braggite (PtPdS), between which an extensive solid solution series exists (Verryn and Merkle, 2002). According to the current nomenclature, the border between vysotskite and braggite sss lies at 10 at% Pt (cf. Cabri, 2002).

There exist several definitions about the composition of PtS (‘cooperite’), PtPdS (‘braggite’) and PdS (‘vysotskite’) in the literature. Analyses of a large number of cooperite, braggite and vysotskite grains done by Verryn and Merkle (2002) indicate a complete solid solution series between cooperite and braggite due to the replacement of Pt by Pd. Cooperite is thus defined as pure PtS with > 95 mol% PtS. Vysotskite can contain up to 10 mol% PtS. The solid solutions between them are named braggite (PtPdS).

On the other hand, experimental data showed that a miscibility gap between braggite and cooperite exists (Cabri *et al.*, 1987; Verryn and Merkle, 2002). Grain analyses plotting within this gap are interpreted to be metastable due to Pd loss to hydrothermal fluids.

PtRh-sulphide: This group comprises PGM being mainly composed of Pt, Rh and S, which are commonly malanite ($CuPt_2S_4$) and cuprorhodsite ($CuRh_2S_4$) (Cabri, 2002). However, since a sss to cuproiridsite ($CuIr_2S_4$) exists as well, minor amounts of Ir do occur.

Pt-telluride: After Cabri (2002) this could be either maslovite (PtBiTe) or moncheite ($PtTe_2$). Furthermore insizwaite ($PtBi_2$) can be assigned to this group.

Pd-telluride: Pd-tellurides are mainly michenerite (PdBiTe) and merenskyite ($PdTe_2$). According to their chemical composition the following PGM can also assigned to this group: froodite ($PdBi_2$), keithconnite (Pd_{3-xTe}), kotulskite (PdTe), polarite and sobolevskite (both PdBi) as well as telluropalladinite (Pd_9Te_4).

Pt-alloys: This group comprises PGM species with Pt as the major component, which is associated with various elements (e.g. Pb, Cu, Hg, Sn, other PGE) except S, Bi and Te. Since lots of variations exist, the individual PGMs are not listed separately.

Pd-alloys: Similar to the Pt-alloys an association with different elements exists with Pd being the major component. Furthermore, stibiopalladinite (PdSb) and plumbopalladinite (Pd_3Pb_2) can be ascribed to this group. As with the Pt-alloys, too many variations exist, and it is therefore referred to Cabri (2002).

This group also comprises RuOsIr-alloys, since they seldom occur and are treated the same way as the Pd-alloys during beneficiation (pers. comm. Corne Schalkwyk, Anglo Research Lab).

Pt-arsenide: This group contains sperrylite ($PtAs_2$) as well as platarsite (PtAsS).

Pd-arsenide: The main constituents of this group are palladoarsenide (Pd_2As), palladobismutharsenide ($Pd_2As_{0.8}Bi_{0.2}$) as well as stillwaterite (Pd_8As_3), but also many other PGM species could be ascribed to this group according to their chemical composition: majakite (PdNiAs), menshikovite ($Pd_3Ni_2As_3$), isomertiite ($Pd_{11}Sb_2As_2$), mertieite I ($Pd_{11}(Sb,As)_4$) and mertieite II ($Pd_8(Sb,As)_3$), palarstanide ($Pd_5(Sn,As_2$) and palladodymite ($(Pd,Rh)_2As$). Most of them can only be distinguished by X-ray diffraction (Augé *et al.*, 2002).

PGE-sulphoarsenide: Most probably the end members of the solid solution series platarsite (PtAsS) – ruarsite (RuAsS) – irarsite (IrAsS) and daomanite ($CuPtAsS_2$) are involved. Additionally, hollingworthite (RhAsS) and osarsite (OsAsS) could be part of this group.

Ferroplatinum: This group includes isoferroplatinum (Pt_3Fe), tetraferroplatinum (PtFe) and ferronickelplatinum ($PtFe_{0.5}Ni_{0.5}$).

Laurite: Pure laurite is made up of S and Ru only (RuS_2), but since sss with ehrlichmannite (OsS_2) and IrS_2 exist, minor amounts of Os and Ir are possible.

The modal mineralogy of the silicate rich fraction of the samples yielded from hydro-separation is presented in figure 4.53. From bottom to top of the stratigraphy declining chromite contents can be recognized (referred to as 'oxides' in the following figures and tables). An exception is the MG4A chromitite layer, showing chromite contents between MG2A and MG2B values. The silicate content decreases in the chromitite layers of the LCZ (i.e. MG1, MG2A and MG2B), whereas in the chromitites of the UCZ increasing silicate contents occur, with the exception of the MG2C layer. The PGM and BMS contents vary and are both highest in the MG3 chromitite layer. The lowest amounts of BMS as well as PGM occur in the MG2A chromitite layer.

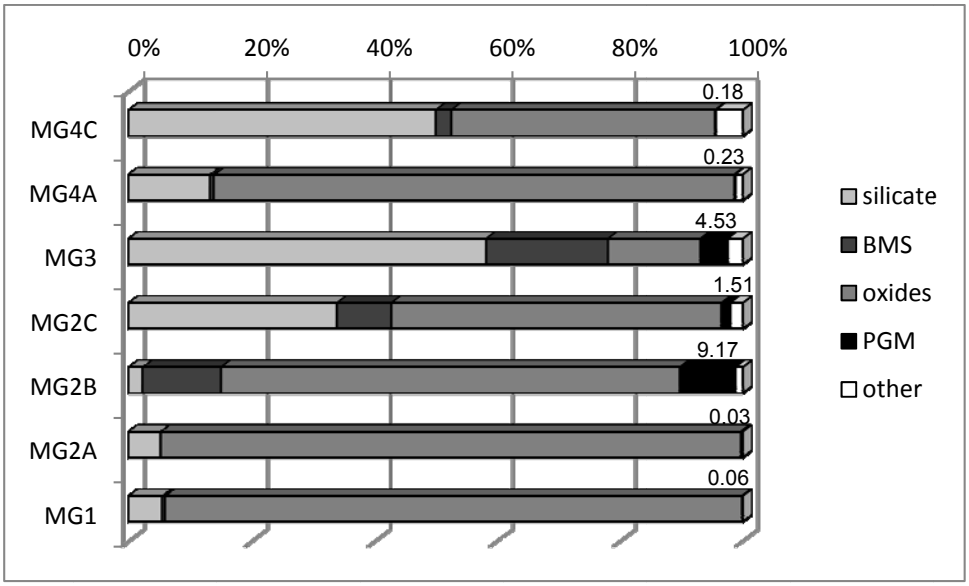

Figure 4.53 Modal mineralogy of the silicate rich fraction of the MG chromitite samples in area %; numbers above bars represent percentages of PGMs gained with the MLA. Data for MG4A, MG3 and MG2C are averages from two samples analysed (cp. Tab. A-2 in appendix A).

These observations suggest a coupled behaviour of the PGM and the BMS, which is corroborated by the high Spearman rank correlation coefficient (r_S= 0.964) for the total of PGM and the total of BMS occurring in the MG chromitite layers (Fig. 4.54A). A similar but weaker positive correlation exists for the PGM and the silicate minerals (r_S= 0.857) suggesting an association of the PGM with the silicate minerals originally being interstitial to chromite (Fig. 4.54B). Due to that, the PGM of the MG chromitite layers seems to show not only a chalcophile but also a siderophile behaviour.

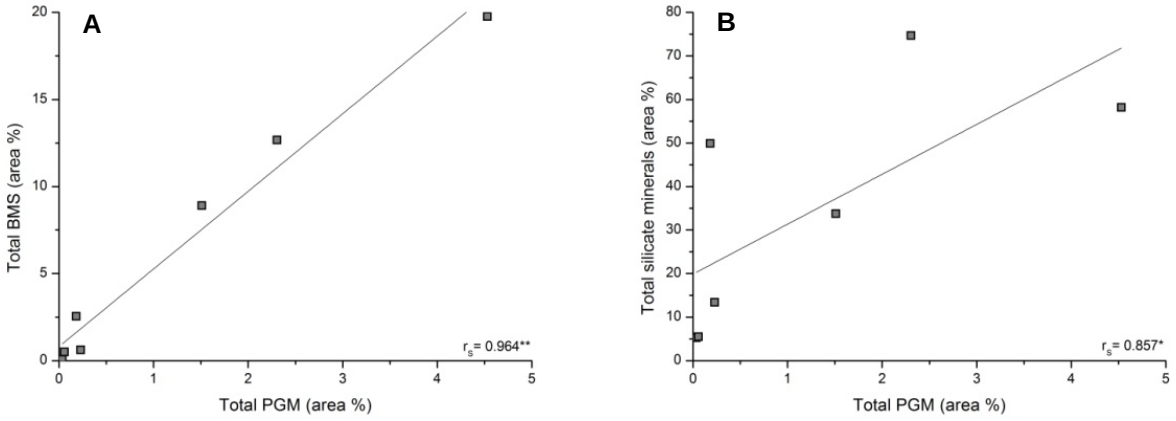

Figure 4.54 Correlation of (**A**) the total amount of BMS and the PGM, and (**B**) the total amount of the PGM and the silicate minerals in area %. r_S**:** Spearman rank correlation coefficient; ** correlation significant at the 0.01 level, * correlation significant at the 0.05 level.

The distribution of the PGM species within the chromitite layers is highly variable, which is illustrated in figure 4.55. Laurite is the most common one in the MG1, MG2A and in the MG4C chromitites, whereas in the other chromitite layers PtRh- sulphides are the dominating PGM species. PtPd- sulphides are the second common PGM species in all the MG chromitite layers. When compared to the other samples, the MG2A chromitite layer hosts a considerable amount of PGE-sulphoarsenides and contemporaneously host the lowest variation of PGM species (cf. Fig. 4.55 and 4.56).

The contents of PGE- tellurides, - arsenides or - alloys are generally low and rarely exceed 3% each. Ferroplatinum also occurs very rare (< 2%). For reasons of presentability their relative proportions are shown in figure 4.56. However, it can be observed, that the Pd-rich varieties are more common than the Pt-rich ones. Especially the MG4C chromitite is enriched in alloys and Pd- tellurides when compared to the other chromitite layers (cf. Tab. 4.19).

As can be obtained from figures 4.55 and 4.56 as well as table 4.19 no general trend in terms of increasing or decreasing amounts of the PGM species related to the stratigraphy can be observed.

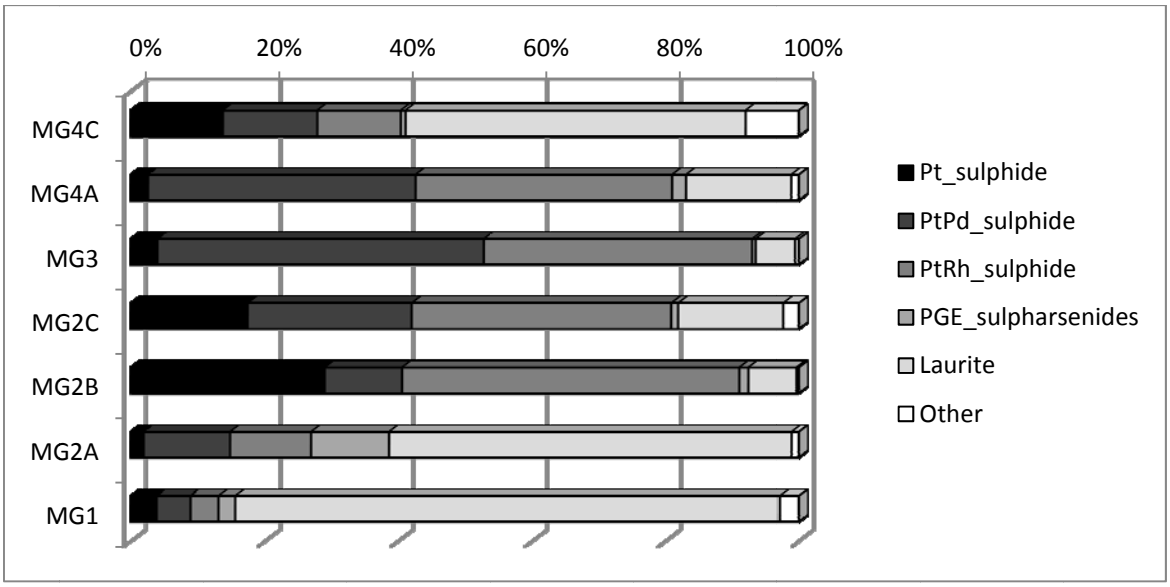

Figure 4.55 Distribution of the individual PGM species found in the silicate rich fraction of the analyzed MG chromitite layers. For data see table 4.18. Data for MG4A, MG3 and MG2C are averages from two samples analysed (cp. Tab. A-2 in appendix A). 'Other' comprises Pt- and Pd-arsenides, -tellurides, -alloys and ferroplatinum; their amount is illustrated in Fig. 4.56.

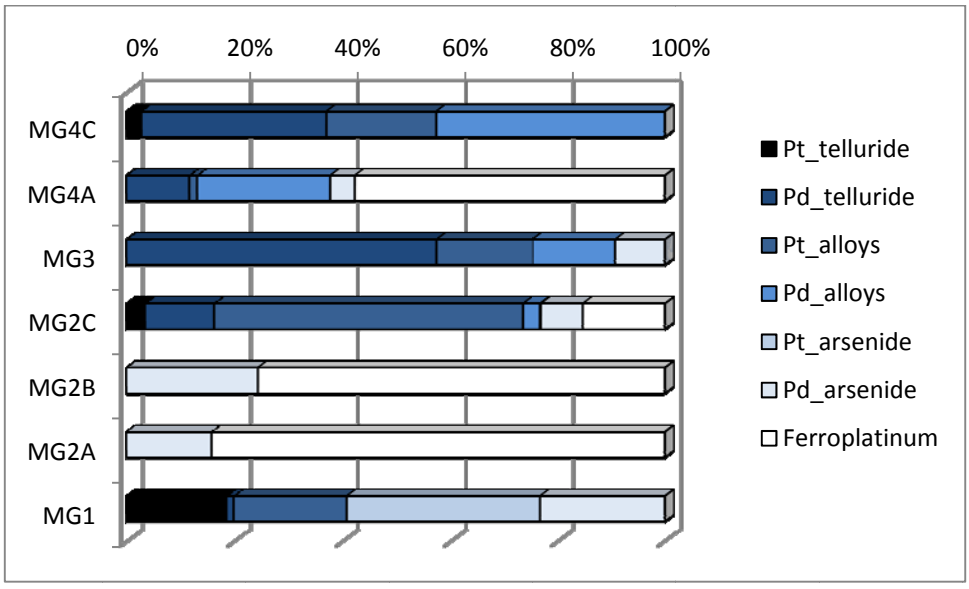

Figure 4.56 Specification of 'other' from figure 4.55. For data see table 4.19. Data for MG4A, MG3 and MG2C are averages from two samples analysed (cp. Tab. A-2 in appendix A).

Table 4.19 Percentages of the PGM species and number of individual grains found in the silicate rich fraction of the analysed MG chromitite layers.

	MG4C		MG4A		MG3		MG2C		MG2B		MG2A		MG1	
No. of grains	154	%	146	%	117	%	152	%	167	%	131	%	125	%
Pt- sulphide	30	19.5	13	8.2	14	11.5	29	15.8	50	29.9	7	5.3	7	5.6
PtPd- sulphide	29	18.8	30	21.1	56	47.3	35	28.9	38	22.8	19	14.5	4	3.2
PtRh- sulphide	28	18.2	45	29.9	35	30.1	45	34.2	63	37.7	25	19.1	9	7.2
Pt- telluride	1	0.6	1	0.4	0	0.0	1	0.3	0	0	0	0	5	4.0
Pd- telluride	11	7.1	0	0	3	2.1	1	1.3	0	0	0	0	2	1.6
Pt- alloys	5	3.2	1	0.3	1	0.4	4	1.4	0	0	0	0	2	1.6
Pd- alloys	15	9.7	3	2.0	1	0.4	1	0.3	0	0	0	0	0	0
Pt- arsenide	0	0	0	0	0	0	1	0	0	0	0	0	4	3.2
Pd- arsenide	0	0	0	0	1	0.4	2	0.3	1	0.6	1	0.8	2	1.6
PGE- sulphoarsenide	8	5.2	7	4.3	1	0.8	5	1.9	2	1.2	15	11.5	12	9.6
ferroplatinum	0	0	2	0.9	1	0.4	2	0.9	1	0.6	1	0.8	0	0
laurite	27	17.5	47	33.0	8	6.4	28	14.7	12	7.2	63	48.1	78	62.4
total	154	100	146	100	117	100	152	100	167	100	131	100	125	100

The ***grain size distribution*** of all PGM grains found within the investigated samples is presented in figure 4.51 assigned with regard to the layers they occur in. Grain sizes are expressed in ECD (cf. subsection 4.3.8.2).

The grain size distribution of the MG1 and MG2A chromitite layers is very similar, and both layers show the smallest grain sizes. Up to 60% of the PGM grains are smaller than 5 µm and only 10% are bigger than 10 µm. In the range from 5 to 10 µm the MG2A chromitite even seems to host smaller PGM grain sizes than the MG1 chromitite.

With height of the stratigraphic column of the MG-sequence the grain sizes seem to increase from MG1/MG2A over MG2C up to the MG3 chromitite layer, with the latter comprising the largest PGM grain sizes within the MG-sequence. From the MG3 up to the uppermost chromitite layer decreasing PGM grain sizes can be observed. The grain size is therefore proportional to the amount of PGE within the chromitite layers, which show increasing contents up to the MG2C and MG3 chromitites and then decreasing amounts of PGE further up to the MG4C chromitite layer (cf. Fig. 4.81 in subsection 4.4.1.2).

The MG4A chromitite shows similarities to the uppermost MG4C chromitite, comparable to findings for the lowermost layers. Of the uppermost chromitite layers only 40% of the PGM are smaller than 5 µm and 20% show grain sizes bigger than 10 µm.

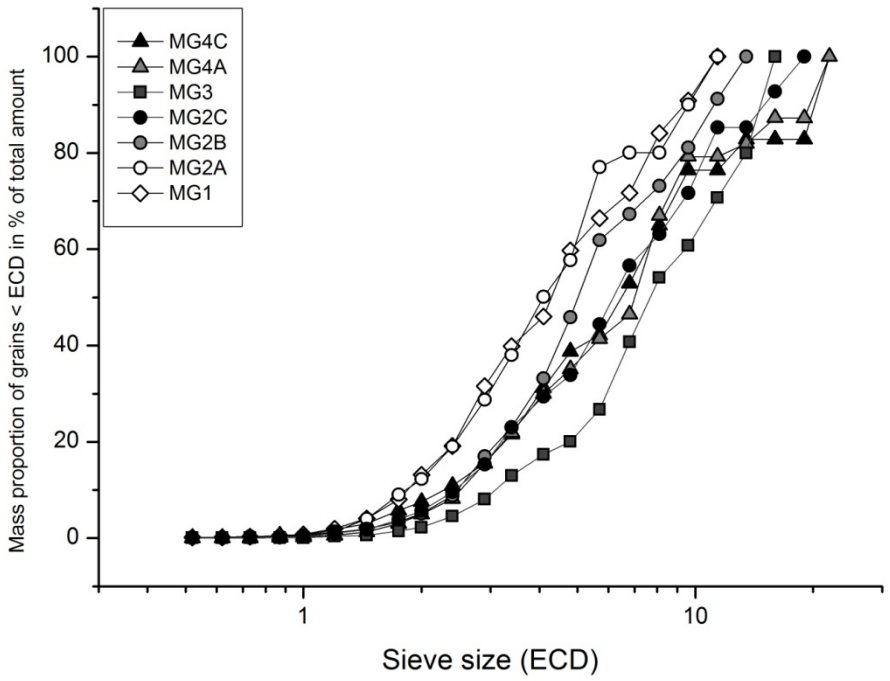

Figure 4.57 Averaged grain size distribution of PGM grains from individual chromitite layers of the MG sequence. Grain size is reported in ECD (µm- equivalent).

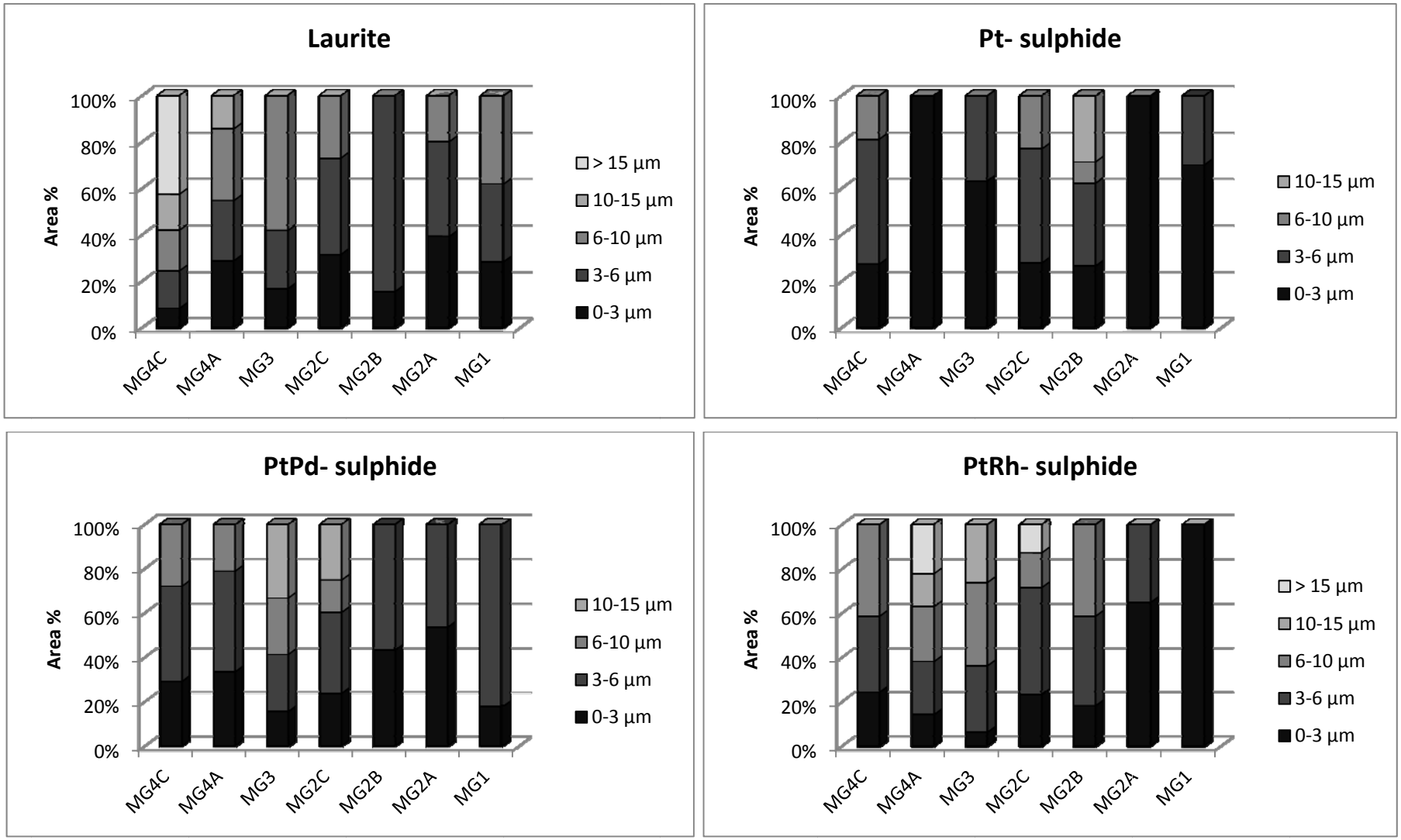

Figure 4.58 Grain size distribution of the PGM in the individual chromitite layers of the MG sequence. Values for MG2C, MG3 and MG4A are averages from two samples. For data see table C-1 in appendix C.

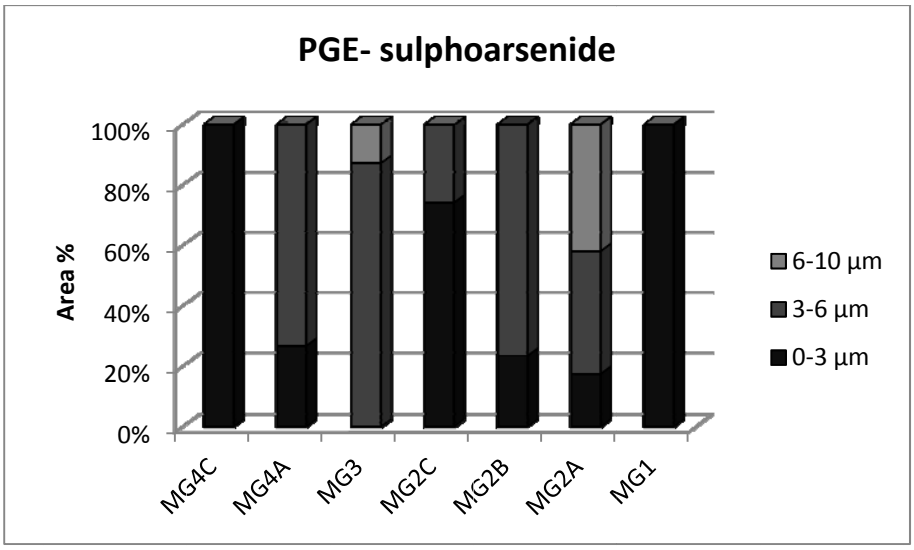

Figure 4.58 *(cont.)* Grain size distribution of the PGM in the individual chromitite layers of the MG sequence. Values for MG2C, MG3 and MG4A are averages from two samples. For data see table C-1 in appendix C.

In figure 4.58 the grain size distribution of laurite, the Pt-, PtPd-, PtRh- sulphides and the PGE- sulphoarsenides of the MG chromitite layers are presented, which make up the major PGM species within them. The other PGM species are only minor constituents (cf. Tab. 4.19) and the majority of them shows grain sizes <3 µm (cf. Tab. C-1 in appendix C).

The major proportion of the PGM presented in Fig. 4.58 have grain sizes <10 µm. Only 5.6% of the grain sizes of the major PGM species (Fig. 4.58) range between 10-15 µm, and only 2.8% are bigger than 15 µm, i.e. laurite and PtRh- sulphide.

In terms of in- or decreasing PGM grain sizes with the stratigraphic column of the MG-sequence no general trend can be observed. With a few exceptions, the lowest range in PGM grain sizes occur in the chromitite layers of the LCZ, i.e. MG1-MG2B. For laurite the greatest range in PGM grain sizes is present in the uppermost chromitite layers, i.e. MG4A and MG4A, whereas the PtPd- sulphides show the greatest grain size range in the MG2C and MG3 chromitites – the chromitite layers that contain highest PGE concentrations (cf. subsection 4.4.1.2). The grain size range of the Pt- sulphides is relatively small (mainly 0-6 µm), with its highest range occurring in the MG2B chromitite (0-15 µm). The PtRh- sulphides as the second common PGM species within the MG chromitite layers have the greatest grain size range in the MG2C and MG4A chromitite layers.

4.3.8.1 Mineral association, mineral locking and mineral liberation

Mineral association, mineral locking and mineral liberation are important parameters to estimate beneficiation success of PGMs from their host hock, which is why they are treated separately. Additionally, the mineral association of the PGM give important implications for the PGE mineralization of the studied samples.

The **mineral association** is due to the mode of occurrence of the PGM within the host rock, i.e. the silicate fraction of the chromitite layers of the MG sequence. The PGM present in the samples occur in six basic modes (see also Fig. 4.59):

- Liberated (L)
- Locked in gangue (G; Gc)
- Attached to gangue (AG; AGc)
- Associated with liberated BMS (SL)
- Associated with BMS that is locked in gangue (SG; SGc)
- Associated with BMS that is attached to gangue (SAG; SAGc)

'Gangue' refers to silicate minerals in the first place, but occasionally oxides (rutile, magnetite) may be involved. The dominant silicate phases are pyroxene and plagioclase; minor phases are amphibole, mica, chlorite and talc. Associations with chromite have been treated separately and are indicated by a little *c* (e.g. G*c*: PGM locked in chromite).

The mineral association of the PGM is summarized in table 4.20. One part shows the mineral association including laurite, and the other one the proportions of mineral association if laurite is excluded from the calculation[8]. Figures 4.60 and 4.61 illustrate the changes of the mineral association of the PGM occurring in the MG chromitite layers.

The majority of the PGM occurring in the MG4C chromitite are associated with BMS locked in gangue (SG; 34.6%) or locked in silicate gangue (G; 26.9%). Liberated PGM occur to 7.7 % only. If laurite is excluded from the calculation, the amount of PGM being locked in chromite (Gc) is reduced to 2.3 % and the number of PGM associated with BMS locked in gangue (SG) increases to 39.5 %.

[8] The exclusion of laurite form the calculation of the mineral associations is mainly done for beneficiation issues, as laurite tends to be locked in chromite and thus is not recoverable. According to this, it is negligible when considering the recovery of the PGM.

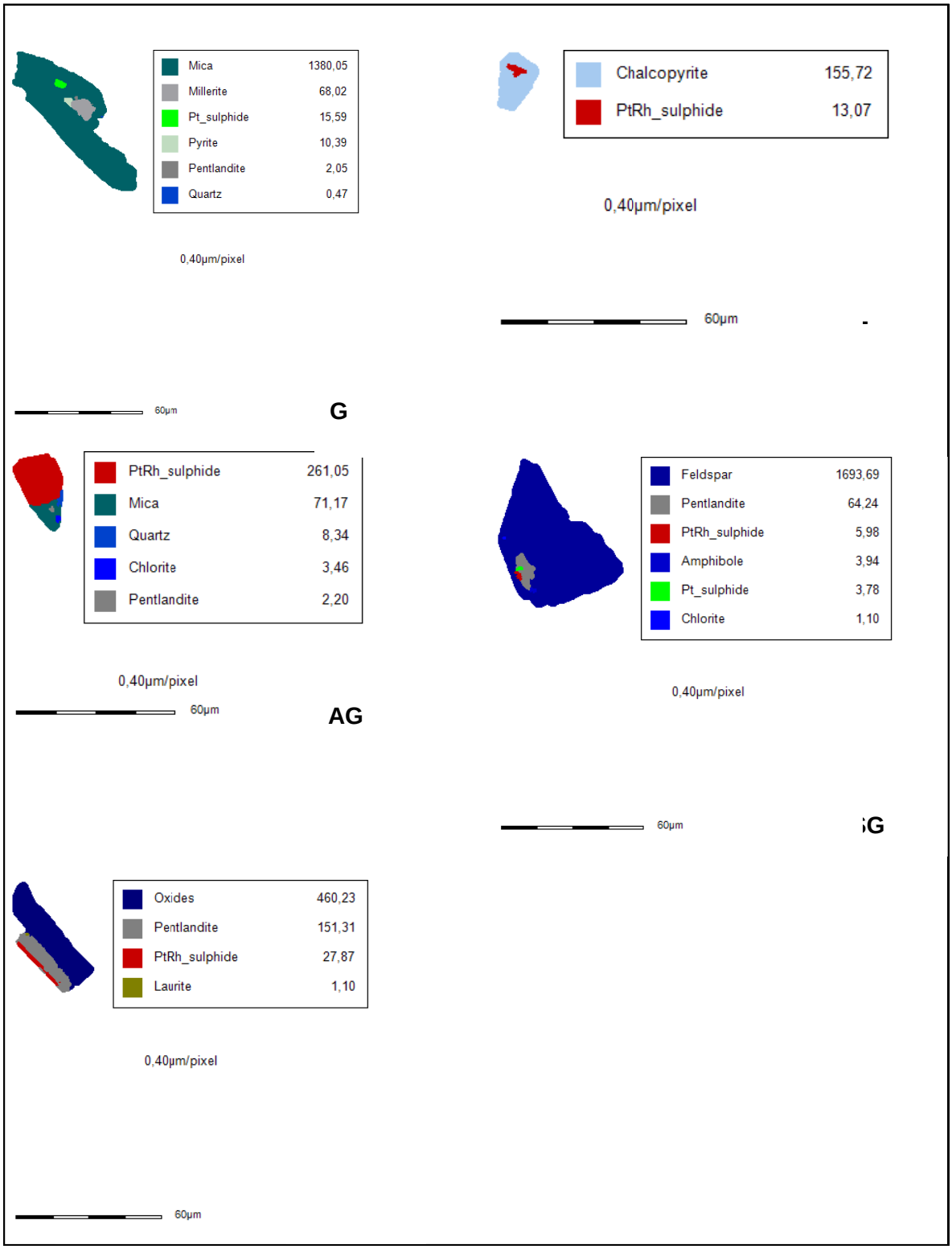

Figure 4.59 Examples of the different modes of occurrences of the PGM. Abbreviations are explained in text. False color images obtained from MLA.

Within the MG4A chromitite layer the major mineral association is PGM locked in chromite (Gc; 27.8 %), followed by PGM being associated with the BMS locked in gangue (SG; 24.3 %). Liberated PGM (L) occur to 17.9 %. The strongest variation occurs at the

association of PGM being locked in chromite, when laurite is excluded: the amount is reduced from 27.8 % to 7.1 % and indicates that within this chromitite layer laurite is the dominant PGM species being locked in chromite. Similar to the MG4C chromitite the number of PGM being associated with BMS locked in gangue (SG) strongly increases to 33.5 %. Minor increases can be observed for liberated PGM (L) and those PGM being attached to gangue.

The majority of the PGM within the MG3 chromitite are whether liberated (L; 24 %) or locked in gangue (G; 23.8 %). Due to only minor changes in the individual numbers at the exclusion of laurite it can be concluded that the amount of this PGM species within this layer is low.

PGM associated with BMS attached to gangue (SAG) is the most common mineral association within the MG2C chromitite (19.8 %). Other quite common associations are PGM locked in chromite (Gc; 16.5 %), PGM associated with BMS locked in gangue (SL; 15.5 %) and liberated PGM (16.7 %). Again laurite seems to be the major PGM species that occurs locked within chromite, since the proportion of PGM occurring locked in chromite (Gc) declines by a quarter when laurite is excluded (cf. Tab. 4.20). Coincidently, the amount of liberated PGM (L) as well as those associated with BMS attached to gangue increases (SAG).

In the MG2B chromitite most of the PGM occur locked in gangue (G; 23.4%), but there is also a relatively high proportion being associated with liberated BMS (SL; 18.6%). Laurite seems to be almost absent within this layer, since the proportions of the individual PGM associations show minor changes only (Tab. 4.20).

Within the MG2A as well as within the MG1 chromitite layer approximately 50% of the PGM are locked in chromite (Gc), which is most likely due to high amounts of laurite. Additional 15.3% or 24% occur associated with BMS locked in gangue (SG). If laurite is excluded from the calculation, the mineral association of the PGM changes considerably (cf. Fig. 4.60 and 4.61). Now the PGM mineral association is found to be dominated by an association with BMS locked in gangue (SG) for both chromitite layers (MG1: 40.4%; MG2A: 29.4%). Although laurite is excluded, there still exists a relatively high proportion of other PGM species in the MG2A chromitite that is locked in chromite (Gc; 14.7%).

Lekghoto (2010) reports a similar mineral association of the PGM for UG2 ore saying that about 50% of the PGM are not associated with the BMS. On that basis she concluded that the PGM occurring in the UG2 are not sufficiently recoverable with the common methods. Merkle and McKenzie (2002) give an overview over the beneficiation of PGE ores, and a detailed description can be found in Cole and Ferron (2002).

Table 4.20 Mineral association of the PGM including and excluding laurite (in %). Values for MG2C, MG3 and MG4A are averages from two samples. Abbreviations as described before.

	including laurite							**excluding laurite**						
	MG4C	MG4A	MG3	MG2C	MG2B	MG2A	MG1	MG4C	MG4A	MG3	MG2C	MG2B	MG2A	MG1
L	7.7	17.9	24.0	16.7	15.6	7.6	4.8	7.8	21.6	24.6	20.0	15.5	13.2	8.5
G	26.9	11.3	23.8	13.0	23.4	6.1	6.4	27.1	11.9	24.7	14.1	23.2	7.4	14.9
Gc	7.1	27.8	3.0	16.5	1.2	49.6	50.4	2.3	7.1	0.9	4.1	0	14.7	4.3
AG	7.7	10.3	12.4	7.4	11.4	2.3	4	6.2	14.3	11.9	8.9	12.3	4.4	4.3
AGc	2.6	1.5	0.9	2.6	1.2	8.4	0	1.6	1.6	0.9	2.8	0	11.8	0
SL	5.1	2.7	13.3	15.5	18.6	6.1	7.2	6.2	4.0	12.8	16.9	19.4	10.3	19.1
SG	34.6	24.3	9.8	7.8	13.8	15.3	24	39.5	33.5	10.5	8.8	14.8	29.4	40.4
SGc	0	0	0	0.6	0	0.8	0.8	0	0	0	0.8	0	1.5	2.1
SAG	8.3	4.2	12.9	19.8	15.0	3.8	2.4	9.3	5.9	13.7	23.5	14.8	7.4	6.4
total	100	100	100	100	100	100	100	100	100	100	100	100	100	100

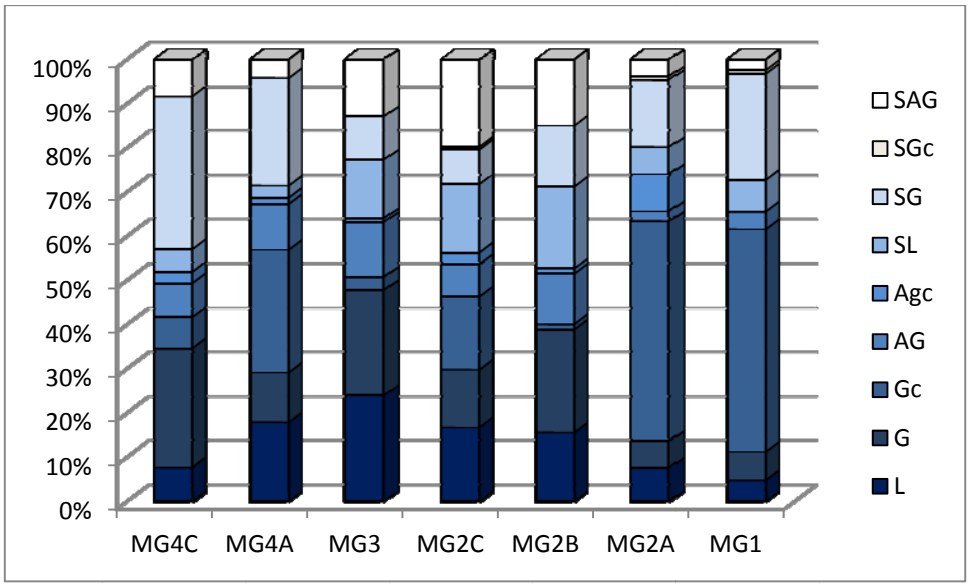

Figure 4.60 Mineral association of the PGM occurring in the silicate fraction of the chromitite layers of the MG sequence from core HEX10 (including laurite). Values for MG2C, MG3 and MG4A are averages from two samples. Data are given in table 4.20.

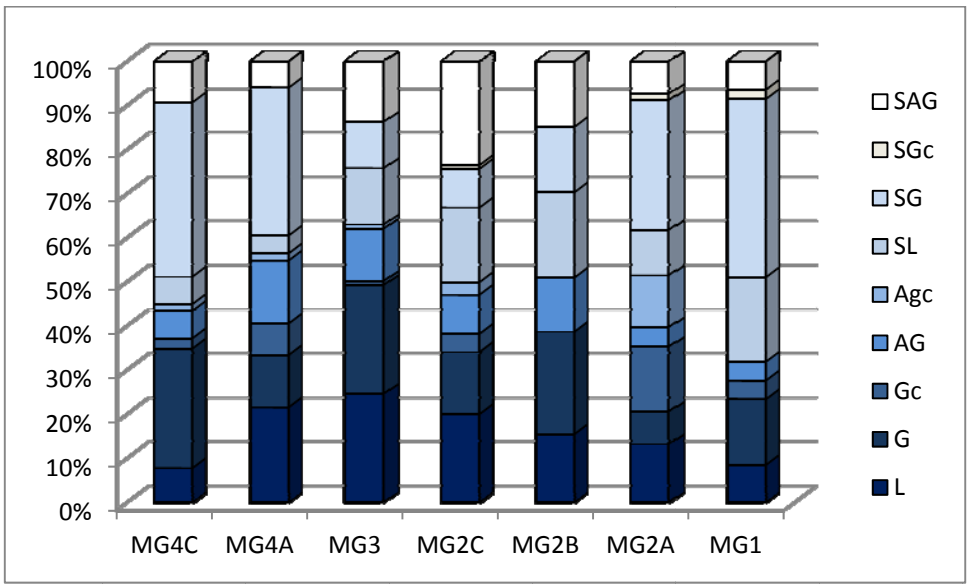

Figure 4.61 Mineral association of the PGM occurring in the silicate fraction of the chromitite layers of the MG sequence from core HEX10 (excluding laurite). Values for MG2C, MG3 and MG4A are averages from two samples. Data are given in table 4.20.

Figure 4.62 summarizes the **mineral locking** parameters of the PGM occurring within the individual chromitite layers of the MG sequence.

The majority of the PGM occurring in the MG1 and MG2A chromitites are locked in oxides, namely chromite. This is most likely due to the high amounts of laurite within these

layers, as have been mentioned before. Locking of the PGM in BMS or even liberation is rare, but a significant number of PGM occurs locked in silicate minerals (cf. table 4.21).

The highest amounts of PGM being locked in BMS are present in the MG2B, MG2C and MG3 chromitite layers, which are the layers with the highest PGE concentrations (cf. Fig. 4.81 in subsection 4.4.1.2). On the other hand, these layers show even higher proportions of PGM being locked in silicate minerals (35.9%, 35% and 35.2%, respectively). Considerable quantities of liberated PGM also occur (Tab. 4.20).

In the MG4A chromitite the major proportion of the PGM occurs locked within silicate minerals (46.2%) and there is also a considerable amount of liberated PGM (28.8%). PGM locking in chromite is 18.7%, and locking in BMS very low (5.7%).

Within the MG4C chromitite the majority of the PGM occur either locked in silicate minerals (41.3%) or in chromite (39.7%).

Although the PGE-richest chromitite layers of the MG-sequence (MG2B, MG2C, MG3) show the strongest association of the PGM with the BMS relative to the other chromitites, there are also considerable amounts of PGM that are locked in silicate minerals ± chromite (Tab. 4.21). The relative proportions of the locking mineral species suggest that the PGM in the PGE-richest chromitites of the MG-sequence tend to dominantly precipitate with the silicate minerals, despite their virtually chalcophile character and therefore their preference of aggregating with the BMS. Another feature is that in chromitite layers with a high amount of laurite the majority of the PGM tend to be locked in chromite, i.e. the MG1 and MG2A chromitite layers (cf. Tab. 4.20). It corroborates the coincidently early precipitation of HT-PGM, i.e. laurite, with chromite observed by other authors, e.g. Merkle (1992).

Table 4.21 Mineral locking parameters of the PGM in the MG chromitites. Values for MG2C, MG3 and MG4A are averages from two samples.

PGM area% locked in...	MG4C	MG4A	MG3	MG2C	MG2B	MG2A	MG1
silicate	41.3	46.2	35.2	35.0	35.9	16.4	12.5
BMS	4.4	5.7	12.5	25.5	23.0	1.7	6.6
oxides	39.7	18.7	5.0	14.1	4.0	70.6	71.5
other	1.2	0.6	1.4	2.6	8.8	1.2	5.4
liberated	13.5	28.8	45.9	22.8	28.2	10.0	4.0
total	100	100	100	100	100	100	100

To show, in which kind of silicates or BMS the PGM are locked in, these groups are splitted into individual minerals. The amounts of the PGM locked therein are presented in figures 4.63 and 4.64.

Locking in silicate minerals: PGM in the MG1 chromitite mainly occur locked in feldspar (64.5%) (Fig. 4.63 and Tab. 4.22). In the MG2A chromitite layer the major locking mineral is mica (44%), but with 23.9% and 21.7% locking in pyroxene or plagioclase is common, too. Similar to the MG1, the PGMs in the MG2B chromitite are mainly locked in feldspar (40.3%).

Within the MG2C chromitite layer 31.6% of the PGM are locked in mica, and 25.4% in feldspar. There are also considerable amounts of PGM being locked in pyroxene (17.5%).

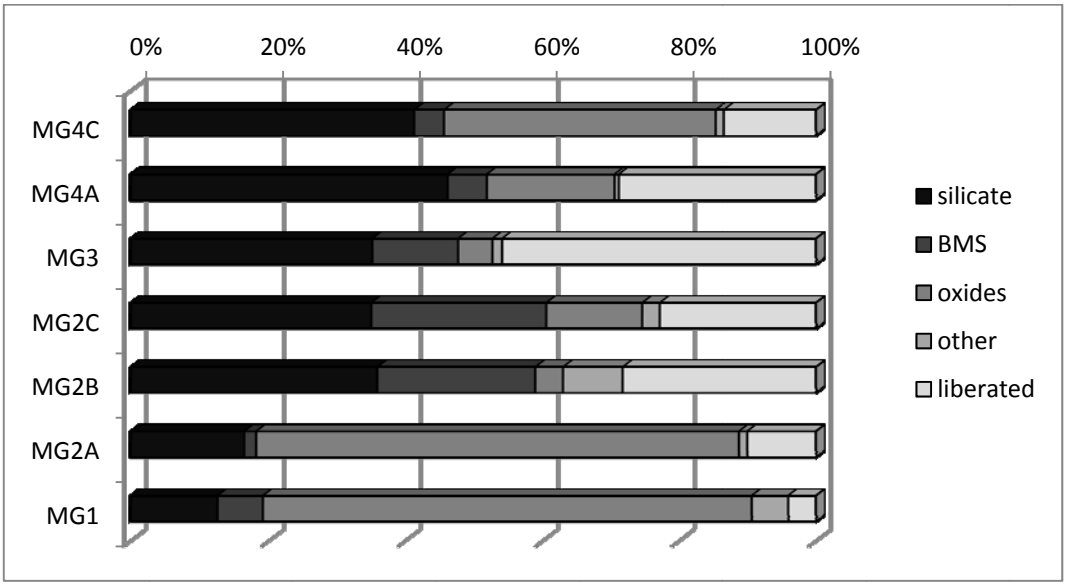

Figure 4.62 Distribution of the PGM from the analysed chromitite layers of the MG sequence occurring locked within several phases or liberated. “Other” describes mineral species deriving from alteration of silicate minerals, i.e. clay minerals. Values for MG2C, MG3 and MG4A are averages from two samples.

Different host minerals are also visible in the MG3 and MG4A chromitites. In the MG3 chromitite 66.7% of the PGM are locked in feldspar and 12.1% in talc. A major association of the PGM with feldspar is also present in the MG4A chromitite layer (43.9%), but there are also 26.3% occurring locked in mica and 22.4% being enclosed by pyroxene.

Feldspar (32.2%) is the major silicate host for the PGM in the MG4C chromitite, followed by 27.3% pyroxene as well as 26.7% amphibole.

It is striking, that in all the chromitite layers a large percentage of the PGM (27.9 to 57.1%) occur in silicate minerals deriving from alteration of the original cumulus silicate minerals, especially pyroxene. Hereto the hydrous minerals amphibole, mica, chlorite and talc belong. This association suggests that at least parts of the PGM could have been formed apart from the primary magmatic process during a late stage event involving fluids.

In fact, there are several studies on PGM associations from the Sudbury Igneous Complex that observed amphibole and biotite being enriched in chlorine (up to 0.2%; e.g. Magyarosi *et al.*, 2002). The enrichment in Cl was interpreted to derive from hydrothermal activity and the authors concluded that the formation of the PGM occurring in these rocks also took place during this event of alteration. A highly saline, Cl-rich fluid acted as complexing agent for the PGM and other metals, remobilizing primary sulphides and PGM. The temperature of the fluid during the precipitation of the PGM was determined to range between 327° and 540°C.

Another study from the Baula Complex in India (Augé *et al.*, 2002) describes a secondary PGM crystallization (Type 2) associated with hydrous silicates being caused by deuteric fluids deriving from an intrusion of gabbro into the host rock along a shear zone. The orthomagmatic, or primary PGM assemblage (Type 1) consists of isoferroplatinum, braggite, sperrylite, laurite and malanite and is not associated with BMS. Type 2 is made up of several PGM belonging to the Pd-As-Sb-Bi-Te system, which is associated with the presence of secondary BMS also deriving from hydrothermal alteration.

A similar study on primary and secondary PGM assemblages exists from the UG2 chromitite layer (Voordouw *et al.*, 2009). According to the authors, the primary PGM assemblage was altered by As-bearing fluids resulting in the formation of secondary PGE-sulphoarsenides. Primary BMS have also been affected by the corrosive action of hydrothermal fluids. The occurrence of disseminated secondary and hydrous silicate minerals led the authors to the conclusion that the fluid derived from a late-stage magmatic process of the UG2 layer itself, moving through it via porous and fracture flow mechanism.

Table 4.22 Locking of the PGM in silicate minerals. Values for MG2C, MG3 and MG4A are averages from two samples.

PGM area% locked in...	MG4C	MG4A	MG3	MG2C	MG2B	MG2A	MG1
amphibole	26.7	5.0	4.3	13.1	8.1	10.4	2.7
chlorite	0.6	0.1	0.6	5.9	5.6	0.0	1.5
feldspar	32.3	43.9	66.7	25.4	40.3	21.7	64.5
mica	8.2	26.3	3.7	31.6	25.8	44.0	19.4
pyroxene	27.3	22.4	5.4	17.5	19.9	23.9	1.4
quartz	4.8	2.3	7.1	5.6	0	0	7.8
talc	0.2	0	12.1	0.8	0.3	0	2.8
total	100	100	100	100	100	100	100

Alteration of silicate minerals and BMS within the chromitite layers has also been determined during this study (cf. subsections 4.2.1 and 4.3.7). Hence, according to the data presented here and the multiple evidence given in other studies, it cannot be entirely excluded that parts of the PGM occurring in the MG chromitite layers are the result of a secondary overprint of the primary PGM assemblage. Since MLA focuses on the LT-PGE and Ru (cf. Tab. 4.18), genetic implications can only be done for PGM containing these elements. Most likely, the PGE-tellurides, -alloys as well as –sulphoarsenides, and eventually also the Pd-arsenides of the MG chromitite layers can be ascribed to derive from a secondary mineralization process.

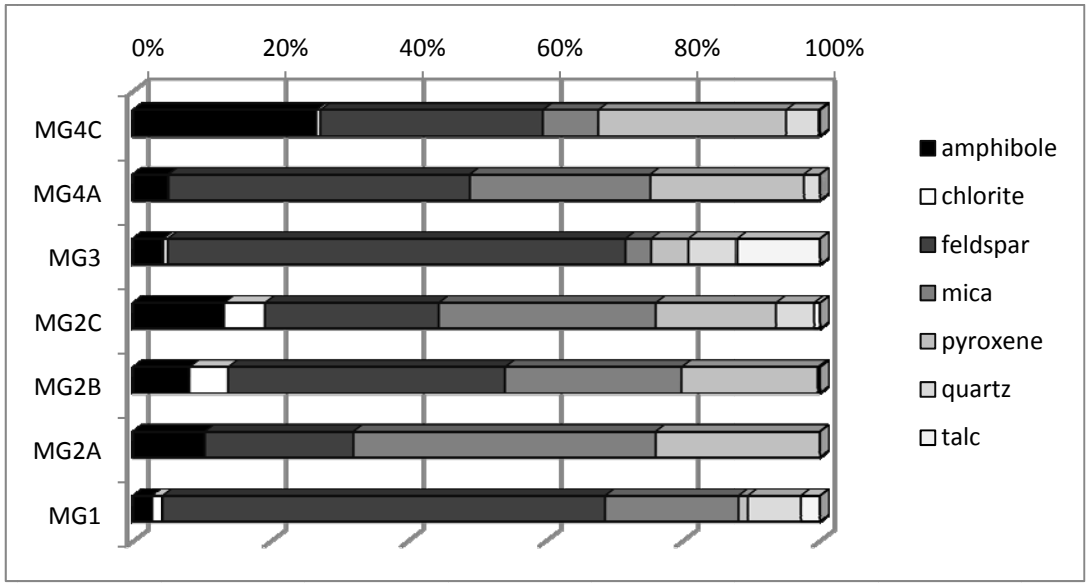

Figure 4.63 Locking of the PGM in the silicates interstitial to chromite. Values for MG2C, MG3 and MG4A are averages from two samples. Data in table 4.22.

Locking in BMS: Only four BMS species have been found to lock PGM, namely chalcopyrite, millerite, pentlandite and pyrite (Tab. 4.23). The dominant PGM-locking BMS is pentlandite (39.6%), followed by chalcopyrite (26.5%). Millerite and pyrite enclose PGM to 16.8% or 17.1%, respectively.

The association of the PGM locked in the individual BMS species changes considerable from one chromitite layer to the next (Tab. 4.23 and Fig. 4.64). Whereas in the MG2A-MG2C chromitites pentlandite is the dominating PGM-hosting BMS (71.1%, 85% or 47%, respectively), 65.1% of the PGM in the lowermost chromitite of the MG-sequence (MG1) are locked in chalcopyrite. In the MG3 chromitite layer 44.6% of the PGM are locked in pyrite. Millerite is the major BMS host for PGM in the MG4A chromitite

(43.5%), whereas in the MG4C chromitite the major locking BMS species are millerite (39.6%) and chalcopyrite (34.6%).

Table 4.23 Locking of the PGM in base metal sulphides. Values for MG2C and MG3 are averages from two samples.

PGM area% locked in...	MG4C	MG4A	MG3	MG2C	MG2B	MG2A	MG1
chalcopyrite	34.6	16.6	4.3	27.9	12.4	24.6	65.1
millerite	39.6	43.5	33.8	0.4	0	0	0
pentlandite	25.8	3.2	17.2	47.0	85.0	71.7	27.4
pyrite	0	36.7	44.6	24.6	2.7	3.6	7.4
total	100	100	100	100	100	100	100

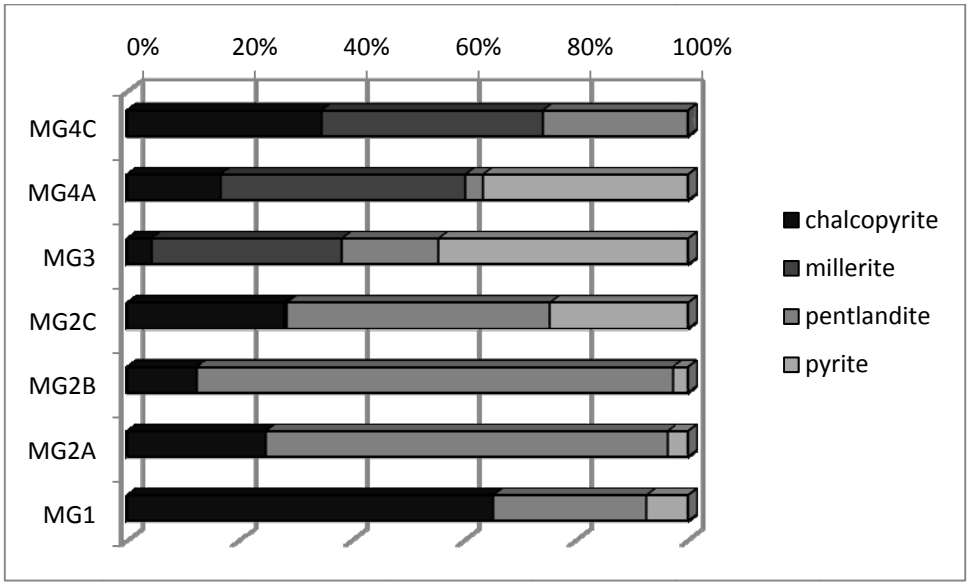

Figure 4.64 Locking of the PGM in BMS. Values for MG2C and MG3 are averages from two samples. Data in table 4.23.

From the results of the mineral association and locking parameters the **degree of liberation** of the PGM can be calculated (cf. subsection 4.3.7.2).

Table 4.24 shows the liberation characteristics of the PGM within the chromitite layers of the MG sequence. The liberation of PGM in the analysed chromitite layers differs a lot. With 45.9% on average it is highest for the MG3 chromitite layer. From the MG2B as well as the MG4A chromitite approximately one third of the PGM occurs liberated.

The majority of PGM within all the analysed samples occurs locked. Since it is important in what kind of mineral they are locked one has to consult the association data

as well. If most of them are associated with liberated BMS they should be recovered during flotation. However, if the locked PGM are associated with silicates or oxides they will be lost to the tailings during beneficiation and are therefore not recoverable with the conventional method of flotation (e.g. Cole and Ferron, 2002; Merkle and McKenzie, 2002).

As figure 4.61 and table 4.20 show, only for the chromitite layers with the highest PGE contents, i.e. the MG2B, MG2C and MG3, considerable amounts of PGM associated with liberated BMS occur. According to this, the amount of recoverable PGM increases to 59.2% for the MG3 chromitite, to 46.8% for the MG2B, and to 38.3% for the MG2C chromitite layers. If laurite is excluded, since it is commonly locked in chromite, the recovery of the MG2C chromitite changes strongly to 56.6%, and decreases very slightly only by 0.5% for the MG3 chromitite (Tab. 4.25). Similar to the MG2B and MG2C chromitites, approximately a third of the PGM being present in the MG4A chromitite layer can be liberated by milling, whereas 67.6% tend to be locked (Tab. 4.24). The recovery of the PGM from this layer is 31.5% including laurite and 32.8% excluding laurite (cf. Tab. 4.25). At present, the PGM don't seems to be economic efficiently recoverable from the other chromitite layers of the MG (MG1, MG2A, MG4C), and even for the MG4A chromitite a valuable recovery is doubtful.

Table 4.24 PGM liberation from chromitite layers of the MG sequence. Values for MG2C, MG3 and MG4A are averages from two samples.

	MG4C	MG4A	MG3	MG2C	MG2B	MG2A	MG1
liberated	13.5	28.8	45.9	22.8	28.2	10.0	4.0
middlings	0	3.6	3.7	10.9	8.3	0	4.8
locked	86.5	67.6	50.4	66.3	63.5	90.0	91.2
total	100	100	100	100	100	100	100

Table 4.25 PGM recovery from the chromitite layers of the MG sequence. Values for MG2C, MG3 and MG4A are averages from two samples. *SL*: PGM associated with liberated BMS; *L*: laurite.

	MG4C	MG4	MG3	MG2C	MG2B	MG2A	MG1
liberated	13.5	28.8	45.9	22.8	28.2	10.0	4.0
SL + L	5.1	2.7	13.3	15.5	18.6	6.1	7.2
SL - L	6.2	4.1	12.8	16.9	19.4	10.3	19.1
recovery + L	18.6	31.5	59.2	38.3	46.8	16.1	11.2
recovery - L	19.7	32.8	58.7	39.7	47.6	20.3	23.1

Although the grain size of most of the PGM is very small (Tab. C-1 in appendix C; see also Fig. 4.58), there is no cut-off in terms of grain sizes (pers. comm. Robert Schouwstra). However, very fine-sized PGM are difficult to recover during flotation (Merkle and McKenzie, 2002). Hence, at least a small portion of the grain size fraction 0-6 µm of the estimates recovery presented in table 4.24 will get lost during flotation.

4.3.8.1.1 Locking of the individual PGM species

In the following, the locking parameters of the analysed PGM species is shown, as this is important for interpretation of PGE mineralization and PGM formation processes. Liberated PGM are excluded from the considerations below (cf. Tab. 4.24).

Laurite is, after the PtRh-sulphides, the second most common PGM occurring in the chromitite layers of the MG sequence (25% of the total PGM amount). It occurs preferentially locked within chromite (66.1%), but there is also a considerably proportion enclosed in the primary silicate minerals orthopyroxene and plagioclase (Fig. 4.65). Nearly 10% are associated with BMS, and only 6% with secondary silicate minerals.

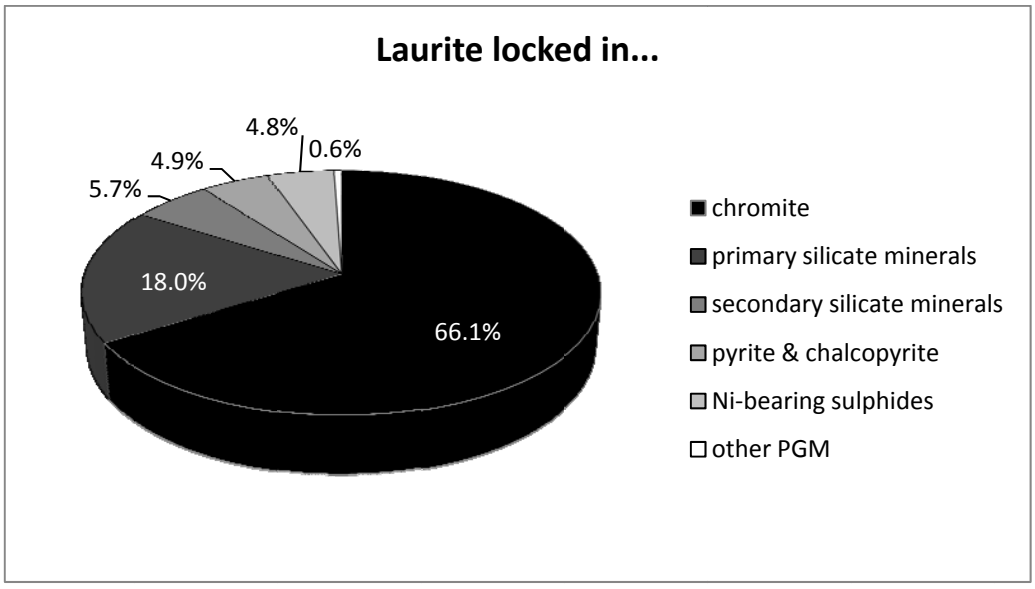

Figure 4.65 Locking parameters of the absolute laurite content of the MG chromitite layers (in area %). *Primary silicate minerals* include orthopyroxene and feldspar; *secondary silicate minerals* are amphibole, chlorite, mica, talc and quartz. The *Ni-bearing sulphides* comprise pentlandite and millerite.

The ***Pt-sulphides*** are the 4th commonest PGM species in the MG chromitite layers (13.8% of the total PGM amount), and are mainly locked in orthopyroxene and plagioclase (Fig. 4.66) and only a minor proportion occurs enclosed in chromite. Different from laurite, the Pt-sulphides show relatively high percentages of association with the BMS (22%) as well as the secondary silicate minerals (16.5%).

With a total of 24.3% the PGM species belonging to the ***PtPd-sulphides*** are among the 3rd commonest. In almost the same proportions they occur enclosed by primary silicate minerals (36.5%) and the BMS (32.8%), whereby locking in the Ni-bearing sulphides dominates over locking in pyrite or chalcopyrite (Fig. 4.67). Nearly 17% are associated with the secondary silicate minerals. As for the Pt-sulphide, the locking in chromite is low (12.1%).

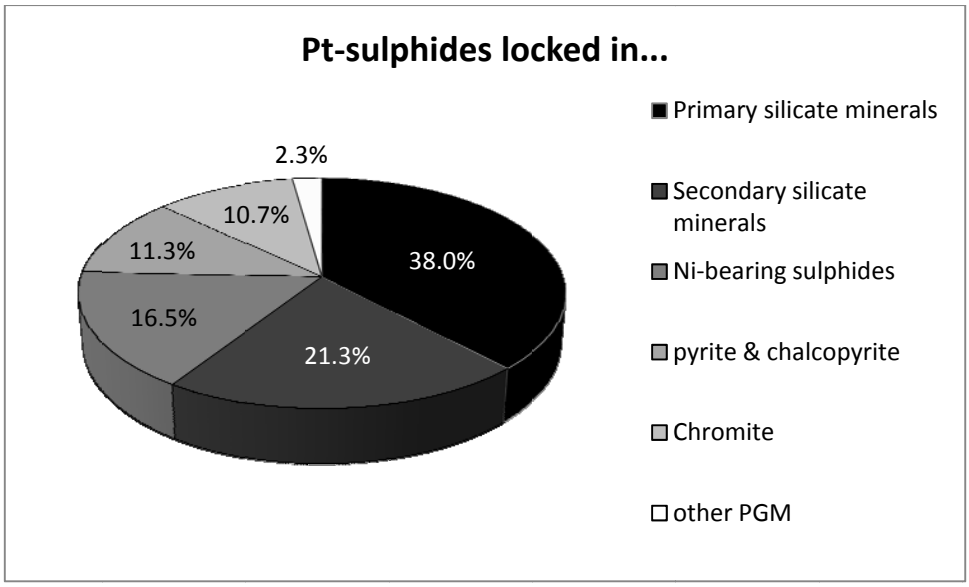

Figure 4.66 Locking parameters of the absolute Pt-sulphide content of the MG chromitite layers (in area %). Descriptions as in figure 4.65.

PtRh-sulphides are the most common PGM species within the chromitite layers of the MG sequence (26.2% of the total PGM amount), which explains the high whole-rock Rh contents described in subsection 4.4.1.2. The majority of this PGM species is associated with orthopyroxene and plagioclase (Fig. 4.68) and approximately ¼ with secondary silicate minerals. Locking in the BMS is among 20% with a dominance of being enclosed in the Ni-bearing sulphides. PtRh-sulphides that are enclosed by chromite are rare (5.7%).

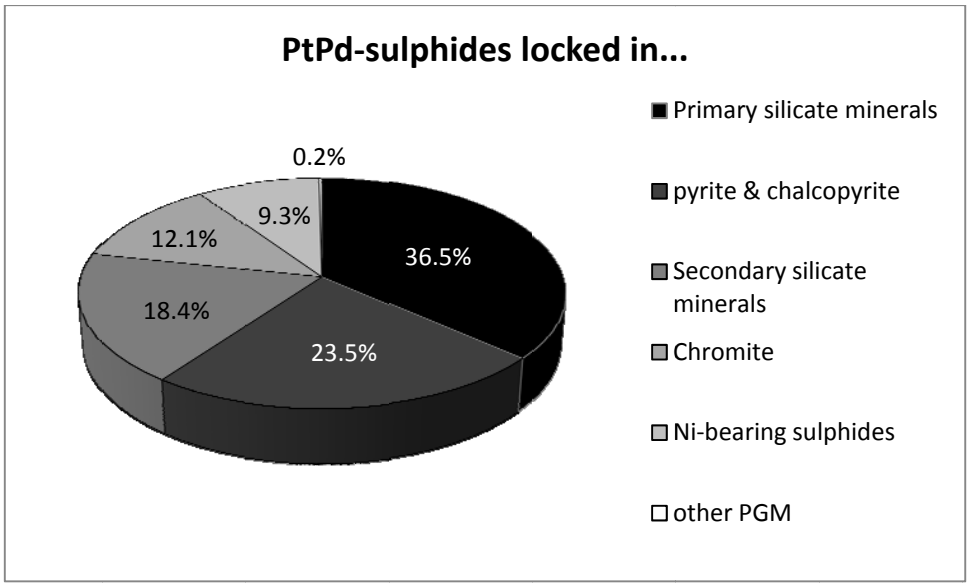

Figure 4.67 Locking parameters of the absolute PtPd-sulphide content of the MG chromitite layers (in area %). Descriptions as in figures before.

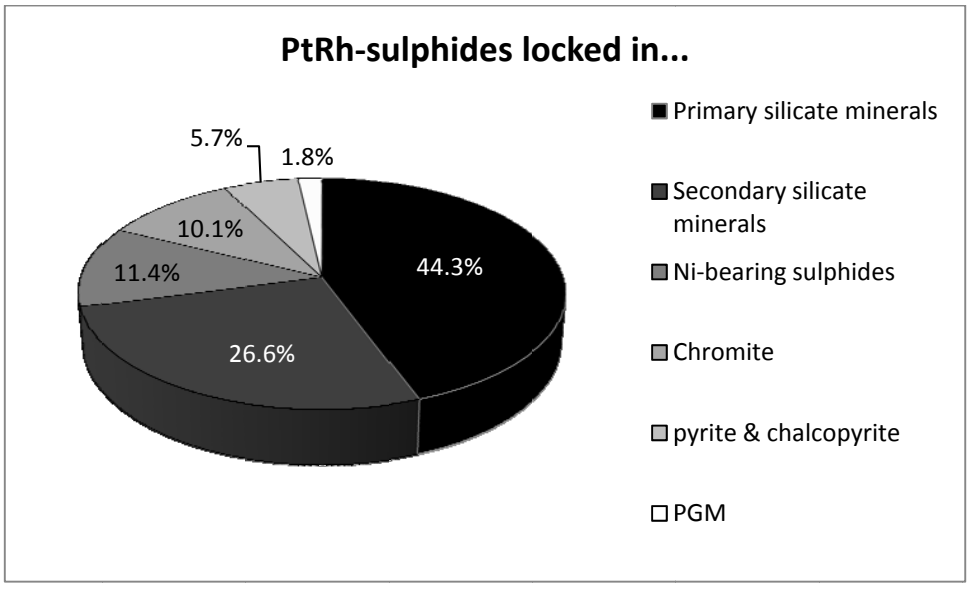

Figure 4.68 Locking parameters of the absolute PtRh-sulphide content of the MG chromitite layers (in area %). Descriptions as in figures before.

The ***PGE-sulphoarsenides*** have a proportion of 4.4% of the total PGM amount occurring within the chromitite layers of the MG sequence. Different from the PGM species presented before, the PGE-sulphoarsenides are mainly associated with secondary silicate minerals (Fig. 4.69). To the same amount they are locked within the BMS (ca. 31%), but dominantly in the Ni-bearing sulphides (20.7%). Approximately 22%

of this PGM species is enclosed by the primary silicate minerals. Locking in chromite occurs to 10% only.

The locking parameters of the **Pt- and Pd-alloys** are shown in table 4.26. The majority of both PGM species is locked in primary silicate minerals, but approximately 44% of the Pd-alloys also occur enclosed in the secondary silicate minerals. To ca. 10% the Pd-alloys are associated with chalcopyrite, whereas this association for the Pt-alloys is 1% only. Locking in chromite is low for both PGM-species. Their total amount among the PGM of the MG chromitite layers is 1.1% for the Pt-alloys and 1.5% for the Pd-alloys.

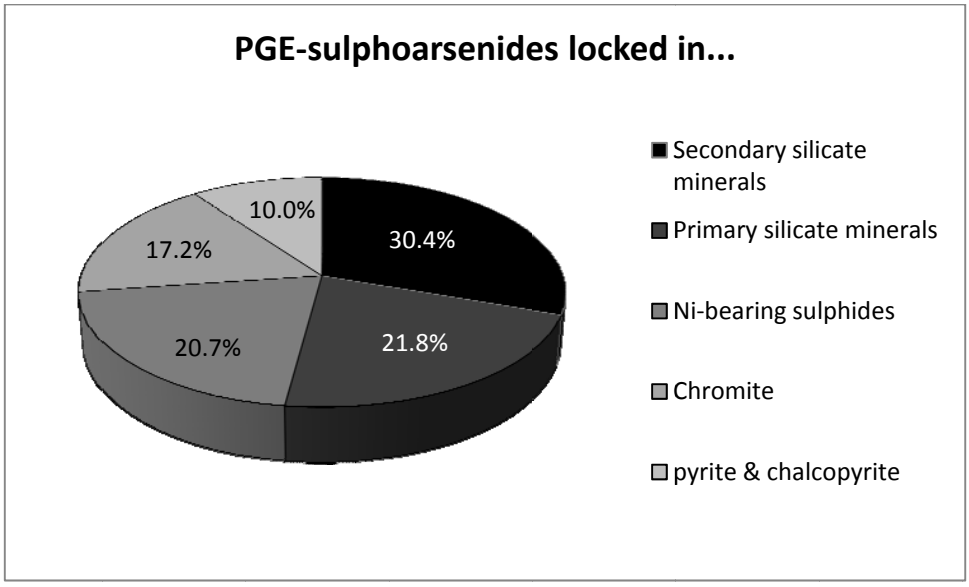

Figure 4.69 Locking parameters of the absolute PGE-sulphoarsenide content of the MG chromitite layers (in area %). Descriptions as in figures before.

Table 4.26 Locking parameters of the absolute Pt-alloy and Pd-alloy contents of the MG chromitite layers. Values in area%.

	Pt-alloys	**Pd-alloys**
primary silicate minerals	96.0	44.9
secondary silicate minerals	-	43.5
chromite	3.1	1.5
chalcopyrite	0.9	10.1

Pt-arsenides dominantly occur locked in plagioclase, whereas only 6.6% of the ***Pd-arsenides*** are associated with primary silicate minerals (Tab. 4.27). The latter are mainly enclosed in chromite, and 29.2% are locked in secondary silicate minerals. Pt-arsenides show lower association with secondary silicate minerals (i.e. mica) as well as chromite.

Distribution of these two PGM species in the BMS is also quite different. Pt-arsenides occur locked in pentlandite only (16.1%), whereas the Pd-arsenides are rather enclosed by chalcopyrite (17.6%) than pentlandite (6.6%).
Together both PGM species make 1% only of the total PGM amount occurring within the chromitite layers of the MG sequence.

Table 4.27 Locking parameters of the absolute Pt-arsenide and Pd-arsenide contents of the MG chromitite layers. Values in area%.

	Pt-arsenides	**Pd-arsenides**
primary silicate minerals	50	6.6
secondary silicate minerals	16.7	29.2
chromite	17.2	40
pentlandite	16.1	6.6
chalcopyrite	-	17.6

Compared to the ***Pt-tellurides***, the ***Pd-tellurides*** occur twice as often in the chromitite layers of the MG sequence (0.7% or 1.4% of the total PGM amount, respectively), but their locking parameters differ considerably (Tab. 4.28).
The Pt-tellurides are to 61.6% locked in the primary silicate minerals. A proportion of 21.4% is associated with pentlandite. 12.5% are enclosed by chromite and only 4.5% are locked in the secondary silicate minerals, i.e. quartz.

The major proportion of the Pd-tellurides is locked in pyrite or chalcopyrite (52.3%), but only 4.4% are locked in millerite. Approximately 22% are associated with the primary silicate minerals. The amount of Pd-tellurides enclosed by chromite or the secondary silicate minerals is low (5% or 2.2%, respectively). However, the Pd-tellurides are the PGM species with the highest proportion that occurs associated with other PGM, mainly PtRh-sulphides.

The total PGM amount of ferroplatinum species in the chromitite layers of the MG sequence is very low (0.6%). Their distribution is as follows: locked in the primary silicate minerals (45.5%), enclosed by chromite (29.5%) and mica (25%). An association with the BMS has not been observed.

Table 4.28 Locking parameters of the absolute Pt-telluride and Pd-telluride contents of the MG chromitite layers. Values in area%.

	Pt-tellurides	Pd-tellurides
primary silicate minerals	61.6	21.8
secondary silicate minerals	4.5	2.2
chromite	12.5	5.0
Ni-bearing sulphides	21.4	4.4
pyrite & chalcopyrite	-	52.3
other PGM	-	14.2

4.3.9 Rutile

Rutile enclosed by chromite is most common within the chromitite layers. As could be shown in subsection 4.2.1 it either occurs as tiny acicular phases or prismatic inclusion (cf. Fig. 4.12 subsection 4.2.1). SEM-EDX analyses resulted in the presence of minor amount of MgO and Cr_2O_3 (< 1%) in prismatic rutile inclusions. It can be ascribed to subsolidus equilibration with chromite.

A positive correlation of FeO and TiO_2 contents in chromite (figure 4.70) is the only one existing for TiO_2 and the major element oxide contents of chromite. Probably, this is an indication that the TiO_2 content in chromite inclines with increasing oxidation state. In fact, the TiO_2 content of chromite from the chromitite layers generally increases upwards the stratigraphic column of the MG sequence (cf. figure 4.24 in subsection 4.3.1), for which a general evolution to less primitive mineral and whole-rock composition have been shown (subsections 4.3.1 and 4.4.1).

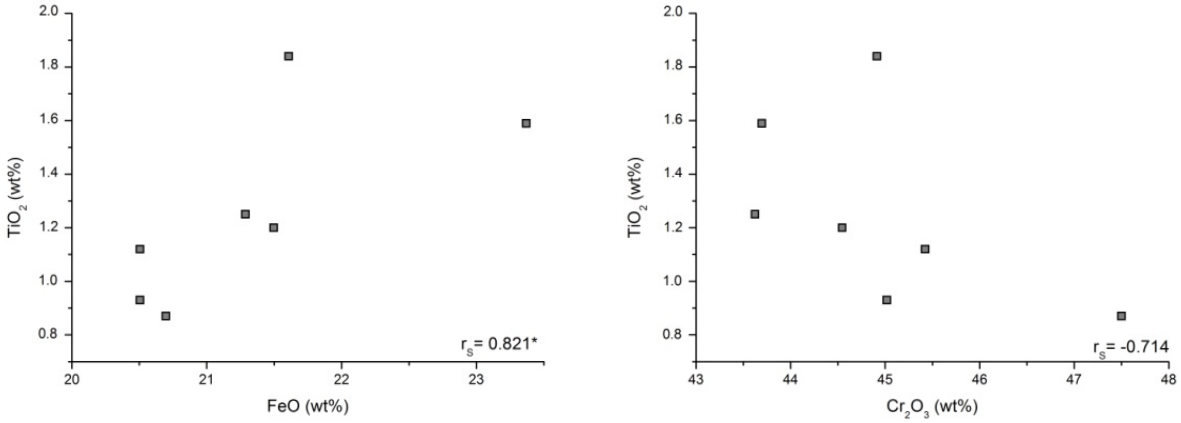

Figure 4.70 Bivariate plots of TiO_2 vs. Fe_2O_3 (left) or Cr_2O_3 (right) obtained from chromite chemistry. TiO_2 values from LA-ICP-MS; Cr_2O_3 and Fe_2O_3 are averages from SEM-EDX analyses of the corresponding chromitite layers. r_S: Spearman rank correlation coefficient.

Although a slight negative correlation between Cr_2O_3 and TiO_2 is visible from figure 4.66, it is not a significant one. However, it demonstrates that Ti^{4+} does not fit into the lattice of chromite, at least not at the present state. The phase diagram Fe_2O_3-TiO_2 shows that at higher temperatures (≥1300°C) pseudobrookite (Fe_2TiO_5) exists as an intermediate phase between hematite and rutile (Lindsley, 1976). Below 585°C pure Fe_2TiO_5 is unstable and disintegrates into Fe_2O_3 and TiO_2. Taking Fe_2O_3 synonymous for the Fe-component of chromite it can be concluded that during cooling exsolution of TiO_2 from the chromite lattice occurs and thus explaining the tiny acicular rutile inclusions that separated orientated to the chromite structure.

Cameron (1979) suggested a combined oxidation-exsolution as the separation process of TiO_2 from the chromite structure forming the acicular inclusions. According to the author the combination is necessary, since charge imbalance due to an excess of cations in the spinel would occur.

The prismatic inclusions cannot simply be explained by exsolution. Their size and especially their shape indicate unimpeded growth, i.e. prior to or contemporaneously to chromite, before being trapped in it. Support is given by the phase diagram Fe_2O_3-TiO_2 showing a field of pseudobrookite separating the hematite field from the field of rutile at temperatures >1000°C. As with the acicular inclusions, the hematite can be taken as synonymous for the Fe-component of chromite. The phase diagram thus also shows that rutile crystallizes contemporaneously to chromite and can be trapped during chromite growth. Additionally, the fact that the majority of chromite grains lack such rutile inclusions and that these inclusions occur in chromite grains of various sizes give textural evidence for rutile formation as distinct crystals apart from chromite.

Hence, these two very different rutile species can be interpreted in terms of two generations of rutile due to their time of formation. The prismatic inclusions represent a first generation and the acicular inclusions the 2nd generation, which formed during cooling of the chromitite layers.

4.4 Whole-rock geochemistry

4.4.1 The chromitite layers

The Cr_2O_3 content within the layers decreases constantly from the bottom to the top of the MG from ca. 46 wt% to 35.4 wt% on average. At the same time, the SiO_2, Al_2O_3 and

CaO contents are increasing and the FeO_{tot} and MnO contents decrease (Tab. 4.29). No variation in the geochemistry is obvious at the boundary LCZ/UCZ (at the top of the MG2C chromitite) (Fig. 4.71).

Table 4.29 Whole-rock geochemistry of the MG chromitite layers obtained from XRF analyses (major element oxides) and ICP-MS analyses (trace elements). *Altogether only 19 of 51 samples have been analysed for their sulphur content. Major element oxides in wt%.

	MG0	MG1	MG2A	MG2B	MG2C	MG3	MG4A	MG4B	MG4C
n	2	9	3	6	4	7	15	2	3
SiO_2	5.6	6.3	4.7	5.4	6.9	8.1	12.2	14.0	14.1
TiO_2	0.6	0.6	0.7	0.7	0.7	0.7	0.6	0.7	0.9
Al_2O_3	13.5	13.9	14.8	14.1	14.7	15.8	17.6	15.0	14.6
Cr_2O_3	45.0	44.9	44.6	43.1	41.8	40.0	36.3	35.3	35.4
Fe_2O_3	2.6	2.5	2.7	2.7	2.6	2.6	2.3	2.5	2.6
FeO	21.2	20.5	22.0	21.5	21.1	21.1	18.8	20.2	20.8
MnO	0.3	0.3	0.3	0.3	0.3	0.3	0.2	0.3	0.3
MgO	8.8	8.4	7.9	8.0	7.8	7.6	8.1	7.7	7.9
CaO	1.6	1.7	1.8	1.7	2.0	2.4	3.1	3.9	3.8
Na_2O	0	0	0	0	0	0.1	0.1	0.2	0.1
NiO	0.1	0.1	0.1	0.1	0.1	0.1	0.1	0.1	0.1
total	99.2	99.2	99.6	97.6	98.0	98.8	99.5	99.9	100.5
Trace elements (ppm)									
V	1720	1814	2409	2011	2073	1932	1888	1616	1667
Co	239	234	252	238	240	241	222	213	218
Ni	768	828	867	869	865	885	851	781	827
Cu	125	99	2248	176	256	229	377	100	2376
Zn	549	502	537	478	448	524	696	465	465
S*	38	48	39	42	48	87	75	28	87
Element ratios									
Mg#	0.27	0.27	0.25	0.25	0.25	0.24	0.28	0.26	0.26
Cr/(Cr+Fe)	0.63	0.63	0.62	0.61	0.61	0.60	0.61	0.58	0.57
Cr/(Cr+Al)	0.81	0.81	0.80	0.80	0.79	0.77	0.73	0.75	0.76

In general, the Mg# decreases from bottom (MG0) to top of the MG3 unit (from 0.27 to 0.24 on average), in a pattern typical of fractional crystallisation (Fig. 4.71). The bottom of MG4A shows a change to a very much more primitive composition (Mg# = 0.28), after which the Mg# decreases again to the top of the succession studied. This increase of the Mg# at the bottom of the chromitite layer was interpreted to result from an injection of primitive magma causing enrichment in MgO of the melt (cf. appendix D).

Besides decreasing Mg# in the MG1, MG2C and MG4A chromitite layers, which is typical for fractional crystallization, the whole-rock Mg# in the remaining chromitites, i.e. MG0, MG2A, MG2B, MG3, MG4B+C, shows a reversed trend with increasing Mg# from the bottom to the top of the layers. It is interpreted to represent increasing amounts of co-precipitating pyroxene.

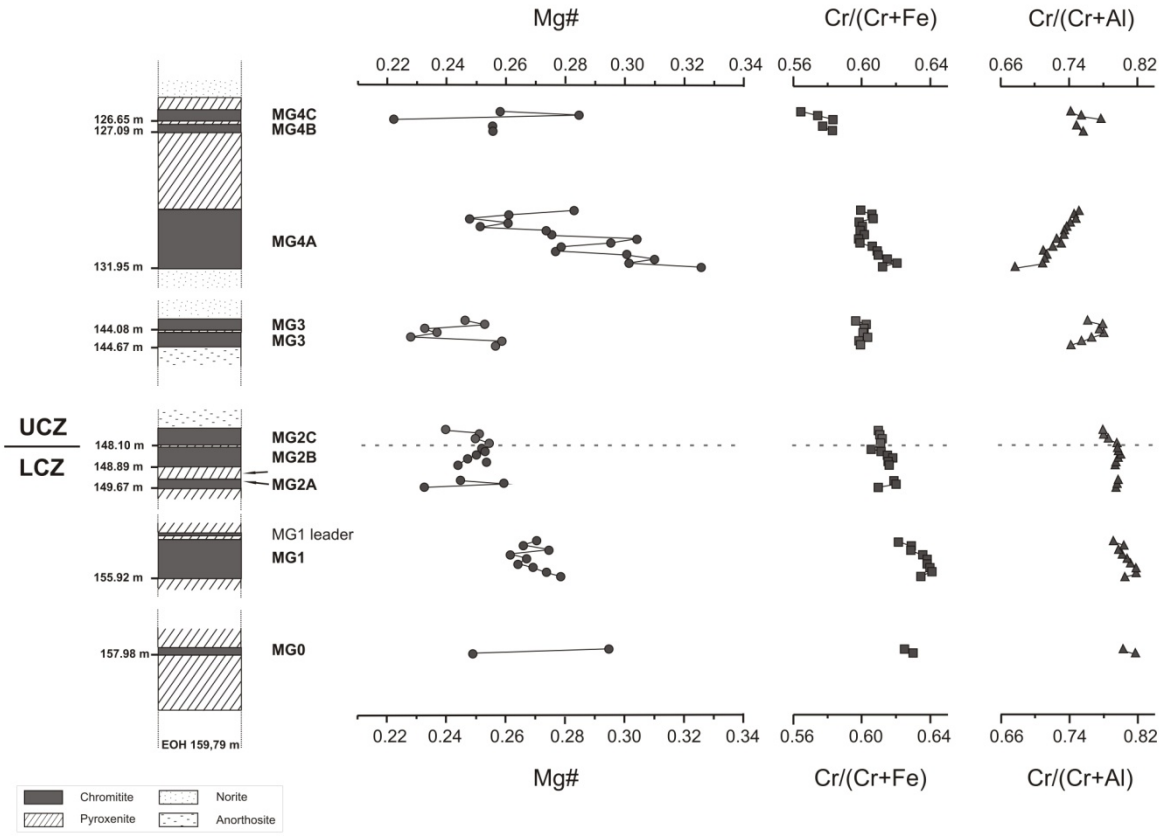

Figure 4.71 Changing whole-rock geochemistry of the MG chromitite layers illustrated by the Mg# and the Cr/(Cr+Fe) and Cr/(Cr+Al) metal ratios. Mg#: MgO/(MgO+FeO). Data are given in table 4.29.

The Cr/(Cr+Fe) ratio decreases in general from bottom to top of the core, but also within each chromitite layer (Fig. 4.71). As in the Mg#, there is an increase in Cr/(Cr+Fe) at the bottom of the MG4A, but of a much slighter magnitude. The general change in the ratio from bottom to top of each chromitite layer may be explained by the normal evolution of the melt, as the melt gets relatively depleted in Cr^{3+} over Fe^{3+}, the latter which is slightly less compatible in the chromite lattice and those of the co-precipitating silicate phases. It thus represents not only the enrichment of Fe relative to Cr in chromite (cf. subsection 4.4.1), but also increasing amounts of co-precipitating pyroxene, which again becomes enriched in Fe relative to Mg as one goes from bottom to top of a chromitite layer.

From bottom to top of the MG sequence, the Cr/(Cr+Al) ratio decreases from the MG0 to the MG4A chromitite (Fig. 4.71) indicating increasing plagioclase precipitation upwards the stratigraphic column. At the bottom of the MG4A the lowest value of the Cr/(Cr+Al) ratio is associated with the highest Mg#. In the UCZ, the Cr/(Cr+Al) ratio and the Mg# behave mirror-inverted; as one increases the other parameter decreases at the same time. On the other hand, in the LCZ they generally show the same behaviour. This feature can be explained by precipitation of cumulus plagioclase, which only starts at the bottom of the UCZ.

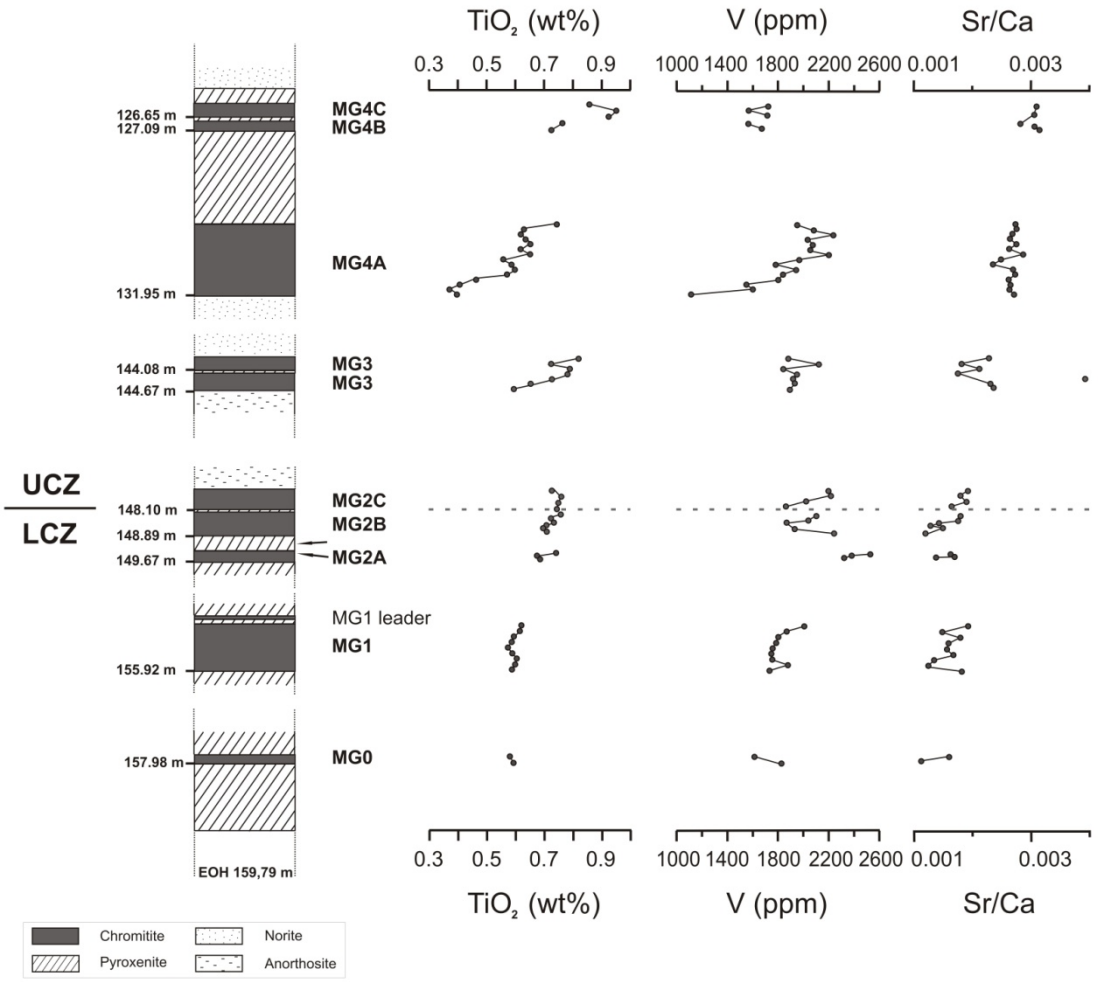

Figure 4.72 Concentrations of selected trace elements and the Sr/Ca ratio (both in ppm) plotted vs. the stratigraphic column. Data are given in table 4.29.

As with the Mg#, the Cr/(Cr+Al) ratio also shows several reversals, i.e. an increasing trend, which is developed in the MG2A, MG2B, MG3 and MG4A chromitite layers. Except for the MG4A chromitite, chromite becomes enriched in Cr relative to Al and ceasing plagioclase crystallization with contemporaneously increasing precipitation of pyroxene is

concluded. Thereby, pyroxene seems to become enriched in Mg relative to Fe towards the top of the chromitite layers, which is depicted in the increasing Mg# with simultaneously decreasing Cr/(Cr+Fe) ratio. In the MG4A fractional crystallisation of pyroxene is illustrated by decreasing Mg# and increasing Cr/(Cr+Fe) ratio. With regard to the increasing Cr/(Cr+Al) ratio, precipitation of plagioclase seems to cease towards the top of the layer.

The TiO_2 concentration increases from the MG0 to the MG4C and also increase within each chromitite layer (Fig. 4.72), which can be explained by the relative incompatibility of this element in the chromite lattice. V increases in the LCZ only, whereas in the UCZ it rather decreases. Although relative incompatible into chromite, too, it is rather incorporated into spinel then silicates, and thus its decrease in the UCZ mirrors decreasing amounts of chromite within the chromitite layers (cf. Fig. 4.7 in subsection 4.2.1). The re-setting of the V and TiO_2 contents at the bottom of MG4A to values below (i.e. more primitive) than that of the MG0 chromitite matches with the high Mg# and Cr/(Cr+Fe) ratio and the low Cr/(Cr+Al) ratio at this point.

The advancing melt evolution is well illustrated by the trend of the Sr/Ca ratio that shows a strong enrichment through the stratigraphy (Fig. 4.72), representing the appearance of plagioclase and its changing composition to less anorthitic varieties (cf. appendix D).

As the Cu content of the chromite cumulates in the UCZ is controlled by the presence of sulphides, Cu can be used as an indicator of the sulphide abundance (Scoon and Teigler, 1994). They calculated Cu background values for the chromitite layers below the UG2 at Union and Brits in the western Bushveld Complex, including the LG, the MG and the UG1. The background ranges between 12 and 20 ppm on average. The Cu values observed for the MG chromitite layers in this study range between 34.4 and 6765 ppm, but most of the values fall between 50 and 200 ppm (Fig. 4.73). Only four samples show extremely high Cu values with more than 1500 ppm. Obviously, the background values for Cu are generally higher in the eastern than in the western Bushveld Complex as determined by Scoon and Teigler (1994), and probably this is a particular feature of the eastern limb. Whether compared to the background values for the western or the eastern Bushveld Complex, all the MG chromitite layers are enriched in Cu, although the appearance of visible BMS is extremely rare (<1 vol %).

Whole-rock analyses for S yielded values between 24 to 108 ppm within the chromitite layers of the MG sequence. Except for the MG4A chromitite layer the whole-rock Cu/S ratio exceeds the Cu/S for chalcopyrite (2:1) (Tab. 4.30), which implies the presence of more Cu than can be precipitated in chalcopyrite. Exemplarily for the incompatible elements La is plotted vs. Cu concentrations (Fig.4.74A) to demonstrate that

the high Cu values in the MG chromitites can also not be ascribed to being enriched in trapped melt. Punctual Cu peaks in chromite grains gathered with the LA-ICP-MS are rare and scarcely can be responsible for the Cu enrichment in the MG chromitite layers (cf. subsection 4.3.1). Thus, sulphide cannot be the (only) Cu-concentrating phase in the MG chromitites and probably another Cu-concentrating phase must be found.

Table 4.30 Cu/S ratio of selected chromitite samples.

layer	sample	Cu/S
MG4C	HEX10/02	2.2
MG4B	HEX10/04	2.6
MG4A	HEX10/08	1.5
	HEX10/14	1.3
	HEX10/15	1.4
	HEX10/19	1.5
MG3	HEX10/21	7.1
	HEX10/22	3.4
	HEX10/27	1.2
MG2C	HEX10/30	2.2
	HEX10/31	5.5
MG2B	HEX10/32	0.6
	HEX10/36	16.4
MG2A	HEX10/38	4.2
	HEX10/39	146.1
MG1	HEX10/41	1.5
	HEX10/43	3.0
	HEX10/49	2.4
MG0	HEX10/51	4.4

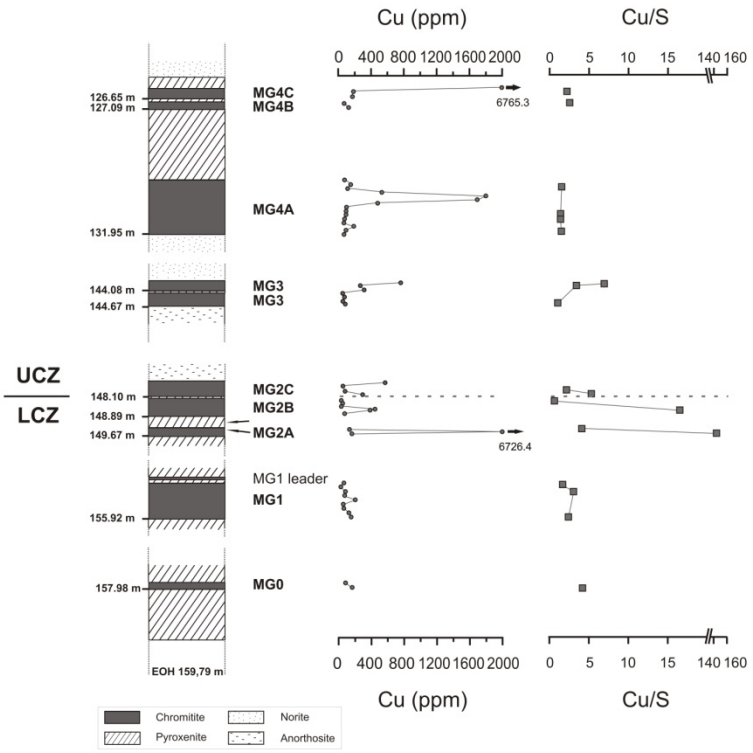

Figure 4.73 Cu content in the MG chromitite layers and Cu/S ratio plotted vs. stratigraphic column of the MG sequence. Arrows illustrate Cu values exceeding 6000 ppm. Data are given in table 4.29.

Although there is no statistically significant correlation of Cu with S (Fig. 4.74B) the weak positive relationship points to Cu consumption during formation of chalcopyrite, as have been mentioned before. However, Cu shows moderately positive correlations with Sb (r_S= 0.594), As (r_S= 0.455) and Zn (r_S= 0.468) on a statistically significant level (Fig. 4.74C and D). It indicates that at least part of the Cu, which is not incorporated into chromite or used to form chalcopyrite, was used to form minerals containing these elements. Especially into question come tetrahedrite ($(Cu,Fe,Ag,Zn)_{12}Sb_4S_{13}$) and tennantite ($(Cu,Ag, Fe,Zn)_{12}As_4S_{13}$), which grow during hydrothermal processes. Since As,

Sb and S moderately correlate with La, they commonly seem to occur in the interstitials to chromite (Fig. 4.74E).

Assuming that tetrahedrite and tennantite are present in the chromitite layers, they have been formed by aqueous fluid, which probably transported Cu from an external source and thus partly redistributed the primary metal content. A similar influence of a fluid has been found to have affected the primary BMS and silicate mineral assemblage of the chromitite layers (cf. subsections 4.2.1 and 4.3.4). Other than the tetrahedrite and tennantite forming fluid that enriched the chromitite layers in Cu, the fluid(s) being responsible for re-distribution of the BMS rather cause Cu-depletion. Hence, two different events of re-distribution of base metals by aqueous fluids in the MG chromitite layers may have occurred.

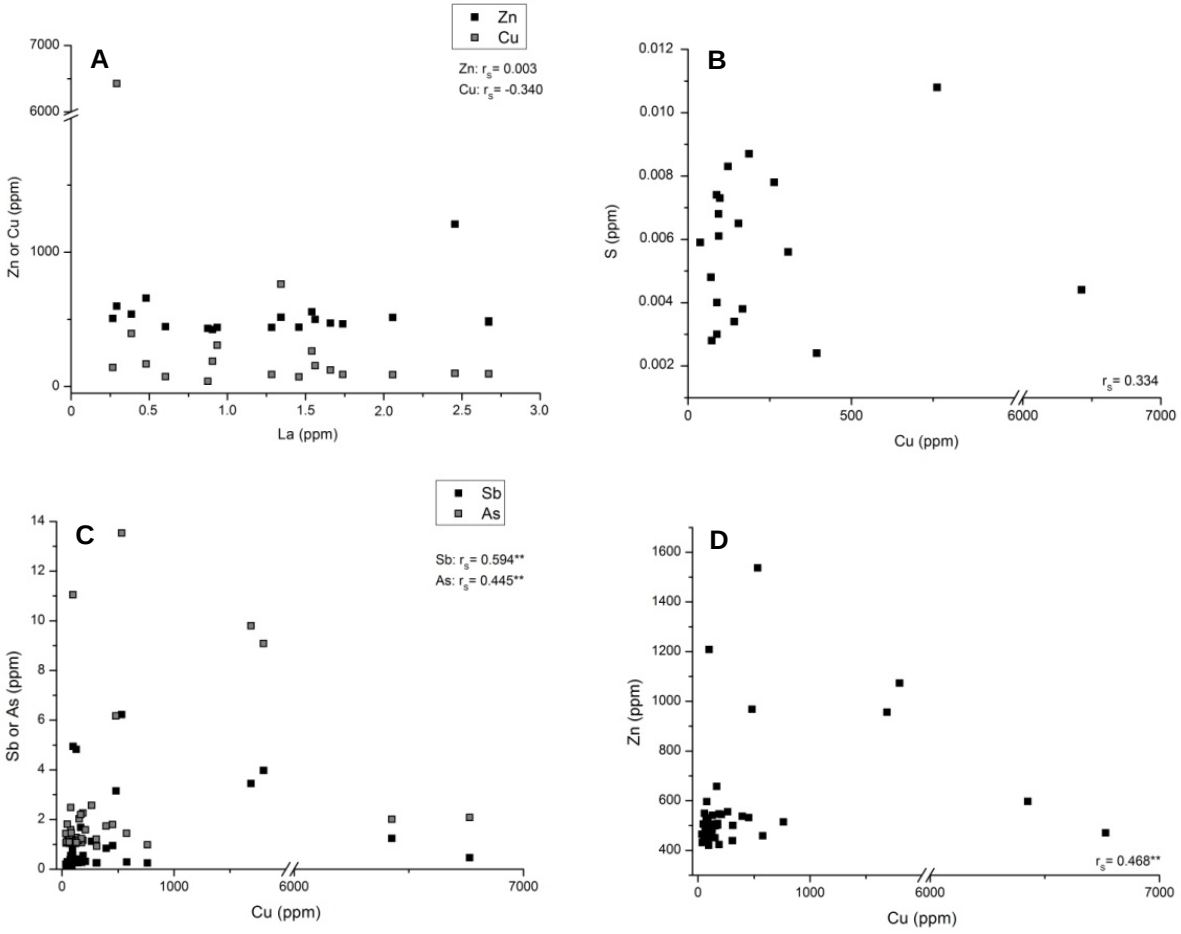

Figure 4.74 (A) Cu and Zn concentration of chromitite samples plotted vs. La content. **(B)** Cu plottet vs. S. **(C)** and **(D)** Moderate correlation of Sb, As or Zn with Cu.

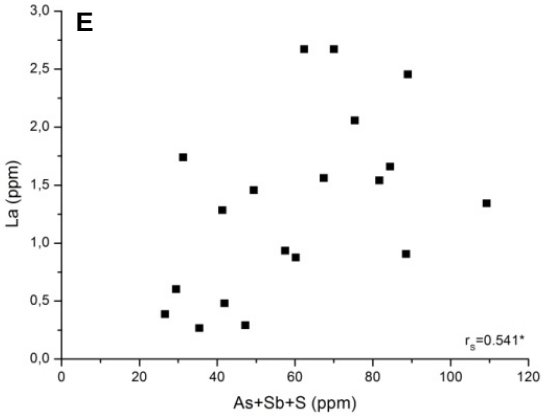

Figure 4.74 *(cont.)* **(E)** Moderate positive correlation of the chalcogenide elements As, Sb and S with La. Note that only samples have been plotted for which the S content has been determined (cf. Tab. A-2 in appendix A).

The C1 normalized REE patterns of the chromitite layers shown in figure 4.75 demonstrate the typical fractionation of light rare earth elements (LREE) versus the heavy ones (HREE) that can be expected from a mantle derived mafic melt (Tab. 4.31). With a value of 0.731, obtained with the $(La_N/Yb_N)/Ce_N$ ratio, the REE are only slightly fractionated. There is only little enrichment of the LREE (Ce/Sm_N = 1.54) and this differs greatly from REE fractionation in the silicate rocks of the CZ (Ce/Sm_N = 3.65), as determined by Maier and Barnes (1998). The HREE are strongly fractionated (Tb/Yb_N = 0.03), exactly reverse to data from silicate rocks (Maier and Barnes, 1998), which show almost no fractionation of the HREE. In general, the REE behave incompatible to chromite, which is the major cumulus phase within massive chromitite, but behave also as incompatible elements towards intercumulus phases like pyroxene and plagioclase.

Table 4.31 REE data from ICP-MS analyses (in ppm). Values are averages for each layer.

	MG0	MG1	MG2A	MG2B	MG2C	MG3	MG4A	MG4B	MG4C
n	2	9	3	7	4	7	15	2	3
La	0.615	1.202	0.235	0.538	1.326	2.166	2.650	0.577	0.720
Ce	1.022	1.998	0.414	0.934	1.993	3.330	4.634	0.930	1.092
Pr	0.117	0.231	0.042	0.108	0.231	0.391	0.543	0.106	0.126
Nd	0.380	0.812	0.155	0.368	0.831	1.390	1.954	0.370	0.437
Sm	0.108	0.183	0.047	0.087	0.184	0.291	0.403	0.084	0.103
Eu	0.058	0.078	0.042	0.055	0.085	0.118	0.183	0.120	0.117
Gd	0.110	0.170	0.038	0.081	0.180	0.294	0.398	0.078	0.089
Tb	0.019	0.028	0.004	0.013	0.026	0.041	0.059	0.012	0.014
Dy	0.123	0.177	0.033	0.080	0.160	0.259	0.361	0.076	0.088
Ho	0.030	0.040	0.008	0.018	0.034	0.055	0.073	0.019	0.021
Er	0.082	0.114	0.023	0.053	0.104	0.152	0.210	0.056	0.066
Tm	0.014	0.018	0.004	0.009	0.016	0.022	0.030	0.012	0.014
Yb	0.100	0.127	0.027	0.061	0.111	0.161	0.229	0.072	0.074
Lu	0.015	0.021	0.005	0.011	0.018	0.026	0.033	0.014	0.014
Y	0.871	1.265	0.292	0.588	1.073	1.647	2.352	0.625	0.705

An exception is Eu, which is compatible with plagioclase (Stosch, 2008). A positive Eu-anomaly of various amplitudes within all the layers is observed, and is due to the appearance of plagioclase that is interstitial only in the LCZ. The MG4B and MG4C chromitite layers have the most positive anomalies, saying that plagioclase is the major intercumulus phase within these chromitite layers (Eu/Eu*= 4.596 or 3.805, respectively). MG1 and MG3 chromitites show only slight positive Eu anomalies (Eu/Eu*= 1.371 or 1.248, respectively).

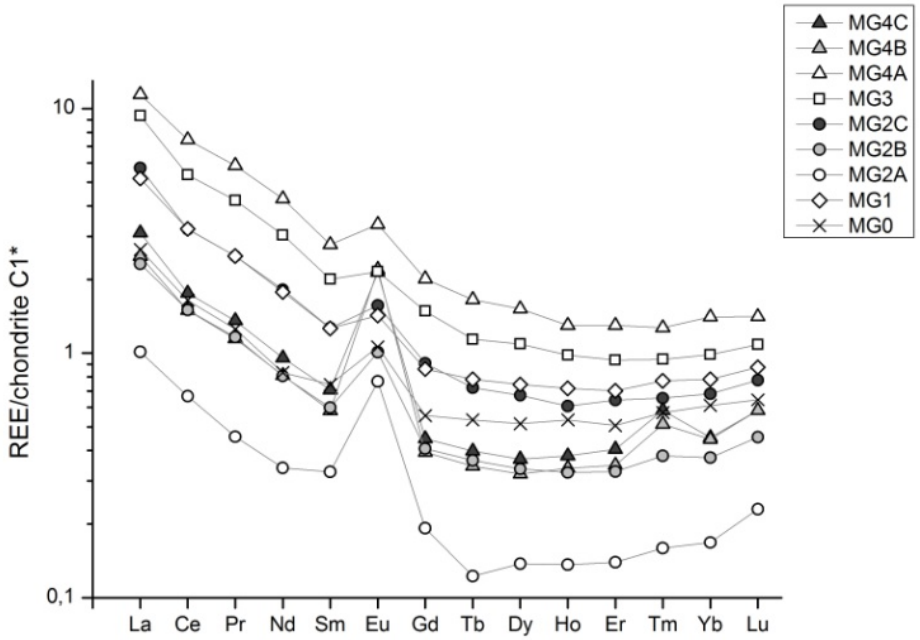

Figure 4.75 Whole-rock REE patterns of the MG chromitite layers. *C1 normalizing values from Lodders (2003). Data are given in table 4.31.

With regard to C1 values for the REE, the MG3 and MG4A seem to be the chromitite layers with the most evolved REE content, as would be expected from a fractional crystallization trend. Compared to the other chromitite layers, the MG2A is relatively depleted in REE, indicating influence of higher amounts of primitive magma.

The multi-element C1 normalized “spider” diagram shows a few distinctive positive and negative anomalies (Fig. 4.76, Tab. 4.32). In all the chromitite layers these are the positive La and Sr peaks, the latter which is strongest in the MG0, MG1, MG4A and MG3 chromitites, reflecting the occurrence of elevated amounts of plagioclase within these layers.

Ti and Ta concentrations are controlled by the presence of accessory minerals like rutile. Due to compatibility in the chromite lattice, the Ti^{4+} (ionic radius: 0.605 Å) is less compatible than the Cr^{3+} (ionic radius Cr^{3+}: 0.52 Å). During the formation of the chromitite layers it gets trapped in chromite, and Ti^{4+} starts to crystallize as rutile, forming an

inclusion in chromite explaining the strong positive Ti anomalies.

Distinctive positive Nb anomalies exist for the MG0, MG1, MG3 and MG4A chromitites. Similar to Ti, Nb concentrations are controlled by the presence of rutile. Due to the chemical character of Nb as a high field strength (HFS) element, it is incompatible into mantle minerals, i.e. perovskite ($CaTiO_3$), and thus enters the melt easily. High anomalies thus point to a high degree of partial melting in the upper mantle or the origin of the melt in the lower mantle, i.e. mantle plume. On the other hand, this feature could also be due to a less depleted Proterozoic mantle relative to the recent one.

The strong negative P peaks are due to the absence of apatite, suggesting that apatite is not a major host for the REE. The absence of further REE concentrating phases, i.e. allanite, monazite and epidote, implies that the REE distribution of the MG chromitites probably is controlled by plagioclase.

Table 4.32 Chondrite normalized data for multi-element diagram (in ppm) gathered with ICP-MS analyses. Values are averages for each layer. Normalizing values from Lodders (2003).

	MG0	**MG1**	**MG2A**	**MG2B**	**MG2C**	**MG3**	**MG4A**	**MG4B**	**MG4C**
n	2	9	3	7	4	7	15	2	3
Ba	31.817	16.991	6.238	9.141	16.089	24.092	45.353	16.020	18.552
Rb	1.193	1.971	1.451	1.418	1.987	1.927	3.105	2.325	2.593
Th	0.087	0.172	0.024	0.060	0.163	0.248	0.284	0.043	0.057
Nb	0.701	0.814	0.610	0.678	0.778	0.914	1.096	0.829	0.874
Ta	0.024	0.025	0.010	0.016	0.025	0.050	0.044	0.017	0.018
La	0.615	1.202	0.235	0.538	1.326	2.166	2.650	0.577	0.720
Ce	1.022	1.998	0.414	0.934	1.993	3.330	4.634	0930	1.092
Sr	12.649	20.184	20.134	18.552	25.507	40.698	59.310	86.728	81.252
Nd	0.380	0.812	0.155	0.368	0.831	1.390	1.954	0.370	0.437
P	110.8	54.9	29.4	43.3	76.1	48.4	124.0	125.5	186.8
Sm	0.108	0.183	0.047	0.087	0.184	0.291	0.403	0.084	0.103
Zr	7.740	8.395	6.805	4.488	7.489	11.830	12.954	3.456	3.384
Hf	0.237	0.235	0.167	0.127	0.210	0.323	0.338	0.088	0.084
Ti	3516.7	3574.8	4191.6	4319.2	4439.3	4354.2	3399.1	4459.8	5463.9
Tb	0.019	0.028	0.004	0.013	0.026	0.041	0.059	0.012	0.014
Y	0.871	1.265	0.292	0.588	1.073	1.647	2.352	0.625	0.705
Tm	0.014	0.018	0.004	0.009	0.016	0.022	0.030	0.012	0.014
Yb	0.100	0.127	0.027	0.061	0.111	0.161	0.229	0.072	0.074

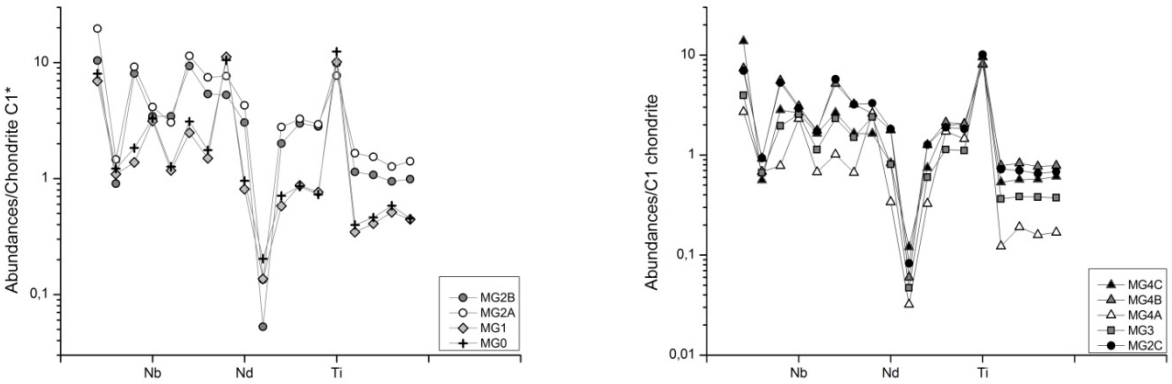

Figure 4.76 Multi-element diagrams for averaged whole-rock data of the MG chromitite layers normalised to C1 chondrite; left: chromitite layers of the LCZ; right: chromitite layers of the UCZ. Data are given in table 4.32.

The modified Harker diagrams have been generated to illustrate how the distribution of the major element oxides changes upwards the stratigraphy relative to Cr_2O_3, which is the major constituent in massive chromitite and therefore plotted on the x-axis (Fig. 4.77). The descriptions regarding these trends are related to the stratigraphy.

Cr_2O_3 vs. SiO_2: The general trend observed here is positive inverse linear with a strong negative correlation (r_S= -0.936), saying that with decreasing Cr_2O_3 content the amount of SiO_2 increases and can be interpreted as the result of progressive melt evolution. From one chromitite layer to the next, three subtrends superimposed by the major trend are present. Two of them follow the tenor of the major trend, but from the MG1 to the MG2A chromitite layer it becomes negative linear. Perhaps the MG2A chromitite layer derives from a more primitive melt mixture than the chromitite layers below, indicating a bigger portion of primitive magma during deposition of the MG2A chromitite.

Cr_2O_3 vs. TiO_2: Variations in the TiO_2 content are mainly controlled by rutile. Although there is no general correlation between TiO_2 and Cr_2O_3 concentrations throughout the stratigraphy of the MG sequence (r_S= -0.015) one can see three small trends developed within it. The lowermost chromitite layers (MG0 and MG1) have a stable TiO_2 content but show various amounts of Cr_2O_3. Varying amounts of chromite are due to fractional crystallization of the mineral. On the other hand, the amount of rutile doesn't change.

Up to the MG3 chromitite an inverse linear trend is present caused by progressive melt evolution the chromite derives from and increasing amounts of rutile. The tenor changes towards the MG4A layer into a negative inverse linear with decreasing amounts of Cr_2O_3 and TiO_2, which is probably caused by the addition of primitive magma similar to the situation described for the MG2A chromitite layer. The change already starts within the MG3 chromitite. From MG4A to the MG4C chromitite the trend changes again to positive inverse linear, indicating further rutile crystallization as well as progressive evolution of the

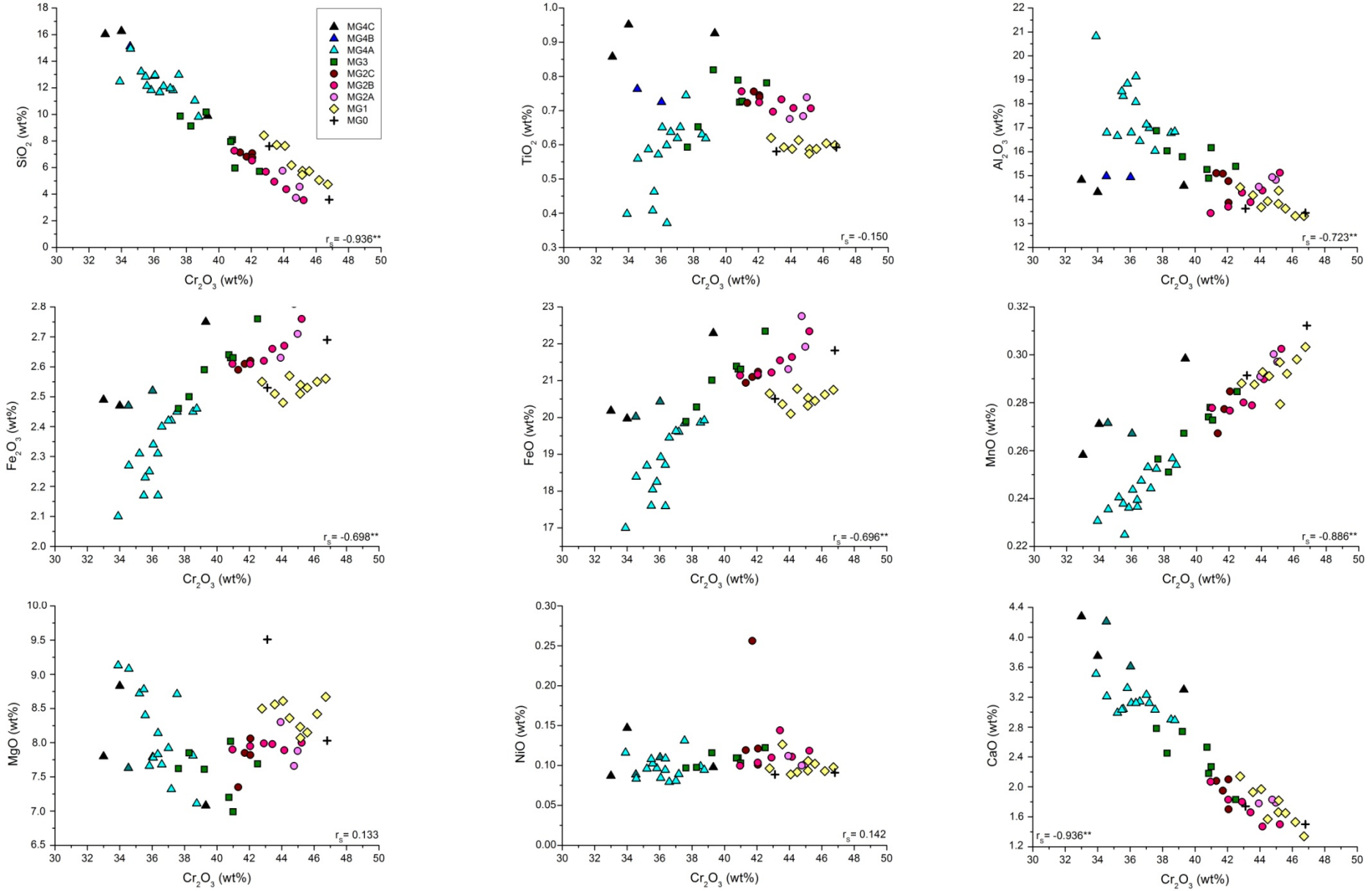

Figure 4.77 Modified Cr_2O_3-Harker plot of the major element oxides related to stratigraphy of the MG sequence. r_S= Spearman rank correlation coefficient. ** Correlation is significant at the 0.01 level. Data are given in table 4.28**.**

melt.

Increasing amounts of rutile with stratigraphy as suggested by the plot Cr_2O_3 vs. TiO_2, confirm the observation of increasing quantities of rutile inclusions in the chromitite layers having already been done by optical microscopy (cf. subsection 4.2.1.1).

Cr_2O_3 vs. Al_2O_3: The Al_2O_3 content within the chromitite layers is controlled by chromite as well as plagioclase. Since the amount of the latter increases in the UCZ, there is a stronger control on the Al_2O_3 content by plagioclase in the UCZ than in the LCZ.

The correlation (r_S= -0.723) is almost as strong as for Cr_2O_3 and SiO_2, but the general inverse linear trend is interrupted by three reversals of this trend becoming negatively inverse linear from the MG2A to MG2B, within the MG4A chromitite and from the MG4A to the MG4C chromitite layers. They are interpreted to be caused by abruptly increasing degrees of plagioclase crystallization due to fractional crystallization of the melt, leading to less Al in chromite.

Cr_2O_3 vs. Fe_2O_3 or FeO: Since the trends for both relations are the same (Fig. 4.77), they are discussed together, although the amount of Fe_2O_3 is controlled by chromite and the one of FeO by chromite as well as orthopyroxene.

Three subtrends are superimposed by a strong negatively inverse linear trend (r_S= -0.698 or -0.696 for Fe_2O_3 and FeO, respectively) upwards the stratigraphy. The general trend is due to progressive evolution of the melt, since Cr and Fe are consumed by chromite as well as pyroxene precipitation. At the bottom (from MG0-MG2A chromitites) and at the top (MG4A-MG4C chromitites) of the MG sequence the direction of the trend changes to positively inverse linear. This inversion to decreasing amounts of Cr_2O_3 and increasing quantities of Fe_2O_3 and FeO can be interpreted as progressive evolution of the mixed melt the chromite and pyroxene derives from, resulting in chromite becoming enriched in Fe relative to Cr.

Cr_2O_3 vs. MnO: Since no MnO has been detected during analyses of chromite grains (cf. subsection 4.3.1), the whole-rock content of Mn is controlled by orthopyroxene only replacing another of the bivalent cations, i.e. Mg^{2+} and Fe^{2+}.

For MnO a general negatively inverse linear trend can be observed (r_S= -0.866). This is interesting, since with decreasing precipitation of chromite the amount of crystallizing orthopyroxene should increase. Hence, decreasing MnO could indicate progressive melt evolution resulting in orthopyroxene with less ‘mafic’ composition, i.e. less Mg. Considering the plot Cr_2O_3-MgO, this is only true up to the middle of the MG3 chromitite layer. From there upwards, increasing amounts of Mg can be observed, replacing Mn as well as Fe in the lattice of orthopyroxene.

Increasing amounts of orthopyroxene with contemporaneously decreasing chromite content can be deduced from the MG4A to the MG4C chromitite layer, since the trend

changes to positively inverse linear.

Cr_2O_3 vs. MgO: No general trend is visible in the plot (r_S= 0.133). Similar to the correlation of Cr_2O_3 and TiO_2 a reversal of trends within the MG3 chromitite layer is visible. Below this layer, both the MgO and Cr_2O_3 content are decreasing, whereas above the MG3 chromitite up to the MG4A the MgO content increases with contemporaneously decreasing Cr_2O_3 concentrations. In the uppermost part of the MG sequence, i.e. from the MG4A to the MG4C chromitite layer, the trend changes again to negatively inverse linear. Thus, below the MG3 chromitite and from MG4A to MG4C progressive melt evolution takes place, leading to decreasing MgO and Cr_2O_3 contents of the chromitite layers. The observed reversal in this trend with increasing MgO concentrations is probably caused by addition of more primitive melt during magma mixing responsible for chromite precipitation. Hence the lower part of the MG3 chromitite is of more evolved composition than the upper part, which is separated from the lower one by a thin pyroxenitic band. This feature has already been shown with the Mg# in figure 4.71.

Cr_2O_3 vs. NiO: With a Spearman rank correlation coefficient of 0.142 correlation is absent, caused by the absence of olivine within the chromitite layers, to which Ni is compatible.

However, from the plot in figure 4.77 a very rough trend is visible with contemporaneously decreasing Cr_2O_3 and NiO contents that can be followed upwards the stratigraphic column. Minor amounts of Ni have been found to be incorporated into the chromite lattice during this study (cf. subsection 4.3.1). Thus, decreasing whole-rock Ni contents are interpreted to represent fractional crystallization of chromite within each layer as well as a general progressive evolution of the melt the chromite grains derive from.

Cr_2O_3 vs. CaO: This is the only correlation (r_S= -0.936) that can be followed throughout the entire stratigraphic column without major interruptions or reversals of trends. The correlation is positively inverse linear, i.e. with decreasing Cr_2O_3 content the amount of CaO increases, which is due to increasing amounts of (cumulus) plagioclase and clinopyroxene in the chromitite layers caused by fractional crystallization. It thus shows progressive evolution of the mixed melt upwards the stratigraphy of the MG-sequence.

However, a tiny interruption with increasing Cr_2O_3 contents is visible within the MG4A chromitite layer, which is ascribed to addition of a small amount of primitive melt to the evolved liquid resulting in an increased precipitation of chromite for a short interval.

As have been shown with the multi-element diagrams in Fig. 4.76, no apatite is present controlling the behaviour of the trace elements of the chromitite layers of the MG-sequence Hence, their distribution seems to be controlled by the intercumulus minerals, i.e. orthopyroxene, plagioclase ± clinopyroxene. Several authors (e.g. Cawthorn and

McCarthy, 1985; Henderson, 1975; Rollinson, 1993) doubt the applicability of incompatible element plots on cumulus rocks. According to them, the incompatible element concentrations in cumulus rocks are controlled by the presence of intercumulus liquid, i.e. high proportions of intercumulus liquid in a cumulate rock will tend to have higher incompatible element concentrations. In the plot shown in Fig. 4.78, the Cr_2O_3 content should represent the relative amount of the cumulus mineral chromite that is plotted versus the Rb/Zr ratio of the individual samples of the MG chromitite layers, since it is sensitive to fractionation. As can be seen, no major fractionation trend is visible from the LCZ chromitites to the chromitites of the UCZ. The data points rather plot in two separate clusters with a minor zone of overlap (from ca. 41-43 wt% Cr_2O_3). However, indications of fractionation by increasing Rb/Zr can be interpreted, illustrated by two subordinated trends within each cluster. It could have been shown in Fig. 4.23 of subsection 4.3.1 that progressive evolution of chromite exists from bottom to top of the MG-sequence by an decreasing Cr/(Cr+Fe) ratio indicating a declining Cr_2O_3 content with progressive fractionation. As chromite is the major cumulus mineral within the chromitite layers, the whole-rock Cr/(Cr+Fe) ratio shows the same trend (Fig. 4.71). Thus, a positive inverse linear trend with decreasing Cr_2O_3 contents as well as an increasing Rb/Zr ratio should be visible in Fig. 4.78. Hence, the subordinated trends within the two clusters represent no real trends of fractionation and are rather caused by various amounts of intercumulus minerals, as is depicted in Fig. 4.7 in subsection 4.2.1. These findings thus confirm the considerations of Cawthorn and McCarthy (1985), Henderson (1975) and Rollinson (1993) mentioned above.

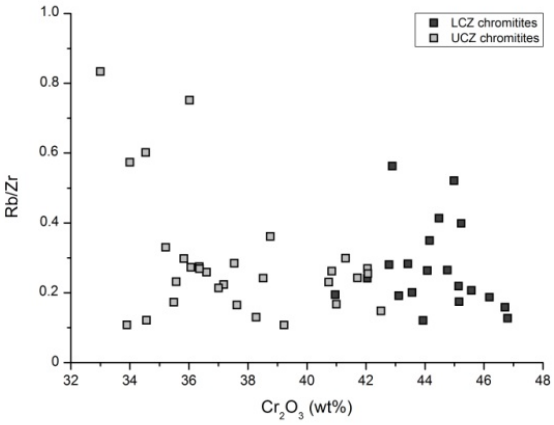

Figure 4.78. Plot of the whole-rock Cr_2O_3 content vs. the Rb/Zr ratio of the individual chromitite samples of the MG chromitite layers.

4.4.1.1 XRD analyses of the chromitite layers

XRD analyses have been carried out to get information about the nature of the co-precipitating silicate minerals occurring in the chromitite layers, since only thick polished sections have been available.

Within all the chromitite layers of the MG sequence orthopyroxene as well as plagioclase have been detected. Orthopyroxene is mainly ferroan enstatite with slightly changing composition (Tab. 4.33). Sometimes two different species of orthopyroxene occur, of which the second one is pure enstatite.

There is more variation in plagioclase composition occurring in the chromitite layers than could have been observed for orthopyroxene (Tab. 4.34). Pure end members are most common, i.e. anorthite or albite, but solid solutions as bytownite are present, too.

Table 4.33 Orthopyroxene (opx) in the chromitite layers. Chemical formulas from Powder Diffraction Files (*.pdf) of X'Pert HighScore.

layer	sample	opx species	chemical formula
MG4A	HEX10/08	orthopyroxene	$(Fe_{0.104}Mg_{0.896})(Fe_{0.703}Mg_{0.254}Ca_{0.043})(Si_2O_6)$
	HEX10/12	orthopyroxene	$(Fe_{0\cdot232}Mg_{0.768})(Fe_{0.570}Mg_{0.387}Ca_{0.043})Si_2O_6$
	HEX10/15	orthopyroxene	$(Fe_{0\cdot232}Mg_{0.768})(Fe_{0.570}Mg_{0.387}Ca_{0.043})Si_2O_6$
		enstatite	$Fe_{0.155}Mg_{0.854}SiO_3$
MG3	HEX10/21	enstatite, ferroan	$(Fe_{0.084}Mg_{0.916})(Fe_{0.414}Mg_{0.586})Si_2O_6$
		enstatite	$Mg_2(Si_2O_6)$
	HEX10/27	enstatite, ferroan	$(Mg_{1.561}Fe_{0.439})Si_2O_6$
MG2C	HEX10/30	enstatite, ferroan	$(Mg_{1.014}Fe_{0.986})Si_2O_6$
	HEX10/31	orthopyroxene	$(Fe_{0.104}Mg_{0.896})(Fe_{0.703}Mg_{0.254}Ca_{0.043})(Si_2O_6)$
MG2B	HEX10/32	enstatite	$MgSiO_3$
		enstatite, ferroan	$(Mg_{1.395}Fe_{0.395}Ca_{0.01}Al_{0.80})(Si_{1.76}Al_{0.24}O_6)$
	HEX10/35	enstatite, ferroan	$(Fe_{0.099}Mg_{0.901})(Fe_{0.399}Mg_{0.601})Si_2O_6$
MG2A	HEX10/38	orthopyroxene	$(Fe_{0.104}Mg_{0.896})(Fe_{0.703}Mg_{0.254}Ca_{0.043})(Si_2O_6)$
MG1	HEX10/41	enstatite, ferroan	$(Fe_{0.099}Mg_{0.901})(Fe_{0.399}Mg_{0.601})Si_2O_6$
	HEX10/46	enstatite, ferroan	$Mg_{1.1}Fe_{0.87}Ca_{0.03}Si_2O_6$
MG0	HEX10/50	enstatite, ferroan	$(Mg_{1.014}Fe_{0.986})Si_2O_6$

Neither for plagioclase, nor for orthopyroxene a regular pattern towards more evolved composition upwards the stratigraphic column can be acquired from the data. Exemplarily for a powder diagram, the powder pattern of sample HEX10/30 is shown in figure 4.79. Phlogopite, muscovite and alteration minerals as chromian chlorite, vermiculite and

montmorillonite only occur in the chromitite layers of the LCZ in detectable amounts (Fig. 4.80).

Table 4.34 Plagioclase (plag) in the MG chromitite layers. Chemical formulas from Powder Diffraction Files (*.pdf) of X'Pert HighScore.

layer	sample	plag species	chemical formula
MG4A	HEX10/08	anorthite, sodian	$Ca_{0.86}Na_{0.14}Al_{1.84}Si_{2.16}O_8$
		anorthite	$Ca(Al_2Si_2O_8)$
	HEX10/12	anorthite	$Ca(Al_2Si_2O_8)$
		albite, high	$Na(AlSi_3O_8)$
	HEX10/15	anorthite	$Ca(Al_2Si_2O_8)$
MG3	HEX10/21	anorthite	$Ca(Al_2Si_2O_8)$
	HEX10/27	anorthite, sodian	$(Ca, Na)(Al, Si)_2Si_2O_8$
		anorthite	$Ca(Al_2Si_2O_8)$
MG2C	HEX10/30	bytownite	$Ca_{0.86}Na_{0.14}Al_{1.84}Si_{2.16}O_8$
		anorthite	$Ca(Al_2Si_2O_8)$
		albite	$(K_{0.22}Na_{0.78})(AlSi_3O_8)$
	HEX10/31	albite	$Na(AlSi_3O_8)$
		bytownite	$Ca_{0.8}Na_{0.2}Al_{1.8}Si_{2.2}O_8$
MG2B	HEX10/32	bytownite	$(Ca_{0.78}Na_{0.22})(Al_{1.78}Si_{0.22})Si_2O_8$
	HEX10/35	albite	$Na(AlSi_3O_8)$
		anorthite, sodian	$Ca_{0.86}Na_{0.14}Al_{1.84}Si_{2.16}O_8$
MG2A	HEX10/38	albite, high	$Na(AlSi_3O_8)$
		anorthite	$Ca(Al_2Si_2O_8)$
MG1	HEX10/41	anorthite	$CaAl_2Si_2O_8$
	HEX10/46	anorthite, annealed	$(Ca_{0.98}Na_{0.02})(Al_{1.98}Si_{0.02})Si_2O_8$
MG0	HEX10/50	albite, calcian	$(Na_{0.84}Ca_{0.16})Al_{1.16}Si_{2.84}O_8$

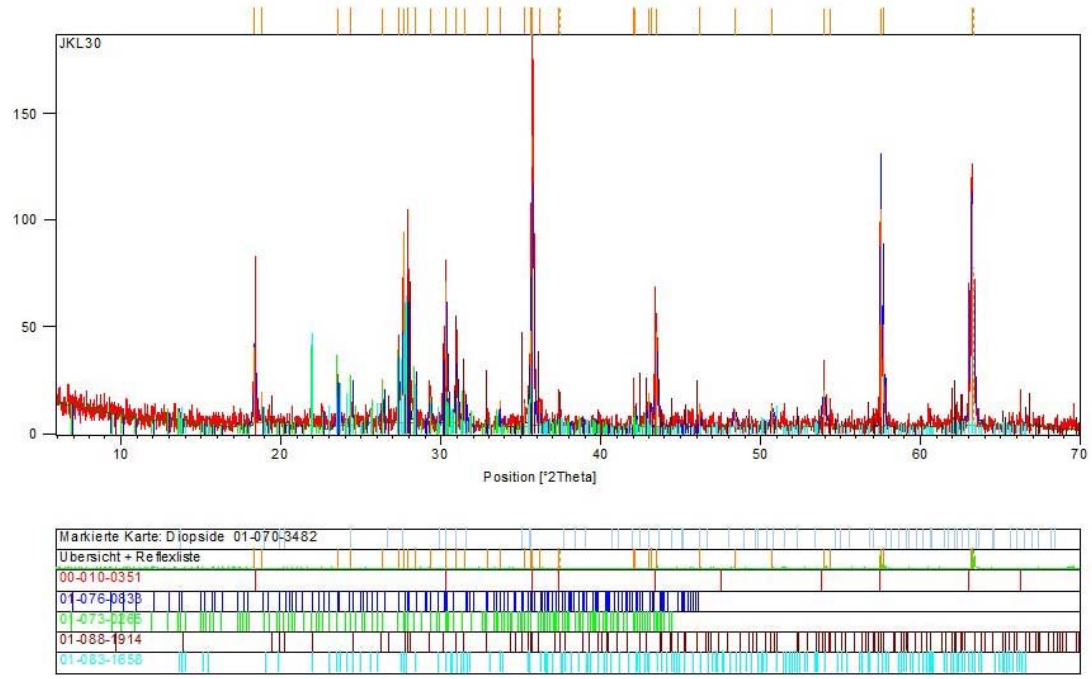

Figure 4.79 XRD pattern from sample HEX10/30 (MG2C). Numbers in the lower part refer to (from top to bottom): magnesiochromite, bytownite, anorthite, ferroan enstatite and albite.

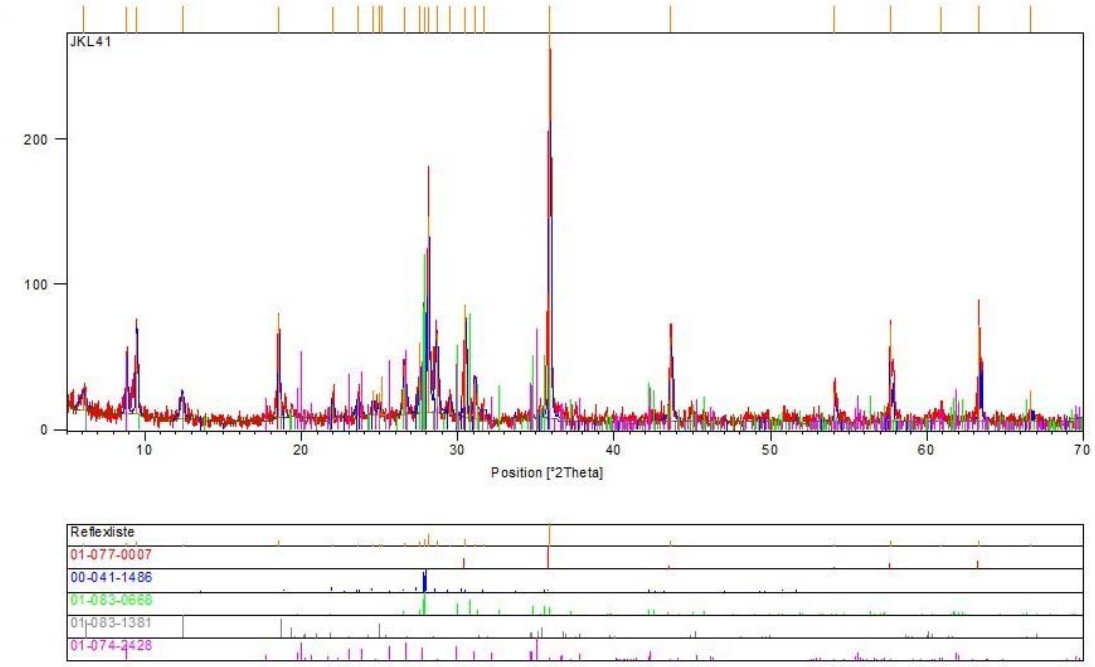

Figure 4.80 XRD pattern from sample HEX10/41 (MG1). Numbers in the lower part refer to (from top to bottom): magnesiochromite, anorthite, ferroan enstatite, chromian chlorite and muscovite.

4.4.1.2 Whole-rock PGE and Au contents of the chromitite layers

In this section, we will follow the definition of Davies and Tredoux (1985), who separated the PGE into two groups according to their melt temperature: the high-temperature PGE (HT-PGE: Os, Ir, Ru), and the low-temperature PGE (LT-PGE: Rh, Pt and Pd). The terms are synonymous for IPGE and PPGE defined by Barnes *et al.* (1985).

All the chromitite layers of the MG sequence show elevated concentrations of PGE. The averaged amounts of the individual PGE and Au per layer are summarized in table 4.35. Detailed results of PGE concentration in chromitite samples are presented in table B-21 in appendix B.

With an average of 3988 ppb PGE+Au the MG2C chromitite layer is the most enriched one, followed by the MG3 that comprises 3910 ppb. Pt is the most common PGE occurring in the MG2C chromitite, and it is also the one showing the highest concentrations of all the other PGE except Pd. Pd is most abundant in the MG3 chromitite layer. The MG4B chromitite shows the lowest PGE+Au content (1366 ppb). Generally, the Au content is low (5-10 ppb) but increases within the chromitite layers upwards the stratigraphy (Tab. 4.35). These values are within the range reported for the same stratigraphic sequence at Thorncliffe (Lee and Parry, 1988).

The data from this study coincide with data from Brits and Union presented by Scoon and Teigler (1994), who also found that the MG2 and MG3 are the chromitite layers richest in Pd and Pt, and that the MG1 and the MG4B chromitites are the poorest. This coincidence implies lateral continuity in PGE mineralisation over the entire Bushveld Complex.

Table 4.35 Average PGE and Au contents of the MG chromitite layers. *Not for every sample Au was detected; number of samples in brackets. *N:* number of samples; *N.d.*: below detection limit. Data are given in ppb.

	MG0	**MG1**	**MG2A**	**MG2B**	**MG2C**	**MG3**	**MG4A**	**MG4B**	**MG4C**
n	2	9	3	6	4	7	15	2	3
Os	79	108	69	124	137	130	114	55	67
Ir	103	102	92	181	200	179	170	65	78
Ru	487	640	334	616	776	691	570	328	419
Rh	199	130	187	266	321	416	273	156	181
Pt	598	388	1650	1633	2109	1420	1335	489	56
Pd	126	282	638	330	436	1063	418	257	219
Au*	n.d.	5 (2)	5 (1)	6 (3)	7 (4)	8 (7)	9 (9)	7 (1)	10 (3)

Figure 4.81 presents the variation in PGE concentration and in the Cr_2O_3 content of the chromitite layers from bottom to top of the stratigraphic column of the MG sequence. It can be seen that up to the MG2C chromitite layer the PGE content strongly increases with contemporaneously decreasing Cr_2O_3 concentration. From there on both are decreasing upwards the stratigraphy. These findings point to decoupled behaviour of the PGE relative to chromite, i.e. high PGE concentration are not necessarily linked to high Cr_2O_3 contents. This relationship is also illustrated by strong negative correlation of Cr_2O_3 and the PGE/Cr_2O_3 ratio plotted in figure 4.82.

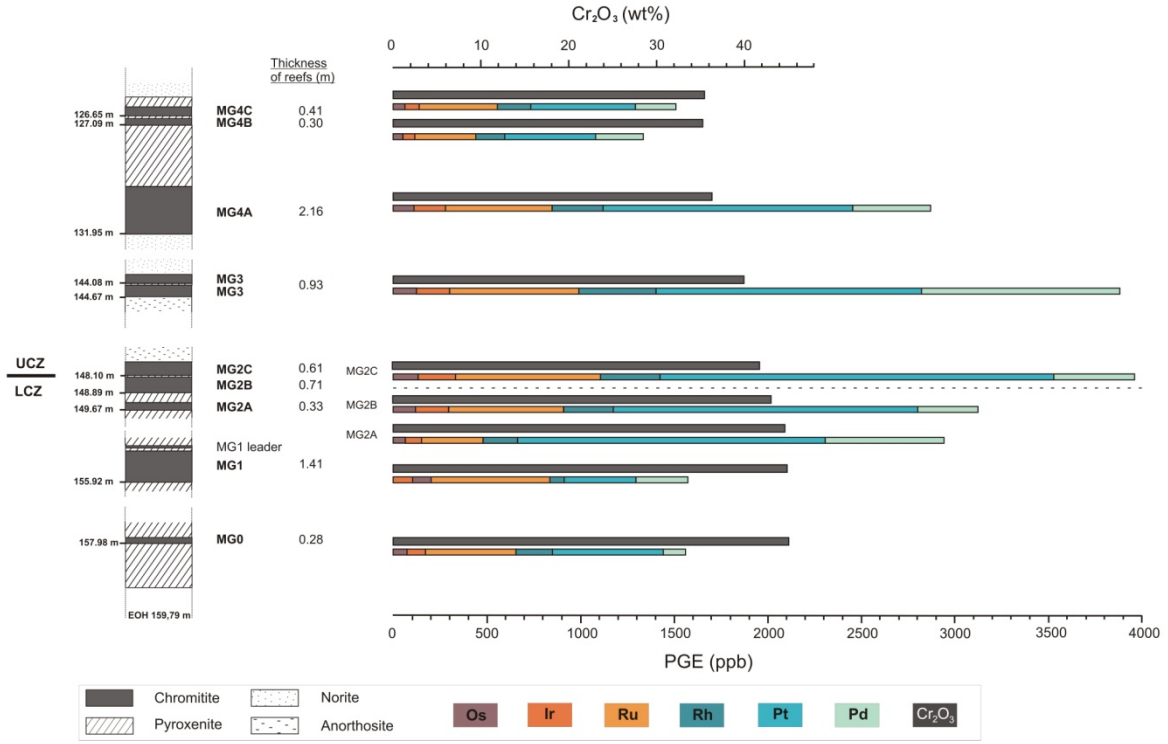

Figure 4.81 Averaged PGE and Cr_2O_3 contents of the MG chromitite layers. Data are given in table 4.35. The variation in Cr_2O_3 content coincides with the amount of chromite vs. silicate in the chromitite layers (cf. subsection 4.2.1).

Steep slopes of normalized PGE patterns of the MG chromitite layers (Fig. 4.77) illustrate fractionation of the PGE relative to each other within the individual chromitite layers of the MG sequence. The highest degree of fractionation occurs within the MG2A layer (Pt/Ir= 17.31), whereas the MG1 chromitite shows the poorest PGE fractionation (Pt/Ir= 3.7). All the MG chromitite layers show the Rh anomaly which is typically associated with chromitite layers (Barnes and Maier, 2002). Compared to the UG2 pattern, to which they are similar, the patterns of the MG chromitite layers show low Pd values. This is perhaps due to alteration. The patterns of the MG chromitites have flatter

slopes compared to the UG2, as they also show higher Os and Ru values for the MG2A, MG2C, MG3 and MG4A chromitite layers. Thus, the MG chromitites are less depleted in HT-PGE relative to LT-PGE, than would be expected from their major mineralogy.

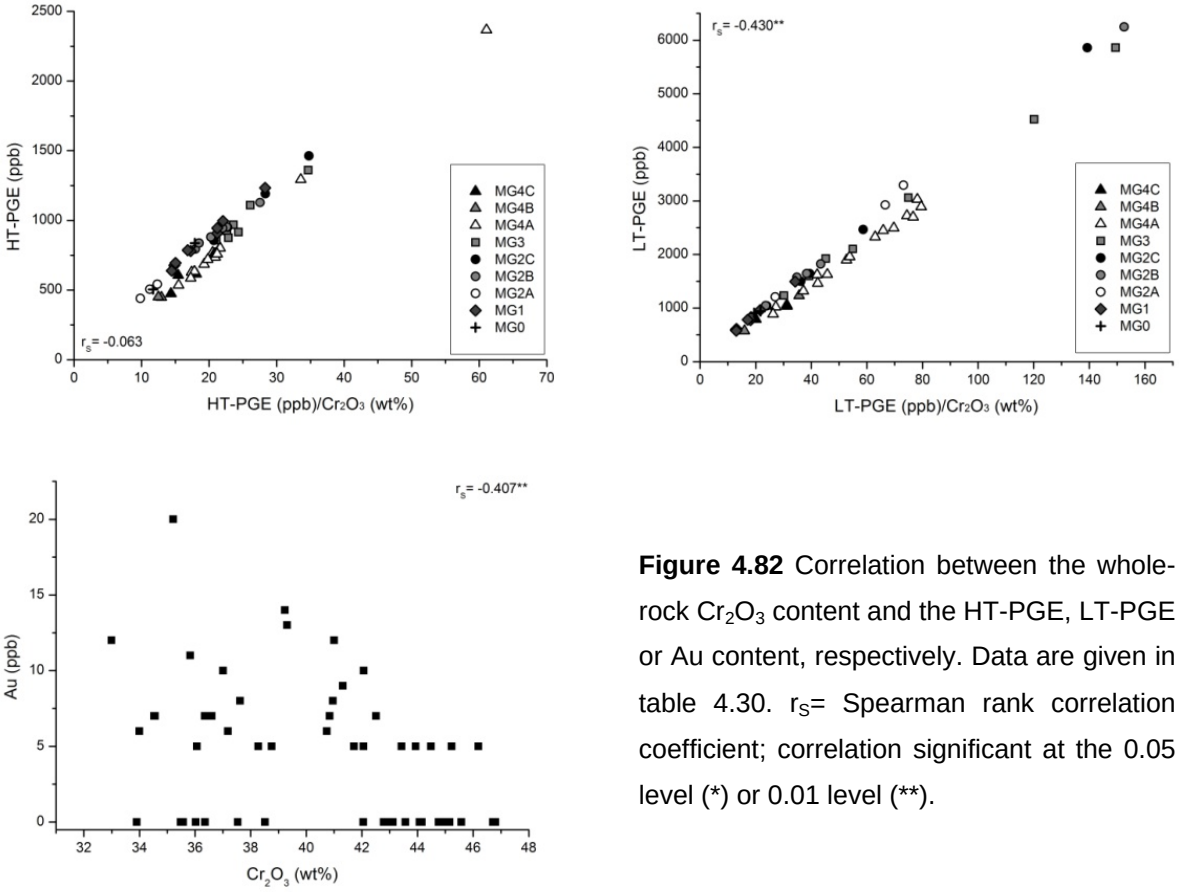

Figure 4.82 Correlation between the whole-rock Cr_2O_3 content and the HT-PGE, LT-PGE or Au content, respectively. Data are given in table 4.30. r_S= Spearman rank correlation coefficient; correlation significant at the 0.05 level (*) or 0.01 level (**).

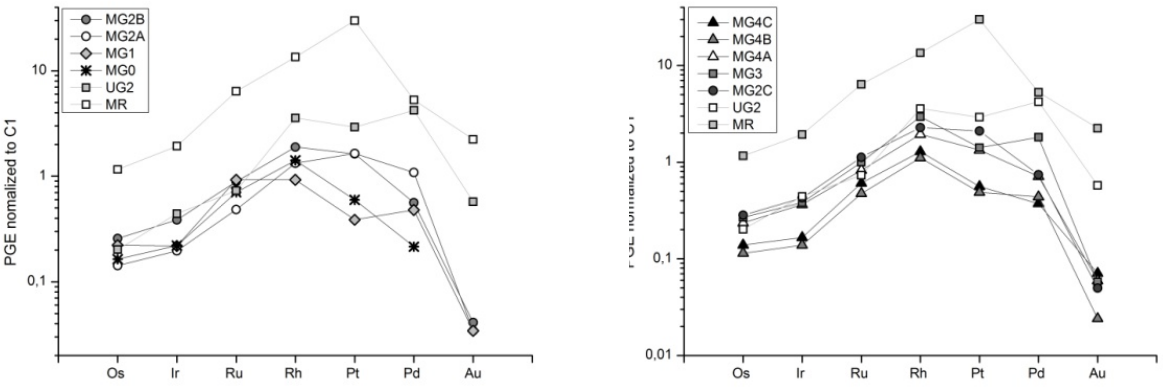

Figure 4.83 C1 normalized PGE and Au patterns of the chromitite layers of the MG sequence. Left: chromitite layers of the LCZ; right: chromitite layers of the UCZ. C1 normalising values are from Lodders (2003). PGE data shown are averages from each layer. Merensky Reef values are averages from the Merensky Reef chromitite; data for the UG2 are from the eastern limb only (Merensky Reef and UG2 data from Barnes and Maier, 2002).

Selected inter-element relationships of the PGE as well as the corresponding Spearman rank correlation coefficients are shown in figure 4.84. As a general rule, the correlations between the HT-PGE are strong to very strong with correlation coefficients ranging between 0.611 and 0.919 (cf. Tab. B-22 in appendix B). These relationships are due to their mode of occurrence. The most likely phase for the HT-PGE is laurite ((Ru, Os, Ir)S_2), which has been shown in subsection 4.3.8. Correlation coefficients of the LT-PGE range between 0.700 and 0.765 and are thus less strong than those observed for the HT-PGE. From Pt-Rh and Pt-Pd plots in figure 4.84 two trends can be interpreted, which is suggested to describe their occurrence in various PGM phases.

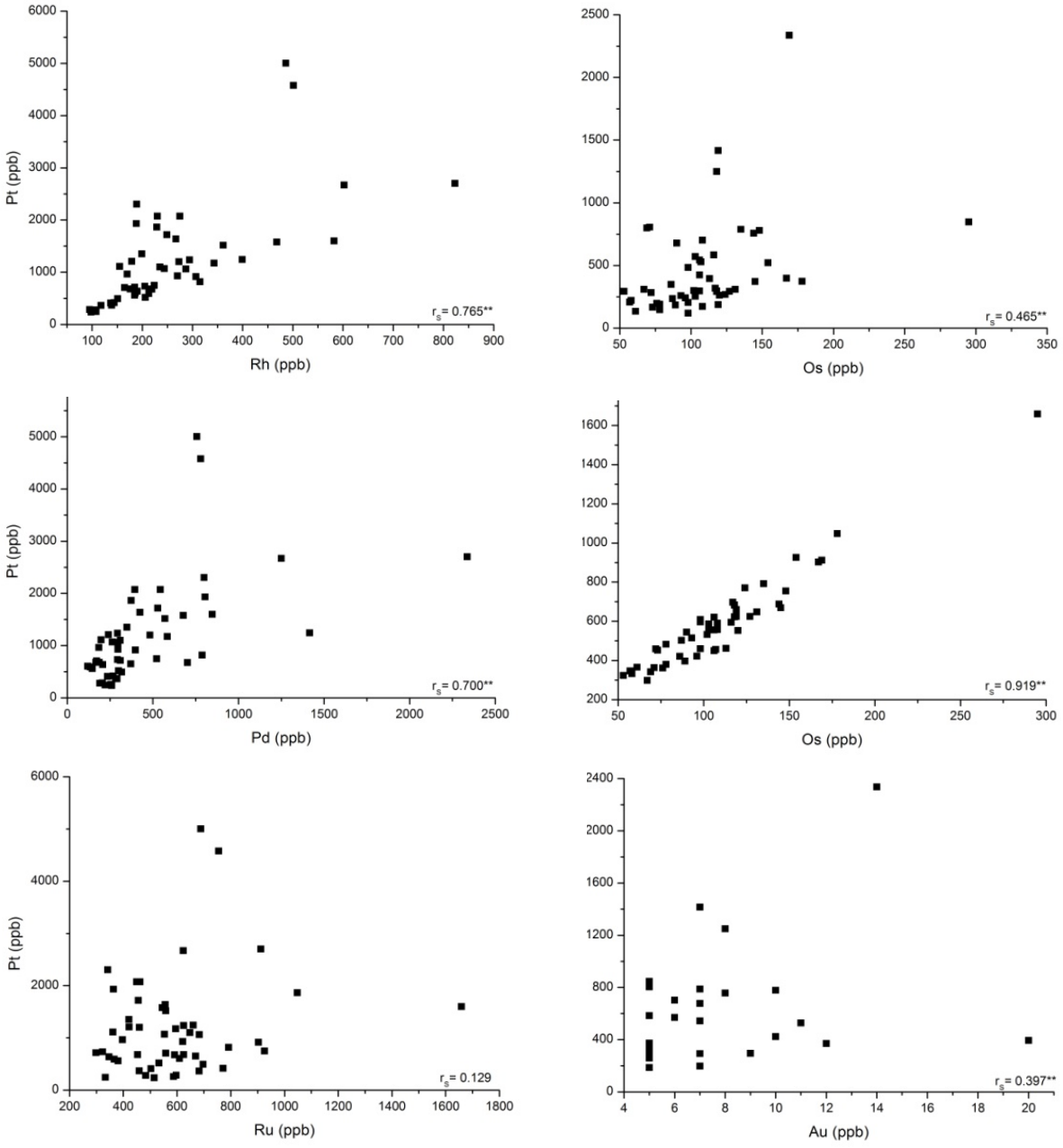

Figure 4.84 Selected interelement relations between the PGE and Pd and Au. r_S= Spearman rank correlation coefficient; correlation significant at the 0.05 level (*) or 0.01 level (**).

The relations between HT-PGE and LT-PGE are less strong correlated, which is depicted in the degree of scattering in the plots (Fig. 4.84). The correlation coefficients range between 0.129 and 0.739 and clearly support the division of the PGE's into two groups. The lowest correlations exist for Ru and Pt or Pd as well as for Os and Pt or Pd.

There is no correlation of the HT-PGE with Au, indicating a different geochemical behaviour of Au. A weak correlation exists for the LT-PGE and Au with decreasing correlation coefficient from Rh to Pd (r_S= 0.479 – 0.452) suggesting limited coincidence of geochemical activities.

A weak correlation exists for Ni and the LT-PGE but is absent for the HT-PGE (Fig. 4.85). The single PGE don't show any correlation with Ni. The LT-PGE do not correlate with Cu, and the HT-PGE show a slight negative correlated relation, which is probably due to temperature control. The lack of significant correlation of the PGE with Ni or Cu, respectively, indicates that the BMS played a subordinated role in PGE fractionation only.

The plot of Ni and Co concentrations of the MG chromitite layers suggests that they are sulphide controlled. There is no indication of a correlation between Ni and Cu illustrating their occurrence in different BMS species. Given that at least part of the Ni is controlled by the presence of BMS, the weak correlation of Ni and the LT-PGE indicate that they are associated with Ni-rich BMS.

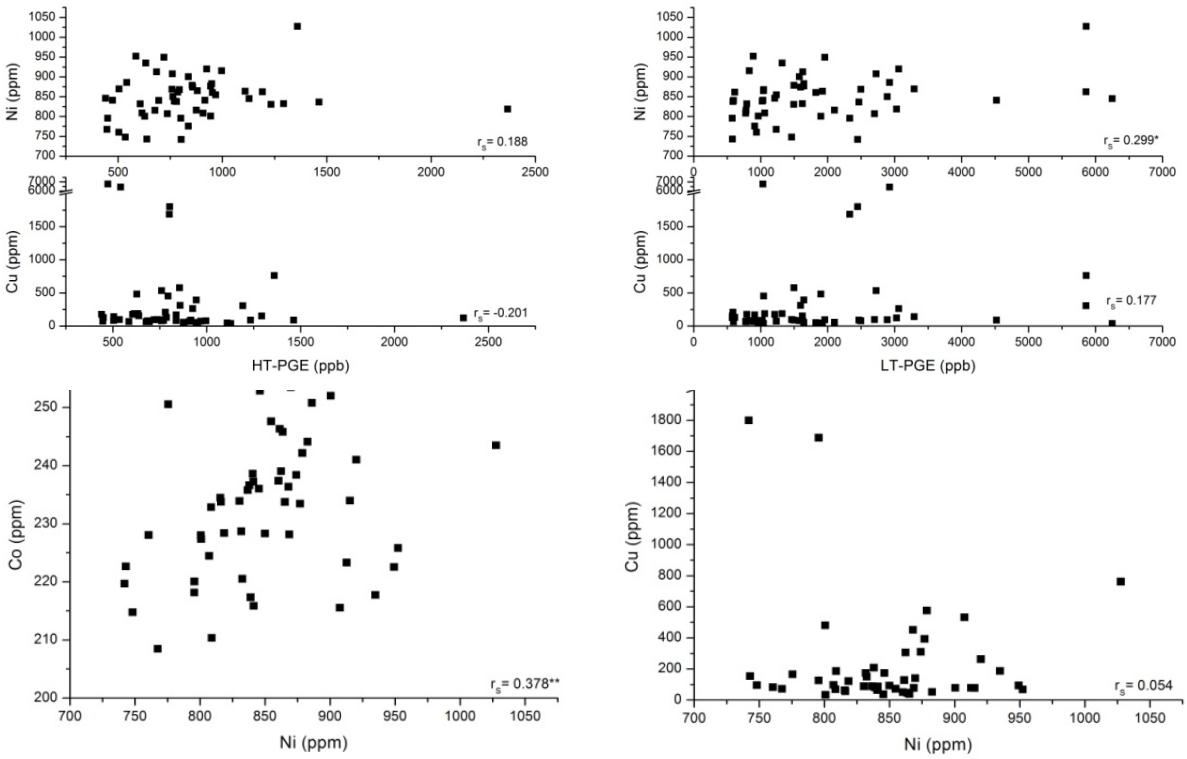

Figure 4.85 Plots illustrating the interrelationships of the two PGE groups with Ni, Co and Cu. r_S= Spearman rank correlation coefficient; correlation significant at the 0.05 level (*) or 0.01 level (**).

After Crocket (2002) a strongly positive Ir/Ni ratio indicates that sulphide liquid immiscibility was the collection mechanism for the PGE. Since the correlation in the chromitite layers of this study is weak only (Fig. 4.86), sulphide liquid immiscibility as the collection mechanism played a limited role only.

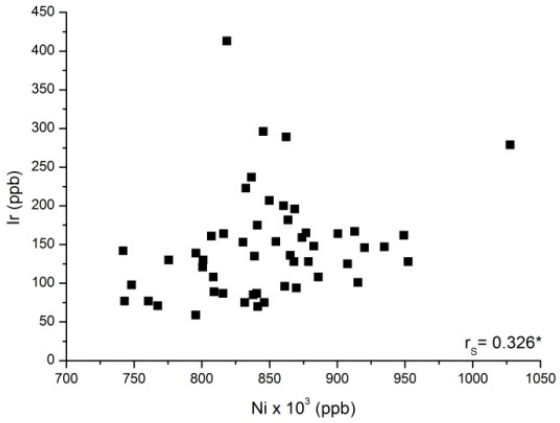

Figure 4.86 Bivariate plot of Ni vs. Ir. r_S= Spearman rank correlation coefficient. *Correlation significant at the 0.05 level.

The S content increases from bottom to top of the MG-sequence (Fig. 4.87). Both, the HT-PGE and the LT-PGE show a turning point from an increasing trend in the LCZ to declining concentrations in the UCZ. Coincidence of positive peaks between HT-PGE and S only occurs in the UCZ; for the LT-PGE and S this is rather the case in the vicinity of the LCZ/UCZ transition zone.

Correlation coefficients are moderate for Rh and Pd with S. Taking into account a low correlation with Ni presented before it suggests a limited fractionation by sulphides. Os, Ir and Ru are not correlated with S. Lacking positive correlations with Ni or Cu indicate their presence independently from the BMS, which further corroborates their occurrence as laurite mentioned before. The poorest correlation exists between Pt and S, indicative of Pt being not only fractionated by sulphide.

LA-ICP-MS studies showed (cf. subsection 4.3.1) that especially Pt (and to a lesser degree Rh and Ir) can be incorporated into the chromite lattice. As this is rather an exception than a regular pattern, incorporation cannot be the major control on Pt fractionation. Hence, there seems to be more than one fractionation path for Pt.

To show if fractionation of the PGE is controlled by temperature the individual PGE have been plotted vs. the whole-rock MgO content of the chromitites. Considering the high melt temperatures of the PGE, the MgO content can be used as an indication for fractionation of the PGE at the source from which the parental melts were extracted (cf. Tredoux *et al.*, 1986). All plots shown in figure 4.88 have a tendency to have a weak negative correlation after reaching maximum PGE concentrations, which are achieved at

MgO contents of ca. 7 wt% for Os, Ir and Ru, 7.6 wt% for Rh and Pd, and 8 wt% for Pt. Thereafter the PGE concentrations decline with increasing MgO concentrations.

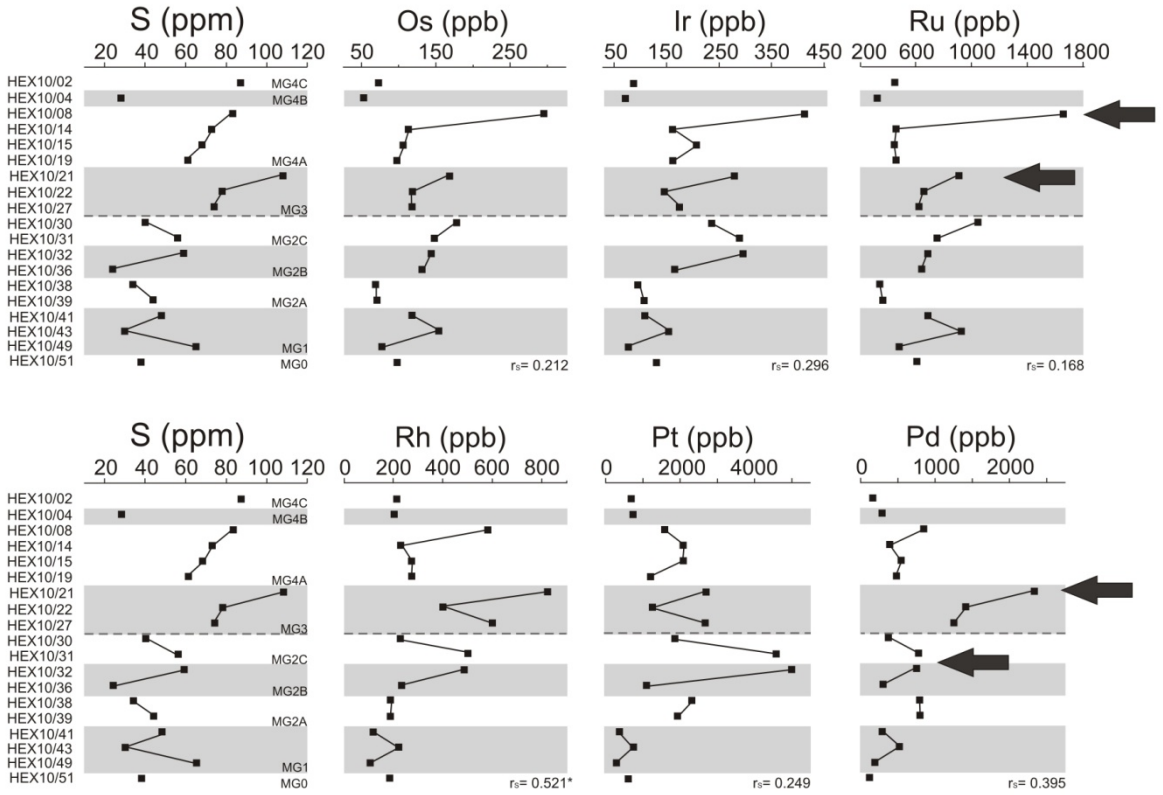

Figure 4.87 Variation of the S and PGE contents of selected samples through the stratigraphy of the MG sequence. Stippled line represents the transition LCZ/UCZ. The arrows indicate peak coincidence. Only samples for which the S content has been determined have been plotted. r_S= Spearman rank correlation coefficient; * correlation significant at the 0.05 level.

According to Tredoux *et al.* (1986) the amount of the HT-PGE even increases with increasing MgO of the rocks, indicating that they are extracted by high degrees of partial melting only, which requires extremely high temperatures. The data of this study do not corroborate these findings, since peak PGE concentrations are achieved at approximately the same MgO content as the LT-PGE. However, the PGE patterns of the MG chromitite layers strongly suggest PGE fractionation. Since the chromitite layers are cumulate rocks, the observed lack of higher HT-PGE concentrations at higher levels of MgO content could result from the process of formation of the cumulate layers that probably altered the characteristic signs of fractionation originally could have been present.

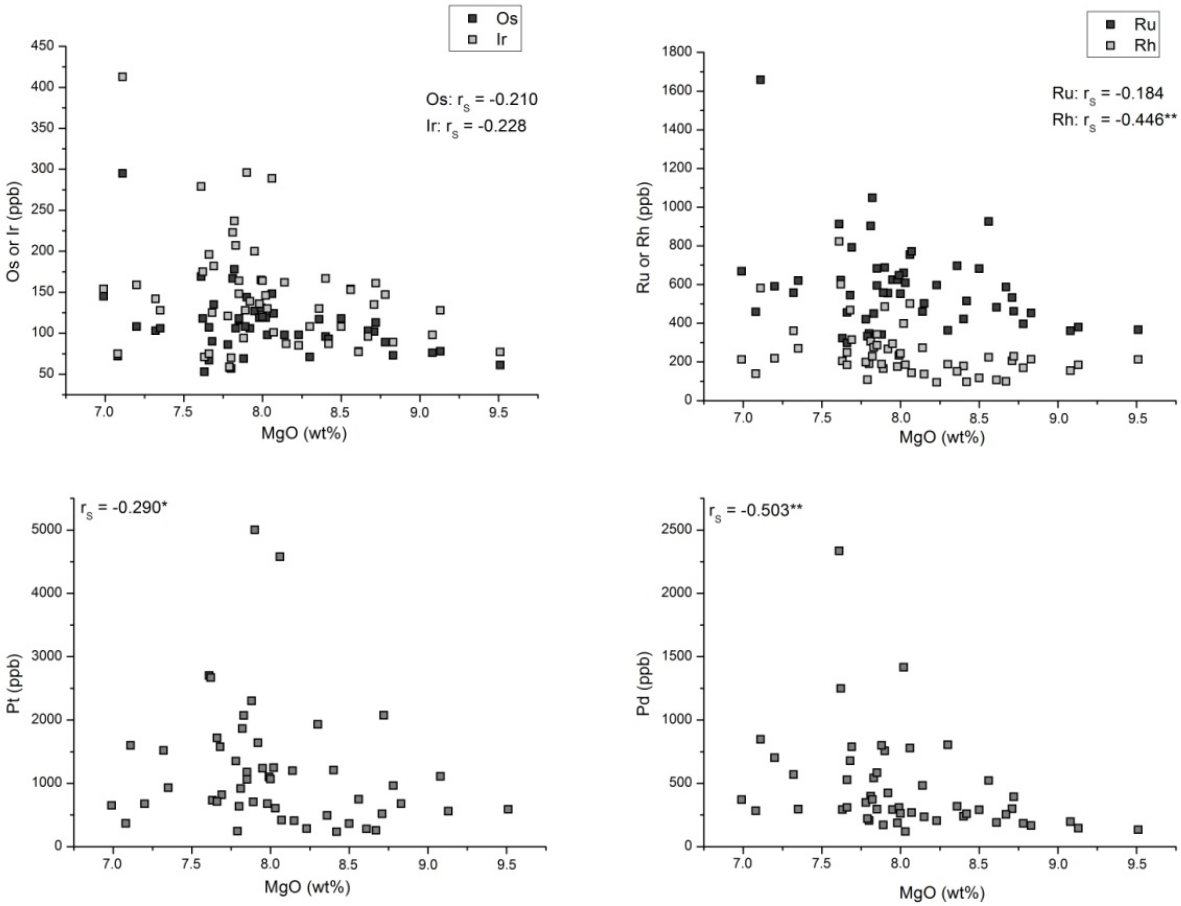

Figure 4.88 Plot of the individual PGE versus the whole-rock MgO content of the MG sequence. r_S= Spearman rank correlation coefficient; **correlation significant at the 0.01 or * the 0.05 level.

By implication this means that upwards the stratigraphy (with decreasing MgO content of the chromitites) the concentration of the HT-PGE relative to the LT-PGE would decrease. Exemplarily for the variation of the relationship of HT-PGE relative to the LT-PGE in the MG sequence the Pt/Ir ratio was plotted vs. the stratigraphic column in figure 4.89. These two elements have been chosen to each represent one of the PGE groups described above. The (Pt+Pd)/(Os+Ir) ratio shows exactly the same trend, indicating that the variations in Pt or Ir alone are representative of the two groups. Generally, the ratio shows an increasing trend, representing an increase of the LT-PGE content relative to the HT-PGE.

As has been shown in subsection 4.4.1, the Mg# of the chromitite layers generally decreases upwards the stratigraphic column of the MG sequence, but a strong reversal to low Mg# at the level of the MG4A chromitite points to addition of primitive magma. As the Pt/Ir ratio in figure 4.89 shows, a strong increase of the HT-PGE relative to the LT-PGE is illustrated in the lower part of the MG4A. Hence, with the postulated addition of primitive melt an addition of the amount of HT-PGE can be interpreted. According to that, primitive melt seems to have a high HT-PGE maturity.

The Pt/Ir ratio shows another few anomalies: In the MG2A and again the middle of the MG4A chromitite layer, the content of the LT-PGE strongly increases relative to the HT-PGE. In addition to the observation of a strong decrease in Pt/Ir ratio in the lower part of the MG4A, a strong increase of the HT-PGE relative to the LT-PGE is also illustrated for the MG2B chromitite layer. With the exception of the MG2C and MG4A chromitite layers, the whole-rock Al_2O_3 content shows exactly the same trend when compared to the Pt/Ir ratio in each cyclic unit (Fig. 4.89). This indicates a connection of PGE fractionation with Al_2O_3 activity of the melt.

There are four different scenarios that can be obtained from bottom to top of the individual chromitite layers (Fig. 4.89):

1. An increasing Al_2O_3 content and an increasing Pt/Ir ratio. It is the most common one and is present in the MG0, MG1, MG4B and MG4C chromitite layers. Since chromite is the dominating mineral within the chromitite layers, the whole-rock Al_2O_3 content is mainly controlled by chromite and only in second order by plagioclase. Hence, increasing Al_2O_3 suggests an enrichment of Al in chromite towards the top of these layers, which is also corroborated by the Cr/(Cr+Al) ratio of the chromitites (cf. subsection 4.4.1). Since investigations with the MLA furthermore showed that the LT-PGE preferentially are associated with plagioclase (cf. subsection 4.4.8.1.1), and these chromitite layers comprise of nearly 35-50% silicate matrix (cf. Fig. 4.7 in subsection 4.2.1), the observed enrichment of the LT-PGE relative to the HT-PGE within these layers is dominantly caused by increasing amounts of co-precipitating plagioclase.
2. Decreasing concentrations of Al_2O_3 and decreasing Pt/Ir ratio. This scenario is developed in the MG2B and MG3 chromitites. Conversely to the findings above, chromite seems to become depleted in Al towards the top of these layers. Additionally, the amount of co-precipitating plagioclase decreases, too. The HT-PGE thus seem to prefer chromite compositions low in Al, which is linked to the enrichment of the HT-PGE relative to the LT-PGE.
3. Increasing Al_2O_3 with contemporaneously decreasing Pt/Ir ratio is developed in the MG2C chromitite layer only. This layer is the first one occurring above the LCZ/UCZ transition. Hence, not only and Al enrichment of chromite but also increasing amounts of plagioclase towards the top of the layer is most likely. In contradiction to case 1, the chromite content in the MG2C chromitite is approximately 15-30% higher relative to the amount of silicate matrix (cf. Fig. 4.7 in subsection 4.2.1). Hence, HT-PGE precipitation is also higher, which leads to the observed enrichment of the HT-PGE relative to the LT-PGE.

4. Decreasing Al_2O_3 concentration and increasing Pt/Ir ratio is present in the MG2A and MG4A chromitite layers. Here, the depletion of chromite in Al is concluded. Additionally, and to compare with case 3, the MG2A and MG4A chromitite layers show higher amounts of silicate matrix than the MG2B and MG3 chromitites. Hence, the MG2A and MG4A chromitite layers are relatively enriched in plagioclase, which explains the enrichment of the LT-PGE relative to the HT-PGE.

Since progressive evolution of melt indicates decreasing temperatures of the melt, the temperature seems to be the major control on PGE fractionation but in dependence of melt composition, i.e. Al_2O_3 concentration.

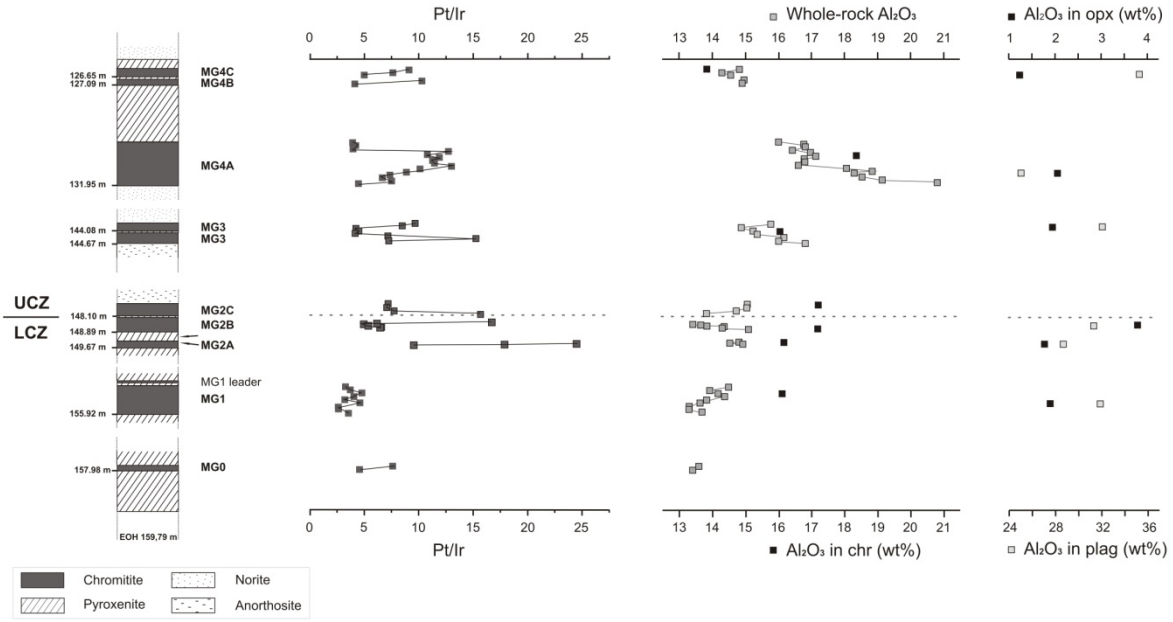

Figure 4.89 Pt/Ir ratio, the whole-rock Al_2O_3 content as well as the Al_2O_3 concentrations of chromite (chr), orthopyroxene (opx) and plagioclase (plag) in the MG chromitite layers plotted vs. the stratigraphic column.

4.4.2 The silicate layers

The silicate layers of the MG are comprised of plagioclase-bearing pyroxenite, norite and anorthosite (cf. subsections 2.3.2 and 4.2.2). From whole-rock analyses the Mg# has been calculated and together with the Al_2O_3 content plotted versus the stratigraphic column of the MG in figure 4.90.

Decreasing Mg# and increasing Al_2O_3 content in the pyroxenites below the MG1 chromitite display the precipitation of orthopyroxene that becomes Fe richer and a slightly increasing plagioclase precipitation. The decreasing Sr/Ca ratio indicates reverse fractionation of plagioclase, which is also displayed in the whole-rock Na_2O content (Tab. 4.36). Above the MG1 chromitite layer, fractional crystallization of orthopyroxene is illustrated by decreasing Mg# after a short interval of increasing Mg content. The latter can be ascribed to the influence of co-precipitating chromite at the bottom of the pyroxenitic layer, which ceases towards the top. With ceasing crystallization of chromite, plagioclase precipitation also seems to diminish, which is depicted in decreasing Al_2O_3 content. As for the MG0 pyroxenite the decreasing Sr/Ca ratio (Fig. 4.90) indicates reverse fractionation of plagioclase. This is corroborated by decreasing amounts of Na_2O as one goes from bottom to top of the layer (cf. Tab. 4.36).

Similar observations can be made for the MG2A pyroxenite, with the significant difference of increasing Sr/Ca ratio illustrating progressive evolution of plagioclase composition. The increasing Mg# at the top of the layer is ascribed to the onset of chromite precipitation, which consumes Fe^{3+} rather than Mg^{2+} and thus resulting in pyroxene becoming enriched in Mg.

Compared to data from the MG2A pyroxenite, the MG2B pyroxenite shows progressive evolution of pyroxene by decreasing Mg# as well as increasing plagioclase precipitation, since the Al_2O_3 content is higher, too. An increased Sr/Ca ratio furthermore indicates fractional crystallization of plagioclase.

A strong shift to lower Mg# and higher Al_2O_3 content can be observed at the bottom of the anorthosite in the hanging wall of the MG2C chromitite layer, which represents the first appearance of cumulus plagioclase within the MG-sequence. Fractional crystallization of orthopyroxene can be gathered from the decreasing Mg# with height. The composition of plagioclase is stable throughout the layer, since the Sr/Ca ratio doesn't show significant changes.

From the leuconorite on top of the MG3 chromitite layer to the norite of the same cyclic unit a decreasing Mg# illustrates an increasing amount of pyroxene (Fig. 4.90). Throughout the norite the Mg# only slightly increases towards the top of the layer, indicating reverse fractionation of pyroxene. The Al_2O_3 content decreases upwards the stratigraphy. The strong decline at the bottom is due to ceasing plagioclase precipitation relative to increasing precipitation of pyroxene.

The development of the Mg# in the MG4A pyroxenite shows several reversals. To picture this and for better understanding of the following remarks, figure 4.91 shows the

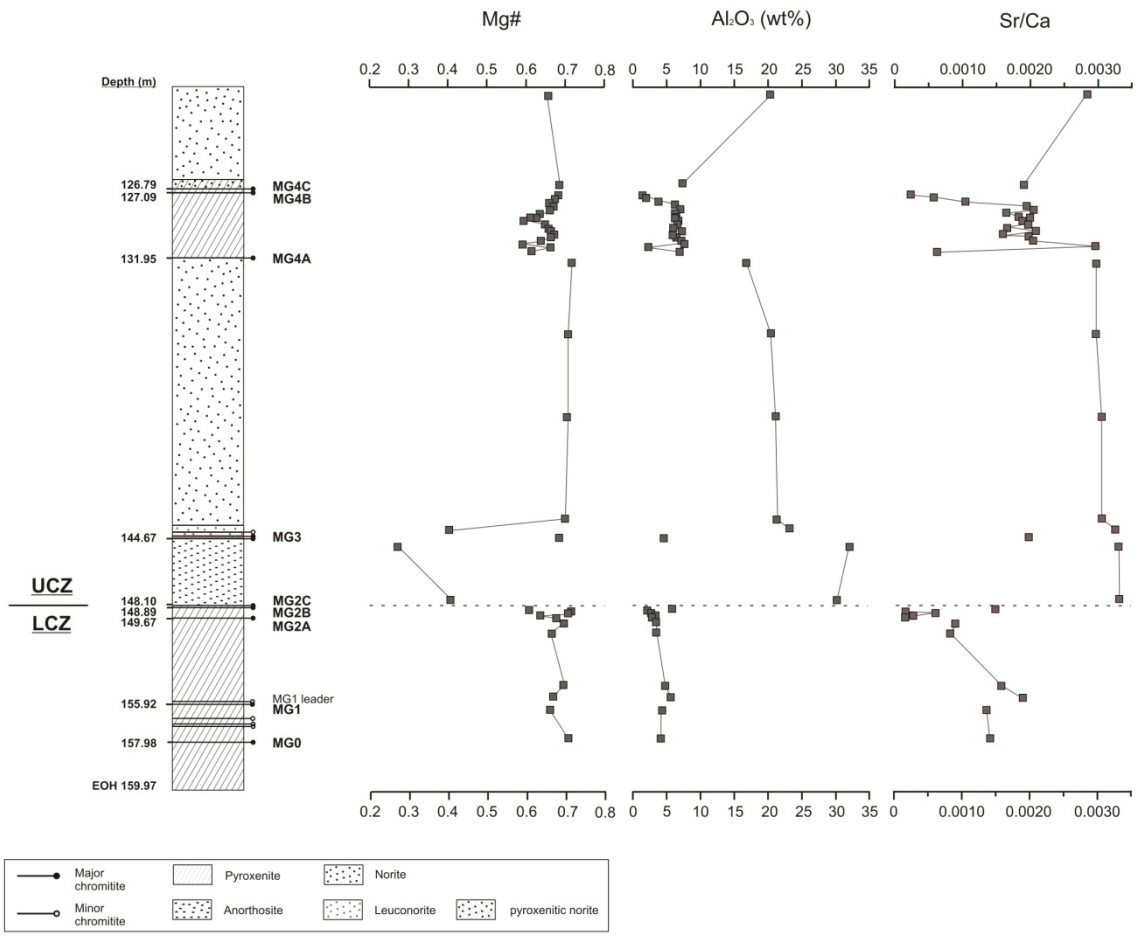

Figure 4.90 Changing whole-rock Mg# and Al_2O_3 content of the different silicate layers of the MG sequence. For illustration of melt evolution, the Sr/Ca ratio has been plotted, too. Dotted line marks the transition LCZ/UCZ. Mg#: MgO/(MgO+FeO_{tot}). Data are given in table 4.36.

development of the Mg# and the Cr_2O_3 content of the MG4A pyroxenite in detail. In the lower half the Mg# first in- and then decreases, just to increase again in the middle up to the top of the layer. By contrast, the Al_2O_3 content and the Sr/Ca ratio decrease throughout the pyroxenitic pile in a saw-tooth manner (Fig. 4.90), but a major bend to stronger declination is visible in the upper third. The lowermost samples contain high amounts of cumulus chromite, which becomes less up to the point, where the first reversal in the Mg# is visible. It again corroborates that the co-precipitation of chromite besides orthopyroxene accounts for the paucity of Fe within the orthopyroxene lattice resulting in increasing Mg# with height. The further decreasing tenor of the Mg# can be correlated with increasing amounts of chromite up to 2/3 of the MG4A pyroxenite. This suggests that the crystallization path in the ternary diagram forsterite-quartz-chromite generally lies upon the cotectic chromite-orthopyroxene. Decreasing Al_2O_3 concentrations and declining Sr/Ca ratio up to this level point to reversed plagioclase crystallization. The declination

Table 4.36 Whole-rock geochemistry of the silicate layers of the MG-sequence obtained from XRF analyses. Sulphur content for some of the samples has been determined with the Eltra CS 800 double dual range. *N.a.:* not analysed. *Total Fe is given in FeO. *Px*: pyroxenite; *no*: norite; *an*: anorthosite; *le-no*: leuconorite; *px-no*: pyroxenitic norite. Major element oxides in wt%.

sample	**JKL22**	**JKL21**	**JKL27**	**JKL28**	**JKL29**	**JKL30**	**JKL31**	**JKL32**	**JKL33**	**JKL34**	**JKL35**	**JKL36**	**JKL37**	**JKL38**
lithology	no	px no	px	px	px	px	px	px	px	px	px	px	px	px
cyclic unit	MG4C	MG4C	MG4A	MG4A	MG4A	MG4A	MG4A	MG4A	MG4A	MG4A	MG4A	MG4A	MG4A	MG4A
SiO_2	51.18	54.14	52.03	52.85	51.06	50.82	49.66	43.66	41.93	39.40	35.01	44.60	48.53	50.33
TiO_2	0.11	0.19	0.32	0.30	0.30	0.26	0.24	0.35	0.36	0.39	0.44	0.30	0.30	0.23
Al_2O_3	20.25	7.39	1.46	2.00	3.73	6.25	7.07	6.15	6.41	6.37	6.70	6.48	5.97	7.30
Cr_2O_3	0	1.03	4.24	4.07	5.14	4.89	5.67	13.26	15.33	19.19	24.67	11.54	8.20	4.80
FeO*	5.93	10.56	12.39	12.44	11.60	11.30	10.84	11.18	11.42	11.57	11.55	10.73	11.19	10.72
MnO	0.11	0.21	0.24	0.23	0.22	0.21	0.20	0.20	0.20	0.21	0.19	0.19	0.21	0.20
MgO	11.51	23.07	26.48	25.78	22.49	22.59	21.30	19.66	19.32	18.08	16.69	19.81	21.45	21.15
CaO	10.92	4.87	2.18	2.30	3.97	3.78	4.19	4.07	3.53	3.37	3.34	3.90	4.74	4.48
Na_2O	0.90	0.25	0	0.02	0.08	0.22	0.28	0.20	0.17	0.13	0.11	0.16	0.14	0.25
K_2O	0	0	0.06	0.08	0.11	0.02	0	0	0	0	0	0	0	0
P_2O_5	0.01	0	0	0.01	0.01	0	0	0	0	0	0	0.01	0.01	0.01
total	101.58	102.87	100.77	101.46	100	101.60	100.66	99.96	99.95	100	100	98.92	101.98	100.67
Trace elements (ppm)														
V	76.989	136.021	203.427	216.495	234.508	221.874	245.024	443.665	477.137	543.406	729.010	394.378	300.661	224.324
Co	39.459	80.094	92.140	91.374	80.198	82.268	82.423	93.081	83.293	89.670	98.397	87.324	79.435	73.753
Ni	224.981	526.959	616.775	621.043	532.835	519.351	508.656	535.300	529.987	532.062	565.435	532.467	476.412	465.608
Cu	23.441	26.927	34.641	32.145	30.819	35.149	39.574	37.262	33.215	29.883	38.802	32.077	30.449	36.628
Zn	33.075	65.386	74.838	74.468	68.008	75.548	77.703	95.743	96.053	102.719	131.307	89.478	74.237	72.709
Ga	17.332	8.070	5.314	4.631	6.603	8.509	8.662	11.939	12.243	14.124	16.280	11.236	9.372	9.061
S	n.a.	30	156	n.a.	79	n.a.	33	n.a.	n.a.	n.a.	65	n.a.	40	n.a.
Selected ratios														
Mg#	0.660	0.686	0.681	0.675	0.660	0.667	0.663	0.638	0.628	0.610	0.591	0.649	0.657	0.664
Ca/Sr	0.003	0.002	0.000	0.001	0.001	0.002	0.002	0.002	0.002	0.002	0.002	0.002	0.002	0.002
Cu/S	n.a.	0.898	0.222	n.a.	0.390	n.a.	1.199	n.a.	n.a.	n.a.	0.597	n.a.	0.761	n.a.

Table 4.36 (cont.)

sample	**JKL39**	**JKL40**	**JKL41**	**JKL42**	**JKL19**	**JKL18**	**JKL17**	**JKL16**	**JKL15**	**JKL14**	**JKL26**	**JKL13**	**JKL12**	**JKL25**
lithology	px	px	px	px	px	no	no	no	no	le no	px	an	an	px
cyclic unit	MG4A	MG4A	MG4A	MG4A	MG4A	MG3	MG4	MG5	MG6	MG7	MG3 inter	MG2C	MG2C	MG2B
SiO_2	51.28	49.98	44.16	35.88	34.36	53.01	52.38	52.23	51.87	36.60	44.53	50.23	47.55	30.90
TiO_2	0.29	0.30	0.34	0.41	0.31	0.12	0.11	0.11	0.10	0.23	0.20	0.10	0.12	0.31
Al_2O_3	5.88	6.29	7.18	7.64	6.92	16.81	20.39	21.10	21.35	23.11	4.55	32.00	30.26	5.80
Cr_2O_3	4.57	5.57	11.17	23.44	28.00	0.62	0.18	0.51	0.92	18.94	13.50	0.13	3.80	31.60
FeO*	10.59	11.10	10.95	11.32	9.99	6.16	5.00	4.90	4.82	5.60	9.98	1.10	2.13	10.98
MnO	0.20	0.20	0.19	0.18	0.17	0.12	0.10	0.10	0.09	0.08	0.19	0.02	0.03	0.17
MgO	21.61	21.25	19.27	16.40	15.91	15.73	11.99	11.46	11.36	3.77	21.93	0.42	1.45	17.12
CaO	4.77	4.13	4.34	3.19	2.94	8.49	10.29	10.58	10.61	10.16	2.40	15.38	14.29	1.77
Na_2O	0.25	0.28	0.30	0.28	0.27	0.53	0.80	0.72	0.82	0.77	0.26	1.24	1.26	0.07
K_2O	0.04	0.04	0	0.01	0	0.02	0.04	0.04	0.03	0.11	0.01	0.25	0.84	0
P_2O_5	0	0	0.01	0	0.01	0	0.01	0.01	0.01	0.01	0.10	0.02	0.01	0.05
total	100.67	100.38	99.13	100	100	102.29	101.84	102.30	102.51	100	98.75	101.00	101.98	100.00
Trace elements (ppm)														
V	243.613	260.877	418.535	755.798	809.084	78.499	60.947	67.600	65.962	499.164	346.042	33.720	105.901	946.062
Co	78.881	80.328	76.861	97.651	98.515	45.717	35.772	36.286	35.036	39.037	90.211	3.271	8.387	104.957
Ni	482.437	483.569	483.547	579.914	659.447	282.412	219.328	211.280	202.911	189.514	585.027	17.783	44.242	738.916
Cu	33.885	52.304	89.855	93.988	70.630	34.971	31.309	28.627	29.101	45.432	47.152	30.921	30.179	61.976
Zn	69.644	73.719	84.799	139.932	136.056	30.988	25.653	24.697	24.668	68.736	78.663	1.352	9.323	149.275
Ga	8.207	7.786	11.098	15.561	17.643	12.762	15.667	16.744	16.362	29.655	8.836	22.650	23.588	15.558
S	17	n.a.	n.a.	n.a.	84	56	n.a.	n.a.	36	n.a.	214	n.a.	57	326
Selected ratios														
Mg#	0.671	0.657	0.638	0.592	0.614	0.719	0.706	0.700	0.702	0.402	0.687	0.275	0.405	0.609
Ca/Sr	0.002	0.002	0.002	0.002	0.002	0.003	0.003	0.003	0.003	0.003	0.002	0.003	0.003	0.002
Cu/S	1.993	n.a.	n.a.	n.a.	0.841	0.624	n.a.	n.a.	0.808	n.a.	0.220	n.a.	0.529	0.190

Table 4.36 (cont.)

sample	**JKL11**	**JKL24**	**JKL23**	**JKL10**	**JKL9**	**JKL8**	**JKL7**	**JKL6**	**JKL5**	**JKL4**
lithology	px	px	px	px	px	px	px	px	px	px
cyclic unit	MG2A	MG2A	MG2A	MG2A	MG1	MG1	MG1	MG1	MG0	MG0
SiO_2	51,94	48.88	42.11	33.87	44.56	43.35	51.80	42.62	36.09	50.83
TiO_2	0.18	0.19	0.23	0.26	0.16	0.25	0.20	0.20	0.22	0.23
Al_2O_3	1.99	2.67	2.72	3.33	3.50	3.35	4.63	5.65	4.23	4.03
Cr_2O_3	5.47	8.87	16.53	28.95	12.57	14.70	4.93	16.43	27.55	6.86
FeO*	10.60	10.82	11.06	11.55	10.32	11.68	10.78	10.13	9.63	10.45
MnO	0.20	0.22	0.21	0.20	0.21	0.22	0.21	0.20	0.18	0.21
MgO	27.05	25.83	23.37	20.05	23.84	23.22	24.48	20.65	18.93	24.76
CaO	1.80	1.92	1.48	1.15	2.49	1.93	3.08	2.68	1.59	2.98
Na_2O	0	0.02	0	0	0	0	0.18	0.30	0.16	0.21
K_2O	0.03	0	0	0	0	0	0.01	0	0.33	0.04
P_2O_5	0.01	0	0	0	0	0	0.03	0	0.01	0
total	100.45	100.61	98.96	100.65	98.79	100	101.54	100	100	101.76
Trace elements (ppm)										
V	200.331	273.333	469.112	922.651	330.880	402.439	200.254	413.581	671.849	214.673
Co	89.028	90.022	97.253	119.082	88.806	100.177	82.993	84.817	97.250	80.029
Ni	626.320	617.927	646.459	740.217	580.068	635.837	506.326	561.696	721.751	511.532
Cu	27.306	32.311	29.598	40.309	29.700	32.596	41.255	48.617	102.930	48.285
Zn	56.402	72.413	97.440	152.582	85.283	107.105	76.621	84.405	118.405	68.440
Ga	3.911	6.085	8.322	13.310	6.642	9.535	6.703	11.168	11.465	7.006
S	n.a.	35	12	n.a.	n.a.	38	91	n.a.	n.a.	781
Selected ratios										
Mg#	0.719	0.705	0.635	0.679	0.698	0.665	0.694	0.671	0.663	0.703
Ca/Sr	0.000	0.001	0.000	0.000	0.001	0.001	0.002	0.002	0.001	0.001
Cu/S	n.a.	0.923	2.467	n.a.	n.a.	0.858	0.453	n.a.	n.a.	0.062

becomes even stronger in the upper third concordantly with increasing Mg#, which again substantiates reverse crystallization.

The first 'real' sequence of fractional crystallization can be obtained from the MG4C cyclic unit developed in the MG sequence: not only from the lithology, i.e. chromitite-pyroxenite-norite, but also from the geochemistry. The latter shows decreasing Mg#, increasing Al_2O_3 concentrations and increasing values of the Sr/Ca ratio, which are all indications for progressive melt evolution.

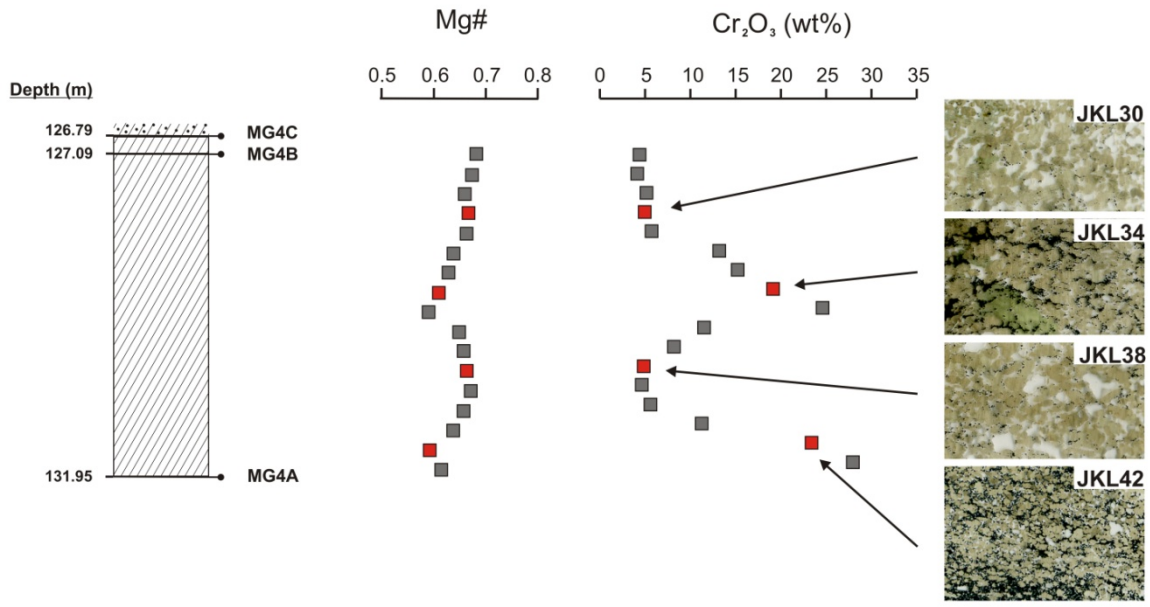

Figure 4.91 Detail of the development with height of the Mg# as well as the Cr_2O_3 content of the plagioclase-bearing MG4A pyroxenite. To emphasize the chromite control on whole-rock Mg#, pictures of scanned thin sections have been added, which stratigraphic positions are indicated by red squares. Legend as in figure 4.90. Data are given in table 4.36.

As a conclusion one can say that reversed crystallization trends are caused by co-precipitating chromite changing the major geochemistry of orthopyroxene as well as plagioclase. To illustrate this, the Cr_2O_3 concentration of the silicate layers has been plotted versus the stratigraphy of the MG sequence (Fig. 4.92). As one can see the Cr_2O_3 content decreases contemporaneously with increasing Mg# (cf. Fig. 4.90).

Figure 4.92 furthermore shows the development of the whole-rock concentrations of TiO_2, V, Ga, Co, Zn and Ni. When the rock types are compared with regard to their absolute amounts of these elements it is obvious that the most primitive one, i.e. the pyroxenites, hosts the highest concentrations. Ga concentrations exactly follow the trend of the Cr_2O_3 concentration, suggesting a chromite control due to relative incompatibility in

silicate minerals. It is most probably incorporated into the chromite lattice. The same applies for Co, Zn and Ni. There seems to be a chromite control for V and TiO_2, too. Although relatively incompatible in the chromite lattice (cf. subsection 4.3.1) they are even more incompatible into silicate minerals, thus concentrating in chromite grains.

The Cu values in the silicate layers are low and range between 23.4 and 102.9 ppm. Most of them (70%) fall between 23.4 and 40 ppm (Fig. 4.93), which is interpreted to represent background values. The remaining 30% of the samples are slightly enriched in Cu. In most cases, this enrichment occurs at the direct contact to the underlying massive chromitite layer. An exception are analyses of samples from the pyroxenite of the MG0 unit both showing Cu enrichment. If one consults the development of the Cr_2O_3 concentration from figure 4.93 one can see that high Cu levels generally coincide with high Cr_2O_3 contents. A bivariate plot presented in figure 4.94A shows moderate positive correlation and thus further proves this relationship. Although coincidence of positive peaks between Cr_2O_3 and Cu at the bottom of the pyroxenitic silicate layers exist, the same is lacking for the norite or the anorthosite, respectively.

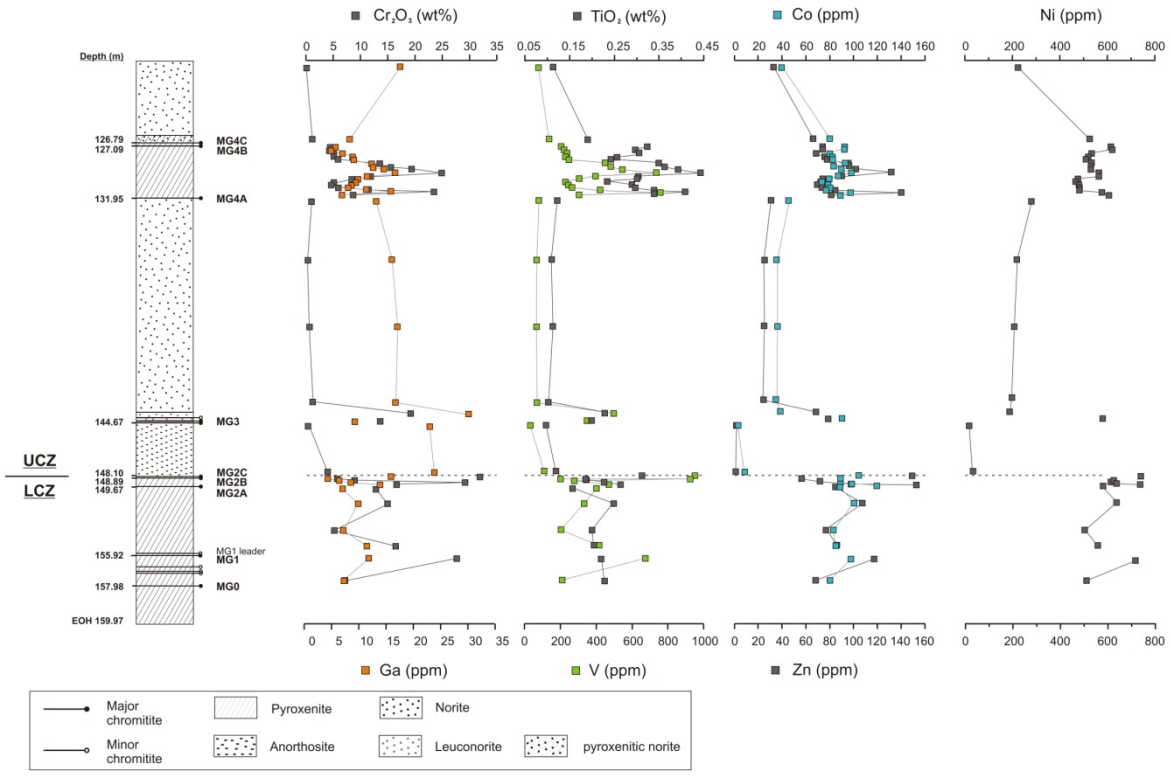

Figure 4.93 Whole-rock Cr_2O_3 and TiO_2 contents as well as whole-rock concentrations of various trace elements plotted versus the stratigraphic column of the MG sequence. Data are given in table 4.36.

The S content of the silicate layers ranges between 12 and 781 ppm (Tab. 4.36) with background values between 12 and 100 ppm. When compared to S contents of the chromitite layers, the silicate layers are enriched in S (cf. subsection 4.4.1). On the other hand, the Cu concentrations in the silicate layers are much lower than those found for the MG chromitites (cf. subsection 4.4.1). Although no BMS could have been detected under the microscope, the Cu/S ratio of the silicates is below the one for chalcopyrite (2:1), which indicates a general excess of sulphur relative to Cu (Tab. 4.36). It could be taken as evidence for S enrichment in the silicate layers due to postcumulus loss of S of the chromitite layers, as has been suggested by several authors (Gain, 1985; von Gruenewaldt *et al.*, 1986; Naldrett *et al.*, 1987). The S profile in figure 4.93 shows that at least at the bottom of the MG1, MG2B and MG4A pyroxenites S enrichment occurs, whereas such enrichment at the bottom of the noritic or anorthositic layers is missing. However, the S enrichment at the bottom of the pyroxenitic layers correlates with Cu enrichment and the positive correlation suggest the presence of chalcopyrite (Fig. 4.94B).

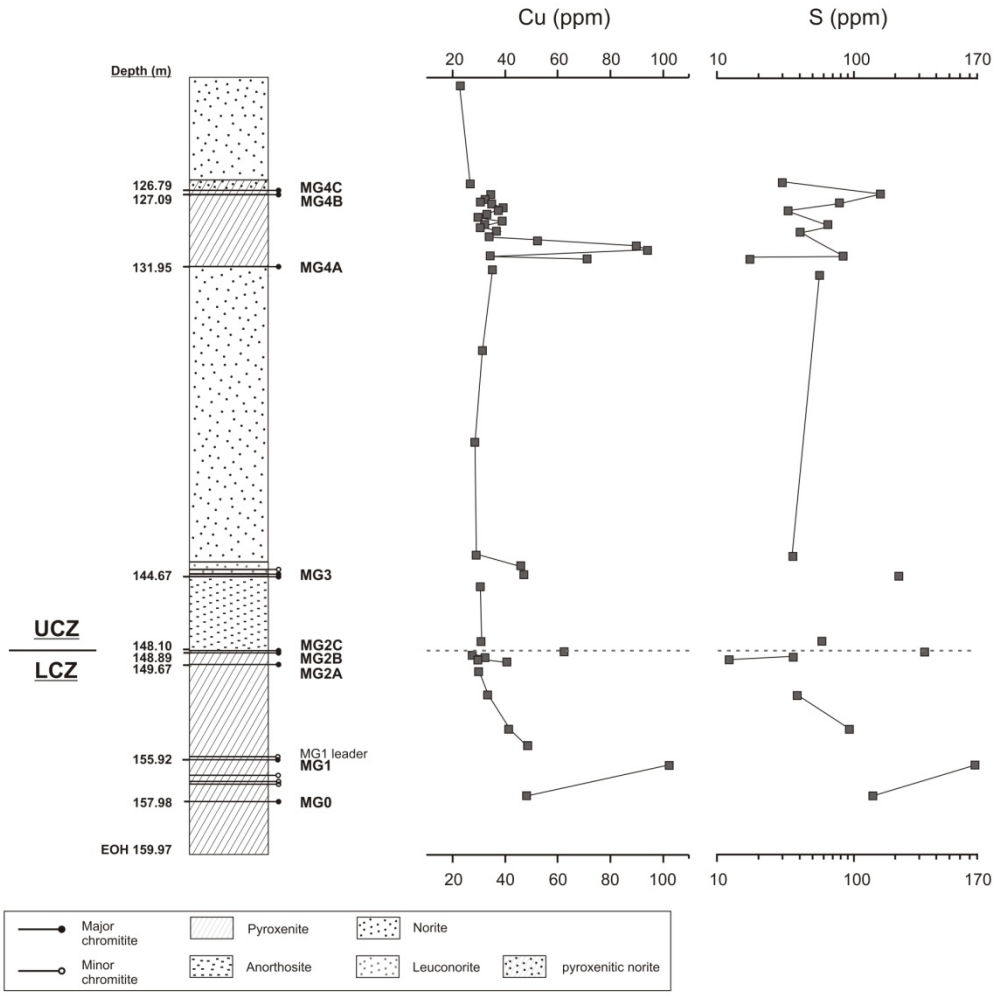

Figure 4.93 Development of Cu concentration as well as the S content of selected samples plotted versus the stratigraphic column of the MG sequence. Data are given in table 4.36.

The negative Rb anomaly presented in the multi-element C1 normalized “spider” diagram (Fig. 4.95) generally coincides with elevated Sr concentrations. The plagioclase-bearing pyroxenites of the UCZ are more enriched in Sr than the pyroxenites from the LCZ indicating higher amounts of plagioclase.

Although positive Ta peaks exist, the lack of positive Ti peaks rules out rutile control. In connection with the negative Nb anomalies this could indicate an involvement of continental crust in magma processes as have been suggested by several authors on the basis of $^{87}Sr/^{86}Sr$ ratio (Kruger, 1994; Kinnaird *et al.*, 2002) or $^{187}Os/^{188}Os$ ratio, respectively (McCandless *et al.*, 1999; Schoenberg *et al.*, 1999) for the chromitite layers.

Coincidently with findings for the chromitite layers the strong negative P peaks illustrate the lack of apatite, thus suggesting the plagioclases to be the major host for the REE.

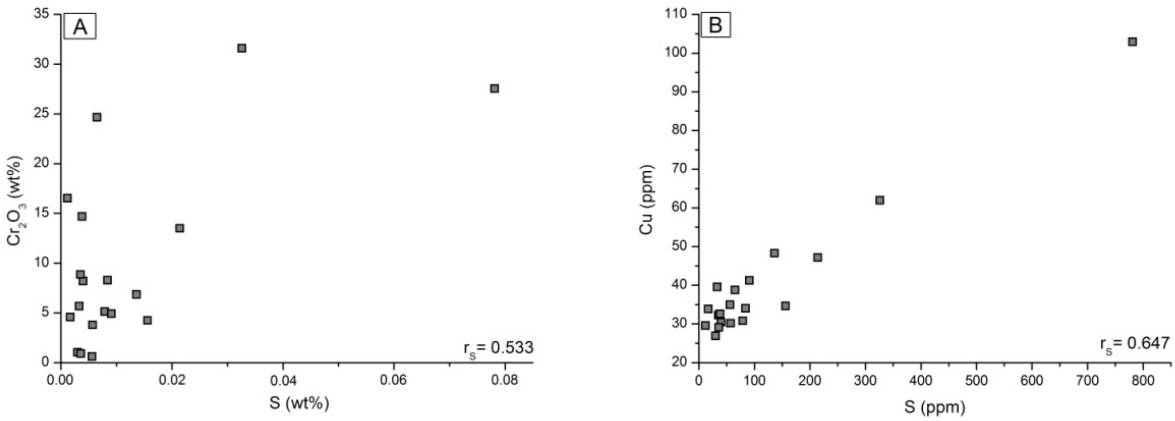

Figure 4.94 Moderate or strong positive correlation of **(A)** the Cr_2O_3 and **(B)** the Cu contents versus S concentrations of the silicate layers of the MG sequence. Data are given in table 4.36. r_S= Spearman rank correlation coefficient.

From the Harker plots in figure 4.96 one perfectly can geochemically discriminate between pyroxenitic and noritic or anorthositic rocks, respectively. This is the reason, why Spearman rank correlation coefficients on whole-rock data in a few cases are so low, although within the pyroxenites medium to strong correlations are visible. The observed changes in the pyroxenite of the MG4A unit are due to changing amounts of chromite within the pyroxenite (cf. Tab 4.36). According to the XRF analyses presented in table 4.36 one can identify three intervals, which already could be shown in figure 4.91.

Table 4.37 Chondrite normalized data for multi-element diagram (in ppm) gathered with XRF analyses. *Values are averages from the layer. Normalizing values from Lodders (2003).

	MG4C	MG4C	MG4A*	MG3*	MG3	MG3	MG2C*	MG2B	MG2A*	MG1*	MG0*
rock type	no	px_no	px	no	le_no	px	an	px	px	px	px
Ba	19.13	20.52	17.72	20.71	57.06	29.88	82.02	2.36	6.32	14.04	71.61
Rb	1.07	1.06	2.37	1.29	2.48	3.98	8.64	0.31	1.97	1.77	8.16
Th	258.41	273.56	293.10	245.87	256.02	325.53	196.94	9092.91	294.45	295.37	277.39
Nb	7.68	10.03	12.91	11.84	10.73	17.69	10.74	36.87	13.50	12.86	15.22
Ta	500.97	400.69	400.32	352.83	164.58	165.49	212.01	45876.74	405.42	400.03	601.74
La	0	0	0	0	0	0	0	0	0	0	0
Ce	0	0	0	0	0	0	0	0	0	0	0
Sr	42.77	13.82	10.71	40.16	50.12	8.74	60.58	2.00	0.83	5.67	5.62
Nd	0	0	0	0	0	0	0	0	0	0	0
P	0.02	0.01	0.02	0.03	0.04	0.47	0.07	0.00	0.01	0.04	0.02
Sm	0	0	0	0	0	0	0	0	0	0	0
Zr	0.64	3.28	2.90	1.60	2.21	2.76	2.33	0.27	2.46	1.89	7.45
Hf	0	0.65	15.07	6.54	0	7.17	20.06	276.07	13.18	3.95	34.68
Ti	2.17	4.30	9.08	2.23	5.27	6.24	2.17	0.03	6.22	5.46	6.75
Tb	0	0	0	0	0	0	0	0	0	0	0
Y	1.05	2.23	3.56	1.61	2.03	9.92	1.62	1.62	3.74	3.14	5.15
Tm	0	0	0	0	0	0	0	0	0	0	0
Yb	0	0	0	0	0	0	0	0	0	0	0

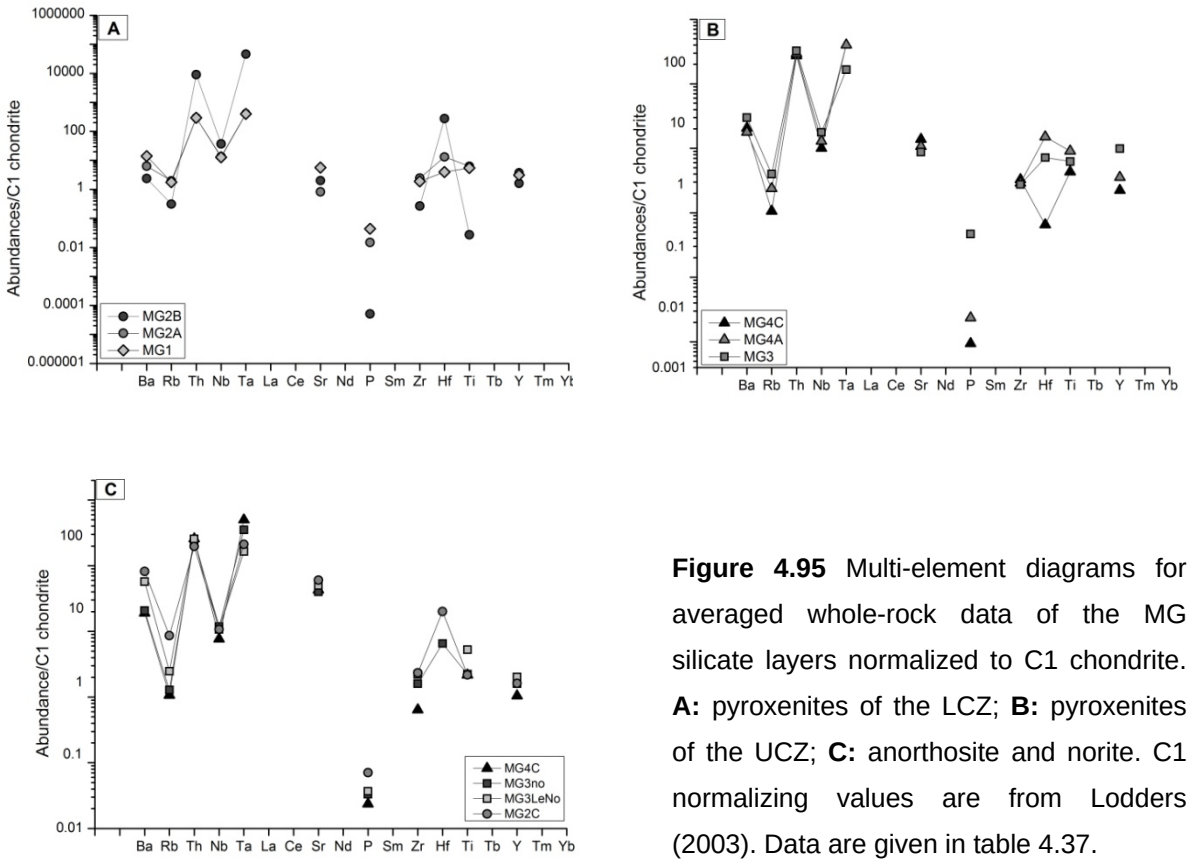

Figure 4.95 Multi-element diagrams for averaged whole-rock data of the MG silicate layers normalized to C1 chondrite. **A:** pyroxenites of the LCZ; **B:** pyroxenites of the UCZ; **C:** anorthosite and norite. C1 normalizing values are from Lodders (2003). Data are given in table 4.37.

The intervals are (from bottom to top of the MG4A pyroxenite):

1) From JKL19 – JKL39
2) From JKL38 – JKL35
3) From JKL34 – JKL27.

The division on the basis of the Cr_2O_3 content has been done, since chromite is the first cumulus mineral that starts to precipitate and therefore strongly influences the composition of the other minerals crystallizing after or with chromite.

MgO vs. SiO_2: With respect to geochemical analyses (cf. Tab. 4.36) the SiO_2 content within the pyroxenitic layers increases from bottom to top and also within the stratigraphic column of the MG sequence. Furthermore, at the bottom of each pyroxenitic layer the MgO content is reset to lower concentrations than have been present at the bottom of the pyroxenitic layer below. In the MG1 and MG2A pyroxenites as well as in the lower and upper third of the plagioclase-bearing MG4A pyroxenite the MgO content increases contemporaneously with increasing SiO_2. Since the Mg# of orthopyroxene in the MG1 pyroxenite yielded by SEM-EDX analyses decreases from bottom to top (cf. Fig. 4.44 in subsection 4.3.6), this feature is simply caused by decreasing chromite precipitation (cf. Cr_2O_3 contents of the pyroxenitic layers in Tab. 4.36). For the MG2A pyroxenite only one value for Mg# of orthopyroxene is available and hence no distinctive statement concerning the fractionation trend of orthopyroxene is feasible.

A different picture can be deduced from the intervals in the plagioclase-bearing MG4A pyroxenite showing increasing amounts of MgO. Here, the Mg# of orthopyroxene contemporaneously increases, which indicates reverse fractional crystallization of orthopyroxene.

From the leuconorite to the norite on top of the MG3 chromitite layer increasing SiO_2 concentration is accompanied by increasing MgO content, indicating increasing amounts of orthopyroxene as well as progressive evolution of the melt both layers derive from. This feature can be followed further up to the top of the noritic layer, although a slightly increasing Mg# of orthopyroxene (cf. Fig. 4.44 in subsection 4.3.6) rather indicates a reverse fractionation trend for orthopyroxene.

Real progressive evolution can be deduced from the anorthosites of the MG2C cyclic unit, since with increasing SiO_2 content the amount of MgO within this layer decreases (also cf. Tab. 4.36).

MgO vs. TiO_2: For the pyroxenitic rocks a negative linear relation is visible. Except for the middle part of the plagioclase-bearing MG4A pyroxenite, where increasing TiO_2 and decreasing MgO point to progressive melt evolution, the other (parts of the) pyroxenitic layers rather show a reverse fractional crystallization trend, if one takes increasing

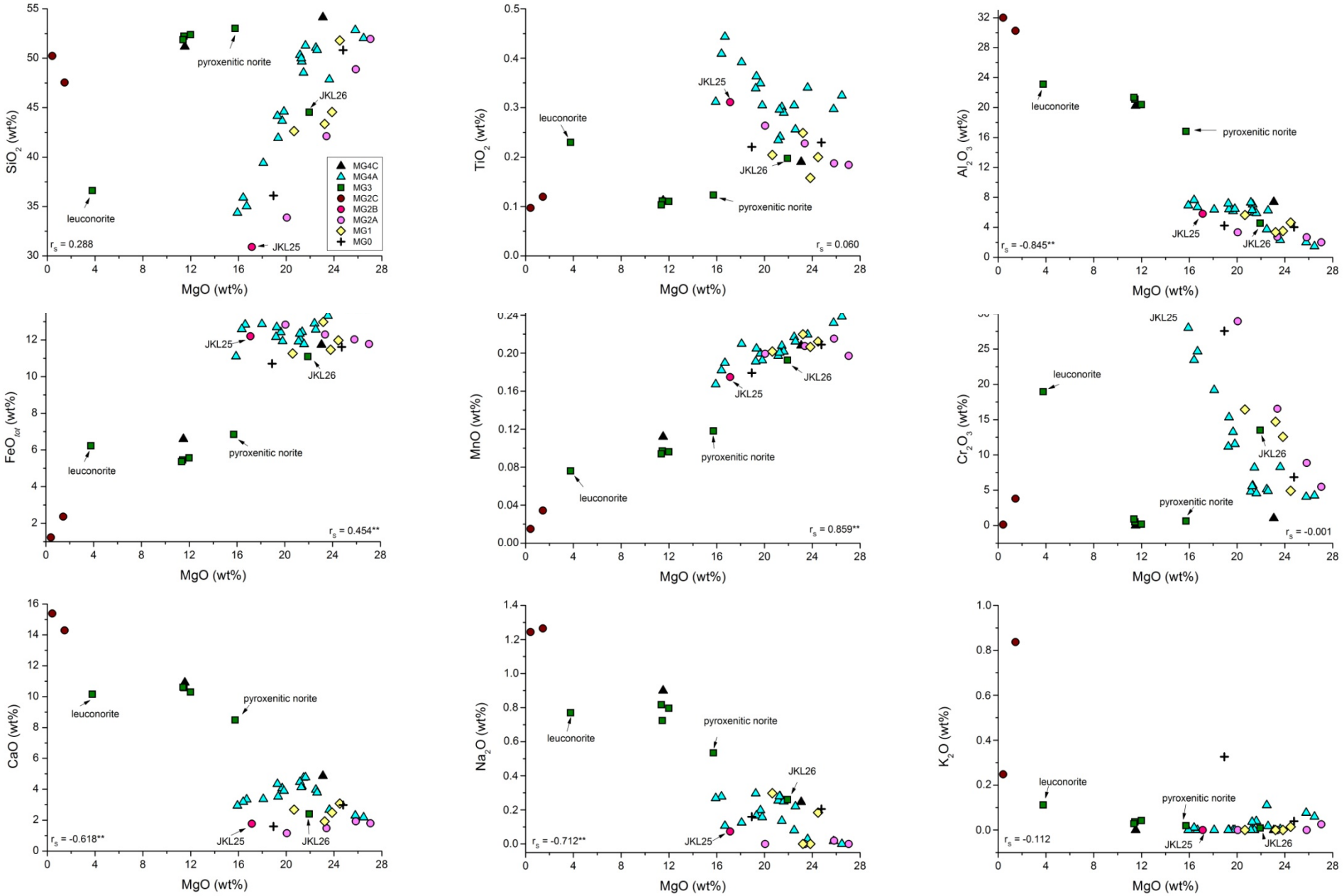

Figure 4.96 Harker plot of the major element oxides of gathered form whole-rock analyses of the silicate layers related to stratigraphy of the MG sequence. r_S = Spearman rank correlation coefficient. **Correlation is significant at the 0.01 level. Data are given in table 4.35.

amounts of TiO_2 as a precursor for progressive melt evolution. However, as have been shown before (Fig. 4.92 and corresponding text), the amount of whole-rock TiO_2 in the silicate layers is controlled by chromite. Thus, the amount of TiO_2 just mirrors the amount of Cr_2O_3 (cf. Tab. 4.36) within the pyroxenites of the MG sequence.

Similar to the pyroxenitic layers, the decreasing TiO_2 concentration from the MG3 leuconorite to norite doesn't reflect decreasing melt evolution (which just have been shown with increasing SiO_2), but rather is linked to decreasing amounts of chromite due to compatibility reasons. In the MG3 norite the TiO_2 content increases independently from the Cr_2O_3 concentration, which is low. Hence, it can be considered to show increasing melt evolution although an increasing Mg# of orthopyroxene exists.

Decreasing TiO_2 in the MG2C anorthosite is linked to decreasing MgO. Since it is linked to decreasing Cr_2O_3 contents as well, chromite control can be considered to be most likely for this feature.

MgO vs. Al_2O_3: A negative linear correlation exists for the pyroxenites. In those of the LCZ Al_2O_3 decreases from bottom to top of each layer with increasing MgO, which is caused by decreasing chromite precipitation consuming less Al as well as decreasing amounts of intercumulus plagioclase within these layers. For the plagioclase-bearing MG4A pyroxenite in the UCZ decreasing Al_2O_3 contents are visible within all the intervals. In the first and the third contemporaneously increasing MgO content indicates decreasing rates of chromite precipitation as well as increasing amounts of orthopyroxene. In the second interval the link with contemporaneously decreasing MgO can be interpreted to show increasing portions of chromite and decreasing amounts of orthopyroxene. The decreasing Mg# of orthopyroxene within this interval points to progressive fractional crystallization during formation of orthopyroxene, whereas for the first and the third interval in each case the Mg# of orthopyroxene increases (cf. Fig. 4.44 in subsection 4.3.6) indicating reverse fractionation.

Decreasing amounts of chromite can also be deduced from decreasing Al_2O_3 concentrations, if one goes from MG3 leuconorite to norite. It is accompanied by increasing amounts of orthopyroxene. Towards the top of the noritic layer, the Al_2O_3 content, and therefore the amount of chromite, further decreases, whereas the amount of orthopyroxene is advancing.

Contemporaneously with decreasing MgO the Al_2O_3 content increases within the anorthosite in the hanging wall of the MG2C chromitite, which points to increasing precipitation of plagioclase and decreasing amounts of orthopyroxene.

MgO vs. FeO_{tot}: The total amount of Fe is influenced by the crystallization of chromite, ortho- and clinopyroxene. The general trend for the pyroxenites visible in figure 4.96 is positive linear. This general trend with increasing MgO and FeO_{tot} content is

present in the in the MG1 pyroxenite as well as within the first and third intervals of the plagioclase-bearing MG4A pyroxenite. This trend implies increasing amounts of orthopyroxene within these layers. By means of the $Mg\#_{opx}$ the former derives from fractional crystallization, whereas for both the latter reverse fractionation is indicated (cf. Fig. 4.44 in subsection 4.3.6). As have been mentioned before, this is caused by different rates of chromite precipitation.

The MG2A pyroxenite shows increasing MgO but decreasing FeO_{tot}, caused by increasing precipitation of orthopyroxene but decreasing amounts of chromite within the layer. In the second interval of the MG4A pyroxenite increasing amounts of chromite and decreasing portions of orthopyroxene are reflected in a positive inverse linear trend. Additionally, the progressive evolution of orthopyroxene composition as deduced from the $Mg\#_{opx}$ (cf. Fig. 4.44 in subsection 4.3.6) further increases the total Fe concentration relative to MgO.

As is shown in figure 4.96, the FeO_{tot} content slightly decreases from the leuconoritic to the noritic layer in the MG3 cyclic unit, contemporaneously with increasing MgO. This is due to the strongly decreasing amounts of chromite. Due to the $Mg\#_{opx}$ (cf. Fig. 4.44 in subsection 4.3.6) the orthopyroxene composition in the norite is of more evolved composition than those occurring in the leuconorite. On the other hand, there are simultaneously increasing FeO_{tot} and MgO amounts within the noritic layer, resulting in a slightly increasing Mg# of orthopyroxene (cf. Fig. 4.44 in subsection 4.3.6), which indicates a gentle reverse fractionation trend for orthopyroxene.

The negative inverse linear trend observed for the MG2C anorthosite reflects decreasing amounts of orthopyroxene as well as chromite from the bottom to the top of this layer.

MgO vs. MnO: As is shown in figure 4.96, the major trend for this relation in the pyroxenite is positive linear with contemporaneously increasing amounts of MgO and MnO. Due to its valence Mn^{2+} generally substitutes for Fe^{2+} or Mg^{2+}, which can be in the pyroxene and the chromite lattice. Except for the second interval of the plagioclase-bearing MG4A pyroxenite, in all the other pyroxenitic layers and intervals rising amounts of orthopyroxene with stratigraphy is present. In the middle of the MG4A pyroxenite decreasing MnO is accompanied by decreasing MgO. Hence it can be concluded that the MnO content of the pyroxenitic layers is controlled by orthopyroxene only.

From the leuconoritic layer up to the lowermost part of the MG3 norite MgO and MnO contents increase simultaneously, caused by increasing amounts of orthopyroxene. As have been mentioned before, Mn^{2+} substitutes for Mg^{2+} within the orthopyroxene lattice. Towards the top of the noritic layer, the orthopyroxene content further increases showing advancing contents of MnO.

The amounts of MgO and MnO decrease simultaneously, which is caused by decreasing orthopyroxene contents towards the top of the MG2C anorthosite.

MgO vs. Cr_2O_3: In the pyroxenitic layers a negative correlation between the two major element oxides exists (Fig. 4.96). The direction of the trend differs according to variations in the amount of chromite and orthopyroxene. It is negative linear in the MG1, MG2A and the lower and upper intervals of the MG4A pyroxenites. It is interpreted to represent the shift of the crystallization path away from the chromite field onto the orthopyroxene-plagioclase cotectic.

In the second interval of the plagioclase-bearing MG4A pyroxenite increasing Cr_2O_3 content is accompanied by decreasing amounts of whole-rock MgO. Thus, there must have been an event causing chromite precipitation, but not the formation of a massive chromitite layer.

A strong decrease in its Cr_2O_3 content is present in the transition from MG3 leuconorite to MG3 norite, which is only caused by decreasing amounts of cumulus chromite (cf. Point Count analyses; Tab. B-1 in appendix B). This feature can be followed up to the top of the MG3 norite, although the declination is less pronounced.

Similar to the relation MgO-FeO_{tot} for the MG2C anorthosite, the negatively inverse linear trend existing between MgO and Cr_2O_3 is interpreted to be caused by contemporaneously decreasing amounts of orthopyroxene as well as chromite.

MgO vs. CaO: CaO is mainly controlled by plagioclase and to a minor extend by the crystallization of clinopyroxene, which is depicted in the buckshot-like distribution in Fig. 4.96. However, the individual layers show distinctive trends.

According to the CIPW norm calculation for samples from the MG1 pyroxenite (cf. Tab. B-2 in appendix B) the amount of plagioclase decreases from bottom to top of the layer, but the clinopyroxene content rather increases. This would explain the varying CaO concentrations within this layer. According to the %An of individual plagioclase grains obtained by SEM-EDX (cf. Fig. 4.44 in subsection 4.3.6) progressive evolution of plagioclase composition is present.

Contemporaneously with increasing MgO the CaO content increases within the MG2A pyroxenite, indicating an increase in orthopyroxene as well as plagioclase precipitation. CIPW norm calculation for this layer (cf. Tab. B-2 in appendix B) suggests decreasing amounts of plagioclase towards the top of the layer, but slightly increasing contents of clinopyroxene. In connection with an increasing Sr/Ca ratio (cf. Fig. 4.90) pointing to progressive fractionation of the plagioclases, the latter scenario seems to be more likely.

The data points of the samples from the plagioclase-bearing MG4A pyroxenite generally show a positive linear trend, i.e. increasing MgO and CaO, indicating increasing

amounts of plagioclase as well as orthopyroxene. This is true for the first and third intervals, but increasing clinopyroxene precipitation cannot be excluded. As depicted by decreasing %An (cf. Fig. 4.44 in subsection 4.3.6) plagioclase derives from progressive fractional crystallization. In the second interval the amounts of CaO as well as MgO are decreasing, which can be interpreted to reflect decreasing amounts of orthopyroxene as well as plagioclase.

The CaO content only slightly increases from the leuconorite to the norite in the hanging wall of the MG3 chromitite (Fig. 4.96) indicating increasing amounts of cumulus plagioclase. An increase in the %An (cf. Fig. 4.44 in subsection 4.3.6) illustrates reverse fractionation.

Although the amount of CaO is declining within the norite, a decreasing %An points to progressive evolution of plagioclase composition. The amount of orthopyroxene increases throughout the entire silicic part of the MG3 cyclic unit.

The CaO content increases within the MG2C anorthosite, pointing to increasing amounts of plagioclase from the bottom to the top of the layer. Since the MgO content decreases at the same time, declining orthopyroxene contents can be deduced.

MgO vs. Na_2O: Similar to the relation MgO-CaO a buckshot-distribution of data points from the pyroxenitic layers is visible (Fig. 4.96), but whole-rock Na_2O concentrations are controlled by plagioclase only. According to table 4.36, the Na_2O content decreases within the MG1 and the second and third interval of the MG4A pyroxenites, implying reverse fractionation of plagioclase. In the lower part of the plagioclase-bearing MG4A pyroxenite Na_2O increases contemporaneously with MgO as well as CaO. From this feature it can be concluded that the precipitation of ortho- as well as clinopyroxene increases with stratigraphy. The amount of plagioclase increases, too, deriving from fractional crystallization.

In the MG2A pyroxenite Na_2O is absent. Hence only anorthosite is present besides pyroxene.

A positively linear trend can be observed from MG3 leuconorite to the norite on top of it, whereas for the norite a negatively linear trend exists. Thus, in the former interval, orthopyroxene and plagioclase contents increase simultaneously, whereas in the latter decreasing amounts of plagioclase is accompanied by further increasing orthopyroxene concentrations.

The variation in the Na_2O content occurring in the MG2C anorthosite is extremely small, which indicates stable plagioclase compositions for this layer.

MgO vs. K_2O: The majority of the pyroxenitic samples doesn't show any K_2O, but in some concentrations of 0.11% in maximum are present (Tab. 4.36). As this is very low no correlation for MgO and K_2O within the pyroxenitic layers exists.

In the transition from leuconorite to norite in the MG3 cyclic unit, the K_2O content decreases, which can be taken as a further evidence for reverse fractionation of plagioclase within this interval, as mentioned before. In the noritic layer above, the amount of whole-rock K_2O is quite stable.

Contradictory to the Na_2O content, there is a decrease in K_2O concentration within the MG2C anorthosite. This is either caused by K-enrichment of anorthitic plagioclase relative to Na, or there is a small portion of orthoclase, which amount decreases towards the top of the layer. The latter is substantiated by CIPW norm calculations (Tab. B-2 in appendix B), showing small, but decreasing amounts of K-feldspar occur within the anorthosite.

Although the SiO_2 content in the silicate layers of the MG4C cyclic unit decreases from bottom to top of the studied section, decreasing amounts of the 'mafic' elements (Cr, Ti, Fe, Mn, Mg) and increasing amounts of the 'felsic' elements (Al, Ca, Na) point to a general progressive evolution with decreasing chromite and orthopyroxene contents as well as increasing plagioclase concentrations.

The samples JKL25 and JLK26 represent small intervals of pyroxenite between the MG2B and MG2C chromitites or the lower and upper parts of the MG3 chromitite layer, respectively. Both are characterized by high amounts of chromite and orthopyroxene by Cr_2O_3 or MgO contents, respectively, as well as low amounts of plagioclase by low CaO contents.

Point Count analyses as well as CIPW norm calculations corroborate the majority of the findings of in- or decreasing amounts of the individual minerals presented above (cf. Tab. B-1 and Tab. B-2 in appendix B).

Due to the absence of apatite as a major control on the distribution of incompatible elements (Fig. 4.95), their distribution in the silicate layers of the MG-sequence as present in core HEX10 seems to be controlled by the intercumulus minerals, i.e. plagioclase ± clinopyroxene. Generally it has been found that incompatible trace element plots of cumulus rocks are rather unreliable (cf. subsection 4.4.1). To illustrate this consideration, the Rb-Zr plot in Fig. 4.97 has been chosen to exemplarily show the behaviour of the incompatible elements in the silicate layers of the MG-sequence. From the positive correlation of these elements coincident enrichment and hence similar distribution coefficients can be concluded.

However, to depict eventually occurring fractionation paths within the silicate layers of the MG-sequence, the Rb/Zr ratio has been plotted vs. the MgO content of the silicate layers (Fig. 4.98), as the Rb/Zr ratio tends to increase with fractionation. As the whole-rock Cr_2O_3 content for the chromitite layers (cf. subsection 4.4.1), the MgO content has been chosen to represent the relative amount of cumulus minerals, i.e. orthopyroxene, in the silicate samples.

The buck-shot distribution of the data points of the LCZ pyroxenites as well as the UCZ pyroxenites doesn't show any fractionation trend (Fig. 4.98). Fractionation is visible towards more evolved compositions, i.e. the noritic and anorthositic samples, which is due to the fact that norite and anorthosite host less orthopyroxene than the pyroxenites as represented by the MgO content.

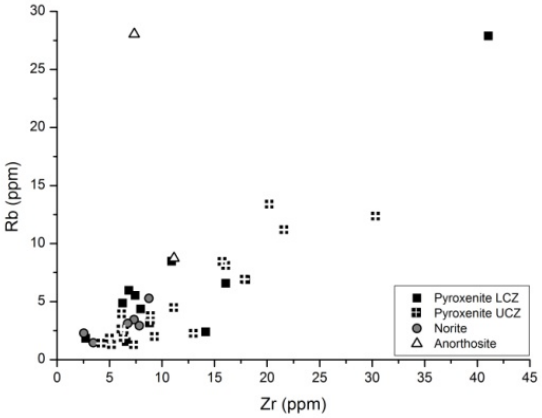

Figure 4.97 Bivariate plot of Zr vs. Rb.

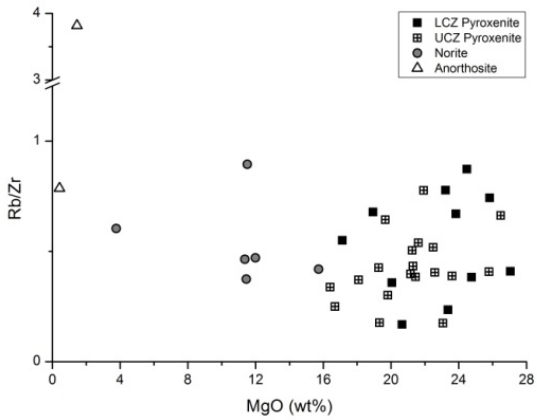

Figure 4.98 Plot of the Rb/Zr ratio vs. the MgO content of the MG silicate samples.

Apart from their use as fractionation indices, plots of incompatible elements can also be taken to identify different magma suites (cf. Rollinson, 1993). For the Bushveld Complex this implies a possibility to identify compositionally different parental magmas for the LCZ and UCZ (cf. Sharpe, 1982, 1985; Kruger and Marsh, 1982; Davies and Tredoux, 1985; Lee and Butcher, 1990; Kruger, 2005).

From figure 4.98 any indication of the presence of two compositionally different liquids (i.e. parental magmas) from which the cumulate rocks derived is present. This is especially well depicted in the data points from the pyroxenitic samples. If a less primitive parental magma had formed the UCZ, the data points of the UCZ pyroxenites would plot above the ones from the LCZ pyroxenites due to higher Rb/Zr ratios. This is not the case. As have been concluded for the chromitite layers (cf. subsection 4.4.1), these plots most likely don't show real relations, as the incompatible elements are rather concentrated in the intercumulus minerals. However, taking into consideration the slight variations depicted by the $Mg\#_{opx}$ (Fig. 4.44 in subsection 4.3.6) and the whole-rock Mg# (Fig. 4.90) as well as the systematic changes of the trace elements with height (Fig. 4.92), the existence of two compositionally different parental magmas responsible for the formation

of the MG-sequence of core HEX10 seems to be unlikely. According to Teigler and Eales (1996) the presence of these slight variations may have been caused by:

(1) Variations in the composition of parental magma(s)
(2) Different degrees of assimilation of country rocks
(3) Secondary processes, e.g. hydrothermal alteration.

Alteration or metasomatic processes, respectively, can be excluded, as the silicate rocks of the MG-sequence show very low degrees of alteration only (cf. subsection 4.2.2). Another possibility is the assimilation of different degrees of country rocks, as e.g. the multi-element diagrams (Fig. 4.95) suggest. Although it can't be excluded, it is rather suggested that the observed variations illustrate subtle changes in parental liquid composition during the formation of the MG-sequence of core HEX10, rather than the presence of two compositionally different magma lineages.

These findings indicate that the MG-sequence from core HEX10 derives from one parental magma only. The noritic and anorthositic layers thus most likely derive from different mixing ratios of replenished parental melt and residual liquid, i.e. during the formation of the norite a higher amount of primitive parental melt mixes with the evolved residual melt in the Bushveld magma chamber. The latter could also show different stages of melt evolution, e.g. it could have been even more evolved during the formation of the anorthosite than during precipitation of the norite. If both or only one of the mentioned cases took place can't be read off the data.

4.4.2.1 Whole-rock PGE and Au contents of the silicate layers

Although much lower than for the chromitite layers the silicate layers host minor PGE concentrations (Tab. 4.38). Generally, the LT-PGE Pt and Pd are most common. With a total of 3465 ppb the MG2B pyroxenite is most enriched, which can probably be ascribed to its exceptionally high amount of chromite (Fig. 4.99). A similar relation between high chromite and PGE content is illustrated for the leuconorite in the hanging wall of the MG3 chromitite layer (2025 ppb). However, the analyses for the MG2A pyroxenite and the MG3 pyroxenitic interlayers, both showing relatively low Cr_2O_3 concentrations, show elevated PGE mineralization relative to the other silicate layers (410 or 369 ppb, respectively). It indicates that another PGE concentrating factor besides chromite could exist. On the other hand, there are also silicate layers being enriched in chromite with negligible PGE concentration, e.g. the pyroxenites of the MG0, MG1 and MG4A units.

The complete results of PGE concentration in silicate samples are compiled in table B-23 in appendix B.

Table 4.38 Averaged whole-rock PGE and Au contents of the silicate layers of the MG sequence (in ppb). **N:** number of analysed samples; **MG3_i:** pyroxenitic interlayer in the MG3 chromitite. ***Px:*** pyroxenite; ***an:*** anorthosite; ***le_no:*** leuconorite; ***no:*** norite; ***px_no:*** pyroxenitic norite. PGE data are given in ppb; Cr_2O_3 in wt %.

unit	**MG0**	**MG1**	**MG2A**	**MG2B**	**MG2C**	**MG3_i**	**MG3**	**MG3**	**MG4A**	**MG4C**
lithology	px	px	px	px	an	px	le_no	no	px	px_no
n	2	2	4	1	2	1	1	1	5	1
Os	7	7	6	34	5	5	33	4	7	0
Ir	8	8	11	87	15	14	81	6	9	1
Ru	47	48	42	192	39	45	215	29	42	2
Rh	14	19	23	193	19	39	252	13	21	5
Pt	47	59	200	2358	99	126	757	36	56	101
Pd	48	135	124	597	35	139	684	19	49	117
Au	6	10	4	4	2	2	3	7	2	4
total	176	286	410	3465	215	369	2025	112	186	230
Cr_2O_3	17.2	12.2	14.9	31.6	1.9	13.5	18.9	0.6	10.2	0.5

Interrelationships between the HT-PGE are very strong (r_S > 0.9) (Tab. B-24 in appendix B). The strongest correlation exists between Os and Ru (r_S = 0.981) (Fig. 4.100), which is most likely due to the presence of laurite $(Ru,Os)S_2$. Correlations between LT-PGE are less strong and range between $0.800 \leq r_S \geq 0.903$ reflecting their occurrence in diverse PGM species (cf. subsection 4.3.8). The high correlation coefficient of 0.808 between Rh and Pd is most likely due to the presence of PGM holding Rh as well as Pd (cf. subsection 4.3.8).

Although still strong, correlation coefficients of Pt with all the other PGE are the weakest, which indicates partly decoupled geochemical behaviour of Pt.

Different from the chromitite layers, no correlation between Au and the PGE exist.

Normalized PGE patterns of the silicates from core HEX10 are shown below (Fig. 4.101 and Fig. 4.102). For comparison, the patterns of the Merensky Reef pyroxenite (MR) and the UG2 reef from the eastern limb are also plotted. Additionally, data from Davies and Tredoux (1985) for the proposed parental magmas of the CZ, i.e. high-Mg basalt and tholeiite, have been added.

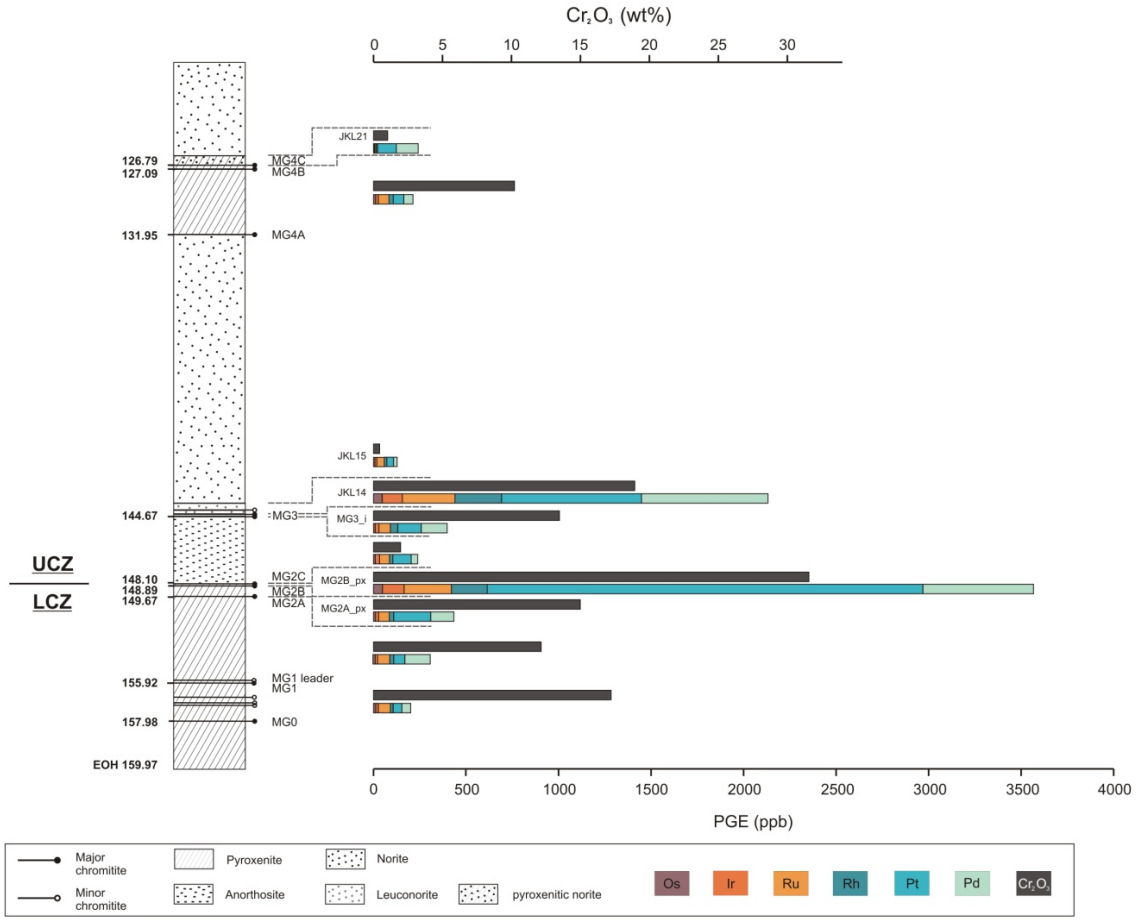

Figure 4.99 PGE and Cr_2O_3 concentrations of the silicate layers of the MG sequence. For the silicate rocks of the MG3 unit three sets of bars are illustrated, since they represent different rock types. These are: ***MG3_i:*** pyroxenitic interlayer within MG3 chromitite; ***JKL14:*** chromitiferous leuconorite; ***JKL15:*** norite. Data are given in table 4.38.

As can be seen from figure 4.101, all the pyroxenitic interlayers are enriched in the PGE relative to the proposed parental magmas. Especially the enrichment in Rh creates a positive Rh anomaly, which has already been described for the chromitite layers of the MG sequence (cf. subsection 4.4.1.2). The PGE tenors of most of the MG silicates are similar to the one of the UG2 suggesting a comparable mineralization style and their precipitation from the same parental magma.

Two exceptions from the dominating patterns can be seen for the MG2A and the MG2B pyroxenites. Both lack the positive Rh anomaly just described and rather show a positive Pt anomaly. They thus mirror mineralization conditions being responsible for the PGE mineralization of the MR pyroxenite. Due to the similarity of their patterns, the tholeiitic suite appears to be the parental magma for the MR pyroxenite. Low Pd concentration in the MG2B pyroxenite is probably due to alteration.

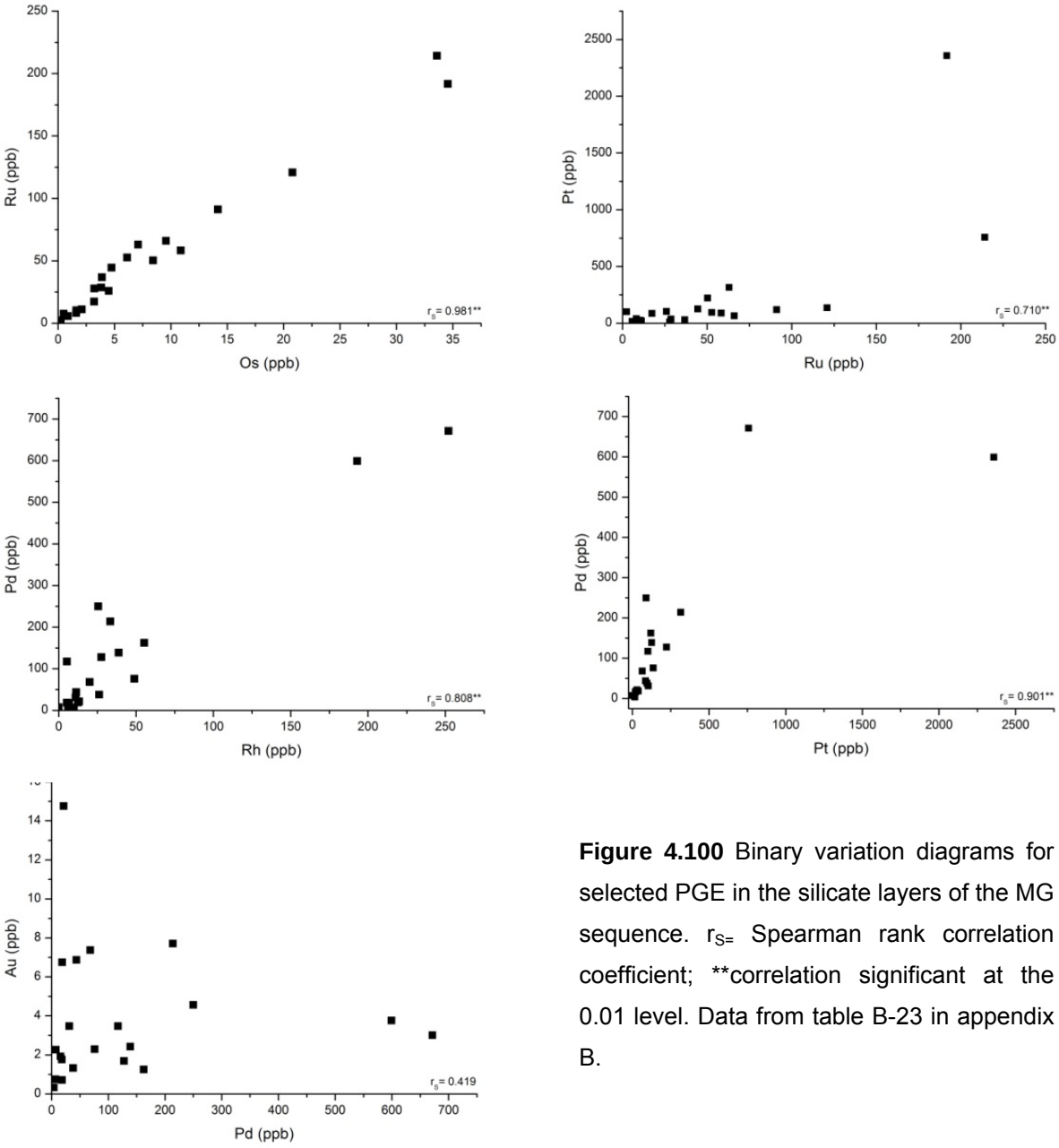

Figure 4.100 Binary variation diagrams for selected PGE in the silicate layers of the MG sequence. $r_{S=}$ Spearman rank correlation coefficient; **correlation significant at the 0.01 level. Data from table B-23 in appendix B.

Exceptionally high PGE concentrations occur within the MG2B pyroxenite. Since it hosts elevated amounts of Cr_2O_3 (cf. Tab. 4.38) a PGE mineralization coupled to the presence of chromite appears to be most likely. On the one hand, this relation is corroborated by the MG3 pyroxenite showing elevated amounts of Cr_2O_3 and high total PGE. On the other hand, the MG0 pyroxenite has low total PGE concentrations but similar amounts of Cr_2O_3 as the MG3 pyroxenite. It thus furthermore indicates that chromite is not the only PGE concentrating factor.

Except for the plagioclase-bearing MG4A pyroxenite, the pyroxenitic interlayers show a slight enrichment of Au relative to the tholeiite and the high-Mg basalt.

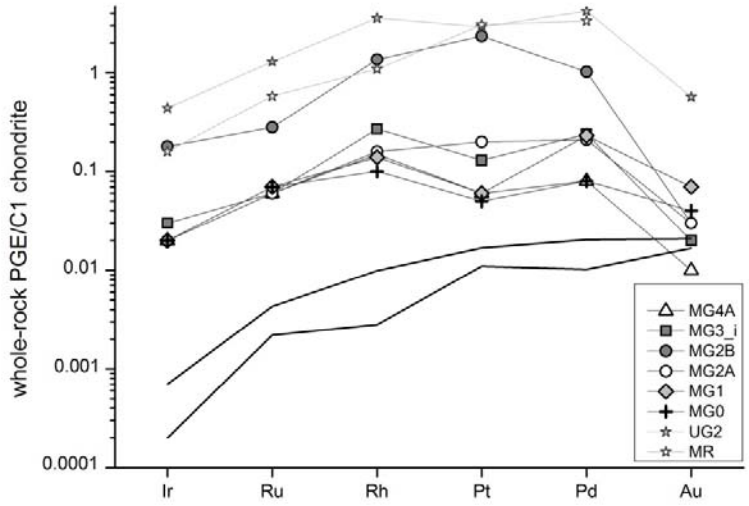

Figure 4.101 Chondrite-normalized PGE and Au patterns of MG pyroxenites. Normalizing C1 values from Lodders (2003). If not otherwise declared, data are averages for each layer. Upper black line: high-Mg basalt; lower black line: tholeiite (Davies and Tredoux, 1985). Data for the Merensky Reef pyroxenite (MR) and the UG2 are from the eastern limb (Barnes and Maier, 2002).

Normalized PGE patterns of the MG anorthosite and norites are also enriched in the PGE when compared to the proposed parental magmas (Fig. 4.102). The leuconorite in the hanging wall of the MG3 chromitite layer is most enriched, which is probably due to its high amount of cumulus chromite (cf. Tab. 4.38).

Except for the silicate sample from the MG4C unit, all the other patterns show the typical positive Rh anomaly noticed before. The similarity of the PGE patterns of these silicate layers with the UG2 pattern is most obvious, suggesting equal style of mineralization and the derivation from the same type of magma.

Although containing the lowest PGE content, highest PGE fractionation (Pt/Ir ratio of 139) is visible in the pyroxenitic norite of the MG4C unit. This pattern is completely different from the other ones and rather similar to the one of the MR pyroxenite. The patterns of the MR pyroxenite resemble the patterns of the tholeiitic suite, which indicates the tholeiitic suite to be the parental magma for this layer.

Highest enrichment of Au can be obtained from the MG3 norite, since the slope rises.

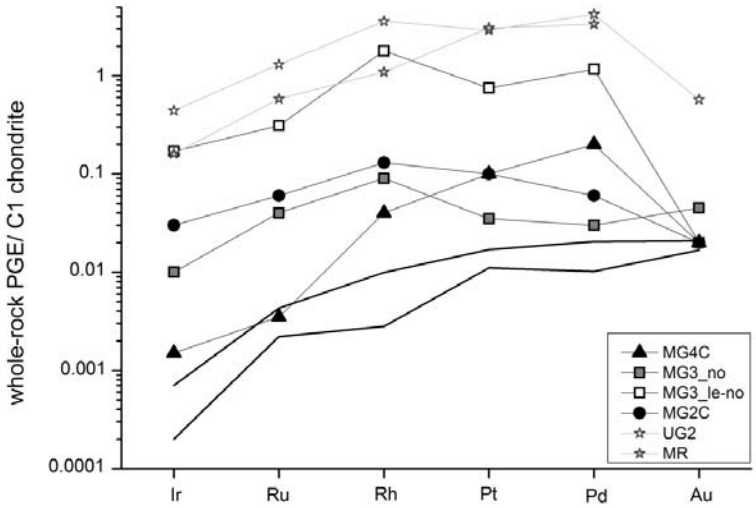

Figure 4.102 Chondrite-normalized PGE and Au patterns of MG norite & anorthosite. Normalizing C1 values from Lodders (2003). If not otherwise declared, data are averages for each layer. Upper black line: high-Mg basalt; lower black line: tholeiite (Davies and Tredoux, 1985). Data for the Merensky Reef pyroxenite (MR) and the UG2 are from the eastern limb (Barnes and Maier, 2002).

Since all the silicate layers show an enrichment in the noble metals relative to the high-Mg basaltic and tholeiitic suites, they must be concentrated by some process during crystallisation. Thus, in the following, the PGE are plotted versus whole-rock Cr_2O_3 and MgO contents of the silicate rocks to show, if correlations exits that can be interpreted to be responsible for enrichment of the PGE within the silicate layers. For the following correlation plots a Spearman rank correlation matrix has been calculated, which is presented in table B-24 in appendix B.

Unlike to findings from the chromitite layers, positive correlations of the PGE with Cr_2O_3 exist and are strongest for Os and Ru, which illustrates the pronounced relationship between the occurrence of laurite and chromite (Fig. 4.103) (e.g. Page and Talkington, 1984; Talkington *et al.*, 1984; Merkle, 1992). The other PGE show moderate correlation coefficients with Cr_2O_3 only, suggesting 'chromite control' on triggering PGE mineralization within the silicate layers. Au mineralization seems to remain unaffected from such a control (Fig. 4.103).

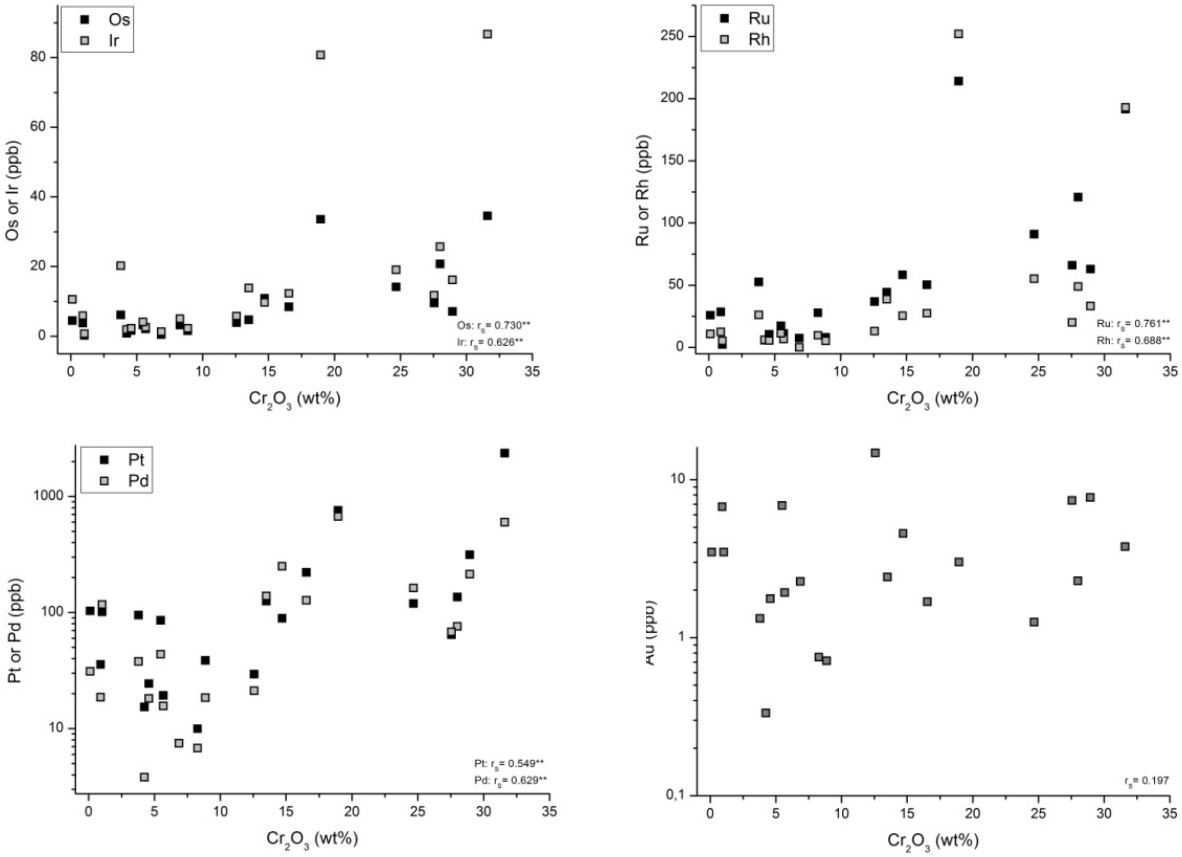

Figure 4.103 Relationship of Cr_2O_3 with the PGE and Au. r_S= Spearman rank correlation coefficient; **correlation significant at the 0.05 level.

The proposed parental magmas of Sharpe (1982) and Davies and Tredoux (1985) have intermediate whole-rock MgO contents when compared to the silicate rocks of the MG (Fig. 4.104), which can be ascribed to the cumulate nature of the MG samples. In the pyroxenites and norites strong negative correlations with the whole-rock MgO content exist for all the PGE, whereas for the leuconoritic and anorthositic rocks a positive linear trend is visible (Fig. 4.104). No correlation exists for Au with the whole-rock MgO content.

The MgO content can be used as an indication of the temperature at which the parental melts were extracted from their source (most likely from the mantle), which has been described by Tredoux *et al.* (1986) for a suite of late Proterozoic to Achaean magmas of mafic to ultramafic composition. They concluded that not the difference in compatibility but rather the melt temperature of the PGE is responsible for the fractionation of the PGE during partial melting of the mantle, as the PGE show varying maximum levels in relation to the whole-rock MgO content. The data from this study show that for the pyroxenitic and noritic rocks highest PGE concentrations are reached at a whole-rock MgO content of approximately 17%. At higher amounts of MgO PGE concentrations within pyroxenites and norites decrease. Since in the leuconorite and the

anorthosite not such high MgO contents are present probably only the rising branch of this correlation is visible.

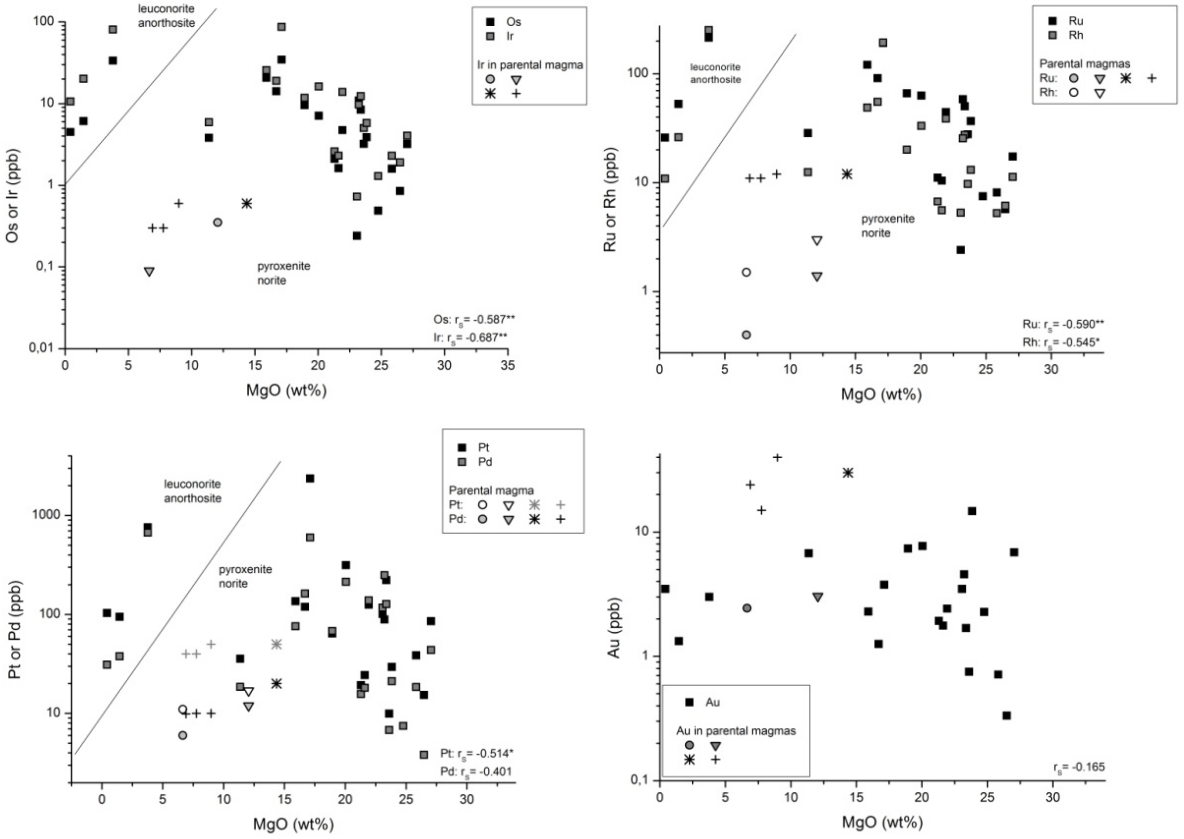

Figure 4.104 Bivariate plots of the whole-rock MgO content of the MG silicate layers vs. PGE and Au contents. For comparison, the data from the proposed parental magmas are plotted. *Circle:* high-Mg basalt; *reversed triangle:* tholeiite (data from Davies and Tredoux, 1985); *snowflake:* B1 magma; *cross:* B2 and B3 magma (data from Sharpe, 1982). r_S= Spearman rank correlation coefficient; ** correlation significant at the 0.01 level, * correlation significant at the 0.05 level.

According to these observations, the MgO-PGE plots do not illustrate fractionation of the PGE at their source, as have been suggested by Tredoux *et al.* (1986), since highest amounts of the PGE are achieved at the same whole-rock MgO concentration. As found for the chromitite layers before (cf. subsection 4.4.1.2), this feature could be due to the cumulate character of the silicate layers of the MG, which distorts the characteristic signs of fractionation originally could have been present.

Due to the chalcophile character of the PGE it is commonly assumed that sulphide is the main phase controlling their fractionation. A plot of the PGE groups versus Cu should show, if the occurrence of PGE is linked to BMS (Fig. 4.105). Cu strongly correlates with S proving that Cu distribution is controlled by BMS, i.e. chalcopyrite (cf. Fig. 4.94B in

subsection 4.4.2). Since a significant correlation of Ni with S is lacking, chalcopyrite seems to be the only/major BMS occurring in the silicate layers of the MG sequence (cf. Tab. B-25 in appendix B).

The only PGE significantly correlating with Cu is Ru (r_S= 0.468), which causes the slight positive correlation observed between Cu and the HT-PGE (Fig. 4.105). A correlation of Cu with the other PGE or Au does not exist.

In figure 4.106 the whole-rock S and PGE contents are plotted in stratigraphic order. The individual PGE do not significantly correlate with S saying that high PGE concentrations are not linked to elevated amounts of whole-rock sulphur (cf. r_S in Fig. 4.106). For some samples a peak coincidence of the PGE and S exists, indicating their presence as PGM sulphides, but it lacks a regular pattern.

However, S, the HT-PGE and Rh show decreasing amounts with height, whereas Pt and Pd show relatively constant or saw-tooth like distribution, respectively (Fig. 4.106). Weak correlation is present for Ru, Os and Ir indicating their precipitation as laurite.

Peak coincidence of the HT-PGE with S appears in samples with Cr_2O_3 contents >20 wt% (JKL5, JKL25, JKL35). For the LT-PGE this is not necessarily the case, since peak coincidence also appears in samples with lower Cr_2O_3 contents, i.e. JKL26 with Cr_2O_3 of 13.5 wt%.

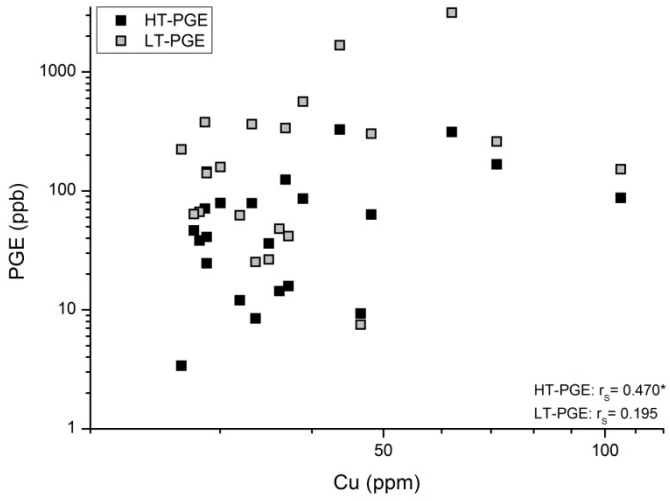

Figure 4.105 HT-PGE and LT-PGE plotted versus the whole-rock Cu contents. r_S= Spearman rank correlation coefficient; * correlation significant at the 0.05 level.

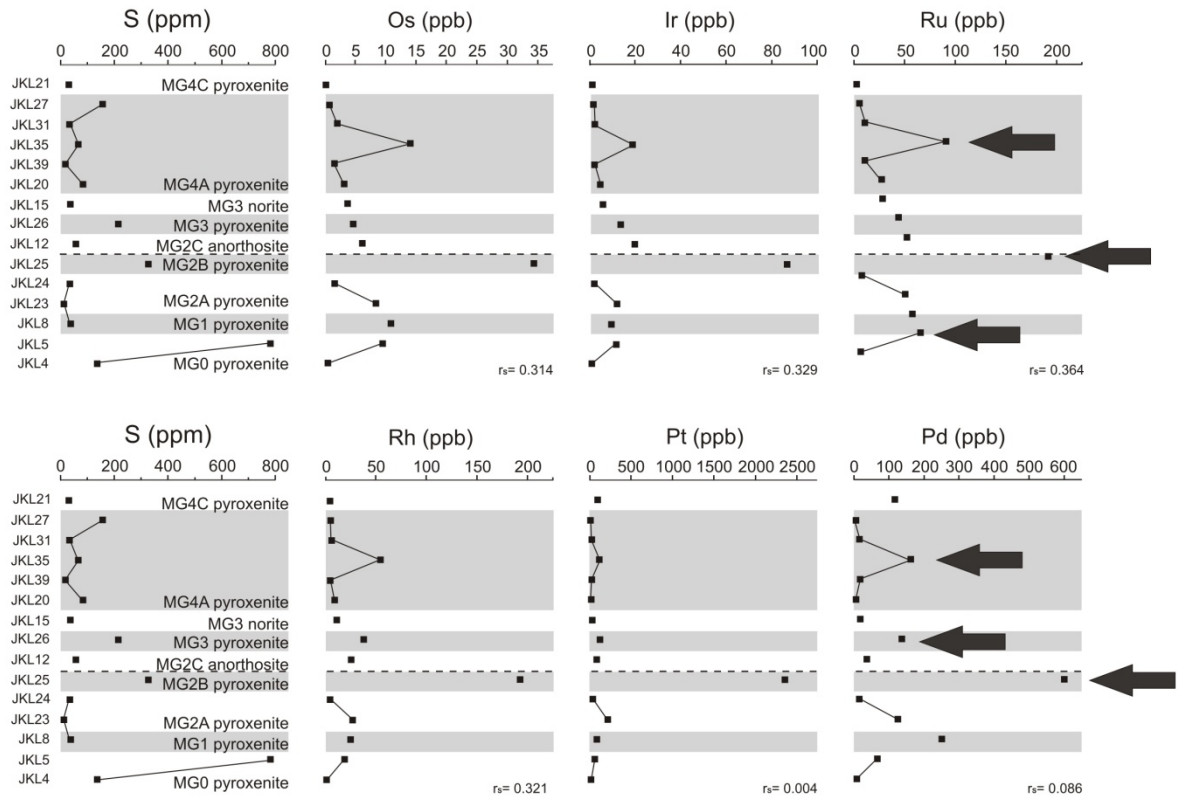

Figure 4.106 Variation of the S and PGE contents of selected samples through the stratigraphy of the MG sequence. Stippled line represents the transition LCZ/UCZ. The arrows indicate peak coincidence. Only samples for which the S content has been determined have been plotted. r_S= Spearman rank correlation coefficient.

In the LCZ the Pt/Ir ratio declines within each pyroxenitic layer with height, describing the enrichment of HT-PGE relative to the LT-PGE (Fig. 4.107). The thin pyroxenitic interlayer above the MG2B chromitite layer is characterized by a strong enrichment of the LT-PGE relative to the HT-PGE. This sample also contains the highest Cr_2O_3 and the lowest SiO_2 contents.

In the UCZ development of PGE contents change within each rock type. An increasing Pt/Ir ratio in the MG2C anorthosite is accompanied by decreasing Cr_2O_3 and increasing SiO_2, which is in contradiction to findings for the pyroxenites of the LCZ. In the short interval from leuconorite to norite in the hanging wall of the MG3 chromitite an enrichment of the HT-PGE relative to the LT-PGE is developed again and coincides with decreasing Cr_2O_3 and increasing SiO_2. The MG4A pyroxenite shows the same features as the MG2C anorthosite.

Since the whole-rock Cr_2O_3 content generally decreases with height and within each silicate layer it cannot be accounted for changes in the individual PGE contents. The same is true for SiO_2, as it steadily increases with stratigraphy.

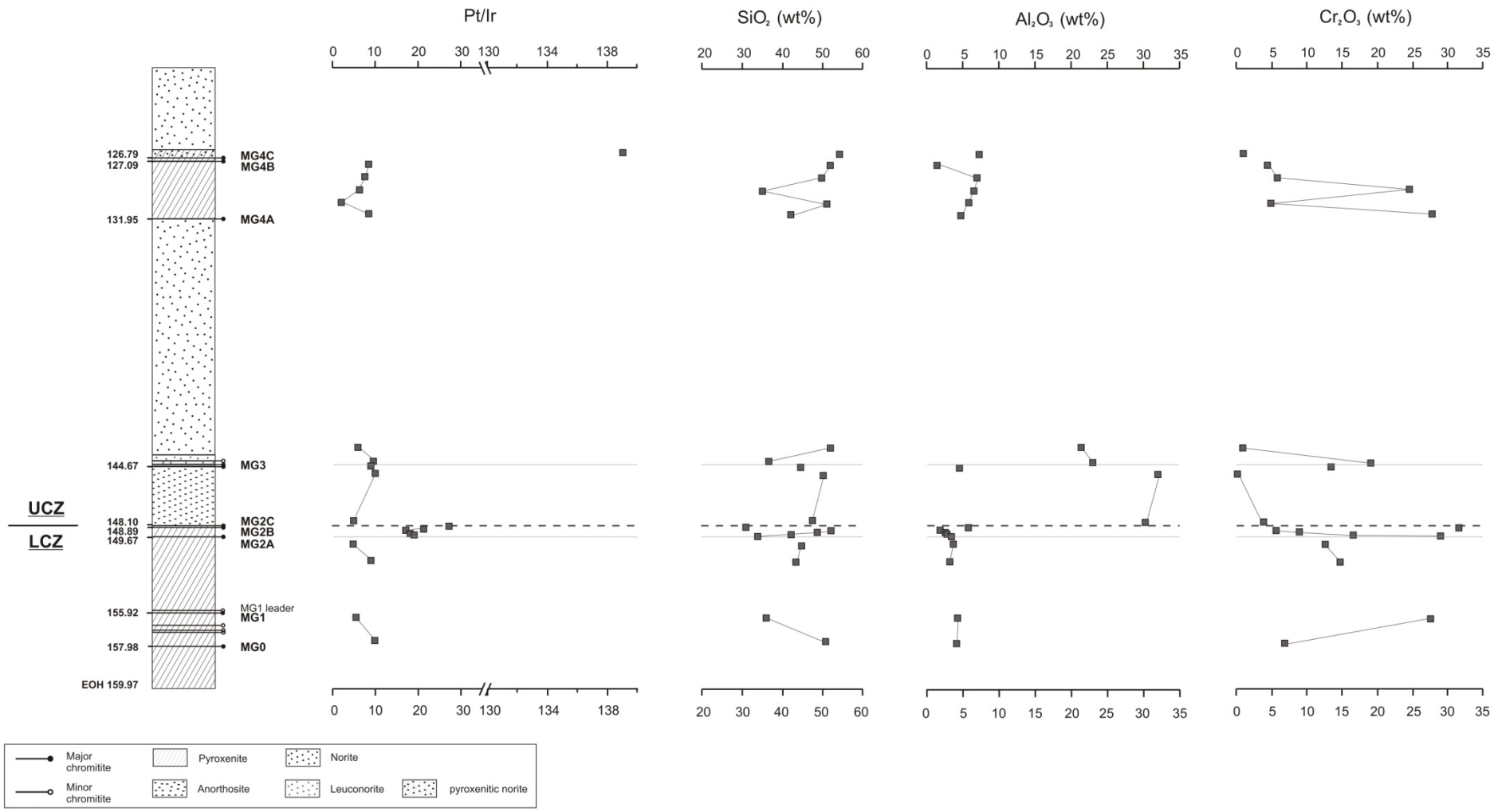

Figure 4.107 Several major element oxide contents and the Pt/Ir ratio plotted versus the stratigraphic column of the MG sequence.

Thus the whole-rock Al_2O_3 content has been plotted versus the stratigraphic column, too (Fig. 4.107). In contradiction to results from the chromitite layers, no such regular patterns between Al_2O_3 content and development of the Pt/Ir ratio can be described. However, enrichment of the LT-PGE relative to the HT-PGE, as can be seen in the anorthosite and the pyroxenite of the UCZ, is linked to increasing Al_2O_3 concentrations. Since in the UCZ cumulus plagioclase occurs, LT-PGE enrichment is probably linked to elevated amounts of cumulus plagioclase. Decreasing amounts of cumulus plagioclase, i.e. decreasing whole-rock concentrations of Al_2O_3, as can be observed from the leuconorite to the norite of the MG3 cyclic unit, are accompanied by an enrichment of the HT-PGE relative to the LT-PGE. In the MG2A pyroxenite the Al_2O_3 content is controlled by chromite (cf. Tab. 4.36 in subsection 4.4.2). Hence, decreasing amounts of Al_2O_3 are linked to decreasing chromite contents, which leads to decreasing Pt/Ir ratio within this layer.

In the pyroxenites of the MG0 and MG1 cyclic units decreasing Al_2O_3 is accompanied by increasing Pt/Ir ratio. Chromite content is relatively high (cf. Tab. 4.36 in subsection 4.4.2), but Al_2O_3 concentration doesn't change contemporaneously with variations in the amount of chromite. Hence, co-precipitation of intercumulus plagioclase is concluded, as already have been shown in subsection 4.2.2.1 (see also Table B-1 in appendix B). As a result, enrichment of the LT-PGE relative to the HT-PGE is observed.

4.5 Comparison with data from other localities of the BC

4.5.1 General considerations

Lateral continuity of the chromitite layers throughout the entire Bushveld Complex has been widely accepted. Although differences in the thickness of individual layers occur (cf. Cameron and Desborough, 1969; Merkle, 1992; Scoon and Teigler, 1994), their lateral continuity can be taken as evidence for the connection of both the western and the eastern limb during formation of the CZ. Further indications are petrologic similarities, as the LCZ/UCZ transition and PGE grades of the individual chromitite layers of the CZ. According to this it is most likely that one main feeder for the entire Bushveld Complex existed.

Kruger (2005) suggests repetitive magma intrusion along the Thabazimbi-Murchison-Lineament (TML), from which the melt spreads towards the south during the formation of the CZ. Major differences in the thicknesses of the Bushveld stratigraphy occur due to the

development of a half-graben to the south that becomes elongated and deepened with further magma addition to the Bushveld magma chamber. The thickest stratigraphic columns occur in the north of the BC (ca. 9 km), since the margin of the half-graben is gently shelving towards the south.

The stratigraphy as well as the lateral extent of the LCZ shows significant differences in the different parts of the BC (Kruger, 2005) and thus Kruger (2005) concluded that during early stages of magma intrusion the Bushveld “magma chamber comprised a network of connected subchambers orientated in an east-west direction south of the TML”, with feeder zones close to the centre of this axis. He furthermore suggests that the Steelpoort fault may also represent a feeder, which has been active during the formation of the LZ.

Local differences in the stratigraphic columns of the LZ and LCZ have also been observed by Hatton and von Gruenewaldt (1985), which the authors explained to represent diverse facies due to differences in parental magma composition. These facies may also have been caused by the presence of several subchambers, as have been suggested by Kruger (2005). Depending on the distance to the main feeder it appears to be possible that the supply with magma varied from subchamber to subchamber, thus explaining the observed differences. It furthermore seems to be likely that slightly different stages of fractionation occurred within these smaller chambers, which could result in compositional differences of the major cumulus minerals of the CZ, e.g. chromite, olivine, orthopyroxene and plagioclase, at the diverse locations of the BC.

For the UCZ chromitites of the MG Schürmann *et al.* (1998) report well-developed thick layers at Tweefontein south of the Steelpoort fault, whereas to the north at Jagdlust they are thin and only poorly developed (Cameron, 1980). However, Kruger (2005) reports that the entire UCZ becomes thinner towards the S of the eastern limb, which is in concordance with a major axis of magma replenishment located in the N of the BC, i.e. along the TML. Probably, the Steelpoort fault has also provided additional magma to the eastern part of the BC during formation of the MG, with a major spreading direction towards the south explaining the higher thicknesses of MG chromitite layers at Tweefontein.

On basis of the Sr-isotopic profile of the Bushveld Complex Kruger (2005) further suggests that the evolution of the Bushveld magma chamber occurred in two stages. The first stage is an open-system Integration stage that resulted in the formation of the LZ, CZ and lower MZ with numerous influxes of magma. The chromitite layers of the CZ have been deposited as a result of repetitive influxes of magma (e.g. Kruger and Marsh, 1982; Kinnaird *et al.*, 2002), recorded by changes in the initial $^{87}Sr/^{86}Sr$ ratio (Kruger, 1994).

The upper MZ as well as the UZ have been formed during a closed-system Differentiation stage without major magma additions, since neither prominent compositional changes nor shifts in the Sr_i ratio occur. According to this, fractional crystallization was the major force during development of the upper MZ and UZ of the BC.

4.5.2 Chromite chemistry

The chromite chemistry from the chromitite layers of the MG from this study has been compared with various data from the literature. The locations the data derive from are summarized in Tab. 4.39 and the locations of the individual farms are shown in Fig. 4.108. The data used for the plot in Fig. 4.109 have been calculated with the spreadsheet of Barnes (2005) and are presented in appendix B (tables B-26 and B-27).

Table 4.39 Origin of comparable data of chromite chemistry to data from this study.

reference	**limb**	**sector**
Cameron (1977)	eastern	Jagdlust-Winterveld (north of the Steelpoort fault)
Hatton and von Gruenewaldt (1985)	eastern	Tweefontein (south of the Steelpoort fault)
	western (N to S)	Amandelbult, Ruighoek, Boshoek, Rustenburg, Marikana
Naldrett *et al.* (2009)	eastern (N to S)	Jagdlust-Winterveld and Clapham (north of the Steelpoort fault), Tweefontein (south of the Steelpoort fault)
	western	Marikana
Scoon and Teigler (1994)	western (N to S)	Union and Brits

MG1: Chromite composition in the eastern limb shows a smaller range in its Cr^{3+} content (58-62%) than those from the western limb (52-62%). In the east, Fe^{3+} is quite stable (8-9%) and Al^{3+} varies by 5% only. Due to larger deviation in Cr^{3+} content, the range of variation in Fe^{3+} and Al^{3+} concentrations in the western limb are larger, too (Fe^{3+}: 5-15%; Al^{3+}: 28-38%).

MG2: The Cr^{3+} content of chromite within this layer is approximately the same in the eastern and the western limb (56-62%), but there are differences in the concentrations of Fe^{3+} and Al^{3+}: chromite in the western limb can contain up to 3% more of each Fe^{3+} and

Al^{3+} than those in the eastern part, due to the wider compositional range in this components.

From Fig. 4.109 can also be deduced that the evolution from MG2A to MG2C in the eastern Bushveld follows the same trend of a less chrome-rich composition, regardless of whether the samples derive from the north (Cameron, 1977) or the south (this study). At the same time, the Fe^{3+} content also decreases, both in favour of Al^{3+}. In contradiction to that, the data from Naldrett *et al.* (2009) for MG2A to MG2C of the western limb show almost no variation in chromite composition.

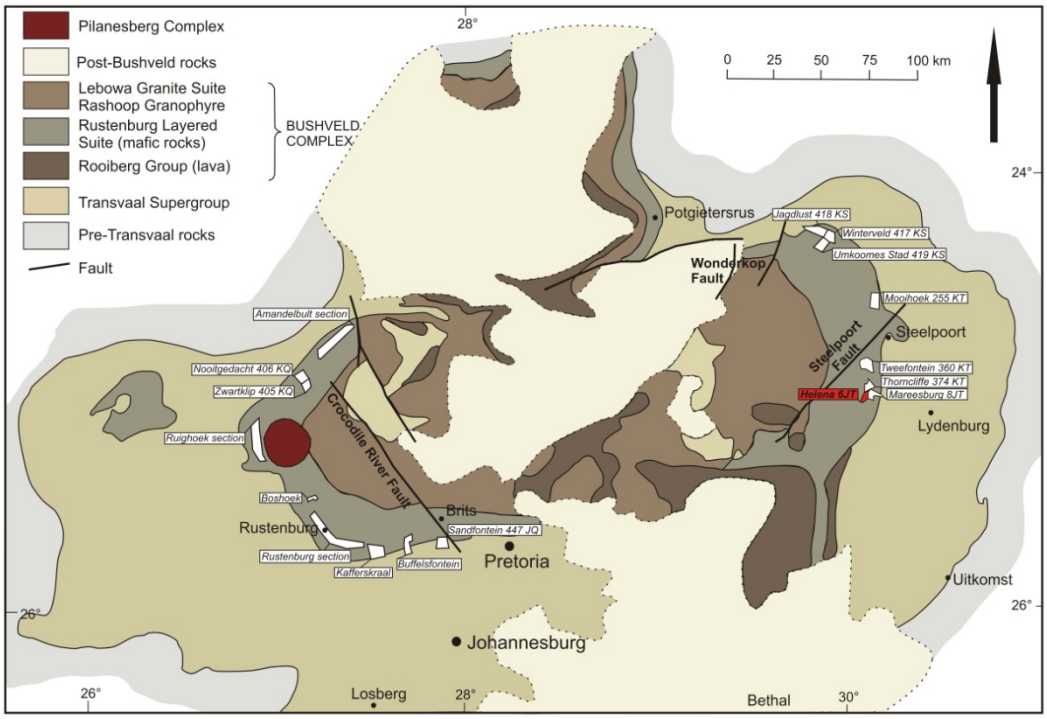

Figure 4.108 Locations of farms, sections and bore cores the data for comparison derive from. ***Western BC:*** Cores Nooitgedacht 406KQ and Zwartklip 405 KG belong to the Union section; farm Kafferskraal represents W-Marikana and farm Buffelsfontein E-Marikana; core Sandfontein 447 JQ belongs to the Brits section. ***Eastern BC:*** Cores Jagdlust 418 KS, Winterveld 417 KS and Umkoomes Stad 419 KS have been investigated by Cameron (1977); core Mooihoek 255 KT belongs to the Clapham section (cf. Naldrett *et al.*, 2009); the cores south of the Steelpoort fault belong to the Tweefontein section.

MG3: Chromite composition in the MG3 chromitite layer of the eastern limb shows relatively stable Cr^{3+} contents (56-59%), whereas in the western part the variation is a bit greater (53-58%) and concentration of Cr^{3+} less. On the other hand, chromite composition

.

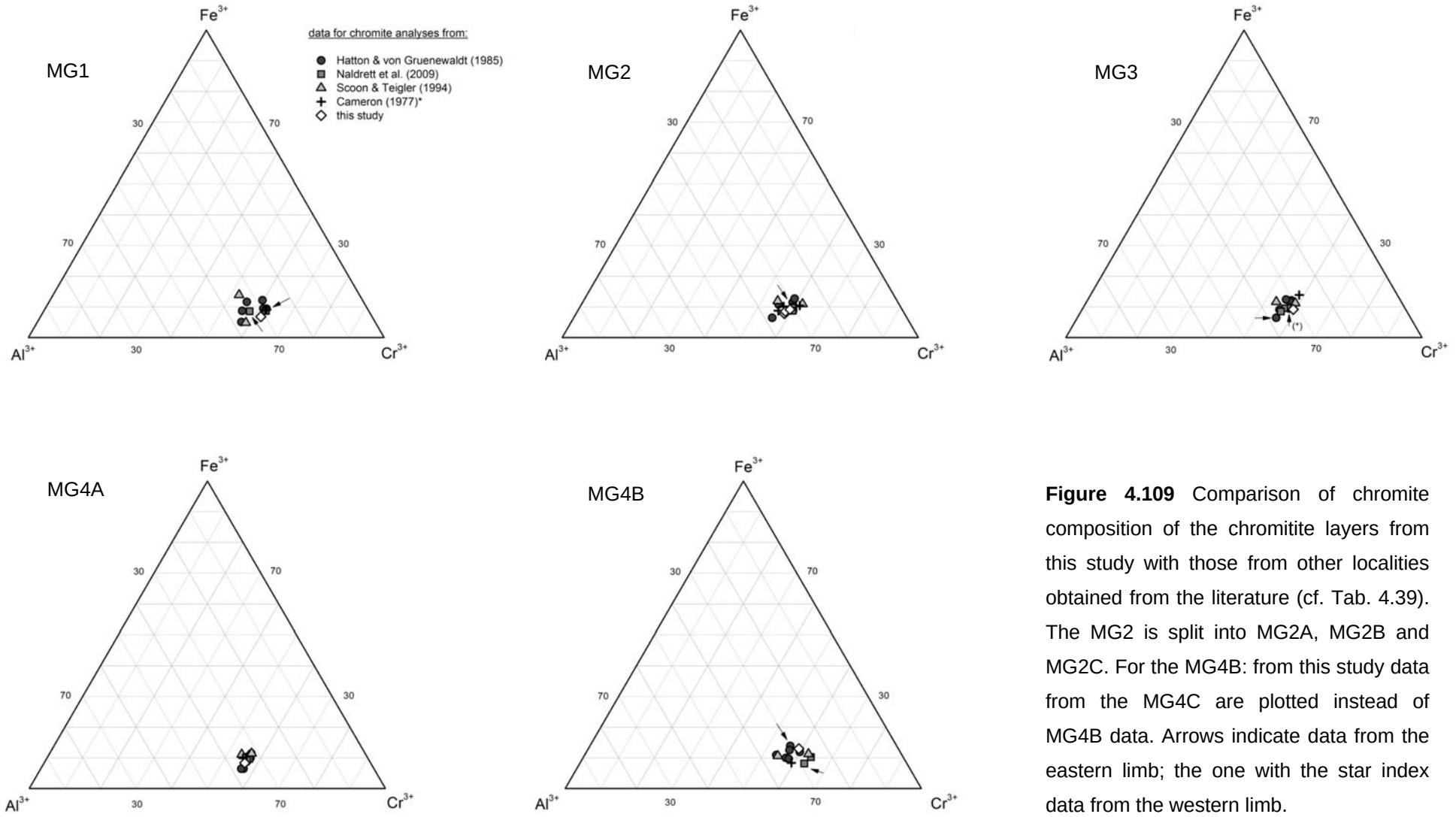

Figure 4.109 Comparison of chromite composition of the chromitite layers from this study with those from other localities obtained from the literature (cf. Tab. 4.39). The MG2 is split into MG2A, MG2B and MG2C. For the MG4B: from this study data from the MG4C are plotted instead of MG4B data. Arrows indicate data from the eastern limb; the one with the star index data from the western limb.

in the eastern part generally shows a wider range of Fe^{3+} (7-14%) and Al^{3+} (28-39%) than those in the western Bushveld (Fe^{3+}: 8-12%; Al^{3+}: 30-36%).

MG4A: The MG4A chromitite layer is the only one showing the smallest variations in chromite composition. Data for the eastern part (Cameron, 1977; this study) are extremely similar and those for the western Bushveld and range a little only (Cr^{3+}: 54-58%; Fe^{3+}: 8-12%; Al^{3+}: 32-38%).

MG4B: The Fe^{3+} contents of chromite are quite similar in the two limbs (E: 8-15%; W: 8-13%). Concentrations of Cr^{3+} and Al^{3+} in the western part show a slightly wider range (Cr^{3+}: 52-65%; Al^{3+}: 25-35%) than those for chromite of the eastern part (Cr^{3+}: 55-63%; Al^{3+}: 28-32%).

Generally, chromite from the western Bushveld shows a wider compositional range with regard to its trivalent cations than those from the eastern part (cf. Fig. 4.109). Nevertheless, sections in the northern parts of both limbs contain chromite with lower Cr^{3+} and higher Al^{3+} concentrations relative to sections in the south (cf. Fig. 4.23 in subsection 4.3.1. and Scoon and Teigler, 1994). Furthermore, chromite from the N of the eastern limb shows higher Mg# than those from this study (cf. Fig. 4.23 in subsection 4.3.1). A decreasing Mg# from N to S has also been described by Eales *et al.* (1988) and Scoon and Teigler (1994) for chromite from the western limb. According to them, the lateral differences in chromite composition are due to fractional crystallisation of magma that intruded through a main feeder located in the vicinity of Union and spreads as a basal flow towards the south, i.e Brits. This is quite similar to the suggestion of Kruger (2005), who postulated repetitive magma replenishment along the TML in the north of the BC, from which the melt spreads towards the south during the formation of the CZ. As have been mentioned in subsection 4.5.1 before, he furthermore suggests the existence of a network of connected subchambers, at least during formation of the LCZ. Hence for the MG1 to the MG2B chromitite layers differences in chromite chemistry could be due to the addition of compositionally varying evolved magma that may has undergone fractional crystallization in the postulated subchambers, rather than simple fractional crystallization as have been described by Scoon and Teigler (1994). This is corroborated by the data of chromite composition from various locations in the western limb, which would be more ‘in line’ from N to S, if they are fed from one fractionating basal flow per cyclic unit only (cf. Tab. B-27 in appendix B).

For chromite in the UCZ of the eastern limb the influence of magma addition from the Steelpoort fault probably occurred additionally to the major fed from the TML, whereas for the western limb magma addition from a feeder conduit south of the TML took place (Kruger, 2005). It may have given rise to the now observed differences in major mineralogy of chromite in the eastern and western limbs.

4.5.2.1 Trace element abundances in chromite grains

As have been shown in subsection 4.3.1, the chromite grains in chromitite layers of the MG sequence in the eastern Bushveld contain much more Zn and Ni than those from the western Bushveld investigated by Paktunc and Cabri (1995).

Scoon and Teigler (1994) noticed a general paucity of olivine in the LCZ of Brits, i.e. of a stratigraphic section in the south, whereas those in the north show abundant. The silicate layers of the MG sequence investigated during this study show the same lack of olivine (cf. subsection 4.2.2) that have been observed for the same stratigraphic sequence at Brits (Scoon and Teigler, 1994). Furthermore, XRD analyses of samples from the MG chromitite layers of this study have shown that olivine is also absent within the MG chromitites of this study. Hence it is concluded that the observed values for Ni in chromite are due to the lack of co-precipitating olivine enriching chromite in Ni. Eventually, the content of BMS is also lower, but no comparative data on sulphur was available.

In subsection 4.3.1, increasing amounts of Zn upwards the stratigraphic column have been linked to melt evolution. However, data of Paktunc and Cabri (1995) for chromite of the western Bushveld showed that chromite from the LG contain higher amounts of Zn than those of the UG. The Zn values of chromite from the MG chromitite layers investigated during this study are even lower. Thus, a simple T control, as can be deduced from melt evolution by decreasing Mg#, for the distribution of Zn in chromite can be ruled out.

Although no significant correlation between Al_2O_3 and Zn content of chromite exists (Fig. 4.110), the chromitite layers with chromite grains showing the lowest $Cr^{3}+/(Cr^{3+}+Al^{3+})$ ratio, i.e. MG2B and MG4A, also have the lowest amount of Zn (cf. figures 4.23 and 4.24 in subsection 4.3.1). Hence, the Zn distribution seems to be rather sensitive to the Al^{3+} content of chromite, but in dependence of Cr^{3+}.

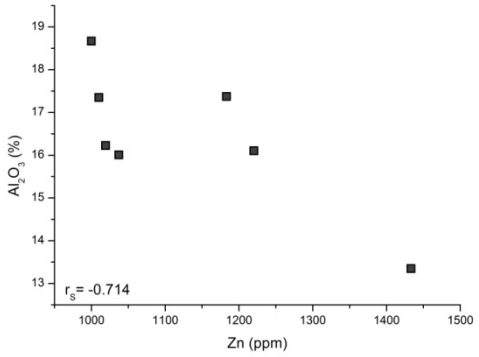

Figure 4.110 Crude negative correlation of Zn and Al_2O_3 content of chromite from chromitite layers of core HEX10. r_S= Spearman rank correlation coefficient; no significant correlation is present.

4.5.3 Silicate chemistry

Limited data of mineral chemistry from the silicate layers of the MG are available in the literature, and thus only two references can be presented in comparison with the data of this study: data from Brits (Teigler *et al.*, 1992) and from Union as well as Brits (Eales *et al.*, 1991).

Values for An content of this study are higher compared to those found for the western BC (Tab. 4.40). To a certain point this is certainly caused by different methods of investigation, i.e. SEM-EDX during this study and EMP data from the literature. Since no exact data of plagioclase analyses have been published, no comparable plot is presented.

Teigler *et al.* (1992) couldn't find a general trend of the %An with stratigraphic height, which is in contradiction to data from this study showing limited progressive evolution towards Na-rich varieties upwards the stratigraphic column (cf. Fig. 4.44 in subsection 4.3.6).

Eales *et al.* (1991) showed that the averaged %An of cumulus plagioclases generally evolves to more Na-rich compositions from the N (Amandelbult) to the SE (Crocodile River Mine) in the western limb. This is in coincidence with the facies model suggested by Scoon and Teigler (1994) for this limb. According to this model more evolved plagioclases, i.e. Na-rich ones, would rather occur distal to a feeder. If one compares data from the NE of the eastern limb, i.e. data from Cameron (1980, 1982) and data from the S (this study), there is no distinct difference in the %An of plagioclase throughout the Middle Group. Only the range in the %An appears to be higher in plagioclase from core HEX10, i.e. the south of the eastern Bushveld, which probably can be taken as evidence for the presence of a more evolved melt in the south of the eastern limb.

Table 4.40 Anorthite content (%An) of plagioclase. *N.a.*: no data available.

	eastern limb	**western limb**	
	this study	Eales *et al.* (1991)	Teigler *et al.* (1992)
cumulus plagioclase	71-95	n.a.	75-81
intercumulus plagioclase	75-90	60-75	53-83
plagioclase as inclusion	78-87		n.a.

Table 4.41 summarizes data for orthopyroxene chemistry from this study and data from the literature. Compared to the CZ of the western BC, variations in MgO content of orthopyroxene from the MG are limited, but more intense for FeO concentrations. Eales *et*

al. (1991) as well as Teigler *et al.* (1992) report decreasing Mg# with stratigraphic height, which in general coincides with data from this study (cf. subsection 4.3.5.2).

Table 4.41 Range of orthopyroxene composition from this study compared with literature data from various locations of the western BC. All data are averages deriving from EMP analyses. Mg# has been calculated as $Mg/(Mg+Fe^{2+})$.

	MgO (wt%)		**FeO (wt%)**		**CaO (wt%)**		**MnO (wt%)**		**Mg#**	
	from	*to*	*from*	*to*	*from*	*to*	*from*	*to*	*from*	*to*
MG sequence (this study)	27.4	32.8	1.2	12.7	0.03	3.3	0.03	0.3	0.72	0.82
Eales *et al.* (1991)	29.5	31.1	9.3	11.7	1.2	1.3	0.2	0.4	0.82	0.86
Teigler *et al.* (1992)	28.3	32	8.2	13	0.9	2.1	0.2	0.3	0.81	0.85

As have been described for chromite chemistry (subsection 4.5.2) these compositional differences at the various sections of the BC may have been caused by different stages of evolved magma from different subchambers entering the two parts of the BC. Higher %An of plagioclase observed for the eastern limb relative to those found in the same stratigraphic sequence in the western limb may be due to the addition of more primitive magma. Since distinct differences in the %An throughout the eastern limb are missing, the magma feeding the north and the south of this limb perhaps intruded along the Steelpoort fault, or magma input additionally to the one from the TML occurred.

4.5.4 Whole-rock PGE geochemistry

4.5.4.1 PGE content of the chromitite layers

In Fig. 4.111 the whole-rock PGE content as well as the Cr_2O_3, Cu and S concentrations of the MG chromitite layers from various sites are presented and compared, and a possible connection of the Cr_2O_3, Cu and S contents with PGE mineralization should be pointed out.

The highest absolute PGE content (Σ 20,578 ppb) can be found in the chromitite layers of the MG sequence of this study, followed by Mooi Nooi chrome mine in the western (Σ 17,589 ppb; Naldrett *et al.*, 2009) and Thorncliffe in the eastern limb (Σ 15,549 ppb; Lee and Parry, 1988). The total PGE concentration of the MG chromitite layers at Kafferskraal (von Gruenewaldt *et al.*, 1986) is 12,394 ppb, whereas those at Union and Brits are below 10,000 ppb (9,081 or 8,890 ppb, respectively; Scoon and Teigler, 1994). The data of this study also yielded highest total Cu, whereas highest total S can be found in the MG chromitite layers at Mooi Nooi chrome mine investigated by Naldrett *et al.* (2009).

Within each sequence the highest PGE concentration exists in the MG2 chromitite layer(s), with the exception of Union and Brits, where the MG3 chromitite layer shows strongest PGE enrichment. Below that point the PGE content increases, whereas above it the PGE concentration decreases from one chromitite layer to the next.

Upwards the stratigraphic column the LT-PGE/HT-PGE ratios at all sites describe a curved line with the turning point at highest PGE concentrations, i.e. MG2 or MG3. The positive branch of the curved line describes an enrichment of the LT-PGE relative to the HT-PGE. From the turning point upwards the stratigraphic column of the MG enrichment of the HT-PGE relative to the LT-PGE is illustrated by the ratio. Interestingly, Brits is the site with the slightest variation in this ratio, ranging between 0.8 and 1.4 only. Furthermore, the turning point in the eastern limb occurs in the chromitite layer above the one with the highest PGE concentration.

As nicely can be seen from figure 4.111, high PGE concentrations are not linked to high whole-rock Cr_2O_3 content, since the latter is generally decreasing with increasing height in the stratigraphic column.

Cu and S values at the various sites differ in their distribution as well as their concentration. Except for Brits, no regular pattern in terms of in- and decreasing contents is visible. Cu contents are generally low and range between 10 and 40 ppm in the western limb, and 15 and 200 ppm on average in the eastern limb. The highest amount of Cu has been determined during this study with values up to 6765 ppm. Background has been found to be 19 ppm Cu at Union (Scoon and Teigler, 1994) but seems to be higher in the eastern limb (subsection 4.4.1). Thus, in the western as well as in the eastern limb enrichment of Cu in the MG chromitite layers is present, but S content is low at all sites.

As figure 4.111 shows neither Cu enrichment nor the amount of S are related to PGE concentration, i.e. high Cu and S concentration is not necessarily linked to elevated amounts of PGE within the chromitite layers. Thus, PGE precipitation with BMS is not supported by the data for the MG.

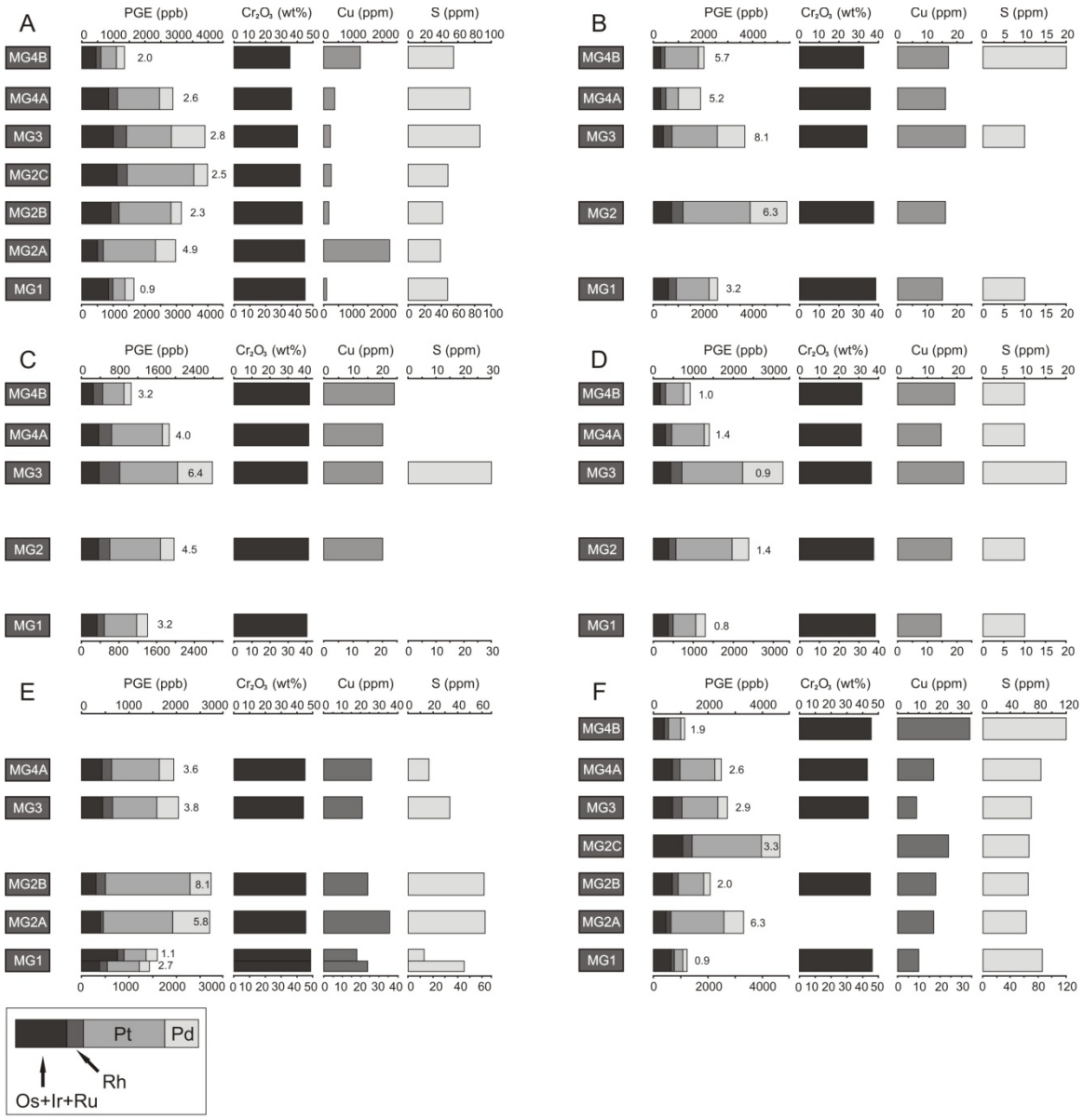

Figure 4.111 Distribution of the PGE, Cr_2O_3, Cu and S in the individual chromitite layers of the MG at various sites. ***A:*** this study; ***B:*** farm Thorncliff 374 KT (Lee and Parry, 1988); ***C:*** Union (Scoon and Teigler, 1994); ***D:*** Brits (Scoon and Teigler, 1994); ***E:*** Kafferskraal, Marikana (von Gruenewaldt *et al.*, 1986); ***F:*** Mooi Nooi chrome mine (Naldrett *et al.*, 2009). *D* and *E* show Ru only for the HT-PGE. Cr_2O_3, Cu and S are whole-rock data except for *E* and *F*, where Cr_2O_3 microprobe data of chromite grains are presented. Numbers next to PGE bars represent LT-PGE/HT-PGE ratio.

The most common PGE at all sites is Pt, followed by Pd and Ru, Rh, Ir and Os (Tab. 4.42). Furthermore, Pt is the most common PGE within every single chromitite layer. Due to the amount of the single PGE in each chromitite layer at the various localities, a slight indication for a vertical PGE zonation is visible. The MG1 at all sites presented here is dominated by Pt and Ru only. The MG2 at Union and Brits in the western (Scoon and Teigler, 1994) and at Tweefontein in the eastern limb (Lee and Parry, 1988) is enriched in

Pt and Pd. On the other hand, when looking at the individual chromitite layers MG2A, MG2B and MG2C at Mooi Nooi (Naldrett *et al.*, 2009), Kafferskraal (von Gruenewaldt *et al.*, 1986) and core HEX10 of this study prominent differences can be observed. Except for the MG2A chromitite at Kafferskraal, which shows enrichment in Pt and Ru, this layer at Mooi Nooi and core HEX10 is dominated by Pt and Pd. In the MG2B the situation is just inversely. The MG2C again is enriched in Pt and Ru.

The MG3 generally shows Pt and Pd enrichment only, but at Mooi Nooi Ru replaces Pd as the second most common PGE.

In the MG4A chromitite layer Rh dominates after Pt, particularly at Union and Brits. At the other locations, Pt and Ru are most important, with the exception of Tweefontein, where Pt and Pd occur as the two most common PGE. The situation of PGE distribution stays the same in the MG4B chromitite layers. Only at Brits Rh is replaced by Ru.

Table 4.42 Total PGE contents from averaged PGE contents per layer of all the chromitite layers at the different sites. Letters correspond to localities presented in figure 4.111.

	A	B	C	D	E	F
Os	739	326	271	0	0	604
Ir	993	638	582	0	0	833
Ru	3958	1397	843	1620	2710	3217
Rh	1753	1481	1301	830	960	1625
Pt	9026	7686	4537	4560	6304	8783
Pd	3426	4021	1547	1880	2420	2527
LT-PGE	14205	13188	7385	7270	9684	12935
HT-PGE	5690	2361	1696	1620	2710	4654
total	19894	15549	9081	8890	12394	17589

4.5.4.2 PGE content of the silicate layers

For comparison with PGE data of the silicate rocks of this study only two references have been found in the literature: Maier and Barnes (1999), who investigated the silicate rocks at Union, and Scoon and Teigler (1994) giving a complete data set for the silicate rocks at Brits. The data of the whole-rock PGE content as well as Cr_2O_3, Cu and S concentrations are presented in figure 4.112.

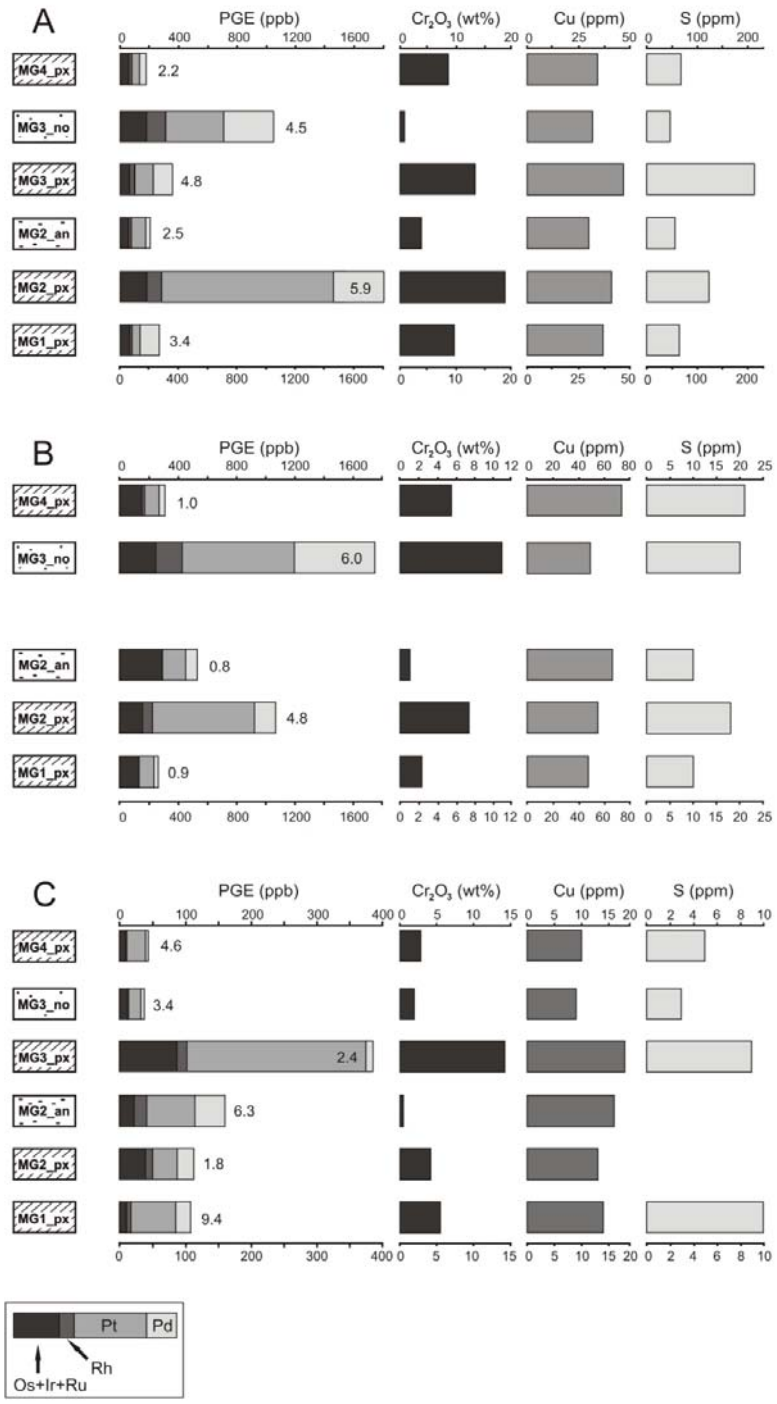

Figure 4.112 Distribution of the PGE, Cr_2O_3, Cu and S in the individual silicate layers of the MG at various sites. ***A:*** this study; ***B:*** Brits (Scoon and Teigler, 1994); ***C:*** Union (Maier & Barnes, 1999). Cr_2O_3, Cu and S are whole-rock data. Numbers next to PGE bars represent LT-PGE/HT-PGE ratio.

At Union and Brits the silicate layer with the highest PGE content can be found in the hanging wall of the most enriched chromitite layer, i.e. the MG3. According to lithological diversity, this is the MG3 pyroxenite at Union and the MG3 norite at Brits. Data from this study show that highest PGE concentration in silicate rocks occur in those comprising a

large amount of cumulus chromite, i.e. MG2 pyroxenite and MG3 norite. An association of the PGE with the amount of Cr_2O_3 can also be obtained from Union and Brits, where PGE enriched silicate layers contain elevated amounts of whole-rock Cr_2O_3 (Fig. 4.112).

As could be shown for the chromitite layers before, no coincidence in the development of Cu, S and the PGE is present. The match of these concentration in some layers, i.e. the MG3 pyroxenite at Union, appears to be accidental and rather due to the presence of PGE sulphides than BMS controlling PGE mineralization.

The development in the PGE concentration in the silicate layers upward the stratigraphic column of the MG at Brits and in core HEX10 from this study is very similar and shows the same pattern of in- and decreasing LT-PGE/HT-PGE ratio. At Union the PGE content first increases up to the MG3 pyroxenite and then decreases again. Furthermore, the development of the LT-PGE/HT-PGE ratio at Union is exactly reverse to the other two sites, and the most enriched layer is enriched in the HT-PGE relative to the LT-PGE when compared to the same stratigraphic level at the other sites.

Table 4.43 Total PGE content from averaged PGE contents per layer of the silicate layers of the MG from **A:** this study; **B:** Brits (Scoon and Teigler, 1994), and **C:** Union (Maier and Barnes, 1999).

	A	B	C
Os	44	0	17
Ir	87	0	38
Ru	306	983	123
Rh	213	268	55
Pt	816	1828	498
Pd	722	843	113
HT-PGE	437	983	177
LT-PGE	1751	2938	665
total	2188	3921	842

4.5.4.3 Summary

The consistence in the relative PGE amount in the MG chromitite layers throughout the entire BC suggests that PGE mineralization occurred by the same process, but most likely apart from the *R*-factor model, since S contents are too low to significantly be

responsible for PGE scavenging. Differences in absolute PGE abundances probably can be ascribed to different evolution stages of melt the respective sites were fed with (cf. subsections 4.5.2 and 4.5.3). Hereby, magma of more primitive composition is most likely enriched in the HT-PGE relative to the LT-PGE, since higher melt temperatures are present and PGE fractionation can result from temperature differences. Hence, high Pt/Ir ratios suggest lower temperature of the melt. Additionally, a PGE pre-concentration of the magma may have occurred in the smaller subchambers postulated by Kruger (2005) to be present at least during formation of the LCZ.

The variations in the S content at the various sites may be also due to different fractionation stages of melts, since progressive melt evolution by fractional crystallization is thought to increase sulphide saturation of a melt (e.g. Naldrett and von Gruenewaldt, 1989). Additionally, the assimilation of varying amounts of S-bearing country rocks is possible to result in the varying S contents.

The enrichment of the MG chromitite and silicate layers in Cu (the whole-rock Cu/S ratio generally exceeds the Cu/S ratio for chalcopyrite; cf. subsections 4.4.1 and 4.4.2; Maier and Barnes, 1999; Scoon and Teigler, 1994) may also derive from an external source, probably from a metal-loaded fluid as have been suggested by Baker *et al.* (2002).

According to the data, PGE fractionation in the MG appears to have occurred on varying paths. Simultaneously high PGE and Cr_2O_3 contents suggest some chromite control. Low S contents indicate that PGE mineralization dominantly took place under sulphide undersaturated conditions. Nevertheless, the occurrence of minor amounts of S (and hence BMS) indicates that minor PGE fractionation by sulphide melt may have occurred.

5. Interpretation and discussion of data

5.1 General considerations

As have been shown in subsection 2.2.1 several models dealing with the formation of chromitite layers exist. The model that can be applied to the MG from core HEX10 not only needs to explain the formation of several massive chromitite layers, but also the precipitation and deposition of the compositionally different silicate cumulate layers. It furthermore should explain the occurrence of reversals in the trends of normal fractional crystallization that have been observed, and fit the progressive evolution of chromite and silicate chemistry throughout the MG sequence.

Additionally, it needs to explain the lateral progressive evolution of chromite and the silicate minerals from proximal to distal facies, as have been pointed out in section 4.4.

There also exist many models on PGE mineralization of chromitite layers (subsection 2.2.2), and some of the chromite formation models can also be applied to PGE mineralization, i.e. those dealing with magma mixing (Irvine *et al.*, 1983; Rice and von Gruenewaldt, 1991, 1995; Kinnaird *et al.*, 2002). However, there are other factors that can control PGE mineralization and distribution, i.e. R-factor or metasomatic processes. It has been shown that high PGE concentrations occurring in the MG sequence are not necessarily linked to high amounts of chromite or sulphur (subsections 4.4.1.2 and 4.3.2.1), and thus the present PGE mineralization of the MG sequence could be the result of several events.

5.2 Formation of the cumulate succession of the MG intersected by borehole HEX10

Due to the lateral extension of individual chromitite layers over several hundred kilometres, a major process guaranteeing the lateral continuity of chromitite formation is needed. The lack of marked compositional changes in silicate chemistry (cf. Fig. 4.44 in subsection 4.3.6) before or after chromite precipitation is indicative for the absence of abrupt pressure changes, as have been suggested by Lipin (1993; cf. subsection 2.2.1). He argues that “the great lateral continuity of the chromite seams implies that the mechanism that caused the chromite seams to form was felt throughout the magma chamber at the same time”, and that “a change in total pressure will be propagated at the

speed of sound". Surely, the speed and efficiency of a pressure change would be greater than magma mixing, but in the eyes of the author of this study can`t be accounted for the lateral evolution of mineral and whole-rock geochemistry of the MG, as has been pointed out during this study (cf. subsections 4.5.2 and 4.5.3). It is commonly assumed that the magma addition in the Bushveld Complex occurred as a fountain (e.g. Cambell *et al.*, 1983), since it is a plume-driven replenishment system (Hatton, 1995). Hence, the magma intrudes with a fast momentum, rather than oozes as stated by Lipin (1993). It can't be excluded that a local pressure increase in the surroundings of the fountain occurred, but in a magma chamber the size of the Bushveld Complex probably wouldn't be laterally consistent. This leads to the conclusion that pressure fluctuations occurred and thus most likely wouldn't result in the accumulation of continuous monomineralic chromitite layers as can be found in the Bushveld Complex.

In the eyes of the author, the shear aggregation model with cascade enrichment proposed by Rice and von Gruenewaldt (1991; 1995), of which a short summary is given in subsection 2.2.1, cannot be ascribed to sufficiently produce massive chromitite layers as are present in the MG sequence. Although the whole-rock Cr_2O_3 content decreases systematically from layer to layer upwards the stratigraphy of the MG sequence, which the authors took as evidence for cascade enrichment, the manifold reversals of the Mg# as well as the $Cr/(Cr+Fe^{3+})$ and Cr/(Cr+Al) ratios that occur within the MG chromitite layers can't be explained with this model. Some authors suggest that geochemical reversal can be induced by pressure changes (e.g. Cameron, 1977; Lipin, 1993). i.e. by decreasing pressure during rupturing events of the magma chamber. If the Bushveld magma(s) hosted sufficient amounts of volatiles, i.e. CO_2, to produce overpressure during cooling is still debatable. Different from the Stillwater Complex, where indications for CO inclusions in olivine exists (Roedder, 1965) any evidence for CO_2- fluid inclusions deriving from primary magmatic events in the Bushveld Complex has been described so far. If the amount of deuteric fluids probably deriving from the cooling Bushveld melts were sufficient enough to produce a pressure increase at all, is also not certain.

Thus, although the considerations of Lipin (1993) about the chromite seam formation of the Stillwater Complex appear to be reasonable, they are probably not directly transferable to an intrusion the size of the Bushveld Complex (which is ca. 8 times the size of the Stillwater Complex).

In view of the results of this study and according to the arguments stated above, a model involving repetitive magma intrusion along the Thabazimbi-Murchison-Lineament (TML) (Kruger, 2005) and magma mixing seem to be the most likely processes for the formation of the cyclic units occurring in the MG of core HEX10. The shifts in mineral as well as in whole-rock geochemistry of the MG sequence of core HEX10 upwards the

stratigraphic column (cf. subsections 4.3.1, 4.3.2, 4.4.1 and 4.4.2) indicate multiple magma replenishment and thus open-system conditions (Kruger, 1994). Hence, this appears to be the most plausible way to describe chromite formation in the Bushveld magma chamber.

The model suggested for the formation of the chromitite layers in the MG sequence of core HEX10 basically is equivalent to the one described by Kinnaird *et al.* (2002). The presence of high initial Sr ratios detected from plagioclases being interstitial to chromite within the chromitite layers of the CZ led Kinnaird *et al.* (2002) to the conclusion of the influence of granophyric roof-rock melt during chromite formation, which triggered chromite saturation and its precipitation in nearly monomineralic layers. While the UG chromitites appear to rather show isotopic shifts than spikes the chromitite layers of the MG show strong increases of the Sr_i ratio properly. Thus, crustal contamination as a trigger for the formation of monomineralic chromitite layers seems to be well applicable for the MG, instead of simple magma mixing only. Although the contamination path with siliceous melt was rejected by Irvine *et al.* (1983), a revival of the theory produced by Irvine (1977) is substantiated not only by data from Kinnaird *et al.* (2002), but also by Spandler *et al.* (2005; 2007). Several indications for crustal contamination can be observed in the samples from the MG, e.g. Na- rich silicate inclusions in chromite of the chromitite layers (cf. subsection 4.3.4.3) and negative Nb anomalies of the silicate layers (Fig. 5.1). Detailed description of the formation of the MG cyclic units of core HEX10 are described in subsections below. For now, only general considerations are portrayed.

Injection of magma most likely occurs in the form of a fountain, since it may be injected with a fast momentum into the residual melt already present in the Bushveld magma chamber (cf. Campbell *et al.*, 1983). Interaction with the granophyric roof rock (i.e. Rooiberg rhyolites of the Kwaggasnek Formation (cf. SACS, 1980; Schweitzer *et al.*, 1995) results in the formation of felsic melt at the top of the Bushveld magma chamber, which is entrained by the highly turbulent motion within the fountain. The resulting hybrid melt shifted the crystallization path into the stability field of chromite, resulting in the precipitation of chromite only (see Fig. 2.7 in subsection 2.2.1). Supercooling during the mixture of the primitive parental liquid with the felsic melt releases high activation energy for nucleation (Campbell, 1996), which is why crystal settling is the major mechanism of crystallization during the formation of the MG chromitite layers. Since the crystal load increases the density of a liquid (Rice and Eales, 1995), the chromite-bearing slurry collects at the base of the fountain and spreads out across the bottom to form a layer. With this slurry interstitial silicate liquid is transported. During cooling of the layer, adcumulus growth of single chromite grains occurs as well as crystallization of the silicate minerals from the interstitial liquid.

At the same time, as the fountain of parental melt is mixing with the felsic roof rock melt, it also interacts with the residual melt in the magma chamber. This leads to the formation of a hybrid layer on top of the chromitite layer, which also spreads laterally. Due to cooling, the hybrid layer can break up into several sublayers of different temperature and densities, separated by diffusive interfaces. According to Huppert and Sparks (1981) the transfer of heat greatly exceeds the transfer of masses at these interfaces. Hence, compositional mixing between the individual sublayers is very limited only.

Crystallization normally should start in the top layer, since it is the coolest and least dense. Increasing pressure in the lowermost layer caused by the weight of the overlying liquid column lowers the liquidus temperature of orthopyroxene (Campbell, 1996). Additionally, more crystallization surfaces are available in the lowermost layer, i.e. the bottom and the walls. Hence, in situ crystallization of orthopyroxene starts in the lowermost layer just on top of the chromitite layer, and not in the uppermost one.

Since crystallization lowers the density of the lowest layer, at some stage overturning occurs due to the equalization of densities in the lowermost and its top layer. The diffusive interface breaks down, and mixing takes place to form another hybrid, probably resulting in the accumulation of norite or anorthosite. Now, the process of crystallization and overturning is repeated.

Due to the different nature of the silicate layers in the LCZ and the UCZ of the MG sequence of core HEX10 the formation of these stratigraphic intervals are discussed separately. However, there is a feature that can be observed within all the silicate layers investigated during this study. They all show a negative Nb anomaly (Fig. 5.1), which perhaps can be taken as evidence for assimilation of continental crust since they resemble the negative peaks of the UCC and LCC patterns. Huppert *et al.* (1985) suggested that at a late stage the introducing magma could have assimilated pre-heated wall rocks, i.e. continental crust, in the feeder conduits. At the beginning of the influx of parental melt, i.e. during chromite formation, the wall rocks of the feeder are relatively cold and hence are not easily incorporated into the entering liquid. With continuous influx the wall rocks get increasingly warmer, and can be assimilated easier, which results in the negative Nb anomaly of the silicate layers. Since the amount of assimilated material is small, major changes in geochemistry do not occur. Isotopic evidence (initial $^{187}Os/^{188}Os$ ratio) for crustal assimilation comes from McCandless *et al.* (1999), who suggested the assimilation of about 5% mafic granulitic lower crust. However, a negative Nb anomaly is lacking for each of the chromitite layers of the MG sequence (Fig. 5.2). Generally, the MG chromitite patterns don't resemble any of the comparative ones (i.e. the normalized patterns for the upper and lower continental crust as well as the primitive mantle) but there are certain features that can be ascribed to the impact of crustal material, e.g. negative Rb

anomalies. As mentioned in subsection 4.4.1, the positive Nb peaks of the chromitite layers could indicate the lower mantle to be the source of the parental melt. Additionally, all the chromitite layers of the MG sequence are enriched in Ti relative to any crustal or mantle patterns.

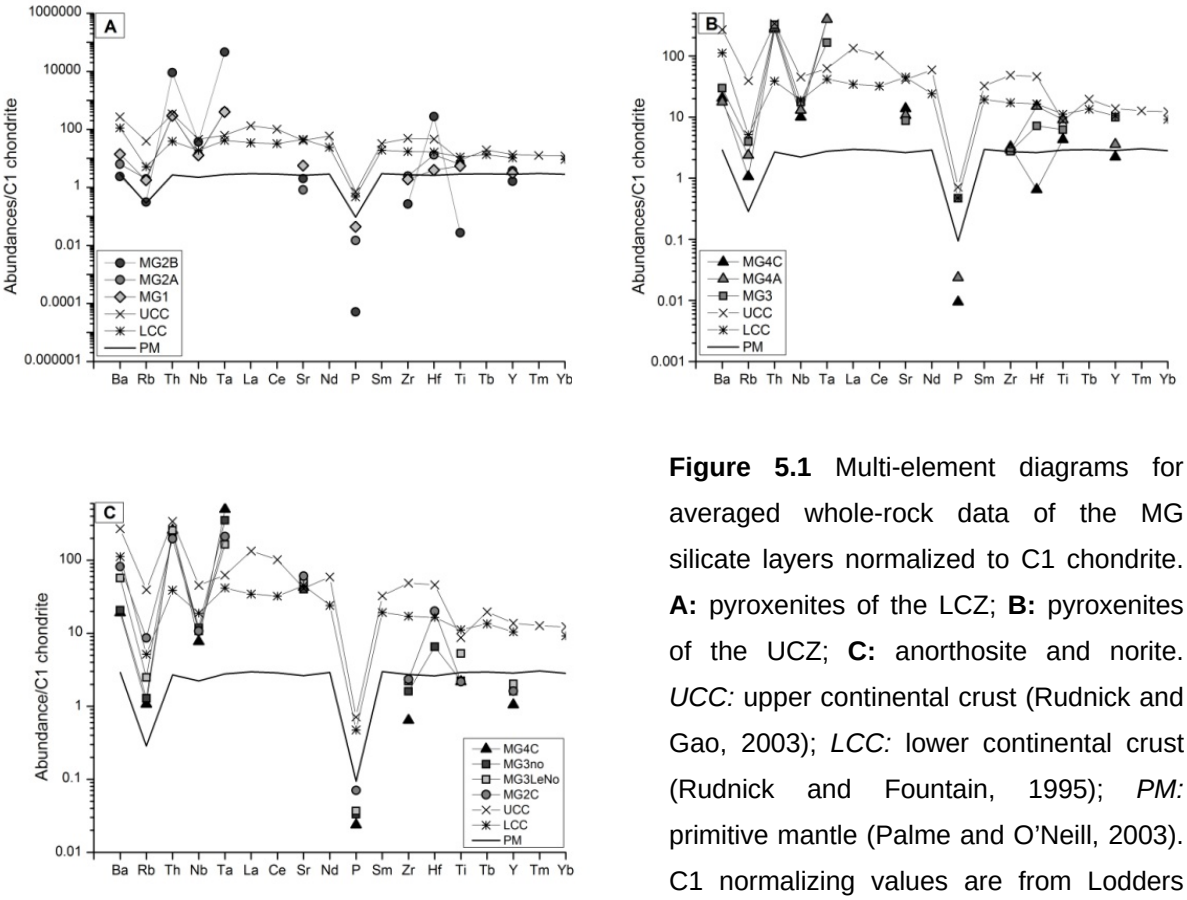

Figure 5.1 Multi-element diagrams for averaged whole-rock data of the MG silicate layers normalized to C1 chondrite. **A:** pyroxenites of the LCZ; **B:** pyroxenites of the UCZ; **C:** anorthosite and norite. *UCC:* upper continental crust (Rudnick and Gao, 2003); *LCC:* lower continental crust (Rudnick and Fountain, 1995); *PM:* primitive mantle (Palme and O'Neill, 2003). C1 normalizing values are from Lodders (2003). Data are given in table 4.36 in subsection 4.3.2.

However, although features of impacts of lower mantle as well as continental crust exist, these contrasting Nb anomalies in each cyclic unit are perhaps caused by the cumulate character of the rocks. As have been mentioned before, Ti as well as Nb are controlled by the presence of rutile. Since rutile occurs in elevated amounts in the chromitite layers, it has consumed large amounts of Ti and Nb from the parental melt during its formation. This results in relative depletion of these elements in the hybrid responsible for the formation of the silicate layer on top of the massive chromitite, which could explain negative peaks for Nb and Ti and consequently the relative dearth of rutile within the silicate layers.

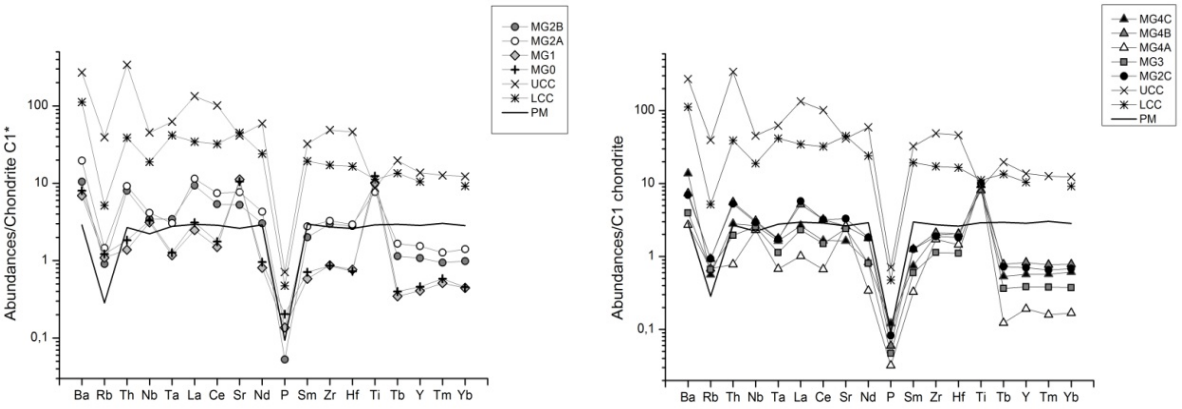

Figure 5.2 Multi-element diagrams for averaged whole-rock data of the MG chromitite layers normalised to C1 chondrite; left: chromitite layers of the LCZ; right: chromitite layers of the UCZ. UCC: upper continental crust (Rudnick and Gao, 2003); LCC: lower continental crust (Rudnick and Fountain, 1995); PM: primitive mantle (Palme and O'Neill, 2003). *C1 normalizing values are from Lodders (2003). Data are given in table 4.32 in subsection 4.4.1.

5.2.1 Cyclic units of the LCZ

In figure 5.3, the formation of the cyclic units of the MG belonging to the LCZ (i.e. MG1 – MG2B) is illustrated. Since each cyclic unit comprises chromitite and pyroxenite only, a residual melt of pyroxenitic composition is suggested (LZ residue), being present in the magma chamber (Fig. 5.3A).

The addition of parental melt and mixing with the granophyric roof rock melt (Fig. 5.3B) leads to the formation of a first hybrid (H_1), according to the contamination path described by Irvine (1977). The composition of H_1 lies within the stability field of chromite, thus only chromite is precipitating (Fig. 5.3F). As mentioned above, crystal load increases the density of a melt. Hence, a chromite bearing slurry settles towards the base of the chamber, tearing silicate liquid with it, being interstitial to chromite (Fig. 5.3C). It is fractionating during cooling, with its composition moving towards and then along the chromite-orthopyroxene cotectic to crystallize orthopyroxene besides chromite (Fig. 5.3F). Eventually it arrives the triple junction chromite-orthopyroxene-plagioclase causing the formation of plagioclase. As long as injection of parental melt is continuous, chromite is crystallizing. At the same time large amounts of silicate liquid emerge, which is a mixture of parental melt, granophyric roof-rock melt as well as residual melt from the Bushveld magma chamber. Since it has a lower density than the chromite-bearing mush, it forms a hybrid layer on top of it (H_2; Fig. 5.3C and 5.3D).

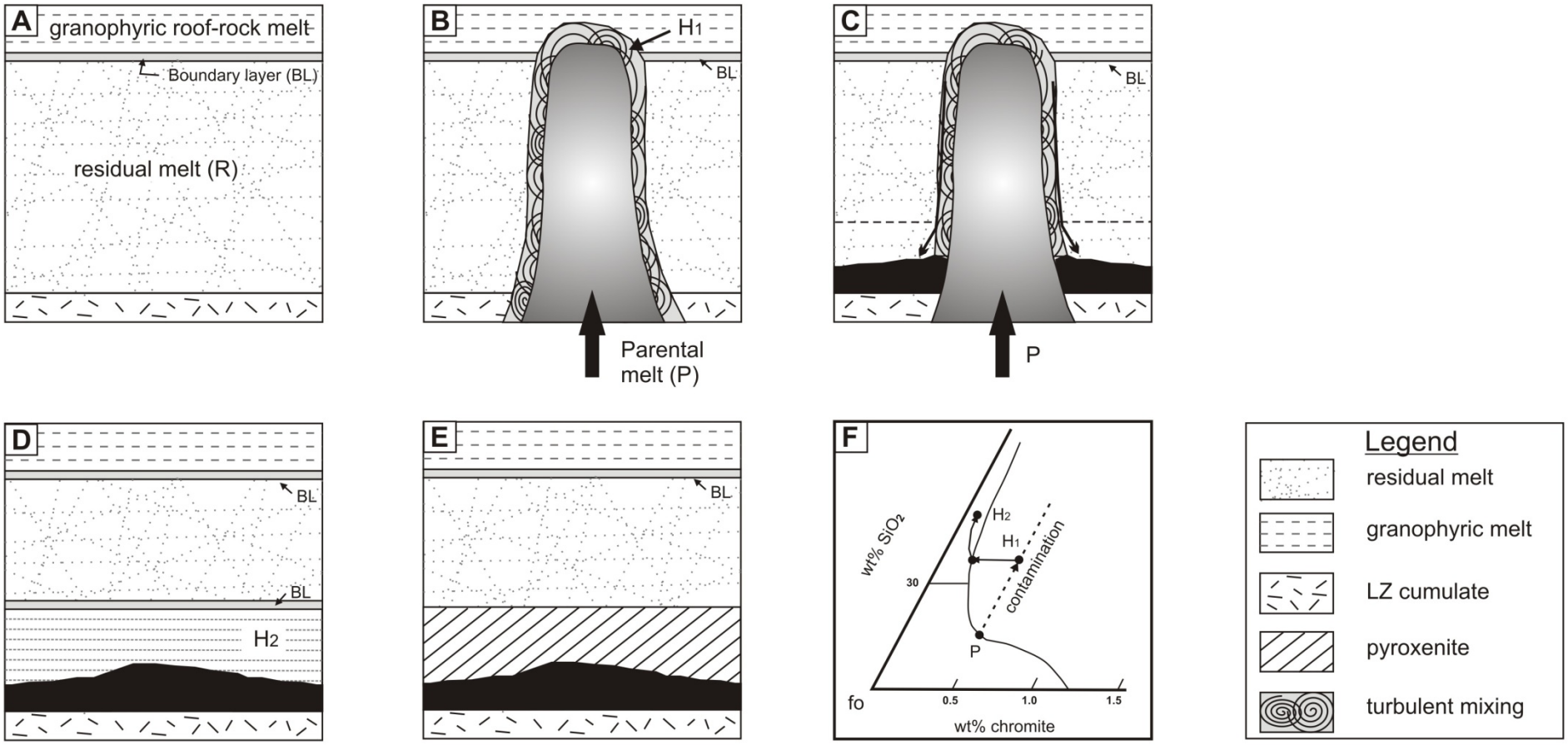

Figure 5.3 Evolution of the cumulates of the LCZ as is present in core HEX10 (modified after Kinnaird *et al.*, 2002). **(A)** Situation in the Bushveld magma chamber after the deposition of the LZ. **(B)** Intrusion of a fountain of parental melt producing a hybrid liquid (H_1) and zones of turbulent mixing and entrainment of pyroxenitic residual melt (R). **(C)** Due to its high gravity, the chromite-bearing mush sinks down producing a massive chromitite layer. **(D)** Further entrainment of pyroxenitic residual melt creates a second hybrid (H_2), from which **(E)** a pyroxenitic layer crystallizes. **(F)** Ternary diagram forsterite-chromite-SiO_2 illustrating the formation of chromite by contamination with a siliceous melt (after Irvine *et al.*, 1983). For details see text.

Chromite is always co-precipitating with the silicate minerals, which can be interpreted to be the basis for the observed adcumulus growth of chromite observed within the chromitite layers of the MG sequence resulting in welding and grain coarsening of chromite (Fig. 4.9 in subsection 4.2.1) and inclusions of former silicate melt (Fig. 4.10 in subsection 4.2.1 and Fig. 4.36 in subsection 4.3.4.3). The Na-rich silicate inclusion that can be found within the chromitite layers (cf. subsection 4.3.4.3) can most likely be taken as evidence for the assimilation of crustal material, i.e. felsic roof rock melt, during the formation of the MG chromitite layers. Isotopic evidence has been provided by Kinnaird *et al.* (2002), who found that plagioclase interstitial to chromite has extremely high Sr_i relative to those occurring in the adjacent silicate layers.

As figure 4.7 in subsection 4.2.1 shows the amount of chromite relative to the co-precipitating silicate minerals increases from the MG1 to the MG2B chromitite regardless of the thickness of the individual layers. This feature is accompanied by a decreasing whole-rock Mg# for the same interval (cf. Tab. 4.25 and Fig. 4.71 in subsection 4.4.1). A high proportion of the whole-rock Mg# is controlled by orthopyroxene. Thus, this feature is linked to the amount of orthopyroxene within the individual chromitite layers and shows declining quantities of orthopyroxene relative to chromite from the MG1 to the MG2B chromitite. One explanation for the declination of orthopyroxene is compaction caused by the crystal and liquid pile. This increases the amount of chromite relative to the silicate minerals by filter pressing. Another possibility is the addition of crystal charged parental melt carrying chromite microphenocrysts. With reference to Eales (2000), the author of this study suggests that this feature of advancing quantities of chromite within the massive chromitite layers is caused by increasing amounts of chromite microphenocrysts being transported with each injection of parental magma into the Bushveld magma chamber.

Another feature that can be observed in the MG chromitites of the LCZ is the increasing Mg# of chromite from MG1 to MG2B (cf. Fig. 4.23 and corresponding text in subsection 4.3.1). After Ulmer (1969) an increase in the fO_2 triggers chromite precipitation resulting in an Mg enrichment of spinels. However, both the MG2A and the MG2B chromitite layer show lowest REE patterns when compared to the other chromitite layers of the LCZ (cf. Fig. 4.75 in subsection 4.4.1) indicating a quite primitive character of the magma mixture they derive from, which rejects an increase in fO_2. Together with the increasing amounts of chromite from the MG1 to the MG2B chromitite layer it is suggested that Cr-microphenocrysts are added with the intruding melt. As have been suggested by Eales (2000) these microphenocryts could derive form a lower-level magma chamber, which would be in accordance with the suggestion of Kruger (2005) of connected subchambers being responsible for the formation of the LCZ. It not only overcomes the multiple stated problems of relatively low amounts of Cr being soluble in silicate melts (Hill

and Roeder, 1974) and the lack of evidence of appropriate residua of source liquid for the CZ, but also explains the features observed within the LCZ chromitite layers during this study.

Data from this study also show that chromite from massive layers have a higher Mg# than those occurring within the silicate layers (cf. tables 4.2, 4.6 and 4.7 in subsections 4.3.1 and 4.3.2), which has been ascribed to co-precipitating silicate minerals changing chromite chemistry by equilibration during cooling (subsection 4.3.3). Cameron and Desborough (1969) ascribed the aspect of higher Mg# to be caused by increasing fO_2. However, Teigler and Eales (1996), who investigated samples deriving from Union in the western Bushveld Complex, reported that the amount of ferric iron in chromite from massive chromitite layers is lower than those occurring in the silicate layers. This is in contradiction to the data from the eastern Bushveld (Cameron and Desborough, 1969; this study) and indicates that changes in fO_2 are rather of regional importance.

As mentioned above, a second hybrid forms contemporaneously to chromite crystallization (Fig. 5.3D). Its composition is situated in the stability field of orthopyroxene, causing the formation of a pyroxenitic layer. Again fractional crystallization drives the composition of the liquid towards the orthopyroxene-plagioclase cotectic, resulting in the co-precipitation of both minerals. Evidence for progressive evolution of orthopyroxene as well as plagioclase composition from bottom to top of the pyroxenitic layers is exemplarily given by decreasing Mg# of orthopyroxene as well as decreasing %An of plagioclase from the pyroxenite of the MG1 cyclic unit (cf. Fig. 4.44 in subsection 4.3.6).

However, both the MG1 and the MG2A pyroxenite show increasing amounts of orthopyroxene but decreasing plagioclase contents towards the top of each layer (cf. Tab. B-1 and B-2 in appendix B) although a decreasing whole-rock Mg# for both layers with height exists (cf. Fig. 4.90 in subsection 4.4.2). An explanation for this feature is given by Boorman *et al.* (2004) suggesting rapid cooling at the bottom of a layer due to crystallization. Since compaction of the cumulate pile occurs at the same time, the interstitial liquid is separated from the hybrid on top of the crystal pile. As a result, the crystallization path is shifted onto the orthopyroxene-plagioclase cotectic. Evidence for compaction occurring in the MG sequence has been shown by the occurrence of dislocation creep (cf. subsection 4.2.2.1). The point that compaction as well as temperature decrease is strongest in the lowermost part of a layer leads to the observed feature of decreasing plagioclase contents and increasing amounts of orthopyroxene from bottom to top of the MG1 and MG2A pyroxenites.

The MG0 cyclic unit differs slightly in chemistry from the cyclic units occurring above it. The chromitite layer shows increasing whole-rock Mg# from bottom to top of the layer as well as decreasing Cr_2O_3 contents. Additionally, increasing Al_2O_3 and CaO contents are

present (cf. Tab. 4.25 in subsection 4.5.1). These features point to increasing amounts of the silicate minerals orthopyroxene as well as plagioclase towards the top of the chromitite layer (cf. Fig. 4.7 in subsection 4.2.1). Hence, weakening influence of granophyric roof rock melt and contemporaneously increasing entrainment of LZ residue into the parental melt could be concluded.

The whole-rock composition of the pyroxenite on top of the massive MG0 chromitite shows decreasing Mg#, which points to progressive evolution of orthopyroxene towards the top of the layer. Additionally, increasing K_2O and decreasing CaO contents are interpreted to illustrate fractional crystallization of plagioclase (cf. Tab. 4.32 in subsection 4.4.2). Here, the same procedure applies that has been described for the formation of the MG1, MG2A and MG2B pyroxenites. The chromite enrichment towards the top of the MG0 pyroxenite demonstrates the onset of chromite precipitation; probably the first chromite grains sank into the pyroxenitic mush. The same sample with the high Cr_2O_3 content also shows the highest amount of K_2O compared to the other pyroxenitic samples of the MG sequence (sample JKL5 with 0.33 wt%; cf. Tab. 4.32 in subsection 4.4.2) and is positioned in the footwall of the MG1 chromitite layer, which can be taken as further evidence of the influence of granophyric roof rock melt triggering the precipitation of massive chromitite.

5.2.2 Cyclic units of the UCZ

According to the whole-rock geochemistry, the MG2C, MG3 and MG4B/4C chromitite layers have been formed during an event quite similar to the one being responsible for the formation of the LCZ chromitites (cf. subsection 5.2.1). During formation of the LCZ, the residual melt in the magma chamber is proposed to have evolved towards noritic composition (LCZ residue). Entrainment of the noritic residual melt into the parental magma caused the formation of plagioclase-rich cumulates, i.e. anorthosite and norite (Fig. 5.4). However, different results for chromite analyses in the course of stratigraphic development occur, which requires detailed considerations for the formation of the UCZ cyclic units.

With the exception of the MG4A chromitite, the Mg# of chromite within the MG chromitite layers of the UCZ decreases on average, which points to progressive evolution of chromite composition crystallizing from an increasingly evolving melt mixture. Decreasing $Cr/(Cr+Fe^{3+})$ and Cr/(Cr+Al) cation ratios of chromite corroborate the existence of an evolving liquid mixture (cf. Fig. 4.23 in subsection 4.3.1). This feature is also depicted within the decreasing whole-rock Mg# (cf. Fig. 4.71 in subsection 4.4.1) that

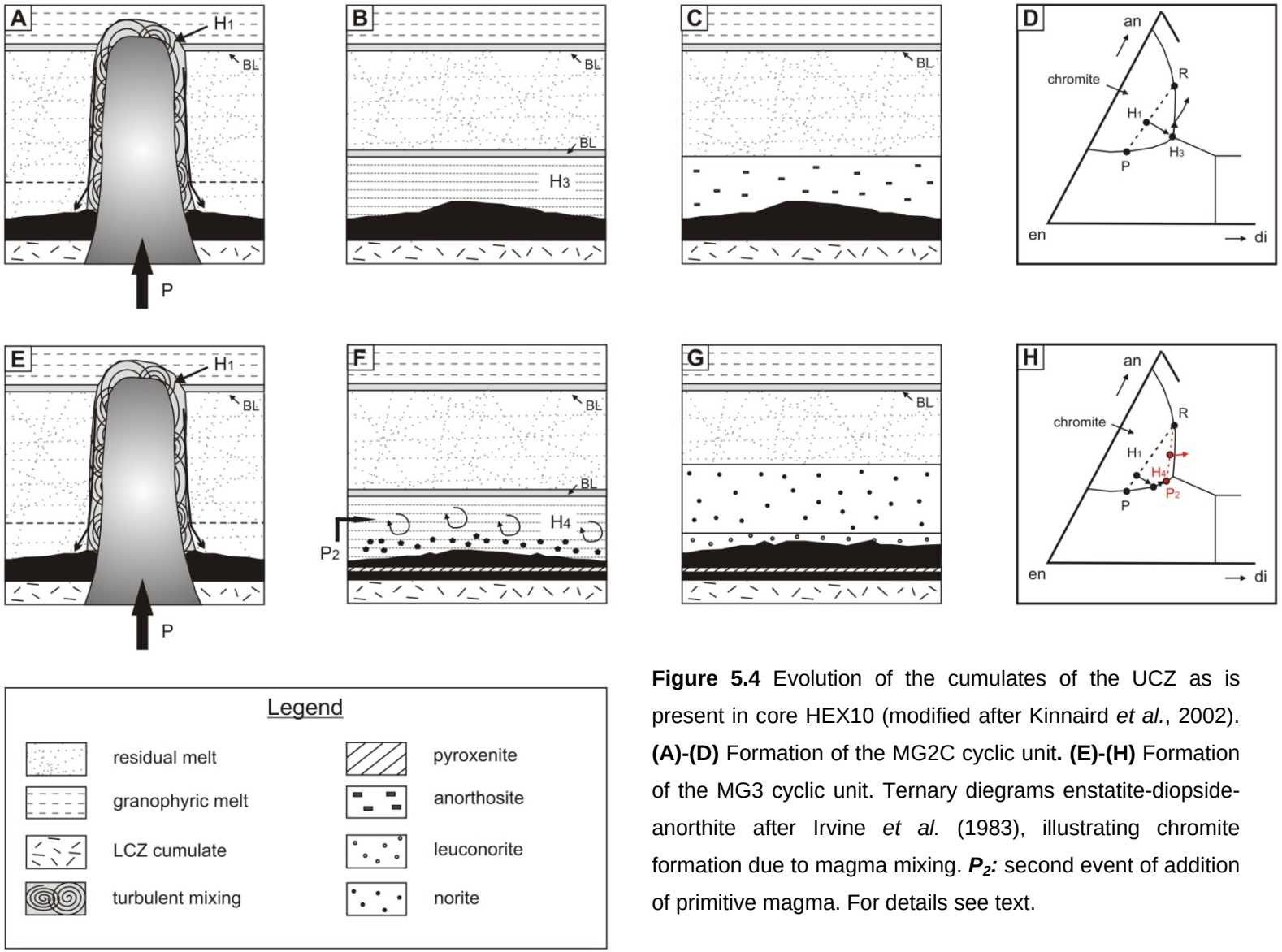

Figure 5.4 Evolution of the cumulates of the UCZ as is present in core HEX10 (modified after Kinnaird *et al.*, 2002). **(A)-(D)** Formation of the MG2C cyclic unit**. (E)-(H)** Formation of the MG3 cyclic unit. Ternary diegrams enstatite-diopside-anorthite after Irvine *et al.* (1983), illustrating chromite formation due to magma mixing. ***P_2:*** second event of addition of primitive magma. For details see text.

furthermore reflects the enrichment of silicate minerals, i.e. orthopyroxene, relative to chromite.

Development of plagioclase chemistry to lower %An (Fig. 4.44 in subsection 4.3.6) as well as decreasing whole-rock Mg# of the MG2C anorthosite (Fig. 4.90 in subsection 4.4.2) point to fractional crystallization within the hybrid layer (H_3), which is a mixture of parental melt, granophyric roof-rock melt and noritic residual melt.

As just have been mentioned, the MG4A chromitite is an exception, since it not only shows chromite with the highest Mg# of the UCZ, but also shows the highest whole-rock Mg# of the entire MG sequence. This feature is most likely due to the influx of a hot and primitive magma into the Bushveld magma chamber. Since the magma seems to be of even more primitive character than the magma forming the LCZ, perhaps a change in the mantle source occurred, i.e. partial melting of 'fresh' mantle material or at melting at higher depths.

According to the modified Harker plot Cr_2O_3-MgO (Fig. 4.74 in subsection 4.4.1) and the tenor of the whole-rock Mg# of the MG3 chromitite layer (Fig. 4.71 in subsection 4.4.1) the change in magma composition mentioned for the MG4A chromitite already started during the deposition of the MG3 chromitite layer. It interrupted the 'original' accumulation of the MG3 cyclic unit by a second event of injection, resulting in the deposition of the upper part of the MG3 chromitite layer with more primitive character. It is suggested that this primitive melt spreads as a basal flow at the level of the hybrid layer responsible for the formation of the MG3 norite, because the density of the primitive basal flow is higher than the one of the hybrid layer as well as the postulated noritic residual melt (Fig. 5.4F and 5.4G). Eventually, the intruding primitive liquid sank into the interstitals of the upper part of the MG3 chromitite mush due to density differences mixing with the interstitial liquid. Since the upper part had continuous supply of 'fresh' primitive liquid and the chromite mush wasn't strongly compacted at that time, it increasingly becomes enriched in Mg-rich orthopyroxene, which is depicted by the increasing whole-rock Mg# (Fig. 4.64 in subsection 4.4.1).

After accumulation of the MG3 chromitite layer, further fractionation of the hybrid layer (H_4) resulted in the deposition of leuconorite, which shows less orthopyroxene than the norite in its hanging wall (cf. tables B-1 and B-2 in appendix B). This is also the reason, why the leuconorite has lower whole-rock Mg# than the norite (Fig. 4.90 in subsection 4.4.2). After the deposition of the leuconorite, the boundary layer between the hybrid layer and the residual melt broke down, as their chemical composition has equalized. This resulted in the deposition of a huge pile of norite (11.26 m, see Tab. A-1 in appendix A).

Since the norite on top of the MG3 chromitite shows higher whole-rock Mg# than the anorthosite in its footwall, elevated quantities of Mg-rich orthopyroxene are present.

Hence, the mixed magma in the emerging hybrid layer seems to have been of more mafic composition. This furthermore could indicate an influx of primitive liquid, as has been mentioned above.

A special feature of the MG3 norite is the presence of spheroidal plagioclase inclusions in orthopyroxene. Their anorthite content has been found to be similar to those plagioclases occurring intercumulus in pyroxenitic layers (cf. subsection 4.3.6), suggesting their derivation as inherited plagioclases from a pyroxenitic layer, probably from the thin pyroxenitic band dividing the MG3 chromitite layer into two parts of different compositions with regard to melt evolution. As the primitive liquid enters in a second injection, plagioclase precipitation is stopped. Mixing of the remaining residual liquid from the hybrid layer with the new batch of primitive liquid induces orthopyroxene crystallization. Perhaps, the small plagioclase crystals had the function of a crystallization seed for orthopyroxene.

As figure 4.44 in subsection 4.3.6 shows, the %An of these inclusions increases from bottom to top of the noritic layer, simultaneously with the one of cumulus plagioclase. It supports the idea of persistent addition of primitive melt interrupting the course of fractionation within the spreading hybrid layer leading to reversals in fractionation trends.

Plagioclase inclusions have also been observed in the western Bushveld in the same stratigraphic sequence, but also in olivine norites and norites of the LCZ and the footwall of the Merensky unit (Eales *et al.*, 1991). They observed a connection between these inclusions and the appearance of geochemical reversals and concluded that this feature is caused by mixing of evolved residual liquid with batches of more primitive liquid. This corroborates the interpretation of the author just given above.

As has been mentioned for the MG4A chromitite layer, addition of primitive liquid can also be seen from modal composition, i.e. chromite content, and the reversals in mineral and whole-rock geochemistry of the plagioclase-bearing pyroxenite in its hanging wall (Fig. 5.5B; also cf. Fig. 4.44 in subsection 4.3.6 and Fig. 4.91 in subsection 4.4.2). The absence of plagioclase inclusions in the reversal part is most likely due to complete resorption.

The MG4B/4C cyclic unit formed during an event similar to the one for the MG2C unit, with the exception of a more mafic residual melt resulting from primitive magma addition. These cyclic units show normal fractionation trends (cf. subsections 4.4.1 and 4.4.2).

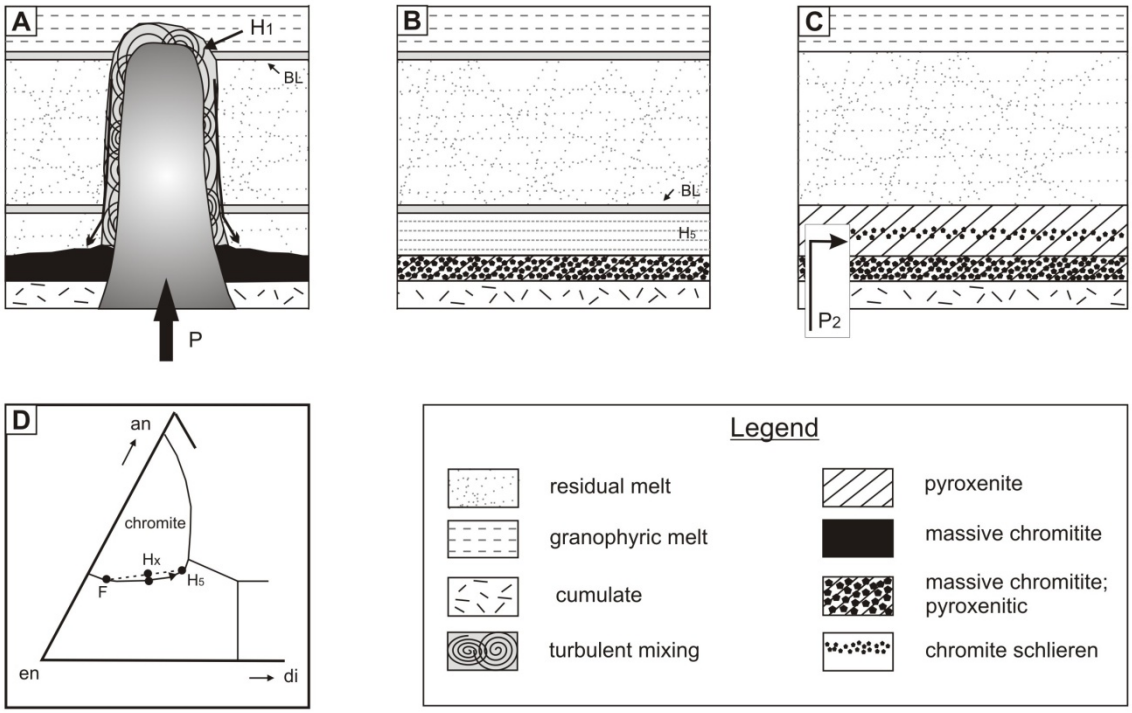

Figure 5.5 Schematic illustration of the formation of the MG4A cyclic unit. (**A-B**) Addition of primitive melt resulting in the formation of the MG4A chromitite layer and a pyroxenitic hybrid (H_5). (**C**) Repetitive influx of primitive magma during accumulation of the MG4A pyroxenite, producing several reversals in the geochemistry of the plagioclase-bearing pyroxenite in the hanging wall of the MG4A chromitite as well as the occurrence of chromitite schlieren. (**D**) shows the formation of the chromitite schlieren (H_x) in the ternary diagram enstatite-forsterite-anorthite (after Irvine, 1983).

5.2.3 Summary

As could be shown, repeated magma injection is the most likely process for the formation of the cumulate succession of the MG sequence of core HEX10. The observed ‘reversals’ in several layers occurring in the UCZ of the MG sequence in core HEX10, i.e. increasing whole-rock Mg# in the MG3 chromitite or the plagioclase-bearing MG4A pyroxenite with stratigraphic height, could be the result of the influence of a feeder supplying the Bushveld magma chamber additionally to a main feeder, which Kruger (2005) postulated to be represented by the TML in the north of the complex. The additional feeder Kruger (2005) suggested to be represented by the Steelpoort fault. As have been shown in subsection 4.3.1 and section 4.4 the mineral chemistry of chromite and the silicate minerals of core HEX10 investigated during this study show a relatively evolved composition when compared to mineral data deriving from the north of the eastern limb. It could indicate a lateral fractionation trend resulting from melt being

injected in the north of the BC and spreading southward, as have been suggested by Kruger (2005) for the entire and Teigler and Eales (1994) for the western Bushveld Complex. Mixing of the southward spreading melt that increasingly evolves on its way with the primitive liquid from the Steelpoort fault could thus result in the observed trends of an increasing Mg# in the UCZ part of core HEX10, as have been mentioned above. The occurrence of the reversal in the UCZ suggests that this feeder zone may have been active only during the formation of the interval from the MG3 up to the MG4A chromitite layers. Since upwards the stratigraphic column of the MG sequence the chromite data from core HEX10 show the same trend as data from the north of the eastern limb (cf. Fig. 4.23 in subsection 4.3.1), the postulated influence of an additional feeder affected whole-rock data only. It thus seems to be most likely that the chromitite layers in the south of the eastern limb, i.e. in core HEX10, host higher proportions of orthopyroxene than those in the north.

In the LCZ part of the MG sequence in core HEX10 the trend of the whole-rock Mg# indicates progressive melt evolution, but the Mg# of chromite point to more primitive conditions during chromite formation (cf. subsections 4.3.1 and 4.4.1). This feature makes it more likely that the intruding melt has been pre-concentrated with microphenocrysts of chromite in several subchambers, which has earlier been suggested by Eales (2000) and Kruger (2005).

5.3 Implications for PGE mineralization and formation of PGM of the Middle Group of core HEX10

5.3.1 PGE mineralization of the MG chromitite layers

Orthomagmatic model and the *R*-factor

As have been described in subsection 2.2.2.1, the dominant model for PGE mineralization of chromitite layers is based on an ISL separating from a silicate magma scavenging the PGE and other metals (e.g. Cu and Ni) due to their chalcophile nature (Naldrett, 1989; Naldrett and von Gruenewaldt, 1989, Li *et al.*, 2001). An important role plays the *R*-factor – a mass ratio of the relative amounts of silicate melt to sulphide liquid. A high *R*-factor can be achieved by high amounts of sulphide liquid, which implies the presence of sufficient amounts of S in the original melt. The chromitite layers of the MG sequence in core HEX10 are very poor in S (28-78 ppm on average; cf. Tab. 4.29 in

subsection 4.5.1) when compared to the UG2 chromitite of the eastern limb (926 ppm; Barnes and Maier, 2002) or the Merensky Reef chromitites of the western limb (3400-4080 ppm; Barnes and Maier, 2002). It suggests that the MG chromitites of core HEX10 seems to lack sufficient amounts of S for achieving a high *R*-factor during PGE mineralization. It is corroborated by the data of Scoon and Teigler (1994), who investigated S-poor chromitites below the UG2 and found that PGE mineralization of these layers was rather triggered by chromite control involving a combination of direct PGM nucleation and localized S saturation.

With high-resolution X-ray computed tomography Godel *et al.* (2010) could show that 95-97% of the PGM in the Merensky Reef chromitites are closely associated with the BMS, mainly located at the borders between the sulphides (pyrrhotite and pentlandite) and other phases as chromite and silicate minerals. Less than 0.7% are entirely enclosed by the BMS. As could have been shown with MLA analyses during this study (subsection 4.3.8) 25-48% of the PGM occurring within the chromitite layers of the MG sequence in core HEX are associated with the BMS (SL, SG, SAG; cf. subsection 4.3.8.1). Relative to the data from Godel *et al.* (2010) a higher proportion of the PGM is entirely enclosed by BMS (1.7-25.5%; cf. Tab. 4.21 in subsection 4.3.8). These differences in the mineral association of the PGM of the Merensky Reef and the MG chromitites may partly be due to the different modes of investigation, i.e. 2D investigation with the MLA and 3D computed tomography, but the data strongly indicate different mineralization types for the S-rich Merensky Reef chromitites and the S-poor MG chromitites of core HEX10.

On basis of their data Godel *et al.* (2010) suggest an initial collection of the PGE by a sulphide liquid, “but that the PGM formation is triggered by local phenomena that take place at the interface between the sulphide blebs and other phases”. This may be well applicable to the observed association of the PGM with the BMS within the Merensky Reef chromitites, although there seems to exist a discrepancy between the BMS assemblage and the PGM association with reference to experimental studies on sulphide liquid separation and PGE compatibility (cf. subsection 2.2.2.1). The BMS assemblage of the Merensky Reef chromitite mainly consists of pyrrhotite and pentlandite with minor chalcopyrite and pyrite (Godel *et al.*, 2010), and therefore should contain more Os,Ir,Ru- and Rh-bearing PGM than PtPd- sulphides. On the other hand, the BMS assemblage of this study has been found to comprise dominantly chalcopyrite and pyrite and minor pentlandite and pyrrhotite (cf. subsection 4.2.1), which should result in the dominance of PtPd- sulphides relative to laurite and Rh-bearing PGM within the MG chromitite layers of core HEX10. As has been shown in subsection 4.3.8 this is not the case. Additionally, the mineral data of the BMS obtained with the SEM (subsection 4.3.7.1) illustrate that a very

small proportion of the PGE occur in solid solution within the BMS only, which make less than 1% of the modal composition of the MG chromitites.

Although the HT-PGE Os, Ir and Ru are thought to be fractionated by mss (Fleet *et al.*, 1993; Peregoedova *et al.*, 2004), substantial correlation is missing for the data presented during this study, which indicates another fractionation path for these PGE. Experimental evidence by Brenan and Andrews (2001) suggests that laurite and an ISL probably can't coexist, since Ru was found to be highly soluble into sulphide liquid (1 ≥ 10 wt%). This characteristic feature has also been corroborated experimentally by other authors, e.g. Fleet *et al.* (1993) and Peregoedova and Ohnenstetter (2002). The lack of significant correlations of the HT-PGE with Ni, Cu or S of the data from this study can be taken as evidence that the HT-PGE are not fractionated by mss and sulphide liquid (cf. subsection 4.4.1.2).

The role of sulphur

Although the parental melt is considered to be sulphide saturated at its source, it becomes undersaturated during its ascent due to decreasing pressure (Ballhaus *et al.*, 2006). Hence, any BMS would precipitate from the silicate melt. However, the presence of PGE-bearing BMS in the MG chromitite layers (cf. subsection 4.3.7) suggests that sulphide saturation is reached at some point during chromite formation, scavenging the remaining PGE (mainly Pt and Pd) from the silicate melt. There are several processes that are thought to trigger sulphide saturation in a silicate melt.

Simply hybridization of Bushveld parental melt with the residual melt in the magma chamber has been discarded by Li *et al.* (2001) to trigger sulphide saturation on the basis of thermodynamic calculations. Since the Bushveld magmas and rocks have a distinct crustal signature (Harmer and Sharpe, 1985; Schiffries and Rye, 1989; Kruger, 1994; McCandless *et al.*, 1999; Schoenberg *et al.*, 1999) any process of crustal contamination can be accounted for lowering the S solubility of the magma and the formation of an immiscible sulphide melt.

Contamination with crustal material may increase the fO_2 causing Fe present in the melt to oxidize (Fe → FeO or Fe_2O_3) (Buchanan and Nolan, 1979). Since S in magmas is bonded to Fe^{2+}, a decrease would reduce the S solubility of the melt and an ISL may form. The most likely process for triggering sulphide saturation during formation of the MG sequence is the addition of external S, for which many paths have been described. Ripley and Alawi (1988) describe partial melting or bulk assimilation of sulphidic country rock, whereas Baker *et al.* (2001) suggest the influence of metal loaded sulphurous fluids, which are released from the country rocks and incorporated into the magma. An indication for the assimilation of country rock is corroborated by presence of Na-rich silicate

inclusions in chromite (cf. subsection 4.3.4.3). An indication for the suggestion of Baker *et al.* (2001) of an incorporation of metal loaded sulphurous fluids into the magma probably is given by the presence of excess Cu in the MG chromitite layers reported during this study (cf. subsection 4.4.1), but further evidence for this is required, e.g. the presence of a sulphur-depleted halo around the Bushveld intrusion.

Hydrothermal model

Another possibility for the PGE mineralization of chromitite layers is assumed to result from upward-migrating halogen-rich deuteric fluids (Boudreau and McCallum, 1992; Reid *et al.*, 1993; Boudreau and Meurer, 1999; Willmore *et al.*, 2000). The proposed models deal with the derivation of a fluid during degassing of the interstitial silicate liquid during cooling. The silicate liquid is assumed to be fluid saturated at a water concentration of approximately 5 wt% (Boudreau and Meurer, 1999). By means of compositionally different fluid inclusions in accessory quartz of the Merensky Reef Ballhaus and Stumpfl (1986) determined a maximum trapping temperature of 730°C at 4-5 bar, which substantiates the fluid derivation from silicate melt. On the other hand, Reid *et al.* (1993) mention that a deuteric fluid deriving from exsolution during crystallisation would be in equilibrium with plagioclase and orthopyroxene (at ~ 1000°C) and thus would not be detectable in the oxygen isotope patterns.

For the BC limited PGE mineralization by deuteric fluids have been observed in the UG2 (e.g. Voordouw *et al.*, 2009) and the Merensky Reef (Reid *et al.*, 1993). In the UG2 Voordouw *et al.* (2009) observed that the leader seam is enriched in PGE-sulphoarsenides and comprises a higher abundance of secondary and hydrous silicates. These observations led the authors to the conclusion that the primary PGM assemblage was altered by As-bearing fluids and resulted in the deposition of a secondary PGM species – the PGE- sulphoarsenides. Based on high amounts of H_2O, CO_2, K, LIL and LREE of the rocks the authors suggest a late-magmatic origin of the fluid. It derives from fractional crystallization of the UG2 chromitite seam moving towards the overlying leader seam.

The presence of altered Na-rich silicate inclusions in chromite of the MG chromitite layers have shown the ability of the rocks of the MG sequence of core HEX10 to produce deuteric fluids at a late magmatic stage (cf. subsection 4.3.4.3). As in the UG2, PGE-sulphoarsenides have been observed in the MG chromitite layers of core HEX10, but their amounts are relatively low (0.8-11.5%; cf. Tab. 4.19 in subsection 4.3.8) and a successive enrichment of this PGM species towards the top of the MG sequence cannot be obtained from the data of this study (cf. Fig. 4.55 in subsection 4.3.8). Additionally, they are randomly distributed in the MG chromitite layers rather than showing increasing

concentrations upward the cumulate pile of the MG sequence as Boudreau and Meurer (1999) suggest to result from such a hydrothermal process. However, due to the major association of the PGE- sulphoarsenides with secondary silicate minerals (cf. subsection 4.3.8.1.1) a non-magmatic origin of this PGM-species cannot entirely be excluded.

Voordouw *et al.* (2009) also report the presence of Ni-rich sulphide in the UG2 chromitite, i.e. millerite, which they furthermore ascribe to secondary alteration of the primary BMS assemblage by deuteric fluids. In the MG chromitite layers of this study millerite is present, too (cf. subsection 4.3.7). In accordance with the interpretations of Voordouw *et al.* (2009) it would indicate deuteric origin for millerite. Since its maximum thermal stability has been determined to be at 379°C (Kullerud and Yund, 1962), the author of this study rather suggests that millerite occurring in the MG chromitites derives from secondary overprint by hydrothermal fluids rather than by precipitation from deuteric fluids (see below).

From their experiments on the volatile transport of the PGE at 1000°C Fleet and Wu (1993) report that significant transport of PGE only occurred in the presence of both S and Cl, from which they concluded the existence of complex ligands (e.g. $S_2Cl_2^{4-}$, S_2Cl^{3-}, SCl_2^{3-}) at high temperatures selectively transporting the PGE in the order Pt > Pd > Ir > Rh. In contrast to that the BMS are transported by Cl-bearing fluids only in the order Fe > Cu > Ni. Such selective transport suggests the formation of zonation in the cumulate pile, as for example has been experimentally determined by Boudreau and Meurer (1999). They observed stratigraphic “offsets” in several layered intrusions with a top zone being enriched in Cu, Ni, Fe, Au and S and a bottom zone being enriched in Pt and Pd but low in S. The authors interpreted this feature to represent peaks resulting from chromatographic separation as the fluid moves stratigraphically upwards through a solidifying igneous crystal pile. In the MG chromitite layers of core HEX10 no reasonable chromatographic separation or zonation of base metals is present, since the BMS content is very low and the base metals are preferentially controlled by other minerals like chromite (i.e. Ni, Fe) and orthopyroxene (Fe). For Cu several paths of consumption have been determined, i.e. chalcopyrite, chromite and secondary complex sulphides (cf. subsection 4.4.1). Additionally, no “offsets” have been observed for the PGE (cf. Fig. 4.81 in subsection 4.4.1.2). Hence, PGM and primary BMS mineralization deriving from a deuteric fluid can be excluded for the MG chromitite layers of this study.

According to these findings, a large proportion of the PGE mineralization of the MG chromitite layers of this study appears to have taken place apart from a PGE-scavenging sulphide liquid or halogen-rich deuteric fluids. It is rather suggested that PGE mineralization and PGM formation of the MG sequence in core HEX10 is basically

governed by PGE-bearing clusters. The processes that may have taken place are separately discussed for the HT-PGE and the LT-PGE in the following.

Origin of the PGE-bearing clusters

Alard *et al.* (2000) reported the existence of two populations of sulphides in mantle lherzolite. The first one is an Fe-Ni mss enriched in Os, Ir, Ru and Rh being enclosed by olivine. The second one consists of intergranular pentlandite and Cu-sulphide (chalcopyrite and isocubanite), which contains Pd and Pt. The authors suggest that during partial melting of the mantle the second population is entrained into the magma, whereas the mss remains trapped in the restite. Only high degrees of partial melting (≥ 20 ± 5%) are considered to liberate the mss, a process that is also thought to produce the parental melt of the BC. Due to the observed positively sloped PGE patterns of mantle derived magmas the authors furthermore propose that the Ru-Os-Ir sulphides and alloys formerly being present in the mss remain in the mantle because of their high melt temperatures. The feature that melt temperatures of PGM greatly exceeds the melt temperature during generation of the partial melts has also been mentioned by Tredoux *et al.* (1995) and Cawthorn and Tredoux (2002). According to Cawthorn and Tredoux (2002) a long period of high degree partial melting could have caused the remaining PGM to enter the melt as micro-xenocrysts or clusters, stabilized by a ligand envelope of S. Thus, the PGE abundances in silicate melts are not governed by partition coefficients between sulphide and silicate liquid (Tredoux *et al.*, 1995; Bockrath and Ballhaus, 2002). This is substantiated by Crocket *et al.* (1992), who stated on the basis of partitioning experiments of Os, Ir and Au that due to the low range in partition coefficients a sulphide liquid is not capable to fractionate the PGE from each other.

As the sizes of the clusters are small, they will be suspended in the silicate melt and thus cause PGE supersaturation despite of the insolubility of PGM in silicate magma. Extraction occurs by physical adherence to accumulating crystals like chromite. Probably, the PGE metal inclusions in chromite from the MG chromitite layers observed during LA-ICP-MS analyses could be taken as an indication for the existence of PGE clusters (subsection 4.3.1).

The HT-PGE

As could be shown with the MLA data (subsection 4.3.8) the HT-PGE occur in one PGM species only (i.e. laurite), which commonly is enclosed by chromite grains (66%; see figure 5.6). Besides its association with chromite laurite in the MG chromitite layers furthermore occurs locked in primary silicate minerals (18%) of which plagioclase is the major host (80%; cf. Tab. 4.22 in subsection 4.3.8.1), and the BMS (ca. 10%) (Fig. 5.6).

This ambivalent feature of laurite association, i.e. with chromite, the silicate minerals or the BMS, strongly suggests that laurite didn't precipitate from a PGE-scavenging sulphide liquid in the first place and is thus interpreted to be a good indication for the correctness of the cluster theory for PGE mineralization.

The capability of chromite of fractionating the HT-PGE from the LT-PGE has been described by several authors not only for the same stratigraphic sequence at other sites of the BC (e.g. Merkle, 1992), but also for other chromitite layers of the CZ (e.g. McLaren and de Villiers, 1982) as well as for other layered intrusions (e.g. Talkington and Lipin, 1986) and ophiolites (e.g. Talkington and Page, 1984; Talkington *et al.*, 1984). It has been suggested that the sulphide mineral laurite can directly precipitate from a silicate magma (McLaren and de Villiers, 1982; Talkington *et al.*, 1984; Prichard *et al.*, 1986; Peck *et al.*, 1992; Amossé *et al.*, 2000). This conclusion is mainly based on petrographic evidence, which point to laurite being a liquidus phase co-precipitating with chromite. Bockrath *et al.* (2004) experimentally proved that "laurite can be a stable liquidus phase of sulphur-bearing, sulphide-undersaturated basaltic melt" and Andrews and Brenan (2002) during their experimental work observed a 'window' in which laurite is already stable, but immiscible Fe-rich monosulphide liquid solution is not.

A much more likely explanation for the observed association of the HT-PGM with chromite in the MG chromitites of core HEX10 gives a nucleation experiment with a Cr_2O_3- and RuO_2-doped picrite carried out by Bockrath *et al.* (2004) that revealed a marked affinity of Ru toward chromite surfaces. The authors concluded that laurite, although possible, does not necessarily have to crystallize directly from a silicate melt, but could also be of 'secondary' origin by reaction of sulphur with the Ru nugget nucleated at the chromite surface. These experiments are in consistence with the cluster model (Tredoux *et al.*, 1995) suggesting cluster stabilization by ligands like S, and also substantiate the consideration of Cawthorn and Tredoux (2002) of a mechanical rather than chemical origin of PGM inclusions, i.e. laurite, in early precipitating chromite. Due to that it appears to be likely that the HT-PGM mineralization of this study mainly resulted from this 'chromite control'.

For laurite occurring locked in the silicate minerals or the BMS it is assumed that HT-PGE bearing clusters being present in the interstitial liquid are locked by crystallizing silicate minerals at low fS_2, whereas at locally high fS_2 the HT-PGE partition into mss. The presence of inclusions of BMS (subsection 4.2.1) in chromite of the MG sequence (Fig. 5.6) indicates that sulphide saturation during chromite crystallization was repeatedly reached. The fact that both types of inclusions (i.e. laurite and BMS) do not occur in the same chromite grains may point out that sulphide saturation occurred locally only during chromite formation. Subsequent cooling to <650°C leads to decomposition of the mss into

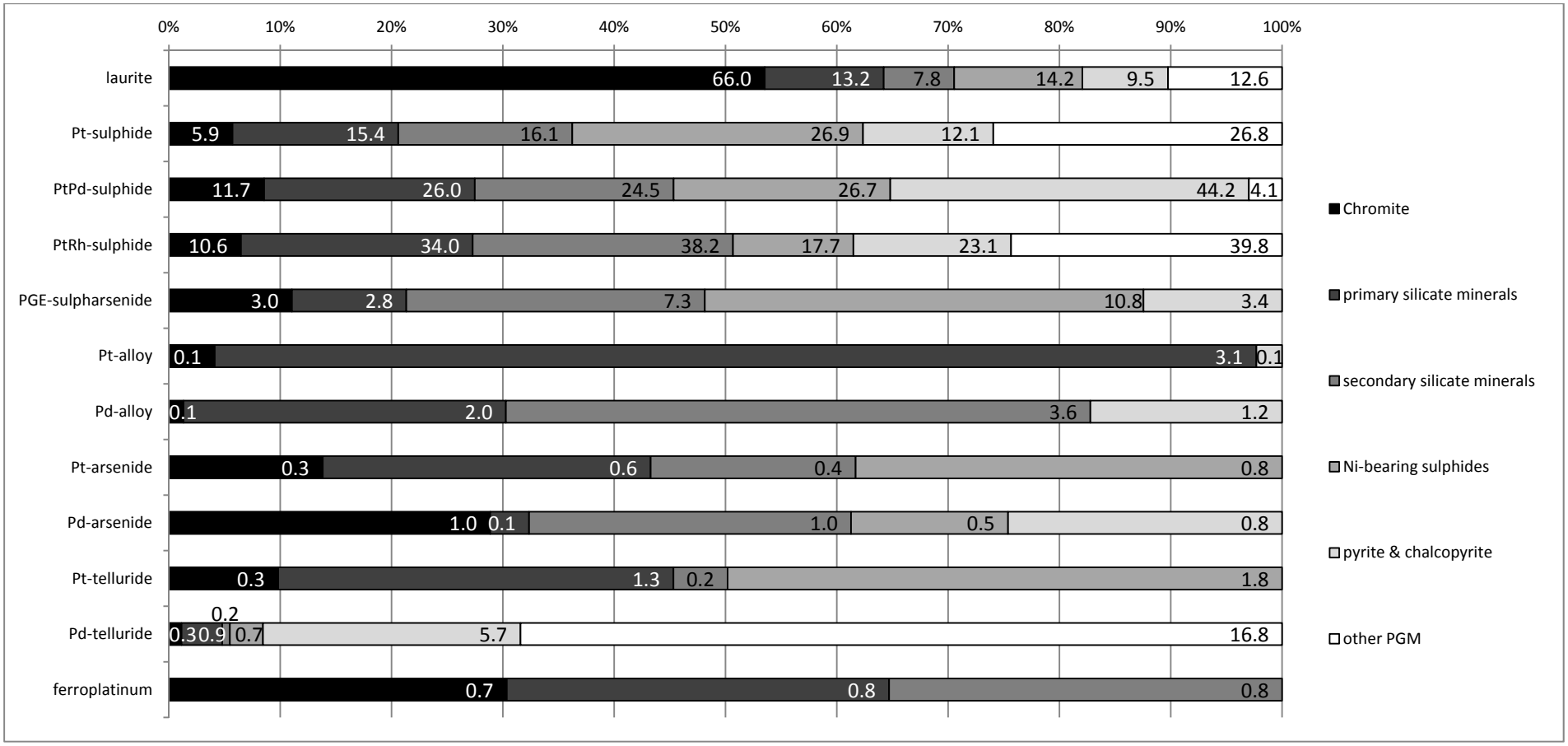

Figure 5.6 Weighted proportions of PGM species in the MG chromitite layers occurring locked in the different minerals. Weighting has been done according to the relative proportion of the individual PGM species at the total PGM amount of the MG chromitite layers. Numbers within or adjacent to the bars represent the percentages of a PGM species relative to the other PGM species in the locking mineral.

pyrrhotite, pentlandite and chalcopyrite (Peregoedova and Ohnenstetter, 2002), explaining the minor association of laurite with the BMS as present in the MG sequence (cf. subsection 4.3.8.1.1).

The LT-PGE

The LT-PGE mainly occur as discrete monosulphides (i.e. cooperite, braggite and Pt-Rh-sulphides) and are dominantly locked in the primary silicate minerals (36-44%) with plagioclase being the major host (63-80%) (cf. Tab. 4.22 in subsection 4.3.8.1; see also Fig. 5.6). The second most association is with the secondary silicate minerals. The Pt-, PtPd- and PtRh-sulphides are associated with the BMS in the third place only. The majority of the Pt- and PtRh-sulphides are related to pentlandite (47 or 55%, respectively), whereas the greater part of the PtPd-sulphides is associated with chalcopyrite (51%). As with the HT-PGM the ambivalent mineral association of the LT-PGM in the MG chromitites of core HEX10 indicates that PGE mineralization and PGM formation most likely took place apart from an ISL scavenging chalcophile elements from the silicate melt, and rather is the result of PGE-clusters being locked during crystallization of the individual mineral species.

The relation of the LT-PGM to primary silicate minerals can probably also be ascribed to locking of PGM clusters during crystallization of orthopyroxene and plagioclase interstitial to chromite at low fS_2, similar to the considerations made for laurite. The association with the BMS rather speaks for the influence of an immiscible sulphide melt segregating from the basaltic parental melt as sulphide saturation is reached. As have been mentioned for the HT-PGE, sulphide saturation only occurs locally in the MG chromitites of core HEX10, which most likely is the reason for the limited association of the PGM with the BMS.

Whole-rock PGE data of this study also revealed statistically significant but only weak or moderate correlations of Rh and Pd with Ni, respectively (cf. subsection 4.4.1.2) suggesting a weak to moderate compatibility of these PGE to Ni-rich sulphide liquid and hence an association with pentlandite. However, partition coefficients $D^{mss/sulphide\ liquid}$ of Rh determined by Fleet *et al.* (1993) and Mungall *et al.* (2005) indicate that Rh is rather incompatible into sulphide liquid. An experimental study of the behaviour of the LT-PGE in the S-poor Fe-Ni-Cu sulphide system done by Peregoedova and Ohnenstetter (2002) yielded that the Fe-Ni-Cu-bearing solid solution, which forms at relatively high temperatures (ca. 1000°C), acts as a temporary collector of Rh, Pt and Pd only. The authors furthermore observed that primary pentlandite isn't stable at high temperatures, which is why pentlandite doesn't directly crystallize from a Cu-bearing sulphide melt. During cooling (at approximately 760°C) the Fe-Ni-Cu solid solution decomposes into

chalcopyrite, pyrrhotite and pentlandite with Pd and Rh partitioning into pentlandite or forming their own minerals. The results presented by this experimental study well explain the correlations of Pd and Rh with Ni observed during this study and also the major association of PtRh-sulphides with pentlandite (cf. subsection 4.3.8.1.1). The PtPd-sulphides to a lesser extent are related to pentlandite (25%) relative to the PtRh-sulphides (55%), but it also matches the observed whole-rock correlation of Ni with Pd.

Under low fS_2 Pt has been found to crystallize as discrete Fe-Pt-alloys (Fleet *et al.*, 1991; Amossé *et al.*, 2000; Peregoedova and Ohnenstetter, 2002). With increasing fS_2 resulting in the segregation of an ISL during fractional crystallization and cooling of the silicate melt the residual Pt present in the silicate melt is entrained into sulphide liquid forming Pt-sulphides associated with the BMS (i.e. pentlandite, chalcopyrite and pyrite) during further cooling (Amossé *et al.*, 2000; Peregoedova and Ohnenstetter, 2002). Hence, the admittedly low amounts of ferroplatinum occurring in the MG chromitite layers most likely represent crystallization of PGM under low fS_2, corroborated by the fact of missing association with the BMS during investigation with the MLA (cf. Fig. 5.6 and subsection 4.3.8.1.1). On the other hand, the Pt-sulphides related to BMS may indicate a 'second-stage' PGM formation at high fS_2 at which the PGE clusters are scavenged from the forming immiscible sulphide liquid resulting in their accumulation associated with the BMS.

Although tellurides, arsenides and alloys of Pt and Pd occur in the chromitite layers of the MG sequence of core HEX10, no correlation of the PGE with the semi-metals exists. This lack of correlation is ascribed to the very low amounts these PGM are present in the massive chromitites (between 0.4 to 1.5%). Fleet *et al.* (1993) describe a late stage event during fractionation of the immiscible sulphide melt at which a semi-metal rich melt segregate from the Cu-rich residual liquid preferentially scavenging Pt and Pd. Due to the low amounts of Pt- or Pd-tellurides, Pt- or Pd-arsenides and Pt- or Pd-alloys occurring in the MG chromitite layers the amount of the segregating semi-metal rich melt must have been small or have not existed at all during formation of the MG chromitite layers of core HEX10.

Positive Rh-anomaly

A special feature of the chromitite layers is their distinctive positive Rh anomaly that can be seen in the chondrite normalized PGE pattern (Fig. 4.53 in subsection 4.4.1.2). It is not unique to the MG chromitite layers of core HEX10, but also has been observed for the chromitite layers of the entire CZ (e.g. von Gruenewaldt and Merkle, 1995). There exists a moderate correlation of Rh with Pt and Pd (see Tab. B-20 in appendix B), which is due to occurrence of PGM bearing Rh, Pt and Pd (cf. subsection 4.3.8). Surprisingly, there is

also a moderate correlation of Rh with Ir (see Tab. B-22 in appendix B), although no Rh-Ir-bearing PGM was detected during investigation with the MLA. Additionally, Rh was absent from laurite, which is the major host PGM for Ir. Hence, coupled substitution has not caused this feature. Probably, Rh is in solid solution in the chromite lattice, as has been suggested by some authors (Grimaldi and Schnepfe, 1969; Capobianco and Drake, 1990; Amossé *et al.*, 2000). The statistically significant but weak negative correlation of the whole-rock Cr_2O_3 content with Rh (r_S= -0.311) could be an indication, suggesting substitution of Cr^{3+} by Rh^{3+}.[9] On the other hand, Ru shows a significant weak positive correlation with whole-rock Cr_2O_3 (r_S= 0.362) that rather is due to the manifold presence of laurite inclusions in chromite and thus coupled substitution appears unlikely.

However, LA-ICP-MS studies on chromite carried out during this study show small but distinctive Rh peaks (cf. Fig. 4.30 in subsection 4.3.1) with sizes of <5 µm, which makes coupled substitution to appear unlikely. These peaks have been interpreted to represent inclusions of Rh-alloys and also can be taken as further evidence for the PGE being transported/present as clusters. Support for this interpretation is given by Ballhaus *et al.* (2006) who carried out nucleation experiments with the PGE and chromite. They found that small Rh alloys are attached to the chromite surface and may be crystallize "piggyback along with chromite", whereas large metal grains are suspended freely in the interstitial liquid. After Peregoedova and Ohnenstetter (2000) Rh is only alloying with Fe at low fS_2, and the model proposed by Ballhaus et al. (2006) does also only work at low fS_2. This is consistent with the assumption given by the author that PGE mineralization of the MG chromitite layers mainly occurred at low fS_2.

Secondary overprint and redistribution of especially the BMS and Pt, Pd and Au

The chromitite layers investigated during this study show clear signs of the influence of aqueous fluids, since part of the primary silicate minerals (i.e. orthopyroxene and plagioclase) within them have been replaced by secondary ones (i.e. plagioclase by an Fe-Mg-Al-Si compound and orthopyroxene by vermiculite; cf. subsections 4.2.1, 4.3.4 and 4.2.8), the BMS show losses Fe, Cu and S (cf. subsection 4.3.7) and the whole-rock Cu/S ratio exceeds the Cu/S ratio for chalcopyrite (cf. subsection 4.4.1). Redistribution of the precious and base metals by fluids, if present, must have taken place after deposition from the melt. This conclusion is based on the proposed high melt temperatures of the PGM (e.g. Cawthorn and Tredoux, 2002) as well as textural evidence of the BMS-silicate mineral assemblage presented in subsection 4.3.7. Additionally, a fluid in coexistence with

[9] At low fS_2 experimental data of Amossé *et al.* (2000) done at 1430°C yielded the existence of Rh as Rh^{3+} and Ru as Ru^{3+} in basaltic melt and thus they are likely to enter the spinel lattice, i.e. chromite.

a sulphide melt would be rather depleted in all the PGE and base metals since they would preferentially partition into the sulphide melt due to their chalcophile character.

PGM (as well as BMS) enclosed by chromite certainly are of primary magmatic origin (Brenan and Andrews, 2001; Andrews and Brennan, 2002; Bockrath *et al.*, 2004) and have been shielded from any secondary processes by the chromite grain. This is especially true for laurite, hosting Ru, Ir and Os, which in total make up approximately 25% of the PGM in the MG chromitite layers of core HEX10. As has been pointed out in subsection 4.3.8, the Pt-, PtPd- and PtRh-sulphides occurring in the MG chromitite layers of this study are associated with (in decreasing order):

1) primary silicate minerals, especially plagioclase
2) secondary silicate minerals
3) BMS.

The PGE-sulphoarsenides as well as the Pd-arsenides are enclosed by secondary silicate minerals in the first place, which leads to the assumption that they derive from a secondary mineralization process taking place after the primary magmatic one. Additionally, re-distribution of Cu, Ni, Fe and S from the BMS being present in the MG chromitite layers (cf. subsection 4.3.7) could have also been caused by a hydrothermal fluid. Due to the lack of substantial evidence for the influence of deuteric fluids on the chromitite layers of the MG sequence present in core HEX10, an externally deriving hydrothermal fluid can probably accounted for to have caused the observed features.

There is manifold evidence for the presence of externally derived fluids in the BC (e.g. Schiffries and Rye, 1990; Mathez and Waight, 2003). Mathez and Waight (2003) noticed a disequilibrium in the lead isotopes between sulphide and plagioclase in the Merensky Reef and interpreted this feature to derive from the addition of crustal fluids after plagioclase has crystallized. On basis of $\delta^{18}O$, δD and $\delta^{13}C$ values from mineral separates deriving from several vein types Schiffries and Rye (1990) concluded that the hydrothermal fluids originated from different rock reservoirs external to the BC, with the dominant component being metamorphic water. Part of the fluids derive from the breakdown of hydrous minerals, another part originate from marine carbonates both occurring in the country rocks. The Cl-rich nature of the fluids has been pointed out by Schiffries and Skinner (1987). Such fluids would be suitable to dissolve the BMS and eventually the PGM and redistribute them.

On basis of BMS data (subsection 4.3.7) it appears to be possible that some of the base metals as well as S have been liberated from the primary BMS by such a Cl-rich hydrothermal fluid and were redistributed locally and/or transported elsewhere. Evidence for local redistribution can be taken from the BMS distribution obtained from investigations with the MLA (cf. Fig. 4.54 in subsection 4.3.8). In the chromitite layers of the UCZ, i.e.

MG3-MG4C, the amount of pentlandite is reduced with contemporaneously increasing concentrations of millerite and pyrite. It suggests decomposition of pentlandite and formation of secondary millerite as well as pyrite. According to the BMS data obtained with the SEM-EDX (cf. subsection 4.3.7) Pt (probably deriving from the breakdown of pentlandite, where it occurred in solid solution) has been enriched in millerite, whereas Pd seems to have been lost and transported with the fluid, eventually up to the Pd-rich UG2. Although this is a small indication only, it could be an explanation of the negative slope visible in the chondrite normalized PGE patterns of the MG chromitite layers (cf. Fig. 4.83 in subsection 4.4.1.2). Even though a great part of the PGM occur locked in secondary silicate minerals, their textures, i.e. pseudo- to idiomorphic grain boundaries, as well as their high melt temperatures (Cawthorn and Tredoux, 2002) indicate that they are more resistant to hydrothermal alteration than the associated BMS and, with the exception of Pd, have probably not been redistributed by a hydrothermal fluid.

The author would like to address the suggestion of Naldrett and Lehmann (1988) that during cooling from 1150°C to 930°C some of the Fe and S of the BMS hosted by chromitite is removed and thus getting enriched in Cu, Ni and the PGE. According to the authors, the ‘excess’ Fe fills vacancies in the chromite lattice, whereas S is lost to the surroundings. In the eyes of the author, Naldrett and Lehmann (1988) completely underestimated the signs of secondary alteration occurring especially in the UG2 that later were described by Li *et al.* (2004) and Voordouw *et al.* (2009). Hence, even if the model proposed by Naldrett and Lehmann (1988) explains the observed features of the BMS, mineralogical and textural evidence in the UG2 as well as in the MG chromitites investigated during this study rather point to aqueous fluids causing this phenomenon.

5.3.2 PGE mineralization of the silicate layers

The general enrichment in the HT-PGE in chromite rich sections of the silicate cumulate (cf. Tab. 4.43 in subsection 4.4.2.1) indicates that HT-PGM mineralization, i.e. laurite, occurred in the same way as have been proposed for the chromitite layers. This is nucleation of HT-PGE-bearing clusters onto the surface of chromite during its crystallization and entrapment during chromite growth at low fS_2. This observation is corroborated by the moderate correlations of the HT-PGE with whole-rock Cr_2O_3 (cf. Fig. 4.103 in subsection 4.4.2.1).

The silicate layers are richer in whole-rock S when compared to the chromitite layers with a general excess in S relative to Cu (cf. subsection 4.4.2). It gives a strong indication for the correctness of the influence of hydrothermal fluids depleting the chromitite layers in

S described before. Hence it can be concluded, that excess S in the silicate layers derives from the underlying chromitite layer of the same cyclic unit. Addition of S to the solidifying silicate cumulate increases the sulphide solubility in the remaining (jnterstitial) liquid, leading to the segregation of a sulphide liquid scavenging the remaining PGE and precipitating them in association with BMS, i.e. chalcopyrite. This would explain the observed positive correlation of Ru with Cu (cf. subsection 4.4.2.1). It is surprising, since Ru is mainly controlled by the presence of laurite being locked in chromite. Perhaps it indicates that laurite in the silicate layers may also occur associated with the BMS, i.e. chalcopyrite, scavenged by sulphide liquid due to the relative lack of enclosing chromite. According to the correlation of Cu with whole-rock S (cf. Fig. 4.94B in subsection 4.4.2), which is the only one existing for S in the silicate layers, chalcopyrite seems to be the dominant BMS. Since any investigation of the silicate layers with the MLA have been carried out during this study, evidence for these conclusions is lacking and additional work is required.

Another possible explanation for the correlation of Cu with Ru is the incorporation of Ru into the lattice of chromite or orthopyroxene. Cu and also Co are compatible to the lattices of these minerals (Arth, 1976). Thus, the moderate positive correlation of Ru with Cu or between Co and Os, Ru, Rh and Pd (Tab. B-25 in appendix B) perhaps indicate that these PGE are also incorporated into chromite or orthopyroxene lattices. Substantial investigations with the LA-ICP-MS on silicate minerals of the silicate layers are required to corroborate or invalidate this argument.

Figure 4.99 in subsection 4.4.2.1 furthermore suggests that samples with high chromite content are most enriched in all the PGE, with Pt and Pd being the most common ones. Moderate correlations of Cr_2O_3 with the LT-PGE are weaker than observed for the HT-PGE, but suggest some ‘chromite control’ on triggering the LT-PGE mineralization in the silicate layers, requiring the presence of chromite. As have been described for the chromitite layers, most of the silicate layers show a positive Rh anomaly in their C1 normalized PGE patterns (cf. figures 4.101 and 4.102 in subsection 4.4.2.1). Strong positive correlations with Pt and Pd (cf. Tab. B-24 in appendix B) indicate the presence of PGM hosting these elements, certainly PtPdRh- sulphides, as have been observed from the chromitite layers.

Lacking correlation of the PGE with whole-rock Ni and S contents (cf. Tab. B-25 in appendix B) indicate that the PGE whether are associated with pentlandite, nor their abundance is connected to the amount of S dissolved in the silicate melt they derive from. Additionally, most of the silicate rocks are depleted in Pt relative to Pd when looking at the C1 normalized PGE patterns (cf. figures 4.101 and 4.102 in subsection 4.4.2.1).

5.3.3 PGE fractionation

As have been shown in subsections 4.4.1.2 and 4.4.2.1, any correlation of the whole-rock PGE concentration with whole-rock MgO content exists, whether for the chromitites nor for the silicate layers of the MG sequence. The MgO content of a magma is proportional to its melting temperature, and hence the PGE, or at least Pd (see footnote 10 below), should correlate with high MgO content. The lack of such a correlation is interpreted to substantiate the cluster origin of the PGE from the mantle, since any fractionation of the PGE at the source of their host magma is indicated by the MgO content although the chondrite normalized PGE patterns point to such a one (cf. Fig. 4.83 in subsection 4.4.1.2 and figures 4.101 and 4.102 in subsection 4.4.2.1). The relative depletion of the HT-PGE is due to their high melt temperatures. As have been mentioned in subsection 5.3.2, the HT-PGM haven't been molten during partial melting of the mantle, but are rather drained in the basaltic melt during partial decomposition of the mss, as the high degree partial melting continued. Ballhaus *et al.* (2006) stated that the enrichment of the HT-PGE is not controlled by partition coefficient during partial melting in the first place. Instead, the segregation of silicate melt causes a volume loss in the mantle source draining the HT-PGE. Hence, the greater part of the HT-PGE remains at the source.

The LT-PGE also have melt temperatures that exceed temperatures during partial melting, with the minor exception of Pd [10] (cf. Tab. 1.4 in chapter 1). As have been described by Lorand *et al.* (2008), the LT-PGE occur in mantle sulphides (i.e. pentlandite and chalcopyrite) interstitial to the silicates. In subsection 5.3.2 it is mentioned, that the LT-PGE are present as discrete nano-xenocrysts in the mantle sulphides. Thus, if not molten during partial melting of the mantle, they are drained into the segregating sulphide melt, which is at 50% sulphide melting according to Ballhaus *et al.* (2006). The authors report that sulphide draining produces Pt-Pd abundances of more than four times the mantle abundances.

Thus, segregation of silicate melt leads to draining of sulphide melt incorporating the LT-PGE and parts of the HT-PGE, since mss as a crystalline phase remains in the mantle. This is why mantle-derived melts show positively sloped C1 or mantle normalized PGE patterns (cf. subsection 2.1.1).

Further PGE fractionation occurs during ascent and emplacement of the silicate magma (Ballhaus *et al.*, 2006). Due to the draining, the sulphides form sulphide droplets in the basaltic melt. During ascent the sulphide solubility of the silicate melt increases

[10] The melt temperature of pure metal Pd is 1552°C and it is assumed that the melt temperature of the mantle during high degree partial melting is around 1600°C (Arndt and Nesbitt, 1982), hence even pure Pd would be molten.

caused by decreasing pressure (Mavgrones and O'Neill, 1999), and the sulphide droplets dissolute in the basaltic melt. Hence, all the PGE are released to the silicate melt and further fractionation may occur.

If one compares the chondrite normalized PGE patterns of the MG chromitite layers (cf. Fig. 4.83 in subsection 4.4.1.2) with the ones of the silicate layers (cf. figures 4.101 and 102 in subsection 4.4.2.1), a much stronger fractionation of the HT-PGE relative to the LT-PGE in the chromitite layers is visible. As has been pointed out before, this is caused by the attachment of HT-PGE bearing PGM, i.e. laurite, onto the chromite surface and entrapment of the PGM as chromite growth continues. Since considerable amounts of chromite are lacking in the silicate layers of the MG sequence, a concentrating pool for the HT-PGE is missing. Additionally, the amount of silicate minerals is much higher in the silicate layers than in the chromitite layers. This is why the silicate layers show less PGE fractionation.

As have been pointed out in subsections 4.4.1.2 and 4.4.2.1, there seems to be some Al_2O_3-induced control on PGE fractionation in the MG sequence. In the lowermost as well as in the uppermost chromitite layers of the MG sequence (i.e. MG0, MG1, MG2A and MG4A, MG4B and MG4C) an enrichment of the LT-PGE relative to the HT-PGE from bottom to top of the individual layer occurs, whereas the remaining chromitite layers (i.e. MG2B, MG2C, MG3) show a relative enrichment of the HT-PGE to the LT-PGE. These features generally have been found to be either caused by Al-depletion of chromite preferentially causing enrichment in the HT-PGE relative to the LT-PGE, or increased co-precipitation of plagioclase, which causes enrichment of the LT-PGE relative to the HT-PGE. The former suggests a compositional dependence of HT-PGM nucleating onto the chromite surface, i.e. chromite relatively low in Al should host more inclusions of HT-PGM than those being relatively Al-enriched. The latter matches the results deriving from investigations with the MLA that the LT-PGM are dominantly associated with plagioclase (cf. subsection 4.3.8). In the silicate layers the Pt/Ir ratio is strongly controlled by the amount of plagioclase, since chromite is a minor phase only. However, the processes observed for the chromitite layers are also applicable to the PGE fractionation in the silicate layers of the MG sequence. Enrichment of the LT-PGE relative to the HT-PGE is linked to increasing whole-rock Al_2O_3 contents, which is caused by increasing amounts of cumulus plagioclase (MG2C anorthosite, plagioclase-bearing MG4A pyroxenite). On the other hand, decreasing amounts of cumulus plagioclase (MG3 leuconorite and MG3 norite) or Al-depletion in chromite (MG2A pyroxenite) is accompanied by a relative enrichment of the HT-PGE over the LT-PGE.

The remaining PGE that have not been precipitated during the processes mentioned above, stay in the silicate melt until sulphide saturation is reached, which in the MG

sequence most likely is achieved by crystallisation during cooling. At this point the PGE fractionation is dominated by sulphide-silicate partitioning and the PGE are collected by the segregating sulphide melt. According to Ballhaus *et al.* (2006), the PGE are not further fractionated relative to each other by the sulphide melt, since they have very similar D values. That only the last stages of PGE fractionation are sulphide dominated can also be concluded from MLA data, since relatively small amounts of the LT-PGM occurring in the chromitite layers of the MG sequence are associated with the BMS (cf. subsection 4.3.8.1.1).

5.4 Parental magmas to the MG sequence

Several workers have suggested the influence of two compositionally different magmas during the formation of the BC (Sharpe, 1981; Davies and Tredoux, 1985; Harmer and Sharpe, 1985). Due to the existence of two types of marginal rocks and sills being linked to the BC intrusion, they suggested the parental magmas to be of the following composition:

1) Ultramafic ("U-type") or B1 (Sharpe, 1981) with boninitic affinity. It corresponds to the high Mg basaltic suite investigated by Davies and Tredoux (1985).
2) Anorthositic/gabbroic ("A-type") or B2 and B3 (Sharpe, 1981). These suites resemble the tholeiitic basaltic suite from Davies and Tredoux (1985). Kruger (2005) suggests the second parental magma to have a noritic lineage.

The ultramafic magma is considered to have formed the LZ and LCZ, whereas the second magma suite is thought to have formed the UCZ and MZ lithologies of the BC (Harmer and Sharpe, 1985). On the other hand, Kruger (2005) says that the second magma formed the UCZ only and postulates a different parental magma for the MZ. Inflections in the $^{186}Sr/^{187}Sr$ ratio (Harmer and Sharpe, 1985) and the $^{187}Os/^{188}Os$ ratio (McCandless *et al.*, 1999; Schoenberg *et al.*, 1999) at the LCZ/UCZ transition furthermore substantiate the two parental magma model.

Although no isotopic investigations took place, the findings of this study do not entirely corroborate the existence of two parental magmas during the formation of the CZ as present in the MG sequence. Especially the inversion in mineral and whole-rock composition in the MG3 and in particular the MG4A chromitite layers to more primitive composition than the chromitite layers in the LCZ (cf. subsections 4.3.1 and 4.4.1) rather suggests the absence of an A-type magma and could be an indication for the presence of one parental magma only. Support for this comes from **Kruger (1994)** and Kinnaird *et al.* (2002) saying that a continuous increasing radiogenity in the Sr_i profile from bottom to top of the CZ exists (cf. section 2.4) rather than a major inflection at the LCZ/UCZ transition.

Furthermore, data from Teigler and Eales (1996) suggest that unequivocal evidence for the existence of an A-type magma during formation of the UCZ is missing. They interpret the overall increase in the Sr_i throughout the CZ to illustrate "a progressive blending-in of liquids with a higher $Sr_{i,}$ or a change in the mantle source". Perhaps "progressive blending-in of liquids with a higher $Sr_{i,}$" describes the mixing of intruding primitive melt with the evolved residual liquid in the Bushveld magma chamber as have been suggested for the formation of the MG sequence of core HEX10 (cf. section 5.2). Progressive evolution of this residual liquid, as is proposed in section 5.2, could thus be accounted for the feature of increasing Sr_i throughout the CZ.

Pollard *et al.* (1975) showed that "sills may propagate as a series of co-planar fingers as a result of instabilities developed in the frontal regions of a magma body". During their work on the Spruitfontein inlier of the southwestern RLS Clarke *et al.* (2000) found an intrusion-related D_1 deformation that caused the development of near-horizontal fractures in the country rocks, which the authors interpreted to have provided "loci for sill-fingers". Although this work was based on rocks of the Marginal Zone, it cannot be excluded that the ongoing filling of the Bushveld magma chamber wouldn't have the same effect onto the surrounding country rocks. According to this, the compositionally different marginal rocks and sills could thus also represent intrusions of different stages of residual melt that have been present in the Bushveld magma chamber during formation of the CZ, rather than reflecting parental melt compositions.

An indication for the considerations given above comes from the PGE data of the silicate rocks from core HEX10 investigated during this study. Figures 4.101 and 4.102 in subsection 4.4.2.1 show the C1-normalized PGE pattern of the silicate layers of core HEX10 in comparison with those from the marginal sills of high Mg basaltic and tholeiitic composition investigated by Davies and Tredoux (1985). As can be seen the high Mg basaltic suite has higher PGE concentrations relative to the tholeiitic suite and a quite even pattern. This could lead to the assumption that the PGE depleted pattern of the tholeiitic suite represents a remnant liquid composition after the fractionation of the individual silicate layers of core HEX10 from the high Mg basaltic suite, especially when looking at the contrasting Rh and Pt anomalies of the tholeiitic basalts and the silicate layers of core HEX10. If this assumption is true then the Sr isotopes of the tholeiitic suite should be higher than those of the silicate layers of the MG from core HEX10. Since no Sr isotope data are available, further work is required for proving or neglecting this theory, respectively. However, besides the geochemical evidence, e.g. the inversions in mineral and whole-rock Mg#, the considerations above would further corroborate the most likely presence of one parental magma only that can be accounted for the formation of the MG sequence in core HEX10. This would be the high Mg basaltic suite of Davies and Tredoux

(1985), whereas the tholeiitic suite investigated by the authors doesn't reflect parental melt composition. Substantial statements have been done by Kruger (2005) who said that "the marginal sills associated with the layered sequence may represent outward expansion of the magma chamber by mixed and residual magmas". Another intriguing point made by Kruger (2005) to corroborate this conclusion is that sills reflecting the composition of true parental magmas are probably restricted to the ultimate vicinity of feeders.

Since all the chondrite normalized PGE patterns in Fig. 4.101 and 4.102 (subsection 4.4.2.1) don't differ significantly they could derive from the same source. Thus, the observed similarities of the MG patterns to the UG2 ± Merensky Reef could be due to their origin from the same parental melt that contributed the PGE to the mineralization of the CZ. As the patterns furthermore suggest, fractionation of the PGE within the stratigraphy of the CZ is low, but absolute PGE abundances increase from bottom to top of the CZ.

6. Summary and conclusions

In the scope of this study, the formation of the chromitite layers and the silicate cumulates of the Middle Group, eastern Bushveld Complex, has been described with a detailed observation of their PGE mineralization and PGM content.

With regard to mineral composition of chromite and whole-rock geochemistry of the chromitite layers, a general progressive evolution upwards the stratigraphic column of the MG sequence is illustrated. By means of the Mg#, the $Cr^{3+}/(Cr^{3+}+Fe^{3+})$ and the $Cr^{3+}/(Cr^{3+}+Al^{3+})$ ratios chromite becomes increasingly enriched in Fe relative to Mg as well as in Al and Fe relative to Cr. No marked compositional changes are present at the LCZ/UCZ transition of the MG sequence. However, at the level of the MG4A chromitite layer a major inflection to more primitive mineral and whole-rock compositions can be observed by means of increasing $Mg\#_{chr}$ and whole-rock Mg# as well as shifts in the $Cr^{3+}/(Cr^{3+}+Fe^{3+})$ and $Cr^{3+}/(Cr^{3+}+Al^{3+})$ ratios of chromite and the chromitite layers. According to Harmer and Sharpe (1985) an increase in Mg# is equivalent to an increase in melt temperature. Thus, the addition of a hot liquid of primitive composition at the level of the MG4A chromitite layer has been concluded. Chromite host considerable amounts of minor elements, as Ni (1400 ppm on average), Zn (1100 ppm on average), Co (400 ppm on average) and Ga (58 ppm on average).

Due to XRD analyses, the silicate minerals interstitial to chromite are dominantly orthopyroxene, i.e. enstatite and ferroan enstatite, and plagioclase of albitic, bytownitic and anorthitic composition. No progressive evolution in the composition of the silicate minerals within the MG chromitite layers upwards the stratigraphic column of the MG sequence could be detected. The observed variations in the An content obtained by SEM-EDX analyses are due to selective sampling.

Chromite composition of chromite occurring in the silicate rocks is strongly influenced by the nature of the co-precipitating silicate minerals. Nevertheless, the data reflect the same general trend of progressive melt evolution from bottom to top of the MG sequence as well as the marked shift to primitive composition at the level of the MG4A cyclic unit.

This shift to primitive composition is also illustrated in the plagioclase-bearing pyroxenite occurring in the hanging wall of the MG4A chromitite layer. The twofold change of plagioclase and orthopyroxene to more primitive compositions points to precipitation from a quite primitive magma mixture resulting from repetitive addition of primitive magma. Generally, progressive evolution of plagioclase as well as orthopyroxene compositions upwards the stratigraphic column of the MG sequence is present. Plagioclase chemistry in the silicate layers ranges from labradorite to bytownite, which is true for cumulus and intercumulus species. The En content of orthopyroxene ranges between 32 and 95%.

Whole-rock geochemistry of the silicate layers is strongly governed by mutual influence of co-precipitating minerals competing for major elements like Mg, Fe, Al or Cr. Thus, no distinct trend with respect to evolution from bottom to top of the stratigraphic column of the MG sequence can be made. For the minor elements Ti, V, Co, Ni, Zn and Ga in the silicate layers a chromite control can be deduced, since their tenors imitate the tenor of the Cr_2O_3 concentration upwards the stratigraphic column.

Although manifold isotopic evidence (Harmer and Sharpe, 1985; McCandless *et al.*, 1999; Schoenberg *et al.*, 1999) as well as studies on marginal rocks and sills of the BC for two compositionally different parental magmas forming the CZ exist (Sharpe, 1981; Davies and Tredoux, 1985), the data from this study don't entirely corroborate these findings. In particular, the strong reversals in mineral and whole-rock composition at the level of the MG4A chromitite layer and its corresponding pyroxenite suggest that the UCZ as present in the MG sequence doesn't derive from mixing of the residual liquid in the Bushveld magma chamber with an A-type magma. In addition, the lack of considerable compositional changes at the LCZ/UCZ transition rather indicates progressive evolution of the residual melt being present in the Bushveld magma chamber during formation of the MG sequence. According to the respective host rocks a pyroxenitic composition is suggested for the residual melt during formation of the LCZ, and a noritic residual melt during the formation of the UCZ. The parental melt is thought to have been of primitive composition (ultramafic-mafic) and derived from a mantle source, as positive Nb anomalies of the MG chromitite layers suggest. Minor contamination with crustal material is indicated positive La and Sr peaks in the multi-element patterns of the MG chromitite layers, as well as positive Ta and negative Rb anomalies in the multi-element patterns of the silicate layers. These findings are in consistence with Os isotope data presented by McCandless *et al.* (1999) suggesting the assimilation of about 5% of granulitic crust.

The similarity of the chondrite normalized PGE patterns of the chromitite and silicate layers to the one of the UG2 strongly indicates their origin from the same magma and suggests a similar style of PGE mineralization. In addition to that, it indicates the presence of one parental magma for the CZ only.

Repetitive replenishment during formation of the MG sequence is not only indicated by the re-setting of the whole-rock Mg# and the $Cr^{3+}/(Cr^{3+}+Fe^{3+})$ ratio of the chromitite layers to low values, but also by increasing whole-rock TiO_2 contents within each chromitite layer.

In the chromitite layers of the MG sequence several silicate inclusions in chromite occur. Their Na-rich nature relative to the silicate minerals interstitial to chromite has led to the conclusion that they may represent a mixture of primitive with siliceous melt, i.e. granophyric roof-rock melt, as has been suggested to trigger chromite precipitation

(Kinnaird *et al.*, 2002; Spandler *et al.*, 2005). Very often they are strongly altered despite being shielded from hydrothermal processes by chromite. In accordance with cracks spreading from these inclusions into the chromite grains it was concluded that during cooling an aqueous fluid phase exsolved, which altered the silicate phases, i.e. orthopyroxene, since it wasn't able to escape. Hence, this can be taken as an indication of the ability of the silicate melt to produce deuteric fluids during a late-stage magmatic process.

The existence of these inclusions in all the MG chromitite layers most likely can been taken as evidence for chromite formation by mixing of primitive melt with a siliceous melt, i.e. granophyric roof-rock melt as suggested by Kinnaird *et al.* (2002). The resulting chromite slurry collects at the base of and spreads out along the bottom of the magma chamber. Restites of entrained roof rock melt are kept in the interstitials to chromite, explaining the unusual high Sr_i values observed by Kinnaird *et al.* (2002). Mixing of primitive melt with felsic melt and residual melt forms hybrid layers on top of the chromitite layers that also spread laterally. The different composition of the residual melt, i.e. pyroxenitic in the LCZ and noritic in the UCZ, mainly influences the composition of the hybrid melt and hence the nature of the precipitating silicate rocks.

As have been shown in subsection 4.4.1.2, the chromitite layers occurring in the vicinity of the LCZ/UCZ transition, i.e. MG2C and MG3, have the highest PGE concentrations with Pt as the most common PGE. Lack of correlation of the PGE content with the amount of Cr_2O_3 implies that high PGE concentrations in the chromitite layers are not necessarily linked to elevated amounts of whole-rock Cr_2O_3. On the other hand, in the silicate layers a strong correlation of the whole-rock Cr_2O_3 content with the HT-PGE exist, which is interpreted to illustrate the pronounced relationship of laurite and chromite observed by other workers before (e.g. Page and Talkington, 1984; Talkington *et al.*, 1984; Merkle, 1992). 'Chromite control' on triggering LT-PGE mineralization of the silicate layers is indicated by weak correlation with whole-rock Cr_2O_3 concentration.

Although whole-rock PGE-MgO plots of chromitite and silicate layers don't indicate PGE fractionation by melt temperature during partial melting of the mantle, as have been suggested by Tredoux *et al.* (1986), the positive sloped chondrite normalized PGE patterns of MG chromitite and silicate layers show fractionation of the HT-PGE relative to the LT-PGE. Hence, the observed features of the MG sequence have been ascribed to the cumulate character of the rocks eliminating the original MgO-PGE relation in the MG sequence.

Additional fractionation of the PGE in the MG chromitite layers by Ni-rich immiscible sulphide liquid have only been found to have affected the LT-PGE by means of whole-

rock data, mainly Pt and Pd. For the silicate layers indications for such a fractionation path are missing.

For both the chromitite and the silicate layers PGE fractionation with decreasing temperature in dependence of the whole-rock Al_2O_3 content from bottom to top of the MG sequence seems to have taken place. As a general rule for the chromitite layers Al-depletion of chromite relative to Cr enriches the HT-PGE relative to the LT-PGE, whereas enrichment in co-precipitating plagioclase results in enrichment of the LT-PGE relative to the HT-PGE. Increasing whole-rock Al_2O_3 content, i.e. increasing amounts of plagioclase, in the silicate layers is accompanied by LT-PGE enrichment, and decreasing amounts of whole-rock Al_2O_3 results in enrichment of the HT-PGE relative to the LT-PGE. The HT-PGE content of the MG4A cyclic unit is additionally influenced by the influx of primitive magma, adding further HT-PGE.

Minor amounts of Pt, and to a lesser extend also Ir, Rh ad Ru, are probably also fractionated from the other PGE by incorporation into the chromite lattice, as LA-ICP-MS analyses showed (subsection 4.3.1). Since any regular pattern has been determined, PGE incorporation into chromite shouldn't affect the tenor of the chondrite normalized PGE patterns.

The primary BMS assemblage of the MG chromitite layers consists of pentlandite, chalcopyrite and pyrite, with chalcopyrite being the most common. Investigations with the MLA yielded the existence of millerite in the UCZ part of the MG sequence, but only minor amounts of pentlandite. This led to the conclusion of millerite replacing pentlandite during a late event involving aqueous fluids that affected the UCZ. A first indication for re-distribution of the BMS occurring in the MG chromitite layers by such fluids is given by their association with secondary silicate minerals like amphibole, mica and chlorite. In addition to that, alteration of the BMS has also been concluded from composition of BMS occurring in the MG sequence showing losses of S, Cu and Fe. Due to that fact, the presence of excess S in the silicate layers as well as the dearth of S relative to the amount of Cu in the chromitite layers could be a result from a re-distribution of base metals from BMS occurring in the MG chromitite layers by aqueous fluids. Cu enrichment of the silicate layers at the direct contact to the underlying chromitite layer further appears to corroborate re-distribution of base metals by dissolution of BMS. This feature seems to be locally restricted and has been interpreted to be the result of externally originating hydrothermal fluids adding Cu to the melt.

Although Cu deriving from the BMS seems to migrate away from the chromitite layers, there still a local Cu enrichment in the chromitite layers to concentrations up to >6000 ppm can be observed. This excess Cu most likely derives from an external source e.g. country rocks (cf. Schiffries and Rye, 1990), which could be metal-loaded

hydrothermal fluids, as suggested by Baker *et al.* (2001). Due to positive correlations of Cu with Sb, As and Zn, the formation of minor amounts of tetrahedrite and tennantite have been suggested as a result of Cu addition to the chromitite layers, which are secondary ore minerals growing during hydrothermal processes.

Investigations of the MG chromitite layers with the MLA yielded the dominance of PtRh- sulphides (26.2%) as the major PGM species, followed by laurite (25%), PtPd- and Pt- sulphides (24.3% or 13.8%, respectively). The remaining 10.7% comprise PGE–sulphoarsenides and PGE- arsenides, Pt- and Pd– alloys and Pt- and Pd- tellurides. Liberation of PGM is low and ranges between 4% for the MG1 chromitite to 45.9% on average for the MG3 chromitite layer. The majority of the PGM species found occur locked in primary silicate minerals like orthopyroxene and feldspar (38.6%), followed by locking in BMS (21.4%). 19.5% of the investigated PGM species are enclosed by chromite, whereas locking in secondary silicate minerals, i.e. amphibole, mica, chlorite, talc and quartz, occurs to 19.1%. Since with common flotation methods only liberated PGM or those attached or closely associated with BMS are extractable (e.g. Merkle and McKenzie, 2002), there is a great range in recovery. It is lowest for the MG1 chromitite layer (11.2%) and highest for the MG3 chromitite (59.2% on average). Hence, to use the MG chromitite layers as a potential PGE ore, the existing recovering methods need to be combined with a new method that is able to recover the PGM from the silicate minerals.

The HT-PGE appear to be concentrated in laurite only, as the strong interelement correlations between them existing in the chromitite and silicate layers already has been shown. Laurite is mainly locked in chromite (66%), which strongly suggests that laurite co-precipitates with chromite as an early phase. Since laurite has been found to not be able to coexist with immiscible sulphide liquid (cf. subsection 5.3.2), low fS_2 was present during the locking process caused by chromite growth. PGM being composed of LT-PGE, i.e. mainly Pt-, PtPd- and PtRh-sulphides, are mainly associated with the silicate matrix of the chromitite layers, which furthermore suggests low fS_2 at the time of their precipitation. Locally occurring sulphide saturation yielded the LT-PGM association with BMS. An eventually occurring segregation of a semi-metal rich melt as a late-stage fractionation process of sulphide melt probably have precipitated the minor amounts of PGE-sulphoarsenides, Pt- or Pd- tellurides, Pt- or Pd- arsenides and Pt- or Pd- alloys.

The observed discrepancy in the PGM association, i.e. their association with silicate minerals, chromite as well as the BMS, appears to make it unlikely that PGE mineralization of the MG chromitite layers can be modelled in terms of the *R*-factor (cf. Naldrett, 1989; Naldrett and von Gruenewaldt, 1989), since it focuses on PGE being scavenged by immiscible sulphide droplets resulting in PGE-rich BMS only. PGM mineralization by deuteric or hydrothermal fluids, alike if primary or secondary, was shown

to be rather unlikely to occur in the MG sequence of core HEX10. However, the cluster theory developed by Tredoux *et al.* (1995) thus seems to be much more plausible to explain the PGE mineralization as present in the MG sequence. According to that, in S-poor environments, i.e. at low fS_2 the PGM will precipitate with silicate minerals and chromite, whereas in S-rich environments, i.e. at high fS_2, they tend to become associated with sulphide melt, resulting in the formation of PGE-bearing BMS. This model is nicely reflected in the data from this study.

Due to the fact that sulphide saturation occurred locally only, the melt the PGM derive from has most likely been sulphide undersaturated at the time of emplacement into the Bushveld magma chamber. Based on studies from e.g. the Duluth complex (Ripley and Alawi, 1988) it has been concluded that the sulphur derives from an external source, e.g. from assimilation of country rock. An indication for the ability of the Bushveld melt to assimilate proportions of country rock is given by the occurrence of Na-rich silicate inclusions in chromite of the MG chromitite layers (subsection 4.3.4.3). Sulphide saturation has been concluded to occur as a late-stage process, as progressive crystallization of the liquid interstitial to chromite increases sulphide saturation. Although PGM association with secondary silicates points to additional PGM mineralization during a hydrothermal event, the idiomorphic shape of the PGM in connection with their high melt temperatures (Cawthorn and Tredoux, 2002) doesn't corroborate such interpretation.

Any analyses with the MLA have been done on silicate samples due to the low PGE abundances. However, as HT-PGE enrichment in the chromite-rich sections of the silicate layers indicates, laurite is associated with chromite. The major BMS appears to be chalcopyrite that is interpreted to have scavenged the remaining LT-PGE and also Ru, as a positive correlation of Cu and Ru suggests. This feature was ascribed to the minor presence of chromite. PGE mineralization in the silicate layers appear to have been taken place under more sulphide saturated conditions than observed for the chromitite layers, which has been caused by the addition of S eventually deriving from the decomposed BMS in the respective underlying chromitite layer.

7. References

Alard, O., Griffin, W.L., Lorand, J.-P., Jackson, S.E. and O'Reilly, S.Y. (2000): Non-chondritic distribution of the highly siderophile elements in mantle sulphides. *Nature*, **407**, 891-894.

Amossé, J., Dablé, P. and Allibert, M. (2000): Thermochemical behaviour of Pt, Ir Rh and Ru vs. $fO2$ and $fS2$ in a basaltic melt. Implications for the differentiation and the precipitation of these elements. *Mineralogy and Petrology*, **68**, 29-62.

Andrews, D.R.A. and Brenan, J.M. (2002): The solubility of ruthenium in sulphide liquid: implications for platinum-group mineral stability and sulphide melt-silicate melt partitioning. *Chemical Geology*, **192**, 163-181.

Anhaeusser, C.R. (2006): Ultramafic and mafic intrusions of the Kaapvaal craton. In: Johnson, M.R., Anhaeusser, C.R. and Thomas, R.J. (eds.): *Geology of South Africa.* Geological Society of South Africa, Johannesburg/Council for Geoscience, Pretoria, 95-134.

Arndt, N.T. and Nesbitt, R.W. (1982): *Komatiites*. Allen and Unwin, London, 526 p.

Arth, J.G. (1976): Behaviour of trace elements during magmatic processes – a summary of theoretical models and their applications. *Journal of Research of the USGS*, **4**, 41-47.

Augé, T., Salpeteur, I., Bailly, L., Mukherjee, M.M. and Patra, R.N. (2002): Magmatic and hydrothermal platinum-group minerals and base-metal sulphides in the Baula complex, India. *The Canadian Mineralogist*, **2**, 277-309.

Baker, D.R., Barnes, S.-J., Simon, G. and Bernier, F. (2001): Fluid transport of sulphur and metals between sulphide melt and basaltic melt. *The Canadian Mineralogist*, **39**, 537-546.

Ballhaus, C. and Stumpfl, E.F. (1986): Sulphide and platinum mineralization in the Merensky reef: evidence from hydrous silicates and fluid inclusions. *Contributions to Mineralogy and Petrology*, **94**, 193-204.

Ballhaus, C., Tredoux, M. and Spaeth, A. (2001): Phase relations in the Fe-Ni-Cu-PGE-S system at magmatic temperature and application to massive sulphide ores of the Sudbury Igneous Complex. *Journal of Petrology*, **42**, 1911-1926.

Ballhaus, C., Bockrath, C., Wohlgemuth-Überwasser, C., Laurenz, V. and Berndt, J. (2006): Fractionation of the noble metals by physical processes. *Contributions to Mineralogy and Petrology*, **152**, 667-684.

Barnes, Stephen J. (1989): Are Bushveld U-type parent magmas boninites or contaminated komatiites? *Contributions to Mineralogy and Petrology*, **101**, 447-457.

Barnes, S.J. (2005): "Calculation of cation proportions in spinel from major element oxides", [online] available at http://www.em.csiro.au/terrain_studies/aboutus/people/stephen_barnes/roeder_spinels.htm

Barnes, S. and Maier, W.D. (1999): The fractionation of Ni, Cu and the noble metals in silicate and sulphide liquids. *Short Course Notes Geological Association of Canada.* **13**; 69-106.

Barnes, S.-J. and Maier, W. D. (2002): Platinum-group element distributions in the Rustenburg Layered Suite of the Bushveld complex, South Africa. *In:* Cabri, L.J. (ed.): *The Geology, Geochemistry, Mineralogy and Mineral Beneficiation of platinum-group elements*. Canadian Institute of Mining, Metallurgy and Petroleum, Special Volume **54**, 431-458.

Barnes, S.-J., Naldrett, A.J. and Gorton, M.P. (1985): The origin of the fractionation of platinum-group elements in terrestrial magmas. *Chemical Geology*, **53**; 3-4, 303-323.

Barton, P.B. Jr. (1973): Solid solutions in system Cu-Fe-S. Part I: The Cu-S and CuFe-S join. *Economic Geology*, **68**, 455-465.

Bates, R.L. and Jackson, J.A. (eds.) (1995): Glossary of geology. 3rd edition, American Geological Institute, Alexandria, Virginia, USA. 788 p.

Bezmen, N.I., Asif, M. Bruegmann, G.E., Romanenko, I.M. and Naldrett, A.J. (1994): Distribution of Pd, Rh, Ru, Ir, Os, and Au between sulphide and silicate metals. *Geochimica et Cosmochimica Acta*, **58**; 4, 1251-1260.

Bockrath, C. and Ballhaus, C. (2002): PGE fractionation between sulphide-bearing mantle and basaltic melt during partial melting and melt segregation. *Abstracts of the 9th International Platinum Symposium*, July 21-25, Billings, Montana, USA.

Bockrath, C., Ballhaus, C. and Holzheid, A. (2004): Stabilities of laurite RuS_2 and monosulphide liquid solution at magmatic temperature. *Chemical Geology*, **208**, 265-271.

Boorman, S., Boudreau, A. and Kruger, F.J. (2004): The Lower zone - Critical zone transition of the Bushveld complex: a quantitative textural study. *Journal of Petrology*, **45**; 6, 1209-1235.

Boudreau, A.E. and McCallum, I.S. (1992): Concentration of platinum-group elements by magmatic fluids in layered intrusions. *Economic Geology*, **87**, 1830-1848.

Boudreau, A.E. and Meurer, W.P. (1999): Chromatographic separation of the platinum-group elements, gold, base metals and sulphur during degassing of a compacting and solidifying crystal pile. *Contributions to Mineralogy and Petrology*, **134**, 174-185.

Boudreau, A.E., Mathez, E.A. and McCallum, I.S. (1986): Halogen geochemistry of the Stillwater and Bushveld complexes: evidence for transport of platinum-group elements by Cl-rich fluids. *Journal of Petrology*, **27**, 957-967.

Brenan, J.M. and Andrews, D. (2001): High-temperature stability of laurite and Ru-Os-Ir alloy and their role in PGE fractionation in mafic magmas. *The Canadian Mineralogist*, **39**, 341-360.

Buchanan, D.L. and Nolan, J. (1979): Solubility of sulphur and sulphide immiscibility in synthetic tholeiitic melts and their relevance to Bushveld complex rocks. *The Canadian Mineralogist*, **17**, 483-494.

Burger, A.J. and Coertze, F.J. (1973-74): Age determinations – April 1972 to March 1974. *Annuals of the Geological Survey of South Africa*, **10**, 135-141.

Burton, K.W., Gannoun, A., Birck, J.-L., Allegre, C.J., Schiano, P., Clocchiatti, R. and Alard, O. (2002): The compatibility of rhenium and osmium in natural olivine and their behaviour during mantle melting and basalt genesis. *Earth and Planetary Science Letters*, **198**, 63-67.

Cabri, L.J. (2002): The platinum-group minerals. *In:* Cabri, L.J. (ed.): *The Geology, Geochemistry, Mineralogy and Mineral Beneficiation of platinum-group elements*. Canadian Institute of Mining, Metallurgy and Petroleum, Special Volume **54,** 13-129.

Cabri, L.J., LaFlamme, J.H.G. and Stewart, J.M. (1978): On cooperite, braggite and vysotskite. *American Mineralogist*, **63**, 832-839.

Cameron, E.N. (1969): Postcumulus changes in the eastern Bushveld complex. *American Mineralogist*, **54**, 754-779.

Cameron, E.N. (1977): Chromite in the central sector of the eastern Bushveld complex, South Africa. *American Mineralogist*, **62**, 1082-1096.

Cameron, E.N. (1979): Titanium-bearing oxide minerals of the Critical Zone of the eastern Bushveld complex. *American Mineralogist*, **64**, 140-150.

Cameron, E.N. (1980): Evolution of the lower Critical Zone, central sector, eastern Bushveld Complex. *Economic Geology*, **75**, 845-871.

Cameron, E.N. (1982): The Upper Critical Zone of the eastern Bushveld complex. *Economic Geology*, **77**, 1307-1327.

Cameron, E.N. and Desborough, G.A. (1969): Occurrence and characteristics of chromite deposits eastern Bushveld complex. *Economic Geology Monograph*, **4**, 23-40.

Campbell, I.H. (1978): Some problems with the cumulus theory. *Lithos*. **11**; 4, 311-323.

Campbell, I.H. (1996): Fluid dynamic processes in basaltic magma chambers. In: Cawthorn, R.G. (ed.): *Layered intrusions.* Elsevier Science B.V., 45-76.

Campbell, I.H., Naldrett, A.J. and Barnes, S.J. (1983): A model for the origin of the platinum-rich sulphide horizons in the Bushveld and Stillwater complexes. *Journal of Petrology*, **24**; 2, 133-165.

Canil, D. (2002) Vanadium in peridotites, mantle redox and tectonic environments: Archean to present. *Earth and Planetary Science Letters*, **195**; 1-2, 75-90.

Capobianco, C.J. and Drake, M.J. (1990): Partitioning of ruthenium, rhodium, and palladium between spinel and silicate melt and implications for platinum group element fractionation trends. *Geochimica et Cosmochimica Acta*, **54**, 869-874.

Capobianco, C.J., Hervig, R.L. and Drake, M.J. (1994): Experiments on crystal/liquid partitioning of Ru, Rh and Pd for magnetite and hematite solid solutions crystallized from silicate melt. *Chemical Geology*, **113**; 1-2, 23-43.

Cawthorn, R.G. (1999): Permeability of the footwall cumulates to the Merensky reef, Bushveld complex. *South African Journal of Geology*, **102**; 3, 293-310.

Cawthorn, R.G. and Barry, S.D. (1992): The role of intercumulus residua in the formation of pegmatoids associated with the UG2 chromitite, Bushveld complex. *Australian Journal of Earth Sciences*, **39**, 263-276.

Cawthorn, R.G and Walraven, F. (1998): Emplacement and crystallization time for the Bushveld complex. *Journal of Petrology*, **39**, 1669-1687.

Cawthorn, R.G. and Webb, S.J. (2001): Connectivity between the western and eastern limbs of the Bushveld complex. *Tectonophysics*, **330**, 195-209.

Cawthorn, R.G. and Tredoux, M. (2002): The possibility of survival of PGM micro-xenocrysts in mantle melts. *Abstracts of the 9th International Platinum Symposium*, July 21-25, Billings, Montana, USA.

Cawthorn, R.G., Biggar, G.M., Graham, C.M., Graham, A., Ford, C.E., Sharpe, M.R. and Davies, G. (1979): Experimental petrological data on the parental magmas to the Bushveld complex. Institute of Geological Research on the Bushveld Complex, University of Pretoria, Research Report **18**, 27 p.

Cawthorn, R.G., McCarthy, T.S. and Davies, G, (1983): Vertical chemical gradients in a single grain of magnetite from the Bushveld complex, South Africa. *Mineralogical Magazine*, **47**, 27-34.

Cawthorn, R.G., Merkle, R.K.W. and Viljoen, M.J. (2002): Platinum-group element deposits in the Bushveld complex, South Africa. In: Cabri, L.J. (ed.): *The geology, geochemistry, mineralogy and mineral beneficiation of platinum-group elements.* Canadian Institute of Mining, Metallurgy and Petroleum, Special Volume **54**, 389-429.

Cawthorn, R.G., Eales, H.V., Walraven, F., Uken, R. and Watkeys, M.K. (2006): The Bushveld complex. In: Johnson, M.R., Anhaeusser, C.R. and Thomas, R.J. (eds.): *Geology of South Africa.* Geological Society of South Africa, Johannesburg/Council for Geoscience, Pretoria, 261-281.

Clarke, B.M., Uken, R. and Watkeys, M.K. (2000): Intrusion mechanism of the Rustenburg Layered Suite as deduced from the Spruitfontein inlier. *South African Journal of Geology*, **103**; 2, 120-127.

Cole, S. and Ferron, C.J. (2002): A review of the beneficiation and extractive metallurgy of the platinum-group elements, highlighting recent process innovations. In: Cabri, L.J. (ed.): *The geology, geochemistry, mineralogy and mineral beneficiation of platinum-group elements.* Canadian Institute of Mining, Metallurgy and Petroleum, Special Volume **54**, 811-844.

Cousins, C.A. (1959): The structure of the mafic portion of the Bushveld igneous complex. *Transactions of the Geological Society of South Africa*, **62**, 179-201.

Craig, J.R. and Scott, S.D. (1974): Sulphide phase equilibria. *Short course notes of the Mineralogical Society of America*, **1**, CS1-CS110.

Crocket, J.H. (2002): Platinum-group element geochemistry of mafic and ultramafic rocks. In: Cabri, L.J. (ed.): *The geology, geochemistry, mineralogy and mineral beneficiation of platinum-group elements.* Canadian Institute of Mining, Metallurgy and Petroleum, Special Volume **54**, 177-210.

Crocket, J.H., Fleet, M.E. and Stone, W.E. (1992): Experimental partitioning of osmium, iridium and gold between basalt melt and sulphide liquid at 1300°C. *Australian Journal of Earth Sciences*, **39**, 427-432.

Czamanske, G.K. and Moore, J.G. (1977): Composition and phase chemistry of sulphide globules in basalt from the Mid-Atlantic ridge rift valley near 37°N lat. *Geological Society of America Bulletin*, **88**, 587-599.

Dare, S.A.S., Pearce, J.A., McDonald, I. and Styles, M.T. (2009): Tectonic discrimination of peridotites using fO_2–Cr# and Ga–Ti–FeIII systematics in chrome–spinel. *Chemical Geology*, **261**, 199–216.

Davies, G. and Tredoux, M. (1985): The platinum-group element and gold contents of the marginal rocks and sills of the Bushveld complex. *Economic Geology*, **80**, 838-848.

De Beer, H., Meyer, R. and Hattingh, P.J. (1987): Geoelectrical and palaeomagnetic studies on the Bushveld complex. *Geodynamics Series*, **17**, 191-205.

Deer, W.A., Howie, R.A. and Zussmann, J. (1963): *Rock-forming minerals; Volume 2A – Single-chain silicates*. 2nd ed., The Geological Society London, 668 p.

Dick, H.J.B. and Bullen, T. (1984): Chromian spinel as a petrogenetic indicator in abyssal and alpine-type peridotites and spatially associated lavas. *Contributions to Mineralogy and Petrology*, **86**, 54-76.

Eales, H.V. (2000): Implications of the chromium budget of the western limb of the Bushveld complex. *South African Journal of Geology*, **103**; 2, 141-150.

Eales, H.V. (2001): A first introduction to the geology of the Bushveld complex and those aspects of South African geology that relate to it. *Popular Geoscience Series*, **2**, pp. 84. The Council for Geoscience, Pretoria.

Eales, H.V. and Cawthorn, R.G. (1996): The Bushveld complex. *In:* Cawthorn, R.G. (ed.): *Layered intrusions.* Elsevier Science B.V., 181-229.

Eales, H.V., Field, M., De Klerk, W.J. and Scoon, R.N. (1988): Regional trends of chemical variation and thermal erosion in the Upper Critical Zone, western Bushveld complex. *Mineralogical Magazine*, **52**, 63-79.

Eales, H.V., de Klerk, W.J. and Teigler, B. (1990): Evidence for magma mixing processes within the critical and lower zones of the northwestern Bushveld complex, South Africa. *Chemical Geology*, **88**; 3-4, 261-278.

Eales, H.V., Maier, W.D. and Teigler, B. (1991): Corroded plagioclase feldspar inclusions in orthopyroxene and olivine of the Lower and Critical Zones, western Bushveld complex. *Mineralogical Magazine*, **55**, 479-486.

Eales, H.V., Teigler, B. and Maier, W.D. (1993): Cryptic variations of minor elements Al, Cr, Ti and Mn in Lower and Critical Zone orthopyroxenes of the western Bushveld complex. *Mineralogical Magazine,* **57**, 257-264.

Eckey, H.-F., Kosfeld, R. and Türck, M. (2008): *Deskriptive Statistik: Grundlagen – Methoden – Beispiele*. 5th revised ed., Wiesbaden, Gabler; 283 p.

Eriksson, P.G., Hattingh, P.J. and Alterman, W. (1995): An overview of the geology of the Transvaal sequence and Bushveld complex, South Africa. *Mineralium Deposita*, **33**, 98-111.

Eriksson, P.G., Altermann, W. and Hartzer, F.J. (2006): The Transvaal Supergroup and its precursors. In: Johnson, M.R., Anhaeusser, C.R. and Thomas, R.J. (eds.): *Geology of South Africa.* Geological Society of South Africa, Johannesburg/Council for Geoscience, Pretoria, 237-260.

Ertel, W., O'Neill, H.St.C., Sylvester, P.J. and Dingwell, D.B. (1999): Solubilities of Pt and Rh in a haplobasaltic melt at 1300°C. G*eochimica et Cosmochimica Acta*, **63,** 2439–2449.

Evans, A.M. (1997): *Ore geology and industrial minerals – An introduction*. 3rd ed., Blackwell Science Ltd. Oxford, 389 p.

Fandrich, R., Gu, Y., Burrows, D. and Moeller, K. (2006): Modern SEM-based mineral liberation analysis. *International Journal of Mineral Processing*, **84**, 310-320.

Farrow, C.E.G. and Watkinson, D.H. (1992): Alteration and the role of fluids in Ni, Cu and platinum-group element deposition, Sudbury Igneous Complex contact, Onaping-Levack area, Canada. *Mineralogy and Petrology*, **46**, 67-83.

Fleet, M.E. and Wu, T.-W. (1993): Volatile transport of platinum-group elements in sulphide-chloride assemblages at 1000°C. *Geochimica et Cosmochimica Acta*, **57**, 3519-3531.

Fleet, M.E., Stone, W.E. and Crocket, J.H. (1991): Partitioning of palladium, iridium, and platinum between sulphide liquid and basalt melt: effects of melt composition, concentration, and oxygen fugacity. *Geochimica et Cosmochimica Acta*, **55**, 2545-2554.

Fleet, M.E., Chryssoulis, S.L., Stone, W.E. and Weisener, C.G. (1993): Partitioning of the platinum-group elements and Au in the Fe-Ni-Cu-S system: experiments on the fractional crystallization of sulphide melt. *Contributions to Mineralogy and Petrology*, **115**, 36-44.

Gain, S.B. (1985): The geologic setting of the platiniferous UG-2 chromitite layer on the farm Maandagshoek, eastern Bushveld complex. *Economic Geology*, **80**; 4, 925-943.

Gammons, C.H. and Bloom, M.S. (1993): Experimental investigations of the hydrothermal geochemistry of platinum and palladium: II. The solubility of PtS and PdS in aqueous sulphide solutions. *Geochimica et Cosmochimica Acta*, **57**, 2451-2467.

Gjibels, R.H., Millared, J.T., Desborough, G.A. and Bartel, A.J. (1974): Osmium, ruthenium, iridium and uranium in silicates and chromite from the eastern Bushveld complex, South Africa. *Geochimica et Cosmochimica Acta*, **38**, 319-327.

Godel, B., Barnes, S.J., Barnes, S.-J. and Maier, W.D. (2010): Platinum ore in three dimensions – Insights from high-resolution X-ray computed tomography. *Geology*, **38**, 1127-1130.

Grimaldi, F.S. and Schnepfe, M.M (1969): Mode of occurrence of platinum, palladium and rhodium in chromitite. *USGS Professional Paper*, **650-C**, C149-C151.

Gu, Y. (2003): Automated scanning electron microscope based mineral liberation analysis. *Journal of Minerals and Materials Characterization and Engineering*, **2**; 1, 33-41.

Hamilton, J. (1977): Sr isotope and trace element studies of the Great Dyke and Bushveld mafic phases and their relation to early Proterozoic magma genesis in Southern Africa. *Journal of Petrology*, **18**, 24-52.

Hamlyn, P.R., Keays, R.R., Cameron, W.E., Crawford, A.J. and Waldron, H.M. (1985): Precious metals in magnesian low-Ti lavas: Implications for metallogenesis and sulphur saturation in primary magmas. *Geochimica et Cosmochimica Acta*, **49**, 1797-1811.

Hanley, J.J., Pettke, T., Mungall, J.E. and Spooner, E.T.C. (2005): The solubility of Pt and Au in NaCl brines at 1.5 kbar, 600 to 800°C: A laser ablation ICP-MS pilot study of synthetic fluid inclusions. *Geochimica et Cosmochimica Acta*, **69**; 10, 2593-2611.

Harmer, R.E. and Sharpe, M.R. (1985): Field relations and strontium isotope systematics of the marginal rocks of the eastern Bushveld complex. *Economic Geology*, **80**; 4, 813-837.

Hattingh, P.J. (1991): Palaeomagnetic constraints on the emplacement of the Bushveld complex. *Journal of African Earth Sciences*, **21**; 4, 549-551.

Hatton, C.J (1982): The effect of pressure, temperature and composition on the distribution of Fe and Mg between olivine, orthopyroxene liquid; an appraisal of the reversal in the normal fractionation trend in the Bushveld complex. Institute of Geological Research on the Bushveld Complex, University of Pretoria, Research Report **38**, 28 p.

Hatton, C.J. and von Gruenewaldt, G. (1985): The geological setting and petrogenesis of the Bushveld complex chromitite layers. Institute of Geological Research on the Bushveld Complex, University of Pretoria, Research Report **57**, 48 p.

Hatton, C.J., Harmer, R.E. and Sharpe, M.R. (1986): Petrogenesis of the middle group of chromitite layers, Doornvlei, eastern Bushveld complex. *In:* Gallagher, M.J., Ixer, R.A., Neary, C.R. and Prichard, H.M. (eds.): *Metallogeny of basic and ultrabasic rocks*. Institute of Mining and Metallurgy London, 241-247.

Haughton, D.R., Roeder, P.L. and Skinner, B.J. (1974): Solubility of sulphur in mafic magmas. *Economic Geology*, **69**, 451-467.

Henderson, P. (1975): Geochemical indicator of the efficiency of fractionation of the Skaergaard intrusion, east Greenland. *Mineralogical Magazine*, **40**, 285-291.

Hess, H.H. (1960): The Stillwater Igneous Complex, Montana: A quantitative mineralogical study. *Memoirs of the Geological Society of Arnerica,* 230 p.

Hiemstra, S.A. (1985): The distribution of some platinum-group elements in the UG-2 chromitite layer of the Bushveld complex. *Economic Geology*, **80**, 944-957.

Hill, R. and Roeder, P. (1974): The crystallization of spinel from basaltic liquid as a function of oxygen fugacity. *Journal of Geology,* **82**, 1709-729.

Hulbert, L.J. and von Gruenewaldt, G. (1985): Textural and compositional features of chromite in the Lower and Critical Zones of the Bushveld complex south of Potgietersrus. *Economic Geology*, **80**, 872-895.

Hunter, R.H. (1996): Texture development in cumulate rocks. In: Cawthorn, R.G. (ed.): *Layered intrusions.* Developments in petrology **15**, Elsevier Amsterdam, 530 p.

Huppert, H.E. and Sparks, J. (1981): The fluid dynamics of a basaltic magma chamber replenished by influx of hot, dense ultrabasic magma. *Contributions to Mineralogy and Petrology*, **75**, 279-289.

Huppert, H.E., Stephen, R. and Sparks, J. (1985): Cooling and contamination of mafic and ultramafic magmas during ascent through continental crust. *Earth and Planetary Science Letters*, **74**; 4, 371-386.

Irvine, T.N. (1975): Crystallization sequences in the Muskox Intrusion and other layered intrusions II: Origin of chromitite layers and similar deposits of other magmatic ores. *Geochimica et Cosmochimica Acta*, **39**; 6-7, 991-1020.

Irvine, T.N. (1977): Origin of chromitite layers in the Muskox Intrusion and other stratiform intrusion; a new interpretation. *Geology*, **5**, 273-277.

Irvine, T.N. (1982): Terminology for layered intrusions. *Journal of Petrology*, **23**; 2, 127-162.

Irvine, T.N. and Sharpe, M.R. (1986): Magma mixing and the origin of stratiform oxide ore zones in the Bushveld and Stillwater complexes. *In:* Gallagher, M.J., Ixer, R.A., Neary, C.R. and Prichard, H.M. (eds.): *The metallogeny of basic and ultrabasic rocks.* Institute of Mining and Metallurgy, London, 183-198.

Irvine, T.N., Keith, D.W. and Todd, S.G. (1983): The J-M platinum-palladium reef of the Stillwater Complex, Montana, II. Origin by double diffusive convective magma mixing and implications for the Bushveld complex. *Economic Geology,* **78**, 1287-1334.

Jackson, E.D. (1970): The origin of ultramafic rocks by cumulus processes. *Fortschritte der Mineralogie*, **48**; 1, 9-10.

Jackson, E.D. (1971): The origin of ultramafic rocks by cumulus processes. *Fortschritte der Mineralogie,* **48**; 1, 128-174.

Jackson, E.D. (1967): Ultramafic cumulates in the Stillwater, Great Dyke and Bushveld intrusions. In: Wyllie, P.J. (ed.) *Ultramafic and related rocks*. John Wiley and Sons, N.Y., 20-38.

Jones, R.T. (1999): Platinum smelting in South Africa. *South African Journal of Science*, **95**, 525-534.

Keays, R.R. (1995): The role of komatiitic and picritic magmatism and S-saturation in the formation of ore deposits. *Lithos*, **34**, 1-18.

Kinnaird, J.A., Kruger, F.J., Nex, P.A.M. and Cawthorn, R.G. (2002): Chromitite formation – a key to understanding processes of platinum enrichment. *Transactions of the Institution of Mining and Metallurgy (Section B: Applied Earth Sciences.*) **111**, B23-B35.

Kruger, F.J. (1994): The Sr-isotopic stratigraphy of the western Bushveld complex. *South African Journal of Geology*, **97**; 4, 393-398.

Kruger, F.J. (2005): Filling the Bushveld complex magma chamber: lateral expansion, roof and floor interaction, magmatic unconformities, and the formation of giant chromitite, PGE and Ti-V-magnetite deposits. *Mineralium Deposita*, **40**, 451-472.

Kruger, F.J. and Marsh, J.S. (1982): Significance of $^{87}Sr/^{86}Sr$ ratios in the Merensky cyclic unit of the Bushveld Complex. *Nature*. **298**; 5869, 53-55.

Kullerud, G. (1963): Thermal stability of pentlandite. *The Canadian Mineralogist*, **7**, 353-366.

Kullerud, G. and Yoder, H.S. (1959): Pyrite stability relations in the Fe-S system. *Economic Geology*, **54**, 533-572.

Kullerud, G. and Yund, R.A. (1962): The Ni-S system and related minerals. *Journal of Petrology*, **3**, 126-175.

Lee, C.A. and Tredoux, M. (1986): Platinum-group element abundances in the Lower and the Lower Critical Zones of the eastern Bushveld complex. *Economic Geology*, **81**, 1087-1095.

Lee, C.A. and Parry, S.J. (1988): Platinum-group element geochemistry of the Lower and Middle Group chromitites of the Eastern Bushveld Complex. *Economic Geology*, **83**, 1127-1139.

Lee, C.A. and Butcher, A.R. (1990): Cyclicity in the Sr isotope stratigraphy through the Merensky and Bastard reef units, Atok section, eastern Bushveld complex. *Economic Geology*, **85**, 877-883.

Legendre, O. and Augé, T. (1986): Mineralogy of platinum-group mineral inclusions in chromitites from different ophiolitic complexes. *In:* Gallagher, M. J., Ixer, R. A., Neary, C. R. and Prichard, H. M.(eds.) *Metallogeny of basic and ultrabasic rocks*. Institution of Mining and Metallurgy, London; 361-372.

Lekghoto, T.B. (2010): Investigation of the behaviour of platinum-group minerals and base metal sulphides during flotation of UG2 ore. *Unpublished M.Sc. thesis, University of the Free State, Bloemfontein; 99 p.*

LeMaitre, R.W. (ed.) (2002): *Igneous rocks: a classification and glossary of terms: recommendations of the International Union of Geological Sciences, Subcommission on the Systematics of Igneous Rocks*. 2nd edition, Cambridge University Press. 236 p.

Lesher, C.M. and Campbell, I.H. (1993): Geochemical and fluid dynamic modelling of compositional variations in Archean komatiite-hosted nickel sulphide ores in Western Australia. *Economic Geology*, **88**; 4, 804-816.

Li, C. and Naldrett, A.J. (1993): High chlorine alteration minerals and calcium-rich brines in fluid inclusions from the Strathcona deep copper zone, Sudbury, Ontario. *Economic Geology*, **88**, 1780-1796.

Li, C., Maier, W.D. and de Waal, S.A. (2001): The role of magma mixing in the genesis of PGE mineralization of the Bushveld complex; thermodynamic calculation and new interpretations. *Economic Geology*, **96**, 653-662.

Li, C., Ripley, E.M. and Merino, E. (2004): Replacement of base metal sulphides by actinolite, epidote, calcite and magnetite in the UG2 and Merensky reef of the Bushveld complex, South Africa. *Economic Geology*, **99**, 173-184.

Lindsley, D.H. (1976): Experimental studies of oxide minerals. *Reviews in Mineralogy*, **3**, L61-L88.

Lipin, B.R. (1993): Pressure increases, the formation of chromite seams, and the development of the ultramafic series in the Stillwater Complex, Montana. *Journal of Petrology*, **34**, 955-976.

Lodders, K. (2003): Solar system abundances and condensation temperatures of the elements. *The Astrophysical Journal*, **591**, 1220-1247.

Lorand, J.-P. and Alard, O. (2001): Platinum-group element abundances in the upper mantle: new constraints from in situ and whole-rock analyses of Massif Central xenoliths (France). *Geochimica et Cosmochimica Acta*, **65**, 2789-2806.

Lorand, J.-P, Luguet, A., Alard, O., Bezos, A. and Meisel, T. (2008): Abundance and distribution of platinum-group elements in orogenic lherzolites: a case study in a Fontete Rouge lherzolite (French Pyrénées). *Chemical Geology*, **248**, 174-194.

Luguet, A., Shirey, S.B., Lorand, J.-P., Horan, M.F. and Carlson, R.W. (2007): Residual platinum-group minerals from highly depleted harzburgites of Lherz massif (France) and their role in HSE fractionation of the mantle. *Geochimica et Cosmochimica Acta*, **71**, 3082-3097.

Magyarosi, Z., Watkinson, D.H. and Jones, P.C. (2002): Mineralogy of Ni-Cu-platinum-group element sulphide ore in the 800 and 810 ore bodies, Copper Cliff South Mine, and P-T-X conditions during the formation of platinum-group minerals. *Economic Geology*, **97**; 7, 1471-1486.

Maier, W.D. (2005): Platinum-group element (PGE) deposits and occurrences: Mineralization styles, genetic concepts and exploration criteria. *Journal of African Earth Sciences*, **41**, 165-191.

Maier, W.D. and Barnes, S.-J. (1998): Concentration of rare earth elements in silicate rocks of the Lower, Critical and Main Zones of the Bushveld complex. *Chemical Geology*, **150**, 85-103.

Maier, W.D. and Barnes, S.-J. (1999): Platinum-group elements in silicate rocks of the Lower, Critical and Main Zones at Union Section, western Bushveld complex. *Journal of Petrology*, **40**; 11, 1647-1671.

Mathez, E.A. and Waight, T.E. (2003): Lead isotopic disequilibrium between sulphide and plagioclase in the Bushveld complex and the chemical evolution of large layered intrusions. *Geochimica et Cosmochimica Acta*, **67**; 10, 1875-1888.

Mathez, E.A. and Webster, J.D. (2005): Partitioning behaviour of chlorine and fluorine in the system apatite-silicate melt-fluid. *Geochimica et Cosmochimica Acta*, **69**, 1275-1286.

Matthey, J. (2011): “Platinum Today – The world’s leading authority on platinum-group metals”, [online] available at http://www.platinum.matthey.com

Mavgrones, J.A. and O’Neill, H.St.C. (1999): The relative effects of pressure, temperature and oxygen fugacity on the solubility of sulphide in mafic magmas. *Geochimica et Cosmochimica Acta*, **63**; 7/8, 1173-1180.

McCandless, T.E., Ruiz, J., Adair, B.I. and Freydier, C. (1999): Re-Os isotope and Pd/Ru variations in chromitites from the Critical Zone, Bushveld complex, South Africa. *Geochimica et Cosmochimica Acta*, **63**; 6, 911-923.

McCormick, K.A. and McDonald, A.M. (1999): Chlorine-bearing amphiboles from the Fraser mine, Sudbury, Ontario, Canada: description and crystal chemistry. *The Canadian Mineralogist*, **37**, 1385-1403.

McLaren, C.H. and de Villiers, J.P.R. (1982): The platinum-group chemistry and mineralogy of the UG-2 chromitite layer of the Bushveld complex. *Economic Geology*, **77**, 1348-1366.

Merkle, R.K.W. (1992): Platinum-group minerals in the Middle Group of chromitite layers at Marikana, western Bushveld complex: Indications for collection mechanisms and postmagmatic modification. *Canadian Journal of Earth Sciences*, **29**, 209-221.

Merkle, R.W. and McKenzie, A.D. (2002): The mining and beneficiation of South African PGE ores – An overview. *In:* Cabri, L.J. (ed.): *The Geology, Geochemistry, Mineralogy and Mineral Beneficiation of platinum-group elements*. Canadian Institute of Mining, Metallurgy and Petroleum, Special Volume **54**, 793-809.

Merkle, R.K.W. and Verryn, S.M.C. (2003): Cooperite and braggite from the Bushveld Complex: implications for the miscibility gap and identification. *Mineralium Deposita*, **38**, 381-388.

Meyer, R. and de Beer, J.H. (1987): Structure of the Bushveld complex from resistivity measurements. *Nature*, **325**, 610-612.

MINTEK (2010a): "Certificate of analysis SARM 65 UG2 chromitite", [online] available at http://www.mintek.co.za/ASD/Certificates/SARM 65.pdf

MINTEK (2010b): "Certificate of analysis SARM 76 Merensky ore" [online], available at http://www.mintek.co.za/ASD/Certificates/SARM 76.pdf

Molnar, F., Watkinson, D.H., Jones, P.C. and Gatter, I. (1997): Fluid inclusion evidence for hydrothermal enrichment of magmatic ore at the contact zone of the Ni-Cu-platinum-group element 4b deposit, Lindsley Mine, Sudbury, Canada. *Economic Geology*, **92**, 674-685.

Molnar, F., Watkinson, D.H. and Everest, J.O. (1999): Fluid-inclusion characteristics of hydrothermal Cu-Ni-PGE veins in granitic and metavolcanic rocks at the contact of the Little Stobie deposit, Sudbury, Canada. *Chemical Geology*, **154**, 279-301.

Molnar, F., Watkinson, D.H. and Jones, P.C. (2001): Multiple hydrothermal processes in footwall units of the North Range, Sudbury Igneous Complex, Canada, and implications for the genesis of vein-type Ni-Cu-PGE deposits. *Economic Geology*, **96**, 1654-1670.

Mondal, S.K. and Mathez, E.A. (2007): Origin of the UG2 chromitite layer, Bushveld complex. *Journal of Petrology*, **48**; 3, 495-510.

Morgan, J.W. (1986): Ultramafic xenoliths – clues to the Earth's late accretionary history. *Journal of Geophysical Research*, **91B**, 12375-12387.

Morimoto, N., Fabries, J., Ferguson, A.K., Ginzburg, I.V., Ross, M., Seifert, F.A. and Zussmann, J. (1988): Nomenclature of pyroxenes. *Mineralogical Magazine*, **52**, 535-550.

Mungall, J.E., Andrews, D.R.A., Cabri, L.J., Sylvester, P.J. and Tubrett, M. (2005): Partitioning of Cu, Ni, Au, and platinum-group elements between monosulphide solid solution and sulphide melt under controlled oxygen and sulphur fugacities. *Geochimica et Cosmochimica Acta*, **69**, 4349–4360.

Murck, B.W. and Campbell, I.H. (1986): The effects of temperature, oxygen fugacity and melt composition on the behaviour of chromium in basic and ultrabasic melts. *Geochimica et Cosmochimica Acta*, **50**, 1871-1887.

Naldrett, A.J. (1981): Platinum-group element deposits. *In:* Cabri, L. J. (ed.): *Platinum-group elements: Mineralogy, geology, recovery*. The Canadian Institute of Mining and Metallurgy, Special Volume **23**, 197-231.

Naldrett, A.J. (1989): Sulphide melts: crystallization temperatures, solubilities in silicate melts, and Fe, Ni, and Cu partitioning between basaltic magmas and olivine. *Reviews in Economic Geology,* **4**; 5-20.

Naldrett, A.J. and Lehmann, J. (1988): Spinel non-stoichiometry as the explanation for Ni-, Cu-, and PGE enriched sulphides in chromitites. *In:* Prichard, H.M., Potts, P.J., Bowles, J.F.W. and Cribbs, S.J. (eds.): *Geo-Platinum '87.* Elsevier Science Publishers Ltd., Essex, U.K.; 93-109.

Naldrett, A.J. and von Gruenewaldt, G. (1989): Association of platinum-group elements with chromitite in layered intrusions and ophiolite complexes. *Economic Geology,* **84**, 180-187.

Naldrett, A.J., Cameron, G., von Gruenewaldt, G. and Sharpe, M.R. (1987): The formation of stratiform platinum-group element deposits in layered intrusions. Institute of Geological Research on the Bushveld Complex, University of Pretoria, Research Report **63**, 100 p.

Naldrett, A.J., Kinnaird, J., Wilson, A., Yudovskaya, M., McQuade, S., Chunnett, G. and Stanley, C. (2009): Chromite composition and the PGE content of Bushveld chromitites: Part 1 – the Lower and Middle Groups. *Transactions of the Institution of Mining and Metallurgy (Section B: Applied Earth Sciences*), **118**, 131-161.

Natural Resources Canada (2011): "WPR-1 – Altered peridotites with gold and platinum-group elements", [online] available at http://www.nrcan.gc.ca/mms-smm/tect-tech/ccrmp/cer-cer/wpr-1-eng.htm

Navrotsky, A. and Kleppa, O.J. (1967): The thermodynamics of cation distribution in simple spinels. *Journal of Inorganic Nuclear Chemistry*, **29**, 2701-2714.

Nehru, C.E., Prinz, M., Dowty, E. and Keil, K. (1974): Spinel-group minerals and ilmenite in Apollo 15 rake samples. *American Mineralogist*, **59**, 1220–1235.

Oberthür, T., Weiser, T.W., Gast, L. and Kojonen, K. (2003): Geochemistry and mineralogy of platinum-group elements at Hartley Platinum Mine, Zimbabwe. *Mineralium Deposita*, **38**, 327–343.

O'Reilly, S.Y., Griffin, W.L. and Ryan, C.G. (1991): Residence of trace elements in metasomatized spinel lherzolite xenoliths: a proton microprobe study. *Contributions to Mineralogy and Petrology*, **109**, 98-113.

Page, N.J. (1971): Sulphide minerals in the G and H chromitite zones in the Stillwater Complex, Montana. *USGS Professional Paper*, **694**, 20p.

Page, N.J. and Jackson, E.D. (1967): Preliminary report on sulphide and platinum-group minerals in the chromitites of the Stillwater Complex. *USGS Paper*, **575D**, 123-126.

Page, N.J. and Talkington, R.W. (1984): Palladium, platinum, rhodium, ruthenium and iridium in peridotites and chromitites from ophiolite complexes in Newfoundland. *The Canadian Mineralogist*, **22**, 137-149.

Page, N.J., Rowe, J.J. and Haffty, J. (1976): Platinum metals in the Stillwater Complex, Montana. *Economic Geology*, **77**, 1352-1363.

Paktunc, A.D. and Cabri, L.J. (1995): A proton- and electron-microprobe study of gallium, nickel and zinc distribution in chromian spinel. *Lithos*, **35**, 261-282.

Palme, H. and O'Neill, H.St.C. (2003): Cosmochemical estimates of mantle composition. *In:* Holland, H.D. and Turekian, K.K. (eds.): *Treatise on geochemistry – Vol. 2, The mantle and core.* Elsevier-Pergamon, Oxford, 1-38.

Pattou, L., Lorand, J.-P. and Gros, M. (1996): Nonchondritic platinum-group element ratios in the Earth's mantle. *Nature*, **379**, 712-715.

Peach, C.L. and Mathez, E.A. (1996): Constraints on the formation of platinum-group element deposits in igneous rocks. *Economic Geology*, **91**; 3, 439-450.

Pearce, J.A., Lippard, S.J. and Roberts, S. (1984): Characteristics and tectonic significance of suprasubduction zone ophiolites. *In:* Kokelaar, B.P. and Holwells, M.F. (eds.): *Marginal Basin Geology,* Blackwell Scientific Publications, Oxford, 77-94.

Peck, D.C., Keays, R.R. and Ford, R.J. (1992): Direct crystallization of refractory platinum-group element alloys from boninitic magmas: Evidence from western Tasmania. *Australian Journal of Earth Sciences*, **39**, 373-387.

Penberthy, C.J. and Merkle, R.K.W. (1999): Lateral variations in the platinum-group element content and mineralogy of the UG2 chromitite layer, Bushveld complex. *South African Journal of Geology*, **102**; 3, 240-250.

Penberthy, C.J., Oosthuyzen, E.J. and Merkle, R.K.W. (2000): The recovery of platinum-group elements from the UG-2 chromitite, Bushveld complex - a mineralogical perspective. *Mineralogy and Petrology*, **68**, 213-222.

Peregoedova, A. and Ohnenstetter, M. (2002): Collectors of Pt, Pd and Rh in a S-poor Fe-Ni-Cu sulphide system at 760°C: experimental data and application to ore deposits. *The Canadian Mineralogist*, **40**, 527-561.

Peregoedova, A., Barnes, S.-J. and Baker, D.R. (2004): The formation of Pt-Ir alloys and Cu-Pd-rich sulphide melts by partial desulphurization of Fe-Ni-Cu-sulphides: results of experiments and implications for natural systems. *Chemical Geology*, **208**, 247-264.

Pollard, D.D., Muller, O.H. and Dockstader, D.R. (1975): The form and growth of fingered sheet intrusions. *Bulletin of the Geological Society of America*, **86**, 351-363.

Prichard, H. M., Neary, C. R. and Potts, P. J. (1986): Platinum-group minerals in the Shetland Ophiolite. *In:* Gallagher, M. J., Ixer, R. A., Neary, C. R. and Prichard, H. M.(eds.) *Metallogeny of basic and ultrabasic rocks*. Institution of Mining and Metallurgy, London; 395-414.

Princivalle, F., Della Costa, A. and Carbonin, S. (1989): Comparative crystal chemistry of spinels from some suites of ultramafic rocks. *Mineralogy and Petrology*, **40**; 2, 117-126.

Reid, D.L., Cawthorn, R.G., Kruger, F.J. and Tredoux, M. (1993): Isotope and trace element patterns below the Merensky reef, Bushveld complex, South Africa: evidence for fluids? *Chemical Geology*, **106**, 171-186.

Rice, A. and von Gruenewaldt, G. (1991): Convective scavenging in Bushveld melts: a proposed mechanism for the concentration of PGE and chromite in mineralized layers. Institute of Geological Research on the Bushveld Complex, University of Pretoria, Research Report **95**, 15 p.

Rice, A. and Eales, H. (1995): The densities of Bushveld melts: textural and hydrodynamic criteria. *Mineralogy and Petrology*, **54**, 45-53.

Rice, A. and von Gruenewaldt, G. (1995): Shear aggregation (convective scavenging) and cascade enrichment of PGEs and chromite. *Mineralogy and Petrology*, **54**, 105-117.

Righter, K., Campbell, A.J., Humayun, M. and Hervig, R.L. (2004): Partitioning of Ru, Rh, Pd, Re, Ir and Au between Cr-bearing spinel, olivine, pyroxene and silicate melts. *Geochimica and Cosmochimica Acta*, **68**; 4, 867-880.

Righter, K., Leeman, W.P. and Hervig, R.L. (2006): Partitioning of Ni, Co and V between spinel-structured oxides and silicate melts: Importance of spinel composition. *Chemical Geology*, **227**, 1-25.

Ripley, E.M. and Alawi, J.A. (1988): Petrogenesis of pelitic xenoliths at the Babitt Cu-Ni deposit, Duluth Complex, Minnesota, USA. *Lithos*, **21**, 143-159.

Robb, L. (2005): *Introduction to ore-forming processes*. Blackwell Science Ltd. Oxford, 373 p.

Roedder, E. (1965): Liquid CO_2 inclusions in olivine-bearing nodules and phenocrysts from basalts. *American Mineralogist,* **50**, 1746-1782.

Rollinson, H. (1993): *Using geochemical data: evaluation, presentation, interpretation*. Pearson Education Ltd., Essex, England.

Rösler, H.J. (1991): *Lehrbuch der Mineralogie*. 5th ed., Deutscher Verlag für Grundstoffindustrie, Leipzig, 844 p.

Rudnick, R.L. and Fountain, D.M. (1995): Nature and composition of the continental crust: a lower crust perspective. *Reviews in Geophysics*, **33**, 267-309.

Rudnick, R.L. and Gao, S. (2003): Composition of the continental crust. *In:* Holland, H.D. and Turekian, K.K. (eds.): *Treatise on geochemistry – Vol. 3, The crust.* Elsevier-Pergamon, Oxford, 1-64.

SACS (South African Committee for Stratigraphy) (1980): Stratigraphy of Southern Africa, Part 1. Lithostratigraphy of South Africa, South West Africa/Namibia and the Republic of Boputhatswana, Transkei and Venda. Geological Survey of South Africa Handbook **8**, 690 p.

Schiffries, C.M. (1982): The platiniferous dunite pipe in the Bushveld complex: Infiltration metasomatism by a chloride solution. *Economic Geology*, **77**, 1439-1453.

Schiffries, C.M. and Skinner, B.J. (1987): The Bushveld hydrothermal system: Field and petrologic evidence. *American Journal of Science*, **287**, 566-595.

Schiffries, C.M. and Rye, D.M. (1989): Stable isotope systematic of the Bushveld complex: I. Constraints of magmatic processes in layered intrusions. *American Journal of Science*, **289**, 841-873.

Schiffries, C.M. and Rye, D.M. (1990): Stable isotope systematic of the Bushveld complex: II. Constraints on hydrothermal processes in layered intrusions. *American Journal of Science*, **290**, 209-245.

Schoenberg, R., Kruger, F.J., Nägler, T.F., Meisel, T. and Kramers, J.D. (1999): PGE enrichment in chromitite layers and the Merensky reef of the western Bushveld complex; a Re-Os and Rb-Sr isotope study. *Earth and Planetary Science Letters*, **172**, 49-64.

Schürmann, L.W., Gräbe, P.-J. and Steenkamp. C.J. (1998): Chromium. *In:* Wilson, M.G.C. and Anhaeusser, C.R. (eds.): *The mineral resources of South Africa*, Handbook **16**, Council for Geoscience, Pretoria, 90-105.

Schweitzer, J.K., Hatton, C.J. and de Waal, S.A. (1995): Regional lithochemical stratigraphy of the Rooiberg Group, upper Transvaal Supergroup: a proposed new subdivision. *South African Journal of Geology*, **98**, 245-255.

Scoon, R. N. and Teigler, B. (1994): Platinum-group element mineralization in the Critical Zone of the western Bushveld complex: 1. Sulphide poor chromitites below the UG2. *Economic Geology*, **89**, 1094-1121.

Scoon, R. N. and Teigler, B. (1995): A new LG-6 chromite reserve at Eerste Geluk in the boundary zone between the central and the southern sectors of the eastern Bushveld complex. *Economic Geology*, **90**, 969-982.

Sharpe, M.R. (1980): Evolution of the Bushveld magma chamber. Institute of Geological Research on the Bushveld Complex, University of Pretoria, Research Report **20**, 57 p.

Sharpe, M.R. (1981): The chronology of magma influxes to the eastern compartment of the Bushveld complex as exemplified by its marginal border groups. *Journal of the Geological Society of London*, **138**; 3, 307-326.

Sharpe, M.R. (1982): Noble metals in the marginal rocks of the Bushveld complex. *Economic Geology*, **77**, 1286-1295.

Sharpe, M.R. (1985): Sr isotope evidence for preserved density stratification in the Main Zone of the Bushveld complex, South Africa. *Nature*, **316**; 11, 119-126.

Sharpe, M.R. and Hulbert, L.J. (1985): Ultramafic sills beneath the eastern Bushveld complex: mobilized suspensions of early Lower Zone cumulates in a parental magma with boninitic affinities. *Economic Geology*, **80**, 849-871.

Spandler, C., Mavrogenes, J. and Arculus, R. (2005): Origin of chromitites in layered intrusions: Evidence from chromite-hosted melt inclusions from the Stillwater Complex. *Geology*, **33**; 11, 893-896.

Spandler, C., O'Neill, H. St C. and Kamenetsky, V.S. (2007): Survival times of anomalous melt inclusions from element diffusion in olivine and chromite. *Nature*, **447**, 303-306.

Stosch, H.-G. (2008): *Geochemie der Seltenen Erden*. Vorlesungen am Mineralogisch-Petrographischen Institut der Universität zu Köln, 1988 – 1993, Skript mit Ergänzungen von 1998, 2000 und 2006. Geologisches Institut, Universität Karlsruhe; p 209.

Sylvester, P.J. (2001): A practical guide to platinum-group element analysis of sulphides by laser ablation ICPMS. *In:* Sylvester, P. (ed.) *Laser-Ablation-ICP-MS in the Earth Sciences, Principles and Applications*. Mineralogical Association of Canada, *Short Course* **29**, 203-311.

Talkington, R.W. and Page, N.J. (1984): Palladium, platinum, rhodium, ruthenium and iridium in peridotites and chromitites from ophiolitic complexes in Newfoundland. *The Canadian Mineralogist*, **22**, 137-149.

Talkington, R.W. and Lipin, B.R. (1986): Platinum-group minerals in chromite seams of the Stillwater Complex, Montana. *Economic Geology*, **81**, 1179-1186.

Talkington, R.W. and Watkinson, D.H. (1986): Whole rock platinum-group element trends in chromite-rich rocks in ophiolitic and stratiform igneous complexes. *In:* M.J. Gallagher and R.A. Ixer (eds.): *The metallogeny of basic and ultrabasic rocks.* Institute of Mining and Metallurgy, London, 427-440.

Talkington, R.W., Watkinson, D.H., Whittaker, P.J. and Jones, P.C. (1984): Platinum-group minerals and other solid inclusions in chromite of ophiolitic complexes: occurrence and petrological significance. *Tschermaks Mineralogische und Petrologische Mitteilungen*, **32**, 285-301.

Teigler, B. (1990): Platinum-group element distribution in the lower and middle group chromitites in the western Bushveld complex. *Mineralogy and Petrology*, **42**, 165-179.

Teigler, B. and Eales, H.V. (1993): Correlation between chromite composition and PGE mineralization in the Critical Zone of the western Bushveld complex. *Mineralium Deposita*, **28**, 291-302.

Teigler, B. and Eales, H.V. (1996): The Lower and Critical Zones of the western limb of the Bushveld complex as intersected by the Nooitgedacht boreholes. Geological Survey of South Africa, *Bulletin* **111**, 126 p.

Teigler, B. Eales, H.V. and Scoon, R.N. (1992): The cumulate succession in the Critical Zone of the Rustenburg Layered Suite at Brits, western Bushveld complex. *South African Journal of Geology*, **95**; 1-2, 17-28.

Tredoux, M. and McDonald, I. (1996): Komatiite WITS-1, low concentration noble metal standard for the analysis of non-mineralized samples. *Geostandards Newsletter*, **20**; 2, 267-276.

Tredoux, M., Lindsay, N.M., Davies, G. and McDonald, I. (1995): The fractionation of platinum-group elements in magmatic systems, with suggestion of a novel causal mechanism. *South African Journal of Geology,* **98**; 2, 157-168.

Ulmer, G.C. (1969): Experimental investigation of chromite spinels. *Economic Geology Monograph*, **4**, 114-131.

Ulmer, G.C. (2011): “Übung Mineralnormierung/Thermobarometrie)”, [online] available at http://eva-elba.unibas.ch/index.cfm?w=117&c=0&f=873&z=12&o=&s=p

USGS (2011a): “Minerals information – Chromium: statistics and information“, [online] available at http://minerals.usgs.gov/minerals/pubs/commodity/chromium/

USGS (2011b): “Minerals information – Platinum-group metals: statistics and information“, [online] available at http://minerals.usgs.gov/minerals/pubs/commodity/Platinum/

Vernon, R.H. (2004): *A practical guide to rock microstructure*. Cambridge University Press, Cambridge, 594 p.

Verryn, S.M.C. and Merkle, R.K.W. (1994): Compositional variation of cooperite, braggite and vysotskite from the Bushveld complex. *Mineralogical Magazine*, **58**, 223-234.

Verryn, S.M.C. and Merkle, R.K.W. (2002): The system PtS-PdS-NiS between 1200 and 700 °C. *The Canadian Mineralogist*, **40**, 571-584.

Viljoen, M.J. and Schürmann, L.W. (1998): Platinum-group metals. *In:* Wilson, M.G.C. and Anhaeusser, C.R. (eds.): *The mineral resources of South Africa*. Handbook **16**, Council for Geoscience, Pretoria, 532-568.

Von Gruenewaldt, G. and Merkle, R.K.W. (1995): Platinum-group element proportions in chromitites of the Bushveld complex: implications for fractionation and magma mixing models. *Journal of African Earth Scienc*es, **21**; 4, 615-632.

Von Gruenewaldt, G., Hatton, C.J., Merkle, R.K.W. and Gain, S.B. (1986): Platinum-group element – chromitite associations in the Bushveld complex. *Economic Geology*, **81**, 1067-1079.

Voordouw, R.J., Gutzmer, J. and Beukes, N.J. (2009): Zoning of PGM assemblages in the UG2 chromitite determined through in-situ SEM-EDX based image analysis. *Mineralium Deposita*, Online: DOI 10.1007/s00126-009-0265-z.

Wager, L.R. (1963): The mechanism of adcumulus growth in the layered series of the Skaergaard intrusion. *Mineralogical Society of America Special Paper*, **1**, 1-9.

Wager, L.R. and Brown, G.M. (1968): Layered igneous rocks. Oliver & Boyd, Edinburgh, 588 p.

Wager, L.R., Brown, G.M. and Wadsworth, W.J. (1960): Types of igneous cumulates. *Journal of Petrology*, **1**; 1, 73-85.

Walraven, F., Armstrong, R.A. and Kruger, F.J. (1990): A chronostratigraphic framework for the north-central Kaapvaal Craton, the Bushveld complex and Vredefort structure. *Tectonophysics*, **171**, 23-48.

White, A.J. (1994): The Potgietersrus prospect – geology and exploration history. *In:* Anhaeusser, C.R. (ed.): *Proceedings of the 15th CMMI Congress*, Volume **3**: Geology. South African Institute of Mining and Metallurgy, 173-181.

Willmore, C.C., Boudreau, A.E. and Kruger, F.J. (2000): The halogen geochemistry of the Bushveld complex, Republic South Africa: Implications for chalcophile element distribution in the Lower and Critical zones. *Journal of Petrology*, **41**; 10, 1517-1539.

Wilson, A. H., Naldrett, A.J. and Tredoux, M. (1989): Distribution and controls of platinum group element and base metal mineralization in the Darwendale subchamber of the Great Dyke, Zimbabwe. *Geology*, **17**; 7, 649-652.

Wilson J. R., Cawthorn, R.G., Kruger, F.J. and Grundvig, S. (1994): Intrusive origin for the unconformity in the northern Gap, western Bushveld complex. *South African Journal of Geology*, **97**, 462–72.

Wood, S.A. (2002): The aqueous geochemistry of the platinum-group elements with applications to ore deposits. *In:* Cabri, L.J. (ed.): *The Geology, Geochemistry, Mineralogy and Mineral Beneficiation of platinum-group elements*. Canadian Institute of Mining, Metallurgy and Petroleum, Special Volume **54**, 211-249.

Appendix – Table of contents

Appendix A

Appendix B

Tables

Figures

Appendix C

Appendix D

Kottke-Levin, J., Tredoux, M. and Gräbe, J.-P. (2009): An investigation of the geochemistry of the Middle Group of the eastern Bushveld complex, South Africa Part 1 – the chromitite layers. *Applied Earth Science (Trans. Inst. Min. Metall. B)*, **118**; 3-4, 111-130.

Table A-1 Core log including depth of individual layers, lithography and thickness of sampling intervals. *CHR* : chromitite; *CHRDISS:* disseminated chromitite; *PX:* pyroxenite; *NO:* norite; *NOLE:* leuconorite; *AN:* anorthosite. *ANMO:* mottled anorthosite; *FR:* fracture; *VNQF:* quartz vein - fracture; *SHZ:* shear zone; *EOH:* end of hole; *HW:* hanging wall; *FW:* foot wall. Chromitite layers are highlighted in grey.

from	to	thickness	lithology	unit	remarks	sample name	sample depth (m)		thickness	remarks
(m)	(m)	(m)					from	to		
110.06	**125.84**	15.78	**NO**		pyroxenitic towards bottom	JKL22	119.71	119.87	0.16	
125.84	**126.24**	0.4	**PX**			JKL21	126.08	126.24	0.16	HW MG4C
126.24	**126.65**	0.85	**CHR**	MG4C	pyroxenite band at 126.65 - 126.79 m	HEX10/01	126.24	126.41	0.17	
						HEX10/02	126.41	126.58	0.17	
						HEX10/03	126.58	126.65	0.07	
126.65	126.79					---			*0.14*	pyroxenite band at 126.65 - 126.79 m
126.79	**127.09**			MG4B		HEX10/04	126.79	126.92	0.13	
						HEX10/05	126.92	127.09	0.17	
127.09	**129.81**	2.72	**PX**		with disseminated chromitite	JKL27	127.30	127.45	0.15	
						JKL28	127.45	127.60	0.15	
						JKL29	127.60	127.75	0.15	
						JKL30	127.75	127.90	0.15	
						JKL31	127.90	128.05	0.15	
						JKL32	128.05	128.20	0.15	
						JKL33	128.20	128.35	0.15	
						JKL34	128.35	128.50	0.15	
						JKL35	128.50	128.65	0.15	
						JKL36	128.65	128.80	0.15	
						JKL37	128.80	128.95	0.15	
						JKL38	128.95	129.10	0.15	
						JKL39	129.10	129.25	0.15	
						JKL40	129.25	129.40	0.15	
						JKL41	129.40	129.55	0.15	
						JKL42	129.55	129.70	0.15	
						JKL19=JKL20	129.70	129.81	0.11	HW MG4A

Cont.

129.81	**131.95**	2.14	**CHR**	MG4A		HEX10/06	129.81	129.95	0.14	
						HEX10/07	129.95	130.09	0.14	
						HEX10/08	130.09	130.23	0.14	
						HEX10/09	130.23	130.37	0.14	
						HEX10/10	130.37	130.51	0.14	
						HEX10/11	130.51	130.65	0.14	
						HEX10/12	130.65	130.79	0.14	
						HEX10/13	130.79	130.93	0.14	
						HEX10/14	130.93	131.07	0.14	
						HEX10/15	131.07	131.21	0.14	
						HEX10/16	131.21	131.35	0.14	
						HEX10/17	131.35	131.49	0.14	
						HEX10/18	131.49	131.63	0.14	
						HEX10/19	131.63	131.77	0.14	
						HEX10/20	131.77	131.91	0.14	
131.95	**143.21**	11.26	**NO**			JKL18	131.91	132.03	0.12	FW MG4A
						JKL17	136.89	136.97	0.08	
						JKL16	137.81	137.99	0.18	
						JKL15	141.53	141.66	0.13	
143.21	**143.48**	0.27	**LENO**			---	143.21	143.48	*0.27*	
143.48	**143.54**	0.06	**CHR**			---	143.48	143.54	*0.06*	
143.54	143.68	0.14	LENO		chromitite band at 143.48 - 143.54 m	JKL14	143.52	143.68	0.16	HW MG3; mottled an (?)
143.68	**144.67**	0.99	**CHR**	MG3	pyroxenite band at 144.08 - 144.15 m	HEX10/21	143.68	143.82	0.14	
						HEX10/22	143.82	143.96	0.14	
						JKL26	---	---	---	pyroxenite band at 144.08 - 144.15 m
						HEX10/23	143.96	144.10	0.14	
						HEX10/24	144.10	144.24	0.14	
						HEX10/25	144.24	144.38	0.14	
						HEX10/26	144.38	144.52	0.14	
						HEX10/27	144.52	144.66	0.14	
144.67	**147.49**	2.82	**ANMO**		disseminated chromitite	JKL13	144.66	144.82	0.16	FW MG3
						JKL12	147.30	147.49	0.19	HW MG2C
147.49	**148.1**	0.61	**CHR**	MG2C		HEX10/28	147.49	147.64	0.15	
						HEX10/29	147.64	147.79	0.15	
						HEX10/30	147.79	147.94	0.15	
						HEX10/31	147.94	148.09	0.15	
148.1	**148.18**	0.08	**PX**			JKL25	148.10	148.18	0.08	

Cont.

148.18	**148.89**	0.71	**CHR**	MG2B		HEX10/32	148.18	148.30	0.12	
						HEX10/33	148.30	148.42	0.12	
						HEX10/34	148.42	148.54	0.12	
						HEX10/35	148.54	148.66	0.12	
						HEX10/36	148.66	148.78	0.12	
						HEX10/37	148.78	148.9	0.12	
148.89	**149.33**	0.44	**PX**			JKL11	148.89	149.00	0.11	FW MG2B
						JKL24	149.08	149.16	0.08	
						JKL23	149.16	149.24	0.08	
						JKL10	149.24	149.33	0.09	HW MG2A
149.33	**149.67**	0.34	**CHR**	MG2A		HEX10/38	149.33	149.48	0.15	
						HEX10/39	149.48	149.63	0.15	
						HEX10/40	149.63	149.78	0.15	
149.67	150.66	0.99	PX			JKL9	149.78	149.90	0.12	FW MG2A
150.66	150.86	0.2	VNQF			---	---	---	---	
150.86	151.39	0.53	PX			JKL8	151.01	151.25	0.24	
151.39	151.46	0.07	CHRDISS	MG1L2		---	---	---		
151.46	151.97	0.51	PX			---	---	---	0	
151.97	152.12	0.15	FR			---	---	---	0	
152.12	152.87	0.75	PX			---	---	---	0	
152.87	153.1	0.23	VNQF			JKL7	153.05	153.16	0.11	
153.1	154.28	1.18	PX		disseminated chromitite band at 151.39 - 154.28 m					
154.28	154.38	0.1	CHR	MG1L1	disseminated	JKL6	154.25	154.33	0.08	
154.38	154.51	0.13	PX			---	---	---	---	
154.51	**155.92**	1.41	**CHR**	MG1		HEX10/41	154.51	154.67	0.16	
						HEX10/42	154.67	154.83	0.16	
						HEX10/43	154.83	154.99	0.16	
						HEX10/44	154.99	155.15	0.16	
						HEX10/45	155.15	155.31	0.16	
						HEX10/46	155.31	155.47	0.16	
						HEX10/47	155.47	155.63	0.16	
						HEX10/48	155.63	155.79	0.16	
						HEX10/49	155.79	155.95	0.16	

Cont.

155.92	156.04	0.12	PX		with chromitite band at 156.04 m	---				
156.04	156.52	0.48	PX			JKL5	155.95	156.13	0.18	"FW MG1"
156.52	156.58	0.06	CHR			---	---	---	---	
156.58	156.82	0.24	PX			---	---	---	---	
156.82	156.9	0.08	CHR			---	---	---	---	
156.9	157.01	0.11	PX			---	---	---	---	
157.01	157.04	0.03	CHR			---	---	---	---	
157.04	157.71	0.67	PX			JKL4	157.48	157.57	0.09	HW MG0
157.71	**157.98**	0.27	**CHR**	MG0	alternating chromitite and pyroxenite bands	HEX10/50	157.71	157.85	0.135	
						HEX10/51	157.85	157.98	0.135	
157.98	158.07	0.09	PX			JKL3	157.93	158.13	0.2	FW MG0
158.07	158.12	0.05	CHR							
158.12	158.85	0.73	PX			---	---		0	
158.85	158.9	0.05	SHZ			---	---		0	
158.9	160	1.1	PX		**EOH**	JKL2	159.64	159.97	0.33	

Table A-2 Analytical methods applied on samples from the chromitite layers.

layer	sample	XRF	ICP-MS	S determ.	XRD	SEM-EDX	LA-ICP-MS	MLA
MG4C	HEX10/01	x	x	-	-	x	x	-
	HEX10/02	x	x	x	-	-	-	x
	HEX10/03	x	x	-	-	x	-	-
MG4B	HEX10/04	x	x	x	-	-	-	-
	HEX10/05	x	x	-	-	-	x	-
MG4A	HEX10/06	x	x	-	-	-	x	-
	HEX10/07	x	x	-	-	-	-	-
	HEX10/08	x	x	x	x	-	-	x
	HEX10/09	x	x	-	-	-	-	-
	HEX10/10	x	x	-	-	-	-	-
	HEX10/11	x	x	-	-	x	x	-
	HEX10/12	x	x	-	x	-	-	-
	HEX10/13	x	x	-	-	-	-	-
	HEX10/14	x	x	x	-	-	-	-
	HEX10/15	x	x	x	x	-	-	x
	HEX10/16	x	x	-	-	-	-	-
	HEX10/17	x	x	-	-	x	-	-
	HEX10/18	x	x	-	-	-	-	-
	HEX10/19	x	x	x	-	-	-	-
	HEX10/20	x	x	-	-	-	-	-
MG3	HEX10/21	x	x	x	x	-	-	x
	HEX10/22	x	x	x	-	x	-	-
	HEX10/23	x	x	-	-	x	x	-
	HEX10/24	x	x	-	-	-	-	-
	HEX10/25	x	x	-	-	-	-	-
	HEX10/26	x	x	-	-	-	-	-
	HEX10/27	x	x	x	x	-	-	x
MG2C	HEX10/28	x	x	-	-	x	x	-
	HEX10/29	x	x	-	-	-	-	-
	HEX10/30	x	x	x	x	-	-	x
	HEX10/31	x	x	x	x	-	-	x
MG2B	HEX10/32	x	x	x	x	-	-	x
	HEX10/33	x	x	-	-	-	-	-
	HEX10/34	x	x	-	-	x	-	-
	HEX10/35	x	x	-	x	-	-	-
	HEX10/36	x	x	x	-	-	-	-
	HEX10/37	x	x	-	-	x	x	-
MG2A	HEX10/38	x	x	x	x	x	x	x
	HEX10/39	x	x	x	-	-	-	-
	HEX10/40	x	x	-	-	x	-	-
MG1	HEX10/41	x	x	x	x	-	-	x
	HEX10/42	x	x	-	-	-	-	-
	HEX10/43	x	x	x	-	x	x	-
	HEX10/44	x	x	-	-	-	-	-
	HEX10/45	x	x	-	-	-	-	-
	HEX10/46	x	x	-	x	x	-	-
	HEX10/47	x	x	-	-	-	-	-
	HEX10/48	x	x	-	-	-	-	-
	HEX10/49	x	x	x	-	-	-	-
MG0	HEX10/50	x	x	-	x	-	x	-
	HEX10/51	x	x	x	-	-	-	-

Table A-3 Analytical methods applied on samples from the silicate layers. *Px*: pyroxenite; *an:* anorthosite; *leno*: leuconorite; *no*: norite; *px_no*: pyroxenitic norite.

unit	sample	lithology	point count	XRF	ICP-MS	S determ.	SEM-EDX	EMP
MG4C	JKL22	px_no	x	x	-	-	-	-
	JKL21	px	x	x	x	x	-	-
MG4A	JKL27	px	-	x	x	x	-	-
	JKL28	px	-	x	-	-	-	-
	JKL29	px	-	x	-	-	-	-
	JKL30	px	x	x	-	-	x	-
	JKL31	px	-	x	x	x	-	-
	JLK32	px	-	x	-	-	-	-
	JKL33	px	-	x	-	-	-	-
	JKL34	px	x	x	-	-	x	x
	JKL35	px	-	x	x	x	-	-
	JKL36	px	-	x	-	-	-	-
	JKL37	px	-	x	-	-	-	-
	JKL38	px	x	x	-	-	x	-
	JKL39	px	-	x	x	x	-	-
	JKL40	px	-	x	-	-	-	-
	JKL41	px	-	x	-	-	-	-
	JKL42	px	x	x	-	-	x	x
	JKL19/20	px	x	x	x	x	x	-
MG3 inter	JKL26	px	-	x	x	x	-	-
MG3	JKL18	no	-	x	-	-	x	x
	JKL17	no	x	x	-	-	-	-
	JKL16	no	x	x	-	-	-	-
	JKL15	no	x	x	x	x	-	-
	JKL14	leno	x	x	x	-	x	-
MG2C	JKL13	an		x	x	-	x	x
	JKL12	an	x	x	x	x	x	-
MG2B	JKL25	px	-	x	x	x	-	-
MG2A	JKL11	px	-	x	x	-	-	-
	JKL24	px	-	x	x	x	-	-
	JKL23	px	-	x	x	x	-	-
	JKL10	px	-	x	x	-	x	x
MG1	JKL9	px	x	x	x	-	x	x
	JKL8	px	x	x	x	x	x	-
	JKL7	px	x	x	-	-	-	-
	JKL6	px	x	x	-	-	-	-
MG0	JKL5	px	x	x	x	x	x	-
	JKL4	px	x	x	x	x	x	-

Table A-4 Standards used for XRF analyses of the silicate samples. References in Geostandard Newsletters, Vol. 18, 1994 (Special issue).

standard	rock type	major element oxides	trace elements
AC-E	Granite	x	x
AGV-1	Andesite	x	-
AL-1	Albite	x	-
ASK-1	Larvikite	x	x
ASK-2	Schist	x	x
ASK-3	Sulphide Ore	-	x
BCR-1	Basalt	x	-
BE-N	Basalt	x	x
BHVO-1	Basalt	x	x
BR	Basalt	x	x
BX-N	Bauxite	x	-
DR-N	Diorite	x	-
DT-N	Disthene	x	x
DTS-1	Dunite	x	-
FK-N	K-Feldspar	x	x
G-1	Granite	x	-
G-2	Granite	x	-
GA	Granite	x	x
GH	Granite	x	x
GL-O	Glauconite	x	-
GR	Granite	x	-
GS-N	Granite	x	x
GSP-1	Granodiorite	x	x
IF-G	Iron Formation Sample	x	-
JA-1	Andesite	x	x
JA-2	Andesite	x	x
JA-3	Andesite	x	-
JB-1	Basalt	x	x
JB-1a	Basalt	x	x
JB-2	Basalt	x	-
JB-3	Basalt	x	x
JCH-1	Chert	x	-
JDO-1	Dolomite	x	-
JF-1	Feldspar	x	-
JF-2	Feldspar	x	-
JG-1	Granodiorite	x	x
JG-1a	Granodiorite	x	-
JG-2	Granite	x	x
JG-3	Granodiorite	x	x
JGB-1	Gabbro	x	-
JGB-2	Gabbro	x	-
JH-1	Hornblendite	x	-
JLK-1	Lake Sediment	x	-
JLS-1	Limestone	x	-
JP-1	Peridotite	x	x
JR-1	Rhyolite	x	-
JR-2	Rhyolite	x	x
JR-3	Rhyolite	x	-
JS1-1	Slate	x	-
JS1-2	Slate	x	-

JSD-1	Stream Sediment	x	-
JSD-2	Stream Sediment	x	-
MAG-1	Marine Mud	x	-
MA-N	Granite	x	x
Mica Fe	Biotite	x	x
Mica Mg	Phlogopite	x	x
NIM-D	Dunite	x	-
NIM-G	Granite	x	x
NIM-L	Lujavrite	x	x
NIM-N	Norite	x	x
NIM-P	Pyroxenite	x	x
NIM-S	Syenite	x	x
PCC-I	Peridotite	x	-
SARM-39	Kimberlite	x	x
SARM-40	Carnonatite	x	-
SARM-41	Carbonaceous Shale	x	-
SARM-42	Soil	x	-
SARM-43	Magnesite	x	-
SARM-44	Sillimanite Schist	x	-
SARM-45	Kinzingiet	x	-
SARM-46	Stream Sediment	x	x
SARM-47	Serpentinite	x	-
SARM-48	Granite	x	x
SARM-49	Quartz	x	-
SARM-50	Dolerite	x	-
SARM-51	Stream Sediment	x	x
SARM-52	Stream Sediment	x	-
SY-2	Syenite	x	x
SY-3	Syenite	x	x
UB-N	Serpentinite	x	-
VS-N	Glass Standard	-	x

Table A-5 Standards used for microprobe analyses of silicate minerals. Analyzing crystals have been: TAP, PET and LIF.

standard	elements analysed	composition
albite	Na, Al, O	O : 48.76%, Na : 8.71%, Al : 10.32%, Si : 32.1%, K : 0.11%
diopside	Mg, Si, Ca	O : 44.33%, Mg : 11.22%, Si : 25.94%, Ca : 18.51%
orthoclase	K	O: 46.47%, Na : 1.01%, Al : 9.81%, Si : 30.4%, K : 12.18%, Ba : 0.13%
rutile	Ti	Ti : 59.95%, O : 40.05%
Cr_2O_3	Cr	Cr : 68.4195%, O : 31.5805%
rhodonite	Mn	O : 37.72%, Mg : 0.98%, Si : 21.63%, Ca : 5.2%, Mn : 33.68%, Fe : 0.79%
hematite	Fe	Fe : 69.9426%, O : 30.0574%

Table A-6 Standards used for analyses of PGE contents for chromitite layers (Xstrata) and the silicate layers (Cardiff University).

standard	Xstrata	Cardiff
SARM-7	x	-
SARM-65	x	-
HGMN.1	x	-
WPR1	-	x
WITS1	-	x

Table B-1 Results of Point Count analyses of the silicate samples. * 'Alteration' are termed areas in the thin sections that are highly altered and where no mineral could be distinguished. Most likely these areas are made up of clay minerals, which can't be determined with the optical microscope. *Opx:* orthopyroxene; *plag:* plagioclase; *chr:* chromite; *cpx:* clinopyroxene; *qtz:* quartz; *hem:* hematite.

cyclic unit	sample	opx	plag	chr	cpx	mica	alteration*	qtz	hem	total	rock type BC nomenclature	rock type modal classification	rock type MG sequence
MG4C	JKL22A	41.33	52.44	0	5.33	0	0.89	0	0	100	norite	pyroxenitic norite	pyroxenitic norite
	JKL21	55.51	31.84	0	6.12	0.82	3.27	1.63	0.82	100	pyroxenite	gabbronorite	plagioclase-bearing pyroxenite
MG4A	JKL30	42.86	25.32	5.19	12.99	0	12.34	1.30	0	100		gabbronorite	
	JKL34	40.64	27.09	25.10	5.98	0	1.20	0	0	100		gabbronorite	
	JKL38	45.40	28.16	9.20	16.67	0	0.57	0	0	100	pyroxenites	gabbronorite	plagioclase-bearing pyroxenites
	JKL42x	31.90	23.30	34.41	7.89	0	1.43	1.08	0	100		gabbronorite	
	JKL20A	30.25	17.83	48.09	0.96	1.27	1.27	0.32	0	100		norite	
MG3	JKL17A	28.85	63.03	0	7.56	0	0	0.56	0	100	norite	norite	norite
	JKL16A	26.03	69.21	0	4.76	0	0	0	0	100	norite	norite	norite
	JKL15A	24.61	70.35	1.58	2.84	0.63	0	0	0	100	norite	norite	norite
	JKL14B	15.44	69.50	13.51	1.16	0.39	0	0	0	100	anorthosite	gabbronorite	leuconorite
MG2C	JKL12A	2.99	87.43	7.19	2.40	0	0	0	0	100	anorthosite	anorthosite	anorthosite
MG1	JKL9B	60.13	11.11	9.15	19.61	0	0	0	0	100	pyroxenite	gabbronorite	pyroxenite
	JKL8B	20.97	13.11	49.44	16.10	0.37	0	0	0	100		gabbronorite	
	JKL8A	39.77	24.43	0	35.80	0	0	0	0	100	pyroxenites	gabbronorite	pyroxenites
	JKL7A	48.04	19.61	9.80	18.14	2.94	1.47	0	0	100		gabbronorite	
	JKL6A	46.95	17.18	30.15	3.05	0	2.67	0	0	100		norite	
MG0	JKL5A	36.08	17.87	33.33	8.59	2.06	2.06	0	0	100			
	JKL4B	57.75	20.19	3.76	15.96	1.88	0.47	0	0	100	pyroxenites	gabbronorites	pyroxenites
	JKL4A	56.27	20.15	15.59	7.98	0	0	0	0	100			

Table B-2 CIPW norm calculation of the silicate rocks from XRF analyses.

cyclic unit	sample	rock type	quartz SiO_2 vol%	plagioclase $CaAl_2Si_2O_8$ vol%	orthoclase $KAlSi_3O_8$ vol%	corundum Al_2O_3 vol%	diopside $CaMgSi_2O_6$ vol%
MG4C	JKL22	px_no	2.87	62.92	0	0	2.02
	JLK21	px	1.96	24.4	0	0	3.95
MG4A	JKL27	px	1.61	4.76	0.47	0	5.84
	JKL28	px	3.09	6.55	0.62	0	5.13
	JKL29	px	4.12	12.66	0.86	0	8.47
	JKL30	px	1.55	21.67	0.15	0	2.25
	JKL31	px	1.71	24.98	0	0	2.25
	JKL32	px	0.2	23.18	0	0	3.77
	JKL33	px	0	24.33	0	0	0.72
	JKL34	px	0.15	24.65	0	0.03	0
	JKL35	px	0	25.46	0	0.44	0
	JKL36	px	1.38	23.96	0	0	1.99
	JKL37	px	1.29	20.87	0	0	6.47
	JKL38	px	2.25	25.43	0	0	2.73
	JKL39	px	3.23	20.62	0.31	0	7.17
	JKL40	px	2.47	22.39	0.31	0	3.85
	JKL41	px	0	27.06	0	0	2.81
	JKL42	px	0	26.12	0	1.39	0
	JKL20	px	1.99	8.46	0	0	6.22
MG3	JKL18	no	5.28	50.54	0.14	0.36	0
	JKL17	no	5.27	61.29	0.27	0.24	0
	JKL16	no	5.87	61.86	0.27	0.48	0
	JKL15	no	4.12	62.59	1.86	0.32	0
	JKL14	le_no	5.62	70.42	0.86	2.82	0
MG3 inter	JKL26	px	1.35	17.99	0.08	0	0.04
MG2C	JKL13	an	8.2	86.87	1.58	1.21	0
	JKL12	an	0	82.13	5.34	0.9	0
MG2B	JKL25	px	0	14.29	0	2.83	0
MG2A	JKL11	px	2.52	6.7	0.24	0	2.93
	JKL24	px	0.86	9.43	0	0	2.03
	JLK10	px	0	8.76	0	1.32	0
	JKL23	px	0	10.22	0	0.03	0
MG1	JKL9	px	0	12.78	0	0	2.52
	JKL8	px	0	12.52	0	0	0.36
	JKL7	px	2.09	16.3	0.08	0	2.7
	JKL6	px	0.52	21.36	0	0.28	0
MG0	JKL5	px	1.34	13.67	3.07	0.78	0
	JKL4	px	1.42	14.53	0.31	0	4.01

Table B-2 *(cont.)*

hypersthene	**llivine**	**rutile**	**ilmenite**	**magnetite**	**hematite**	**apatite**	**chromite**	**total**
$FeMg_2Si_2O_6$ vol%	$FeMg_2SiO_4$ vol%	TiO_2 vol%	$FeTiO_3$ vol%	Fe_3O_4 vol%	Fe_2O_3 vol%	$Ca_5(F,OH,Cl)(PO4)_3$ vol%	Cr_2O_3 vol%	vol%
30.97	0	0	0.13	1.08	0	0.02	0	100.01
67.95	0	0	0.24	1.04	0	0	0.46	100
83.46	0	0	0.45	1.32	0	0	2.09	100
80.9	0	0	0.4	1.31	0	0.02	1.97	99.99
69.69	0	0	0.42	1.24	0	0.02	2.52	100
70.55	0	0	0.34	1.17	0	0	2.32	100
66.88	0	0	0.32	1.13	0	0	2.73	100
64.22	0	0	0.5	1.26	0	0	6.87	100
64.3	0.75	0	0.54	1.31	0	0	8.06	100.01
62.77	0	0	0.6	1.37	0	0	10.44	100.01
55.24	2.66	0	0.71	1.43	0	0	14.06	100
65.08	0	0	0.44	1.2	0	0.03	5.93	100.01
65.76	0	0	0.4	1.18	0	0.02	4.01	100
65.84	0	0	0.32	1.11	0	0.02	2.29	99.99
65.03	0	0	0.38	1.1	0	0	2.18	100.02
66.73	0	0	0.4	1.16	0	0	2.7	100.01
61.72	1	0	0.48	1.21	0	0.03	5.7	100.01
56.34	0.9	0	0.65	1.39	0	0	13.21	100
77.21	0	0	0.49	1.34	0	0	4.28	99.99
42.14	0	0	0.14	1.14	0	0	0.27	100.01
31.8	0	0	0.13	0.91	0	0.02	0.08	100.01
30.28	0	0	0.13	0.88	0	0.02	0.21	100
29.74	0	0	0.11	0.87	0	0.02	0.37	100
9.94	0	0.08	0.17	0	0.8	0.02	9.26	99.99
71.75	0	0	0.29	1.13	0	0.26	7.09	99.98
1.75	0	0	0.11	0.19	0	0.04	0.05	100
8.18	1.42	0	0.13	0.36	0	0.02	1.51	99.99
60.37	0.81	0	0.55	1.48	0	0.15	19.53	100.01
83.51	0	0	0.26	1.13	0	0.02	2.69	100
81.75	0	0	0.27	1.19	0	0	4.48	100.01
67.3	3.22	0	0.45	1.51	0	0	17.44	100
77.5	1.51	0	0.35	1.32	0	0	9.07	100
74.93	1.71	0	0.23	1.18	0	0	6.64	99.99
75.39	3.64	0	0.37	1.37	0	0	6.35	100
75.02	0	0	0.26	1.12	0	0.07	2.37	100.01
67.67	0	0	0.31	1.16	0	0	8.7	100
63.45	0	0	0.35	1.22	0	0.03	16.1	100.01
74.98	0	0	0.31	1.1	0	0	3.34	100

Table B-3 Analyses of chromite in chromitite layers obtained with the SEM-EDX. FeO and Fe_2O_3 have been recalculated using a method described by Prof. Ulmer (cf. chapter 3.2.2.10).

layer	sample_analyses	SiO_2 wt%	TiO_2 wt%	Al_2O_3 wt%	Cr_2O_3 wt%	Fe_2O_3 wt%	FeO wt%	MgO wt%	Na_2O wt%	total wt%
MG4C	HEX10/01_01	0	1.7	12.9	44.6	9.9	23.7	8.1	0	101.0
	HEX10/01_02	0.7	1.6	13.1	43.6	10.8	23.4	8.0	0	101.1
	HEX10/01_03	0	1.4	13.8	43.5	10.9	22.9	8.6	0	101.1
	HEX10/01_04	0	1.5	14.0	43.4	10.5	23.3	8.3	0	101.1
	HEX10/01_10	0.7	1.3	13.6	43.4	10.7	23.0	8.3	0	101.1
	HEX10/01_11	0	1.7	14.1	44.3	8.6	24.1	7.9	0	100.9
	HEX10/01_12	0	1.3	14.7	44.0	9.4	23.1	8.4	0	100.9
	HEX10/01_13	0	1.2	14.0	43.2	10.6	23.3	8.0	0.8	101.1
	HEX10/01_16	0.6	1.6	14.3	43.2	9.6	23.4	8.3	0	101.0
MG4A	HEX10/11_01	0.7	0	17.4	44.8	7.8	21.1	9.1	0	100.8
	HEX10/11_02	0.6	1.0	17.3	44.0	6.7	22.0	9.0	0	100.7
	HEX10/11_05	0.8	1.0	18.4	42.1	7.7	21.0	9.8	0	100.8
	HEX10/11_05	0	0.9	19.1	43.1	6.8	20.8	10.0	0	100.7
	HEX10/11_07	0	0.9	18.8	44.5	4.9	22.3	9.1	0	100.5
	HEX10/11_08	0.9	0.7	18.7	43.5	6.9	20.8	9.2	0	100.7
	HEX10/11_10	0	0.9	18.1	44.1	6.6	21.4	9.6	0	100.7
	HEX10/11_11	0	1.0	19.0	42.8	7.0	20.8	10.1	0	100.7
	HEX19/23_08	1.0	1.1	16.1	45.4	6.8	20.8	9.6	0	100.7
	HEX19/23_10	1.0	0.9	15.8	45.3	7.2	21.4	9.1	0	100.7
	HEX19/23_11	0.8	1.2	16.1	45.8	6.1	21.4	9.3	0	100.6
	HEX19/23_13	0	1.3	17.1	44.0	7.4	21.5	9.5	0	100.7
	HEX19/23_15	0	0.9	16.7	43.4	9.0	21.7	9.2	0	100.9
MG2C	HEX10/28_01	0.9	0.9	16.9	44.8	6.5	21.7	9.1	0	100.7
	HEX10/28_04	1.0	0.9	17.2	44.2	6.8	21.0	9.5	0	100.7
	HEX10/28_06	1.1	1.1	16.9	44.8	5.8	21.7	9.2	0	100.6
	HEX10/28_08	0	1.2	17.7	43.4	6.6	21.4	9.6	0.8	100.7
	HEX10/28_09	0	0.9	17.4	45.0	6.5	21.3	9.5	0	100.7
	HEX10/28_10	1.1	0.8	17.7	44.6	5.6	21.7	9.1	0	100.6
	HEX10/28_11	1.1	0.9	16.9	45.2	5.9	21.5	9.1	0	100.6
	HEX10/28_12	0.9	1.1	17.0	44.4	6.3	21.7	9.2	0	100.6
MG2B	HEX10/37_02	0	1.2	17.1	44.3	5.6	20.5	10.8	0	99.5
	HEX10/37_05	0	1.3	17.6	45.2	7.8	20.3	10.3	0	102.5
	HEX10/37_08	0	1.1	16.1	45.4	6.1	20.6	10.2	0	99.4
	HEX10/37_09	0	0.7	17.5	45.9	7.0	20.7	9.9	0	101.7
	HEX10/37_10	0	0.8	17.3	44.9	6.6	20.6	9.9	0	100.1
	HEX10/37_11	0	0.8	17.7	44.4	7.4	20.3	9.9	0.7	101.1
MG2A	HEX10/38_01	0	1.2	16.3	45.0	7.7	20.6	10.0	0	100.8
	HEX10/38_03	0	1.2	15.6	45.7	6.9	21.2	9.3	0.7	100.7
	HEX10/38_05	0	1.1	15.6	46.5	7.0	20.7	9.8	0	100.7
	HEX10/38_06	0	1.3	16.2	45.3	7.0	21.2	9.7	0	100.7
	HEX10/38_07	0.7	1.0	16.1	45.4	7.2	20.4	9.9	0	100.7
	HEX10/38_08	0	1.2	16.0	45.6	7.3	20.6	10.0	0	100.7
	HEX10/38_09	0	0.8	16.9	45.5	7.5	19.8	10.3	0	100.7
	HEX10/38_10	0	0.9	16.4	44.4	8.3	20.0	10.1	0.8	100.8

Table B-3 *(cont.)*

MG1	HEX10/43_01	0.9	1.0	16.4	46.3	5.7	20.4	9.8	0	100.6
	HEX10/43_02	0.9	0.8	15.9	47.6	5.1	21.1	9.1	0	100.5
	HEX10/43_05	2.1	0.6	16.7	45.9	5.8	19.7	9.8	0	100.6
	HEX10/43_06	0	0.9	15.6	47.4	6.4	20.5	9.8	0	100.6
	HEX10/43_08	0	0	17.8	47.7	5.2	20.2	9.7	0	100.5
	HEX10/43_09	0.8	0.6	16.8	46.6	5.9	20.0	9.9	0	100.6
	HEX10/43_10	0.9	0.7	16.2	46.8	5.9	20.2	9.7	0	100.6
	HEX10/43_11	0.7	0.3	13.4	51.6	3.7	23.4	7.1	0	100.4

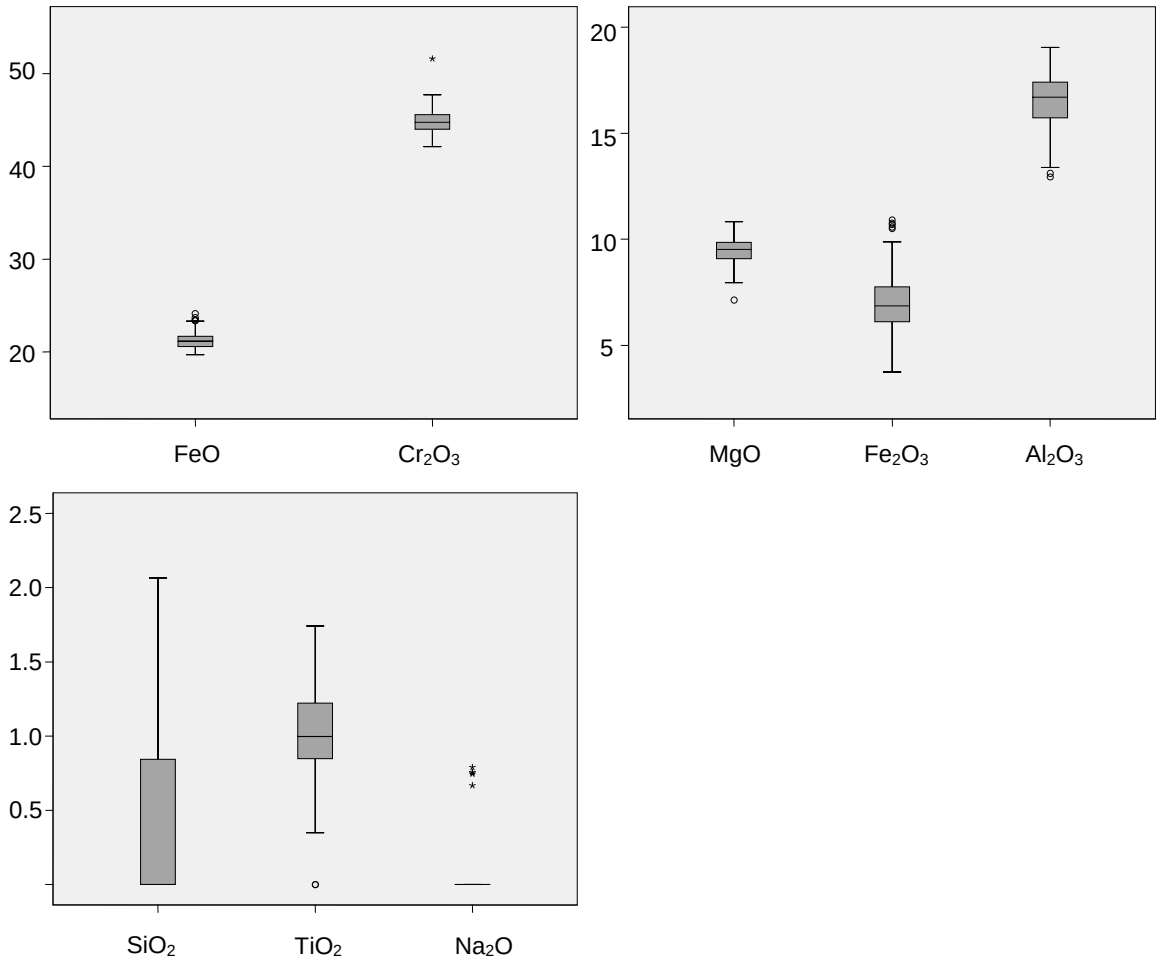

Figure B-1 Box plots of the major element oxides from chromite analyses in chromitite layers. All data sets are not normally distributed and contain outliers (°: moderate outlier; *: extreme outlier). N= 52. Data used are presented in table B-3.

Table B-4 Correlation matrix using the Spearman rank coefficient of correlation. N=7. Except TiO_2, the data for major element oxides of chromite grains derive from SEM-EDX analyses and are averages from the grain analyses of the chromitite layers MG1, MG2A, MG2B, MG2C, MG3, MG4A and MG4C. Data for TiO_2, V, Co, Ni, Zn and Ga derive from LA-ICP-MS analyses and are averages from grain analyses of the same chromitite layers. Significant correlations are bold.
* Correlation is significant at the 0.05 level; ** Correlation is significant at the 0.01 level.

		SiO_2	TiO_2	Al_2O_3	Cr_2O_3	Fe_2O_3	FeO	MgO	V	Co	Ni	Zn	Ga
SiO_2	Correlation Coefficient	1.000											
	Sig. (2-tailed)	.											
TiO_2	Correlation Coefficient	0.000	1.000										
	Sig. (2-tailed)	1.000	.										
Al_2O_3	Correlation Coefficient	-0.036	-0.286	1.000									
	Sig. (2-tailed)	0.939	0.535	.									
Cr_2O_3	Correlation Coefficient	0.071	-0.714	-0.250	1.000								
	Sig. (2-tailed)	0.879	0.071	0.589	.								
Fe_2O_3	Correlation Coefficient	-0.679	0.536	-0.536	-0.214	1.000							
	Sig. (2-tailed)	0.094	0.215	0.215	0.645	.							
FeO	Correlation Coefficient	0.393	**0.821***	-0.464	-0.607	0.286	1.000						
	Sig. (2-tailed)	0.383	0.023	0.294	0.148	0.535	.						
MgO	Correlation Coefficient	-0.500	-0.679	0.607	0.393	-0.214	**-0.964****	1.000					
	Sig. (2-tailed)	0.253	0.094	0.148	0.383	0.645	0.000	.					
V	Correlation Coefficient	0.107	0.571	-0.036	-0.714	0.321	0.714	-0.607	1.000				
	Sig. (2-tailed)	0.819	0.180	0.939	0.071	0.482	0.071	0.148	.				
Co	Correlation Coefficient	0.250	0.750	-0.214	**-0.821***	0.179	**0.857***	-0.750	0.643	1.000			
	Sig. (2-tailed)	0.589	0.052	0.645	0.023	0.702	0.014	0.052	0.119	.			
Ni	Correlation Coefficient	-0.250	0.714	0.071	-0.607	0.286	0.321	-0.143	0.000	0.500	1.000		
	Sig. (2-tailed)	0.589	0.071	0.879	0.148	0.535	0.482	0.760	1.000	0.253	.		
Zn	Correlation Coefficient	-0.036	0.250	-0.179	-0.321	0.429	0.429	-0.393	**0.857***	0.286	-0.393	1.000	
	Sig. (2-tailed)	0.939	0.589	0.702	0.482	0.337	0.337	0.383	0.014	0.535	0.383	.	
Ga	Correlation Coefficient	-0.464	0.107	0.714	-0.679	0.000	-0.143	0.357	0.250	0.214	0.429	0.000	1.000
	Sig. (2-tailed)	0.294	0.819	0.071	0.094	1.000	0.760	0.432	0.589	0.645	0.337	1.000	.

Table B-5 Analyses of chromite grains of the silicate layers obtained with the SEM-EDX. FeO and Fe_2O_3 have been recalculated with a method described by Prof. Ulmer (cf. subsection 3.2.2.10).

layer	sample_analyses	SiO_2 wt%	TiO_2 wt%	Al_2O_3 wt%	Cr_2O_3 wt%	Fe_2O_3 wt%	FeO wt%	MgO wt%	CaO wt%	Na_2O wt%	total wt%
MG4A_px	JKL30A_01	0.8	0.8	17.5	54.0	0	21.5	3.7	0	1.7	100
	JKL30A_02	0	1.2	14.7	57.3	0	22.4	4.4	0		100
	JKL30A_03	0	3.0	9.1	38.4	15.9	32.6	2.6	0	0	102
	JKL30A_04	0	1.1	19.3	53.3	0	22.9	3.5	0	0	100
	JKL34A_01	2.6	1.5	11.1	55.1	0	26.2	3.3	0	0.2	100
	JKL34A_02	0	2.6	30.1	4.8	29.5	28.6	7.4	0	0	103
	JKL34A_03	0	3.8	13.4	53.1	0	24.3	5.4	0	0	100
	JKL34A_04	1.3	1.1	14.7	54.7	0	24.6	3.1	0.6	0	100
	JKL34A_05	5.1	0	19.4	48.9	0	20.6	5.6	0.4	0	100
	JKL38A_01	0	0.7	18.5	55.0	0	22.0	3.8	0	0	100
	JKL38A_02	5.6	0	26.2	42.1	0	15.1	6.8	0.7	2.7	99
	JKL38A_03	2.6	0.9	23.5	48.3	0	16.2	5.7	0.8	2.0	100
	JKL38A_04	0	1.3	18.8	55.2	0	20.1	4.6	0	0	100
	JKL38A_05	0	0	31.6	45.0	0	13.6	9.8	0	0	100
	JKL42A_01	0	1.2	13.6	59.0	0	22.0	4.1	0	0	100
	JKL42A_02	1.4	0.9	15.2	57.6	0	19.5	4.1	0.4	1.0	100
	JKL42A_03	0	0.7	16.9	57.2	0	20.6	4.6	0	0	100
	JKL42A_04	0	0.9	13.3	59.7	0	21.7	4.4	0	0	100
	JKL42A_05	0	1.0	14.6	59.2	0	20.3	3.8	0	1.1	100
	JKL20A_01	0	1.1	41.5	7.3	18.9	20.6	12.6	0	0	102
	JKL20A_02	0	0.1	15.9	49.0	6.2	18.8	10.5	0	0	101
MG3_no	JKL18A_01	0	11.1	8.9	14.6	24.9	41.4	1.6	0	0	102
	JKL14A_01	3.9	0.7	20.9	27.6	14.4	25.5	5.6	0.8	2.0	101
	JKL14A_02	0	0.7	17.0	57.5	0	19.8	4.9	0	0	100
	JKL14A_03	0	0.7	18.6	57.2	0	18.0	5.6	0	0	100
	JKL14B_01	0	0.7	15.4	57.7	0	23.3	3.0	0	0	100
	JKL14B_02	0	1.0	16.2	56.5	0	20.4	4.6	0	1.3	100
	JKL14B_03		0.7	16.5	58.3	0	19.3	5.2	0	0	100
	JKL14B_04	1.8	0.6	16.6	42.8	6.5	26.5	5.3	0.5	0	101
	JKL14B_05	0.8	0.4	15.4	42.8	16.2	8.3	17.3	0.5	0	102
	JKL14B_06	0.9	0	17.1	58.3	0	18.6	5.0	0	0	100
MG3_leno	JKL14B_07	1.3	0.4	12.5	59.7	0	22.9	2.1	1.1	0	100
MG2C_an	JKL13A_01	0.4	1.3	8.5	47.0	9.9	31.4	1.4	0	0	100
	JKL13A_02	0.9	1.1	11.8	48.6	2.6	31.5	1.6	0	1.4	99
	JKL12A_01	0.6	0.8	13.3	56.1	0	26.5	2.6	0	0	100
MG2A_px	JKL10A_01	0.6	0.3	21.2	53.9	0	15.8	6.9	0	1.2	100
	JKL10A_02	5.7	0	19.7	8.4	38.7	20.5	7.7	0.6	1.4	103
	JKL10A_03	12.6	0	26.4	35.3	0	10.7	13.6	1.3	0	100
MG1_px	JKL9A_01	2.6	0.6	18.4	51.6	0	22.0	4.1	0.8	0	100
	JKL9A_02	0	0	16.2	55.5	0	22.8	4.1	0	1.4	100
	JKL9A_03	3.7	0	18.4	50.8	0	17.6	7.6	0	1.9	100
	JKL9A_04	0.5	1.3	19.4	52.5	0	19.5	5.2	0	1.6	100
	JKL9A_05	0	0	16.4	34.6	17.4	26.7	5.1	0	1.6	102
	JKL9A_06	3.0	0.5	16.8	51.7	0	22.4	4.6	0.9	0	100
	JKL9A_07	13.5	0	15.9	40.2	1.4	16.5	7.4	4.0	0	99
	JKL8B_01	0.6	0.7	19.1	54.6	0	20.2	4.8	0	0	100
	JKL8B_02	2.2	0.3	22.7	47.5	0	20.5	6.8	0	0	100
MG0_px	JKL5A_01	0.7	0.8	19.4	56.4	0	16.9	5.9	0	0	100
	JKL4A_01	0	0	13.5	21.9	35.8	27.9	4.5	0	0	104
	JKL4A_02	0	0.9	13.8	43.9	9.4	28.5	4.4	0	0	101

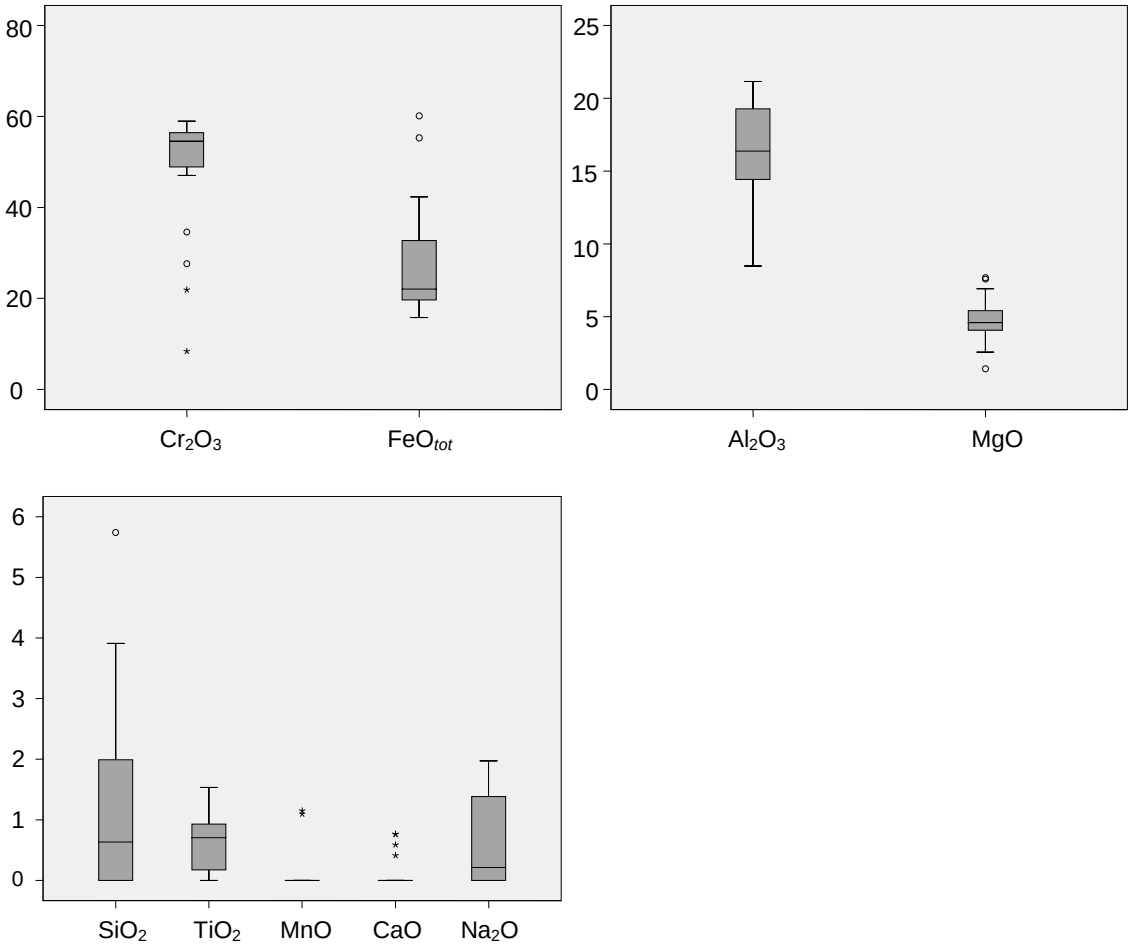

Figure B-2 Box plots of the major element oxides from chromite analyses in silicate layers. All data sets are not normally distributed and contain outliers (°: moderate outlier; *: extreme outlier). N= 50. Data used are presented in table B-5.

Table B-6 Correlation matrix using the Spearman rank coefficient of correlation. N=19. The data for major element oxides of chromite grains derive from SEM-EDX analyses given in table B-5. Significant correlations are bold. * Correlation is significant at the 0.05 level; ** Correlation is significant at the 0.01 level.

		SiO_2	TiO_2	Al_2O_3	Cr_2O_3	FeO_{tot}	MnO	MgO	CaO	Na_2O
SiO_2	Correlation Coefficient	1.000								
	Sig. (2-tailed)	.								
TiO_2	Correlation Coefficient	-0.025	1.000							
	Sig. (2-tailed)	0.918	.							
Al_2O_3	Correlation Coefficient	0.381	-0.412	1.000						
	Sig. (2-tailed)	0.107	0.079	.						
Cr_2O_3	Correlation Coefficient	-0.383	**0.467***	-0.311	1.000					
	Sig. (2-tailed)	0.105	0.044	0.196	.					
FeO_{tot}	Correlation Coefficient	-0.160	-0.223	-0.237	**-0.496***	1.000				
	Sig. (2-tailed)	0.513	0.359	0.329	0.031	.				
MnO	Correlation Coefficient	0.253	0.092	-0.231	-0.267	0.090	1.000			
	Sig. (2-tailed)	0.295	0.708	0.342	0.270	0.715	.			
MgO	Correlation Coefficient	0.309	**-0.458***	**0.854****	-0.395	-0.125	-0.207	1.000		
	Sig. (2-tailed)	0.197	0.048	0.000	0.094	0.611	0.395	.		
CaO	Correlation Coefficient	**0.626****	-0.184	0.327	-0.315	0.202	0.110	0.116	1.000	
	Sig. (2-tailed)	0.004	0.452	0.172	0.189	0.408	0.653	0.637	.	
Na_2O	Correlation Coefficient	0.293	-0.307	**0.469***	-0.417	0.093	-0.166	**0.545***	0.205	1.000
	Sig. (2-tailed)	0.224	0.201	0.043	0.075	0.706	0.496	0.016	0.399	.

Table B-7 Analyses of Ca-rich plagioclase from the chromitite layers obtained with SEM-EDX.

layer	sample_analyses	SiO_2 wt%	Al_2O_3 wt%	Cr_2O_3 wt%	FeO_{tot} wt%	MgO wt%	CaO wt%	Na_2O wt%	total wt%
MG4C	HEX10/03_2-3	44.3	38.0	0	0	0.7	15.4	1.7	100
	HEX10/03_2-4	39.3	32.5	0	5.5	0.8	21.9	0	100
MG4A	HEX10/17_2-5	51.7	32.1	0	0	0.7	10.7	4.8	100
MG3	HEX10/22_1-1	49.1	33.5	0	0	0.7	13.3	3.4	100
	HEX10/22_2-4	48.9	33.9	0	0	0.8	13.1	3.4	100
	HEX10/22_2-5	48.6	33.8	0	0	0.8	13.3	3.5	100
	HEX10/22_2-7	49.2	33.4	0	0	0.8	13.1	3.5	100
	HEX10/22_3-4	48.9	33.8	0	0	0.6	13.1	3.6	100
	HEX10/22_3-7	48.6	34.0	0	0	0.7	13.4	3.4	100
	HEX10/22_5-3	49.9	32.8	0	0	0.9	12.8	3.6	100
MG2B	HEX10/34_3-1	47.5	35.6	0.7	0	0.8	12.3	3.1	100
	HEX10/34_3-3	47.9	35.2	0	0	0.8	12.8	3.3	100
	HEX10/34_3-4	48.3	35.1	0	0	0.9	12.4	3.3	100
	HEX10/34_4-4	45.3	33.4	0	6.0	0.6	12.0	2.7	100
	HEX10/34_6-4	48.2	35.1	0	0	0.7	12.8	3.3	100
	HEX10/34_8-5	47.7	35.2	0	0	0.7	13.2	3.1	100
MG2A	HEX10/40_2-3	48.5	34.8	0	0	0	13.9	2.9	100
	HEX10/40_4-5	48.6	34.2	0	0	0.7	13.3	3.2	100
MG1	HEX10/46_1-3	49.1	34.2	0	0	0	13.3	3.4	100
	HEX10/46_1-4	49.9	33.7	0	0	0	12.9	3.5	100
	HEX10/46_1-6	50.0	32.9	0	0	0.9	12.4	3.8	100
	HEX10/46_2-5	49.6	33.1	0	0	1.2	12.4	3.7	100
	HEX10/46_5-2	47.1	32.4	0	4.9	0	11.9	3.8	100
	HEX10/46_7-2	46.9	31.9	0	5.1	0.6	12.0	3.6	100
	HEX10/46_7-3	49.9	33.2	0	0	0.7	12.4	3.8	100

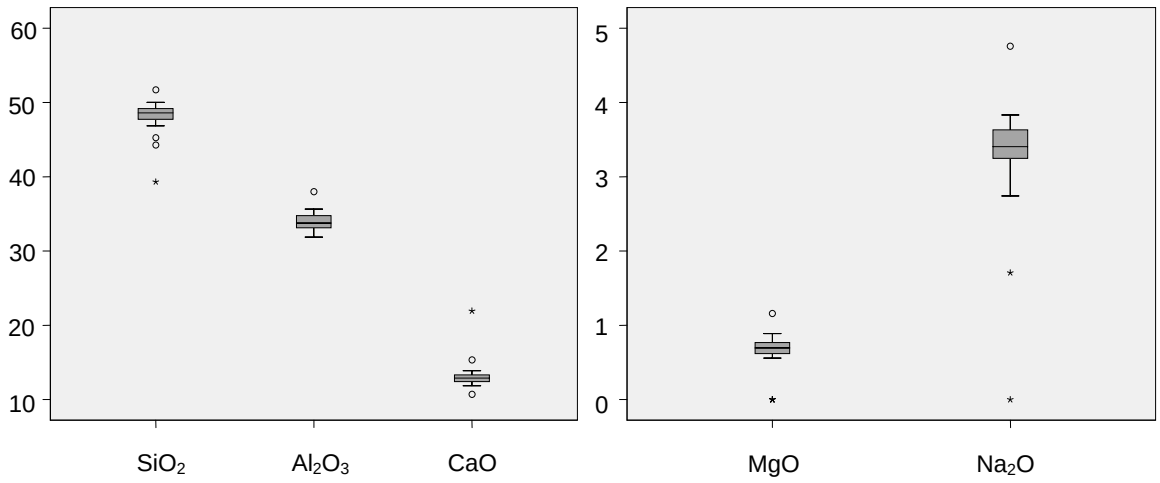

Figure B-3 Box plots of the major element oxides from analyses of Ca-rich plagioclase in chromitite layers. All data sets are not normally distributed and contain outliers (°: moderate outlier; *: extreme outlier). N= 25. Data used are presented in table B-7.

Table B-8 Correlation matrix using the Spearman rank coefficient of correlation. N=25. The data for major element oxides of Ca-rich plagioclase derive from SEM-EDX analyses presented in table B-7. Significant correlations are bold. ** Correlation is significant at the 0.01 level ; * Correlation is significant at the 0.05 level.

		SiO_2	Al_2O_3	Cr_2O_3	FeO_{tot}	MgO	CaO	Na_2O
SiO_2	Correlation Coefficient	1.000						
	Sig. (2-tailed)	.						
Al_2O_3	Correlation Coefficient	-0.317	1.000					
	Sig. (2-tailed)	0.123	.					
Cr_2O_3	Correlation Coefficient	-0.198	0.311	1.000				
	Sig. (2-tailed)	0.342	0.130	.				
FeO_{tot}	Correlation Coefficient	**-0.593****	**-0.514****	-0.089	1.000			
	Sig. (2-tailed)	0.002	0.009	0.673	.			
MgO	Correlation Coefficient	0.252	-0.099	0.113	-0.248	1.000		
	Sig. (2-tailed)	0.225	0.639	0.589	0.232	.		
CaO	Correlation Coefficient	-0.115	**0.400***	-0.226	-0.257	-0.141	1.000	
	Sig. (2-tailed)	0.583	0.048	0.276	0.216	0.500	.	
Na_2O	Correlation Coefficient	**0.695****	**-0.648****	-0.226	-0.137	0.117	**-0.498***	1.000
	Sig. (2-tailed)	0.000	0.000	0.276	0.513	0.577	0.011	.

Table B-9 Analyses of Na-rich plagioclase from the chromitite layers obtained with SEM-EDX. Those analyses from Na-rich plagioclases occurring in silicate melt inclusions are highlighted in grey.

layer	**sample_analyses**	**SiO_2** wt%	**Al_2O_3** wt%	**Cr_2O_3** wt%	**FeO_{tot}** wt%	**MgO** wt%	**CaO** wt%	**Na_2O** wt%	**SrO** wt%	**total** wt%
MG4A	HEX10/17_2-3	66.2	21.2	0	0	0	0.7	11.9	0	100
	HEX10/17_10A-2	66.5	21.9	0	0	0	0.5	11.1	0	100
MG3	HEX10/22_3-3	61.4	21.6	0	4.6	0	1.2	11.2	0	100
MG2B	HEX10/34_2-2	56.1	18.0	0	0	0.5	0.4	11.1	13.9	100
	HEX10/34_6-2	62.9	23.2	0	0	0.6	2.0	11.3	0	100
MG2A	HEX10/40_2-4	70.5	16.9	0	0	0	0	12.6	0	100
	HEX10/40_4-4	65.1	22.2	1.1	0	0	0	11.7	0	100
MG1	HEX10/46_5-3	63.1	23.5	0	0	0.6	2.7	10.0	0	100
	HEX10/46_7D-2	58.1	22.2	0	6.5	1.2	2.9	9.1	0	100
	HEX10/46_7D-3	56.9	22.5	0	6.6	2.2	2.5	9.2	0	100

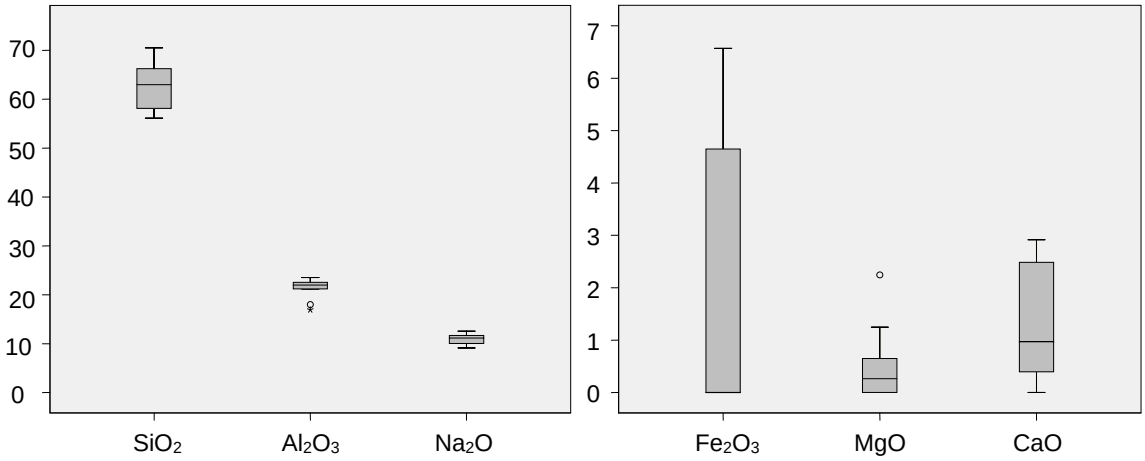

Figure B-4 Box plots of the major element oxides from analyses of Na-rich plagioclase in chromitite layers. The data sets are not normally distributed and contain outliers (°: moderate outlier; *: extreme outlier). N= 10. Data used are presented in table B-9.

Table B-10 Correlation matrix using the Spearman rank coefficient of correlation. N=10. The data for major element oxides of Na-rich plagioclase derive from SEM-EDX analyses presented in table B-9. Significant correlations are bold. * Correlation is significant at the 0.05 level.

		SiO_2	**Al_2O_3**	**Cr_2O_3**	**FeO_{tot}**	**MgO**	**CaO**	**Na_2O**	**SrO**
SiO_2	Correlation Coefficient	1.000							
	Sig. (2-tailed)	.							
Al_2O_3	Correlation Coefficient	-0.212	1.000						
	Sig. (2-tailed)	0.556	.						
Cr_2O_3	Correlation Coefficient	0.174	0.174	1.000					
	Sig. (2-tailed)	0.631	0.631	.					
FeO_{tot}	Correlation Coefficient	-0.589	0.172	-0.214	1.000				
	Sig. (2-tailed)	0.073	0.636	0.552	.				
MgO	Correlation Coefficient	**-0.692***	0.588	-0.309	0.549	1.000			
	Sig. (2-tailed)	0.027	0.074	0.384	0.100	.			
CaO	Correlation Coefficient	-0.474	0.626	-0.466	0.591	**0.759***	1.000		
	Sig. (2-tailed)	0.166	0.053	0.175	0.072	0.011	.		
Na_2O	Correlation Coefficient	**0.709***	-0.455	0.290	-0.619	**-0.756***	**-.0736***	1.000	
	Sig. (2-tailed)	0.022	0.187	0.416	0.056	0.011	0.015	.	
SrO	Correlation Coefficient	-0.522	-0.406	-0.111	-0.214	0.062	-0.291	-0.174	1.000
	Sig. (2-tailed)	0.122	0.244	0.760	0.552	0.865	0.415	0.631	.

Table B-11 Analyses of orthopyroxene in chromitite layers obtained with the SEM-EDX. Orthopyroxene analyses from silicate melt inclusions are highlighted in grey.

layer	sample_analyses	SiO_2 wt%	TiO_2 wt%	Al_2O_3 wt%	Cr_2O_3 wt%	FeO_{tot} wt%	MgO wt%	CaO wt%	Na_2O wt%	total wt%
MG4C	HEX10/03_3-1	55.5	0	1.3	0	6.8	36.4	0	0	100
	HEX10/03_4-6	62.2	0	1.2	0	5.7	30.9	0	0	100
MG4A	HEX10/17_3-1	55.1	0	2.0	0	6.3	35.9	0	0.8	100
	HEX10/17_3-3	49.4	0	3.1	4.4	6.5	35.9	0.0	0.7	100
	HEX10/17_6-1	53.5	0	2.1	1.4	5.4	36.6	0	1.0	100
	HEX10/17_10A-1	50.4	0	1.2	0.7	12.2	35.5	0	0	100
MG3	HEX10/22_1-3	54.5	0	1.8	1.4	6.4	35.9	0	0	100
	HEX10/22_2-1	54.8	0	1.6	0	8.0	34.8	0	0.8	100
	HEX10/22_2-2	58.9	0	3.5	0	3.9	32.5	0	1.1	100
	HEX10/22_4-3	55.7	0	0.9	0	6.2	37.2	0	0	100
MG2B	HEX10/34_3-5	55.2	0	1.0	0	4.9	38.0	0	0.9	100
	HEX10/34_5-1	53.3	0	2.1	0.8	7.5	35.6	0.7	0	100
	HEX10/34_5-2	50.4	0	4.1	0.8	14.0	28.6	1.2	1.0	100
	HEX10/34_5-3	55.3	0	1.9	0	6.7	36.1	0	0	100
	HEX10/34_5-5	48.6	4.9	7.1	1.9	4.5	28.9	4.1	0	100
	HEX10/34_6-3	55.9	0	0.9	0	4.9	38.2	0	0	100
	HEX10/34_7-1	55.9	0	1.1	0	5.2	37.2	0	0.6	100
MG2A	HEX10/40_1-2	62.4	0	1.9	0	3.2	31.4	0	1.166	100
	HEX10/40_1-5	63.4	0	1.7	0	0	34.9	0	0	100
	HEX10/40_3-1	55.3	0	1.0	0	5.0	37.9	0	0.8	100
	HEX10/40_5-2	51.8	0	2.0	0	13.2	30.4	1.5	1.1	100
	HEX10/40_5-4	55.3	0	1.7	0	4.8	37.3	0	0.9	100
	HEX10/40_11-1	54.6	0	1.6	1.0	5.4	36.7	0	0.8	100
MG1	HEX10/46_5-4	54.9	0	1.1	0	6.6	36.3	0.2	1.0	100
	HEX10/46_6A-1	53.5	1.1	4.1	2.1	3.8	28.5	5.0	1.9	100
	HEX10/46_6B-1	52.9	0	0.5	1.3	5.9	38.3	0	1.2	100

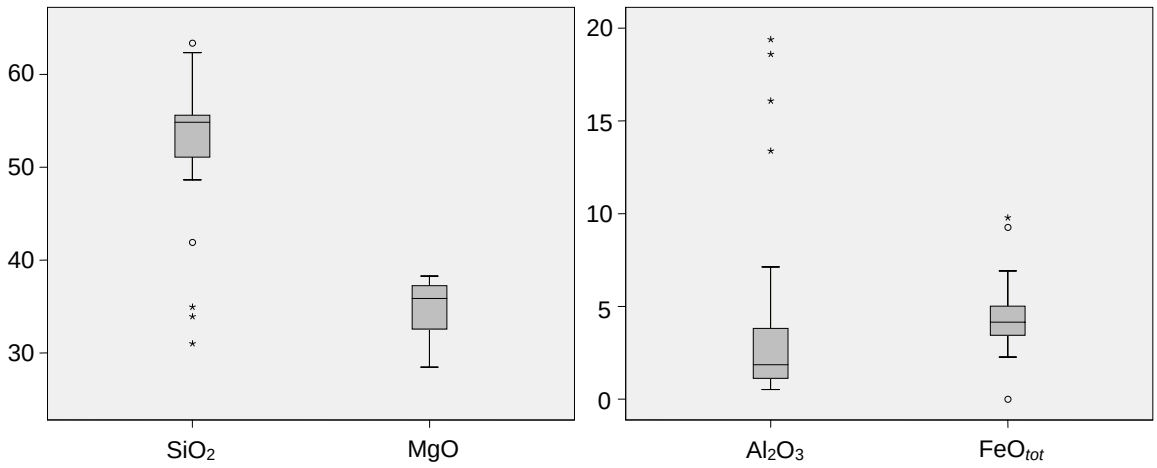

Figure B-5 Box plots of the major element oxides from orthopyroxene analyses in chromitite layers. All data sets are not normally distributed and contain outliers (°: moderate outlier; *: extreme outlier). N=28. Data used are presented in table B-11.

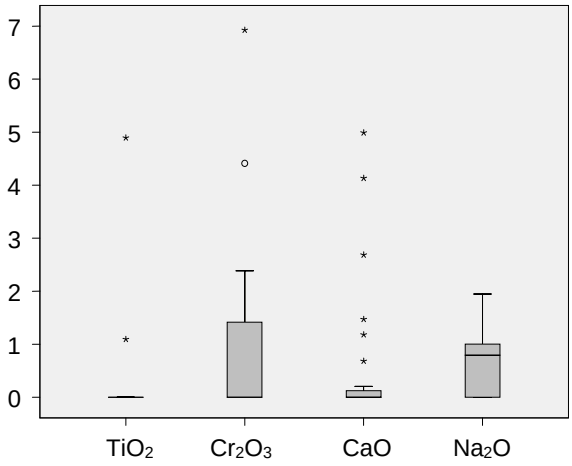

Figure B-5 *(cont.)* Box plots of the major element oxides from orthopyroxene analyses in chromitite layers.

Table B-12 Correlation matrix using the Spearman rank coefficient of correlation. N=26. The data for major element oxides of orthopyroxene grains derive from SEM-EDX analyses given in table B-11. Significant correlations are bold. ** Correlation is significant at the 0.01 level; * Correlation is significant at the 0.05 level.

		SiO_2	TiO_2	Al_2O_3	Cr_2O_3	FeO_{tot}	MgO	CaO	Na_2O
SiO_2	Correlation Coefficient	1.000							
	Sig. (2-tailed)	.							
TiO_2	Correlation Coefficient	-0.227	1.000						
	Sig. (2-tailed)	0.246	.						
Al_2O_3	Correlation Coefficient	**-0.657****	0.309	1.000					
	Sig. (2-tailed)	0.000	0.109	.					
Cr_2O_3	Correlation Coefficient	**-0.751****	0.368	**0.615****	1.000				
	Sig. (2-tailed)	0.000	0.054	0.000	.				
FeO_{tot}	Correlation Coefficient	**-0.570****	-0.359	0.233	0.180	1.000			
	Sig. (2-tailed)	0.002	0.061	0.234	0.359	.			
MgO	Correlation Coefficient	0.170	**-0.428***	**-0.576****	-0.181	-0.149	1.000		
	Sig. (2-tailed)	0.388	0.023	**0.001**	0.357	0.450	.		
CaO	Correlation Coefficient	**-0.523****	**0.559****	**0.428***	**0.488****	0.251	**-0.556****	1.000	
	Sig. (2-tailed)	0.004	0.002	0.023	0.009	0.197	0.002	.	
Na_2O	Correlation Coefficient	-0.204	0.055	0.186	0.081	-0.115	-0.129	0.165	1.000
	Sig. (2-tailed)	0.298	0.779	0.344	0.680	0.561	0.513	0.401	.

Table B-13 Analyses of plagioclase in silicate layers obtained with the EMP. *Px:* pyroxenite; *no:* norite; *an:* anorthosite.

cyclic unit	lithology	sample_analysis	SiO_2 wt%	TiO_2 wt%	Al_2O_3 wt%	Cr_2O_3 wt%	FeO wt%	MnO wt%	MgO wt%	CaO wt%	Na_2O wt%	K_2O wt%	total wt%
MG4A	px	JKL42A_1	51.96	0.03	30.19	0	0.19	0.01	0.05	13.49	3.77	0.31	100.02
		JKL42A_4	51.41	0.03	30.40	0	0.30	0	0.02	13.67	3.84	0.34	100.00
		JKL42A_8	53.44	0.03	30.35	0	0.12	0	0.03	11.08	4.62	0.39	100.06
MG3	no	JKL18A_5	48.84	0.02	32.25	0	0.19	0.03	0.02	15.95	2.52	0.17	99.99
MG2C	an	JKL13A_2	49.50	0.07	31.86	0	0.33	0.03	0.03	15.39	2.64	0.16	100.01
		JKL13A_3	48.78	0.03	32.61	0.01	0.31	0	0.02	15.73	2.37	0.13	99.99
		JKL13A_4	49.44	0.02	31.99	0.01	0.28	0	0.02	15.53	2.60	0.13	100.02
		JKL13A_5	49.76	0.05	32.61	0.03	0.24	0	0.02	14.64	2.49	0.14	99.99
MG1	px	JKL9A_4	48.20	0	32.29	0.01	0.40	0	0.23	16.41	2.45	0.06	100.06
		JKL9A_8	48.73	0.03	32.08	0	0.19	0.01	0.03	16.17	2.62	0.14	100.02

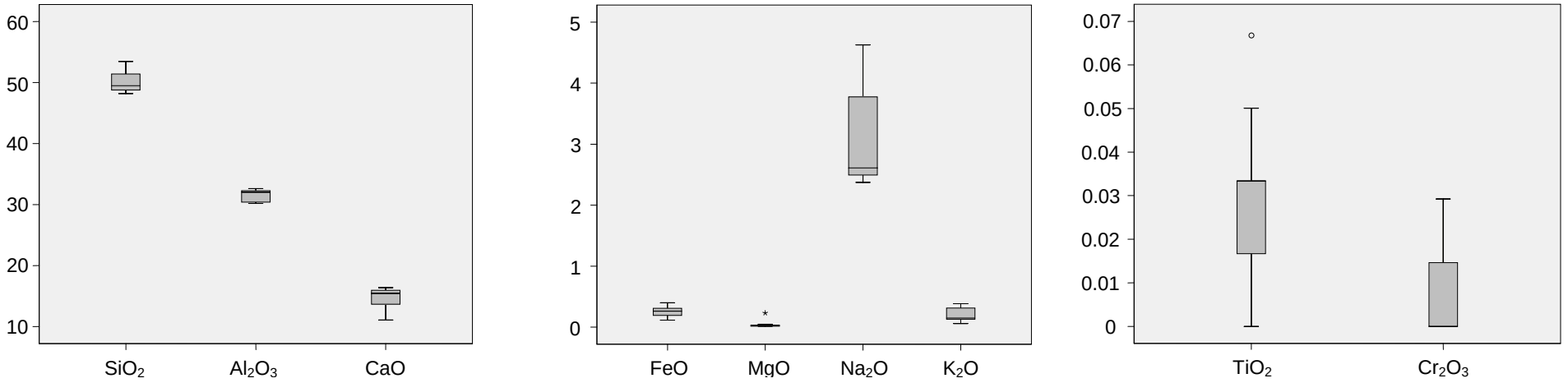

Figure B-6 Boxplots of the major element oxides from plagioclase analyses in silicate layers. All data sets are not normally distributed and contain outliers (°: moderate outlier; *: extreme outlier). N= 10. Data used are presented in table B-13.

Table B-14 Correlation matrix using the Spearman rank coefficient of correlation. N=10. The data for major element oxides of plagioclase grains derive from EMP analyses given in table B-13. Significant correlations are bold. * Correlation is significant at the 0.05 level; ** Correlation is significant at the 0.01 level.

		SiO_2	TiO_2	Al_2O_3	Cr_2O_3	FeO	MnO	MgO	CaO	Na_2O	K_2O
SiO_2	Correlation Coefficient	1.000									
	Sig. (2-tailed)	.									
TiO_2	Correlation Coefficient	0.467	1.000								
	Sig. (2-tailed)	0.173	.								
Al_2O_3	Correlation Coefficient	**-0.699***	-0.130	1.000							
	Sig. (2-tailed)	0.024	0.720	.							
Cr_2O_3	Correlation Coefficient	-0.333	-0.130	**0.737***	1.000						
	Sig. (2-tailed)	0.347	0.721	0.015	.						
FeO	Correlation Coefficient	-0.472	-0.039	0.394	0.428	1.000					
	Sig. (2-tailed)	0.168	0.914	0.260	0.217	.					
MnO	Correlation Coefficient	-0.083	0.192	-0.221	-0.630	-0.195	1.000				
	Sig. (2-tailed)	0.821	0.596	0.540	0.051	0.589	.				
MgO	Correlation Coefficient	-0.059	-0.091	-0.362	-0.278	0.033	0.208	1.000			
	Sig. (2-tailed)	0.871	0.802	0.304	0.437	0.927	0.563	.			
CaO	Correlation Coefficient	**-0.988****	-0.513	**0.669***	0.270	0.411	0.165	0.059	1.000		
	Sig. (2-tailed)	0.000	0.130	0.035	0.450	0.238	0.648	0.871	.		
Na_2O	Correlation Coefficient	**0.758***	0.298	**-0.930****	**-0.756***	-0.485	0.165	0.216	**-0.721***	1.000	
	Sig. (2-tailed)	0.011	0.402	0.000	0.011	0.156	0.648	0.548	0.019	.	
K_2O	Correlation Coefficient	**0.817****	0.349	**-0.740***	**-0.750***	-0.611	0.249	-0.007	**-0.762***	**0.854****	1.000
	Sig. (2-tailed)	0.004	0.323	0.014	0.01	0.061	0.487	0.986	0.010	0.002	.

Table B-15 Analyses of orthopyroxene in silicate layers obtained with the EMP. *Px:* pyroxenite; *no:* norite; *an:* anorthosite.

cyclic unit	lithology	sample_analyses	SiO_2 wt%	TiO_2 wt%	Al_2O_3 wt%	Cr_2O_3 wt%	FeO wt%	MnO wt%	MgO wt%	CaO wt%	Na_2O wt%	K_2O wt%	total wt%
MG4A	px	JKL34A_1	55.49	0.08	1.25	0.47	10.02	0.31	30.65	1.62	0.05	0.01	99.96
		JKL34A_2	55.49	0.10	1.25	0.47	10.24	0.27	30.56	1.55	0.05	0.02	100.01
		JKL34A_3	55.58	0.10	1.28	0.44	10.58	0.30	30.61	1.02	0.04	0.04	99.98
		JKL34A_5	64.86	0.08	1.44	0.23	1.57	0.03	31.47	0.03	0.28	0.01	100.01
		JKL34A_6	55.37	0.13	1.34	0.44	10.30	0.25	30.02	2.01	0.12	0.02	100.00
		JKL34A_7	65.18	0.03	0.74	0.09	1.18	0.03	32.55	0.06	0.13	0.01	100.01
		JKL42A_2	54.79	0.17	1.00	0.34	10.47	0.21	32.20	0.80	0.01	0	99.99
		JKL42A_3	54.64	0.12	1.30	0.53	11.01	0.21	30.16	1.94	0.04	0.01	99.97
		JKL42A_5	54.87	0.13	1.10	0.44	11.35	0.22	31.09	0.76	0.01	0	99.97
		JKL42A_6	54.70	0.15	1.08	0.51	10.90	0.23	30.56	1.85	0.03	0.01	100.02
		JKL42A_7	56.65	0.15	1.11	0.32	8.43	0.17	32.50	0.66	0.01	0	100.00
		JKL42A_9	56.99	0.15	1.13	0.31	7.56	0.21	32.75	0.87	0.01	0.01	100.00
		JKL42A_10	57.12	0.13	1.17	0.35	7.68	0.26	32.05	1.19	0.04	0.01	100.01
		JKL42A_11	57.29	0.18	1.27	0.28	7.38	0.18	32.47	0.90	0.05	0	100.00
MG3	no	JKL18A_1	54.32	0.15	1.19	0.54	11.87	0.25	30.71	0.87	0.08	0.02	100.00
		JKL18A_2	54.77	0.18	1.08	0.44	11.41	0.18	30.61	1.15	0.13	0.02	99.98
		JKL18A_3	52.90	0.48	0.74	0.54	11.69	0.23	31.84	1.47	0.09	0.01	100.01
		JKL18A_4	54.89	0.15	1.17	0.47	10.86	0.15	30.84	1.29	0.11	0.05	99.98
		JKL18A_6	56.20	0.12	1.30	0.47	8.83	0.13	31.56	1.29	0.08	0.01	99.98
		JKL18A_7	55.28	0.12	1.47	0.45	8.43	0.17	32.62	1.34	0.07	0.04	99.98
		JKL18A_8	55.75	0.13	1.27	0.47	8.89	0.17	32.02	1.12	0.12	0.04	99.97

Table B-15 (cont.)

MG2A	px	JKL10A_1	55.81	0.07	1.34	0.37	9.12	0.28	31.77	1.20	0.03	0	100.00
		JKL10A_2	55.58	0.13	1.34	0.34	9.21	0.21	31.99	1.18	0.03	0	100.00
		JKL10A_3	55.22	0.10	1.38	0.42	9.47	0.15	32.05	0.99	0.16	0.05	100.00
		JKL10A_6	55.00	0.13	1.30	0.42	10.55	0.31	30.70	1.54	0.04	0	100.00
MG1	px	JKL9A_1	54.96	0.20	1.17	0.48	11.90	0.25	28.61	2.22	0.16	0.02	99.97
		JKL9A_2	54.38	0.17	1.11	0.38	12.17	0.26	30.20	1.30	0.01	0	99.98
		JKL9A_3	54.94	0.08	1.32	0.35	12.16	0.30	29.65	1.13	0.05	0.01	100.00
		JKL9A_5	54.21	0.15	1.23	0.53	11.60	0.31	28.54	3.32	0.11	0.01	100.00
		JKL9A_6	54.42	0.17	1.23	0.44	11.46	0.30	28.94	2.92	0.11	0.01	100.00
		JKL9A_7	55.17	0.20	1.28	0.41	12.05	0.28	29.70	0.64	0.15	0.07	99.97
		JKL9A_11	61.72	0.15	0.89	0.34	9.07	0.13	27.38	0.15	0.12	0.06	100.01

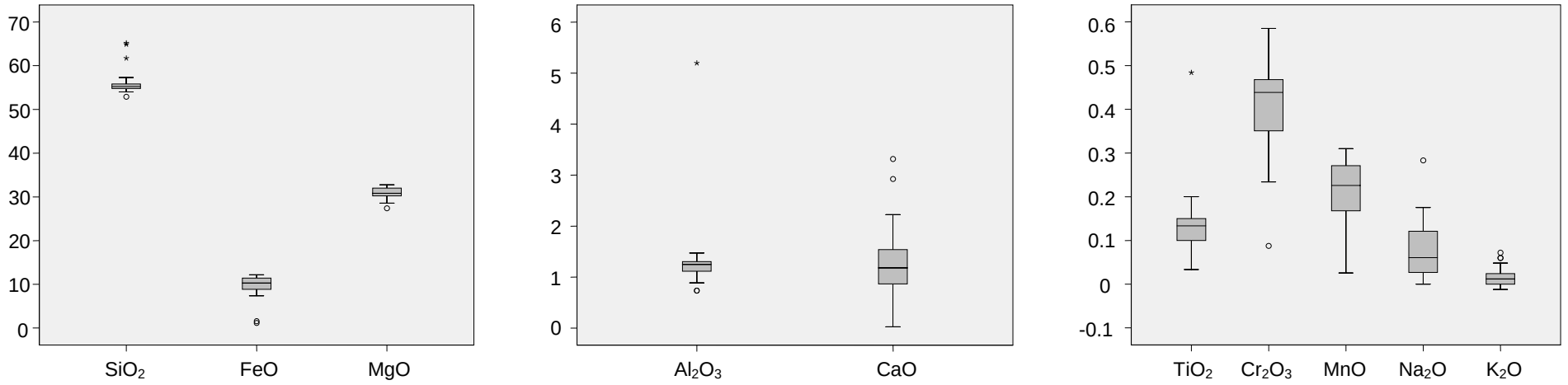

Figure B-7 Box plots of the major element oxides from orthopyroxene analyses in silicate layers. All data sets are not normally distributed and contain outliers (°: moderate outlier; *: extreme outlier). N= 34. Data used are presented in table B-15.

Table B-16 Correlation matrix using the Spearman rank coefficient of correlation. N=34. The data for major element oxides of orthopyroxene grains derive from EMP analyses given in table B-15. Significant correlations are bold. * Correlation is significant at the 0.05 level; ** Correlation is significant at the 0.01 level.

		SiO_2	TiO_2	Al_2O_3	Cr_2O_3	FeO	MnO	MgO	CaO	Na_2O	K_2O
SiO_2	Correlation Coefficient	1.000									
	Sig. (2-tailed)	.									
TiO_2	Correlation Coefficient	**-0.339***	1.000								
	Sig. (2-tailed)	0.050	.								
Al_2O_3	Correlation Coefficient	0.108	**-0.570****	1.000							
	Sig. (2-tailed)	0.545	0.000	.							
Cr_2O_3	Correlation Coefficient	**-0.690****	0.077	0.053	1.000						
	Sig. (2-tailed)	0.000	0.664	0.768	.						
FeO	Correlation Coefficient	**-0.764****	**0.459****	-0.220	0.458**	1.000					
	Sig. (2-tailed)	0.000	0.006	0.212	0.006	.					
MnO	Correlation Coefficient	-0.337	0.111	0.028	0.213	**0.588****	1.000				
	Sig. (2-tailed)	0.052	0.531	0.877	0.228	0.000	.				
MgO	Correlation Coefficient	**0.442****	-0.177	0.019	**-0.400***	**-0.687****	**-0.496****	1.000			
	Sig. (2-tailed)	0.009	0.316	0.916	0.019	0.000	0.003	.			
CaO	Correlation Coefficient	**-0.497****	0.103	0.138	**0.658****	**0.370***	**0.479****	**-0.444****	1.000		
	Sig. (2-tailed)	0.003	0.563	0.436	0.000	0.031	0.004	0.008	.		
Na_2O	Correlation Coefficient	-0.032	-0.014	0.184	0.242	-0.037	-0.306	-0.255	0.040	1.000	
	Sig. (2-tailed)	0.856	0.935	0.299	0.168	0.836	0.079	0.146	0.821	.	
K_2O	Correlation Coefficient	-0.099	-0.028	0.127	**0.412***	0.066	-0.195	-0.288	0.048	**0.715****	1.000
	Sig. (2-tailed)	0.576	0.874	0.473	0.016	0.711	0.268	0.099	0.788	0.000	.

Table B-17 Analyses of clinopyroxene in silicate layers obtained with the SEM-EDX. *Px:* pyroxenite; *no:* norite; *leno:* leuconorite; *an:* anorthosite.

cyclic unit	sample_analyses	lithology	SiO_2 wt%	TiO_2 wt%	Al_2O_3 wt%	Cr_2O_3 wt%	FeO_{tot} wt%	MgO wt%	CaO wt%	Na_2O wt%	K_2O wt%	total wt%
MG4A	JKL34A_8-1	px	47.1	0	2.8	0	16.8	17.3	15.0	1.0	0	100.0
	JKL34A_8-5	px	44.9	0	2.7	0	21.4	18.4	11.8	0.8	0	99.9
MG3	JKL18A_3-3	no	55.7	0	4.3	0	2.2	18.5	18.1	1.2	0	100.0
	JKL18A_4-4	no	55.5	0	3.3	0	2.8	18.5	18.8	1.1	0	100.0
	JKL18A_5-3	no	49.7	0	2.1	1.1	11.3	17.2	17.7	0.9	0	100.0
	JKL18A_5-5	no	50.6	0	2.4	0	12.0	17.8	16.0	1.2	0	100.0
	JKL16A_5-1	no	37.6	0	2.5	0	33.6	17.6	6.5	2.2	0	100.0
	JKL16A_6-4	no	42.6	0	2.4	0	25.1	21.2	6.7	2.0	0	100.0
	JKL14B_1-1	no	56.3	0	2.9	0	2.5	20.1	16.7	1.5	0	100.0
	JKL14B_4-1	leno	55.6	0	3.0	0	2.5	20.0	17.8	1.1	0	100.0
	JKL14B_4-2	leno	54.9	0	3.0	1.1	3.1	20.1	16.9	0.9	0	100.0
MG2C	JKL13A_1-1	an	56.3	0.5	4.9	0	2.9	18.3	15.7	1.4	0	100.0
	JKL13A_1-2	an	54.7	0.5	5.2	0	3.8	16.5	17.5	1.2	0	99.5
	JKL13A_1-5	an	56.3	0	4.1	0.6	3.2	16.4	17.6	1.4	0	99.6
	JKL12A_1-2	an	53.7	6.4	2.4	0	0.0	16.4	20.2	0.9	0	100.0
MG2A	JKL10A_2-1	px	44.3	0	2.5	0	23.3	19.1	9.2	1.6	0	100.0
	JKL10A_2-3	px	40.4	0	2.5	0	29.6	21.0	4.5	1.9	0	100.0
MG1	JKL9A_5-1	px	48.6	0	2.2	0	14.4	18.6	15.1	1.0	0	100.0
	JKL9A_5-2	px	53.5	0	7.9	0	3.4	23.8	9.2	1.9	0.3	100.0
	JKL9A_5-6	px	49.2	0	2.2	0	15.3	18.8	13.4	1.0	0.1	100.0
	JKL8B_2-1	px	55.8	0	3.2	0	2.5	22.9	14.0	1.6	0	100.0
MG0	JKL4A_4-2	px	40.5	0	3.9	0	26.7	18.3	7.9	2.7	0	100.0
	JKL4A_4-3	px	45.9	0	5.7	0	16.2	18.9	9.3	4.0	0	100.0

Table B-18 Correlation matrix using the Spearman rank coefficient of correlation. N=23. The data for major element oxides of clinopyroxene grains derive from SEM-EDX analyses given in table B-17. Significant correlations are bold. ** Correlation is significant at the 0.01 level; * Correlation is significant at the 0.05 level.

		SiO_2	**TiO_2**	**Al_2O_3**	**Cr_2O_3**	**FeO_{tot}**	**MgO**	**CaO**	**Na_2O**	**K_2O**
SiO_2	Correlation Coefficient	1.000								
	Sig. (2-tailed)	.								
TiO_2	Correlation Coefficient	0.260	1.000							
	Sig. (2-tailed)	0.231	.							
Al_2O_3	Correlation Coefficient	0.412	0.148	1.000						
	Sig. (2-tailed)	0.051	0.501	.						
Cr_2O_3	Correlation Coefficient	0.260	-0.149	-0.086	1.000					
	Sig. (2-tailed)	0.231	0.497	0.696	.					
FeO_{tot}	Correlation Coefficient	**-0.909****	-0.340	-0.289	-0.138	1.000				
	Sig. (2-tailed)	0.000	0.112	0.182	0.531	.				
MgO	Correlation Coefficient	-0.028	**-0.460***	0.122	-0.206	0.003	1.000			
	Sig. (2-tailed)	0.900	0.027	0.581	0.346	0.989	.			
CaO	Correlation Coefficient	**0.745****	0.347	0.070	0.327	**-0.820****	**-0.419***	1.000		
	Sig. (2-tailed)	0.000	0.105	0.750	0.128	0.000	0.047	.		
Na_2O	Correlation Coefficient	-0.280	-0.176	0.402	-0.326	0.381	0.375	**-0.643****	1.000	
	Sig. (2-tailed)	0.196	0.423	0.057	0.129	0.073	0.077	0.001	.	
K_2O	Correlation Coefficient	-0.020	-0.119	0.044	-0.119	0.018	0.311	-0.236	0.034	1.000
	Sig. (2-tailed)	0.927	0.588	0.840	0.588	0.934	0.148	0.277	0.876	.

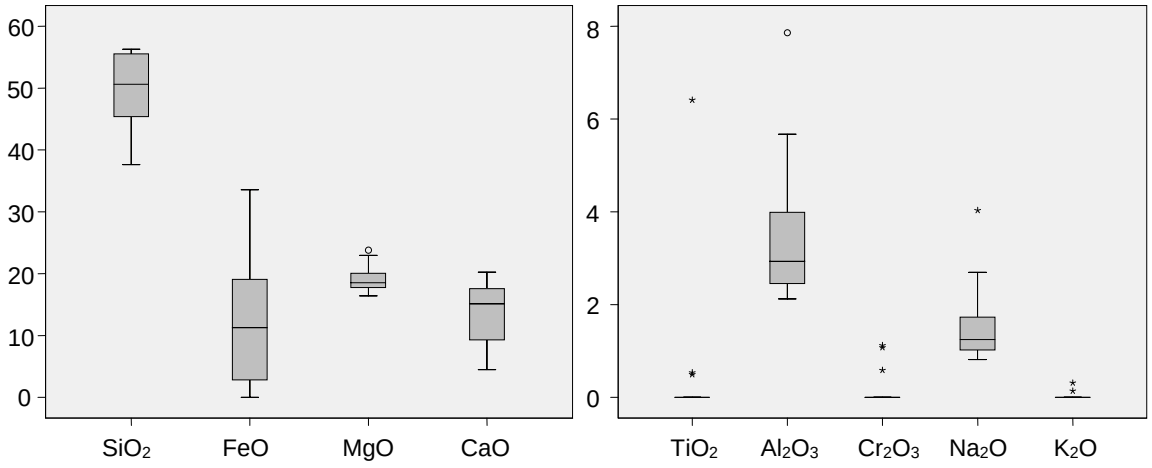

Figure B-8 Box plots of the major element oxides from clinopyroxene analyses in silicate layers. All data sets are not normally distributed and contain outliers (°: moderate outlier; *: extreme outlier). N= 23. Data used are presented in table B-17.

Table B-19 SEM-EDX analyses of pentlandite, millerite, chalcopyrite and pyrite occurring in the chromitite layers. Data in %. Norm compositions from Rösler (1991).

Ni-bearing sulphides ($N_{pentlandite}$=11; $N_{millerite}$=4)

layer	sample	mineral	Fe	Ni	Pt	Pd	S	total
MG4C	HEX10/03_6	pentlandite	21.5	36.9	0	5.7	35.9	100.0
MG4A	HEX10/17_1	millerite	0	60.8	2.2	0	37.0	100.0
MG3	HEX10/22_3	millerite	0	62.3	1.9	0	35.8	100.0
	HEX10/22_5	millerite	0	60.0	2.6	0	37.5	100.0
MG2B	HEX10/34_2	pentlandite	21.4	39.8	1.5	0	37.4	100.0
	HEX10/34_2	pentlandite	3.0	54.5	2.8	0	39.7	100.0
	HEX10/34_4	pentlandite	25.9	34.1	2.4	0	37.6	100.0
	HEX10/34_9	pentlandite	44.3	27.4	0	0	28.3	100.0
	HEX10/34_9	pentlandite	21.4	38.8	2.0	0	37.9	100.0
MG1	HEX10/46_2	millerite	0	60.2	1.8	0	38.0	100.0
	HEX10/46_2	pentlandite	22.9	41.2	0	0	35.9	100.0
	HEX10/46_3	pentlandite	23.2	42.0	0	0	34.7	100.0
	HEX10/46_4	pentlandite	23.4	40.7	1.7	0	34.1	100.0
	HEX10/46_4	pentlandite	22.3	41.3	2.4	0	34.1	100.0
	HEX10/46_5	pentlandite	21.9	40.7	2.0	0	35.3	100.0

Table B-19 *(cont.)* SEM-EDX analyses of pentlandite, millerite, chalcopyrite and pyrite occurring in the chromitite layers.

chalcopyrite (N=27)

layer	sample	Fe	Cu	Os	Ir	Ru	Pt	S	total
MG4C	HEX10/03_5	30.6	32.3	0	0	0	2.2	34.9	100.0
	HEX10/03_8	30.0	32.4	0	0	0	0	37.6	100.0
	HEX10/03_2	26.8	36.7	0	0	0	1.8	34.6	100.0
	HEX10/03_2	29.3	31.2	0	0	0	2.3	37.2	100.0
	HEX10/03_4	25.9	28.8	8.2	0	0	2.3	34.8	100.0
	HEX10/03_4	28.7	32.7	0	0	0	2.3	36.3	100.0
MG4A	HEX10/17_1	30.2	33.1	0	0	0	0	36.7	100.0
	HEX10/17_2	29.5	30.8	0	0	0	2.1	37.5	100.0
	HEX10/17_5	29.0	33.8	0	0	0	0	37.2	100.0
MG3	HEX10/22_3	33.6	32.5	0	0	0	0	33.9	100.0
	HEX10/22_3	28.2	30.7	0	0	6.6	0	34.5	100.0
	HEX10/23_9	29.5	33.5	0	0	0	1.6	35.4	100.0
MG2C	HEX10/28_5	28.6	32.3	0	0	0	2.2	36.9	100.0
	HEX10/28_13	29.4	32.8	0	0	0	1.7	36.1	100.0
MG2B	HEX10/37_3	29.9	33.4	0	0	0	0	36.7	100.0
MG2A	HEX10/38_4	30.8	31.2	0	0	0	0	38.0	100.0
	HEX10/40_1A	28.8	31.9	0	0	0	1.5	37.8	100.0
	HEX10/40_2	25.8	36.5	0	1.6	0	1.6	34.5	100.0
	HEX10/40_2	28.6	33.5	0	0	0	0	37.9	100.0
	HEX10/40_4	26.9	35.5	0	0	0	1.7	36.0	100.0
	HEX10/40_4	27.6	33.5	0	0	0	2.4	36.5	100.0
	HEX10/40_4	28.3	34.1	0	0	0	0	37.6	100.0
	HEX10/40_4	30.4	37.1	0	0	0	1.8	30.7	100.0
	HEX10/40_4	29.2	33.4	0	0	0	0	37.4	100.0
	HEX10/40_5	28.0	35.3	0	0	0	0	36.8	100.0
	HEX10/40_10	30.8	32.5	0	0	0	0	36.7	100.0
MG1	HEX10/46_4	28.9	35.1	0	0	0	0	36.0	100.0

pyrite (N=9)

layer	sample	Fe	Os	Ir	Pt	Zn	Ru	Ga	S	total
MG4C	HEX10/03_9	43.5	0	0	0	0	0	0	56.5	100.0
MG4A	HEX10/11_9	42.5	0	0	0	2.6	0	0	54.8	100.0
	HEX10/17_2	41.6	0	2.2	0	0	0	0	56.1	100.0
	HEX10/17_5	42.6	0	0	2.1	0	0	0	55.3	100.0
	HEX10/17_5	43.6	0	0	1.9	0	0	0	54.5	100.0
MG2B	HEX10/34_4	39.6	0	0	2.5	0	0	0	57.9	100.0
MG1	HEX10/46_8	43.6	0	0	2.6	0	0	0	53.8	100.0
	HEX10/46_8	43.6	0	0	2.3	0	0	0	54.1	100.0
	HEX10/46_8	43.5	0	0	2.6	0	0	0	53.8	100.0

Table B-20 Norm compositions of the BMS (in %) (from Rösler, 1991).

mineral	Fe	Cu	Ni	S	total
pentlandite	32.6	-	34.2	33.2	100
millerite	-	-	64.7	35.3	100
chalcopyrite	30.4	34.6	-	34.9	99.9
pyrite	46.6	-	-	53.4	100

Table B-21 Whole-rock PGE and Au concentration in the chromitite layers of the MG from core HEX10 gathered by ICP-MS. *X:* below detection limit. Data in ppb.

elements		Os	Ir	Ru	Rh	Pt	Pd	Au
detection limit		2	2	2	1	2	2	5
cyclic unit	**sample**							
MG4C	HEX10/01	57	70	347	190	637	207	12
	HEX10/02	73	89	453	214	679	167	6
	HEX10/03	72	75	459	139	369	283	13
MG4B	HEX10/04	53	71	323	205	733	293	7
	HEX10/05	58	59	333	108	245	221	X
MG4A	HEX10/06	102	135	533	206	517	299	X
	HEX10/07	167	223	903	307	917	398	X
	HEX10/08	295	413	1659	582	1600	847	5
	HEX10/09	90	125	545	468	1578	678	7
	HEX10/10	103	142	558	361	1518	570	6
	HEX10/11	106	139	556	267	1639	424	10
	HEX10/12	86	121	421	199	1351	349	5
	HEX10/13	76	98	361	155	1111	197	7
	HEX10/14	113	161	462	230	2075	394	20
	HEX10/15	106	207	450	275	2073	543	7
	HEX10/16	107	196	456	249	1718	528	11
	HEX10/17	96	167	422	179	1209	240	X
	HEX10/18	89	147	397	170	965	184	X
	HEX10/19	98	162	460	273	1201	483	X
	HEX10/20	78	128	380	185	559	146	X
MG3	HEX10/21	169	279	912	823	2703	2336	14
	HEX10/22	119	146	660	399	1246	1416	7
	HEX10/23	108	159	591	219	676	702	6
	HEX10/24	135	182	792	315	820	788	7
	HEX10/25	145	154	669	213	651	371	12
	HEX10/26	116	164	595	343	1176	584	5
	HEX10/27	118	175	623	602	2670	1250	8
MG2C	HEX10/28	106	128	621	270	931	296	9
	HEX10/29	118	148	683	287	1062	296	5
	HEX10/30	178	237	1048	229	1864	373	5
	HEX10/31	148	289	755	501	4579	779	10

Table B-21 *(cont.)*

MG2B	HEX10/32	144	296	688	486	5005	757	8
	HEX10/33	127	200	625	294	1238	293	X
	HEX10/34	119	136	625	176	679	187	5
	HEX10/35	108	128	558	165	707	172	X
	HEX10/36	131	165	648	235	1101	309	X
	HEX10/37	120	164	553	244	1070	262	5
MG2A	HEX10/38	69	94	342	189	2304	799	X
	HEX10/39	71	108	363	188	1933	805	5
	HEX10/40	67	75	298	185	715	310	X
MG1	HEX10/41	118	108	682	118	366	291	X
	HEX10/42	117	130	697	151	494	318	5
	HEX10/43	154	153	926	224	748	522	X
	HEX10/44	124	101	771	144	418	268	X
	HEX10/45	98	85	597	95	285	205	X
	HEX10/46	87	87	503	137	410	235	X
	HEX10/47	93	87	515	98	236	259	5
	HEX10/48	103	96	587	100	258	254	X
	HEX10/49	78	77	483	107	280	190	X
MG0	HEX10/50	61	77	366	213	591	134	X
	HEX10/51	98	130	609	186	606	119	X

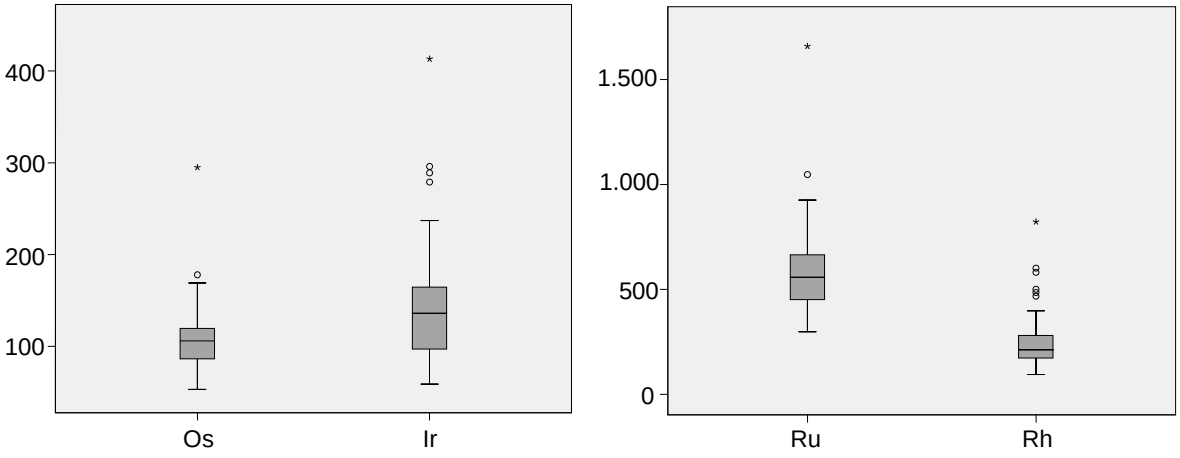

Figure B-9 Box plots of PGE analyses of the chromitite layers. All data sets are not normally distributed and contain outliers (°: moderate outlier; *: extreme outlier). N= 51. Data used are presented in table B-19.

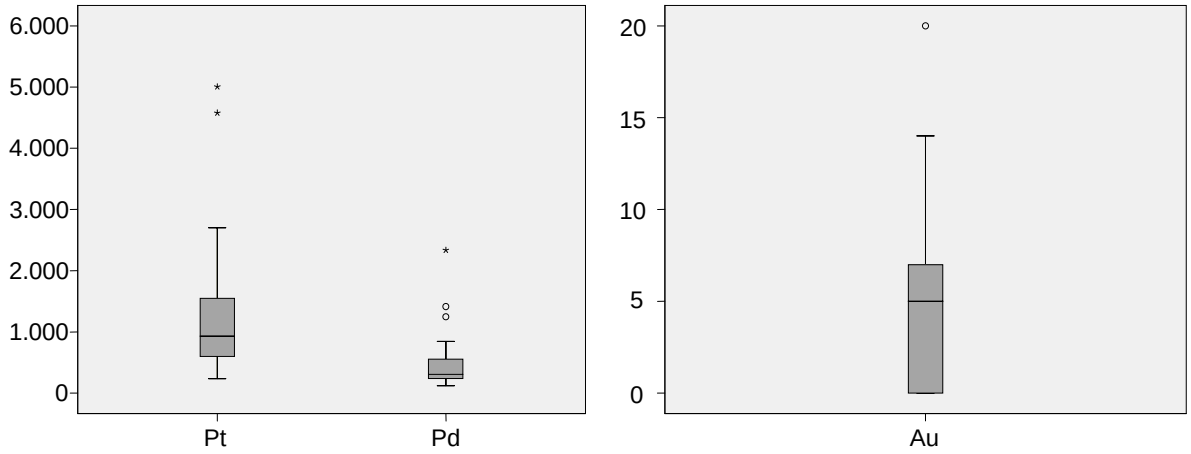

Figure B-9 *(cont.)* Box plots of PGE analyses of the chromitite layers.

Table B-22 Correlation matrix using the Spearman rank coefficient of correlation. N=51. The data are given in table B-19. Significant correlations are bold. ** Correlation is significant at the 0.01 level; * Correlation is significant at the 0.05 level.

		Os	Ir	Ru	Rh	Pt	Pd	Au
Os	Correlation Coefficient	1.000						
	Sig. (2-tailed)	.						
Ir	Correlation Coefficient	**0.811****	1.000					
	Sig. (2-tailed)	0.000	.					
Ru	Correlation Coefficient	**0.919****	**0.611****	1.000				
	Sig. (2-tailed)	0.000	0.000	.				
Rh	Correlation Coefficient	**0.536****	**0.739****	**0.412****	1.000			
	Sig. (2-tailed)	0.000	0.000	0.003	.			
Pt	Correlation Coefficient	**0.341***	**0.669****	0.129	**0.765****	1.000		
	Sig. (2-tailed)	0.014	0.000	0.368	0.000	.		
Pd	Correlation Coefficient	**0.465****	**0.574****	**0.371****	**0.721****	**0.700****	1.000	
	Sig. (2-tailed)	0.001	0.000	0.007	0.000	0.000	.	
Au	Correlation Coefficient	0.159	0.243	0.086	**0.479****	**0.457****	**0.452****	1.000
	Sig. (2-tailed)	0.264	0.086	0.551	0.000	0.001	0.001	.

Table B-23 Whole-rock PGE and Au concentrations in the silicate layers of the MG from core HEX10 gathered by ICP-MS. Data in ppb.

element		Os	Ir	Ru	Rh	Pt	Pd	Au
detection limit		0.005	0.008	0.01	0.006	0.01	0.01	0.005
cyclic unit	**sample**							
MG4C	JKL21	0	1	2	5	101	117	3
MG4A	JKL27	1	2	6	6	15	4	0
	JKL31	2	3	11	7	19	16	2
	JKL35	14	19	91	55	119	162	1
	JKL39	2	2	10	6	24	18	2
	JKL20	3	5	28	10	10	7	1
	JKL19	21	26	121	49	136	76	2
MG3	JKL15	4	6	29	12	36	19	7
	JKL14	34	81	214	252	757	671	3
	JKL26	5	14	44	39	126	139	2
MG2C	JKL13	4	11	26	11	103	31	3
	JKL12	6	20	53	26	95	38	1
MG2B	JKL25	35	87	192	193	2358	599	4
MG2A	JKL11	3	4	17	11	86	44	7
	JKL24	2	2	8	5	39	18	1
	JKL23	8	12	50	28	222	128	2
	JKL10	7	16	63	33	315	214	8
MG1	JKL9	4	6	37	13	29	21	15
	JKL8	11	10	58	25	89	250	5
MG0	JKL5	10	12	66	20	64	68	7
	JKL4	0	1	8	0	0	7	2

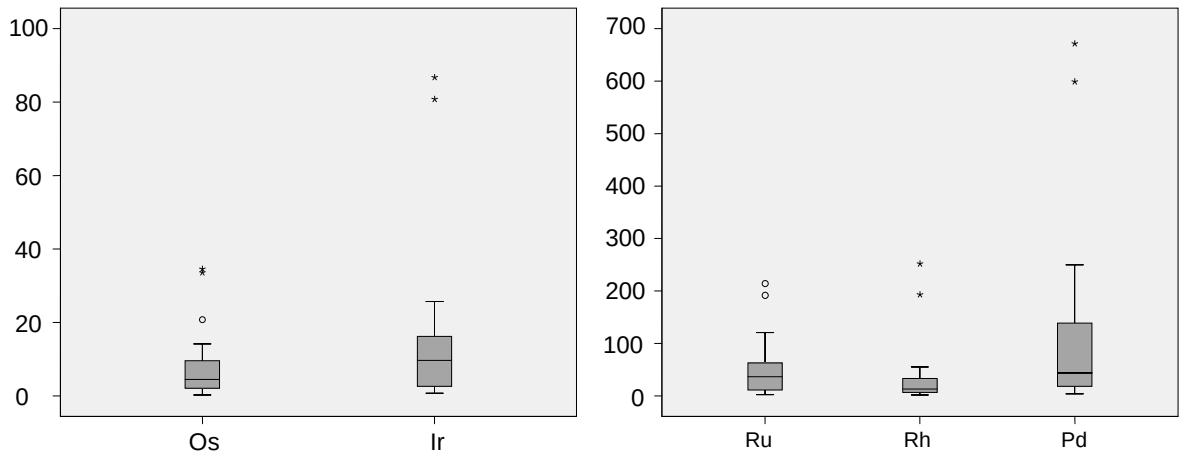

Figure B-10 Box plots of PGE analyses of the silicate layers. All data sets are not normally distributed and contain outliers (°: moderate outlier; *: extreme outlier). N= 21. Data used are presented in table B-21.

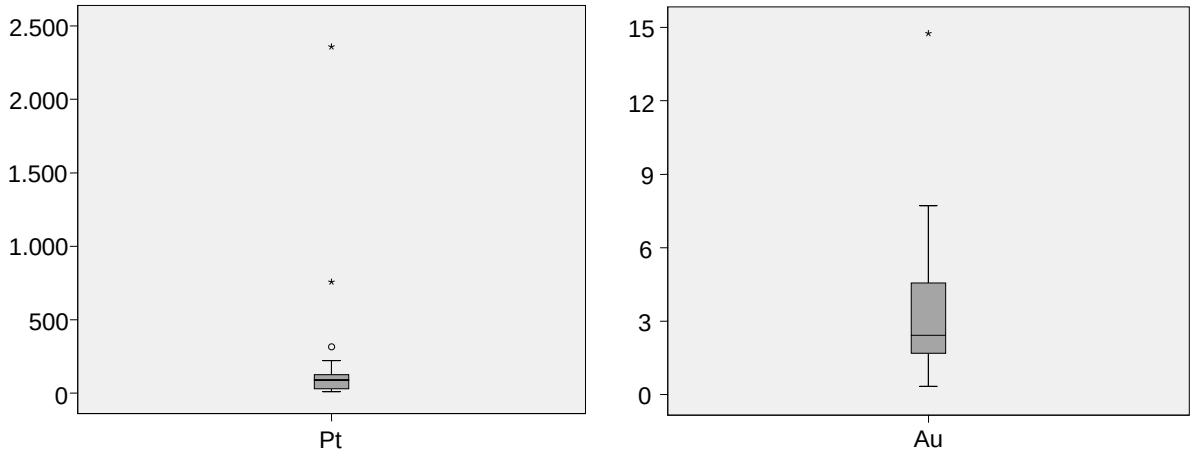

Figure B-10 *(cont.)* Box plots of PGE analyses of the silicate layers.

Table B-24 Correlation matrix using the Spearman rank coefficient of correlation. N=21. The data are given in table B-21. Significant correlations are bold. *Sig.*: significance. ** Correlation is significant at the 0.01 level.

		Os	Ir	Ru	Rh	Pt	Pd	Au	Cr_2O_3	MgO
Os	Correlation Coefficient	1.000								
	Sig. (2-tailed)	.								
Ir	Correlation Coefficient	**0.934****	1.000							
	Sig. (2-tailed)	0.000	.							
Ru	Correlation Coefficient	**0.982****	**0.943****	1.000						
	Sig. (2-tailed)	0.000	0.000	.						
Rh	Correlation Coefficient	**0.931****	**0.949****	**0.937****	1.000					
	Sig. (2-tailed)	0.000	0.000	0.000	.					
Pt	Correlation Coefficient	**0.756****	**0.809****	**0.732****	**0.812****	1.000				
	Sig. (2-tailed)	0.000	0.000	0.000	0.000	.				
Pd	Correlation Coefficient	**0.789****	**0.729****	**0.773****	**0.817****	**0.890****	1.000			
	Sig. (2-tailed)	0.000	0.000	0.000	0.000	0.000	.			
Au	Correlation Coefficient	0.226	0.143	0.277	0.185	0.174	0.334	1.000		
	Sig. (2-tailed)	0.339	0.548	0.238	0.435	0.462	0.150	.		
Cr_2O_3	Correlation Coefficient	**0.735****	**0.592****	**0.749****	**0.668****	**0.493***	**0.614****	0.119	1.000	
	Sig. (2-tailed)	0.000	0.006	0.000	0.001	0.027	0.004	0.618	.	
MgO	Correlation Coefficient	**-0.559***	**-0.674****	**-0.586****	**-0.520***	**-0.471***	-0.338	-0.095	-0.056	1.000
	Sig. (2-tailed)	0.010	0.001	0.007	0.019	0.036	0.145	0.691	0.816	.

Table B-25 Correlation matrix using the Spearman rank coefficient of correlation showing correlations of the PGE and Au with the base metals Ni, Cu and Co, and S. N=21; N for S is 15 only. Significant correlations are bold. *Sig.*: significance. ** Correlation is significant at the 0.01 level; * Correlation is significant at the 0.05 level.

		Co	Ni	Cu	Os	Ir	Ru	Rh	Pt	Pd	Au	S
Co	Correlation Coefficient	1.000										
	Sig. (2-tailed)											
Ni	Correlation Coefficient	**0.913****	1.000									
	Sig. (2-tailed)	0.000										
Cu	Correlation Coefficient	0.422	0.332	1.000								
	Sig. (2-tailed)	0.057	0.141									
Os	Correlation Coefficient	**0.460***	0.327	0.426	1.000							
	Sig. (2-tailed)	0.036	0.148	0.054								
Ir	Correlation Coefficient	0.322	0.199	0.403	**0.943****	1.000						
	Sig. (2-tailed)	0.154	0.388	0.070	.000							
Ru	Correlation Coefficient	0**.440***	0.323	**0.468***	**0.981****	**0.945****	1.000					
	Sig. (2-tailed)	0.046	0.153	0.033	.000	0.000						
Rh	Correlation Coefficient	**0.435***	0.281	0.365	**0.938****	**0.953****	**0.942****	1.000				
	Sig. (2-tailed)	0.049	0.218	0.104	.000	0.000	0.000					
Pt	Correlation Coefficient	0.371	0.284	0.169	**0.748****	**0.794****	**0.710****	**0.808****	1.000			
	Sig. (2-tailed)	0.097	0.211	0.464	0.000	0.000	0.000	0.000				
Pd	Correlation Coefficient	**0.449***	0.331	0.186	**0.775****	**0.723****	**0.753****	**0.808****	**0.901****	1.000		
	Sig. (2-tailed)	0.041	0.143	0.420	0.000	0.000	0.000	0.000	0.000			
Au	Correlation Coefficient	0.081	0.221	-0.026	0.274	0.203	0.305	0.258	0.268	0.419	1.000	
	Sig. (2-tailed)	0.729	0.336	0.911	0.229	0.378	0.179	0.258	0.241	0.058		
S	Correlation Coefficient	0.350	0.371	**0.761****	0.314	0.329	0.364	0.321	0.004	0.086	0.179	1.000
	Sig. (2-tailed)	0.201	0.173	0.001	0.254	0.232	0.182	0.243	0.990	0.761	0.524	

Table B-26 Chromite chemistry of the eastern Bushveld complex gained from the literature. The cation fractions have been calculated with the spreadsheet of Barnes (2005). If indicated by the authors, the core details have been added in brackets. [1] MG4C instead of MG4B; * MG2 only.

MG4B	Farm	Cr^{3+}	Fe^{3+}	Al^{3+}	Reference
N	Jagdlust-Winterveld	0.593	0.083	0.323	Cameron (1977)
	Tweefontein	0.562	0.139	0.299	Hatton and von Gruenewaldt (1985)
	Tweefontein (8JT7)	0.631	0.081	0.288	Naldrett *et al.* (2009)
S	Helena (HEX10)[1]	0.591	0.130	0.279	this study
MG4A					
N	Jagdlust-Winterveld	0.551	0.099	0.351	Cameron (1977)
	Tweefontein	0.558	0.102	0.340	Hatton and von Gruenewaldt (1985)
	Tweefontein (8JT7)	0.570	0.096	0.334	Naldrett *et al.* (2009)
S	Helena (HEX10)	0.563	0.084	0.353	this study
MG3					
N	Jagdlust-Winterveld	0.586	0.138	0.276	Cameron (1977)
	Clapham (MH-37)	0.569	0.095	0.336	Naldrett *et al.* (2009)
	Tweefontein (8JT7)	0.583	0.097	0.320	Naldrett *et al.* (2009)
	Tweefontein	0.573	0.121	0.306	Hatton and von Gruenewaldt (1985)
S	Helena (HEX10)	0.593	0.092	0.315	this study
MG2C					
N	Jagdlust-Winterveld	0.563	0.087	0.350	Cameron (1977)
	Tweefontein*	0.590	0.114	0.295	Hatton and von Gruenewaldt (1985)
	Tweefontein (8JT7)	0.601	0.092	0.307	Naldrett *et al.* (2009)
S	Helena (HEX10)	0.585	0.078	0.337	this study
MG2B					
N	Jagdlust-Winterveld	0.571	0.102	0.328	Cameron (1977)
	Tweefontein*	0.590	0.114	0.295	Hatton and von Gruenewaldt (1985)
	Tweefontein (8JT7)	0.602	0.094	0.304	Naldrett *et al.* (2009)
S	Helena (HEX10)	0.511	0.075	0.289	this study
MG2A					
N	Jagdlust-Winterveld	0.614	0.104	0.281	Cameron (1977)
	Tweefontein*	0.590	0.114	0.295	Hatton and von Gruenewaldt (1985)
	Tweefontein (8JT7)	0.603	0.087	0.310	Naldrett *et al.* (2009)
S	Helena (HEX10)	0.594	0.092	0.315	this study
MG1					
N	Jagdlust-Winterveld	0.624	0.091	0.285	Cameron (1977) (MG1B)
	Jagdlust-Winterveld	0.621	0.089	0.290	Cameron (1977) (MG1A)
	Tweefontein	0.622	0.094	0.284	Hatton and von Gruenewaldt (1985)
	Clapham (MH-37)	0.579	0.086	0.335	Naldrett *et al.* (2009)
S	Helena (HEX10)	0.620	0.068	0.313	this study

Table B-27 Chromite chemistry of the western Bushveld complex gained from the literature. The cation fractions have been calculated with the spreadsheet of Barnes (2004). If indicated by the authors, the core details have been added in brackets. * MG2B.

MG4B	Farm	Cr^{3+}	Fe^{3+}	Al^{3+}	Reference
N	Amandelbult	0.579	0.097	0.324	Hatton and von Gruenewaldt (1985)
	Union	0.538	0.109	0.353	Hatton and von Gruenewaldt (1985)
	Union (NG-1,2,3)	0.544	0.106	0.350	Scoon and Teigler (1994)
	Boshoek	0.569	0.100	0.331	Hatton and von Gruenewaldt (1985)
	Rustenburg	0.567	0.125	0.308	Hatton and von Gruenewaldt (1985)
	Marikana	0.599	0.119	0.282	Hatton and von Gruenewaldt (1985)
	Marikana (TF-21)	0.639	0.102	0.259	Naldrett *et al.* (2009)
S	Brits (SF-7)	0.626	0.113	0.261	Scoon and Teigler (1994)
MG4A					
N	Amandelbult	0.563	0.064	0.373	Hatton and von Gruenewaldt (1985)
	Union	0.566	0.114	0.319	Hatton and von Gruenewaldt (1985)
	Union (NG-1,2,3)	0.541	0.111	0.348	Scoon and Teigler (1994)
	Ruighoek	0.569	0.064	0.366	Hatton and von Gruenewaldt (1985)
	Boshoek	0.571	0.099	0.329	Hatton and von Gruenewaldt (1985)
	Rustenburg	0.567	0.087	0.346	Hatton and von Gruenewaldt (1985)
	Marikana	0.565	0.108	0.327	Hatton and von Gruenewaldt (1985)
	Marikana (TF-21)	0.565	0.093	0.342	Naldrett *et al.* (2009)
S	Brits (SF-7)	0.567	0.114	0.318	Scoon and Teigler (1994)
MG3					
N	Union (NG-1,2,3)	0.533	0.117	0.351	Scoon and Teigler (1994)
	Ruighoek	0.555	0.091	0.355	Hatton and von Gruenewaldt (1985)
	Boshoek	0.558	0.064	0.377	Hatton and von Gruenewaldt (1985)
	Rustenburg	0.556	0.124	0.320	Hatton and von Gruenewaldt (1985)
	Marikana	0.569	0.118	0.313	Hatton and von Gruenewaldt (1985)
	Marikana (TF-21)	0.587	0.099	0.313	Naldrett *et al.* (2009)
	Brits	0.581	0.094	0.325	Hatton and von Gruenewaldt (1985)
S	Brits (SF-7)	0.588	0.113	0.300	Scoon and Teigler (1994)
MG2	Amandelbult	0.557	0.064	0.378	Hatton and von Gruenewaldt (1985)
N	Union (NG-1,2,3)	0.545	0.120	0.335	Scoon and Teigler (1994)
	Boshoek	0.554	0.108	0.339	Hatton and von Gruenewaldt (1985)
	Rustenburg	0.589	0.127	0.284	Hatton and von Gruenewaldt (1985)
	Marikana	0.597	0.099	0.303	Hatton and von Gruenewaldt (1985)
	Marikana (TF-21)*	0.600	0.098	0.303	Naldrett *et al.* (2009)
S	Brits (SF-7)	0.620	0.109	0.271	Scoon and Teigler (1994)
MG1					
N	Amandelbult	0.558	0.087	0.356	Hatton and von Gruenewaldt (1985)
	Union (NG-1,2,3)	0.522	0.139	0.338	Scoon and Teigler (1994)
	Ruighoek	0.556	0.116	0.328	Hatton and von Gruenewaldt (1985)
	Boshoek	0.574	0.051	0.376	Hatton and von Gruenewaldt (1985)
	Rustenburg	0.597	0.122	0.281	Hatton and von Gruenewaldt (1985)
	Marikana	0.623	0.092	0.285	Hatton and von Gruenewaldt (1985)
	Marikana (TF-21)	0.624	0.087	0.289	Naldrett *et al.* (2009)
	Brits	0.614	0.094	0.292	Hatton and von Gruenewaldt (1985)
S	Brits (SF-7)	0.587	0.049	0.365	Scoon and Teigler (1994)

Table C-1 Grain size distribution of the PGM species occurring in the individual chromitite layers including laurite. Data for the MG2C, MG3 and MG4A chromitite are averages from two samples each.

MG1	size classes					
	0-4.1	4.1-8.1	8.1-11.4	11.4-16.0	16.0-22.0	total
Pt-sulphide	100	0	0	0	0	100
PtPd-sulphide	17.8	82.2	0	0	0	100
PtRh-sulphide	100	0	0	0	0	100
Pt-telluride	100	0	0	0	0	100
Pd-telluride	100	0	0	0	0	100
Pt-alloys	100	0	0	0	0	100
Pd-alloys	0	0	0	0	0	0
Pt-arsenide	100	0	0	0	0	100
Pd-arsenide	100	0	0	0	0	100
PGE-sulphoarsenides	100	0	0	0	0	100
ferroplatinum	0	0	0	0	0	0
laurite	34.6	44.0	21.4	0	0	100

MG2A	size classes					
	0-4.1	4.1-8.1	8.1-11.4	11.4-16.0	16.0-22.0	total
Pt-sulphide	100	0	0	0	0	100
PtPd-sulphide	65.7	34.3	0	0	0	100
PtRh-sulphide	21.7	78.3	0	0	0	100
Pt-telluride	0	0	0	0	0	0
Pd-telluride	0	0	0	0	0	0
Pt-alloys	0	0	0	0	0	0
Pd-alloys	0	0	0	0	0	0
Pt-arsenide	0	0	0	0	0	0
Pd-arsenide	100	0	0	0	0	100
PGE-sulphoarsenides	31.6	68.4	0	0	0	100
ferroplatinum	100	0	0	0	0	100
laurite	53.8	26.4	19.8	0	0	100

MG2B	size classes					
	0-4.1	4.1-8.1	8.1-11.4	11.4-16.0	16.0-22.0	total
Pt-sulphide	32.4	39.1	0	28.5	0	100
PtPd-sulphide	56.1	43.9	0	0	0	100
PtRh-sulphide	28.4	36.1	35.4	0	0	100
Pt-telluride	0	0	0	0	0	0
Pd-telluride	0	0	0	0	0	0
Pt-alloys	0	0	0	0	0	0
Pd-alloys	0	0	0	0	0	0
Pt-arsenide	0	0	0	0	0	0
Pd-arsenide	100	0	0	0	0	100
PGE-sulphoarsenides	23.5	76.5	0	0	0	100
ferroplatinum	100	0	0	0	0	100
laurite	35.9	64.1	0	0	0	100

MG2C	size classes					
	0-4.1	4.1-8.1	8.1-11.4	11.4-16.0	16.0-22.0	total
Pt-sulphide	36.9	40.3	22.9	0	0	100.005
PtPd-sulphide	32	33.1	9.8	25.2	0	100
PtRh-sulphide	29.9	43.5	13.9	0	12.7	100
Pt-telluride	100	0	0	0	0	100
Pd-telluride	100	0	0	0	0	100
Pt-alloys	74.	25.6	0	0	0	100
Pd-alloys	100	0	0	0	0	100
Pt-arsenide	100	0	0	0	0	100
Pd-arsenide	100	0	0	0	0	100
PGE-sulphoarsenides	100	0	0	0	0	100
ferroplatinum	100	0	0	0	0	100
laurite	39.3	33.8	26.9	0	0	100

MG3	size classes					
	0-4.1	4.1-8.1	8.1-11.4	11.4-16.0	16.0-22.0	total
Pt-sulphide	66.8	33.2	0	0	0	100
PtPd-sulphide	21.4	29.5	15.9	33.3	0	100
PtRh-sulphide	16.1	36.6	21.2	26.1	0	100
Pt-telluride	0	0	0	0	0	0
Pd-telluride	100	0	0	0	0	100
Pt-alloys	100	0	0	0	0	100
Pd-alloys	100	0	0	0	0	100
Pt-arsenide	0	0	0	0	0	0
Pd-arsenide	100	0	0	0	0	100
PGE-sulphoarsenides	12.8	87.2	0	0	0	100
ferroplatinum	0	0	0	0	0	0
laurite	22.2	55.8	22	0	0	100

MG4A	size classes					
	0-4.1	4.1-8.1	8.1-11.4	11.4-16.0	16.0-22.0	total
Pt-sulphide	100	0	0	0	0	100
PtPd-sulphide	37.8	55.3	6.8	0	0	100
PtRh-sulphide	21	33.6	8.2	14.9	22.1	99.85
Pt-telluride	100	0	0	0	0	100
Pd-telluride	0	0	0	0	0	0
Pt-alloys	100	0	0	0	0	100
Pd-alloys	100	0	0	0	0	100
Pt-arsenide	0	0	0	0	0	0
Pd-arsenide	0	0	0	0	0	0
PGE-sulphoarsenides	35.5	64.5	0	0	0	100
ferroplatinum	100	0	0	0	0	100
laurite	41.1	35.6	9.1	14.3	0	100

MG4C	size classes					
	0-4.1	4.1-8.1	8.1-11.4	11.4-16.0	16.0-22.0	total
Pt-sulphide	39.3	60.7	0	0	0	100
PtPd-sulphide	46.3	25.8	27.9	0	0	100
PtRh-sulphide	40.4	59.6	0	0	0	100
Pt-telluride	100	0	0	0	0	100
Pd-telluride	100	0	0	0	0	100
Pt-alloys	100	0	0	0	0	100
Pd-alloys	100	0	0	0	0	100
Pt-arsenide	0	0	0	0	0	0
Pd-arsenide	0	0	0	0	0	0
PGE-sulphoarsenides	100	0	0	0	0	100
ferroplatinum	0	0	0	0	0	0
laurite	13.9	10.7	17.5	15.5	42.3	100

An investigation of the geochemistry of the Middle Group of the eastern Bushveld complex, South Africa Part 1 – the chromitite layers

J. Kottke-Levin*[1,2], M. Tredoux[1] and P.-J. Gräbe[3]

This paper presents whole-rock geochemical and mineral chemical data for chromitite layers of the Middle Group of the eastern Bushveld complex. It reports on compositional variations of chromite from the chromitite layers, and special attention is paid to the platinum-group element (PGE) content and mineralisation within the chromitite layers. The discussion is focused on possible mechanisms by which the association of PGE enrichment within the chromitite layers can be modelled. The MG chromitites from bottom (MG0) to top (MG4C) are characterised by progressive melt evolution, showing decreasing Mg# and Cr/(Cr+Fe) ratio and increasing Cr/(Cr+Al) ratio, TiO_2 and V concentrations. An increase in the Mg# together with a drop in the Cr/Cr+Al) and an increasing Cr/(Cr+Fe) ratio at the base of the MG4A chromitite strongly suggests the addition of hot and primitive magma. High Cu concentrations in the chromitite layers with coincident low S values suggest the application of Naldrett *et al.*[36] Fe-loss model during cooling. With the help of the La/Cu and Cu/S ratios it could be shown that Cu is concentrated neither in base metal sulphides nor in trapped silicate melt and thus the model is not applicable. Laser ablation inductively coupled plasma mass spectrometry studies of single chromite grains also have not revealed Cu to be in solid solution and thus another Cu concentrating phase must be found. The PGE patterns of the MG chromitite layers are very similar to the one of the UG2 suggesting that they derived from the same magma and the same style of mineralisation did apply. It furthermore implies the presence of one parental magma only for the entire Critical Zone. Due to low S contents in the MG chromitite layers, it seems unlikely that the PGE have been concentrated by base metal sulphides only. About a sixth of the platinum-group mineral observed is associated with As, Bi and Te, and therefore PGE concentration by the cluster model is favoured. Enrichment of the high-temperature PGE over the lower-temperature PGE in the lowermost MG chromitite layers and the MG4A is probably due to the presence of high temperatures of the chromitite forming melt, and thus temperature could play a role in the fractionation of the two PGE groups.

Keywords: Middle Group, Chromitite layers, PGE mineralisation, Bushveld complex

Introduction

Besides being also the world's largest ore deposit for chrome and vanadium, the Rustenburg Layered Suite (RLS) in the Bushveld complex contains approximately 75 and 50% of the world's platinum (Pt) and palladium (Pd) resources respectively.[2,39] With a surface extension

[1]Department of Geology, University of the Free State, PO Box 339, Bloemfontein 9300, South Africa
[2]Martin-Luther-University Halle-Wittenberg, Von Seckendorff-Platz 3, 06120 Halle (Saale), Germany
[3]Xstrata Alloys, Xstrata Head Office, PO Box 2131, 0300 Rustenburg, South Africa

*Corresponding author, email KottkeLevinJ.SCI@ufs.ac.za

Published by Maney on behalf of the Institute and The AusIMM
Received 2 August 2009; accepted 12 November 2009
DOI 10.1179/174327509X12550990457960

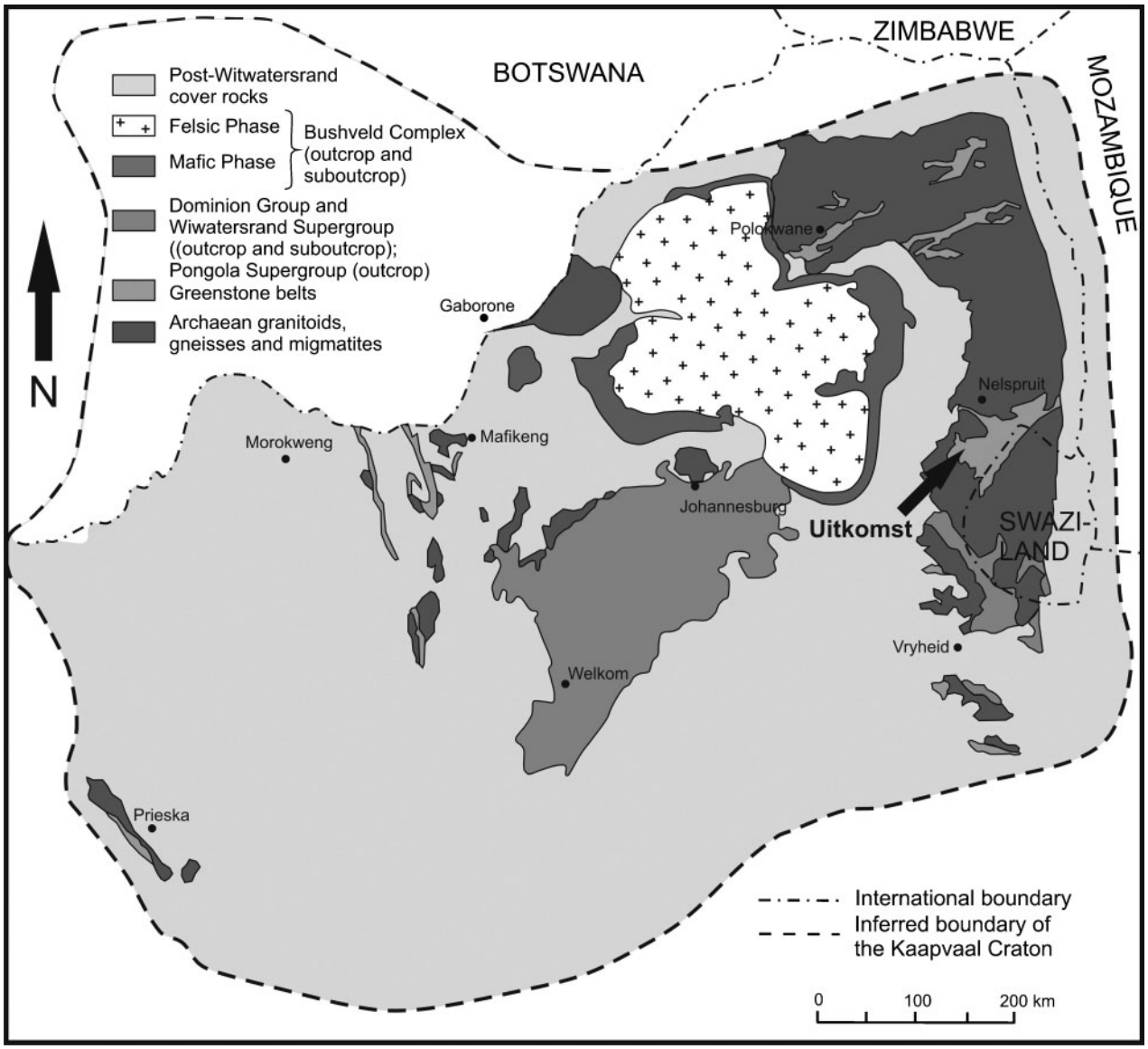

1 The Bushveld complex and the satellite intrusion at Uitkomst (indicated with an arrow, from Anhaeusser[1])

of 65 000 km^2, it is also the largest layered mafic intrusion on Earth. The Bushveld complex comprises:

(i) mafic sills that intruded into the Transvaal Supergroup
(ii) the felsic and minor basic volcanics of the Rooiberg Group
(iii) the ultramafic and mafic rocks, referred to as the RLS
(iv) the Rashoop Granophyre Suite and the Lebowa Granite Suite both overlying the RLS.[7]

Although no accurate age for the mafic sills is available, they are interpreted to represent an early stage of pre-Bushveld magmatism.[7] An age of 2·06 Ga for the Rooiberg Group is provided by Hatton and Schweitzer[21] and these rocks thus are coeval with the RLS that has been dated at 2·061 Ga by Walraven *et al.*[54] Age determinations of the Rashoop Granophyre Suite and the Lebowa Granite Suite by several authors (e.g. Coertze *et al.*;[10] Walraven;[52] Walraven *et al.*;[53] and Walraven and Hattingh[55]) have shown radiometric ages ranging from 2·09 to 1·40 Ga.

The RLS is made up of five limbs: the western, eastern, northern, far western and Bethal limbs, of which the first four are indicated in dark grey in Fig. 1. The Bethal limb has been identified by a gravitational high and its lithology is only known from borehole information.[7] There are also several satellite intrusions that are thought to be coeval with the RLS (*see* Fig. 1), e.g. the Molopo Farms complex in Botswana[19] and the Uitkomst intrusion to the east of the eastern limb near the town of Badplaas.[6,9,13]

The RLS in the western and eastern limbs are vertically subdivided into five stratigraphic zones: the Marginal Zone at the bottom (mainly mafic to ultramafic sills and chill zones), followed by the ultramafic Lower Zone and then the Critical, Main and Upper Zones (Fig. 2). The rocks become progressively less mafic and more Fe-rich towards the top of the RLS.[15]

The Critical Zone (CZ) contains the important platinum-group element (PGE) ore horizons: the Merensky Reef and the UG2 chromitite layer, both occurring towards its top. It also hosts a number of

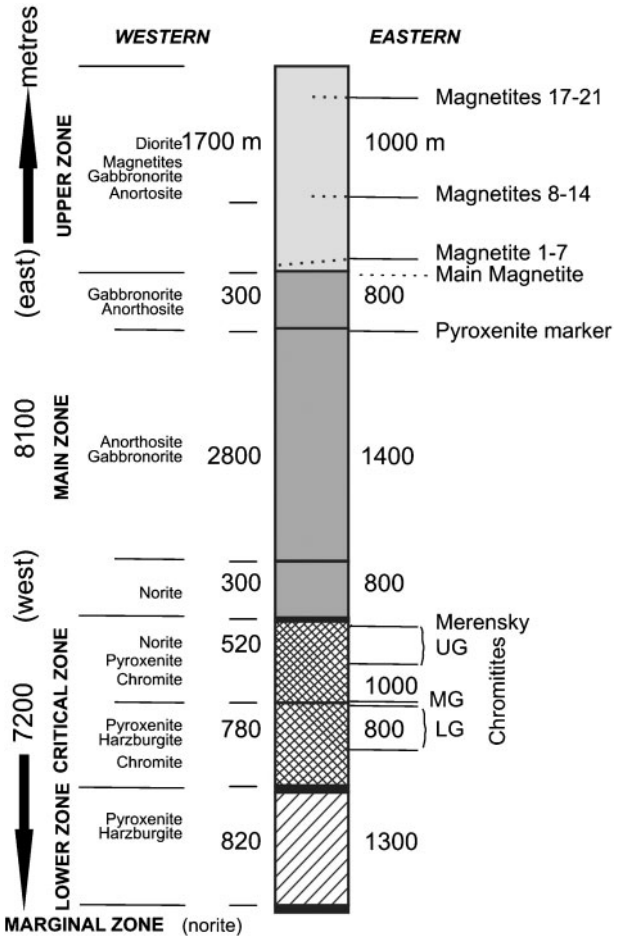

2 General stratigraphic column for the western and the eastern Bushveld complex[8,56]

other chromitite layers. These are divided into three groups, called the Lower, Middle and Upper Groups, depending on their position in the CZ stratigraphy. The Middle Group (MG) is situated at the transition zone from an ultramafic (pyroxenite) to a more mafic rock assemblage (pyroxenite, norite, anorthosite), which marks the transition from the Lower Critical Zone (LCZ) to the Upper Critical Zone (UCZ). This boundary is identified by the first appearance of cumulus plagioclase, and in the eastern limb, where this study was based, it occurs between the chromitite layers 2 and 3 of the MG (MG2 and M3 respectively).[7,16]

The formation of chromitite layers

Previous work on chromitite layers of the CZ showed that they are enriched in the PGE relative to the silicate rocks of the cumulate succession,[27,35,43] suggesting that PGE mineralisation is connected to the formation of chromite. Irvine[24] was the first who provided a model for chromite formation. With an olivine-chromite-silica ternary plot he explained the crystallisation paths in a mafic magma when mixing with a newly introduced magma or contamination with siliceous material (e.g. felsic country rocks) occurs. Both events are able to shift the 'normal' crystallisation path into the stability field of chromite, thus resulting in the precipitation of chromite only. The idea of contamination leading to the formation of mono-mineralic chromitite layers has expanded by Kinnaird *et al.*,[25] who corroborated the contamination with detailed Sr_i data from interstitial plagioclase from chromitites and different silicate host rocks of the entire CZ. According to this information, the influx of new magma into the magma chamber with Sr_i=0·705–0·706 causes interaction with the highly radiogenic overlying granophyric roof rocks (Sr_i> 0·72). This contamination by a highly siliceous melt yielded short events of chromite precipitation. The chromite grains settled to the floor of the magma chamber, dragging small fragments of magma with them; the latter then crystallised to form the interstitial silicates with enriched isotopic ratios. As PGE enrichment is connected to chromitite layers, Kinnaird *et al.*[25] suggest that the contamination process leading to chromite formation also caused the PGE precipitation, due to the reduction of the magmatic environment as Fe^{3+} and Cr^{3+} are withdrawn by the chromite.

A study on silicate melt inclusions in chromite grains from the Stillwater Complex led Spandler *et al.*[44] to propose the same model for chromite formation that has been suggested by Kinnaird *et al.*:[25] a new magma influx interacting with the roof of the Stillwater magma chamber that led to partial melting of the roof rock and mixing with the residual melt in the magma chamber. Spandler *et al.*[44] interpret the inclusions in the chromite to be trapped melt that has been locked in during chromite growth and hence can be used to provide information about chromite formation. The chemical composition of the inclusions shows variable degrees of mixing between the parental magma, i.e. high-Mg basalt, and a Na-rich trondhjemitic melt, the latter probably deriving from partial melting of country rocks. More recent research[45] has shown mobility of rare earth elements through olivine and chromite suggests a degree of interaction between the inclusion and surrounding silicate melt. This has cast doubt on whether silicate inclusions in chromite and olivine record pristine melt compositions but the unusually Na-rich character of the Stillwater inclusions and the highly radiogenic Sr isotope signatures found in plagioclase associated with chromite still support the idea that chromite crystallisation took place in the presence of unusually silicic melt.

Although the discussion about the formation of the chromitite layers is manifold, there still is the problem how chromitite layers can form in the Bushveld complex. It is evident that large intrusions such as the Bushveld complex are not emplaced in a single magma injection, but are the results of multiple magma addition (Kruger;[27] Cawthorn and Walraven[6]); therefore the formation of all the chromitite layers in the CZ of the Bushveld complex (total thickness of 9·5 m)[14] would require around 15 km of magma.[14] This seems very unlikely, unless large volumes of Cr-depleted residua are missing.[14]

As stated by Eales,[14] there appears to be more Cr present in the Bushveld complex than can be accounted for by its solubility in the mafic parental magmas, assuming that the present column represents the entire magma mass. He therefore suggests the presence of ~3% microphenocryts of chromite in the magma for the formation of the CZ, in addition to the Cr being dissolved in the melt. Mondal and Mathez[30] adopted the

model proposed by Eales[14] to explain the formation of the UG2 and its pyroxenitic host rock. The Cr-rich ultramafic sills of the eastern Bushveld complex are interpreted by Sharpe and Hulbert[46] and Davies and Tredoux[12] as having been formed in a crustal chamber before the intrusion into the Bushveld magma chamber, and this model should give support to the Cr-microphenocryst model proposed by Eales.[14]

PGE concentration within chromitite layers

Petrogenetic models for PGE mineralisation are typically based on high silicate/sulphide partition coefficients and the so-called *R* factor.[33] However, these arguments were neglected by von Gruenewaldt *et al.*[51] in their discussion of the chromitite layers below the UG2, as the S content of these layers is extremely low.

Scoon and Teigler[40] ascribed the PGE mineralisation in sulphide-poor layers to chromite control. However, Naldrett and Lehmann[34] suggest a model whereby the original sulphide content of the magma is re-distributed during cooling, leading to Fe loss of the base metal sulphides (BMS). The Fe is incorporated into vacancies in high-temperature chromite grains and the S is lost to the surroundings, producing sulphides that are enriched in Cu, Ni and the PGE. Naldrett *et al.*[36] extended this model by postulating a multi-stage magma chamber, in which the FeS component of earlier sulphides is gradually dissolved by sulphide-undersaturated magma passing through the staging chamber. The remaining sulphide will thus become enriched in Ni, Cu and especially the PGE. Cawthorn[5] in turn suggested that oxidation processes are responsible for the loss of Fe and S from the chromitites, and rejected a desulphidation process. He considered that, because of low BMS abundances in the chromitite layers, the sulphides have never been there.

Several authors also ascribed the PGE enrichment in the chromitite layers to the process of contamination and magma mixing (e.g. Kinnaird *et al.*;[25] Schoenberg *et al.*[42]). As mentioned earlier, Kinnaird *et al.*[25] suggest that platinum-group mineral (PGM) formation was initiated because of changes in physics and chemistry which the magma underwent during contamination and mixing. The Os isotope data of the PGE deposits of the Bushveld complex seem to indicate that the magma chamber have had a significant crustal input,[42] and these authors also argued that contamination of the residual magma by a siliceous crustal melt initiated PGM precipitation. Teigler[48] ascribed the increasing content of rhodium (Rh), platinum (Pt) and palladium (Pd) relative to osmium (Os), iridium (Ir) and ruthenium (Ru) with height in the stratigraphic column of the RLS, to the same process.

Post-cumulus overprinting and redistribution of PGE mineralisation were discussed by Teigler and Eales.[49] As new S-undersaturated magma mixes with the supernatant liquid in the magma chamber, the stability field of chromite is entered, and chromite grains start to precipitate. By this process, the solubility of S in the hybrid silicate liquid changes dramatically, leading to the formation of high-temperature (HT) PGMs such as laurite and PGE alloys.

A mechanical, rather than chemical, association between the PGE and sulphide is proposed by the cluster theory of Tredoux *et al.*,[50] according to which the PGE are present as metallic clusters in the melt and which are stabilised by surface adsorption of chalcogenides, such as S, As, Sb and Te. In an S-rich environment, the clusters will associate with the sulphide melt and will precipitate to form PGE, arsenides, antimonides, tellurides and complex sulphides. Remaining clusters will precipitate with the BMS and form sub-microscopic inclusions within them. On the other hand, in an S-poor environment, the clusters will remain in the silicate melt. Eventually, they will coalesce to form PGE alloys and thus probably can act as nucleation centres for early-forming oxide and silicate minerals. The high melting points of Os and Ir, as well as their tendency to form the most stable clusters, coincide with the appearance of these two elements with early cumulates.

In this paper, we will consider a continuous section through the MG chromitites in the eastern Bushveld, with the specific view to investigate the interrelationship between the Cr and PGE enrichment, and the mechanisms that may be responsible for the geochemical features observed.

Analytical techniques

The samples for this study derive from a core that was drilled by Xstrata in the eastern Bushveld complex in the Mpumalanga province, South Africa – for the geographical position of the bore hole (*see* Fig. 3). The log of the section of the core which was sampled is given in Fig. 4; as is clear from this figure there are nine distinctive chromitite layers numbered from bottom to top: MG0, MG1, MG2A-2C, MG3 and MG4A-4C.

Fifty-one samples of the MG chromitite layers have been sampled at intervals of $\sim$15 cm, and from each of them a thick polished section was prepared, for study by reflected light optical microscopy. Half of each sample was crushed, and the major element oxide contents and some minor and trace element concentrations were analysed with a PANanalytical WDXRF Axios spectrometer at the Department of Geology at the University of the Free State, South Africa (UFS). The spectrometer works with the SuperQ Version 4 Software and an accelerator voltage of 60 kV in maximum. The PGE and Au contents were analysed by Xstrata and were determined by NiS fire assay pre-concentration, followed by solution inductively coupled plasma mass spectrometry (ICP-MS) using the procedure described by Wilson *et al.*[57] The major element chemistry of selected chromite grains were investigated with the SEM-EDX at the UFS, with a Shimadzu SSX-550 scanning electric microscope using an accelerating voltage of 15 kV. The trace element analyses of chromite grains were carried out by Laser ablation inductively coupled plasma mass spectrometry (LA-ICP-MS) at the School of Earth and Ocean Sciences at the University of Cardiff using a method described by Dare *et al.*[11] Elements analysed by LA-ICP-MS were Ti, V, Co, Ni, Cu, Zn, Ga, As, Sb, Te, Bi, S and the PGE. Only Co, Ga, Co and Ni were quantified in the chromite. The other elements were used to monitor the presence or absence of sulphide inclusions and/or ilmenite exsolution features within the volume sampled by the laser.

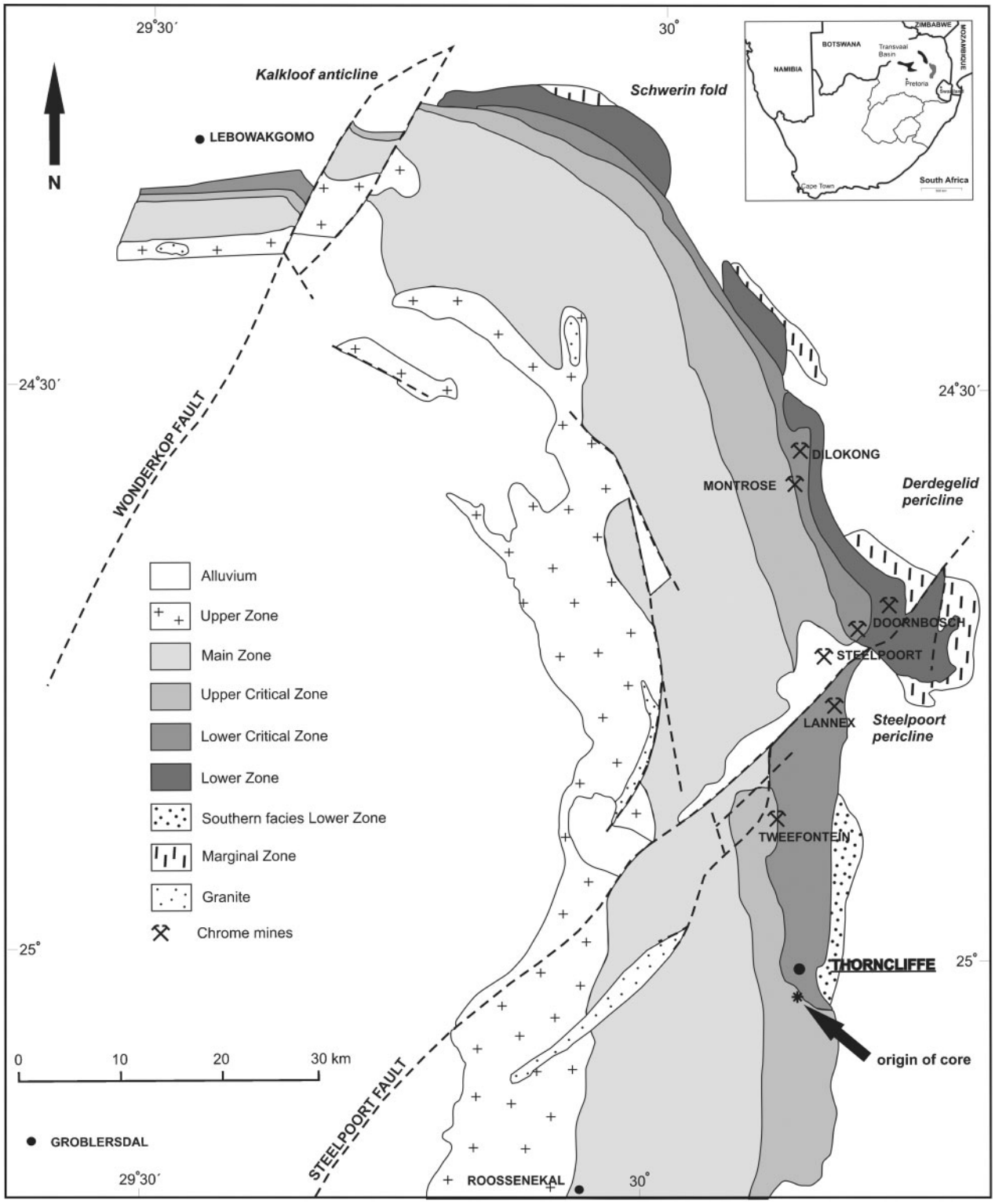

3 Map of the eastern Bushveld complex.[38] The arrow indicates the approximate origin of the core

From SEM-EDX data, the Mg#, the $Cr/(Cr+Fe^{3+})$ and $Cr/(Cr+Al)$ ratios of spinels were calculated, using the spreadsheet of S. Barnes, which is available on the internet.[58]

The mineral liberation analyser (MLA) at Mintek, Johannesburg, was used to gather information about the PGM species occurring in the chromitite layers and their equivalent circle diameter (ECD). The measurements were run at 25 kV using a SPL_DZ MLA measurement and a spot size of 7·6. A 300-fold magnification was used during measurements with a scan speed of 1 μs.

Results

Petrography

The MG chromitites occurring within the LCZ, namely the MG0, MG1, MG2A and MG2B chromitites, are

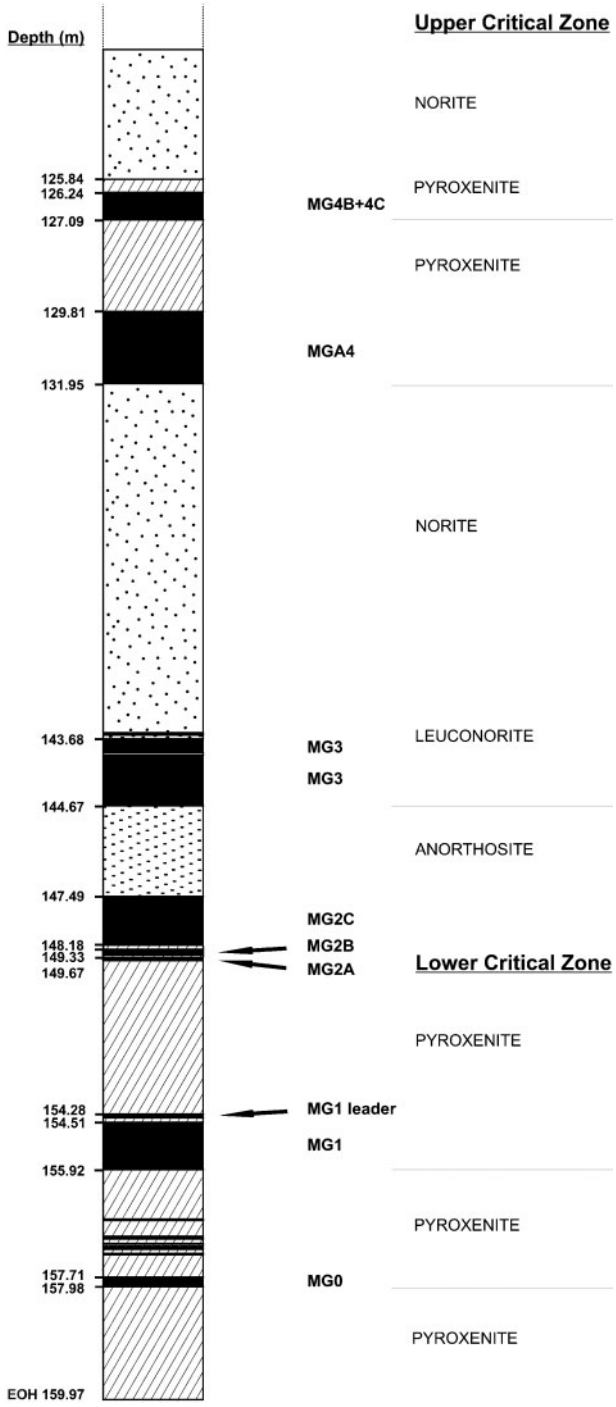

4 Log of the stratigraphy of the Middle Group from core HEX10

hosted by pyroxenites only (Fig. 4) whereas those in the UCZ are sometimes also hosted by anorthositic and noritic cumulates (Fig. 4). In the UCZ only the MG4A to MG4C chromitites are entirely hosted by pyroxenite, whereas the MG2C is sandwiched between a pyroxenitic footwall and anorthositic hanging wall. The MG3 chromitite is hosted by anorthosite, but within the MG3 a thin (6 cm thick) pyroxenitic band occurs.

The amounts of chromite and silicate phases differ in the individual chromitite layers. The chromite content ranges between 66 and 82 modal per cent. The chromite grains are very heterogeneous in size, which ranges between 24 and 584 μm in maximum dimension. The grains are generally rounded and partly euhedral and are cemented by silicate gangue (Fig. 5A). A common feature is the occurrence of annealed grains (Fig. 5B) resulting from postcumulus reactions. The most common shape of these chromite grains is polygonal with grains meeting at triple junctions. Lobate structures are rather rare (Fig. 5C), but probably represent coalescence and annealing of former disseminated and smaller grains (cf. Hulbert and von Gruenewaldt[23]).

Poikilitically enclosed chromite grains in orthopyroxene can often be found in the MG chromitite layers of the UCZ (Fig. 5D), as also have been observed by Hulbert and von Gruenewaldt.[23] Base metal sulphides are very uncommon (<1 vol.-%). Often they are disseminated within the silicate gangue, but also occur as inclusions in chromite grains. Only four different BMS could be determined with the optical microscope: pyrite and chalcopyrite as the major BMS phases, with minor pentlandite and rarely pyrrhotite (Fig. 5E–F). Often, they occur as multi-phase sulphides. von Gruenewaldt *et al.*[51] give BMS data for the MG chromitite layers in the southwestern part of the Bushveld complex (Marikana area). They also observed chalcopyrite as the most abundant BMS, followed by minor pentlandite. Pyrite occurs in small amounts only in their samples, but siegenite is relatively abundant. von Gruenwaldt *et al.*[51] also recorded the absence of pyrrhotite, suggesting post-magmatic modification of the BMS. Except for the fact that pyrite is more abundant in the MG chromitites observed during this study the BMS species appear to be very similar in the western and eastern parts. Siegenite has not been found. Although no microscopic evidence for post-magmatic modification has been observed in the samples of the MG chromitite layers, the presence of pyrite, together with the scarcity of pyrrothite, could emphasise the model of S loss suggested by Naldrett and Lehmann.[34]

Rutile inclusions in chromite grains are very common and vary in size from 1 to 35 μm in size, but most of them are in the range 12 to 20 μm. They occur in all the chromitite layers (Fig. 5G–H).

Platinum-group minerals have only been observed twice by their very high reflectance (Fig. 5I–J), as they are normally too small to be seen with the optical microscope (3–5 μm on average, as pointed out by Merkle[31]). Preliminary observations with the MLA showed the existence of nine different PGM species, based on 286 grains. They are dominated by sulphides, mainly laurite [Ru(Os,Ir)S], braggite [PtPd(Ni)S] and cuprorhodsite [PtRhCuS]. Minor tellurides and arsenides also occur. Except in MG3, laurite is the dominating PGM species within the chromitite layers and is mostly locked in chromite. The majority of the PGM have grain sizes between 2 and 4 equivalent circle diameter (ECD; μm equivalent), followed by grain sizes between 4–6 ECD, and 8–10 ECD. Although the PGM mostly are sulphides, the PGM themselves are not linked to the appearance of BMS, as shown in Fig. 6.

Chromite composition

Chemical data for single chromite grains were obtained by SEM-EDX for the major elements and by LA-ICP-MS for the trace elements. The ternary plot in Fig. 7 illustrates the averaged relative element proportions of

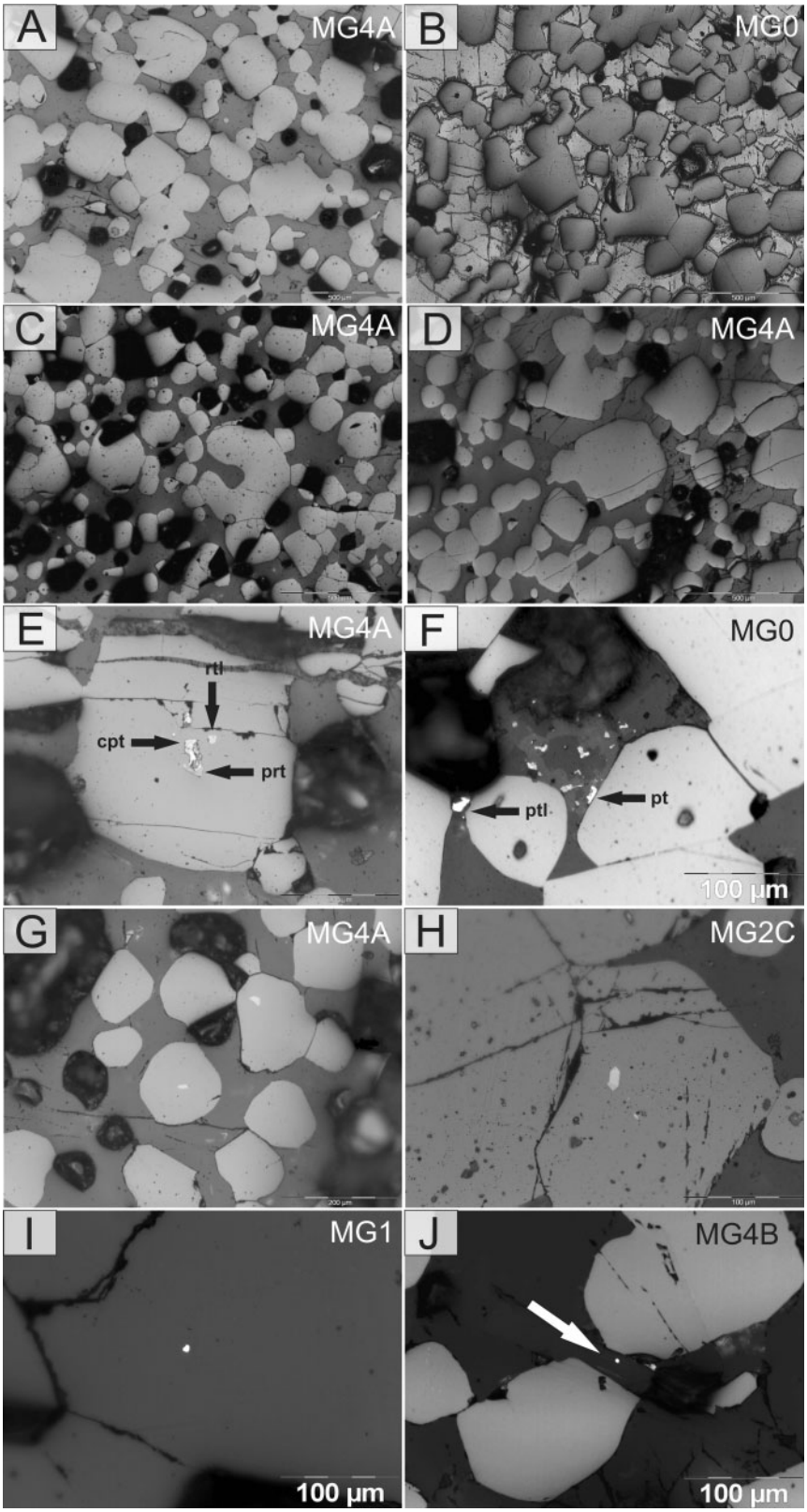

5 Reflected light photomicrographs showing textural features of chromitite layers. The annealing of grains is a very common feature, as can be seen in Fig. 5(A)–(D). BMS hardly can be found. (A) and (B) General overview of chromite grains with heterogeneous grains sizes, hosted by silicate gangue. (C) Lobate structure of chromite, probably caused by sintering and annealing of former individual grains. (D) Poikilitically enclosed chromite grains in pyroxene. (E) Multiphase BMS inclusion in chromite, consisting of chalcopyrite (cpt) and pyrrhotite (prt). As the latter one is very rare, it probably represents part of an unmodified BMS which was trapped within a chromite grain. A rutile inclusion can also be observed. (F) Disseminated BMS in silicate gangue. The major phase is chalcopyrite, accompanied by minor pyrite (pt) and pentlandite (ptl). (G) and (H) Rutile inclusions of different size and shape. (I) PGM inclusion in chromite. (J) PGM inclusion in silicate (indicated by white arrow). Both PGMs could only be observed because of their high birefringence, causing blurry grain boundaries

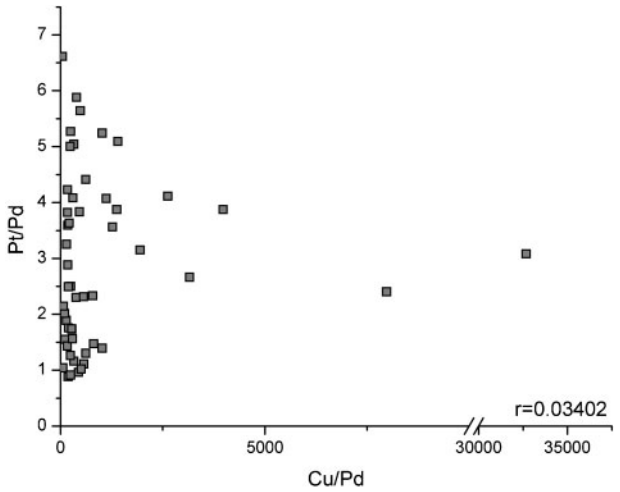

6 Minimally negative correlation* between base metal sulphides and platinum-group elements (*according to the interpretation of Eckey *et al.*[17])

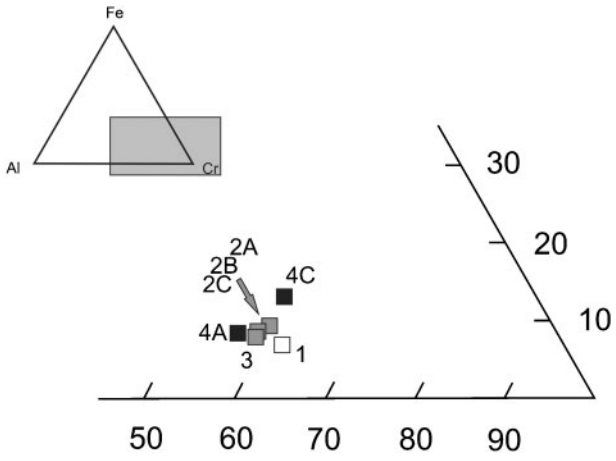

7 Ternary phase diagram Al–Cr–Fe showing average element contents in chromite grains. Numbers represent individual layers. Data see Table 1

Al, Cr and Fe within the chromite grains for each layer. Cr and Al are the major elements in the chromite grains and they behave mirror inverted; as the one increases the other one decreases at the same time. It speaks for mutual substitution. The Fe contents are generally low, but as the Cr_2O_3 content decreases throughout the stratigraphy, the FeO_{tot} content increases.

From SEM-EDX data the Mg#, Cr/(Cr+Fe) and Cr/(Cr+Al) ratios were calculated and included into the whole-rock plots (*see* Table 2 and Fig. 8). The same has been done for TiO_2 and V (*see* Fig. 9). The Mg# and the Cr/(Cr+Al) ratio obtained from single chromite grains are in the range of those from whole-rock data and show the same trends. The values for TiO_2 and V in chromite are higher than the whole-rock data, but follow the same trends. The only exception is the Cr/(Cr+Fe) ratio of the chromite grains, which is approximately two times higher but has the same trend when compared to Cr/(Cr+Fe) ratio from the whole-rock data.

The chromite grains show prominent amounts of Ni, Zn and Co (average values of 1400, 1100 and 400 ppm respectively). Ga contents of 58 ppm on average have also been detected. Ni values are in the range found for other layered intrusions, such as the Bird River Sill, Manitoba, and the Mechanic Intrusion, New Brunswick.[37] Values detected from the other groups of chromitite layers in the Bushveld complex range between 393–1179 ppm and 450–997 ppm for the LG, and 943–1022 ppm and 672–861 ppm for the UG chromitites.[37] The Ni values of the MG chromitites determined during this study are considerably higher. Paktunc and Cabri[37] also determined Zn values in the LG and the UG chromitites, which range between 642–5784 ppm and 426–3923 ppm for the LG and 884–2169 ppm and 981–1657 ppm for the UG chromitite layers. As we determined a Zn concentration of 1100 ppm on average, the Zn contents from chromite grains of the MG chromitite layers fall into the range of the LG. Ga was also determined by Paktunc and Cabri,[37] and the concentrations range between 28–54 ppm for the LG and 70–73 ppm for the UG chromitites. Thus, the Ga concentrations of the MG chromitites we studied

Table 1 Averaged mineral data from the MG chromitite layers for the ternary AFM diagram

		Cr/3+*	Fe/3+*	Al/3+*
HEX10/01	MG4C	0·591	0·130	0·279
HEX10/11	MG4A	0·563	0·084	0·353
HEX10/23	MG3	0·593	0·092	0·315
HEX10/28	MG2C	0·585	0·078	0·337
HEX10/37	MG2B	0·511	0·075	0·289
HEX10/38	MG2A	0·594	0·092	0·315
HEX10/43	MG1	0·620	0·068	0·313

*Calculated with a spreadsheet from S. Barnes[58]

Table 2 Averaged mineral data from the MG chromitite layers for Mg#, the Cr/(Cr+Fe) and Cr/(Cr+Al) ratios

		Mg#*	Cr/(Cr+Fe)*	Cr/(Cr+Al)*	TiO_2, wt-%	V, ppm
HEX10/01	MG4C	0·385	0·679	0·820	1·59	7537
HEX10/05	MG4B	na	na	na	1·11	2664
HEX10/06	MG4A	na	na	na	1·37	6757
HEX10/11	MG4A	0·442	0·615	0·871	1·25	3555
HEX10/23	MG3	0·429	0·653	0·866	1·84	5042
HEX10/28	MG2C	0·435	0·635	0·882	1·20	6129
HEX10/37	MG2B	0·412	0·559	0·764	0·93	3001
HEX10/38	MG2A	0·461	0·654	0·866	1·12	5067
HEX10/43	MG1	0·446	0·665	0·901	0·87	4414
HEX10/50	MG0	na	na	na	0·86	3022

*Calculated with a spreadsheet from S. Barnes[32]

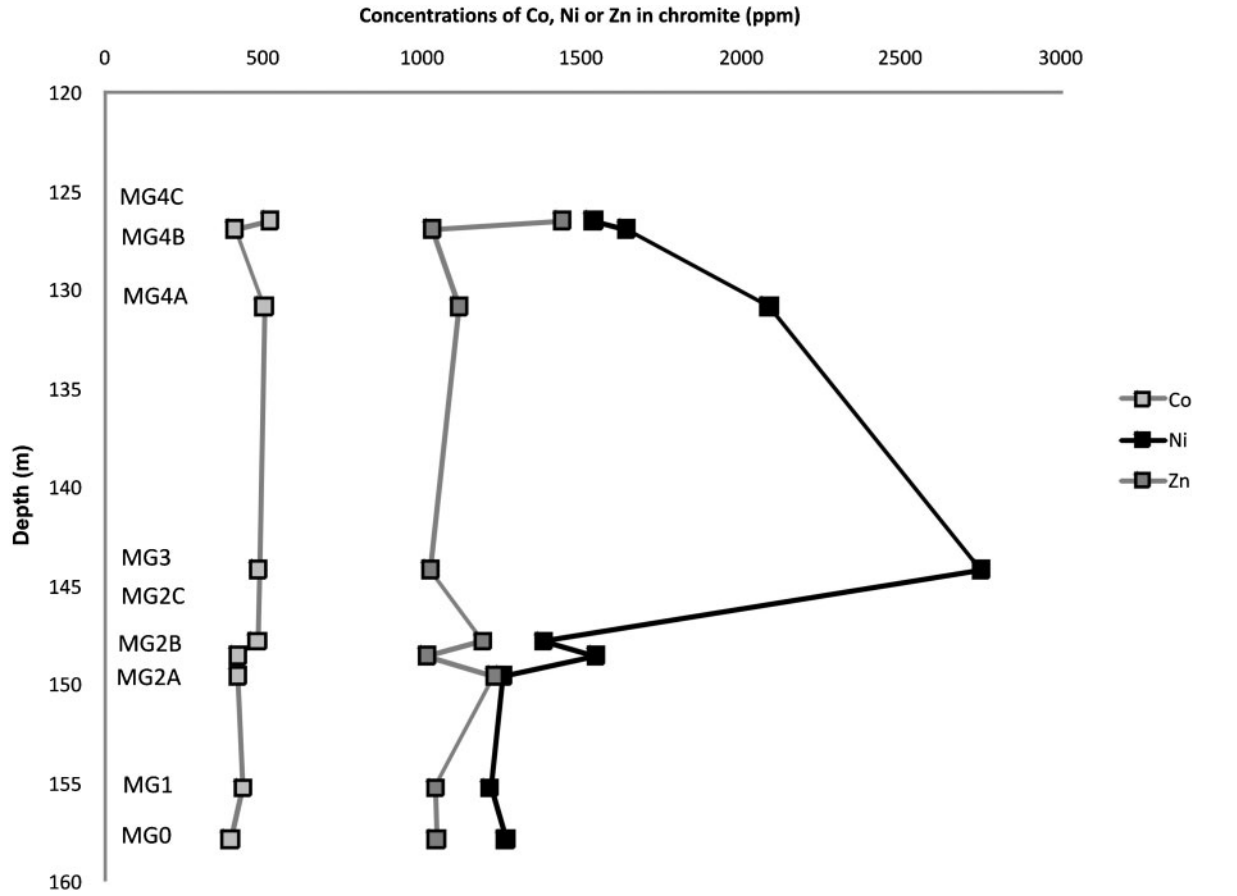

8 Variations in the Co, Ni and Zi concentrations in single chromite grains from individual chromitite layers with stratigraphic height

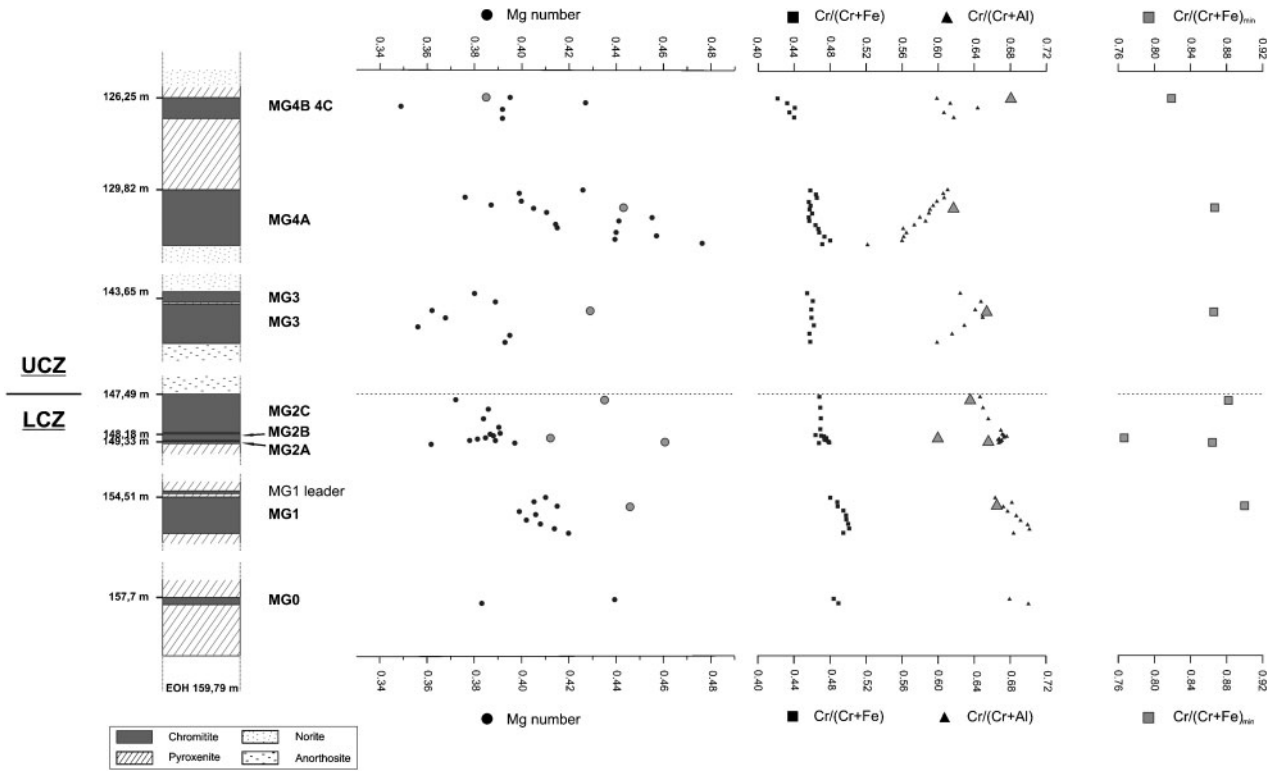

9 Whole-rock data of the chromitite layers of the Middle Group showing the Mg#, the Cr/(Cr+Fe) and the Cr/(Cr+Al) ratios (black symbols). Grey symbols illustrate mineral chromite data gathered with the SEM-EDX

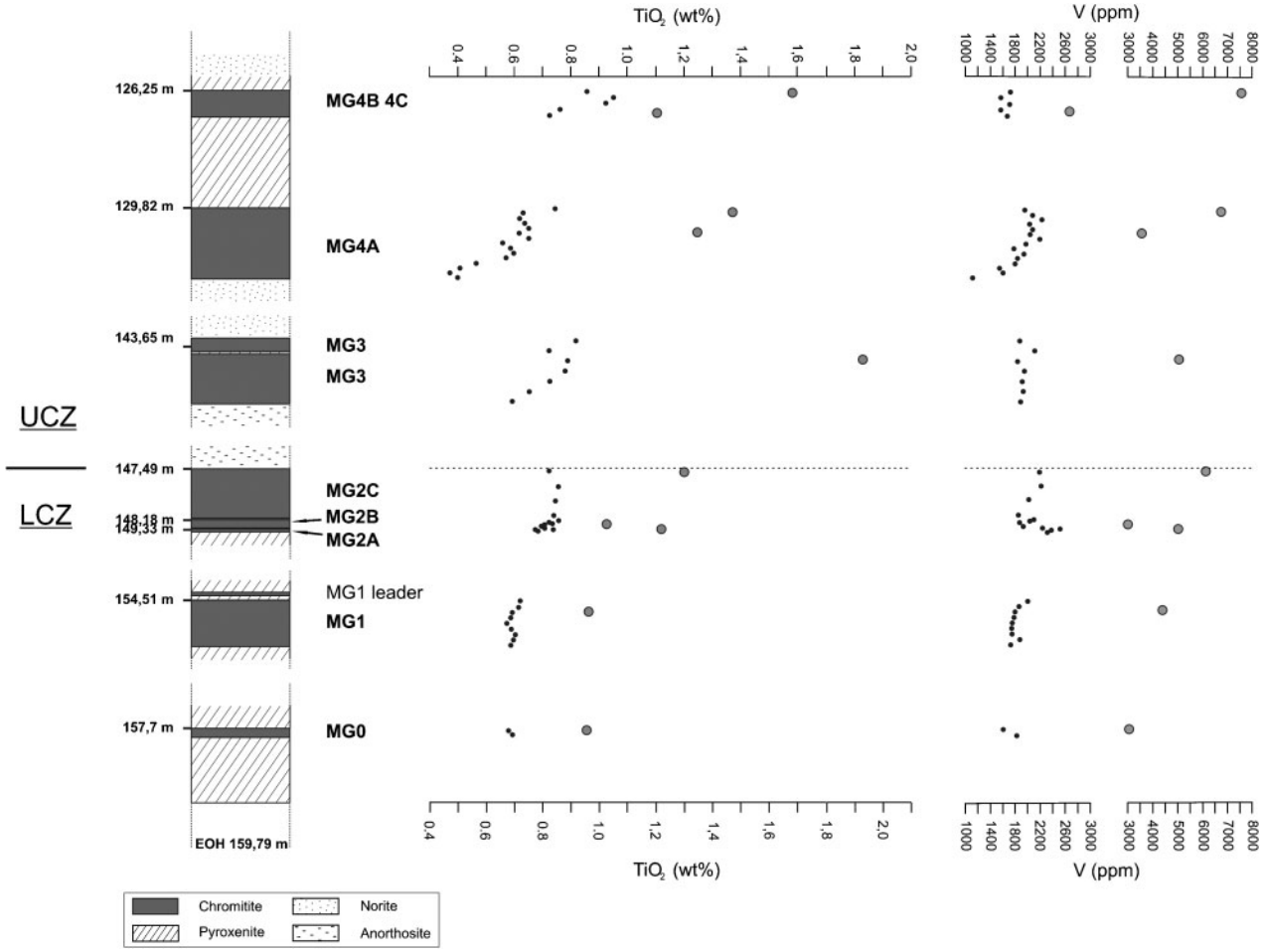

10 Whole-rock data for the chromitite layers of the MG showing the TiO_2 and V contents plotted versus the stratigraphy (small black points). Grey symbols are mineral data from chromite grains gathered with the LA-ICP-MS

(58 ppm) fall into the middle of LG and UG values and describe an increasing trend through the stratigraphy of the CZ.

Although all the above mentioned elements also occur in sulphides, their distribution in the chromitite layers is mainly chromite controlled and they occur in solid solution in chromite grains as we determined with the LA-ICP-MS. Co and Zn concentrations show similar variations with stratigraphic height (Fig. 8), which are the inverse of the Ni concentrations. For data see Table 3.

Table 3 Co, Ni and Zn concentrations in chromite grains obtained with the LA-ICP-MS

	Av. depth, m	Co, ppm	Ni, ppm	Zn, ppm
MG4C	126·50	519·27	1530·00	1433·18
MG4B	126·92	408·77	1634·22	1025·78
MG4A	130·86	499·21	2080·77	1110·99
MG3	144·17	482·43	2744·64	1019·15
MG2C	147·79	479·37	1375·22	1183·11
MG2B	148·54	419·50	1538·22	1010·12
MG2A	149·56	418·24	1247·27	1220·26
MG1	155·23	433·03	1207·33	1037·16
MG0	157·85	394·63	1256·00	1039·52

Whole rock geochemistry

The Cr_2O_3 content within the layers decreases constantly from the bottom to the top of the MG. At the same time, the SiO_2, Al_2O_3 and CaO contents are increasing and the FeO_{tot} and MnO contents decrease.

A variation in the geochemistry is obvious at the boundary LCZ/UCZ (between MG2B and MG2C), where the major element oxide contents show a change. Analytical data for the whole-rock Mg#, the Cr/(Cr+Fe) Cr/(Cr+Al) and Sr/Ca ratios and selected elements (TiO_2, V, Cu) are summarised in Table 4 and Figs. 9–11.

The Mg# decreases from bottom (MG0) to top of the MG3 unit (from 0·4 to 0·35 on average), in a pattern typical of fractional crystallisation. The bottom of MG4A shows a change to a very much more primitive composition (Mg#=0·48), after which the Mg# decreases again to the top of the succession studied. The increase in the Mg# within the chromitite layers may result from an injection of primitive magma causing enrichment in MgO of the melt.

The Cr/(Cr+Fe) ratio decreases in general from bottom to top of the core, but also within each chromitite layer. As in the Mg#, there is an increase in Cr/(Cr+Fe) at the bottom of the MG4A, but of a much slighter magnitude. The general change in the ratio may be explained by the normal evolution of the

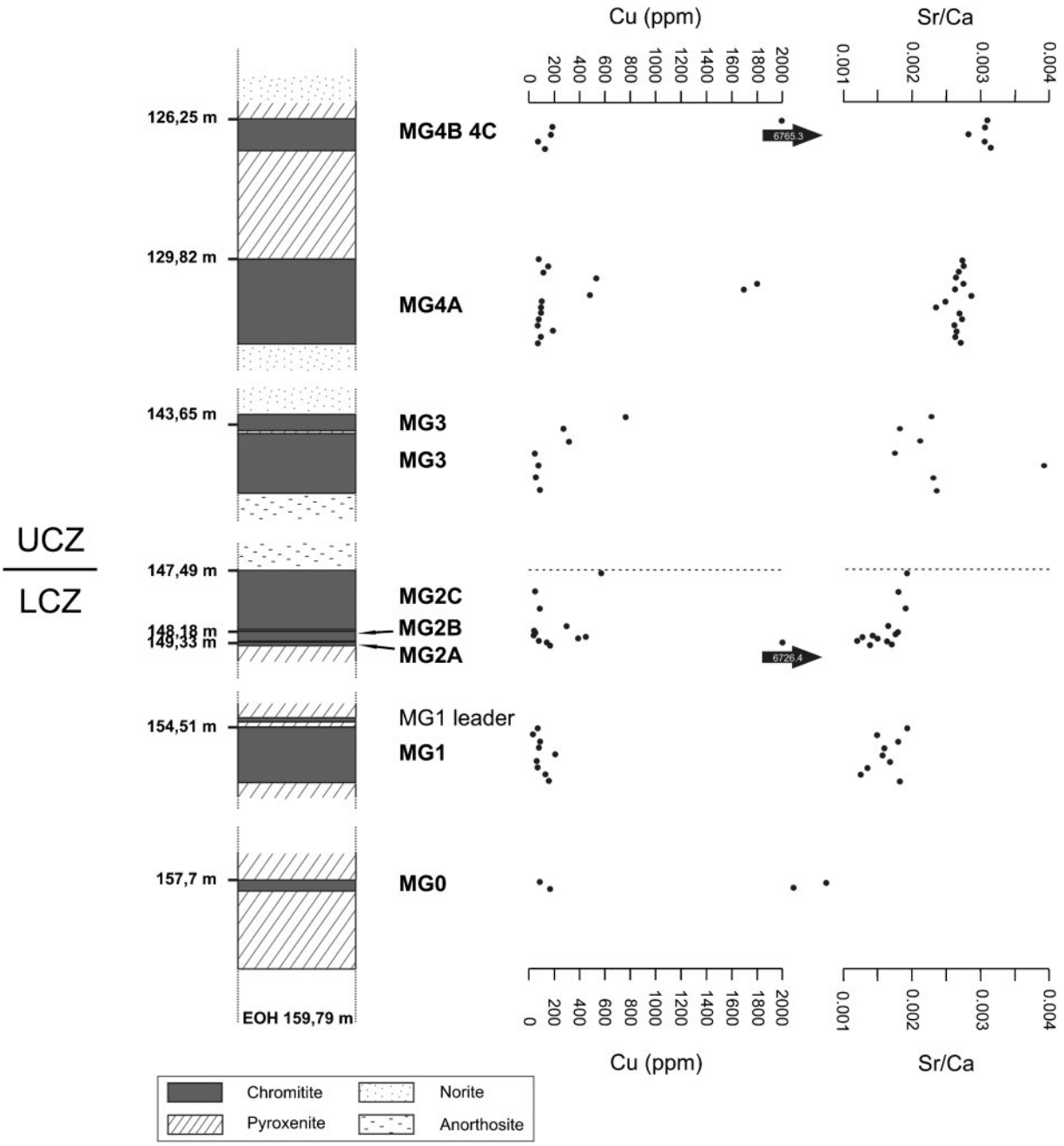

11 Whole-rock data for the chromitite layers of the MG showing the Cu content and the Sr/Ca ratio plotted versus the stratigraphy. Black arrows indicate high peaks in the Cu concentrations; the values are inserted into the arrows

melt, as the melt gets relatively depleted in Cr^{3+} over Fe^{3+}, the latter which is slightly less compatible in the chromite lattice and those of the co-precipitating silicate phases.

Although in general decreasing within the stratigraphic column from the MG0 to the MG4A, the Cr/(Cr+Al) ratio in the individual chromitite layers first increases and then decreases, as plagioclase joins pyroxene on the solidus. At the bottom of the MG4A the lowest value of the Cr/(Cr+Al) ratio is associated with the highest Mg#. In general, the Cr/(Cr+Al) ratio and the Mg# behave mirror-inverted; as one increases the other parameter decreases at the same time.

The TiO_2 and V concentrations increase from the MG0 to the MG4C and also increases within each chromitite layer (Fig. 10), which can be explained by the relative incompatibility of these elements in the chromite lattice. The re-setting of the V and TiO_2 contents at the bottom of MG4A to values below (i.e. more primitive) than that of the MG0 chromitite matches with the high Mg# and Cr/(Cr+Fe) ratio and the low Cr/(Cr+Al) ratio at this point.

The advancing melt evolution is well illustrated by the trend of the Sr (ppm)/Ca (ppm) ratio that shows a strong enrichment through the stratigraphy (Fig. 11), representing the appearance of plagioclase and its changing composition to less anorthitic varieties.

As the Cu content of the cumulates in the UCZ is controlled by the presence of sulphides, Cu can be used as an indicator of the sulphide abundance.[40] Scoon and Teigler[40] calculated Cu background values for the chromitite layers below the UG2 at Union and Brits in the western Bushveld complex, including the Lower Group (LG), the MG and the UG1. The background ranges between 12 and 20 ppm on average. The Cu values observed for the MG chromitite layers in this study range between 34·4 and 6765 ppm, but most of the values fall between 50 and 200 ppm. Only four samples show extremely high Cu values with more than 1500 ppm. Obviously, the background values for Cu are generally higher in the eastern than in the western Bushveld complex as determined by Scoon and Teigler,[40] and probably this is a particular feature of the eastern limb. Whether compared to the background values for the western or the eastern Bushveld complex, all the MG chromitite layers are enriched in Cu, although the appearance of visible BMS is extremely rare (probably <1 vol.-%).

Preliminary whole-rock analyses for S by Eltra CS 800 Double Dual Range indicated values between 24 to 108 ppm. As the Cu/S ratios show (Table 5), no correlation exists between Cu and S. Except for the MG4A chromitite layer the whole-rock Cu/S ratio also

Table 4 Whole rock data for Mg#, the Cr/(Cr+Fe) and Cr/(Cr+Al) ratios, some minor and trace elements and the Cr/Ca ratio

		Mg#*	Cr/(Cr+Fe)*	Cr/(Cr+Al)*	TiO_2, wt-%	V, ppm	Cu, ppm	Sr/Ca
HEX10/01	MG4C	0·395	0·599	0·423	0·858	1719	6765	0·003
HEX10/02		0·427	0·614	0·433	0·951	1566	187	0·003
HEX10/03		0·349	0·644	0·441	0·926	1716	175	0·003
HEX10/04	MG4B	0·392	0·607	0·436	0·763	1565	73	0·003
HEX10/05		0·392	0·618	0·441	0·725	1668	126	0·003
HEX10/06	MG4A	0·426	0·611	0·459	0·744	1958	83	0·003
HEX10/07		0·399	0·606	0·465	0·630	2088	151	0·003
HEX10/08		0·376	0·607	0·466	0·619	2244	122	0·003
HEX10/09		0·400	0·599	0·457	0·637	2039	533	0·003
HEX10/10		0·387	0·595	0·459	0·651	2082	1800	0·003
HEX10/11		0·405	0·592	0·458	0·619	2060	1688	0·003
HEX10/12		0·410	0·590	0·461	0·651	2206	481	0·003
HEX10/13		0·455	0·580	0·457	0·559	1972	96	0·002
HEX10/14		0·441	0·587	0·458	0·587	1788	98	0·002
HEX10/15		0·414	0·574	0·465	0·598	1949	94	0·003
HEX10/16		0·415	0·561	0·468	0·571	1846	78	0·003
HEX10/17		0·440	0·566	0·469	0·463	1808	79	0·003
HEX10/18		0·457	0·562	0·475	0·408	1555	188	0·003
HEX10/19		0·439	0·560	0·481	0·371	1605	94	0·003
HEX10/20		0·476	0·522	0·472	0·398	1121	68	0·003
HEX10/21	MG3	0·380	0·625	0·455	0·819	1874	763	0·002
HEX10/22		0·389	0·648	0·462	0·724	2122	264	0·002
HEX10/23		0·362	0·642	0·460	0·789	1842	310	0·002
HEX10/24		0·368	0·650	0·460	0·781	1949	47	0·002
HEX10/25		0·356	0·630	0·463	0·727	1916	73	0·004
HEX10/26		0·395	0·616	0·458	0·652	1932	57	0·002
HEX10/27		0·393	0·599	0·459	0·593	1891	88	0·002
HEX10/28	MG2C	0·372	0·647	0·469	0·722	2196	577	0·002
HEX10/29		0·386	0·650	0·470	0·756	2220	52	0·002
HEX10/30		0·384	0·656	0·471	0·745	2020	89	0·002
HEX10/31		0·391	0·670	0·470	0·740	1855	307	0·002
HEX10/32	MG2B	0·387	0·672	0·465	0·756	2101	38	0·002
HEX10/33		0·388	0·673	0·471	0·724	2040	52	0·002
HEX10/34		0·385	0·677	0·474	0·733	1870	40	0·001
HEX10/35		0·381	0·673	0·477	0·707	1872	452	0·001
HEX10/36		0·389	0·668	0·475	0·697	1936	394	0·001
HEX10/37		0·377	0·667	0·476	0·706	2243	79	0·001
HEX10/38	MG2A	0·378	0·671	0·479	0·739	2529	142	0·002
HEX10/39		0·397	0·670	0·480	0·676	2378	6426	0·002
HEX10/40		0·362	0·668	0·468	0·684	2319	175	0·001
HEX10/41	MG1	0·410	0·664	0·481	0·620	2007	70	0·002
HEX10/42		0·405	0·682	0·489	0·614	1869	34	0·001
HEX10/43		0·415	0·673	0·489	0·593	1801	89	0·002
HEX10/44		0·399	0·678	0·496	0·587	1785	78	0·002
HEX10/45		0·406	0·687	0·499	0·574	1758	209	0·002
HEX10/46		0·402	0·692	0·499	0·588	1746	64	0·002
HEX10/47		0·408	0·700	0·501	0·604	1755	65	0·001
HEX10/48		0·414	0·702	0·502	0·599	1877	129	0·001
HEX10/49		0·420	0·684	0·496	0·588	1731	154	0·002
HEX10/50	MG0	0·439	0·680	0·485	0·581	1614	83	0·001
HEX10/51		0·383	0·700	0·490	0·593	1826	167	0·001

*Calculated with a spreadsheet from S. Barnes[58]

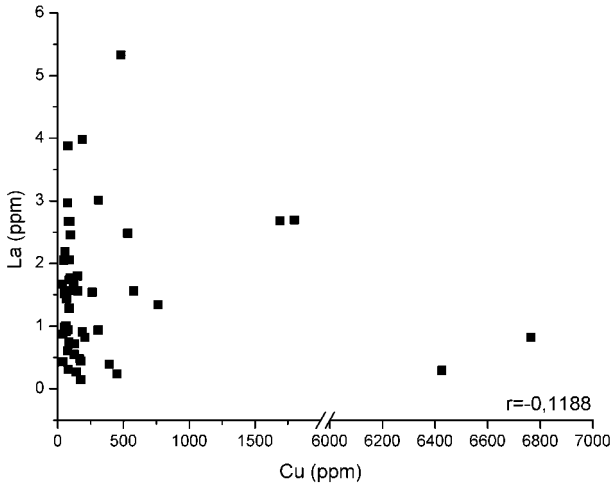

12 Cu concentrations of individual chromitite samples plotted against La to show, that the high Cu values of the MG chromitites are not concentrated in trapped melt

exceeds the Cu/S for chalcopyrite (2:1), which implicates the presence of more Cu than can be precipitated in chalcopyrite. Figure 12 presents a plot of La versus Cu demonstrating that the high Cu values in the MG chromitites can also not be ascribed to being enriched in trapped melt.

Table 5 Whole rock data for the Cu/S ratio of selected chromitite samples

		Cu/S
HEX10/02	MG4C	2·15
HEX10/04	MG4B	2·61
HEX10/08	MG4A	1·47
HEX10/14		1·34
HEX10/15		1·38
HEX10/19		1·54
HEX10/21	MG3	7·06
HEX10/22		3·38
HEX10/27		1·19
HEX10/30	MG2C	2·22
HEX10/31		5·48
HEX10/32	MG2B	0·64
HEX10/36		16·42
HEX10/38	MG2A	4·16
HEX10/39		146·05
HEX10/41	MG1	1·47
HEX10/43		2·96
HEX10/49		2·38
HEX10/51	MG0	4·39

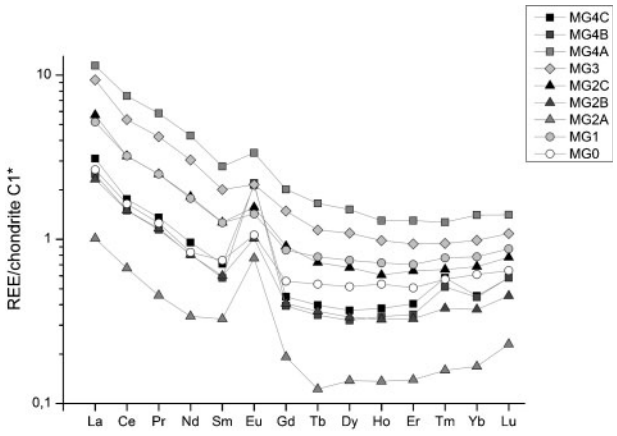

13 Whole-rock REE patterns of the chromitite layers. *CI normalising values from Lodders[29]

The CI normalised REE patterns of the chromitite layers shown in Fig. 13 demonstrate the typical fractionation of light rare earth elements (LREE) versus the heavy ones (HREE) that can be expected from a mantle derived mafic melt (Table 6). With a value of 0·731, obtained with the $(La_N/Yb_N)/Ce_N$ ratio, the REE are only slightly fractionated. There is only little enrichment of the LREE ($Ce/Sm_N=1·54$) and thus differ greatly from REE fractionation in the silicate rocks of the CZ ($Ce/Sm_N=3·65$), as determined by Maier and Barnes.[30] The HREE are strongly fractionated ($Tb/Yb_N=0·03$), exactly reverse to data from silicate rocks (Maier and Barnes[30]), which show almost no fractionation of the HREE. In general, the REE are incompatible with chromite, which is the major cumulus phase, but behave also as incompatible elements towards intercumulus phases such as pyroxene and plagioclase. An exception is Eu, which is compatible with plagioclase.[47]

A positive Eu-anomaly of various amplitudes within all the layers is observed, and is due to the appearance of plagioclase that is interstitial only in the LCZ. The MG4B and MG4C chromitite layers have the most positive anomalies, saying that plagioclase is the major intercumulus phase within these chromitite layers (Eu/Eu*=4·596 or 3·805 respectively). MG1 and MG3 show only slight positive Eu anomalies (Eu/Eu*=1·371 or 1·248 respectively).

With regard to CI values for the REE, the MG3 and MG4A seem to be the chromitite layers with the most

Table 6 Averaged REE data CI normalised after Lodders[29]

	La	Ce	Pr	Nd	Sm	Eu	Gd	Tb	Dy	Ho	Er	Tm	Yb	Lu
MG4C	3·102	1·758	1·358	0·956	0·709	2·142	0·447	0·398	0·369	0·380	0·405	0·584	0·452	0·583
MG4B	2·485	1·498	1·146	0·810	0·582	2·197	0·393	0·345	0·320	0·339	0·348	0·513	0·444	0·583
MG4A	11·420	7·462	5·850	4·277	2·780	3·359	2·012	1·654	1·519	1·299	1·299	1·270	1·406	1·411
MG3	9·338	5·362	4·214	3·042	2·008	2·155	1·485	1·139	1·090	0·982	0·938	0·944	0·987	1·084
MG2C	5·714	3·209	2·494	1·818	1·267	1·565	0·909	0·722	0·673	0·607	0·642	0·654	0·682	0·776
MG2B	2·318	1·503	1·164	0·806	0·599	1·010	0·407	0·364	0·336	0·325	0·328	0·380	0·374	0·453
MG2A	1·012	0·667	0·455	0·339	0·327	0·767	0·192	0·123	0·138	0·137	0·140	0·159	0·168	0·230
MG1	5·180	3·218	2·494	1·778	1·263	1·429	0·860	0·782	0·744	0·717	0·701	0·771	0·782	0·874
MG0	2·651	1·646	1·256	0·832	0·745	1·062	0·556	0·534	0·515	0·533	0·506	0·571	0·611	0·645

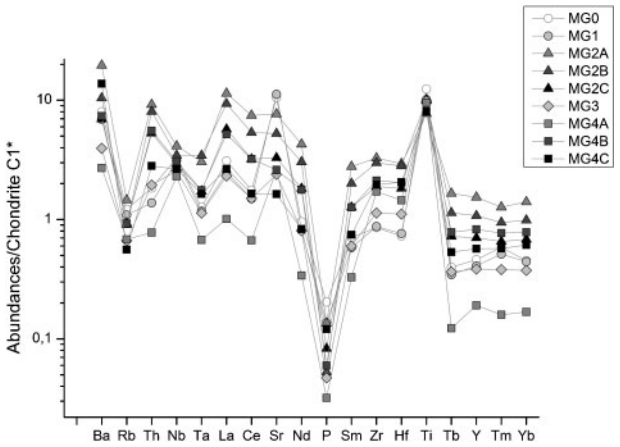

14 Multi-element diagram for average whole-rock data of the MG chromitite layers normalised to CI chondrite[29]

evolved REE content, as would be expected from a fractional crystallisation trend. Compared to the other chromitite layers, the MG2A is relatively depleted in REE.

The multi-element CI normalised 'spider' diagram shows a few distinctive positive and negative anomalies (Fig. 14 and Table 7). The negative Rb anomaly coincides with the positive Sr values, the latter one increasing to the top of the stratigraphy and reflecting the increasing occurrence of more evolved plagioclase.

Ti, Nb and Ta concentrations are controlled by the presence of accessory minerals such as ilmenite, rutile or sphene. Due to compatibility in the chromite lattice, the Ti^{4+} (ionic radius: 0·605 Å)[59] is less compatible than the Cr^{3+} (ionic radius Cr^{3+}: 0·52 Å),[59] but compatible in the silicates. As it gets trapped in chromite, Ti^{4+} starts to crystallise as rutile, forming an inclusion in chromite. Distinctive positive Nb anomalies, which also should be rutile controlled, only exist for MG2A, MG2B, MG4B and MG4C.

The strong negative P peaks are due to the absence of apatite, suggesting that apatite is not a major host for the REE. The absence of further REE concentrating phases, i.e. allanite, monazite and epidote, implies that the REE distribution of the MG chromitites probably is controlled by plagioclase.

PGE data

In this section, we will follow the definition of Davies and Tredoux,[12] who separated the PGE into two groups according to their melt temperature: the high-temperature PGE (HT-PGE: Os, Ir, Ru), and the low-temperature PGE (LT-PGE: Rh, Pt and Pd). The data used for the plots are summarised in Table 8.

In Fig. 15, the Pt/Ir ratio has been plotted against the stratigraphy. These two elements (Pt and Ir) have been chosen to each represent one of the PGE groups described above. The (Pt+Pd)/(Os+Ir) ratio shows exactly the same trend, indicating that the variations in Pt or Ir alone are representative of the two groups. Generally, the ratio shows an increasing trend, indicating that the LT-PGE content increases relative to that of the HT-PGE. There are a few anomalies: in MG2A and again the middle of MG4A, the content of the LT-PGE strongly increases relative to the HT-PGE.

Plots of PGE/Cr over PGE show a strong negative correlation between the whole-rock Cr and PGE contents (Fig. 16). This is true for both the HT-PGE and the LT-PGE. The Cr/(Os+Ir) or Cr/(Pt+Pd) ratios in Fig. 15 respectively, also illustrate this relationship at least up to MG3. Within MG4A-4C the PGE content decreases as the Cr content further decreases. As for example MG2A has the highest PGE content but not the highest Cr_2O_3 concentration, higher PGE contents are not necessarily linked to a higher Cr_2O_3 concentration.

Looking at the CI normalised PGE patterns of the MG chromitite layers, it is obvious that they are similar to the one of the UG2 (Fig. 17, Table 9). All the MG layers show the Rh anomaly which is typically associated with chromitite layers.[1] Compared to the UG2 pattern, the patterns of the other chromitite layers show low Pd values. This is probably due to alteration. The patterns of the MG chromitite layers have flatter slopes compared to the UG2, as they also show higher Os and Ru values for MG2A, MG2C, MG3 and MG4A. Thus, the Middle Group chromitites are less depleted in HT-PGE relative to LT-PGE, than would be expected from their major mineralogy.

Discussion and conclusions

The MG chromitites from bottom (MG0) to top (MG4C) are characterised by progressive melt evolution, which is depicted in the mineral data and the whole-rock geochemistry. Cryptic variations of chromite compositions are expressed by changing Mg#, Cr/(Cr+Fe) and Cr/(Cr+Al) rations and TiO_2 and V concentrations (*see* Figs. 8 and 9). The chromite composition seems to be influenced by the

Table 7 Averaged whole-rock data for the multi-element plot normalised to CI (after Lodders[28])

	Ba	Rb	Th	Nb	Ta	La	Ce	Sr	Nd	P	Sm	Zr	Hf	Ti	Tb	Y	Tm	Yb
MG4C	1·217	1·834	3·297	1·268	3·102	1·758	10·498	0·956	0·203	0·709	0·855	0·727	12·418	0·398	0·461	0·584	0·452	1·217
MG4B	1·091	1·380	3·130	1·174	2·485	1·498	11·205	0·810	0·136	0·582	0·873	0·764	10·136	0·345	0·409	0·513	0·444	1·091
MG4A	1·458	9·199	4·136	3·049	11·420	7·462	7·663	4·277	0·135	2·780	3·271	2·938	7·725	1·654	1·537	1·270	1·406	1·458
MG3	0·905	8·038	3·449	3·440	9·338	5·362	5·258	3·042	0·053	2·008	2·987	2·811	9·896	1·139	1·076	0·944	0·987	0·905
MG2C	0·933	5·284	2·935	1·728	5·714	3·209	3·295	1·818	0·083	1·267	1·891	1·824	10·089	0·722	0·702	0·654	0·682	0·933
MG2B	0·666	1·950	2·559	1·131	2·318	1·503	2·397	0·806	0·047	0·599	1·133	1·108	9·816	0·364	0·384	0·380	0·374	0·666
MG2A	0·681	0·778	2·303	0·674	1·012	0·667	2·601	0·339	0·032	0·327	1·718	1·452	9·526	0·123	0·191	0·159	0·168	0·681
MG1	0·925	5·554	3·072	1·759	5·180	3·218	2·608	1·778	0·060	1·263	2·120	2·040	8·125	0·782	0·827	0·771	0·782	0·925
MG0	0·560	2·813	2·646	1·638	2·651	1·646	1·634	0·832	0·120	0·745	1·955	2·062	7·992	0·534	0·569	0·571	0·611	0·560

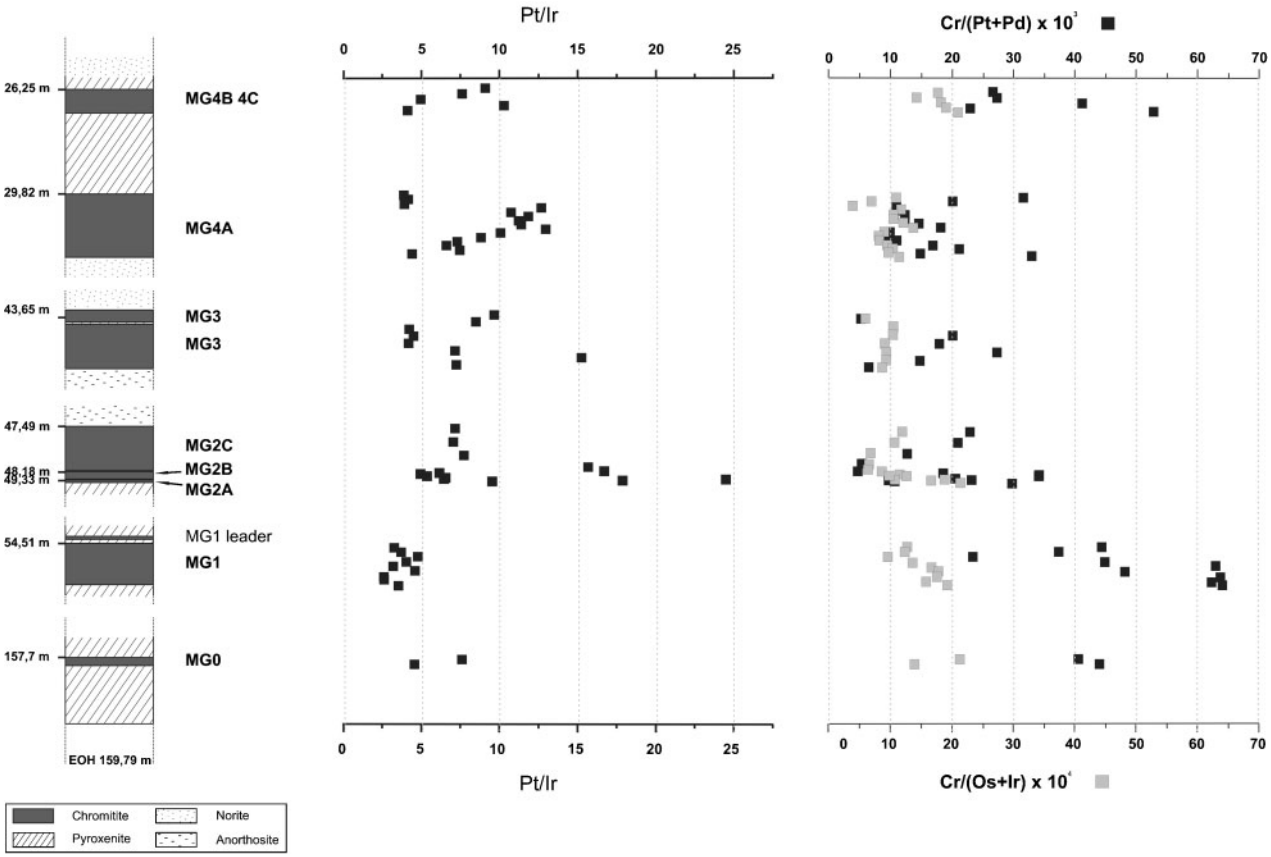

15 Relationship between the HT-PGE and LT-PGE (represented by the ratio Pt/Ir) and between the HT-PGE (Os+Ir) and LT-PGE (Pt+Pd) in relation to the chrome content, plotted versus the stratigraphy

co-precipitating silicate phase. This is especially well illustrated by the Cr/(Cr+Al) ratio that decreases as long as the chromitite layers are hosted by pyroxenite. The increase in the ratio for chromite grains in MG3 is due to the competition for Al between the plagioclase in the anorthositic and noritic host rocks and the chromite grains within the MG3.

The decreasing Mg# from the MG0 to the MG3 chromitite generally illustrates a trend typical for fractional crystallisation. Decreasing Mg# in spinels is normally attributed to decreasing crystallisation temperature,[19] thus an increase in Mg# could imply an increase in temperature, as it is the case for the MG4A chromitite. This increase is most likely explained by addition of hot (and more primitive) magma to the residual melt within the magma chamber. This furthermore would also explain the drop in the Cr/Cr+Al) and the increasing Cr/(Cr+Fe) ratios within the chromite grains of MG4A, as with this addition the 'new' mixed melt is more primitive than the residual one. The resetting of the V and TiO_2 contents at the bottom of MG4A to values below (i.e. more primitive) than that of the MG0 chromitite matches with the high Mg# and Cr/(Cr+Fe) ratio and the low Cr/(Cr+Al) ratio at this point and lends further support to the possibility of an influx of new magma.

The incompatibility of Ti^{4+} in the chromite lattice causes enrichment in TiO_2 in chromite grains from chromitite layers further up in the stratigraphy, illustrated by the advancing trend from MG0 to MG3. With progressive melt evolution Ti^{4+} is 'forced' into the chromite lattice and thus an increasing TiO_2 content could be used as an indicator for melt evolution. The drop of the TiO_2 concentration at the bottom of MG4A is another observation which strongly suggests a new influx of primitive magma resetting the melt composition by magma mixing. This offers further support for the model of Kinnaird *et al.*,[25] who determined the initial Sr ratios of the chromitite layers of the CZ by using interstitial or cumulus plagioclases. The value they obtained from interstitial plagioclases from the MG4 chromitite layer (Sr_i=0·70569) of borehole AM38 shows a lower Sr_i than samples below or above the MG4.

As chromite with more than 60 modal per cent is the major phase, the bulk geochemistry of the chromitite layers is mainly controlled by chromite. The whole-rock data therefore show the same trends as those that have been observed for the chromite grains. This especially includes the strong changes of the Mg# and the Cr/(Cr+Fe) and Cr/(Cr+Al) ratios at the bottom of MG4A, indicating magma addition and mixing. The general progressive melt evolution in the MG is furthermore illustrated by the increasing Sr/Ca ratio. It exemplifies the advancing plagioclase content within the chromitite layers and the development of more evolved compositions.

With LA-ICP-MS it could be shown that high Ni concentrations within the chromitite layers are due to Ni being in solid solution in chromite grains, whereas for

high Cu values no adequate explanation could be found. Furthermore, Cu is concentrated neither in trapped melt nor in chalcopyrite, as could have been shown with La/Cu and Cu/S ratios. On that basis, the S-loss model by Naldrett and Lehmann[34] is not applicable for the sulphide (and PGE) mineralisation of the MG chromitite layers and the Cu concentration phase has still to be found and requires further research.

The lower MG layers are enriched in the HT-PGE relative to the LT-PGE, which we interpret as the presence of high melt temperatures and therefore more primitive magma. Besides any geochemical control exerted by the co-crystallising phases, temperature could thus also be responsible for PGE fractionation. The HT-PGE would then preferentially be concentrated in chromitite layers further down in the stratigraphy. This seems to be the case for the CZ as a whole, because the overlying UG2 and Merensky reefs are enriched in the LT-PGE relative to the MG layers. Within the MG chromitite layers, the Pt/Ir ratio shows that the lowermost chromitite layers (MG0 and MG1) have the highest HT-PGE concentrations relative to the LT-PGE content and could be therefore had derived from hotter hybrid liquids than the chromitite layers above them. At the bottom of the MG4A the Pt/Ir ratio shows a relatively low value, also due to the enrichment of HT-PGE relative to LT-PGE. With the whole-rock and mineral data discussed above, it could be an indication

Table 8 Whole-rock PGE data and several ratios used for plots

		HT-PGE	LT-PGE	HT-PGE/Cr	LT-PGE/Cr	Cu/Pd	Pt/Pd	Pt/Ir	Cr/(Pt+Pd)	Cr/(Os+Ir)
HEX10/01	MG4C	474	1034	$2{\cdot}099\times10^{-6}$	$4{\cdot}58\times10^{-6}$	32 683	3·08	9·10	267 508	1 777 767
HEX10/02		615	1060	$2{\cdot}644\times10^{-6}$	$4{\cdot}557\times10^{-6}$	1120	4·07	7·63	274 969	1 435 950
HEX10/03		606	791	$2{\cdot}253\times10^{-6}$	$2{\cdot}941\times10^{-6}$	618	1·30	4·92	412 527	1 829 714
HEX10/04	MG4B	447	1231	$1{\cdot}892\times10^{-6}$	$5{\cdot}21\times10^{-6}$	249	2·50	10·32	230 300	1 905 547
HEX10/05		450	574	$1{\cdot}826\times10^{-6}$	$2{\cdot}329\times10^{-6}$	572	1·11	4·15	528 897	2 106 547
HEX10/06	MG4A	770	1022	$2{\cdot}998\times10^{-6}$	$3{\cdot}979\times10^{-6}$	277	1·73	3·83	314 743	1 083 672
HEX10/07		1293	1622	$4{\cdot}906\times10^{-6}$	$6{\cdot}155\times10^{-6}$	381	2·30	4·11	200 411	675 744
HEX10/08		2367	3029	$8{\cdot}926\times10^{-6}$	$1{\cdot}142\times10^{-5}$	144	1·89	3·87	108 366	374 538
HEX10/09		760	2724	$3{\cdot}035\times10^{-6}$	$1{\cdot}088\times10^{-5}$	786	2·33	12·62	110 995	1 164 677
HEX10/10		803	2449	$3{\cdot}157\times10^{-6}$	$9{\cdot}627\times10^{-6}$	3158	2·66	10·69	121 835	1 038 331
HEX10/11		801	2330	$3{\cdot}163\times10^{-6}$	$9{\cdot}202\times10^{-6}$	3982	3·87	11·79	122 738	1 033 502
HEX10/12		628	1899	$2{\cdot}545\times10^{-6}$	$7{\cdot}695\times10^{-6}$	1379	3·87	11·17	145 164	1 192 167
HEX10/13		535	1463	$2{\cdot}263\times10^{-6}$	$6{\cdot}187\times10^{-6}$	487	5·64	11·34	180 776	1 358 939
HEX10/14		736	2699	$3{\cdot}055\times10^{-6}$	$1{\cdot}12\times10^{-5}$	249	5·27	12·89	97 587	879 349
HEX10/15		763	2891	$3{\cdot}068\times10^{-6}$	$1{\cdot}162\times10^{-5}$	172	3·82	10·01	95 073	794 608
HEX10/16		759	2495	$3{\cdot}096\times10^{-6}$	$1{\cdot}018\times10^{-5}$	149	3·25	8·77	109 140	809 004
HEX10/17		685	1628	$2{\cdot}814\times10^{-6}$	$6{\cdot}689\times10^{-6}$	329	5·04	7·24	167 967	925 416
HEX10/18		633	1319	$2{\cdot}607\times10^{-6}$	$5{\cdot}432\times10^{-6}$	1019	5·24	6·56	211 321	1 028 848
HEX10/19		720	1957	$2{\cdot}894\times10^{-6}$	$7{\cdot}866\times10^{-6}$	195	2·49	7·41	147 732	956 851
HEX10/20		586	890	$2{\cdot}526\times10^{-6}$	$3{\cdot}837\times10^{-6}$	466	3·83	4·37	329 015	1 125 997
HEX10/21	MG3	1360	5862	$5{\cdot}067\times10^{-6}$	$2{\cdot}184\times10^{-5}$	326	1·16	9·69	53 268	599 141
HEX10/22		925	3061	$3{\cdot}31\times10^{-6}$	$1{\cdot}095\times10^{-5}$	186	0·88	8·53	104 985	1 054 600
HEX10/23		858	1597	$3{\cdot}078\times10^{-6}$	$5{\cdot}729\times10^{-6}$	442	0·96	4·25	202 277	1 043 964
HEX10/24		1109	1923	$3{\cdot}813\times10^{-6}$	$6{\cdot}611\times10^{-6}$	59	1·04	4·51	180 891	917 581
HEX10/25		968	1235	$3{\cdot}451\times10^{-6}$	$4{\cdot}402\times10^{-6}$	197	1·75	4·23	274 489	938 219
HEX10/26		875	2103	$3{\cdot}341\times10^{-6}$	$8{\cdot}03\times10^{-6}$	97	2·01	7·17	148 808	935 365
HEX10/27		916	4522	$3{\cdot}558\times10^{-6}$	$1{\cdot}757\times10^{-5}$	70	2·14	15·26	65 670	878 595
HEX10/28	MG2C	855	1497	$3{\cdot}025\times10^{-6}$	$5{\cdot}296\times10^{-6}$	1948	3·15	7·27	230 371	1 207 973
HEX10/29		949	1645	$3{\cdot}325\times10^{-6}$	$5{\cdot}763\times10^{-6}$	177	3·59	7·18	210 183	1 073 042
HEX10/30		1463	2466	$5{\cdot}084\times10^{-6}$	$8{\cdot}57\times10^{-6}$	238	5·00	7·86	128 634	693 383
HEX10/31		1192	5859	$4{\cdot}141\times10^{-6}$	$2{\cdot}035\times10^{-5}$	394	5·88	15·84	53 722	658 683
HEX10/32	MG2B	1128	6248	$4{\cdot}025\times10^{-6}$	$2{\cdot}229\times10^{-5}$	50	6·61	16·91	48 638	636 939
HEX10/33		952	1825	$3{\cdot}309\times10^{-6}$	$6{\cdot}343\times10^{-6}$	176	4·23	6·19	187 919	879 829
HEX10/34		880	1042	$2{\cdot}962\times10^{-6}$	$3{\cdot}507\times10^{-6}$	211	3·63	4·99	343 098	1 165 187
HEX10/35		794	1044	$2{\cdot}628\times10^{-6}$	$3{\cdot}455\times10^{-6}$	2626	4·11	5·52	343 729	1 280 245
HEX10/36		944	1645	$3{\cdot}216\times10^{-6}$	$5{\cdot}605\times10^{-6}$	1275	3·56	6·67	208 158	991 563
HEX10/37		837	1576	$2{\cdot}705\times10^{-6}$	$5{\cdot}093\times10^{-6}$	303	4·08	6·52	232 329	1 089 656
HEX10/38	MG2A	505	3292	$1{\cdot}641\times10^{-6}$	$1{\cdot}07\times10^{-5}$	177	2·88	24·51	99 189	1 888 237
HEX10/39		542	2926	$1{\cdot}803\times10^{-6}$	$9{\cdot}734\times10^{-6}$	7983	2·40	17·90	109 788	1 679 329
HEX10/40		440	1210	$1{\cdot}437\times10^{-6}$	$3{\cdot}951\times10^{-6}$	564	2·31	9·53	298 782	2 156 700
HEX10/41	MG1	908	775	$3{\cdot}102\times10^{-6}$	$2{\cdot}648\times10^{-6}$	242	1·26	3·39	445 553	1 295 257
HEX10/42		944	963	$3{\cdot}102\times10^{-6}$	$3{\cdot}164\times10^{-6}$	108	1·55	3·80	374 820	1 232 203
HEX10/43		1233	1494	$4{\cdot}136\times10^{-6}$	$5{\cdot}012\times10^{-6}$	170	1·43	4·89	234 724	971 009
HEX10/44		996	830	$3{\cdot}223\times10^{-6}$	$2{\cdot}686\times10^{-6}$	293	1·56	4·14	450 410	1 373 250
HEX10/45		780	585	$2{\cdot}525\times10^{-6}$	$1{\cdot}894\times10^{-6}$	1020	1·39	3·35	630 345	1 687 809
HEX10/46		677	782	$2{\cdot}171\times10^{-6}$	$2{\cdot}508\times10^{-6}$	270	1·74	4·71	483 471	1 792 175
HEX10/47		695	593	$2{\cdot}199\times10^{-6}$	$1{\cdot}876\times10^{-6}$	250	0·91	2·71	638 450	1 755 737
HEX10/48		786	612	$2{\cdot}459\times10^{-6}$	$1{\cdot}915\times10^{-6}$	507	1·02	2·69	624 292	1 606 220
HEX10/49		638	577	$2{\cdot}115\times10^{-6}$	$1{\cdot}913\times10^{-6}$	813	1·47	3·64	641 733	1 945 900
HEX10/50	MG0	504	938	$1{\cdot}709\times10^{-6}$	$3{\cdot}18\times10^{-6}$	621	4·41	7·68	406 883	2 137 609
HEX10/51		837	911	$2{\cdot}614\times10^{-6}$	$2{\cdot}845\times10^{-6}$	1401	5·09	4·66	441 686	1 404 483

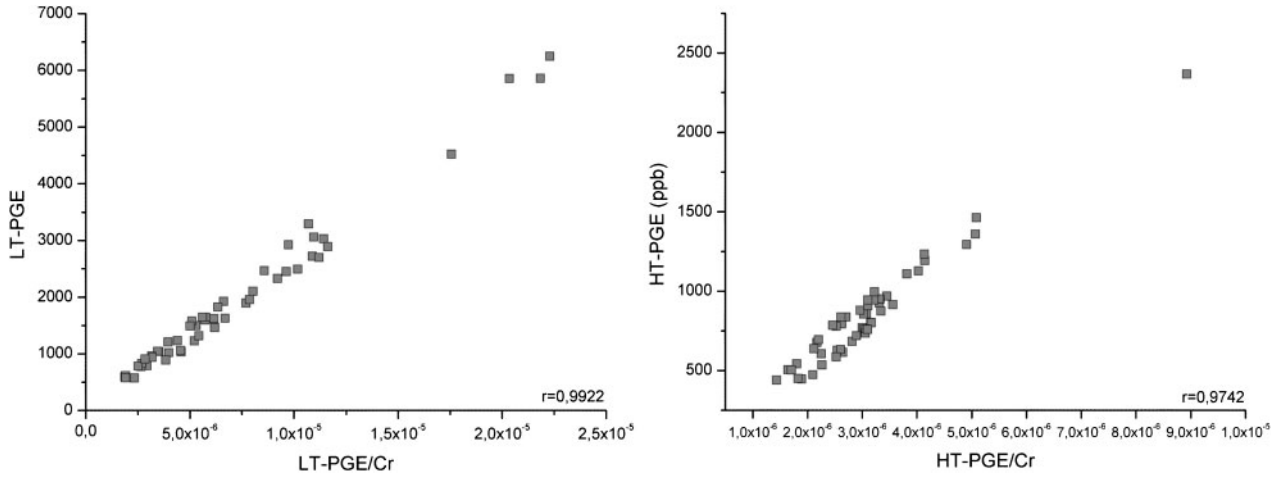

16 Correlation between the Cr_2O_3 content and the HT-PGE and the LT-PGE

that magma addition of primitive nature is most likely at the bottom of MG4A.

Many workers, e.g. Harmer and Sharpe,[20] Davies and Tredoux[12] and Barnes and Maier,[2] have identified two different magma types which were probably responsible for the formation of the LZ and CZ of the Bushveld complex: a high-Mg basalt (B1) and a tholeiite (B2), the first one being the parental magma for the LZ and the LCZ. A mixture of B2 magma with a residual phase of B1 yielded the formation of the UCZ. However, the PGE patterns of the MG chromitites show the same trends, which indicate the same style of mineralisation. It is a strong indication that the PGE, whether associated with the LCZ or UCZ, were derived from the same magma. Because the UG2 show a very similar PGE pattern as the MG chromitite layers, the PGE in the UG2 probably were also derived from the same parental melt. This is of cause contradictory to the thesis of Harmer and Sharpe,[20] Davies and Tredoux[12] and Barnes and Maier[2] described before, but with their model of chromite formation, Kinnaird *et al.*[25] give a plausible explanation for the contradiction. With each magma introduction into the chamber, the fountain incorporated a component of melted roof. The contamination immediately causes precipitation of chromite leading to the formation of a chromitite layer. The remaining magma within the chamber is thus a mixture of intruded, primitive magma and partial roof rock melt. We suggest that, at the stage of the formation of the UCZ, the magma mixture in the chamber was comparable with the proposed B2 magma of Harmer and Sharpe.[20] Thus, not two different magma types caused

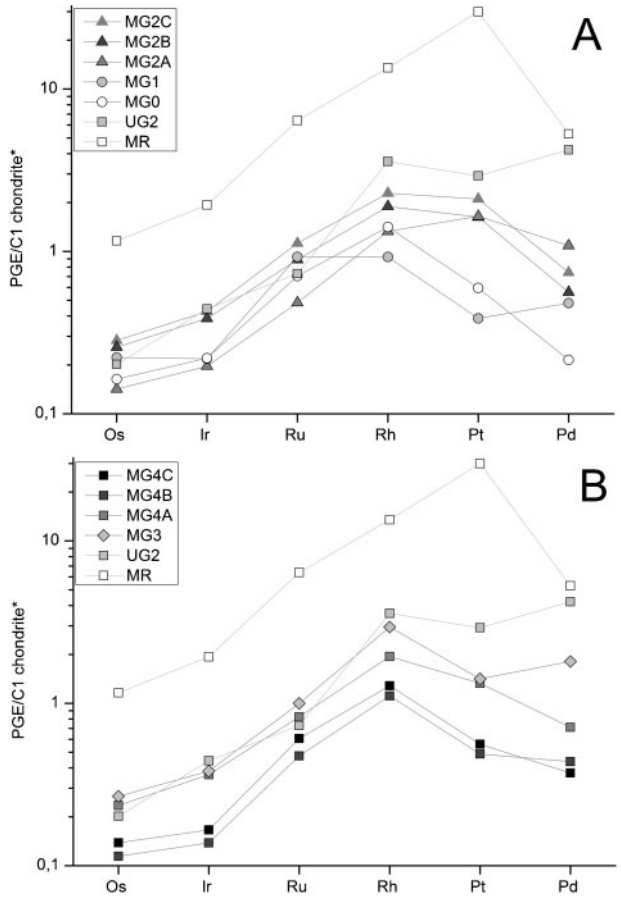

17 Cl normalised PGE patterns of the chromitite layers of the Middle Group. (A) Chromitite layers of the LCZ; (B) Chromitite layers of the UCZ. *Cl normalising values from Lodders.[29] PGE data shown are averages of samples taken from each layer. Merensky Reef values are averages form Merensky Reef chromitites and UG2 data are from the eastern limb only (MR and UG2 data from Barnes and Maier[2])

Table 9 Averaged whole-rock PGE data Cl normalized after Lodders[29]

	Os/Cl	Ir/Cl	Ru/Cl	Rh/Cl	Pt/Cl	Pd/Cl
MG4C	0·139	0·166	0·606	1·284	0·559	0·372
MG4B	0·114	0·138	0·474	1·110	0·487	0·437
MG4A	0·235	0·364	0·825	1·941	1·330	0·712
MG3	0·267	0·383	1·000	2·952	1·415	1·809
MG2C	0·283	0·427	1·122	2·282	2·101	0·741
MG2B	0·257	0·386	0·890	1·891	1·627	0·561
MG2A	0·142	0·196	0·483	1·329	1·644	1·085
MG1	0·222	0·218	0·925	0·925	0·387	0·480
MG0	0·164	0·220	0·704	1·415	0·596	0·215
UG2	0·202	0·443	0·730	3·582	2·920	4·218
MR	1·160	1·932	6·393	13·496	29·954	5·297

the formation of the CZ, but a mixture of primitive melt and roof rock melt. The PGE load would also derive from the primitive magma only, which perfectly explains the very similar appearance of the PGE patterns of the MG chromitites.

As the chromitite layers are enriched in PGE relative to their silicate host rocks (Kottke-Levin *et al.*,[26] in prep.),[28] some kind of entrapment during chromitite formation must have led to these high PGE abundances. The very low S concentrations in the MG layers and the lack of correlation between Cu and Pt/Pd makes it necessary to think about PGE concentration models beyond the *R*-factor and sulphide control. For example, Naldrett *et al.*[36] observed a decreasing Cu/Pd ratio across the pre-Merensky cyclic unit of the Eastern Platinum mine, western Bushveld complex, which is referred to progressive cannibalisation of earlier sulphides by removing the FeS component and thus causing the enrichment of Ni, Cu and PGE in the remaining sulphide. This could not be proved for the sample interval during this study, where the Cu/Pd ratio strongly varies on average between 200 and 7000 throughout the stratigraphy and no trend could be detected

With respect to low Pd and Au contents obtained from the PGE patterns of the MG chromitites, the loss of S is rather due to secondary alteration processes[3] than to the Fe loss of sulphides during cooling.

Although high *R* factors seem to be a plausible explanation for the enrichment of PGE in sulphides, approximately a sixth of the PGM observed contain As, Te and Bi and thus another enrichment process should be considered: the authors of this article give preference to the cluster theory of Tredoux *et al.*[50] They do not neglect the chalcophile character of the PGE, but restrain the applicability of conventional sulphide models for especially the HT-PGE, as their behaviour may be influenced by temperature. According to this model, the PGE would have been transported by the melt as micro- or nano-xenocrysts or clusters of about 100–1000 atoms stabilised by surface adsorption of chalcogenides (S, As and Te), indicating that they (esp. the HT-PGE) may never have been molten during partial melting processes in the mantle. This would explain the PGE enrichment in the cumulate rocks, i.e. chromitite layers, of the RLS when compared to the rocks being thought to represent their parent liquids.[8]

The cluster model also envisages the trapping of PGE-bearing clusters as micro-inclusions in cumulus-phases that also could have been acted as nucleation seeds. As we found many laurite inclusions rarely, exceeding grain sizes of 6 μm on average, within chromite grains of the MG chromitite layers it is possible that they represent such micro-inclusions. Although there is no connection between the Cr and the PGE contents in the MG chromitite layers, the whole-rock $Cr/(Cr+Fe^{3+})$ versus Pt/Ir plot (Fig. 15) suggests some chromitite control based on geochemistry influencing the fractionation of the PGE. The enrichment of LT-PGE relative to the HT-PGE in the stratigraphic column of the MG indicates that the PGE were differentiated with height, obviously connecting higher LT-PGE concentrations to evolved liquids and probably lower temperatures. The fractionation of the PGE is not yet fully understood and still debated, as redistribution of the original PGE content during postcumulus processes may have occurred,[18,51] which probably is reflected by the low Pd content in the CI normalised patterns.

In our opinion, an enrichment mechanism working with mechanical concentration, such as the cluster model, seems to offer a much more reasonable explanation for the behaviour of PGE than the 'standard' sulphide partitioning theory, given that the S content of the rocks we studied is very low. The stability of the clusters is likely to be promoted by a low fS_2.[12] Furthermore, the link between high chromite contents and elevated concentrations of PGE cannot be verified for all the MG chromitite layers. Thus it seems most likely that the cluster model, together with temperature control, determined the PGE concentrations and fractionation within the MG chromitite layers.

Acknowledgements

The authors would like to thank Xstrata Alloys for providing the sample material and granting permission to publish the results. This research is kindly funded by the University of the Free State, Bloemfontein, South Africa and Xstrata Alloys. Further expressions of thanks go to the two anonymous reviewers whose helpful comments and suggestions helped to improve the paper.

References

1. C. R. Anhaeusser: 'Ultramafic and mafic intrusions of the Kaapvaal craton', in 'Geology of South Africa', (ed. M. R. Johnson *et al.*), 95–134; 2006, Pretoria, Geological Society of South Africa, Johannesburg/Council for Geoscience.
2. S.-J. Barnes and W. D. Maier: 'Platinum-group element distributions in the Rustenburg Layered Suite of the Bushveld complex, South Africa', in 'The geology, geochemistry, mineralogy and mineral beneficiation of platinum-group elements', (ed. L. J. Cabri), Special Volume 54, 431–458; 2002, Montreal, Canadian Institute of Mining, Metallurgy and Petroleum.
3. P. B. Barton, Jr: *Sulfide petrol.. Miner. Soc. Amer. Spec. Pap.*, 1970, **3**, 187–98.
4. R. G. Cawthorn: 'The platinum and palladium resources of the Bushveld Complex', *S. Afr. J. Sci.*, 1999, **95**, 481–489.
5. R. G. Cawthorn: 'Platinum-group element mineralization in the Bushveld Complex—a critical reassessment of geochemical models', *S. Afr. J. Geol.*, 1999, **102**, 268–81.
6. R. G. Cawthorn and F. Walraven: 'Emplacement and crystallization time for the Bushveld Complex', *J. Petrol.*, 1998, **39**, 1669–1687.
7. R. G. Cawthorn, R. K. W. Merkle and M. J. Viljoen: 'Platinum-group element deposits in the Bushveld complex, South Africa', in 'The geology, geochemistry, mineralogy and mineral benefication of platinum-group elements', (ed. L. J. Cabri), Special Volume 54, 389–429; 2002, Montreal, Canadian Institute of Mining, Metallurgy and Petroleum.
8. R. G. Cawthorn, C. A. Lee, R. P. Schouwstra and P. Mellowship: 'Relationship between PGE and PGM in the Bushveld complex', *Can. Miner.*, 2002, **40**, 311–328.
9. R. G. Cawthorn, H. V. Eales, F. Walraven, R. Uken and M. K. Watkeys: 'The Bushveld Complex', in 'Geology of South Africa', (ed. M. R. Johnson *et al.*), 261–281; 2006, Pretoria, Geological Society of South Africa, Johannesburg/Council for Geoscience.
10. F. J. Coertze, A. J. Burger, F. Walraven, A. G. Marlow and D. R. Maccaskie: 'Field relations and age determinations in the Bushveld Complex', *Trans. Geol. Soc. S. Afr.*, 1987, **81**, (1), 1–11.
11. S. A. S. Dare, J. A. Pearce, I. McDonald and M. T. Styles: 'Tectonic discrimination of peridotites using fO_2–Cr# and

Ga–Ti–FeIII systematic in chrome–spinel', *Chem. Geol.*, 2009, **261**, 199–216.
12. G. Davies and M. Tredoux: 'The platinum-group element and gold contents of the marginal rocks and sills of the Bushveld complex', *Econ. Geol.*, 1985, **80**, 838–848.
13. S. A. de Waal, W. D. Maier, R. A. Armstrong and C. D. K. Gauert: 'Parental magma and emplacement of the stratiform Uitkomst Complex, South Africa', *Can. Miner.*, 2001, **2**, 557–571.
14. H. V. Eales: 'Implications of the chromium budget of the western limb of the Bushveld complex', *S. Afr. J. Geol.*, 2000, **103**, (2), 141–150.
15. H. V. Eales: 'A first introduction to the geology of the Bushveld Complex and those aspects of South African geology that relate to it', Popular Geoscience Series, Vol. 2, 84; 2001, Pretoria, The Council for Geoscience.
16. H. V. Eales and R. G. Cawthorn: 'The Bushveld Complex', in 'Layered Intrusions', (ed. R. G. Cawthorn), 181–230; 1996, Amsterdam, Elsevier.
17. H.-F. Eckey, R. Kosfeld and M. Türck: 'Deskriptive Statistik: Grundlagen – Methoden – Beispiele', 5th, revised edn, 283; 2008, Wiesbaden, Gabler.
18. S. B. Gain: 'The geological setting of the platiniferous UG-2 chromitite layer on the farm Maandagshoek, eastern Bushveld complex', *Econ. Geol.*, 1985, **80**, 925–943.
19. D. Gould, P. A. Rathbone, G. S. Kimbell, A. J. Burley, R. J. Peart, M. E. Parker and S. F. Pease: 'The geology of the Molopo Farms Complex, southern Botswana', *Bull. Geol. Surv. Botswana*, 1987, **21**, 178.
20. R. E. Harmer and M. R. Sharpe: 'Field relations and strontium isotope systematic of the marginal rocks of the eastern Bushveld complex', Research Report 50, Inst. Geol. Res. Univ., Pretoria, South Africa, 1984.
21. C. J. Hatton and J. K. Schweitzer: 'Evidence for synchronous extrusive and intrusive Bushveld magmatism', *J. S. Afr. Earth Sci.*, 1995, **21**, 579–594.
22. R. Hill and P. Roeder: 'The crystallization of spinel from basaltic liquid as a function of oxygen fugacity', *J. Geol.*, 1974, **82**, 709–729.
23. L. J. Hulbert and G. von Gruenewaldt: 'Textural and compositional features of chromite in the lower and Critical Zones of the Bushveld Complex South of Potgietersrus', *Econ. Geol.*, 1985, **80**, 872–895.
24. T. N. Irvine: 'Crystallization sequences in the Muskox intrusion and other layered intrusions-II. Origin of chromitite layers and similar deposits of other magmatic ores', *Geochim. cosmochim. Acta*, 1975, **39**, 991–1020.
25. J. A. Kinnaird, F. J. Kruger, P. A. M. Nex and R. G. Cawthorn: 'Chromitite formation—a key to understanding processes of platinum enrichment', *Trans. Inst. Min. Metall.* (*Sect. B: Appl. Earthsci.*), 2002, **111**, B23–B35.
26. J. Kottke-Levin, M. Tredoux and P.-J. Grabe: 'An investigation of the geochemistry of the Middle Group of the eastern Bushveld complex, South Africa. Part II: the silicate cumulates', in prep.
27. F. J. Kruger: 'Filling the Bushveld complex magma chamber: lateral expansion, roof and floor interaction, magmatic unconformities, and the formation of giant chromitite, PGE and Ti-V-magnetite deposits', *Miner. Depos.*, 2005, **40**, 451–472.
28. C. A. Lee and S. J. Parry: 'Platinum-group element geochemistry of the Lower and Middle Group chromitites of the Eastern Bushveld Complex', *Econ. Geol.*, 1988, **83**, 1127–1139.
29. K. Lodders: 'Solar system abundances and condensation temperatures of the elements', *Astrophys. J.*, 2003, **591**, 1220–1247.
30. W. D. Maier and S.-J. Barnes: 'Concentrations of rare earth elements in silicate rocks of the Lower, Critical and Main Zones of the Bushveld Complex', *Chem. Geol.*, 1998, **150**, 85–103.
31. R. K. W. Merkle: 'Platinum-group minerals in the middle group of chromitite layers at Marikana, western Bushveld Complex: indications for collection mechanism and postmagmatic modification', *Can. J. Earth Sci.*, 1992, **29**, 209–221.
32. S. K. Mondal and E. A. Mathez: 'Origin of the UG2 chromitite layer, Bushveld Complex', *J. Petrol.*, 2007, **48**, (3), 495–510.
33. B. W. and I. H. Campbell: 'The effects of temperature, oxygen fugacity and melt composition on the behaviour of chromium in basic and ultrabasic melts', *Geochim. Cosmochim. Acta*, 1986, **50**, 1871–1887.
34. A. J. Naldrett and J. Lehmann: 'Spinel non-stoichiometry as the explanation for Ni-, Cu- and PGE-enriched sulphides in chromitites', in 'Geo-platinum '87', (ed. H. M. Prichard *et al.*); 1987, London, Elsevier Science publishing Ltd.
35. A. J. Naldrett and G. von Gruenewaldt: 'Association of platinum-group elements with chromite in layered intrusions and ophiolite complexes', *Econ. Geol.*, 1989, **84**, 180–187.
36. A. J. Naldrett, A. Wilson, J. Kinnaird and G. Chunnett: 'PGE tenor and metal ratios within and below the Merensky Reef, Bushveld Complex: implications for its genesis', *J. Petrol.*, 2009, **50**, (4), 625–659.
37. A. D. Pactunk and L. J. Cabri: 'A proton- and electron-microprobe study of gallium, nickel and zinc distribution in chromian spinel', *Lithos*, 1995, **35**, 261–282.
38. A. Rice and G. von Gruenewaldt: 'Shear aggregation (convective scavenging) and cascade enrichment of PGEs and chromite', *Miner. Petrol.*, 1995, **54**, 105–117.
39. L. W. Schürmann, P.-J. Gräbe and C. J. Steenkamp: 'Chromium', in 'The mineral resources of South Africa, Handbook 16', (ed. M. G. C. Wilson and C. R. Anhaeusser); 90–105; 1998, Pretoria, Council for Geoscience.
40. R. N. Scoon and B. Teigler: 'Platinum-group element mineralization in the critical zone of the western Bushveld Complex; I, Sulfide poor-chromitites below the UG2', *Econ. Geol.*, 1994, **89**, 1094–1121.
41. R. N. Scoon and W. J. de Klerk: 'The relationship of olivine cumulates and mineralization to cyclic units in part of the upper Critical Zone of the western Bushveld complex', *Can. Miner.*, 1987, **25**, 51–77.
42. R. Schoenberg, F. J. Kruger, T. F. Nägler, T. Meisel and J. D. Kramers: 'PGE enrichment in chromitite layers and the Merensky Reef of the western Bushveld Complex; a Re–Os and Rb–Sr isotope study', *Earth Planet. Sci. Lett.*, 1999, **172**, 49–64.
43. M. R. Sharpe: 'Noble Metals in the Marginal Rocks of the Bushveld Complex', *Econ. Geol.*, 1982, **77**, 1286–1295.
44. C. Spandler, J. Mavrogenes and R. Arculus: 'Origin of chromitites in layered intrusions: evidence from chromite-hosted melt inclusions from the Stillwater Complex', *Geology*, 2005, **33**, 893–896.
45. C. Spandler, H. St. C. O'Neill and V. S. Kamenetsy: 'Survival times of anomalous melt inclusions from element diffusion in olivine and chromite', *Nature*, 2007, **447**, 303–306.
46. M. R. Sharpe and L. J. Hulbert: 'Ultramafic sills beneath the eastern Bushveld complex: mobilized suspensions of early Lower Zone cumulates in a parental magma with boninitic affinities', *Econ. Geol.*, 1985, **80**, 849–871.
47. H.-G. Stosch: 'Geochemie der Seltenen Erden', Lecture script of the Department of Mineralogy and Petrology at the University of Cologne, Germany, Version 3.1, 2008, 209.
48. B. Teigler: 'Platinum-group element distribution in the lower and middle group chromitites in the western Bushveld Complex', *Miner. Petrol.*, 1990, **42**, 165–179.
49. B. Teigler and H. V. Eales: 'Correlation between chromite composition and PGE mineralization in the Critical Zone of the western Bushveld Complex', *Miner. Depos.*, 1993, **28**, 291–302.
50. M. Tredoux, N. M. Lindsay, G. Davies and I. McDonald: 'The fractionation of platinum-group elements in magmatic systems, with the suggestion of a novel causal mechanism', *S. Afri. J. Geol.*, 1995, **98**, 157–167.
51. G. von Gruenewaldt, C. J. Hatton, R. K. W. Merkle and S. B. Gain: 'Platinum-group element – chromitite associations in the Bushveld Complex', *Econ. Geol.*, 1986, **81**, 1067–1079.
52. F. L. Walraven: 'Notes on the age and genetic relationships of the Makhutso Granite, Bushveld Complex, South Africa', *Chem. Geol.*, 1988, **72**, 17–28.
53. F. Walraven, E. A. Retief, A. J. Burger, D. J. V. de Swanepoel: 'Implications of new U-Pb zircon age dating on the Nebo Granite of the Bushveld Complex', *S. Afr. J. Geol.*, 1987, **90**, 344–351.
54. F. Walraven, R. A. Armstrong and F. J. Kruger: 'A chromostratigraphic framework for the north-central Kaapvaal craton, the Bushveld complex and Vredefort structure', *Tectonophysics*, 1990, **171**, 23–48.
55. F. Walraven and E. Hattingh: 'Geochronology of the Nebo Granite, Bushveld Complex', *S. Afr. J. Geol.*, 1993, **96**, 31–41.
56. J. A. White: 'The Potgietersrus project: geology and exploration history', Proc. 15th CMMI Cong., Johannesburg, South Africa, 1994, S.Afr. Inst. Min. Metall., 173–182.

57. A. H. Wilson, A. J. Naldrett and M. Tredoux: 'Distribution and controls of platinum group element and base metal mineralization in the Darwendale subchamber of the Great Dyke, Zimbabwe', *Geology*, 1989, **17**, 649–652.
58. http://www.em.csiro.au/terrain_studies/aboutus/people/stephen_barnes/spincalc_dec04.xls
59. http://www.environmentalchemistry.com/yogi/periodic/ionicradius.html